Contributions to the reliability of numerical simulations in fluid mechanics. Application to the flow simulation of thermodynamically complex gases

Pietro Marco Congedo

UNIVERSITY OF BORDEAUX 1

HDR

Defended by

Pietro Marco CONGEDO

Contributions to the reliability of numerical simulations in fluid mechanics. Application to the flow simulation of thermodynamically complex gases.

Defense on December 6, 2013

Jury :

President :	Christophe CORRE	-	Institut National Polytechnique de Grenoble
Reviewers :	Charbel FARHAT	-	Stanford University
	Pierre SAGAUT	-	Université Pierre et Marie Curie - Paris 6
	Carlo POLONI	-	University of Trieste
Examinators :	Bernhard MULLER	-	Norwegian University of Science and Technology
	Mejdi AZAIEZ	-	Institut Polytechnique de Bordeaux
	Rémi ABGRALL	-	INRIA and Institut Polytechnique de Bordeaux

Contributions to the reliability of numerical simulations in fluid mechanics. Application to the flow simulation of thermodynamically complex gases.

Abstract: At the interface of physics, mathematics, and computer science, Uncertainty Quantification (UQ) aims at developing a more rigorous framework and more reliable methods to characterize the impact of uncertainties on the prediction of Quantities Of Interest (QOI). Despite significant improvements done in the last years in UQ methods for Fluid Mechanics, there is nonetheless a long way to go before there can be talk of an accurate prediction when considering all the numerous sources of uncertainties of the physical problem (boundary conditions, physical models, geometric tolerances, etc), in particular for shock-dominated problems.

This manuscript illustrates my main contributions for improving the reliability of the numerical simulation in Fluid Mechanics: i) the development of efficient and flexible schemes for solving at low-cost stochastic partial differential equations for compressible flows, ii) various works concerning variance-based and high-order analysis, iii) the design of some low-cost techniques for the optimization under uncertainty. The application of interest is the robust design of turbines for Organic Rankine Cycles (ORC). Some contributions to the numerical flow prediction of the thermodynamically complex gases involved in ORC will be presented.

This manuscript is divided in two parts. In the first part, some intrusive algorithms are introduced that feature an innovative formulation allowing the treatment of discontinuities propagating in the coupled physical/stochastic space for shock-dominated compressible flows. Then, variance and higher-order based decompositions are described, that could alleviate problems with large number of uncertainties by performing a dimension reduction with an improved control. Some ANOVA-based analyses are also applied to several flows displaying various types of modeling uncertainties, be it cavitation, thermodynamic or turbulence modeling. Two algorithms for handling stochastic inverse problems are then introduced for improving input uncertainty characterization by directly using experimental data. Finally, robust-optimization algorithms are introduced, that are efficient when dealing with a large number of uncertainties, relying on different formulations, *i.e.* with de-coupled/coupled approaches between the stochastic and the optimization solvers.

The second part is devoted to the study of dense gas flow in ORC-cycles, which represent a highly demanding field of application as far as flow simulation reliability is concerned. The numerical ingredients necessary for this kind of simulation are described. Then, some recent results are illustrated : i) high-fidelity turbine computations; ii) a feasibility study concerning the appearance and the occurrence of a Rarefaction Shock Wave, using experimental data and different operating conditions (in monophasic and two-phase flows); iii) a stochastic study concerning the thermodynamic model uncertainties.

This set of research works has produced several papers in international journals and peer-reviewed conferences. **Keywords:** Uncertainty Quantification, intrusive and non-intrusive methods, inverse problem, robust optimization, CFD, thermodynamics, dense-gas, BZT.

Contents

Chapter 1

Context and Introduction

Contents

1.1 Reliable numerical prediction in Fluid Mechanics

1.1.1 Some basic notions

Science aims at providing a complete and accurate description of how the real world works. In particular, the so-called Computational Science (CS) relies on the three Pillars of Knowledge (see Fig. 1.1), *i.e.* Computation, Experiment and Theory, for making available reliable and predictive tools. These three aspects should be considered at the same time, providing complementary tools for a complete understanding of a given phenomenon. Over the years, experiments represented a unique source of knowledge for computations and theory validation. In more recent years, computations are more and more used as a numerical low-cost experiment. Moreover, computations can also provide some useful indication to set-up experimental conditions via numerical simulation and statistical characterization. Computational Science aims at developing a reliable and predictive numerical tool relying on and exploiting the interaction between the three aforementioned Pillars. The idea is not only to reproduce a given phenomenon but also to predict the reality, *i.e.* using the numerical tools in conditions for which the tool has not been specifically validated nor tested.

An intrinsic limit of this process is given by the nature of observations, that are aleatory, since they are obtained through some interfaces (our senses, measurements tools, etc). As a consequence, our capacity (or inability) to predict or to control any type of phenomenon is conditioned by this original "sin" : it is not directly our mind that looks at the world, but this one is observed through some natural or artificial layers which alter the reality. In this sense, we are as prisoners in a Cave [1], and we need to break the chains for capturing the real physics.

The worldwide use of simulations and models in very different fields is motivated by the need to predict reality with a good accuracy and for a low computational cost (with respect to the experiment

[1] The Republic, *Plato*.

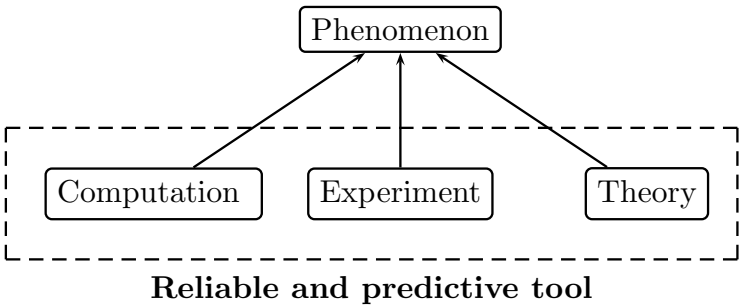

Figure 1.1: Three pillars of Knowledge.

for example). Since these models rely on some approximation of the observations, it is of greatest importance to assess the fidelity of these modeling and simulation aspects.

In fact, observations are affected by multiple sources of error (see [Ebert 2013]). Let us list some of these errors:

- Biases in frequency or value
- Instrument error
- Random error or noise
- Reporting errors
- Subjective observations
- Representativeness error
- Precision and conversion error
- Analysis error
- ...

Since several techniques exist for selecting, filtering, verifying the experimental data in order to reduce the global level of uncertainty, not considering this information (*i.e.* the statistical variability) as a fundamental one for assessing the reliability of the numerical simulation can lead to erroneous estimation and predictions. In this case, the comparison of experimental data with a numerical solution does not provide useful information, thus yielding wrong conclusions and leading consequently to bad decisions in a design procedure. A key question is therefore : how experimental data can best be taken into account when performing a numerical simulation ?

Let us draw a very schematic view of input/output for a CFD (Computational fluid-dynamics) numerical code (Figure 1.2), since algorithms, methods and results discussed in this manuscript are focused on mathematical models that are represented by partial differential equations for Fluid Mechanics.

Obviously, experimental data are directly associated to the definition of boundary conditions, initial conditions and geometry for the numerical simulation. These data are naturally affected by some uncertainties. This kind of uncertainty is defined as *aleatory*, since this is the physical variability present in the system, due above all to the measurement errors. Even with very accurate measurements tools, this uncertainty can not be reduced, because it is intrinsically aleatory. Note that aleatory uncertainty is normally characterized using probabilistic approaches. On the contrary,

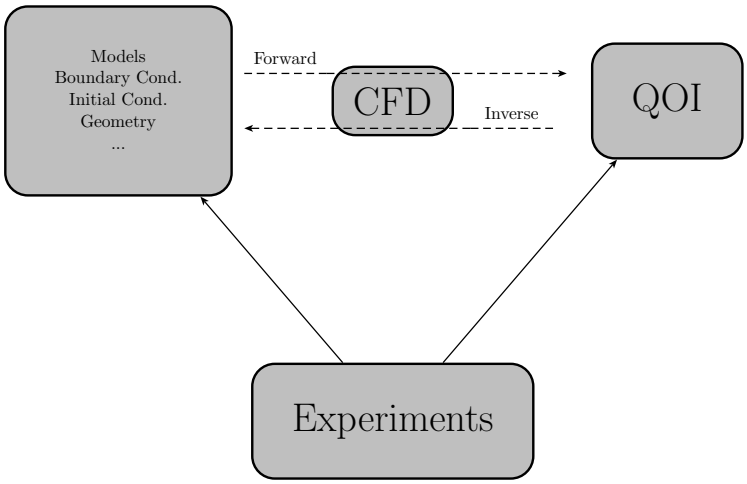

Figure 1.2: Flow chart of interaction between CFD and experiments. QOI stands for "Quantity Of Interest" that is the main physical quantity one wishes to estimate from the CFD computation.

models are usually calibrated using some experimental data, thus yielding some empirical model-parameters. Usually, these parameters are then tuned in order to generate a numerical solution closer to the experimental outputs. These uncertainties are defined as *epistemic*, since this is a potential deficiency that is due to a lack of knowledge (see [AIAA 1998]). More generally, they can be generated from assumptions introduced in the derivation of the mathematical model used or from simplifications related to the correlation or dependence between physical processes.

These sources of uncertainty should be considered in the numerical simulation for a reliable simulation. All these physics-driven uncertainties are not the only perturbation factors of the numerical simulation reliability. It is mandatory to consider also the error coming from the numerical solution of the system of equations. This leads directly to the distinction between error and uncertainty (see [Iaccarino 2008]). In this manuscript, the term *error* is associated to the translation of a mathematical formulation into a numerical algorithm (and a computational code). Typically, errors are also further classified as follows [Trucano 2006]

- implementation mistakes (bugs) or usage errors
- errors or bugs introduced by the coder in the preparation of the input/output for the numerical code.
- numerical errors resulting from computing the discretized solution of the mathematical model on a digital computer ((a) spatial and temporal discretization errors in the numerical solution of Partial Differential Equations (PDEs), and (b) iterative solution errors usually resulting from the selected solution approach for the set of nonlinear equations.)

Remark that the first and second sources refer to human errors.

Using the present definition of errors, the uncertainties are naturally associated to the choice of the physical models and to the specification of the input parameters required for performing the analysis, as already specified. When dealing with a numerical code, the term *Verification* [Trucano 2006] is used for the process of verifying that the numerical algorithms are correctly implemented in the computer code, of identifying errors in the software, of determining the correctness of the numerical accuracy of the solution, and so on. Thus, the *Verification* process is not associated to experimental data.

Let us now come back to the flow chart of Figure 1.2. Once defined the boundary/initial conditions and the physical models used in the system of equations, the output, *i.e.* the Quantity of Interest (QOI)), of the numerical simulation should be compared to the reality. The term *Validation* is used for the process of assessing whether the mathematical/physical formulation is appropriate for the flow physics to analyze. This is accomplished by means of a comparison with experimental data. For a very comprehensive survey of verification and validation processes, please refer to [Oberkampf 2010].

Validation cannot be performed in a robust way without explicitly accounting for the uncertainties present in both the measurements and the computations. This is why Uncertainty Quantification (UQ) plays a fundamental role in assessing the reliability of the numerical simulation. The introduction of uncertainty in numerical simulations does not alter this process but introduces considerable difficulties in each phase. At the interface of physics, mathematics, and computer science, Uncertainty Quantification (UQ) aims at developing a more rigorous framework and more reliable methods to characterize the impact of uncertainties on the prediction of Quantities Of Interest (QOI).

This manuscript is essentially devoted to two types of analysis for what is a very complex problem in terms of methods, algorithms, computational cost, and post-processing management. Most of the studies presented are focused on uncertainty propagation problems, designed in Figure 1.2 as *Forward* problems. This means that uncertainties are taken into account in the following way: i) first, input uncertainties on the model, boundary/initial conditions and so on (in terms of intervals and probability density functions (pdf)) are defined, ii) then some stochastic methods are used for taking into account these uncertainties in the numerical simulation, iii) a numerical solution (including the computation of a QOI) is generated with an associated numerical error bar, iv) numerical and experimental error bars are compared.

The second kind of problem treated in this manuscript is called *Inverse* problem. In this case, the experimental data (with the experimental measurement errors) available for the output of the numerical simulation are used for building the statistical properties of some inputs of the numerical code. Let us imagine a space vehicle undergoing atmospheric re-entry (this complex case is treated in the second part of this manuscript). In such a case, the available experimental data, *pressure and heat flux at the stagnation point of the vehicle*, correspond to the output of the numerical simulation. In this kind of problem, the aim is to compute the pdf of the free-stream conditions, *i.e.* the input of the numerical simulation, by using directly the numerical code and the experimental data known for the output of the simulation (the stagnation point measurements).

The question of computing confidence level in numerical simulation is especially complex in the context of flow simulation. Measurements in fluid mechanics devices are delicate and expensive due mainly to unsteadiness, turbulence, multiphase nature of the flow, and so on. This makes much more complicated the measures, thus increasing the amount of uncertainties associated. As a consequence, in this field, it is even more important to estimate the variability of the numerical solution by taking into account possibly scarce and inaccurate experimental data. Moreover, numerical simulation for compressible flows is strongly affected by some peculiar physical phenomena, such as compressibility, discontinuities (compression shocks), turbulence, multi-scale phenomena, etc. These aspects make the numerical simulation even more complex to solve and also much more expensive, thus complicating the fact to include uncertainties in the numerical loop.

In order to clarify how complexity can rapidly increase when designing a device from flow simulations, we next detail reliability issues for a particular application, the Organic Rankine cycle (ORC). In fact, dense gas flow in ORC-cycles represent a highly demanding field of application as far as flow simulation reliability is concerned.

1.1.2 Application of interest: ORC-based system

An Organic Rankine cycle (ORCs) is a closed power cycle composed of four basic components. Heat is supplied to a heater where the compressed liquid is converted into a superheated vapor at constant

pressure. The vapor is then expanded through a turbine stage to produce a work output. For an impulse turbine stage, the flow is expanded through a stator stage or through nozzles. Vapor leaving the turbine then enters the condenser where heat is removed until the vapor is condensed into the liquid state. Saturated liquid is then delivered to a pump, which raises the pressure of the liquid and is then delivered back to the heater from which point the cycle is then repeated. Thus, ORCs are similar to the large steam Rankine cycle but the main difference is that ORCs utilize heavy working fluids, *i.e.* organic compounds, which result in superior efficiency over steam Rankine cycle engines for heat source temperatures below around 900 K. ORCs typically require only a single-stage expander which consists of a single rotating component for the entire system in the turbine stage, making them much simpler than multi-stage expanders typical of the steam Rankine cycle.

Typically, the working fluids are of retrograde type. Therefore it is not necessary to use a reheat which greatly simplifies the cycle structure. Moreover the risk of blade erosion is avoided due to the absence of moisture in the vapor nozzle. ORCs are an appealing option for remote, low-power applications because of their mechanical simplicity. The point of interest in this particular application is that a dense gas flow in a turbine cascade is characterized by a significant uncertainty on the physical parameters and on the operating conditions at the turbine inlet. The ORCs are mainly used in biomass and geothermal applications - development in solar and heat recovery applications are also expected - where the **renewable heat sources** display a non-negligible level of variability. This is obviously a strong source of uncertainty.

One solution for optimizing the efficiency of ORC-based systems could be the use of BZT fluids. BZT fluids are dense gases, that are characterized by very specific thermodynamic properties. Dense gases are usually defined as single-phase vapors whose thermodynamic state is close to saturation conditions, at temperatures and pressures of the order of magnitude of the critical ones. At these conditions, real gas effects play a crucial role in the dynamic behavior of the fluid. The dynamics of dense gases is governed by a thermodynamic parameter known as the Fundamental Derivative of Gas-dynamics [Thompson 1971]:

$$\Gamma = 1 + \frac{\rho}{a}\left(\frac{\partial a}{\partial \rho}\right)_s \tag{1.1}$$

(with ρ the fluid density and a the sound speed), which represents a measure of the rate of change for the local speed of propagation of weak pressure disturbances. For perfect gases, $\Gamma = (\gamma + 1)/2$, where the specific heat ratio γ is always greater than 1 for thermodynamic stability reasons so that $\Gamma > 1$. This is also true for most of light fluids with simple molecules, as water vapor for instance. For more complex fluids, Γ may become lower than 1 in the dense gas region. In such conditions, Eq. (1.1) shows that $(\frac{\partial a}{\partial \rho})_s < 0$, *i.e.* the behavior of the speed of sound in the course of an isentropic transformation is reversed with respect to classical fluids : the speed of sound increases when the fluid is expanded and decreases when it is compressed. Most of the fluids exhibiting this reversed behavior are of the retrograde type, *i.e.* they display a negative slope of the liquid/vapor coexistence curve in the temperature-entropy plane $T - s$. This feature makes them particularly suitable as working fluids in low-temperature energy-conversion cycles, since they do not condense upon expansion and consequently no undesired liquid droplets are formed. Finally, a particular class of highly-complex heavy fluids may exhibit negative values of Γ in a subset of the dense gas region next to the saturation curve. Such fluids are usually referred-to as Bethe-Zel'dovich-Thompson fluids (BZT), from the researchers who first postulated their existence; the thermodynamic region characterized by negative values of Γ is called the inversion zone, and the $\Gamma = 0$ contour is said the transition curve. It has been theoretically shown that, for $\Gamma < 0$, compression waves are smoothed out. As an example, Fig. 1.3 illustrates the calculated negative-Γ thermodynamic region in the temperature-entropy thermodynamic plane for siloxane D6, a candidate BZT fluid selected for the first experiments in a shock-tube configuration [Colonna 2008a].

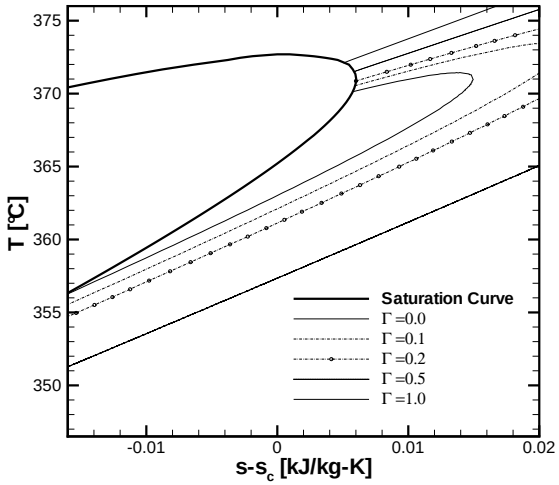

Figure 1.3: Close-up of the dense-gas region for a BZT fluid, namely D6, computed using the PRSV equation of state. Subscript c indicates critical point-properties.

Compression shocks within the inversion zone violate the entropy inequality, and are therefore inadmissible; conversely, rarefaction shocks are allowed (see for instance [Thompson 1971, Cramer 1992, Monaco 1997]). According to several thermodynamic models, a region of negative Γ exists for molecularly complex fluids such as heavy hydrocarbons, perfluorocarbons, and siloxanes [Colonna 2003]. The possibility of observing non-classical waves increases for substances possessing large specific heats and molecular weight. Precisely, it strongly depends on the ratio $c_{v\infty}(T_c)/R$, $c_{v\infty}(T_c)$ being the specific heat at constant volume in the dilute gas limit and at the critical temperature, and $R = R/M$ the gas constant (with R the universal constant of gases and M the gas molecular weight). The peculiar properties of BZT fluids can be exploited in energy conversion cycles to improve isentropic efficiency of turbines and compressors: theoretically, using a working fluid characterized by low values of Γ may allow operating turbomachinery blades at near-sonic tip speeds without any losses due to shock waves and to the related induced boundary-layer separation. This is in clear contrast to the classical behavior of regular gases (such as air, oxygen, nitrogen, water steam as well as *classical* organic fluids used in ORC turbines such as isopentane and toluene) which exhibit much lower critical Mach numbers (around 0.75 or even less); this behavior thereby significantly limits the flow-speed in the relative frame of reference and the amount of power that can be extracted from the potential thermodynamic energy in the flowing gas. Nonclassical gas dynamics effects could be exploited to considerably increase the efficiency of supersonic turbines for small-capacity Organic Rankine Cycle power systems [Brown 2000], whereby the detrimental effect of **compression shocks** in the flow passages can be largely reduced, or even suppressed, as non-classical compression fans are instead predicted [Monaco 1997, Colonna 2004].

The use of BZT working fluids at properly chosen conditions would be sufficient, by itself, to increase the turbine critical Mach number. This effect can be further improved with a specific **robust shape optimization** [Cinnella 2008b], allowing to use smaller rotation speed, with consequent technical simplifications and improved lifetime of the rotor and bearings, or, for a given rotation speed, to elaborate the available pressure ratio using a reduced number of stages. Up till now no experimental data are available for flows of heavy fluids in the dense gas region. Experiments are difficult because of high temperature and pressure conditions, and fluid decomposition or inflammability in presence of air.

Note that BZT fluids demand very accurate equations of state for describing the region close to the saturation curve, since a perfect gas equation of state can not capture the physics of these gases. Note also that the thermophysical properties of dense gases are themselves characterized by a strong uncertainty [Cinnella 2010, Cinnella 2011]: the experimentally measured values of the critical parameters and of the caloric properties are known with an uncertainty that can exceed 5%. The determination of critical-point data for dense gases is indeed delicate because such gases may decompose, totally or partly, at temperatures close to the critical one; in this case, critical point values just rely on estimates. A **large number of uncertain parameters** are therefore present in the analysis of an ORC-based system.

An attempt to experimentally prove for the first time the existence of non-classical gas dynamics is underway at the Delft University of Technology. A newly built shock tube [Colonna 2008a], called Flexible Asymmetric Shock Tube (FAST), will be used to generate a Rarefaction Shock Wave (RSW) in the dense vapor of a siloxane fluid at high reduced temperature and pressure. A major consideration emerged from these studies: if non-classical gas dynamics effects do exist, they are relatively weak, if compared, for instance, to compression shock waves, and can occur only if the experimental conditions are controlled within a relatively small range of pressures and temperatures, as illustrated in Fig. 1.3.

The accurate simulation of the RSW experiment can provide valuable insights both for defining the initial operating conditions of the experiment and for interpreting the expected results. Flow simulation can also be used to design ORC turbines exploiting non-classical effects. In any case, it is deemed crucial to be able to properly take into account the uncertainty introduced by the thermodynamic model in the first place but also by the measurement and setting of the initial condition (for the shock tube) or the inlet boundary condition (for the turbine). In this case, it is necessary to quantify the uncertainties associated with the numerical simulations of the TU Delft dense gas shock tube experiments. The considered sources of uncertainty are on the one hand the parameters of the fluid thermodynamic model and on the other hand the measurements performed by the control system of the FAST setup in charge of setting the operating conditions. Correctly assessing the level of accuracy needed to set the initial experimental conditions could help maximizing the probability of actually observing the expected non-classical RSW. This is a so-called (**inverse problem**), that will be presented and analyzed in the following. To address this problem, several approaches have been proposed. The maximum likelihood method provides the identification of probabilistic models of random coefficients based on the maximum likelihood principle [Desceliers 2006]. Another method based on Bayesian inference [Ma 2009b], where unknown parameters are considered as random variables, seeks the probabilistic distributions of the unknown. Other known approaches are the spectral stochastic method [Asokan 2004], the sparse grid collocation [Zabaras 2008] and a sensitivity derivative approach [Ngnepieba 2007]. These methods are applied in different domains, from civil engineering [Abusam 2009] to finance [Ait-Sahalia 2007] and water technology [Abusam 2003].

Finally, a reliable simulation of this kind of system demands the development of several methods/algorithms in UQ context: i) techniques for considering problems with a large number of uncertainties (thermodynamic model, inlet conditions, geometric tolerances, turbulence model, etc), ii) efficient stochastic methods for capturing shocks in the coupled physical/stochastic space (a correct simulation of the shock in the turbine is an essential element for correctly computing the efficiency and its variability), iii) low-cost strategies for optimizing the turbine geometry taking into account the great level of variability of the energy sources, iv) accurate methods for solving inverse problems starting from the experimental data. These items correspond to the main objectives of my research, as will be now presented in the next section.

1.2 Objective of my research

The main objectives of my research are focused on several topics that I presented in the previous section. In particular, concerning methods and numerical algorithms, I focused my attention on major issues for a reliable numerical simulation in compressible flows for realistic systems : stochastic methods for shock-dominated flows, problems with a large number of uncertainties, efficient algorithm for solving inverse problems, robust design optimization. Finally, the other part of my studies is focused on the physics of dense-gas flows and ORC systems for a reliable simulation of such systems.

1.2.1 Stochastic methods for shock-dominated compressible flows

The problem is to find an efficient representation of the stochastic solution, when the flow presents some discontinuities, thus producing a shock evolving in the coupled physical/stochastic space. Probabilistic uncertainty quantification (UQ) approaches represent the inputs as random variables and seek to construct a statistical characterization of few quantities of interest.

Let us first sketch some UQ techniques to fix ideas.

The most popular and known method for the uncertainty quantification (UQ) is the Monte Carlo. Its development led back to the research on the nuclear devices in the context of the Manhattan project and is due to Fermi, von Neumann and Ulam. This method is based on a stochastic procedure to represent realizations of the solution for which the statistic moments can be computed. Despite its solid mathematical framework it represents a very expensive approach for most practical application because it requires a great number of realizations. Several improved versions of the classical Monte Carlo method have been proposed in literature for increasing the convergence rate, see for instance the recent work presented in [Graham 2011], but they still remain unfeasible for complex problems when the evaluation of samples is expensive, as in most engineering problems.

Classically, among the UQ techniques, the polynomial chaos (PC) has shown its efficiency in the case of smooth responses (see [Le Maître 2010b]). Wan and Karniadakis have introduced an adaptive class of methods for solving the discontinuity issues by using local basis functions, the multi-element generalized Polynomial Chaos (ME-gPC) (see [Foo 2010]). This strategy deals with an adaptive decomposition of the domain on which local bases are employed. Long-time integration problems could be encountered [Wan 2006b], where this behavior is due to the modification in time of the statistic properties of the solution that induces an efficiency loss of the polynomial basis in time. Recently, Gerritsma [Gerritsma 2010] proposed a time-dependent generalized Polynomial Chaos scheme based on the research of a time varying optimal polynomial basis. Another class of method is based on the stochastic collocation (SC) approach [Babuška 2010]. This strategy is based on building interpolating polynomials, of the same dimensionality as the stochastic space, in order to approximate the solution. In order to reduce the computational cost for high-dimension problems, these methods are often coupled to sparse grids techniques. The sparse grid strategy has been proposed by Smolyak [Smolyak 1963b] allowing interpolation of the function in a reduced subset of points with respect to the full tensorization set. This strategy is a cure against the so-called curse of dimensionality [Bellman 1961] problem, i.e. the exponential growth of the number of points with respect to the stochastic dimensions [Ganapathysubramanian 2007, Griebel 2006]. In the work of Agarwall [Agarwal 2009], an adaptive stochastic collocation method, based on the recursive splitting of the domain, has been proposed. In this case the splitting of the domain and the adaptivity is applied directly to the sparse grid basis. A sparse grid collocation strategy, based on piecewise multilinear hierarchical basis functions, has been adopted by Ma and Zabaras [Ma 2009c] to recover the convergence loss by a global polynomial approximations in presence of discontinuities. Chantrasmi and Iaccarino in [Chantrasmi 2009] proposed a multi-dimensional approach based on Pade-Legengre approximation for CFD applications in presence of shock waves. A new iterative formulation to improve the convergence of standard stochastic collocation approach has been presented by Poëtte

and Lucor in [Poëtte 2012]. The author demonstrated the capability of the method to achieve a better convergence with no additional cost, *i.e.* the additional operation with respect to the standard spectral method are all performed in the post-processing phase. This method has been successfully applied to Euler system of equations in [Poëtte 2012, Lucor 2012]. More recently, in the context of the simplex approach [Witteveen 2010], Witteveen and Iaccarino introduced the concept of sub-cell resolution for problems in which the discontinuities in the random space are directly related to their physical counterparts [Witteveen 2013]. The presence of a sparsity character of the solution, *i.e.* only few coefficients in the PC basis are really non-null, has been employed by Doostan and Owhadi in [Doostan 2011] to obtain a non-adapted sampling method. A direct comparison between the iterative spectral approach, the sub-cell resolution technique within the simplex method and the adaptive important sampling for compressing sensing has been proposed for some test cases in [Lucor 2012].

In order to treat discontinuous response surfaces, [Le Maître 2004b, Le Maître 2004a] applied a multiresolution analysis to Galerkin projection schemes. The intrusive Galerkin approach may lead to an optimal representation of the solution, exhibiting an exponential convergence, if a proper basis is chosen. However the intrusive Galerkin approach results in a larger system of equations than in the deterministic case with, in addition, a different structure that requires a new class of solver and numerical code. Despite this issue, the intrusive Galerkin approach can be demonstrated to display substantial advantages with respect to non-intrusive approach, not only for idealized systems, but also for large-scale applications [Le Maître 2004b]. In this context, advancements have been achieved in the Galerkin intrusive scheme where the wavelets formulation has been used in order to modify the basis of approximation [Tryoen 2010]. It modifies the basis, by enriching the space with a hierarchical structure according to the regularity of the solution. However the Galerkin approach presented in [Tryoen 2010] remains very problem-dependent. In fact, using a Roe-type solver requires to know the eigenstructure of the Roe matrix explicitly; this can be very complex. Moreover, *ad hoc* entropy fix should be adopted, thus increasing the numerical cost associated to the representation of discontinuous solutions [Tryoen 2011]. This original approach has been further improved to obtain a more efficient scheme employing a multiresolution adaptive strategy [Tryoen 2012]. However, actually this approach is limited by the spatial and time discretization accuracy that could dominate the overall accuracy of the global scheme. In [Pettersson 2013], an intrusive formulation of the stochastic Euler equations based on Roe variables is presented. It is shown that the Roe variable formulation is robust for supersonic problems where the conservative variable formulation fails, but only for localized basis functions of the generalized chaos representation. For global Legendre polynomials, the discontinuities in stochastic space lead to oscillations and unphysical behavior of the solution and numerical instability. Wavelet functions are more robust for this aspect, and do not yield oscillations around discontinuities in stochastic space, but need very regular grids.

Efficient algorithms for stochastic compressible computational fluid-dynamics should display the following features :

- Handling of any kind of pdf (derived from experimental data in particular). For unsteady flows, experimental data should be described by an unsteady pdf.
- Taking into account a very large number of uncertainties. The stochastic problem can indeed depend on a very large number of uncertainties, depending on the flow configuration.
- Treating discontinuities. Remark that a physical discontinuity should propagate in the coupled physical/stochastic space, thus yielding a very stiff problem to solve with classical approaches.
- Adaptation in the coupled physical/stochastic space at the same time.

- Reduction of the computational cost while preserving the accuracy (for both forward and inverse problems)

1.2.2 Variance-based and high-order decomposition

An alternative solution for reducing the cost of a UQ method is based on approaches attempting to identify the relative importance of the input uncertainties on the output. If some dimensions could be identified as negligible, they could be discarded in a reduced stochastic problem. If the number of uncertainties could be reduced, a better statistic estimation could be achieved with a lower computational cost.

Concerning the computation of the most influential parameters, it is important to determine the uncertain inputs which have the largest impact on the variability of the model output. In the literature, Global sensitivity analysis (GSA) aims at quantifying how uncertainties in the input parameters of a model contribute to the uncertainties in its output (see for example [Borgonovo 2003]), where global sensitivity analysis techniques are applied to probabilistic safety assessment models). Sometimes, GSA classifies the inputs according to their importance on the output variations and it gives a hierarchy of most important ones.

Traditionally, GSA is performed using methods based on the decomposition of the output variance [Sobol 2001], *i.e.* ANOVA (ANalysis Of VAriance). The ANOVA approach involves splitting a multi-dimensional function into contributions from different groups of sub-dimensions. In 2001, Sobol used this formulation to define global sensitivity indices [Sobol 2001], displaying the relative variance contributions of different ANOVA terms. In [Rabitz 1999], the authors introduced two High-Dimensional Model Reduction (HDMR) techniques to capture input-output relationships of physical systems with many input variables. These techniques are based on ANOVA-type decompositions.

In order to avoid to perform a large number of function evaluations, several techniques have been developed to compute the different so-called sensitivity indices at a reduced cost [Saltelli 2010]. In [Sudret 2008, Crestaux 2009, Blatman 2010a], generalized Polynomial Chaos Expansions (gPC) are used to build surrogate models for computing the Sobol's indices analytically as a post-processing of the PC coefficients. In [Foo 2010], multi-element polynomial chaos is combined with analysis of variance (ANOVA) functional decomposition to enhance the convergence rate of polynomial chaos in high dimensions and in problems with low stochastic regularity. In [Yang 2012], the use of adaptive ANOVA decomposition is investigated as an effective dimension-reduction technique in modeling incompressible and compressible flows with high-dimension of random space. In Sudret [Blatman 2010b], sparse Polynomial Chaos (PC) expansions are introduced in order to compute sensitivity indices. An adaptive algorithm allows to build a PC-based metamodel that only contains the significant terms whereas the PC coefficients are computed by least-square regression.

Other approaches are developed in the case where the assumption of independence of the input parameters is not valid. New indices have been proposed to address the dependence [Xu 2007, Xu 2008], but this attempts are limited to a linear correlation. In [Borgonovo 2007], they introduce a global sensitivity indicator which looks at the influence of input uncertainty on the entire output distribution without reference to a specific moment of the output (moment independence) and which can be defined also in the presence of correlations among the parameters. In [Caniou 2011], a gPC methodology to address global sensitivity analysis for this kind of problems is introduced. A moment-independent sensitivity index that suits problems with dependent parameters is reviewed. Recently, in [Borgonovo 2012], a numerical procedure is set-up for moment-independent sensitivity methods.

The ANOVA-based analysis creates a hierarchy of the most important input parameters for a given output when variations are computed in terms of variance. A strong limitation of this approach is the fact that it is based on the variance since the second central moment can not be considered as a general indicator for a complete description of output variations. For example, any Gaussian signal is completely characterized by its mean and variance. Consequently the 3rd order moment

of a Gaussian signal is zero. Unfortunately, many signals encountered in practice have non-zero high-order statistics, but second-order statistics contain no phase information. As a consequence, phase signals cannot be correctly identified by a 2nd-order technique. Remark also that many measurement noises are Gaussian, and so in principle the high-order statistics are less affected by Gaussian background noise than the 2nd order measures. For correctly describing the complexity of engineering systems, the computation of Higher-Order (HO) statistics is of primary importance. In particular, attention should be paid to the third order moment, the *skewness* (measure of the non-symmetry of the distribution, *i.e.* any symmetric distribution will have a third central moment of zero), and to the fourth order moment, the *kurtosis* (measure of whether the distribution is tall or short, compared to the normal distribution of the same variance). If we wish to determine the most influential parameters for a given output, the hierarchy of important parameters based on 2nd-order statistical moment (like in ANOVA analysis) is not the same if a different statistic order is considered. Depending on the problem, a n-order decomposition could be of interest. It seems of primary importance to collect the set of hierarchies obtained from n-order statistical moment decomposition, for a correct ranking of all the uncertainties.

The objective in this research field is directed towards efficient and low-cost methods permitting to analyze high-order statistics. The idea is to determine whether there are some dimensions to neglect for reducing the problem complexity. Another issue is also the formulation of global suitable criteria for ranking uncertainties according to the different statistical moments.

1.2.3 Robust design optimization

In most engineering applications, the use of deterministic models within an optimization cycle is no longer considered a satisfactory strategy in order to obtain reliable solutions. Design procedure must explicitly take into account the system uncertainties, because the overall performance might be overly sensitive to these uncertainties leading to an unacceptable variability in the operating environment. The risk is to obtain final designs with good performances at the design point but poor off-design characteristics, an undesirable property that is well-known in the literature as over-optimization. The goal of robust design optimization [Schueller 2008] is to determine a design which is relatively insensitive with respect to physical and modeling uncertainties.

Robust optimization processes may require a prohibitive computational cost when dealing with a large number of uncertainties and a highly non-linear fitness function. Efforts in the development of numerical method are directed mainly toward the reduction of the number of deterministic evaluations necessary for solving the optimization problem and for performing the uncertainty quantification (UQ) of the performances of interest [Parussini 2010, Beyer 2007, Doltsinis 2004, Mitra 2005, Park 2006, Schueller 2008, Carlberg 2011, Carlberg 2008]. When UQ and optimization are decoupled, *i.e.* optimization strategy is not influenced by the presence of uncertainties, the overall cost is typically the product of the cost of the two approaches [Diwekar 2003]. Decoupled approaches are simple but more expensive than necessary.

Robust Design method, also called the Taguchi Method, was pioneered in [G. 1989] and is quoted here for the sake of proper referencing even though the approach suffers important limitations from an optimization efficiency point of view. Several methods incorporate the uncertainties into the optimization problem. For example, the meta-model approach uses the data to build a meta-model of the robustness measures by using a set of given design points. In this context, the response surface methodology, neural networks, Kriging models, have been proposed as meta-modeling techniques [Jensen 2007, Namura 2011, Xu 2003]. In general, meta-modeling techniques are not well suited for large scale robust optimization problems when the number of design variables is large. Another class of methods, usually referred to as the deterministic approach to robust optimization, calculate explicitly the desired robustness measures. In this class, several methods prove their efficiency for

high-dimensional uncertain parameter (see for example [Sankaran 2010, M. S. Eldred 2008]). The large amount of computational effort required for considering a large number of uncertainties is well known in the literature under the designation "Curse of Dimensionality" [Bellman 1961]. Two different methodologies have been proposed to tackle this issue in the Uncertainty Quantification framework. First, a strategy to reduce the number of points required for the numerical integration, named Sparse grid [Gao 2011, Ma 2009a], has been introduced. This technique can lead to a strong reduction of the quadrature points for moderate dimensional problem, provided that the function has some regularity. It is based essentially on some results of the interpolation theory. Certainly the Sparse Grid allows to avoid the exponential growth of the number of points with the stochastic dimension, so in this sense prevents from the curse of dimensionality, but for high dimensional stochastic spaces the number of simulations required could still be prohibitive. More recently, the attention has shifted to both the number of points required and the number of stochastic dimensions. There are a few studies [Sankaran 2010], exploring the possibility to identify the most important uncertainties and as a consequence to reduce the number of dimensions of the stochastic space. If the number of uncertainties could be reduced, a better statistics estimation could be achieved with a lower computational cost. This reduction strategy can be used into a robust optimization framework, thus decreasing the final cost for obtaining the optimal individual. Generally, ANOVA-based approaches are used in order to decompose the variance according to the different contributions, permitting to create a ranking of the most predominant uncertainties [Congedo 2011c].

For robust optimization problems, computational cost can easily become prohibitive. Let us consider for example a decoupled approach, *i.e.* a stochastic problem is solved for each set of parameters to optimize : the global cost is crudely the cost of a single stochastic problem times the number of iterations of the optimization algorithm. As a consequence, the challenge consists in computing accurate solution by retaining a low computational cost.

1.2.4 Understanding of dense-gas physics

Up to now, no experimental data are available for flows of heavy fluids in the dense gas region. Experiments are difficult because of high temperature and pressure conditions, and fluid decomposition or inflammability in presence of air. This has motivated the use of numerical simulation as a favoured tool for dense gas flow analysis, but only a limited number of papers have been devoted to the computation of dense gas flows. With a view to support the design of experimental devices allowing to demonstrate the occurrence of BZT phenomena, shock tube simulations have been performed in [Fergason 2001] and more recently in [Colonna 2008a, Congedo 2012]. External flows over airfoils have been computed in [Congedo 2007, Cinnella 2005a, Brown 2000] while BZT flows in turbines have been simulated in [Monaco 1997, Brown 2000, Colonna 2004] and more recently in [Turunen-Saaresti 2010a, Turunen-Saaresti 2010b, Congedo 2011b] with complex EoS to describe the thermodynamic behavior of the gas. With no experimental validation yet available for any of these configurations, care must be taken in the analysis of the computed flow fields because of their sensitivity to the thermodynamic model and to the numerical ingredients of the discretization scheme [Cinnella 2011].

The objective of this research field is to provide a very reliable simulation tool that could be used also for the prediction, since no comparison with experimental data is possible. A particular attention is paid to code validation and model assessment. The effect of the boundary conditions should be also investigated: specifically, boundary conditions which ensure an oscillation-free behavior for thermodynamic quantities such as enthalpy and entropy at the turbine inlet and outlet are developed, so as to allow an accurate evaluation of the loss coefficients for a turbine stage.

The finely computed turbine stage should be integrated into a more global cycle analysis in order

to derive performance indices such as efficiencies based on the first and second laws as well as the net specific work of the cycle. The elements included in this analysis should combine fluid properties with cycle working conditions, namely : high and low temperatures and pressures. In this cycle analysis, the turbine is the only simulated component but its computed performances depend on the whole cycle conditions (super-heating or not, multistage expansion, etc).

Because of the strong existing sources of uncertainty in ORC cycles, another objective should be to take into account uncertainty quantification (UQ) to increase the reliability of the coupled local/global approach and the robustness of the proposed designs.

A last point to assess for the reliability concerns turbulence models. Turbulence models currently used in dense-gas flow simulations (RANS) depend on some tuning parameters, generally calibrated with respect to a perfect gas equation of state. More complex models (LES-DNS) should be used to calibrate these parameters for more complex equations of state.

1.3 Highlights on my contributions to methods and applications

I summarize here my main contributions in terms of methods and results[2]. These are organized along two main axes.

The first axis is focused on the development, use and application of UQ and Robust-Optimization methods, both intrusive and non-intrusive, for various models and problems (see Fig. 1.4). Note that I studied uncertain operating conditions (and more generally boundary conditions), and various models with uncertain model-parameters (for turbulence, thermodynamics, two-phase flows). Looking at Fig. 1.4, activities focused on CFD, UQ and Robust Optimization deal with so-called uncertainty propagation problem, *i.e.* starting from a definition of input uncertainties, output statistics are computed by using different methods. On the contrary, activities related to experiments dealt with a so-called inverse problem, *i.e.* the use of output experimental data for characterizing input uncertainties.

The second axis is devoted to advancements for the simulation of dense gas flows in CFD numerical codes. In particular, I worked on the modifications of some numerical schemes for taking into account non-ideal equations of state [20], on the development and use of very accurate equations of state [13,19], on the physics of dense-gas turbulent flows [16,17], on the shape optimization of profiles and turbines [9,16,18]. A very recent activity concerns the simulation of two-phase flow with dense-gases by means of very accurate equations of state [2]. All these activities are summarized in Fig. 1.5.

In order to give a clear idea of my contributions in terms of methods and applications, I list below some highlights concerning methods and results for UQ and Robust Optimization.

Intrusive methods for shock-dominated compressible flows

- The Semi-Intrusive method (SI) [7] allows the computation of statistics of linear and non linear PDEs solutions. This method proves to be very efficient to deal with any form of probability density function, long-term integration and discontinuities in the stochastic space. Given a PDE and starting from a description of the solution in terms of a space variable and a (family) of random variables that may be correlated, the solution is numerically described by its conditional expectancies of point values or cell averages. This is done via a tessellation of the random space as in finite volume methods for the space variables. Then, using these conditional expectancies and the geometrical description of the tessellation, a piecewise polynomial approximation in the random variables is computed using a reconstruction method that is standard for high order finite volume space, except that the measure is no longer the standard Lebesgue measure

[2]Note that each reference number is associated to the list of my publications (see Section 12.6).

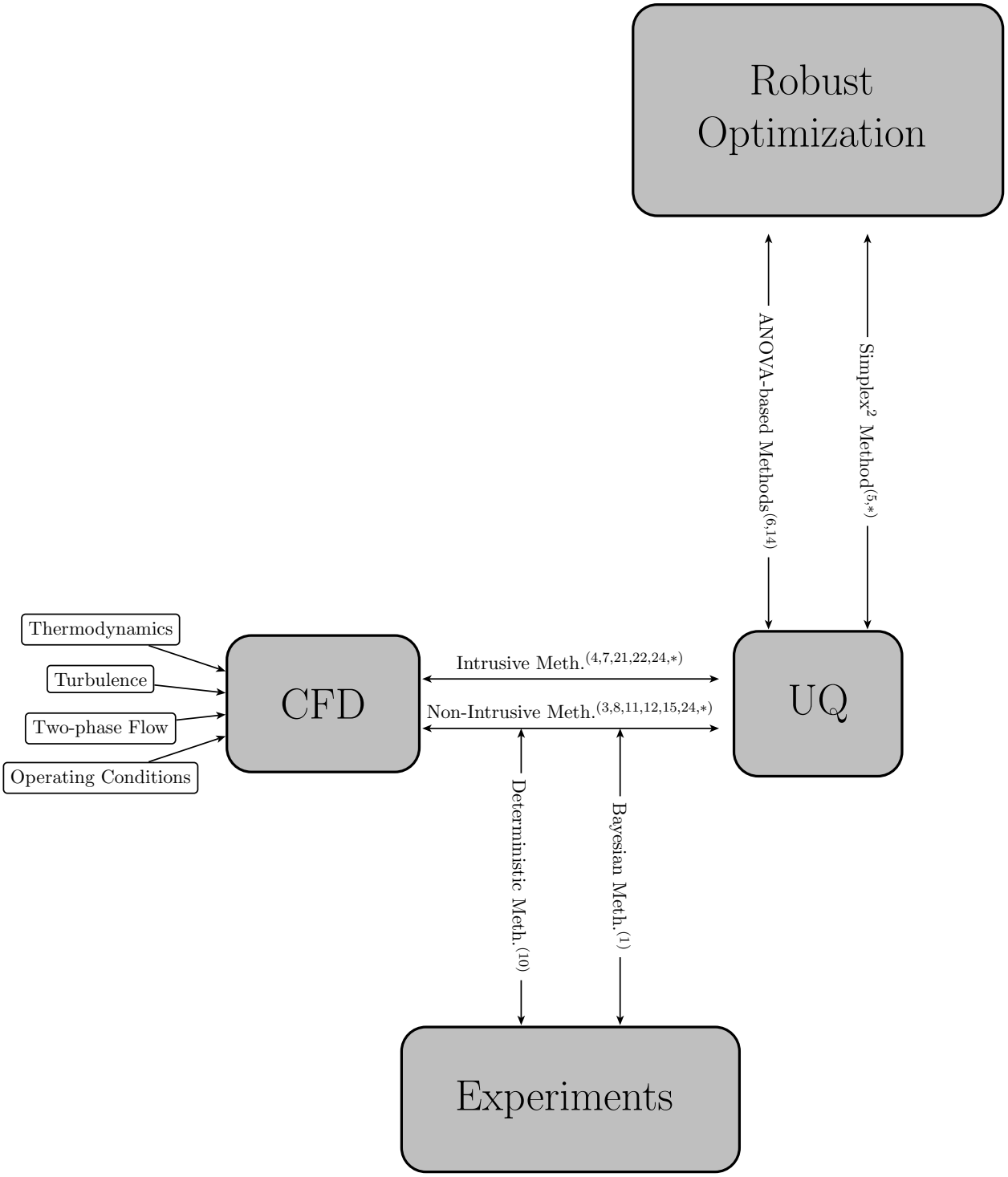

Figure 1.4: UQ and Robust-Optimization activities and contributions. Each reference number is associated to the list of my publications (see Section 12.6), with the asterisk indicating a work-in-progress.

but the probability measure. Starting from a given scheme for the deterministic version of the PDE, this reconstruction is used to formulate a scheme for the numerical approximation of the solution. This new approach is said semi-intrusive because it requires only a limited amount of modification in a deterministic flow solver to quantify uncertainty on the flow state when the

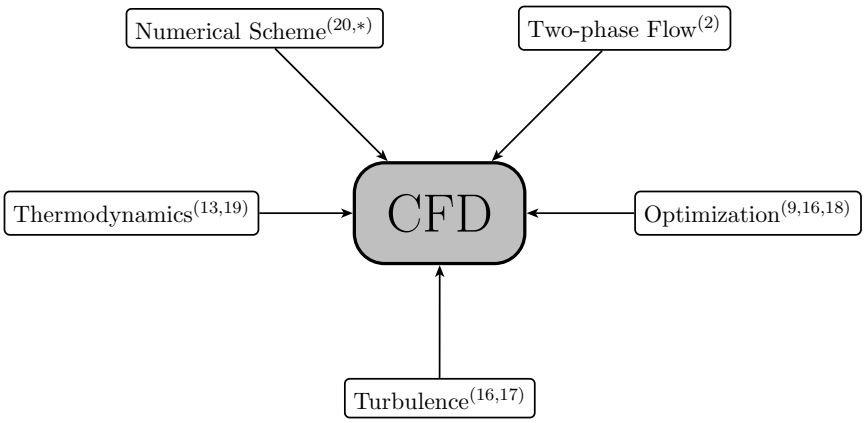

Figure 1.5: Dense-gas activities and contributions. Each reference number is associated to the list of my publications (see Section 12.6), with the asterisk indicating a work-in-progress.

flow solver includes uncertain variables. This method is described in Section 3.1.

- TE Algorithm [4] is a novel adaptive strategy for stochastic problems, inspired from the classical Harten's framework. The proposed algorithm allows building, in a very general manner, stochastic numerical schemes starting from any type of deterministic schemes and handling a large class of problems, from unsteady to discontinuous solutions. Its formulations permits to recover the same results concerning the interpolation theory of the classical multiresolution approach, but with an extension to uncertainty quantification problems. The interest of the present strategy is demonstrated by performing several numerical problems where different forms of uncertainty distributions are taken into account, such as discontinuous and unsteady custom-defined probability density functions.
  Remark that the basic version of this algorithm is non-intrusive, although its following extensions are intrusive, since a weak coupling between physical and stochastic space is applied. This method is presented in the cell-average setting in Section 3.2.

- The TE method is extended to the so-called spatial-TE (sTE), for partial differential equations and applied to the heat equation [24]. Moreover, the flexibility of the proposed method is demonstrated by proposing a simple algorithm coupling high-resolution schemes in the physical and in the stochastic spaces at the same time, and by applying it to the Burgers equation [22]. These methods are not reported in this manuscript. Please refer any interested reader to [22,24].

- aSI method [21] deals with a multiresolution strategy applied to SI scheme for compressible fluids problems. The mathematical framework of the multiresolution framework is presented for the cell-average setting and the coupling with the existing semi-intrusive scheme is described from both the theoretical and practical point-of-view. Some reference test-cases are performed to demonstrate the convergence properties and the efficiency of the overall scheme: the linear advection problem for both smooth and discontinuous initial conditions, the inviscid Burgers equation and the 1D Euler system of equations to model an uncertain shock tube problem obtained by the well-known Sod shock problem. This method is described in Section 3.2

- aSI method is coupled with a DEM (Discrete Equation Method) approach for taking into account uncertainties in a multiphase problem (the paper is in preparation). This shows the great flexibility of the aSI stochastic scheme permitting an easy coupling also with a very complex code, such as a DEM-based code. Some highlights of this work are presented in Section 11.3.

- aSI method is extended for taking into account up to three dimensions in the stochastic space. Some highlights of this work are presented in Section 11.3.

Variance-based and high-order decomposition

- ANOVA analysis is a very common numerical technique for computing a hierarchy of most important input parameters for a given output when variations are computed in terms of variance. This second central moment can not be retained as an universal criterion for ranking some variables, since a non-gaussian output could require higher order (more than second) statistics for a complete description and analysis. I studied how decomposing High-order statistics (HOSD) [23]. In particular, how third and fourth-order statistic moments, *i.e.* skewness and kurtosis, respectively, can be decomposed. It is shown that this decomposition is correlated to a polynomial chaos expansion, permitting to easily compute each term. Then, new sensitivity indices are proposed, based on the computation of the kurtosis. A part of this work is presented in Section 4.1.

- ANOVA based analysis is applied for studying various sources of uncertainties in different flow configuration: turbulent and cavitating flows [3,8], thermodynamically complex flows [11,15], and the influence of operating/boundary conditions [8,14]. Some of these works are presented in Sections 4.2, 6.4 and in Chapter 9.

Robust optimization

- Simplex^2 Method [5] is an efficient algorithm for uncertainty quantification (UQ) in computational problems with random inputs. Its formulation, based on simplex tessellation, high degree polynomial interpolation and adaptive refinements can be employed in problems involving optimization under uncertainty. The optimization approach used is the Nelder-Mead algorithm (NM), also known as Downhill Simplex Method. The resulting SSC/NM method, called Simplex^2, is based on i) a coupled stopping criterion and ii) the use of an high-degree polynomial interpolation in the optimization space for accelerating some NM operators. This method is presented in Section 6.3.3.2.

- ANOVA-based method [6] is an efficient algorithm used in order to perform a variance-based decomposition and to reduce stochastic dimension basing on an appropriate criterion. A massive use of metamodels allows reconstructing response surfaces for sensitivity indexes in the design variables plan. This method is presented in Section 6.2.

Inverse problem

- A Backward uncertainty propagation method is proposed [10]. This is an innovative, flexible and efficient algorithm combining computational fluid dynamics (CFD), uncertainty quantification (UQ) tools and metamodel-based optimization in order to obtain a reliable estimate for the probability of occurrence of a given phenomenon and to prescribe the experimental accuracy requirements ensuring the reproducibility of the measurements with sufficient confidence. This method is illustrated in Section 10.1.

- A new methodology to rebuild freestream conditions for the trajectory of a re-entry vehicle from measurements of stagnation-point pressure and heat flux is presented [1]. Uncertainties

due to measurements and model parameters are taken into account and a Bayesian setting is used to solve the associated stochastic inverse problem. A sensitivity analysis based on a stochastic spectral framework is first investigated to study the impact of uncertain input data on stagnation-point measurements. An original backward uncertainty propagation method is then proposed, for which only the uncertainties that have the most impact are retained. This method is presented in Section 5.1.

Concerning dense-gases numerical simulation, I list some exciting results obtained recently:

- The reliability of thermodynamic models has been assessed [11,15], focusing in particular on fluids displaying BZT properties. The sensitivity of numerically computed flow fields to uncertainties in thermodynamic models for complex organic fluids has been investigated. Precisely, our focus is on the propagation of uncertainties introduced by some popular thermodynamic models into the numerical results of a computational fluid dynamics solver for flows of molecularly complex gases close to saturation conditions (dense gas flows). A chaos collocation method is used to perform both a priori and a posteriori tests on the output data generated by thermodynamic models for dense gases with uncertain input parameters. A priori tests check the sensitivity of each equation of state to uncertain input data via some reference thermodynamic outputs, such as the saturation curve and the critical isotherm. A posteriori tests investigate how the uncertainties propagate into the computed field properties and aerodynamic coefficients for a flow around an airfoil placed into a transonic dense gas stream. This study is presented in Chapter 9.

- Feasibility study on the RSW (Rarefaction Shock Wave) appearance is explored [10]. The backward uncertainty propagation method presented before is applied to the study of rarefaction shock waves (RSW) in a dense-gas shock tube. Previous theoretical and numerical studies have shown that a RSW is relatively weak and that the prediction of its occurrence and intensity are highly sensitive to uncertainties on the initial flow conditions and on the fluid thermodynamic model. It is shown that requirements on the experimental uncertainties are hardly achievable for ensuring a high probability to observe the RSW. This work is presented in Chapter 10.

- The appearance of a RSW in a two-phase flow has been recently investigated [2]. A discrete equation method (DEM) for the simulation of compressible multiphase flows including real-gas effects is introduced. So a numerical approximation of a reduced five-equation model is obtained. A simple procedure is then proposed for using a more complex equation of state, thus improving the quality of the numerical prediction. A computational study on the occurrence of rarefaction shock waves (RSW) in a two-phase shock tube is presented, with dense vapors of complex organic fluids. Since previous studies have shown that a RSW is relatively weak in a single-phase (vapor) configuration, its occurrence and intensity are investigated considering the influence of the initial volume fraction, initial conditions and the thermodynamic model. This work is presented in Chapter 10.

- High-fidelity turbine computation of dense-gas turbines are performed by using cross-validation between flow solvers [13]. This study is devoted to the numerical study of dense gas flows in turbomachinery and the assessment of their interest as working fluids in energy-conversion cycles. A structured and an unstructured dense-gas solver are used to ensure the reliability of the computed results for dense gas flows through a turbine cascade. The physical analysis is focused on the effect of the working fluid and its operating thermodynamic conditions on turbine performance. This work is presented in Chapter 8. Some recent results obtained with a high-order residual distribution schemes are presented in Section 11.3.

1.4 Organization of the manuscript

This manuscript is divided in two main parts. The first one is devoted to Uncertainty Quantification (UQ) and robust design optimization. In particular, my main contributions in terms of methods and results are illustrated. The second part is focused on dense-gas CFD (Computational fluid-dynamics). I briefly describe the main numerical ingredients for a well-posed and accurate numerical simulation of thermodynamically complex flows. Then, the most important results in terms of physical understanding of BZT flows and advancements in their investigation are presented. Even though the two parts are presented separately, several studies have been performed which mix UQ and robust optimization with dense gas flow analysis.

Part I

Uncertainty quantification and Robust Optimization

Chapter 2

Introduction to UQ

Contents

2.1 Some definitions

Let us introduce the mathematical setting, used for the UQ analysis in the context of partial differential equations. Let us consider an output of interest $u(\mathbf{x}, t, \boldsymbol{\xi}(\omega))$ depending from the physical space $\mathbf{x} \in \Omega \subset \mathbb{R}^{n_d}$, the time $t \in T$ and a vector of parameters $\boldsymbol{\xi} \in \Xi$ where Ξ is the sample space. The output of interest u can be a conserved (or primitive, or another flow variable) variable of a system of conservation laws.

We suppose that the output of interest is governed by an algebraic or differential operator $\mathcal{L}$ with a source term $\mathcal{S}$:

$$\mathcal{L}(\mathbf{x}, t, \boldsymbol{\xi}(\omega); u(\mathbf{x}, t, \boldsymbol{\xi}(\omega))) = \mathcal{S}(\mathbf{x}, t, \boldsymbol{\xi}(\omega)). \tag{2.1}$$

Initial and boundary conditions, that could depend from the parameter vector $\boldsymbol{\xi}$, should be provided for a well-posed problem. Both the operators $\mathcal{L}$ and the source term $\mathcal{S}$ are defined on the domain $\Omega \times T \times \Xi$.

Let us define a measurable space (Ξ, Σ, p) where Σ is its $\sigma-$algebra of events and p a probability measure with the following properties:

- $p(A) \geq 0$ for all $A \in \Sigma$;
- Countable additivity: if $A_i \in \Sigma$ are disjoint sets then $p(\bigcup_i A_i) = \sum_i p(A_i)$;
- as probability measure p is normalized on Ξ: $p(\Xi) = 1$.

The $\mathbb{R}^d-$valued random variable $\boldsymbol{\xi}$ specifies a set of events with a corresponding probability. More formally, the random variable $\boldsymbol{\xi}$ is a measurable function that maps the measurable space (Ξ, Σ, p) to another measurable space, the Borel $\mathcal{B}^d$ $\sigma-$algebra of the real space $(\mathbb{R}^d, \mathcal{B}^d, \mathbb{P})$. There is some set of events ω, that $\boldsymbol{\xi}$ maps to an output event $A \in \mathcal{B}^d$ with the probability of occurrence of A, $\mathbb{P}(A)$ equal to the probability of ω:

$$\mathbb{P}(A) = p(\boldsymbol{\xi}^{-1}(A)) = p(\omega : \boldsymbol{\xi}(\omega) \in A). \tag{2.2}$$

As usual in the literature, we consider that $\mathbb{P}(A) = p(\boldsymbol{\xi} \in A) = p(\boldsymbol{\xi})$.

The aim of UQ analysis is to find statistical quantities of the solution $u(\mathbf{x}, t, \boldsymbol{\xi})$, the statistical moments or the probability distribution.

Assuming $u(\boldsymbol{\xi}) \in L_2(\Xi, p)$, mean and variance can be computed as follows:

$$\begin{aligned} \mathcal{E}(u, \mathbf{x}, t) &= \int_\Xi u(\mathbf{x}, t, \boldsymbol{\xi}) p(\boldsymbol{\xi}) \mathrm{d}\boldsymbol{\xi} \\ \mathrm{Var}(u, \mathbf{x}, t) &= \int_\Xi \left(u(\mathbf{x}, t, \boldsymbol{\xi}) - \mathcal{E}(u)\right)^2 p(\boldsymbol{\xi}) \mathrm{d}\boldsymbol{\xi}. \end{aligned} \tag{2.3}$$

2.2 Organization of this part

In the first part of this manuscript, I resume my main contributions to UQ and Robust Optimization methods. Chapter 3 is devoted to some intrusive approaches for Partial Differential Equations (PDE), in particular for hyperbolic systems: i) the Semi-Intrusive (SI) method, ii) the aSI method, that is the coupling between SI and a multi-resolution inspired strategy, called TE method. Other intrusive methods that are not reported in this manuscript, are then briefly described.

In Chapter 4, non-intrusive approaches are considered. In particular, high-order statistical moments decomposition is presented. The interest of using ANOVA-based analysis is highlighted in a study about the uncertainty propagation through some turbulence models.

Chapter 5 illustrates some recent results obtained with two algorithms for inverse problems in dense-gas flows and in an aerospace application.

Finally, in Chapter 6, the focus is on my contributions to Robust Optimization methods: the Simplex^2 Method, and an ANOVA-based optimization method. Finally, the shape optimization of an airfoil in a BZT flow is illustrated.

Chapter 3

Intrusive Approaches

Contents

In this chapter, I describe the work done on two intrusive approaches, *i.e.* the methods SI and aSI. Other methods not reported in this manuscript, are briefly resumed in Section 3.3.

3.1 Semi-intrusive method

3.1.1 Principles of the method

3.1.1.1 General formulation of the method

Let us start from some model represented by a PDE, say

$$\mathcal{L}(u) = 0, \tag{3.1}$$

defined in a domain K of $\mathbb{R}^d$ subjected to boundary conditions, and if needed initial conditions. The operator depends in some way of parameters (for example the equation of state, or the parameter of a turbulent model, to give an example in fluids), that in many cases are not well known. Hence we assume they are random variables defined on some universe Ω, and that these random variables are measurable with respect to a measure $d\mu$ defined on Ω. Hence our problem can formally be seen as a "stochastic" PDE of the type

$$\mathcal{L}(u, X) = 0, \tag{3.2}$$

defined in a domain K of $\mathbb{R}^d$, subjected to initial and boundary conditions, and where X is a random variable defined on Ω. By abuse of language, we use the same notation $\mathcal{L}$ for the problem. The operator $\mathcal{L}$ depend on $u := u(x, t, X)$ or $u := u(x, X)$ depending on of the problem is time dependent or not and $X := X(\omega)$ where $x \in \mathbb{R}^d$ for $s \in \{1, 2, 3\}$ and $t \in \mathbb{R}^+$ are the usuals and respectively space and time parameters, the event ω belongs to Ω. The random variable may also depend on space and time, as well as the measure μ.

We will identify Ω to some subset of $\mathbb{R}^s$, s being the number of random parameter to define X. Thus we can also see (3.2) as a problem defined on a subset K' of $\mathbb{R}^d \times \mathbb{R}^s$.

For any realization of Ω, we assume to be able to solve the following approached deterministic form of (3.2) in space and time, by some numerical method:

$$\mathcal{L}_h(u_h, X(\omega)) = 0. \tag{3.3}$$

In order to approximate a solution of (3.2), the first step is to discretize the probability space Ω. We construct a partition of Ω, i.e. a set of Ω_j, $j = 1, \ldots, N$ that are mutually independent

$$\mu(\Omega_i \cap \Omega_j) = 0 \text{ for any } i \neq j \tag{3.4}$$

and that cover Ω

$$\Omega = \cup_{i=1}^{N} \Omega_i. \tag{3.5}$$

We assume $\mu(\Omega_i) = \int_{\Omega_j} d\mu > 0$ for any i. We wish to approximate the solution of (3.2) by the average conditional expectancies $E(u_h|\Omega_j)$

$$E(u_h \mid \Omega_j) = \frac{\int_{\Omega_j} u_h d\mu}{\int_{\Omega_j} d\mu} \tag{3.6}$$

from the knowledge of the operator $\mathcal{L}_h$.

Let us illustrate how this idea can be made effective. If an iterative technique is used for solving (3.3), as it is often the case, a deterministic solution can be written as

$$u_h^{n+1} = \Im(u_h^n) \tag{3.7}$$

where the operator $\Im$ is a succession of additions, multiplications and function evaluations. In (3.7), the index n can be the index of the iteration *stricto sensu*, or the index of the time step in the case of an explicit method for a time dependent problem, etc. This leads to

$$E\left(u_h^{n+1} \mid \Omega_j\right) = E\left(\Im(u_h^n) \mid \Omega_j\right). \tag{3.8}$$

This scheme is fully defined if $E(\Im(u_h^n) \mid \Omega_j)$ can be evaluated. We show how to do that in sections 3.1.1.2 and 3.1.1.3. Thus we are able to construct a sequence $\left(E\left(u_h^{n+1} \mid \Omega_j\right)\right)_{n\geq 0}$. If the problem is steady and *if this sequence converges in some sense*, the limit is the sought solution. In the case of time dependent problems, (3.8) represents an approximation of the conditional expectancy at time t_{n+1}. In the case of explicit/implicit methods, as for dual time stepping, the interpretation of (3.8) can easily be done in the relevant context.

3.1.1.2 Consistency of the method

Given the conditional expectancies $E(X \mid \Omega_j)$, can we estimate for a given f, $E(f(X))$?

We assume $X = (X_1, \ldots, X_n)$. The idea is the following: For each Ω_j, we first define a stencil, i.e. a set $\mathcal{S}_i = \{\Omega_j\}_{j\in I_i}$ with $\Omega_i \in \mathcal{S}_i$ and we wish to evaluate a polynomial $P_i \in \mathbb{R}[x_1, \cdots, x_n]$ of degree p such that

$$E(X \mid \Omega_j) = \frac{\int_{\mathbb{R}^n} 1_{\Omega_j}(x_1, \cdots, x_n) P(x_1, \cdots, x_n) d\tilde{\mu}}{\mu(\Omega_i)} \qquad \text{for } j \in \mathcal{S}_i \tag{3.9}$$

where $d\tilde{\mu}$ is the image of $d\mu$. [1]

[1] for example $d\mu$ is the sum of a Gaussian and a Dirac at x_0,

$$\int_{\mathbb{R}^n} P(x) d\tilde{\mu} = \alpha \frac{1}{\sqrt{2\pi\sigma}} \int_{\mathbb{R}} P(x) e^{-\frac{(x-m)^2}{2\sigma}} dx + (1-\alpha) P(x_0)$$

This problem is reminiscent of what is done in finite volume schemes to compute a polynomial reconstruction in order to increase the accuracy of the flux evaluation thanks the MUSCL reconstruction. Among the many references that have dealt with this problem, with the Lebesgue measure $dx_1 \dots dx_n$, one may quote [Harten 1987] and for general meshes [Barth 1990, Abgrall 1994a]. A systematic method for computing the solution of problem (3.9) is given in [Abgrall 1997b].

Assume that the stencil $\mathcal{S}_i$ is defined, the technical condition that ensure a unique solution to problem (3.9) is that the Vandermonde–like determinant (given here for one random variable for the sake of simplicity)

$$\Delta_i = \det\left(E(x^l|\Omega_j)\right)_{0\le l\le n, j\in\mathcal{S}_i}. \tag{3.10}$$

is non zero. In the case of several random variable, the exponent l above is replaced by a multi–index. A necessary condition, in 1D, is that $\#\mathcal{S}_i \ge \frac{p(p+1)}{2}$. Similar, but more complex expressions of this type exist for multivariate polynomials.

Once the solution of (3.9) is known, we can estimate

$$E\left(f(X)\right) \approx \sum_{j=1}^{N} \int_{\Omega_j} f\left(P\left(x_1, \cdots, x_n\right)\right) d\tilde{\mu} \tag{3.11a}$$

by using a relevant quadrature formula in each Ω_j. For example, if $d\tilde{\mu}$ has a density in Ω_i, we can do

$$\int_{\Omega_j} f\big(P(x)\big) d\tilde{\mu} \approx \sum_{k=1}^{m_i} w_k^i f\left(P\big(x_k^i\big)\right) \tag{3.11b}$$

where the weights are the w_k^i and the quadrature points are the x_k^i. If $d\tilde{\mu}$ has no density, the ad hoc formula must be used, but the principle stays the same.

We have the following approximation results : if $f \in C^1(\mathbb{R}^n) \cap L^1(\Omega, \mu)$ and X of class Cr, $r \ge p+1$ then

$$\left|E\left(f(X)\right) - \sum_{j=1}^{N} \int_{\mathbb{R}^n} 1_{\Omega_j}\left(x_1, \cdots, x_n\right) f\left(P\left(x_1, \cdots, x_n\right)\right) d\tilde{\mu}\right| \\ \le \max ||D^{p+1}X||_\infty \max_{\Omega_i} \min_{\omega_i\in\Omega_i} E(||(\omega-\omega_i)^{p+1}||\ |\Omega_i).$$

for a set of regular stencils. The proof of this results is given in [Abgrall 2013b].

We notice that we never need to make any additional assumption on the structure of X to evaluate P in (3.9). In particular, there is no need to assume that the random variables X_i are mutually independent.

3.1.1.3 Polynomial reconstruction

In this section, we provide explicit examples and applications of the reconstruction technique that we have abstractly sketched in the previous paragraph. Let us subdivide the space Ω into non overlapping measurable subsets. For the simplicity of exposure we will consider one source of uncertainty, thus the subsets can be identified, via the measure $d\mu$, to N intervals of $\mathbb{R}$ which are denoted by $\Omega_j = [\omega_{j-1/2}, \omega_{j+1/2}]$. The case of multiple sources can be considered by tensorisation of the probabilistic mesh. Note it does not mean that $d\mu$ is of the form $d\mu = d\mu_1 \otimes \dots \otimes d\mu_s$ as it would be the case for independent variables: this formalism enables to consider correlated random variables, as we show later in the text. Note that the subsets $\Omega_{j+1/2}$, seen as subsets of $\mathbb{R}^n$ may well be unbounded, the only relevant information is that their *measure* $\mu(\Omega_{j+1/2})$ is bounded. This is obviously the case because μ is a probability measure.

Let us describe in details what is done for one source of uncertainties. In the cell Ω_i, the polynomial $P_i \in \mathbb{P}^k(\mathbb{R})$ of degree k is fully described by a stencil $\mathcal{S}_i = \{\Omega_i, \Omega_{i_1+1/2}, \ldots\}$ such that in any cell $[\omega_{j-1/2}, \omega_{j+1/2}] \in \mathcal{S}_i$ we have

$$E(P_i|[\omega_{j-1/2}, \omega_{j+1/2}]) = E(u|[\omega_{j-1/2}, \omega_{j+1/2}]). \tag{3.12}$$

It is easy to see that there is a unique solution to that problem provided that the cells of $\mathcal{S}_i$ do not overlap, which is the case, and if $k = \#\mathcal{S}_{i+1/2} - 1$. In the numerical examples, we consider three reconstruction mechanisms :

- a first order reconstruction: we simply take $\mathcal{S}_i = \{\Omega_i\}$ and the reconstruction is piecewise constant,
- a centered reconstruction: the stencil is $\mathcal{S}_{i+1/2} = \{i - 1/2, i + 1/2, i + 3/2\}$ and the reconstruction is piecewise quadratic. At the boundary of Ω, we use the reduced stencils $\mathcal{S}_{1/2} = \{1/2, 3/2\}$ for the first cell $[\omega_0, \omega_1]$ and $\mathcal{S}_{N-1/2} = \{N - 1/2, N - 3/2\}$ for the last cell $[\omega_{N-1}, \omega_N]$, i.e. we use a linear reconstruction at the boundaries.
- An ENO reconstruction : for the cell $[\omega_{i-1/2}, \omega_{i+1/2}]$, we first evaluate two polynomials of degree 1. The first one, p_i^-, is constructed using the cells $\{[\omega_{i-1/2}, \omega_{i+1/2}], [\omega_{i-3/2}, \omega_{i-1/2}]\}$ and the second one, p_i^+, on $\{[\omega_{i-1/2}, \omega_{i+1/2}], [\omega_{i+1/2}, \omega_{i+3/2}]\}$. We can write (with $\omega_i = \frac{\omega_{i-1/2}+\omega_{i+1/2}}{2}$)

  $$p_i^+(\xi) = a_i^+(\xi - \omega_i) + b_i^+ \text{and } p_i^-(\xi) = a_i^-(\xi - \omega_i) + b_i^-.$$

  We choose the least oscillatory one, i.e. the one which realizes the oscillation $\min(|a_i^+|, |a_i^-|)$. In that case, we take a first order reconstruction on the boundary of Ω.

Other choices are possible such as WENO-like interpolants.

Once the polynomial is reconstructed, we need to evaluate conditional expectancies. This amounts to perform numerical integrations over Ω_j. If $d\mu = \mu(\omega)d\omega$, this can be done thanks to a classical quadrature method, as the following third order Gaussian quadrature:

$$\int_a^b h(\omega)d\omega \approx \frac{b-a}{2}(h(\xi_1) + h(\xi_2)), \tag{3.13}$$

where $\xi_1 = \frac{a+b}{2} - \frac{b-a}{2}\frac{\sqrt{3}}{3}$ and $\xi_2 = \frac{a+b}{2} + \frac{b-a}{2}\frac{\sqrt{3}}{3}$.

In all the practical illustrations, we will use only one or two sources of uncertainty even though the method can be used for any number of uncertain parameters, this leading to other known problems such that the curse of dimensionality. Using classical quadrature formulas in multi-dimensional stochastic problem, the computational cost can increase exponentially [Smolyak 1963a], and others methods, as the sparse grid methods must be used [Gerstner 1998, Ma 2009a]. These methods are based on a linear combination of tensor product of one dimensional quadrature formulas.

3.1.1.4 1D-1D Discretization

Fundamental concepts have been introduced in the previous sections, and we will now focus on a detailed discretization of an 1D-1D PDE. By "1D-1D", we mean one dimension in the geometric space and one dimension in probabilistic space. Let us consider the following equation

$$\frac{\partial u}{\partial t} + \frac{\partial f(u)}{\partial x} = S, \tag{3.14}$$

Initial and/or boundary conditions,

defined in a domain $K = D \times \Omega \subset \mathbb{R}^2$, where $u := u(x,t,X(\omega))$, $S := S(x,t,X(\omega))$ is a source term and $t > 0$. The space parameter x is defined on $D \subset \mathbb{R}$, ω and X are respectively a random parameter and a random variable, defined on the probability space $(\Omega, d\mu)$ where $d\mu$ is the probability measure and $\Omega \subset \mathbb{R}$. The initial conditions, boundary conditions and the domain D may be random.

As explained previously in section 3.1.1.1, the discretization of (3.14) is based on two steps, the integration of the deterministic part of the system and the integration of the probabilistic part.

Deterministic formulation

We consider a spatial discretization for (3.14) with nodes points $x_i = i\Delta x$ where i belongs to some subset of $\mathbb{Z}$, a time step $\Delta t > 0$ and a set $t_n = \Delta t$, $n \in \mathbb{N}$. The control volume is as usual the intervals $C_i = [x_{i-1/2}, x_{i+1/2}]$ with $x_{i+1/2} = (x_i + x_{i+1})/2$. We start from a finite volume scheme, and for the simplicity of exposure, we only consider a first order in time.

Thus we define the *deterministic scheme* (i.e. for any fixed ω) as

$$\begin{aligned} u_i^{n+1}(X(\omega)) = u_i^n(X(\omega)) \\ - \frac{\Delta t}{|C_i|}\Big(F(u_{i+1}^n(X(\omega)), u_i^n(X(\omega))) - F(u_i^n(X(\omega)), u_{i-1}^n(X(\omega)))\Big) \\ + \int_{C_i} S(x, t^n, X(\omega))\, dx, \end{aligned} \tag{3.15}$$

where F is a consistent approximation of the continuous flux f. The cell-averaged quantity is defined as

$$u_i^n(X(\omega)) = \frac{1}{|C_i|}\int_{C_i} u(x, t^n, X(\omega))dx. \tag{3.16}$$

Probabilistic formulation

The next step is the discretization of the probabilistic part of the equation, where the variables must be represented by their conditional expectancies. We consider a probabilistic discretization for (3.15) with nodes points $\omega_{j+1/2} = (j + 1/2)\Delta\omega$ where j belongs to some subset of $\mathbb{Z}$. The control volume is the intervals $\Omega_j = [\omega_{j-1/2}, \omega_{j+1/2}]$.

Thus we define the *probabilistic scheme* as

$$\begin{aligned} u_{i,j}^{n+1} = u_{i,j}^n - \frac{\Delta t}{|C_i|}\Big(E(F(u_{i+1}^n, u_i^n)|\Omega_j) - E(F(u_i^n, u_{i-1}^n)|\Omega_j)\Big) \\ + \frac{\Delta t}{|C_i|}E\Big(\int_{C_i} S(x, t^n, X(\omega))dx\Big|\Omega_j\Big) \end{aligned} \tag{3.17}$$

where the cell-averaged conditional expectancy is defined as

$$u_{i,j}^n = E(u_i^n(X)|\Omega_j) = \frac{1}{\mu(\Omega_j)}\int_{\Omega_j} u_i^n(X(\omega))d\mu(\omega). \tag{3.18}$$

Numerical flux evaluation

The expectancy of the numerical flux can be approached as it is shown in section 3.1.1.2 by

$$E(F(u_{i+1}^n, u_i^n)|\Omega_j) \approx \frac{1}{\mu(\Omega_j)}\int_{\Omega_j} F(P_{i+1,j}^n, P_{i,j}^n)\, d\mu, \tag{3.19}$$

where $P_{i,j}$ is a piecewise polynomial reconstruction of the probabilistic solution. Assuming that we require all polynomial reconstructions $P_{i,j}$ to have the correct cell average, we have

$$E(P_{i,j}|\Omega_j) = E(u_i|\Omega_j). \tag{3.20}$$

To achieve the second order accuracy, there are many reconstruction methods. As it is shown in section 3.1.1.3 one can use a second order centered method, where polynomial reconstruction have the following form:

$$P_{i,j}(\omega) = a + b(\omega - \omega_j) + c(\omega - \omega_j)^2,$$

and where $\omega_j = \dfrac{\omega_{j+1/2} + \omega_{j-1/2}}{2}$.

We rephrase in the present context the discussion of section 3.1.1.3 to clarify as much as possible. The coefficients a, b and c are determined using the previous requirement (3.20), thus for $l \in \{j-1, j, j+1\}$

$$E(P_{i,l}|\Omega_l) = E(u_i|\Omega_l).$$

By linearity of expectancy, this leads to resolve the system

$$\begin{aligned} a + b\ E(\omega - \omega_{j+1/2}|\Omega_l) + c\ E((\omega - \omega_{j+1/2})^2|\Omega_l) \\ = E(u_{i,l}|\Omega_l) \text{ for any } l \in \{j-1, j, j+1\}. \end{aligned}$$

Once reconstructed, the polynomial is injected in the numerical flux F. For the simplicity of the exposure let's formulate F thanks to the Roe's method:

$$F(P^n_{i+1,j}, P^n_{i,j}) = \frac{1}{2}\big(f(P^n_{i+1,j}) + f(P^n_{i,j}) - |A(P^n_{i+1,j}, P^n_{i,j})|(P^n_{i+1,j} - P^n_{i,j})\big) \tag{3.21}$$

where $|A(u^n_{i+1,j}, u^n_{i,j})|$ is the Jacobian matrix evaluated at the Roe's average, see [Roe 1981] for details. Of course other method are applicable.

Time stepping procedure

To finish with the discretization, the time step evolution is evaluated taking into account Δt_{Ω_j} for any realization Ω_j, which is obtained under classical CFL stability conditions. Thus the general time step is evaluated as

$$\Delta t = \min_{\Omega_j} \Delta t_{\Omega_j}. \tag{3.22}$$

Implementation issues

The deterministic scheme is sketched in the Algorithm 1 in order to better show in the Algorithm 2 what are the modifications. The Algorithm 3 shows how to implement the stochastic resolution of the system (3.14). As indicated, the modifications to the deterministic code are rather small. The first loop, on top of all the others, is a loop over the iterative parameter introduced in (3.8). It already exists in the deterministic method, see Algorithm 1.

Algorithm 1: Flow chart for the deterministic scheme (3.7).

Initialise U^0
for n:= 1 to $nmax$: Deterministic loop **do**
  From U^n, evaluate the relevant parameters V^n for the solver $\Im$,
  Evaluate $\Im(V^n) = U^{n+1}$.

The second loop, enclosed by the previous one, is a loop over the subsets Ω_j which also does not induce any modification of the code. In this loop, we first evaluate the reconstruction polynomials (in the stochastic direction), and for each quadrature points in (3.11), we evaluate the relevant data to be sent to the deterministic solver. Then we apply the deterministic solver $\Im$ on this datum. Once this loop is done, we evaluate U^{n+1}, the vector made of $\{E(U^n|\Omega_j)\}_{\Omega_j}$ as in the quadrature formula (3.11).

This method is further exemplified for (3.14) in algorithm 3.

Algorithm 2: Flow chart for the system (3.14). The deterministic sequence are underlined, they corresponds to the steps of the deterministic algorithm 1.

for j:=1 to $jmax$: Probabilistic loops **do**
  Evaluate U_j^0, the initial condition.
for $n := 1$ to $nmax$: Deterministic loop **do**
  for j:=1 to $jmax$: Probabilistic loops **do**
    For each Ω_i, evaluate the reconstruction polynomial $R(U^n)_i(x,\omega)$.
    for $j^{quad} := 1$ to j_{max}^{quad} : Quadrature loop: **do**
      Evaluate the relevant parameters $V^n_{jquuad} = R(U^n)_i(x,\omega_{j^{quad}})$
      Evaluate $\Im(V^n_{j^{quad}}) = U^{n+1}_{j^{quad}}$.
    From the $\{U^{n+1}_{j^{quad}}\}_{j^{quad}}$, evaluate U^{n+1} from the quadrature formula (3.11).

Algorithm 3: Flow chart for the system (3.14). The deterministic steps are underlined

for n:= 1 to $nmax$: Deterministic loop **do**
  for j:=1 to $jmax$: Probabilistic loops: **do**
    for $j^{quad} := 1$ to j_{max}^{quad} : Quadrature loop: **do**
      Reconstruct a piecewise polynomial $u^n_{j_{quad}}(x)$ of $u^n(x, X(\omega))$ in each cell Ω_j
      for $i := 1$ to i_{max} : Deterministic loop **do**
        reconstruct a piecewise polynomial $u^n_{i,j^{quad}}$ of $u^n_{j^{quad}}(x)$ in each cell C_i
        Compute fluxes $F(u^n_{i+1,j_{quad}}, u^n_{i,j_{quad}})$, ... using deterministic solver
        Control time step $\Delta t_{\Omega_{j_{quad}}}$
      compute expectancies $E(F(u^n_{i+1}, u^n_i)|\Omega_j)$, ... using quadrature formula
      update probabilistic time step $\Delta t_{\Omega_j} = \min_{\Omega_{j_{quad}}}(\Delta t_{\Omega_{j_{quad}}})$
    update total time step $\Delta t = \min_{\Omega_j}(\Delta t_{\Omega_j})$
  for $j := 1$ to j_{max} : Probabilistic loop **do**
    for $i := 1$ to i_{max} : Deterministic loop **do**
      update values

$$u^{n+1}_{i,j} = u^n_{i,j} + \frac{\Delta t}{|C_i|}\Big(E(F(u^n_{i+1}, u^n_i)|\Omega_j) - E(F(u^n_i, u^n_{i-1})|\Omega_j)\Big)$$

3.1.2 Some significant results

3.1.2.1 Kraichnan-Orszag problem

The Kraichnan Orszag three-modes problem has been introduced by Kraichnan [Kraichnan 1963] and Orszag [Orszag 1967]. It has been intensively studied to study the loss of accuracy of gPC expansion for problems involving long time integration. In [Wan 2005], the exact solution is given, and different computations have been performed in [Wan 2005, Wan 2006a, Foo 2008, Gerritsma 2010, Agarwal 2009, Ma 2009a]. This problem is defined by the following system of nonlinear ordinary differential equations

$$\begin{aligned} \frac{\mathrm{d}y_1}{\mathrm{d}t} &= y_1 y_3, \\ \frac{\mathrm{d}y_2}{\mathrm{d}t} &= -y_2 y_3, \\ \frac{\mathrm{d}y_3}{\mathrm{d}t} &= -y_1^2 + y_2^2 \end{aligned} \tag{3.23a}$$

subject to stochastic initial conditions

$$y_1(0) = y_1(0;\omega), \qquad y_2(0) = y_2(0;\omega), \qquad y_3(0) = y_3(0;\omega). \tag{3.23b}$$

In general, uniform distributions are considered, except in [Wan 2006a] where beta and Gaussian distributions are also taken into account. The computational cost of SI method for the K-O problem is compared to that of other methods, namely a quasi-random Sobol (MC-SOBOL) sequence with $8\dot{1}0^6$ iterations, and a Polynomial Chaos Method (PC) with Clenshaw-Curtis sparse grid. The error in variance of y_1 is considered at a final time t_f of 50. We define the error between two numerically integrated functions $f_1(t_j)$ and $f_2(t_j)$, $j = 1, \cdots, n_t$, as:

$$\varepsilon_{L^2} = \frac{\frac{1}{n_t}\sqrt{\sum_{j=1}^{n_t}\left(f_1(t_j) - f_2(t_j)\right)^2}}{\frac{1}{n_t}\sqrt{\sum_{j=1}^{n_t}\left(f_1(t_j)\right)^2}},$$

where f_1 is considered the Monte Carlo converged solution. Similarly, the L_∞ error is defined by

$$\varepsilon_{L^\infty} = \frac{max_{j=1,\ldots,n_t}\left|f_1(t_j) - f_2(t_j)\right|}{max_{j=1,\ldots,n_t}\left|f_1(t_j)\right|}.$$

For different error levels, corresponding computational cost is computed.

1D

First, we study the 1D problem corresponding to initial conditions of the form

$$y_1(0) = 1.0, \qquad y_2(0) = 0.1\xi, \qquad y_3(0) = 0.0,$$

where ξ is a uniformly distributed random variable varying in $[-1, 1]$. We use SI, MC-SOBOL and PC method to compute the variance of y_1. In Table 3.1.2.1, we show the results in terms of number of samples required to reach a prescribed error in the L^2 and L^∞ norms. The performance of the SI method are comparable and even better than PC method, at least on this problem.

Then, the same problem described previously but with a different probability distribution for $y_2(0)$ has been considered. In particular, ξ is discontinuous on $[a, b] = [-1, 1]$ with a density defined by :

$$f(\gamma) = \frac{1}{M} \times \begin{cases} \dfrac{1+\cos(\pi x)}{2} & \text{if } x \in [-1, 0] \\ 10 + \dfrac{1+\cos(\pi x)}{2} & \text{if } x \in [0, 1] \\ 0 & \text{else} \end{cases} \tag{3.24a}$$

Error level ε_{L^2}	$MC-SOBOL$	PC	SI
10^{-1}	75	24	24
10^{-2}	520	37	36
10^{-3}	4500	85	82

Table 3.1: Number of samples required for the 1D K-O problem for time $t\,\varepsilon\,[0,10]$. The error norm is L_∞.

and $M = \frac{11}{2}$ to ensure normalization.

Because of the discontinuous pdf, only MC-SOBOL and SI solutions can be compared, showing the great flexibility given by SI method with respect to the form of the pdf. In Figure 3.1, variance of $y_1(t)$ is reported for the converged solutions obtained with MC-SOBOL and SI. The SI method permits to reproduce exactly MC-SOBOL solution. In Figure 3.2, a convergence study for SI is reported by using an increasing number of points in the stochastic space. In Table 3.2, we reported number of samples required to reach a prescribed error ε_{L^2}. The SI method shows to be very competitive in terms of efficiency and computational cost with respect to MC-SOBOL method when whatever form of pdf is used (a discontinuous pdf in this case). Let us remark that a uniform grid is used in the stochastic plane *without* any type of adaptation. This displays the great potentiality of this method if coupled with an adaptive methods.

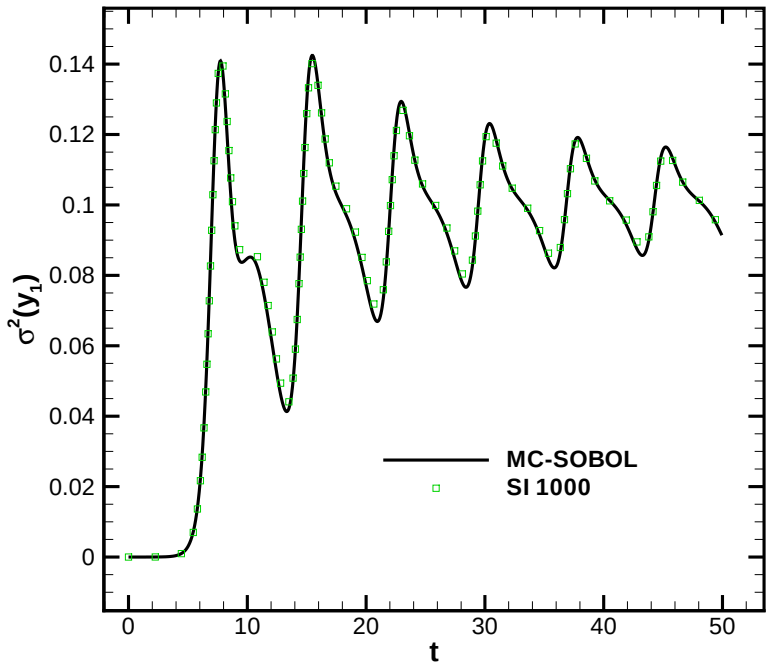

Figure 3.1: Variance of y_1 computed by means of SI and MC-SOBOL methods.

2D

Then, we use SI method to study the K-O problem with two-dimensional random inputs:

$$y_1(0) = 1.0, \qquad y_2(0) = 0.1\xi_1, \qquad y_3(0) = \xi_2,$$

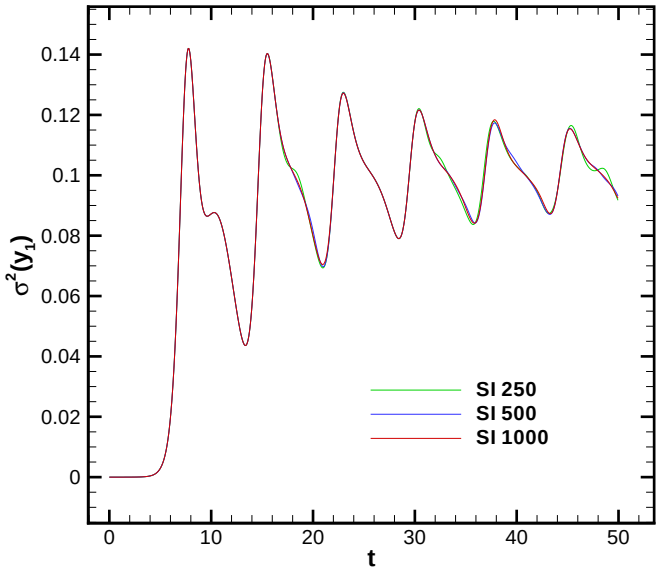

Figure 3.2: Variance of y_1 computed by means of SI for different meshes in the stochastic space.

Error level ε_{L^2}	$MC-SOBOL$	SI
10^{-1}	60	15
10^{-2}	450	240
10^{-3}	3500	1400

Table 3.2: Number of samples required for the 1D-discontinuous K-O problem for time $t\,\varepsilon\,[0,50]$. The error norm is L_∞.

where ξ_1 is discontinuous on $[a,b]=[-1,1]$ with a density defined by (3.24) and ξ_2 is a uniform random variable in [-1,1].

In Figure 3.1.2.1, the SI capability to reproduce exactly MC-SOBOL solution is represented. The SI and MC-SOBOL solutions are nearly coincident also for long time ($t=50$). The mesh convergence study in the stochastic space for SI is reported in Figure 3.1.2.1 showing that the solution obtained with a mesh of 320×320 is well converged. In Table 3.3, the computational cost required to reach a prescribed error of ε_{L^2} is reported. Reductions from 50% to 66% are obtained using SI with respect to MC-SOBOL solutions. Once again, let us emphasis that these results have been obtained *without* any mesh adaptation, contrarily to [Gerritsma 2010]. In our case, adaptivity is doable and certainly much better results in term of cost could be obtained in that case. Our emphasis here is to show the potential of the method without any fancy subtilities and improvements.

Error level ε_{L^2}	$MC-SOBOL$	SI
10^{-1}	400	170
10^{-2}	18000	4000
10^{-3}	400000	160000

Table 3.3: Number of samples required for the 2D-discontinuous K-O problem for time $t\,\varepsilon\,[0,50]$. The error norm is L_∞.

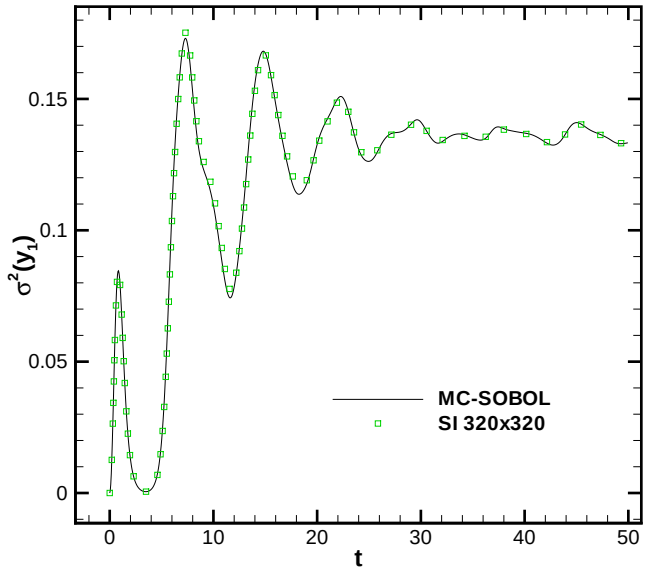

Figure 3.3: Variance of y_1 computed by means of SI and MC-SOBOL methods.

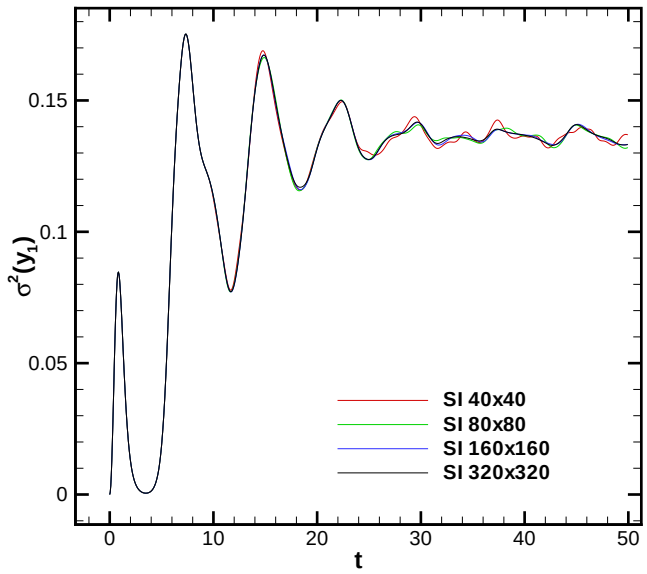

Figure 3.4: Variance of y_1 computed by means of SI for different meshes in the stochastic space.

3.1.2.2 Nozzle flow with shock

The steady shocked flow in a convergent-divergent nozzle is taken into account with a fixed (deterministic) geometry:

$$A(x) = \begin{cases} 1 + 6(x - \frac{1}{2})^2 & \text{for} \quad 0 < x \leq \frac{1}{2} \\ 1 + 2(x - \frac{1}{2})^2 & \text{for} \quad \frac{1}{2} < x \leq 1 \end{cases}$$

The outlet pressure (subsonic outlet flow with $p_e = 1.6529$ bar) is chosen in order to have a compression shock in the divergent part of the nozzle, exactly located at $x = 0.75$. For the other boundary conditions, a subsonic inlet flow with a stagnation pressure $p_0 = 2$ bar and a stagnation temperature $T_0 = 300$ K are considered. The mean γ is 1.4. Two test-cases are considered. First, an uncertain heat coefficient ratio γ is assumed. The random parameter $\omega = \gamma$ varies within the range $[1.33, 1.47]$, following various choices of pdf (uniform and discontinuous) described below. In the second test-case, two-uncertainties stochastic problem is solved where γ follows a discontinuous pdf and the subsonic outlet flow varies uniformly within the range $1.6529 \pm 2\%$.

The random parameter ω (defining either the heat ratio or the subsonic outlet flow) ranges between ω_{min} and ω_{max}; the interval $[\omega_{min}, \omega_{max}]$ is mapped onto $[a, b]$ by a linear transformation and the pdf on $[a, b]$ is either :

- uniform with $\omega \in [a, b] = [0, 1]$,
- discontinuous on $[a, b] = [0, 1]$ with a density defined (3.24).

Again, various stochastic methods are used to compute statistics of the supersonic nozzle. In a first step, a uniform pdf on γ is used in order to compare MC-SOBOL, PC and SI. In a second step, γ follows (3.24) and we compare MC-SOBOL and SI to demonstrate the flexibility, and the accuracy, offered by the SI method.

After a study on the grid convergence, the 1D physical space is divided in 201 points (with the normalized geometric domain that varies from 0 to 1). The base scheme is a standard TVD scheme using MUSCL extrapolation on the characteristic variables with Roe flux and Harten-Yee entropy fix. The scheme is implicit to speed up the convergence to steady state. The code has been modified along the lines of the algorithms 2. A preliminary convergence study with respect to the stochastic estimation has been realized, by using an increasing refinement of the probabilistic space discretization in the case of the SI method, and an increasing polynomial order in the case of PC method. The probabilistic space discretization varies from 5 to 160 points (in practice: 5, 10, 20, 40, 80, 160 points), while the polynomial order varies from 2 to 100. Next, the stochastic solutions are compared computing the mean and the variance of the Mach number and pressure distributions along the nozzle using various choices of pdf for γ. Finally, a comparison in terms of computational cost is performed by computing error ε_{L^2} with respect to x. In Figure 3.5, the mean solutions of Mach number and the pressure along the 1D nozzle are reported, where the mean stochastic solutions are computed with the SI method using 10 points in the probabilistic space and the PC method using a 10th order polynomial, with γ described by a uniform pdf (γ varying between 1.33 and 1.47). As can be observed in Figure 3.5, the mean flow is characterized by an isentropic region of increasing speed or Mach number between $x = 0$ and the mean shock location in the divergent (the flow becoming supersonic at the nozzle throat located in $x = 0.5$), followed by a subsonic flow behind the shock with decreasing speed. The mean solutions computed by the two UQ methods are coincident. Next the standard deviation of the Mach number is computed along the nozzle by using different refinement levels for the probabilistic space in the case of the SI method and different polynomial order in the case of the PC method, always keeping a uniform pdf for γ. In Table 3.4, the number of samples required to reach a prescribed error ε_{L^2} is reported for each strategy. The SI method demands fewer points in the stochastic space for a given level of error.

Error level ε_{L^2}	$MC-SOBOL$	PC	SI
10^{-1}	5	6	5
10^{-2}	24	19	10
10^{-3}	70	59	40

Table 3.4: Number of samples required for the 1-uncertainty nozzle problem, uniform pdf.

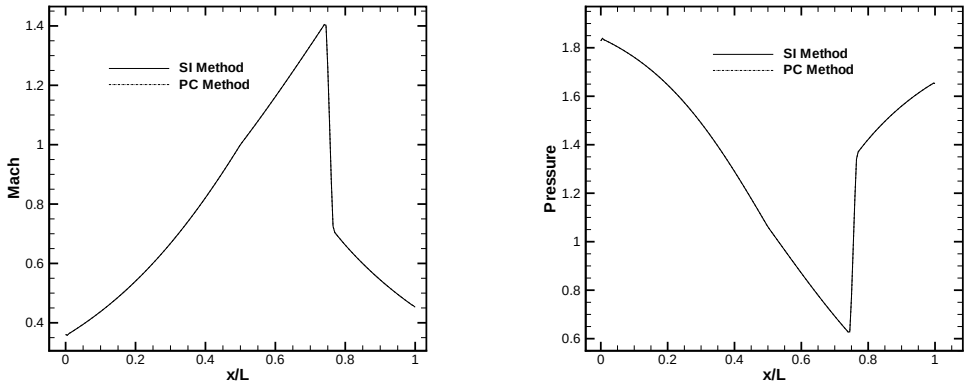

Figure 3.5: Nozzle flow with uncertain γ (uniform pdf). Computed mean distribution for the Mach number (left) and the static pressure (right) using the semi-intrusive method with 10 points in the probabilistic space and the PC method with a 10th order polynomial.

Then, a discontinuous pdf is considered for the stochastic γ. It is interesting to show the kind of innovative contribution the SI method can bring with respect to the PC method (in its classical version). To this end, in Figure 3.6, the standard deviation of Mach is reported along the nozzle when the discontinuous pdf (3.24) is considered. Note that choosing (3.24)) to describe the random variable γ introduces no change whatsoever in the application of the SI method (while the PC method can no longer be used. The standard deviation of the Mach number distribution computed for this discontinuous pdf is plotted in Figure 3.6 for several levels of discretization refinement in the probabilistic space: here again the result can be considered as almost converged with no more than a 40-point discretization and fully converged with a 80-point discretization. In Figure 3.7, the standard deviation of the Mach is reported along the nozzle for the discontinuous pdf by using SI and MC-SOBOL methods. The standard deviation distributions computed by means of the SI and MC-SOBOL methods are coincident, even for the maximal standard deviation. The stochastic estimation remains globally very similar for the newly proposed SI approach and the well-established MC-SOBOL method, which allows to validate the SI method results for the case of a discontinuous pdf on γ. Let us estimate the respective computational cost of SI, MC-SOBOL for this case. In Table 3.1.2.2, the number of samples required to reach a prescribed error for ε_{L^2} is reported for the SI and MC-SOBOL methods. A drastic reduction of the computational cost is obtained by using the SI method with respect to MC-SOBOL solutions.

Error level ε_{L^2}	$MC-SOBOL$	SI
10^{-1}	4	5
10^{-2}	42	20
10^{-3}	250	40

Table 3.5: Number of samples required for the 1-uncertainty nozzle problem, discontinuous pdf

Next, a two-uncertainties stochastic problem is considered by assuming a discontinuous pdf for γ and a uniform pdf for p_e. In Figure 3.8, the standard deviation of the Mach is reported along the nozzle for SI and MC-SOBOL. The standard deviation distributions computed by means of SI and MC-SOBOL are coincident. As shown in Table 3.6, the SI method allows strongly reducing the computational cost until six times with respect to MC-SOBOL method.

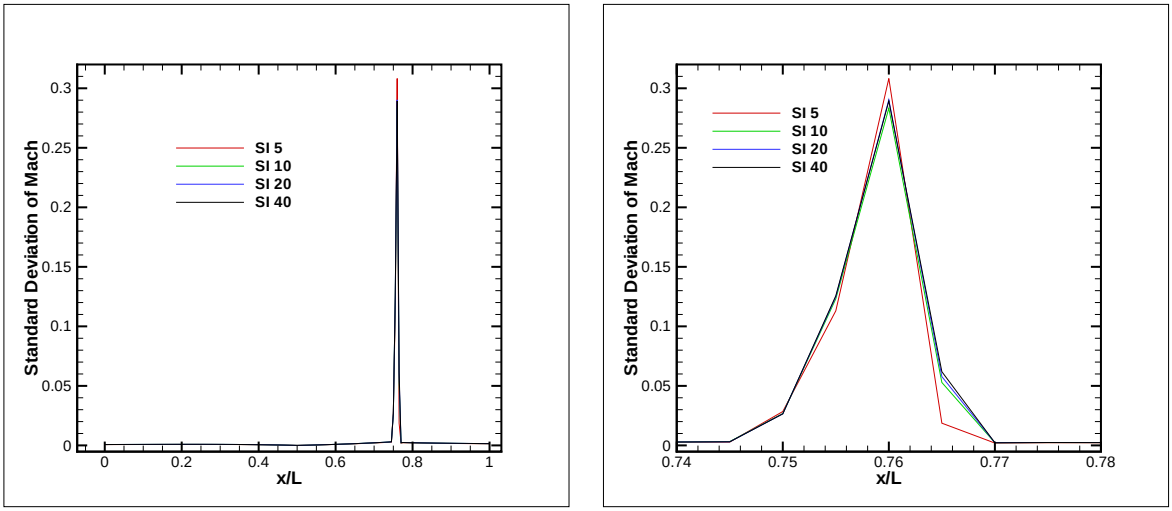

Figure 3.6: Nozzle flow with uncertain γ (discontinuous pdf). Convergence study for the standard deviation on the Mach number distribution computed using the SI method.

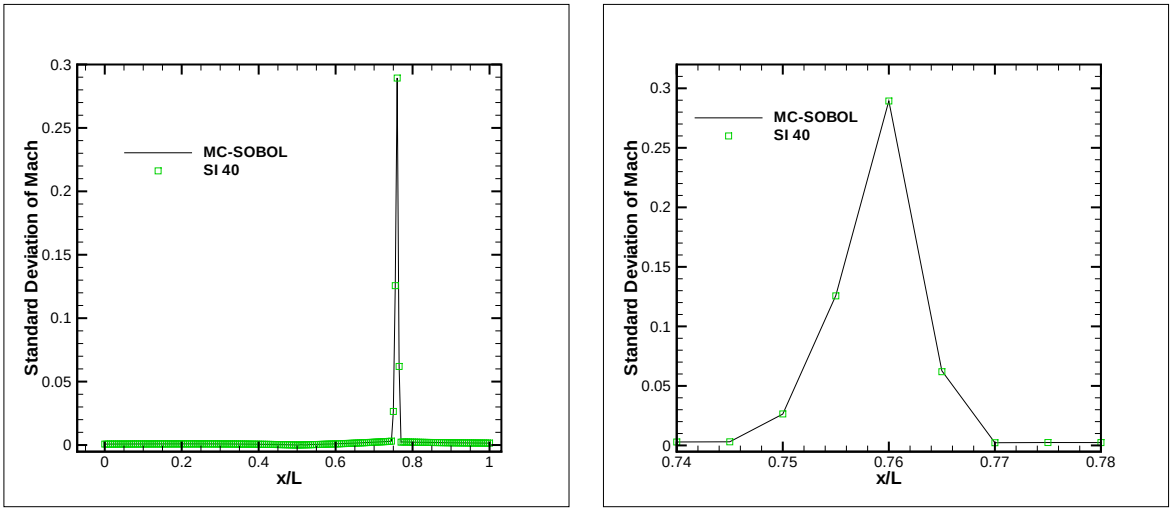

Figure 3.7: Nozzle flow with uncertain γ (discontinuous pdf). Standard deviation for the Mach number distribution for MC-SOBOL and SI methods. Left : global view; right : close-up on the shock region.

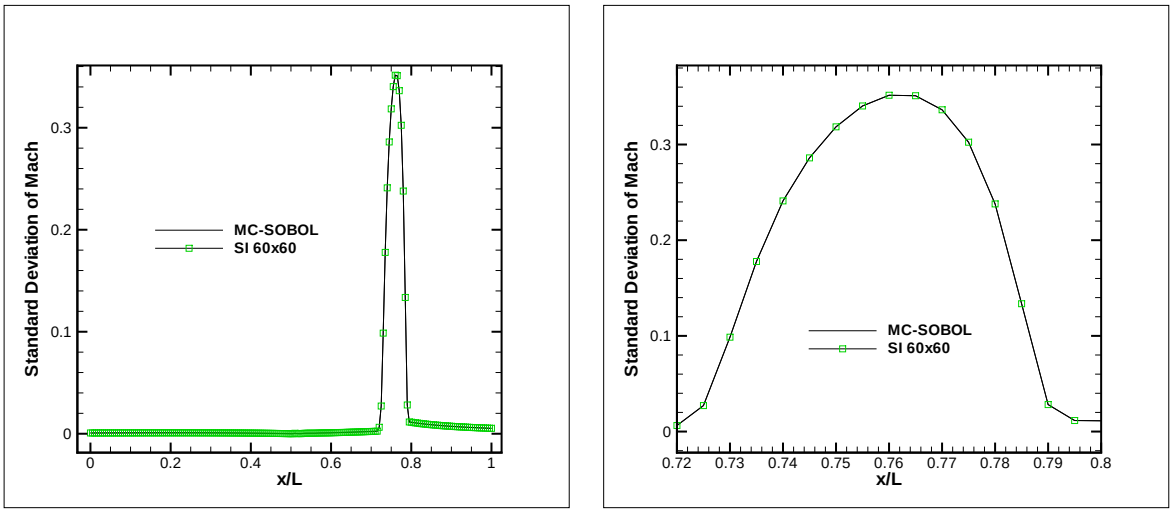

Figure 3.8: Nozzle flow with uncertain γ (discontinuous pdf) and p_e (uniform pdf). Standard deviation for the Mach number distribution for MC-SOBOL and SI methods. Left : global view; right : close-up on the shock region.

Error level ε_{L^2}	$MC-SOBOL$	SI
10^{-1}	35	25
10^{-2}	1000	400
10^{-3}	20000	3600

Table 3.6: Number of samples required for the 2-uncertainties nozzle problem, discontinuous pdf

3.1.2.3 Viscous Burgers equation

In this section, we show how higher order reconstruction techniques affect the accuracy of the numerical solution with respect to a reference analytical solution. Let us consider the viscous Burger's equation

$$\frac{1}{2}\frac{\partial u^2}{\partial x} = \nu \frac{\partial^2 u}{\partial x^2}, \tag{3.25}$$

where $x \in [0,1]$ and $u(0) = 1$ and $u(1) = -1$. We take

$$\nu = 0.1 + 0.2\big(\cos(2\pi\omega) + 1.\big) \tag{3.26}$$

with a uniform $\omega \in [0,1]$.

The computation is initialized by using $u^0 = 1-2x$ and run up to convergence. For this equation, it is possible to compute exactly the solution $u_\nu(x) = \tanh\left(\frac{x}{2\nu}\right)$ and the associated variance.

Several probabilistic reconstructions have been used, here are our notations for the Figures

- O3 and centered five points: for the cell j, use $j-2$, $j-1$, $j+1$ and $j+2$ (probabilistic indices).
- O2 and centered 3 points : for the cell j, use $j-1$ and $j+1$ (probabilistic indices).
- ENO : ENO reconstruction using the cells j $j-1$ and $j+1$ for the cell j,
- O1 : use the cell j only.

The figure 3.9 displays the solution (with a zoom on the right) for $\Delta x = \frac{1}{41}$, $\delta\omega = \frac{1}{11}$.

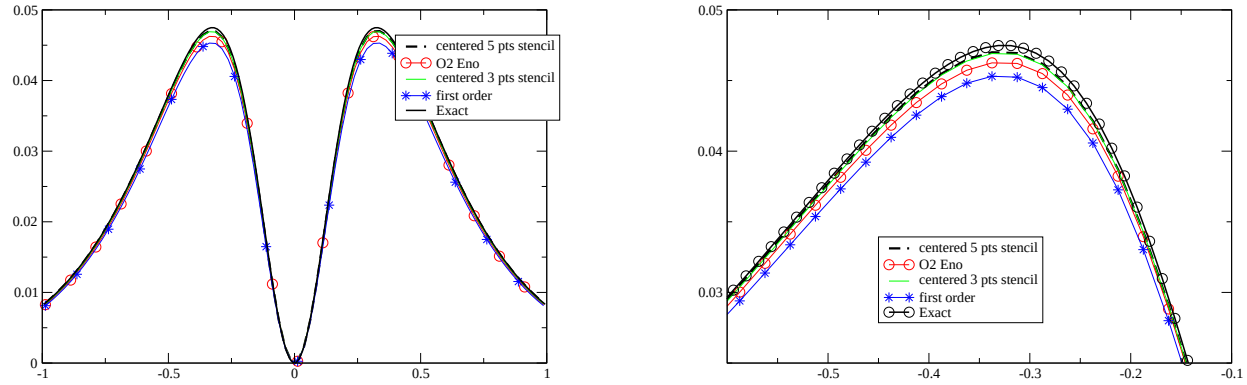

Figure 3.9: For a fixed spatial resolution and a fixed "probabilistic" resolution, comparison of the O3,O2,ENO and first order reconstructions. The exact variance is obtained from the exact solution with $\Delta x = 1/160$ and $\Delta\omega = 1/40$.

As expected higher is the formal accuracy, better are the results. In particular, the centered 3 points reconstruction gives the best results with respect to the exact solution while the less accurate solution have been obtained by using the first order reconstruction.

These behavior is confirmed by a convergence analysis, as shown in Figure 3.10, where L^2 and L^∞ norms of the variance have been reported for several spatial resolutions. Remark that the error saturates (i.e. if $\delta\omega$ is too large, the main error is the spatial error), and this error decreases when Δx decreases. Finally, these results show how the statistics accuracy can be improved by using an higher reconstruction order in the stochastic space.

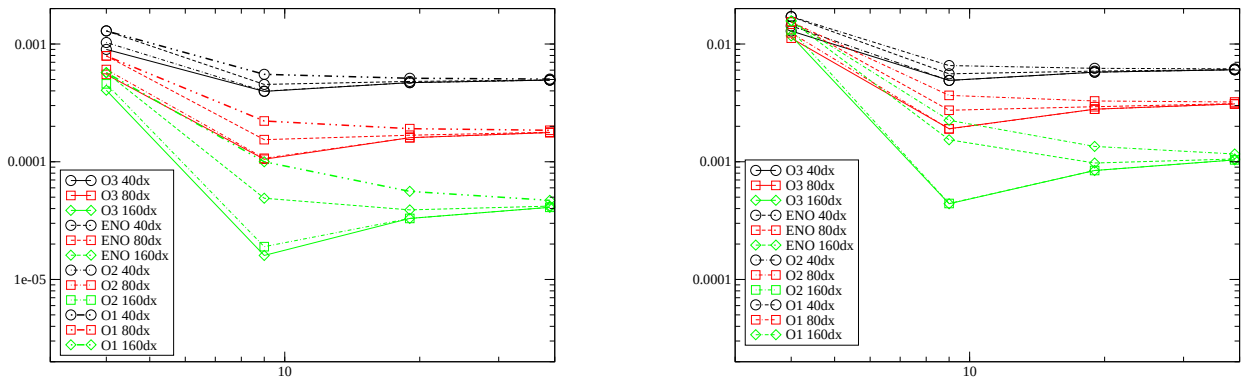

Figure 3.10: For the O3,O2,ENO and first order reconstruction, evaluation of the (spatial) L^2 and L^∞ norms of the variance for the spatial resolutions of $\Delta x = 1/40, 1/80, 1/160$. Left : L^2 norm, right :L^∞ norm

3.1.3 Conclusions

This study deals with the formulation of a semi-intrusive (SI) method allowing the computation of statistics of linear and non linear PDEs solutions. This method is said semi-intrusive because it requires only a limited amount of modifications in a deterministic flow solver to quantify uncertainty on the flow state when the flow solver includes uncertain variables. Then, it can be considered as very easy to implement in comparison with other intrusive methods, like as Polynomial Chaos. This method shows to be very efficient to deal with probability density function of whatsoever form, long-term integration and discontinuities in stochastic space. Several test cases have been considered. First, a modified version of the Kraichnan-Orszag three-modes problem has been taken into account by considering a discontinuous pdf for the stochastic variable. This test is very challenging seeing that other intrusive methods well known in literature can suffer of long time integration problems even for uniform pdf. The SI method displays good results and a drastic improvement in computational time with respect to Monte Carlo solutions. Secondly, a stochastic nozzle flow has been considered with discontinuous pdf again, where SI shows large reduction of computational cost with respect to Monte Carlo solution. Then, SI has been applied to solve the viscous Burgers equation with several probabilistic reconstruction of stochastic space. As expected, higher order reconstruction allow to reduce the error by using the same number of points in the stochastic space, displaying the interest to use more accurate reconstruction in order to improve numerical accuracy of statistic properties.

Let us emphasis that the results presented in this study have been obtained by using always a uniform grid in the stochastic space without any kind of adaptivity. For this reason, a multi-resolution based algorithm has been developed. This is illustrated in the next section.

3.2 Adaptive semi-intrusive Method

3.2.1 Introduction and motivation

Following the general idea of a semi-intrusive propagation of the uncertainties, we introduced in [4] (see Section 12.6) a point-value setting in the multiresolution (MR) framework to represent data in the stochastic space. The multiresolution representation of data permits to increase the efficiency of the numerical code for the solution of stochastic partial differential equations. The idea of introducing the MR representation of data, in the context of stochastic problem, is not totally new. In [Le Maître 2010b], a multiresolution basis is employed to represent the solution of a partial differential equations after fixing the physical coordinate. This representation is very efficient but limited to the case where the stochastic representation is used at a fixed physical location. To overcome this issue, more recently, Tryoen et al. introduced in [Tryoen 2010] a multiresolution wavelets representation in the context of intrusive Galerkin projections. However, the Galerkin approach presented remains very problem-dependent. This approach is limited by the spatial and time discretization accuracy (only first order) that could dominate the overall accuracy. Moreover, the approach that we proposed in [4] has the advantage to remain very general, not limited from the order of the spatial and time discretization, from the probability density function (that can be even discontinuous and time varying) and, eventually, from the geometry of the stochastic space in the case of multidimensional problems.

In this section, the MR is presented in the cell-average framework and the representation is implemented in the SI scheme. Moreover, we demonstrate the advantages of the introduction of a real-time adaptivity in the stochastic space, by following the evolution of the solution in the overall physical and stochastic space. This is shown by comparing the accuracy, at a fixed computational cost, with and without the adaptivity based on the MR framework on the original SI scheme. Different reference test-cases are performed for which the reference solution can be obtained in an analytical or semi-analytical approach.

Section 3.2.2 illustrates the multi-resolution framework of Harten, generalized for the stochastic space, where a cell-average setting is chosen. In particular the Truncate and Encode algorithm is presented in Section 3.2.2.1 where the representation of the discrete data is obtained from the coarsest level towards the finest. The semi-intrusive scheme is detailed for the MUSCL-Hancock method in Section 3.2.3. The overall formulation of the adaptive semi-intrusive scheme is presented in Section 3.2.4. Several numerical results are presented in Section 3.2.5. In particular, the introduction of the adaptive representation of data in the stochastic space is demonstrated to improve the spatial convergence and to cure the staircase approximation phenomenon with respect to an equivalent not adapted solution. The linear advection equation, the inviscid Burgers equation and an uncertain version of the Sod shock tube are performed as test-cases. Concluding remarks are reported in Section 3.2.6.

3.2.2 The cell-average multiresolution setting

In this section, the multiresolution framework in a cell-averaged representation of data is presented. The original Harten's framework [Harten 1993, Harten 1994, Harten 1995, Abgrall 1998] is here modified to allow an efficient representation of data with respect to a general weighted function. In the context of UQ, the weighted function is easily identified as the probability distribution of the input parameters.

In this study, only the cell-average framework is analyzed and this choice allows a straightforward extension of the finite volume representation of data in the coupled physical/stochastic space as already shown in [Abgrall 2011] employing only uniform meshes in both spaces (see later Section 3.2.3).

The Harten framework can be considered, as pointed out by Aràndiga and Donat in [Arandiga 2000], as a rearrangement of the information in a set of discrete data representing different resolution levels. This rearrangement of data with the addition of a truncation procedure could yield a reduction of the computational cost and of the memory usage associated to the representation/calculation and memorization of discrete data.

The Harten framework can be viewed as a more general framework with respect to the classical wavelets framework in which the hierarchical representation of data is obtained by means of a functional basis based on a dilating equation and a so called mother wavelets. As presented in [Arandiga 2009] the dilating equation in a general space can be difficult to solve, especially for domains of complex geometries. The Harten framework is capable to avoid the solution of a dilating equation obtaining a local polynomial basis for general geometries with, eventually, data-dependent strategies for the representation of data. All this features makes the Harten framework, an optimal starting point for the development of a general framework for the representation of data.

Two building blocks exist: a discretization operator $\mathcal{D}_k$ and a reconstruction operator $\mathcal{R}_k$. Both operators operates between the continuous space to represent (the stochastic space in this context) and one of its discrete representation, for instance the resolution level $k-$th. The knowledge of the these two operators allow to define in an unique way two other operators working on data rearrangement between different resolution levels. These discrete operators between consecutive levels k (higher resolution) and $k-1$ (lower resolution) are the operators of decimation D_k^{k-1} and prediction P_{k-1}^k.

In this section, we consider the cell-average framework. Let us consider a function $f = f(\boldsymbol{\xi})$, $f : \Xi \subset \mathbb{R}^d \to \mathbb{R}$ with d the number of uncertain parameters. In the classical MR cell-average framework, $f \in \mathcal{F}$ where $\mathcal{F}$ is the functional space of the absolutely integrable functions $\mathcal{F} = L^1(\Xi)$. However, in the context of UQ, $\mathcal{F}$ is identified with L^2 to deal with function with finite variance. Let us consider the probability density function $p(\boldsymbol{\xi})$ and let us define the following measure:

$$\mathrm{d}\mu(\boldsymbol{\xi}) = p(\boldsymbol{\xi})\mathrm{d}\boldsymbol{\xi}. \tag{3.27}$$

If the stochastic space is represented by means of a non-overlapping tessellation

$$\Xi = \bigcup_{j=1}^{N_\xi} \Xi_j, \quad \text{with} \quad \Xi_i \cap \Xi_j = 0 \quad \text{if} \quad i \neq j. \tag{3.28}$$

the measure of each element of the tessellation can be found as follows

$$\mu(\Xi_j) = \int_{\Xi_j} \mathrm{d}\mu(\boldsymbol{\xi}). \tag{3.29}$$

Let us consider a set of discrete operators of discretization $\{\mathcal{D}_k\}_{k=0}^{L}$, each of them defined on a vectorial space of finite dimension

$$\mathcal{D}_k : \quad \mathcal{F} \to V_k \quad \text{with} \quad \dim(V_{k+1}) > \dim(V_k) = J_k. \tag{3.30}$$

The sequence $\{\mathcal{D}_k\}_{k=0}^{L}$ has to be nested according to the following properties:

- $\mathcal{D}_k$ is onto
- the null space of each level include the null space associated to the previous resolution level $\mathcal{N}(\mathcal{D}_k) \subset \mathcal{N}(\mathcal{D}_{k+1})$.

These properties reflect in the following relation between discretization operators

$$\mathcal{D}_{k+1}(f) = 0 \Rightarrow \mathcal{D}_k(f) = 0 \quad \forall f \in \mathcal{F}. \tag{3.31}$$

A such operator on the k-th level can be defined over the j-th cell Ξ_j^k as

$$(\mathcal{D}_k f)_j \overset{\text{def}}{=} \frac{1}{\mu(\Xi_j^k)} \int_{\Xi_j^k} f(\boldsymbol{\xi}) \mathrm{d}\mu(\boldsymbol{\xi}) = v_j^k. \tag{3.32}$$

Thanks to the onto property of each operator $\mathcal{D}_k$, the reconstruction operator $\mathcal{R}_k$ can be defined as its right-inverse

$$\mathcal{R}_k : \quad V_k \to \mathcal{F}. \tag{3.33}$$

The reconstruction operator is not required to be linear and this makes the Harten's multiresolution more general with respect to the wavelets framework [Getreuer 2008].

The reconstruction operator $\mathcal{R}_k$ for the cell average setting originally has been introduced by Harten in the 1D case employing the concept of reconstruction via primitive function. In practice, the cell-averaged function is replaced by a point valued function that corresponds to its primitive in the nodes of the mesh. A more convenient approach can be adopted, following Abgrall and Sonar [Abgrall 1997a], even for multidimensional problems on unstructured meshes [Abgrall 1998]. Fixed a polynomial degree of reconstruction r, a stencil $\mathcal{S}_j^k$ of cells with cardinality $s = s(r) = \mathrm{card}(\mathcal{S}_j^k)$ can be fixed. On each stencil $\mathcal{S}_j^k$, a polynomial $\mathcal{P}_j^k(\boldsymbol{\xi}; f)$ of degree r can be constructed. The admissibility of this stencil obeys to a Vandermonde condition (see for further details [Abgrall 1997a]). Supposing the stencils admissible, the conditions to satisfy for the computation of $\mathcal{P}_j^k$ is

$$\mathcal{D}_k(\mathcal{P}_j^k(\boldsymbol{\xi}; f))_l = \mathcal{D}_k(f)_l, \quad \forall l \in \mathcal{S}_j^k. \tag{3.34}$$

The reconstruction operator $\mathcal{R}_k$ in this case is exactly equal to the union of all the polynomial $\mathcal{P}_j^k$ defined on all the cells Ξ_j^k.

The two operators $\mathcal{D}_k$ and $\mathcal{R}_k$ should satisfy a consistency relationship between them

$$(\mathcal{D}_k \mathcal{R}_k)(v) = v \quad \forall v \in V_k, \tag{3.35}$$

thus implying $\mathcal{D}_k\mathcal{R}_k = \mathrm{I}_k$ where I_k is the identity operator on V_k.

For the nested sequence whose elements are defined in (3.30), the decimation operator D_k^{k-1} can be defined, which is a linear mapping between V_k onto V_{k-1}:

$$\mathrm{D}_k^{k-1}: \quad V_k \to V_{k-1}, \tag{3.36}$$

where

$$\mathrm{D}_k^{k-1} v^k = \mathcal{D}_{k-1} f \in V_{k-1} \quad \forall v^k = \mathcal{D}_k f \in V_k. \tag{3.37}$$

The decimation operator, independent from the particular f, is employed to generate recursively the set of discrete data from the highest resolution level ($k = L$) to the lowest ($k = 0$) $\{v^k\}_{k=0}^{L-1}$,

$$v^{k-1} = \mathrm{D}_k^{k-1} v^k \quad \forall k = L, L-1, \ldots, 1. \tag{3.38}$$

By an agglomeration (splitting) procedure, for a generic mesh, even non structured, it is always possible to obtain a less (higher) resolution level. To each cell Ξ_j^k at the lower resolution level corresponds a number of cell ($\bar{l}_c$) at the higher resolution level. To preserve the nested character between levels, the following properties between meshes should hold:

$$\Xi_j^k = \sum_l^{\bar{l}_c} \Xi_l^{k+1}. \tag{3.39}$$

In the following, without loss of generality, $\bar{l}_c = 2$. This happens naturally for the 1D case of equally splitted cells between levels in the case of regular nested meshes.

In this case, the decimation operator (see Figure 3.11) could be obtained as follows

$$\begin{aligned}(\mathrm{D}_k^{k-1} v^k)_j = (\mathrm{D}_k^{k-1}\mathcal{D}_k f)_j = (\mathcal{D}_{k-1} f)_j &= \frac{1}{\mu(\Xi_j^{k-1})} \int_{\Xi_j^{k-1}} f(\boldsymbol{\xi}) \mathrm{d}\mu(\boldsymbol{\xi}) \\ &= \frac{1}{\mu(\Xi_j^{k-1})} \left(\mu(\Xi_{2j}^k)(\mathcal{D}_k f)_{2j} + \mu(\Xi_{2j-1}^k)(\mathcal{D}_k f)_{2j-1} \right).\end{aligned} \tag{3.40}$$

Moreover, the prediction P_{k-1}^k allows to approximate the set of data v^k from v^{k-1}

$$v^k = \mathcal{D}_k f \approx \mathcal{D}_k(\mathcal{R}_{k-1} v^{k-1}). \tag{3.41}$$

This leads to the definition of the prediction operator P_{k-1}^k between discrete data on successive resolution level as

$$\mathrm{P}_{k-1}^k \stackrel{\text{def}}{=} \mathcal{D}_k \mathcal{R}_{k-1}: \quad V^{k-1} \to V^k. \tag{3.42}$$

The prediction operator P_{k-1}^k is obtained following the definition (3.42) and using first the reconstruction procedure (3.34) for the level $k-1$th, and then applying the discretization operator $\mathcal{D}_k(\mathcal{P}_j^{k-1})$ relative to the level k.

A consistency property can be defined, $\mathrm{D}_k^{k-1}\mathrm{P}_{k-1}^k = \mathrm{I}_k$, that follows from

$$v^{k-1} = \mathrm{D}_k^{k-1} v^k = \mathrm{D}_k^{k-1}\mathcal{D}_k f = \mathrm{D}_k^{k-1}\mathcal{D}_k\mathcal{R}_{k-1} v^{k-1} = \mathrm{D}_k^{k-1}\mathrm{P}_{k-1}^k v^{k-1}. \tag{3.43}$$

The last element of the MR framework is constituted by the prediction error e^k

$$e^k \stackrel{\text{def}}{=} v^k - \mathrm{P}_{k-1}^k v^{k-1} = (\mathrm{I}_k - \mathrm{P}_{k-1}^k \mathrm{D}_k^{k-1}) v^k. \tag{3.44}$$

The prediction error satisfies (from the consistency property (3.43))

$$\mathrm{D}_k^{k-1} e^k = \mathrm{D}_k^{k-1}(v^k - \mathrm{P}_{k-1}^k v^{k-1}) = v^{k-1} - v^{k-1} = 0, \tag{3.45}$$

then it is in the null space of the decimation operator $e^k \in \mathcal{N}(\mathrm{D}_k^{k-1})$. Using the definition (3.36) and applying the rank theorem, it is possible to write

$$\dim(V_k) = \dim(\mathcal{N}(\mathrm{D}_k^{k-1})) + \dim(V_{k-1}) \rightarrow \dim(\mathcal{N}(\mathrm{D}_k^{k-1})) = \dim(V_k) - \dim(V_{k-1}) = J_k - J_{k-1}. \tag{3.46}$$

The linear independent coordinates of e^k are called wavelets or details d^k. Two operators can be defined to link the prediction error to the details, E^k and G^k, as follows

$$e^k \overset{\text{def}}{=} E^k d^k, \quad d^k \overset{\text{def}}{=} G^k e^k \quad \text{with} \quad E^k G^k : V^k \rightarrow \mathcal{N}(\mathrm{D}_k^{k-1}). \tag{3.47}$$

Using all the operators described in this section, a multi-resolution representation of data can be defined.

This is obtained by two procedure: the *encoding* and the *decoding*. The *encoding* moves from the highest resolution level to the lowest one applying recursively (for all $k = L, \ldots, 1$) the decimation operator and computing the details

$$\begin{cases} v^{k-1} = \mathrm{D}_k^{k-1} v^k \\ d^k = G_k(\mathrm{I}_k - \mathrm{P}_{k-1}^k \mathrm{D}_k^{k-1}) v^k. \end{cases} \tag{3.48}$$

The multi-resolution representation v_{MR} refers to the possibility to obtain a one-to-one correspondence between the highest resolution level v^L and the sequence of the details d^k in addition to the lowest resolution level v^0:

$$v_{\mathrm{MR}} \overset{\text{def}}{=} \{v^0, d^1, \ldots, d^L\}. \tag{3.49}$$

The *decoding* procedure is the dual procedure with respect to the *encoding*: recursively moves from the lowest resolution level v^0 together with the prediction error e^k for all the levels $k = 1, \ldots, L$

$$v^k = \mathrm{P}_{k-1}^k v^{k-1} + E_k d^k. \tag{3.50}$$

Ideally, *decoding* and *encoding* permit an ideal exchange of information among different resolution levels. In order to be useful, these operations are coupled with an operator of data truncation. This additive operator allows, under a certain tolerance, to eliminate the over abundant information. The compression capability opens several possibilities to the application of the multi-resolution framework to compress the data as, for instance, in the signal/image representation schemes [Arandiga 2009] or as a fundamental brick in the solution of intrinsically multi scales problems, as demonstrated already in the first seminal works of Harten [Harten 1994, Harten 1995].

The truncation is instead based on the elimination of the wavelets d^k under a prescribed tolerance. The problem statement is the following: given a sequence of scale coefficients or wavelets for a fixed level d^k and assigned a level dependent tolerance criterion ε_k, we should generate $\hat{d}^k = \left\{\hat{d}_j^k\right\}_{j=1}^{J_k - J_{k-1}}$ according to

$$\hat{d}_j^k = \mathrm{tr}(d_j^k, \varepsilon_k) = \begin{cases} 0 & |d_j^k| \leq \varepsilon_k \\ d_j^k & \text{otherwise.} \end{cases} \tag{3.51}$$

Different choices exist in literature for the threshold parameter ε_k: a level independent choice $\varepsilon_k = \varepsilon$ or a dependent criterion $\varepsilon_k = \varepsilon / 2^{L-k}$. Since the original work of Harten, the stability of the MR representation of the data has been studied. Harten proposed [Harten 1993] to modify the *encoding* procedure in order to preserve the following condition

$$||v^L - \hat{v}^L|| \leq C\varepsilon, \tag{3.52}$$

with a constant C and measured in some norms as the L^1 and L^∞.

In this work, the main contribution is to adapt this framework performing the one-time encoding and truncated procedure in order to obtain a compact representation of the data in the stochastic space. This fundamental brick of the algorithm is described in the following section.

3.2.2.1 A one-time truncate and encode cell-average representation

In this section, the truncate and encode TE algorithm is described in the case of cell-average quantities. The pivotal idea of the algorithm is to identify in the prediction error e^k at a certain $k-$th level, a measure of the quality of the predictor operator P_{k-1}^k.

From classical interpolation results (see for instance [Quarteroni 2008]), note that the interpolation error diminishes, moving from a coarser level to a finer one, with respect to the local regularity of the function and to the local polynomial order of the interpolation. On the contrary, in presence of discontinuities, the error remains constant and of the order $\mathcal{O}[1]$. This means that, starting from the knowledge of a fine level k (using the discretization operators $\mathcal{D}_k$), the recursive combinations of prediction operations via the operators P_{k-1}^k and evaluations of the error e^k permits to determine the region, where the solution respects a certain accuracy criterion. In particular, if the criterion is equal to the truncation operation described above, at the end of the algorithm, the discretized set of data $\{v^k\}_{k=0}^L$ is directly related to the data $\{\hat{v}^k\}_{k=0}^L$ obtained under the same truncation criterion by the classical MR framework.

The algorithm starts with the definition of the coarsest level of resolution $k = 1$. On this level the discretization operator is applied obtaining the discrete data v^1: $v^1 = \mathcal{D}_1 f$. By decimation, it is also possible to obtain the discrete data on the level $k = 0$ knowing only v^1:

$$v^0 = \mathrm{D}_1^0 v^1. \tag{3.53}$$

An *encoding* step (analogous to what is normally done in the classical MR (see (3.48))) is then completed, by computing the linear independent coefficients d^k of e^k for $k = 1$:

$$d^k = G_k(\mathrm{I}_k - \mathrm{P}_{k-1}^k \mathrm{D}_k^{k-1}) v^k. \tag{3.54}$$

The truncation is applied on d^1 with respect to the threshold ε, defined by the user, and to the relation $\varepsilon_k = \varepsilon_k(\varepsilon, k)$:

$$\hat{d}^1 = \mathrm{tr}(d^1, \varepsilon_k). \tag{3.55}$$

This operation relies on the knowledge of the finest level ($k = L$), where the threshold is always equal to ε (see (3.51)). The integer $k = L$ is assigned to the finest level if the coarsest is marked as $k = 0$ and at each refinement k is increased by one.

The data d^1 are analyzed in order to locate the region of the domain, where the accuracy of the prediction, via P_{k-1}^k, is not adequate. This is accomplished in a very simple way after the truncation, by identifying the non-zero wavelets d_j^1. At each non-zero (truncated) wavelets, corresponds a region where the knowledge of the solution is not sufficient under the criterion used in the truncation (3.55). Then, further information are added. In particular, after the generation of the mesh on the level $k = 2$, on all the cells/points inside the regions (at level $k = 0$) used to generate the corresponding wavelets d_j^1, the discretization operator $\mathcal{D}_2$ is applied. On the contrary, in the region marked as well-described, the *decoding* procedure is performed:

$$v^2 = \mathrm{P}_1^2 v^1 + E_2 d^2 \simeq \mathrm{P}_1^2 v^1. \tag{3.56}$$

The assumption in the equation (3.56) means that for every null wavelets at a level $k - 1$, the corresponding wavelets at level k are null too. In the case of non null details, the equation (3.56) is not applied, but substituted by a direct (exact) discretization of the function by means of the operator $\mathcal{D}_k$ for $k = 2$.

Knowing v^2 and v^1, the *encoding* is performed by computing d^2 and their truncated counterpart $\hat{d}^2$ by (3.51). The algorithm is then repeated until reaching the finest level L or a full satisfactory prediction, *i.e.* $d_j^k = 0$ for all $j = 1, \ldots, J_k - J_{k-1}$.

To make things clear, the algorithm is now presented in the case of 1D stochastic space. Some preliminary operation are first performed:

- Generation of a nested set of meshes $\mathcal{G}^k$ for $k = 0, \dots, L$ (0 is the coarsest mesh):

$$\mathcal{G}^k = \left\{\Xi_j^k\right\}_{j=1}^{J_k} \quad \text{where} \quad \Xi_j^k = [\xi_{j-1}^k, \xi_j^k]. \tag{3.57}$$

  In this case the case of bounded probability density function is addressed and a topological tessellation for the mesh can be obtained, *i.e.* each cell has the same Lebesgue measure equal to $1/J_k$. Otherwise, in the case of unbounded pdf, the set of meshes can be built on a nested sequence of cells with the same probability measure $\mathrm{d}\mu$.

- Definition of the operator $\mathcal{D}_k$, $\mathcal{R}_k$, D_k^{k-1} and P_{k-1}^k according to §3.2.2:

$$\begin{cases} (\mathcal{D}_k f(\xi))_j = \dfrac{1}{\mu(\Xi_j^k)} \displaystyle\int_{\Xi_j^k} f(\xi) p(\xi) \mathrm{d}\xi \\ \mathcal{R}_k : (\mathcal{D}_k \mathcal{R}_k v^k)_l = (\mathcal{D}_k f(\xi))_l \quad \text{with} \quad l \in \mathcal{S}_j^k \\ (\mathrm{P}_{k-1}^k v^{k-1})_j = (\mathcal{D}_k \mathcal{R}_{k-1} v^{k-1})_j = \dfrac{1}{\mu(\Xi_j^k)} \displaystyle\int_{\Xi_j^k} \mathcal{R}_{k-1} v^{k-1} p(\xi) \mathrm{d}\xi. \end{cases} \tag{3.58}$$

  The decimation operator can be defined when the topological relation between the cells at two different resolution levels is known. Let us consider the situation sketched in Figure 3.11. We assume that the cells generated by the splitting of Ξ_j^{k-1}, are named as Ξ_{2j-1}^k and Ξ_{2j}^k even if this numeration does not correspond to the index j of the generating stochastic cell at the lower resolution level. The indexes numeration in Figure 3.11 is exactly matched only if all the cells are splitted from a resolution level to the higher one. In that case, the dimensions of the spaces of the two levels $k-1$ and k are related by the following relation, $J_k/J_{k-1} = 2$. In the following, the abstract indexes $2j$ and $2j-1$ are employed to make evident the dependence of the two cells, at level k, from the generating cell Ξ_j^{k-1}. However, the indexes should always be intended in the sense described above. When a cell is split to obtain the higher resolution level (see Figure 3.11), the measure $\mathrm{d}\mu$ is defined as follows:

$$\begin{cases} \mu(\Xi_j^{k-1}) = \mu(\Xi_{2j-1}^k) + \mu(\Xi_{2j}^k) \\ \mu(\Xi_{2j-1}^k) = \mu(\Xi_{2j}^k). \end{cases} \tag{3.59}$$

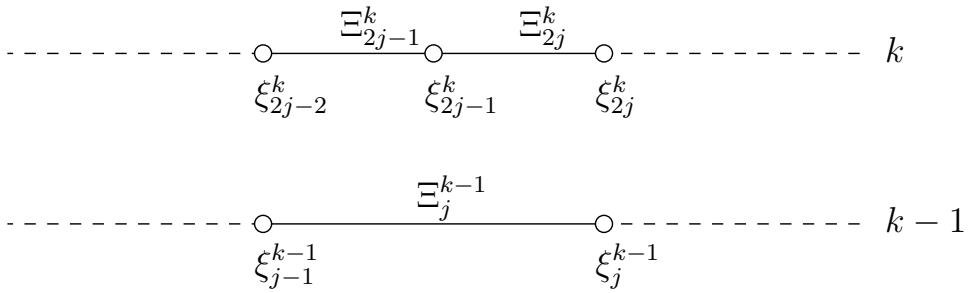

Figure 3.11: Example of 1D stochastic nested meshes for the cell-average setting decimation procedure.

  Then, the decimation operator is simply obtained as

$$(\mathrm{D}_k^{k-1} v^k)_j = v_j^{k-1} = \frac{1}{\mu(\Xi_j^{k-1})} \left(\mu(\Xi_{2j}^k) v_{2j}^k + \mu(\Xi_{2j-1}^k) v_{2j-1}^k\right) \tag{3.60}$$

- Setting a proper threshold ε and a proper relation for $\varepsilon_k = \varepsilon_k(\varepsilon, k; L)$

- Discretization of the level $k = 1$: $(v^1) = (\mathcal{D}_1 f)$;
- Decimation of the discrete data v^1 to obtain $(v^0) = (\mathrm{D}_1^0 v^1)$.

The TE algorithm for cell-average setting in 1D stochastic space can be explicitly written as:

Algorithm 4: Truncate and Encode algorithm for the cell average setting in 1D stochastic space.

while $2 \leq k \leq L$ **do**
  for $j = 1, \ldots, J_{k-2}$ **do**
    Encoding:
    $(d^{k-1})_j = v_{2j}^{k-1} - (\mathrm{P}_{k-2}^{k-1} v^{k-2})_{2j} = v_{2j}^{k-1} - \left(\frac{1}{\mu(\Xi_{2j}^{k-1})} \int_{\Xi_{2j}^{k-1}} \mathcal{R}_{k-2} v^{k-2} p(\xi) \mathrm{d}\xi \right)$;
    Truncation: $\hat{d}_j^{k-1} = \mathrm{tr}(d_j^{k-1}, \varepsilon_{k-1})$;
  end
  for $j = 1, \ldots, J_{k-1}$ **do**
    if $\hat{d}_j^{k-1} > 0$ **then**
      Discretization: $v_{2j}^k = (\mathcal{D}_k f)_{2j} = \frac{1}{\mu(\Xi_{2j}^k)} \int_{\Xi_{2j}^k} f(\xi) p(\xi) \mathrm{d}\xi$;
      Discretization: $v_{2j-1}^k = (\mathcal{D}_k f)_{2j-1} = \frac{1}{\mu(\Xi_{2j-1}^k)} \int_{\Xi_{2j-1}^k} f(\xi) p(\xi) \mathrm{d}\xi$;
    end
  end
end

At this level, remark that the sequence of discretization operators should be nested and $\mathcal{N}(\mathcal{D}_k) \subset \mathcal{N}(\mathcal{D}_{k+1})$. This means that the error vector e^k can be represented by means of only its independent components, the wavelets d^k, thanks to the relation (3.47). It is always possible to write, recalling the definition of the error vector e_k (3.44) and the nested property of the discretization operator (3.40), as follows

$$\begin{aligned} e_{2j-1}^k &= v_{2j-1}^k - (\mathrm{P}_{k-1}^k v^{k-1})_{2j-1} \\ &= \frac{1}{\mu(\Xi_{2j-1}^k)} \left(\mu(\Xi_j^{k-1}) v_j^{k-1} - \mu(\Xi_{2j}^k) v_{2j}^k \right) - \frac{1}{\mu(\Xi_{2j-1}^k)} \left(\mu(\Xi_j^{k-1}) v_j^{k-1} - \mu(\Xi_{2j}^k) (\mathrm{P}_{k-1}^k v^{k-1})_{2j} \right) \\ &= \frac{\mu(\Xi_{2j}^k)}{\mu(\Xi_{2j-1}^k)} \left(\mathrm{P}_{k-1}^k v^{k-1})_{2j} - v_{2j}^k \right) = -\frac{\mu(\Xi_{2j}^k)}{\mu(\Xi_{2j-1}^k)} d_j^k. \end{aligned} \tag{3.61}$$

The first loop should be performed in order to compute all the *wavelets* d_j^k, while the second loop is performed over the whole set of cells belonging to the resolution level. In particular, the error vector component is compared with the threshold for deciding whether the discretization via the model evaluation is necessary. In the second loop, in the case of a nested sequence, with splitting based on the probability measure, the local error is equal to *wavelet* computed over the same cell Ξ_j^{k-1} (see equation (3.61)). Therefore, the truncated wavelet is exactly equal to the truncated component of the error.

In the classical framework, the first step is the *encoding* procedure moving from the finest level to the coarsest. In this case, the explicit evaluation of the function f is performed at the finest level while the other levels are obtained by agglomeration. In the present paper, the encoding is performed proceeding from the coarsest level. Each time a higher resolution level is added, *i.e* k, the function is explicitly evaluated via the discretization operator $\mathcal{D}_k$. Due to numerical errors, the relation (3.37) could not hold. In such a case, the wavelets d^k are not the linear independent components of the error vector e^k. For represent-

ing the error vector in terms of its independent components d^k, the Discetrize Agglomerate Decimate (DAD) algorithm is introduced. The DAD algorithm consists in the following operations

Algorithm 5: DAD algorithm.

Discretization:

$$v_{2j}^k = \frac{1}{\mu(\Xi_{2j}^k)} \int_{\Xi_{2j}^k} f(\xi)p(\xi)\mathrm{d}\xi \ ;$$

$$v_{2j-1}^k = \frac{1}{\mu(\Xi_{2j-1}^k)} \int_{\Xi_{2j-1}^k} f(\xi)p(\xi)\mathrm{d}\xi \ ;$$

Agglomeration:

$$\mu(\Xi_j^{k-1}) = \mu(\Xi_{2j-1}^k) + \mu(\Xi_{2j}^k) \ ;$$

Decimation:

$$(\mathrm{D}_k^{k-1} v^k)_j = v_j^{k-1} = \frac{1}{\mu(\Xi_j^{k-1})} \left(\mu(\Xi_{2j}^k) v_{2j}^k + \mu(\Xi_{2j-1}^k) v_{2j-1}^k \right)$$

The DAD algorithm should be always performed before the *Encoding* in the TE algorithm 5. The introduction of the DAD algorithm is a peculiarity of the cell-average framework, while the point-value setting does not require any similar procedure because two successive levels are constituted by a set of points in the intersection of the two spaces.

Another peculiarity of the cell average framework is the presence of integral quantities that requires different evaluation in each cell, according to the numerical rule used to obtain the integrals in the discretization operator (3.32). The family of Newton-Cotes formula, employing only equally spaced points, is the best choice in term of computational cost; this family of quadrature rule is both nested and based on equally spaced points. The three point quadrature rule of Newton Cotes, known also as the Cavalieri-Simpson rule, is employed in this work:

$$\int_a^b f(\xi)\mathrm{d}\mu(\xi) \approx \frac{b-a}{6} \left(f(a) + 4f\left(\frac{a+b}{2}\right) + f(b) \right). \tag{3.62}$$

When a cell is split, it is easy to see that only three of the six points required (three for each cells) should be computed again. On the contrary, the points employed at the previous level can be re-employed thanks to the nested nature of the meshes. This makes the sequence of cell evaluations from the coarsest resolution level to the finest one, only a hierarchical representation without extra computational effort. For instance, if a Gauss (two points) quadrature rule would be employed, the point of a previous level could not be used for the evaluation, of the integrals, at successive resolution levels. This feature is a key aspect when the MR framework is coupled (see section §3.2.4) with the semi-intrusive scheme presented in the following section.

3.2.2.2 ENO polynomial reconstruction for the MR setting

In this section, further details on the polynomial interpolation are provided. The $\mathcal{R}_k$ operator, from a practical point of view, can be obtained by the union of all the polynomial obtained by the conservative interpolation techniques described by the equation (3.34). Two different operations are relative to the piecewise polynomial approximation $\mathcal{P}_j$. The first is to obtain $\mathcal{P}_j^k$ from the mesh at the resolution level k and, of course, from the cell average quantities at this resolution level. The second operation is the prediction of a cell average value (for a cell entirely contained in the support of the polynomial $\mathcal{P}_j^k$) at the successive resolution level (see equation (3.42)). To make things clearer, the case of uniform probability distribution is here addressed. The first task is to define the polynomial representation for a second order polynomial piecewise approximations ($r = 2$), over the stochastic cell Ξ_j:

$$\mathcal{P}_j = a(\xi - \xi_j)^2 + b(\xi - \xi_j) + c, \tag{3.63}$$

where ξ_j is the coordinate of the center of the stochastic cell.

To obtain the coefficients a, b and c, the conditions (3.34) must be fulfilled for a certain stencil. In the case of centered reconstruction, the stencil is fixed and equal to $\mathcal{S}_j = \{\Xi_{j-1}, \Xi_j, \Xi_{j+1}\}$. A

linear system can be obtained as

$$\begin{cases} \mathbb{E}(\mathcal{P}_j^k \,|\, \Xi_{j-1}) = \dfrac{1}{\mu(\Xi_{j-1}^k)} \displaystyle\int_{\Xi_{j-1}^k} \mathcal{P}_j^k \mathrm{d}\xi = \mu(\Xi_{j-1}^k) v_{j-1}^k \\ \mathbb{E}(\mathcal{P}_j^k \,|\, \Xi_j) = \dfrac{1}{\mu(\Xi_j^k)} \displaystyle\int_{\Xi_j^k} \mathcal{P}_j^k \mathrm{d}\xi = \mu(\Xi_j^k) v_j^k \\ \mathbb{E}(\mathcal{P}_j^k \,|\, \Xi_{j+1}) = \dfrac{1}{\mu(\Xi_{j+1}^k)} \displaystyle\int_{\Xi_{j+1}^k} \mathcal{P}_j^k \mathrm{d}\xi = \mu(\Xi_{j+1}^k) v_{j+1}^k, \end{cases} \tag{3.64}$$

where the linear operator $\mathbb{E}(\bullet \,|\, \Xi)$ becomes (on the generic cell Ξ_j)

$$\mathbb{E}(\mathcal{P}_j^k \,|\, \Xi_j) = a\, \mathbb{E}((\xi - \xi_j)^2 \,|\, \Xi_j) + b\, \mathbb{E}((\xi - \xi_j) \,|\, \Xi_j) + c. \tag{3.65}$$

If the integration is performed analytically, with respect to the parameter $(\xi - \xi_j)$, the system becomes

$$\begin{pmatrix} \mathbb{E}((\xi-\xi_j)^2 \,|\, \Xi_{j-1}) & \mathbb{E}((\xi-\xi_j) \,|\, \Xi_{j-1}) & 1 \\ \mathbb{E}((\xi-\xi_j)^2 \,|\, \Xi_j) & \mathbb{E}((\xi-\xi_j) \,|\, \Xi_j) & 1 \\ \mathbb{E}((\xi-\xi_j)^2 \,|\, \Xi_{j+1}) & \mathbb{E}((\xi-\xi_j) \,|\, \Xi_{j+1}) & 1 \end{pmatrix} \begin{pmatrix} a \\ b \\ c \end{pmatrix} = A(\xi - \xi_j) \begin{pmatrix} a \\ b \\ c \end{pmatrix} = \begin{pmatrix} \mu(\Xi_{j-1}^k) v_{j-1}^k \\ \mu(\Xi_j^k) v_j^k \\ \mu(\Xi_{j+1}^k) v_{j+1}^k \end{pmatrix}, \tag{3.66}$$

where the matrix $A = A(\xi - \xi_j)$ is dependent from the stochastic cell Ξ_j via its coordinate ξ_j. From a practical point of view, when the polynomial reconstruction should be performed over a cell Ξ_j, the matrix $A^{-1}(\xi - \xi_j)$ is first evaluated and then the vector of coefficients is obtained by the matrix vector product with the right hand side that depends from both the resolution level k and the stencil $\mathcal{S}_j$.

However, the procedure described above should be modified if the ENO interpolation is required. The only modification concerns the choice of the stencil: the procedure select the less oscillatory one between the following $\{\Xi_{j-2}, \Xi_{j-1}, \Xi_j\}, \{\Xi_{j-1}, \Xi_j, \Xi_{j+1}\}$ and $\{\Xi_j, \Xi_{j+1}, \Xi_{j+2}\}$. The smoothest one is selected choosing the one with $\min(|a|)$ following [Abgrall 1994b]. Obviously, at the boundaries of the domain, the stencil is always modified to be inside the domain. This is a key aspect if the higher accuracy is desired. With the modification of the stencil, the scheme preserves its maximal accuracy as it is shown for the solution of the stochastic linear advection equation with smooth solution in §3.2.5.1.

The second task to solve is the prediction of a cell average v_j^{k+1} at the next following resolution level, if the polynomial $\mathcal{P}_j^k$ reconstruction at the previous resolution level is available (the cell $\Xi_j^{k+1} \subset \Xi_j^k$ as required by the nested character of the discretization procedure). This task is accomplished analytically in the following way. The expectancy operator is applied to the polynomial $\mathcal{P}_j^k$ over the stochastic cell $\Xi_j^{k+1} \subset \Xi_j^k$

$$\mathbb{E}(\mathcal{P}_j^k \,|\, \Xi_j^{k+1}) = a\, \mathbb{E}((\xi - \xi_j^k)^2 \,|\, \Xi_j^{k+1}) + b\, \mathbb{E}((\xi - \xi_j^k) \,|\, \Xi_j^{k+1}) + c, \tag{3.67}$$

where the terms $\mathbb{E}((\xi - \xi_j^k)^2 \,|\, \Xi_j^{k+1})$ and $\mathbb{E}((\xi - \xi_j^k) \,|\, \Xi_j^{k+1}) + c)$ can be analytically evaluated when the cell Ξ_j^{k+1} is defined.

The procedure described in this section is used in SI scheme in order to obtain the polynomial representation of the functions along the stochastic space to evaluate the expectancy of the flux function.

3.2.3 The semi-intrusive finite volume formulation for PDEs

In this section, the semi-intrusive (SI) method is coupled to a second order MUSCL-Hancock method (MHM) for the deterministic part of the scheme. This result, to the best of our knowledge, is the

first adaptive intrusive scheme of high-order. Another adaptive intrusive strategy based on data-independent wavelets limited only to first order in time and space is the work of Tryoen et al. [Tryoen 2011]. This work is the first to introduce wavelets adaptivity into an intrusive stochastic formulation by means of the polynomial chaos technique, but remain very limited in its generality requiring for each case *ad hoc* modifications.

3.2.3.1 MUSCL-Hancock deterministic numerical formulation

The MHM is a slightly different approach with respect to the classical predictor-corrector MUSCL approach. It requires only the computation of slopes in the predictor step. Moreover, it does not require the solution of Riemann problems in the predictor step. The corrector step is based on the evolution of cell-average quantities, taking into account their contribution related to the flux at interfaces obtained by the solution of a Riemann problem. Let us consider a 1D scalar conservation law

$$\frac{\partial u(x,t)}{\partial t} + \frac{\partial f(u(x,t))}{\partial x} = 0, \tag{3.68}$$

where $x \in \Omega \subset \mathbb{R}$ is the physical space and $t \in T \subset \mathbb{R}^+$ is the time space. The physical space is divided in a set of non-overlapping cells $\mathcal{C}_i$ with $\Omega = \bigcup_i \mathcal{C}_i$. The classical first order Godunov scheme, applied to (3.68), is obtained introducing the so-called cell-average $\bar{u}_i$ on each cell $\mathcal{C}_i$:

$$\bar{u}_i(t) = \frac{1}{|\mathcal{C}_i|} \int_{\mathcal{C}_i} u(x,t) \mathrm{d}x, \tag{3.69}$$

where $|\mathcal{C}_i|$ indicates the volume of the cell. Van Leer [LeVeque 2002, Toro 1997] proposed to consider non-constant data on each cell to achieve a higher accuracy in the so-called Monotone Upstream-centred Scheme for Conservation Laws (MUSCL). The piecewise linear approximation is used for the solution $u(x,t)$ on the cell $|\mathcal{C}_i|$:

$$u(x,t_n) = \bar{u}_i^n + \sigma_i^n (x - x_i) \quad \text{with} \quad x_{i_L} \leq x \leq x_{i_R}, \tag{3.70}$$

with σ_i^n the so-called slope. Of course, the choice of $\sigma_i^n = 0$ leads to the Godunov scheme. A slope limiter should be introduced near the discontinuity to avoid oscillations. In this work, both the Roe's superbee limiter and the van Leer limiters are employed. The superbee limiter in its limited slope form is

$$\begin{cases} \sigma_i^n = \text{maxmod}\left(\sigma_{(1)}^n, \sigma_{(2)}^n\right) \\ \sigma_{(1)}^n = \text{minmod}\left(\left(\dfrac{\bar{u}_{i+1}^n - \bar{u}_i^n}{|\mathcal{C}_i|}\right), 2\left(\dfrac{\bar{u}_i^n - \bar{u}_{i-1}^n}{|\mathcal{C}_i|}\right)\right) \\ \sigma_{(2)}^n = \text{minmod}\left(2\left(\dfrac{\bar{u}_{i+1}^n - \bar{u}_i^n}{|\mathcal{C}_i|}\right), \left(\dfrac{\bar{u}_i^n - \bar{u}_{i-1}^n}{|\mathcal{C}_i|}\right)\right), \end{cases} \tag{3.71}$$

where the minmod and maxmod functions are defined as follows

$$\text{minmod}(a,b) = \begin{cases} a & \text{if} \quad |a| < |b| \quad \text{and} \quad ab > 0 \\ b & \text{if} \quad |a| > |b| \quad \text{and} \quad ab > 0 \\ 0 & \text{if} \quad ab <= 0 \end{cases}$$

$$\text{maxmod}(a,b) = \begin{cases} a & \text{if} \quad |a| > |b| \quad \text{and} \quad ab > 0 \\ b & \text{if} \quad |a| < |b| \quad \text{and} \quad ab > 0 \\ 0 & \text{if} \quad ab <= 0. \end{cases}$$

The van Leer limiter, in the form of slope limiter, is defined as (see Toro [Toro 1997] for further details)

$$\sigma_i^n = \begin{cases} \text{MIN}\left(\dfrac{2R}{1+R}, \dfrac{2}{1+R}\right) \dfrac{\bar{u}_{i+1}^n - \bar{u}_{i-1}^n}{2\Delta x} & \text{if} \quad R > 0 \\ 0 & \text{if} \quad R \leq 0, \end{cases} \tag{3.72}$$

where R is the ratio between successive slopes $R = (\bar{u}_i^n - \bar{u}_{i-1}^n)/(\bar{u}_{i+1}^n - \bar{u}_i^n)$.

The MHM is then introduced in order to avoid the problem related to the solution of the so-called generalized Riemann problem, in which the two states are not constant. The fully discrete second order MHM, for computing the cell averaged solution $\bar{u}_i^{n+1}$, consists of the following three steps:

- Step 1 - For each cell $\mathcal{C}_\ell \in \{\mathcal{C}_{i-1}, \mathcal{C}_i, \mathcal{C}_{i+1}\}$, the solution at the interface is computed according to

$$\begin{cases} u_{\ell_L}^n = \bar{u}_\ell^n - \sigma_\ell^n \dfrac{|\mathcal{C}_\ell|}{2} \\ u_{\ell_R}^n = \bar{u}_\ell^n + \sigma_\ell^n \dfrac{|\mathcal{C}_\ell|}{2} \end{cases} \tag{3.73}$$

- Step 2 - On each cell $\mathcal{C}_\ell \in \{\mathcal{C}_{i-1}, \mathcal{C}_i, \mathcal{C}_{i+1}\}$, the solution evolved of a half time step employing the flux function $f = f(u)$:

$$\begin{cases} u_{\ell_R}^{\Uparrow} = \bar{u}_{\ell_R} + \dfrac{1}{2}\dfrac{\Delta t}{|\mathcal{C}_\ell|}\left(f(u_{\ell_L}^n) - f(u_{\ell_R}^n)\right) \\ u_{\ell_L}^{\Uparrow} = \bar{u}_{\ell_L} + \dfrac{1}{2}\dfrac{\Delta t}{|\mathcal{C}_\ell|}\left(f(u_{\ell_L}^n) - f(u_{\ell_R}^n)\right) \end{cases} \tag{3.74}$$

- Step 3 - The cell-averaged value on the cell $\mathcal{C}_i$ evolves following

$$\bar{u}_i^{n+1} = \bar{u}_i^n - \frac{\Delta t}{|\mathcal{C}_i|}\left(\mathcal{F}^{\text{RM}}\left(u_{i-1_R}^{\Uparrow}, u_{i_L}^{\Uparrow}\right) - \mathcal{F}^{\text{RM}}\left(u_{i_R}^{\Uparrow}, u_{i+1_L}^{\Uparrow}\right)\right). \tag{3.75}$$

The symbol $\mathcal{F}^{\text{RM}}$ is employed to indicate the flux evaluated at the interface, after the solution of the Riemann problem defined by two constant states based on the evolved extrapolated values. For the linear advection §3.2.5.1 and Burgers equation §3.2.5.2, an exact Riemann solver is used. Moreover, in the case of the Euler system of equations §3.2.5.3, the Roe-Pike method is employed with the Harten-Hyman entropy fix following [Toro 1997].

The time advancing formula is then limited to a stencil of only three cells $\mathcal{C}_{i-1}$, $\mathcal{C}_i$ and $\mathcal{C}_{i+1}$ but the computation of the slopes for the cells $\mathcal{C}_{i-1}$ and $\mathcal{C}_{i+1}$ requires (see (3.71) and (3.72)) also to know the solution on the two sourrounding cells $\mathcal{C}_{i-2}$ and $\mathcal{C}_{i+2}$. The average solution $\bar{u}_i^{n+1}$, on each cell $\mathcal{C}_i$ at time $t_{n+1} = t_n + \Delta t$, can be computed knowing the solution on the augmented stencil $\left\{\bar{u}_{i-2}^n, \bar{u}_{i-1}^n, \bar{u}_i^n, \bar{u}_{i+1}^n, \bar{u}_{i+2}^n\right\}$. In the following, the notation $\bar{u}_i^{n+1} = \text{MHM}\left(\bar{u}_{i-2}^n, \bar{u}_{i-1}^n, \bar{u}_i^n, \bar{u}_{i+1}^n, \bar{u}_{i+2}^n, \Delta t\right)$ is used to identify the ensemble of the operation described above. The aim is to evaluate the updated value in time of a certain cell $\bar{u}_i^{n+1}$, knowing the solution at the previous time step.

3.2.3.2 Semi-intrusive formulation for the MHM

The SI version of the MHM (here presented in the 1D stochastic case without loss of generality) can be obtained adding one dimension more (the stochastic space) with a finite-volume like representation. In particular, the conditional expectancy operator, defined on the stochastic cell Ξ_j, is introduced according to the following definition:

$$\mathbb{E}(\bullet \,|\, \Xi_j) = \frac{1}{\mu(\Xi_j)} \int_{\Xi_j} \bullet(x, \xi, t)\, p(\xi, t)\, \mathrm{d}\xi. \tag{3.76}$$

If the conditional expectancy operator is applied to the step three of the MHM scheme (3.75), the following scheme is obtained:

$$\mathbb{E}(u_i^{n+1} \,|\, \Xi_j) = \mathbb{E}(u_i^n \,|\, \Xi_j) - \frac{\Delta t}{|\mathcal{C}_i|} \left(\mathbb{E}(\mathcal{F}^{\mathrm{RM}} \left(u_{i-1_R}^{\Uparrow}, u_{i_L}^{\Uparrow} \right) \,|\, \Xi_j) - \mathbb{E}(\mathcal{F}^{\mathrm{RM}} \left(u_{i_R}^{\Uparrow}, u_{i+1_L}^{\Uparrow} \right) \,|\, \Xi_j) \right). \quad (3.77)$$

The evaluation of the updated conditional expectancy value on the cell Ξ_j, is obtained by evaluating the conditional expectancy contribution related to the numerical fluxes $\mathbb{E}(\mathcal{F}^{\mathrm{RM}} \left(u_{i-1_R}^{\Uparrow}, u_{i_L}^{\Uparrow} \right) \,|\, \Xi_j)$ and $\mathbb{E}(\mathcal{F}^{\mathrm{RM}} \left(u_{i_R}^{\Uparrow}, u_{i+1_L}^{\Uparrow} \right) \,|\, \Xi_j)$. To evaluate this integral contribution, a polynomial representation of the physical averaged solution with respect to the stochastic dimensions, has to be obtained. The conservative interpolation procedure, already presented in §3.2.2 to obtain the reconstruction operator $\mathcal{R}_k$, can be adopted requiring for the polynomial $\mathcal{P}_j(\xi)$:

$$\mathbb{E}(P_\ell(\xi) \,|\, \Xi_\ell) = \mathbb{E}(u \,|\, \Xi_\ell) \quad \forall \Xi_\ell \in \mathcal{S}_j \quad (3.78)$$

If the stencil $\mathcal{S}_j$ is chosen with a cardinality $s = s(r) = \mathrm{card}(\mathcal{S}_j) = r + 1$ (for a 1D space), a polynomial $\mathcal{P}_j(\xi)$ of degree r can be built.

The polynomial representation $\mathcal{P}_j(\xi)$ can be injected into the steps 1 (3.73) and 2 (3.74) of the MHM. If the Cavalieri-Simpson rule (using three quadrature points $ng = 3$) is adopted for the quadrature, the SI scheme for the MHM can be recasted in a form that makes easy the use of MR stochastic representation of data.

We assume a uniform tessellation for the physical and stochastic space, with a number of cells equal to N_x and N_ξ, respectively and a constant time step Δt. The first step is to evaluate the initial condition in terms of conditional expectancies. This can be obtained easily via a tensorization of the quadrature rule and evaluating the analytical value of the function $u(x, \xi, 0)$. This step yields the stochastic initial condition $\mathbb{E}(u_i(x, \xi, 0) \,|\, \Xi_j)$ for all $i = 1, \ldots, N_x$ and $j = 1, \ldots, N_\xi$.

The SI algorithm becomes:

Algorithm 6: Semi-intrusive version of the MUSCL-Hancock method for a 1D stochastic space.

for $n = 1, \ldots, N_t$ **do**
  for $i = 1, \ldots, N_x$ **do**
    for $j = 1, \ldots, N_\xi$ **do**
      Polynomial reconstruction (via (3.78)) over $\Xi_j = [\xi_{j-1}, \xi_j] \Rightarrow \mathcal{P}_j(\xi)$;
      for $ng = 1, \ldots, 3$ **do**
        $\xi_{ng} = \xi_{j-1} + \frac{\xi_j - \xi_{j-1}}{2}(ng - 1)$;
        Step 1 (see (3.73)) $\Rightarrow \forall \mathcal{C}_\ell \in \{\mathcal{C}_{i-1}, \mathcal{C}_i, \mathcal{C}_{i+1}, \} \rightarrow \left\{ u_{\ell_L}^n(\xi_{ng}), u_{\ell_R}^n(\xi_{ng}) \right\}$;
        Step 2 (see (3.74)) $\Rightarrow \forall \mathcal{C}_\ell \in \{\mathcal{C}_{i-1}, \mathcal{C}_i, \mathcal{C}_{i+1}, \} \rightarrow \left\{ u_{\ell_L}^{\Uparrow}(\xi_{ng}), u_{\ell_R}^{\Uparrow}(\xi_{ng}) \right\}$;
      end
      Flux expectancy computation:
      $\mathbb{E}(\mathcal{F}_L^{\mathrm{RM}} \,|\, \Xi_j) = \sum_{ng=1}^{3} w_{ng}\, \mathcal{F}^{\mathrm{RM}} \left(u_{i-1_R}^{\Uparrow}(\xi_{ng}), u_{i_L}^{\Uparrow}(\xi_{ng}), \xi_{ng} \right)$;
      $\mathbb{E}(\mathcal{F}_R^{\mathrm{RM}} \,|\, \Xi_j) = \sum_{ng=1}^{3} w_{ng}\, \mathcal{F}^{\mathrm{RM}} \left(u_{i_R}^{\Uparrow}(\xi_{ng}), u_{i+1_L}^{\Uparrow}(\xi_{ng}), \xi_{ng} \right)$;
      Time update:
      $\mathbb{E}(\bar{u}_i^{n+1} \,|\, \Xi_j) = \mathbb{E}(\bar{u}_i^n \,|\, \Xi_j) - \frac{\Delta t}{|\mathcal{C}_i|} \left(\mathbb{E}(\mathcal{F}_L^{\mathrm{RM}} \,|\, \Xi_j) - \mathbb{E}(\mathcal{F}_R^{\mathrm{RM}} \,|\, \Xi_j) \right)$
    end
  end
end

where $\mathbb{E}(\mathcal{F}_L^{\mathrm{RM}} \,|\, \Xi_j) = \mathbb{E}(\mathcal{F}^{\mathrm{RM}} \left(u_{i-1_R}^{\Uparrow}, u_{i_L}^{\Uparrow} \right) \,|\, \Xi_j)$ and $\mathbb{E}(\mathcal{F}_R^{\mathrm{RM}} \,|\, \Xi_j) = \mathbb{E}(\mathcal{F}^{\mathrm{RM}} \left(u_{i_R}^{\Uparrow}, u_{i+1_L}^{\Uparrow} \right) \,|\, \Xi_j)$.

3.2.4 The overall multiresolution adaptive-SI scheme

In the previous section, the SI scheme applied to the MHM is presented. In this section, the adaptive version of the numerical algorithm (aSI) is described. The main difference, referring to the algorithm 6 is in the internal loop, on j, concerning the stochastic cells. This loop should be substituted by the application of the TE algorithm 4. The discretization step is performed by the application of the MHM, as presented in the internal loop (on j), in the algorithm 6. The complete aSI scheme is:

Algorithm 7: Semi-intrusive version of the MUSCL-Hancock method for a 1D stochastic space.

for $n = 1, \dots, N_t$ **do**
  for $i = 1, \dots, N_x$ **do**
    while $2 \leq k \leq L$ **do**
      for $j = 1, \dots, J_{k-2}$ **do**
        Encoding:
        $d_j^{k-1} = v_{2j}^{k-1} - (\mathrm{P}_{k-2}^{k-1} v^{k-2})_{2j} = v_{2j}^{k-1} - \left(\frac{1}{\mu(\Xi_{2j}^{k-1})} \int_{\Xi_{2j}^{k-1}} \mathcal{R}_{k-2} v^{k-2} p(\xi) \mathrm{d}\xi \right)$;
        Truncation: $\hat{d}_j^{k-1} = \mathrm{tr}(d_j^{k-1}, \varepsilon_{k-1})$;
      end
      for $j = 1, \dots, J_{k-1}$ **do**
        if $\hat{d}_j^{k-1} > 0$ **then**
          Discretization:
          for $\Xi_q \in \left\{ \Xi_{2j-1}^k, \Xi_{2j}^k \right\}$ **do**
            for $ng = 1, \dots, 3$ **do**
              Polynomial evaluation: $\bar{u}(x, \xi_{ng}, t_n) \simeq (\mathcal{D}_k \mathcal{R}_L v^L(t_n))(\xi_{ng})$
              Step 1 (see (3.73)) $\Rightarrow \forall \mathcal{C}_\ell \in \{\mathcal{C}_{i-1}, \mathcal{C}_i, \mathcal{C}_{i+1}, \} \rightarrow \left\{ u_{\ell_L}^n(\xi_{ng}), u_{\ell_R}^n(\xi_{ng}) \right\}$
              Step 2 (see (3.74)) $\Rightarrow \forall \mathcal{C}_\ell \in \{\mathcal{C}_{i-1}, \mathcal{C}_i, \mathcal{C}_{i+1}, \} \rightarrow \left\{ u_{\ell_L}^{\Uparrow}(\xi_{ng}), u_{\ell_R}^{\Uparrow}(\xi_{ng}) \right\}$
            end
            Flux expectancy computation:
            $\mathbb{E}(\mathcal{F}_L^{\mathrm{RM}} \,|\, \Xi_q) = \sum_{ng=1}^3 w_{ng} \, \mathcal{F}^{\mathrm{RM}} \left(u_{i-1_R}^{\Uparrow}(\xi_{ng}), u_{i_L}^{\Uparrow}(\xi_{ng}), \xi_{ng} \right)$
            $\mathbb{E}(\mathcal{F}_R^{\mathrm{RM}} \,|\, \Xi_q) = \sum_{ng=1}^3 w_{ng} \, \mathcal{F}^{\mathrm{RM}} \left(u_{i_R}^{\Uparrow}(\xi_{ng}), u_{i+1_L}^{\Uparrow}(\xi_{ng}), \xi_{ng} \right)$
            Cell agglomeration of $\mathbb{E}(u_i^n \,|\, \Xi_q)$ via equation (3.79)
            Time update:
            $\mathbb{E}(\bar{u}_i^{n+1} \,|\, \Xi_q) = \mathbb{E}(\bar{u}_i^n \,|\, \Xi_q) - \frac{\Delta t}{|\mathcal{C}_i|} \left(\mathbb{E}(\mathcal{F}_L^{\mathrm{RM}} \,|\, \Xi_q) - \mathbb{E}(\mathcal{F}_R^{\mathrm{RM}} \,|\, \Xi_q) \right)$
          end
        end
      end
    end
    Reconstruction: $(\mathcal{D}_L \mathcal{R}_L v^L)_l = (\mathcal{D}_L \bar{u}(x_i, \xi, t_{n+1}))_l \quad \text{with} \quad l \in \mathcal{S}_j^L$;
  end
end

The reconstruction operator $\mathcal{R}_k$ for each cell Ξ_j is the polynomial $\mathcal{P}_j$ reconstructed for the SI scheme. A link between the MR representation and the SI scheme exists since the polynomial representation of the data in the stochastic space is the same for the SI and TE. The polynomial reconstruction is carried out when the algorithm attain the highest resolution level (indicated in

the algorithm by $k = L$) and the reconstruction operator $\mathcal{R}_L$ is then obtained and stored. The reconstruction operator is then used, for the polynomial evaluation before Step 1. The physical cell-averaged values are obtained, for each quadrature points ξ_{ng}, applying the discretization operator $\mathcal{D}_k$. Moreover, a conservative interpolation is also present into the MR algorithm, where the operator $\mathcal{R}_k$ is used to obtain the wavelets during the *encoding* procedure.

One important feature of the aSI algorithm is the possibility to locally refine/derefine the stochastic space, as a function of the variation of the solution during the computation. At the end of each time step, for each physical location, the algorithm produces a sequence of conditional expectancies $\mathbb{E}(u^n \,|\, \Xi_j)$ with different measures $\mu(\Xi_j)$, due to the local refinement/derefinement of the tessellation. The TE strategy starts from the coarsest level to the finest (until some cell have to be split or the maximum resolution level is reached). In practice, if a cell has not to be splitted, it is moved at the highest resolution level. The local variation of the cell measure yields a strong relation between the actual level of evaluation of the scheme, and the maximum level (locally) reached at the previous time step (and consequently the measure of each cell). Two problems exist: the agglomeration of a cell at a time n, and the splitting of a cell at a time $n+1$. The MR framework presented is based on a nested subdivision of the cell. Then, at the end of the TE algorithm, each cell belonging to the coarsest level $k = 0$, will result in a set of cells. When the TE algorithm requires the application of the SI-MHM at a generic level k, an equivalent conditional expectancy $\mathbb{E}(u \,|\, \Xi_j^k)$ evaluated at time n is computed by applying the equation (3.77). This conditional expectancy should be obtained by the agglomeration of all the stochastic cells belonging to Ξ_j^k at time n, following the exact definition:

$$\mathbb{E}(u \,|\, \Xi_j^k) = \frac{1}{\mu(\Xi_j^k)} \sum_{\Xi_\ell \subseteq \Xi_j^k} \mu(\Xi_\ell) \mathbb{E}(u \,|\, \Xi_\ell). \tag{3.79}$$

Obviously, it is easy to verify that the limit case is the one with a cell not subdivided, then the equation (3.79) reduces to an identity. Due to the nested sequences of operators and meshes, a cell would be always constituted by an integer number of cells at the end of the TE algorithm (see algorithm 4). A sketch of a possible situation for the agglomeration of a cell Ξ_j^k is reported in Figure 3.12.

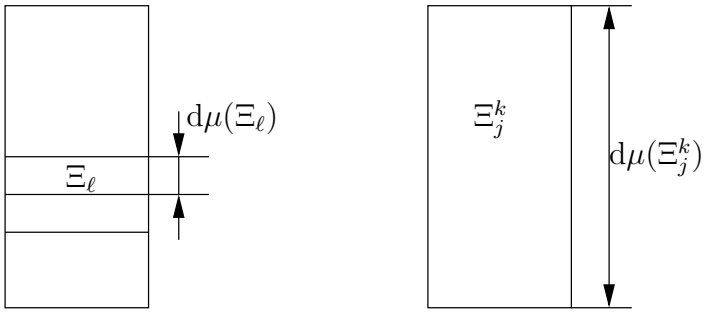

Figure 3.12: Example of the agglomeration procedure to obtain a coarser cell Ξ_j even if the TE algorithm yields a set of children cells.

The other issue is related to reduce the computational cost basing on the computed quantities, when a cell has to be split. For this reason, the quadrature rule of Newton-Cotes is adopted. In this case, the entire set of degrees of freedom (dof) can be saved, if the cell has to be split. Let us consider the Figure 3.13, where the Cavalieri-Simpson rule is used. On the left, the cell at level k is represented with its dof, the circles are used for the value of $\bar{u}_i$ obtained via the polynomial $\mathcal{P}_j$ (the polynomial evaluation step in the algorithm 7), and squares for the fluxes obtained after the application of the step 1 and 2 of the MHM. When the cell is split in two cells, only three points have to be added (the numerical scheme has to be applied). On the contrary, the other points can

be obtained directly from the mother cell at level k. In the Figure 3.13, the black circle/squares represent the new points to compute. In practice, the black points are associated to the values for $\bar{u}_i$ obtained by interpolation and the fluxes are obtained via the Step 1 and 2; otherwise, they are only recovered from the mother cell. Finally, the fluxes conditional expectancy computation is performed easily combining the new fluxes (black) and the old ones (white) with the correct weights for the quadrature.

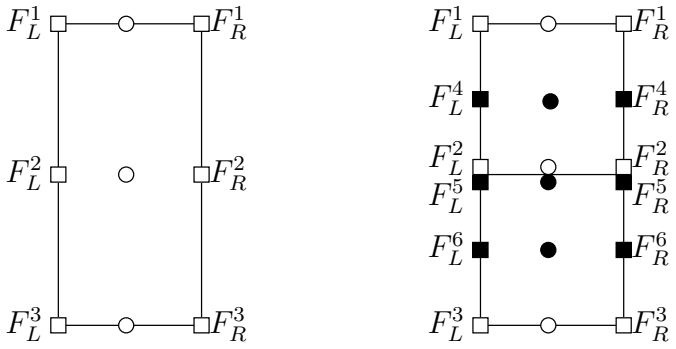

Figure 3.13: Example of a splitting procedure to save the computational cost associated to the degree of freedom already computed. On the left the cell at level of resolution k is reported while on the right the corresponding split cells are reported with the new points to explicitly add (black symbols).

The nested procedure described above allows to extend the accuracy of the quadrature rule even to high-order Newton-Cotes formula. Moreover, in the present work, the three points Cavalieri-Simpson rule (see (3.62)) is employed. The error is proportional to the fourth derivative of the integrand, so the rule is fully accurate to polynomial function of order equal or less than three (see [Quarteroni 2008] for further details). In the following, the variance of the outputs of interest is computed. In this case, the quadrature of the polynomial $\mathcal{P}_j$ squared has to be evaluated on each cell $\Xi_j = [\xi_a, \xi_b]$. In order to attain the exact integration of $\mathcal{P}_j^2$, the closed four points Newton-Cotes rule (also known as the Boole's rule) is employed

$$\int_{\Xi_j} f(\xi)\mathrm{d}\xi = \frac{\xi_b - \xi_a}{90}\left(7f(\xi_a) + 32f\left(\xi_a + \frac{\xi_b - \xi_a}{4}\right) + 12f\left(\xi_a + \frac{\xi_b - \xi_a}{2}\right) + 32f\left(\xi_a + 3\frac{\xi_b - \xi_a}{4}\right) + 7f(\xi_b)\right). \tag{3.80}$$

The last five points rule has an error $\mathcal{O}(f^{(6)}(\eta))$, where $\eta \in]\xi_a, \xi_b[$, so it is able to integrate exactly polynomial function of order equal to five.

3.2.5 Numerical results

In this section, the aSI scheme derived in Section 3.2.4 is applied to several problems. The aim is to show the convergence properties and to provide some evidence of the advantage to employ an adaptive representation of the solution in the stochastic space. For all the problems, the expectancy and the variance of the some outputs are computed according to the definitions (2.3) with respect to their exact value. Different 1D-1D test cases are taken into account. The linear advection problem is solved for both smooth and discontinuous initial conditions in section §3.2.5.1. In the first case, the uncertainty is considered in the initial condition, while in the discontinuous case an uncertain advection velocity is considered. For this test case, both the convergence curves for the first order Godunov method and the MHM are reported to demonstrate the ability of the scheme to maintain the convergence properties of the deterministic scheme. The Burgers equation is then solved employing a smooth initial, but uncertain, initial condition (§3.2.5.2). This case is chosen to demonstrate the

ability of the scheme to capture (refining the stochastic space) a discontinuous solution (along the stochastic dimension) even if the discontinuities form during the evolution of a smooth solution. This property is a key feature in the development of numerical schemes for UQ in compressible flows applications. The last test case is the stochastic analysis of the uncertain shock tube problem solving the Euler system of equations in section §3.2.5.3. In this case, the statistics of the density are compared to the semi-analytical solution of the Euler equations, considering an uncertain parameter on the initial conditions.

Systematically in this study, the spatial norms are computed employing the following definitions

$$\begin{cases} \mathrm{err}_{\mathcal{E}^m}|_{L_p} = ||\mathcal{E}^m(x) - \mathcal{E}^m_{\mathrm{ref}}(x)||_{L_p} = \left(\dfrac{1}{N_x} \displaystyle\sum_{i=1}^{N_x} |\mathcal{E}^m(\bar{u}_i) - \mathcal{E}^m_{\mathrm{ref}}(\bar{u}_i)|^p \right)^{1/p} \\ \mathrm{err}_{\mathcal{E}^m}|_{L_\infty} = ||\mathcal{E}^m(x) - \mathcal{E}^m_{\mathrm{ref}}(x)||_{L_\infty} = \max\limits_i |\mathcal{E}^m(\bar{u}_i) - \mathcal{E}^m_{\mathrm{ref}}(\bar{u}_i)| \,, \end{cases} \tag{3.81}$$

where the integer $p = 1, 2$ for the L_1 and L_2 norms in the physical space and $\mathcal{E}^m$ indicates a statistical moment, *i.e.* the expectancy or the variance.

3.2.5.1 Linear advection

The first test case is the linear advection problem here reported, for $\Omega = [0, 1]$, in its general stochastic formulation

$$\begin{cases} \dfrac{\partial u(x,\xi,t)}{\partial t} + a(\xi,t)\dfrac{\partial u(x,\xi,t)}{\partial x} = 0 \\ u(x,\xi,0) = u_0(x,\xi), \end{cases} \tag{3.82}$$

where both the advection velocity a and the initial condition u_0 can depend on a random parameter.

Let us consider first the smooth test-case with an initial condition equal to $u_0(x,\xi,t) = sin(4\pi x + 20\xi)$, with the random parameter uniformly distributed $\xi \sim \mathcal{U}[0, 1]$. The problem is solved until the time $t = 1$ with a constant advection velocity equal to $a = 0.1$ and with periodic boundary conditions. The exact solution can be computed analytically as follows

$$u(x,\xi,1) = sin(4(x - 0.1t)\pi + 20\xi) \tag{3.83}$$

The exact statistics can be computed as function of the $i-$th cell $\mathcal{C}_i = [x_i - \frac{|\mathcal{C}_i|}{2}, x_i + \frac{|\mathcal{C}_i|}{2}]$, integrating first with respect to the stochastic space and then with respect to the space

$$\begin{cases} \mathcal{E}(\bar{u}_i) = \dfrac{1}{|\mathcal{C}_i|} \displaystyle\int_{\mathcal{C}_i} \int_\Xi u(x,\xi,1)\,\mathrm{d}\xi\,\mathrm{d}x \\ \mathrm{Var}(\bar{u}_i) = \dfrac{1}{|\mathcal{C}_i|} \displaystyle\int_{\mathcal{C}_i} \int_\Xi u^2(x,\xi,1)\,\mathrm{d}\xi - \left(\int_\Xi u^2(x,\xi,1)\,\mathrm{d}\xi \right)^2 \mathrm{d}x. \end{cases} \tag{3.84}$$

Expressions for both statistics are obtained using the MAPLE software. Numerical simulations are carried out on equally spaced spatial meshes of 51, 101, 201 and 401 points, with $N_t = 200$ time steps and $\Delta t = 5 \times 10^{-3}$.

In Figure 3.14, both the expectancy of the solution 3.14(a) and the variance 3.14(a) for the linear advection problem (3.82) with smooth initial condition and constant advection velocity are reported. The continuous lines indicate the solution obtained via the scheme without compression, while with the dashed lines the solution obtained via the application of the aSI algorithm. In particular, the polynomial reconstruction is taken as a centered second-order polynomial except for the two boundary cells where the stencil is fully shifted into the numerical domain in order to maintain the order of accuracy. In particular, both the Godunov first order scheme and the MHM are reported to show that the numerical scheme is able to preserve the expected order of convergence even with compression.

To preserve the formal second order of accuracy, the slope for the MHM is evaluated by a centered approximation without any limiter function. The full solution is obtained on an equally spaced mesh of 128 stochastic cells while the aSI algorithm is applied starting from a coarse level of 16 cell ($m_0 = 4$) to a higher resolution level of 128 cells ($m = 7$) and a threshold equal to $\varepsilon = 10^{-3}$. Note that the finest level is indicated as m. This case is reported in order to show the formal accuracy of the method because the solution is regular enough to minimize the gain associated to the compression of the solution. In particular, the average number of cells employed by the aSI scheme is 126 against the 128 of the full solution. Of course, the level of compression could be easily increased in this case employing a higher order polynomial $\mathcal{P}_j$ for the reconstruction. Remark that, looking at the accuracy, the stochastic reconstruction (quadratic polynomial) is sufficiently accurate with respect to the spatial and time accuracy (second order in the case of MHM). On the contrary, looking at the compression, a higher polynomial order can yield a stronger compression keeping the second order convergence rate.

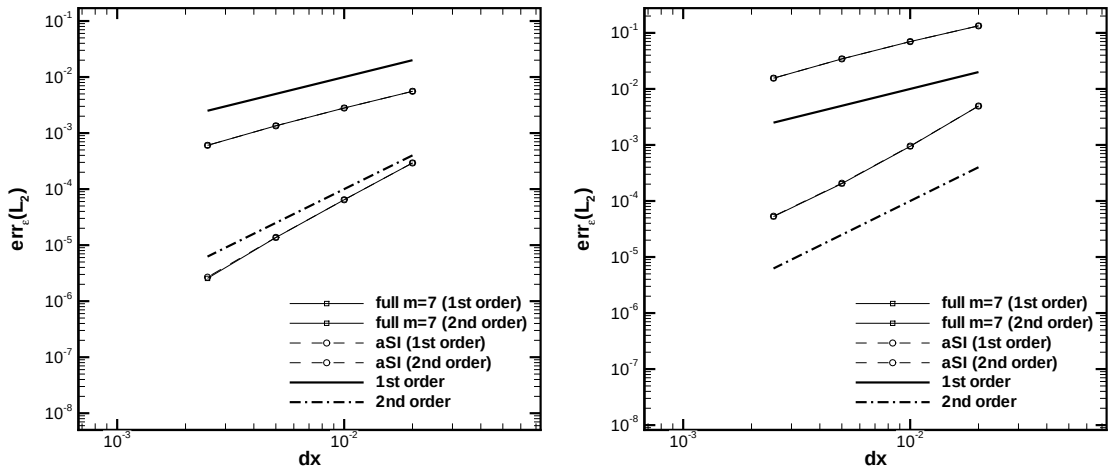

(a) (b)

Figure 3.14: Spatial convergence for the linear advection problem with smooth initial condition (3.83). The statistics of the solution (mean (a) and variance (b)) obtained with (aSI) and without (full) compression are reported for both the Godunov first order scheme and the MHM method with a centered slope.

Let us consider now the linear advection problem (3.82), that is solved with an uncertain advection ($\xi \sim \mathcal{U}[\frac{1}{5}, \frac{4}{5}]$) velocity defined as

$$a(\xi) = \frac{1}{40} e^{5\xi^2} + \frac{1}{5}, \tag{3.85}$$

considering a discontinuous initial condition (in the physical space)

$$u(x, \xi, 0) = \begin{cases} 1 & \text{if} \quad \frac{2}{5} \leq x \leq \frac{3}{5} \\ 0 & \text{if} \quad \text{otherwise.} \end{cases} \tag{3.86}$$

In this case, the problem is solved until the final time of $t = 0.4$ with 200 equal steps of $\Delta t = 2 \times 10^{-3}$. The exact solution is derived for the first two statistical moments employing the following procedure. Referring to the Figure 3.15, starting from the initial condition (defined by the points A_1, A_2, B_2, B_1) the new points (coordinates in the physical space) at the final time ($t = 0.4$) can be

computed as follows

$$\begin{cases} A_1'^{,x} = A_1^x + a\left(\frac{1}{5}\right)t = \frac{12}{25} + \frac{1}{100}e^{\frac{1}{5}} \\ A_2'^{,x} = A_2^x + a\left(\frac{1}{5}\right)t = \frac{12}{25} + \frac{1}{100}e^{\frac{1}{5}} \\ B_1'^{,x} = B_1^x + a\left(\frac{1}{5}\right)t = \frac{12}{25} + \frac{1}{100}e^{\frac{16}{25}} \\ B_2'^{,x} = B_2^x + a\left(\frac{1}{5}\right)t = \frac{12}{25} + \frac{1}{100}e^{\frac{16}{25}}. \end{cases} \tag{3.87}$$

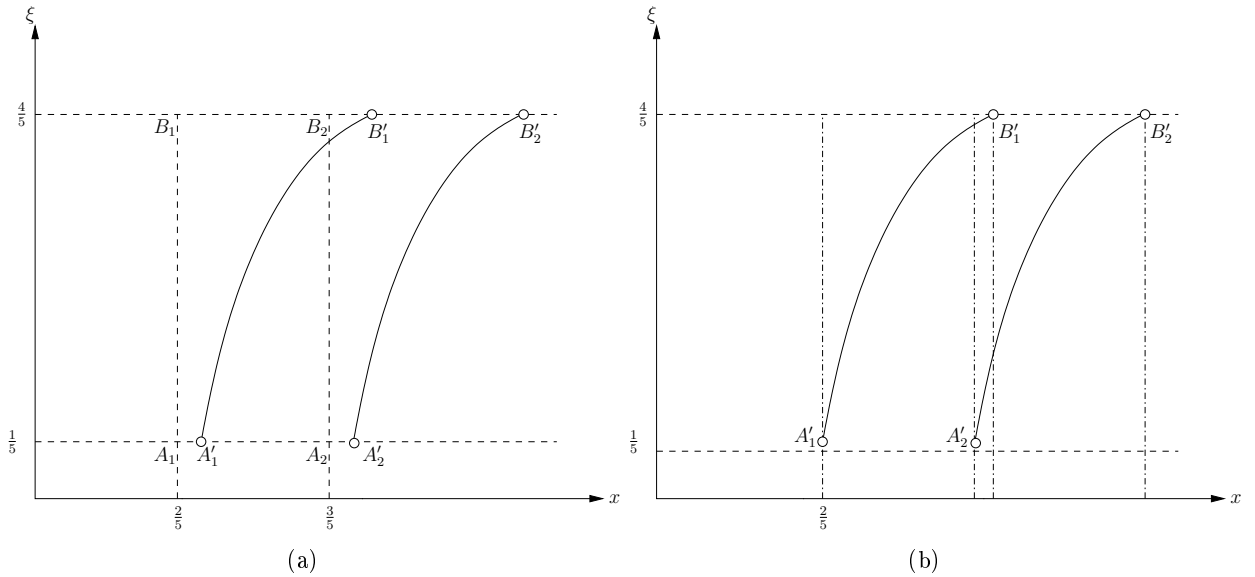

Figure 3.15: Schematic representation of the evolution between the initial condition (points A_1, A_2, B_1, B_2) and the final condition at time $t = 0.4$ (points A_1', A_2', B_1', B_2') (a). The regions in which the exact solution should be computed, at the final time $t = 0.4$, are reported in (b).

At the final time step, four different regions can be identified (see Figure 3.15(b)). The solution in the external region, where $x \leq A_1'^{,x}$ and $x \geq B_2'^{,x}$, is easily identified as $u(x, \xi, t) = 0$. For the remaining regions, the position of the discontinuity has to be computed. In particular, it is possible to define the two functions $\xi_d^1 = \xi_d^1(x)$ and $\xi_d^2 = \xi_d^2(x)$ as the positions of the discontinuities for each x belonging respectively to the intervals $[A_1'^{,x}, B_1'^{,x}]$ and $[A_2'^{,x}, B_2'^{,x}]$. If x belongs to the interval defined above, the following relations must hold

$$\begin{cases} x = A_1'^{,x} + a\left(\xi_d^1\right)t = \frac{12}{25} + \frac{1}{100}e^{(\xi_d^1)^2} & \text{if} \quad x \in [A_1'^{,x}, B_1'^{,x}] \\ x = A_2'^{,x} + a\left(\xi_d^2\right)t = \frac{17}{25} + \frac{1}{100}e^{(\xi_d^2)^2} & \text{if} \quad x \in [A_2'^{,x}, B_2'^{,x}]. \end{cases} \tag{3.88}$$

As a consequence, the position of the discontinuities, for a certain physical position can be derived

$$\begin{cases} \xi_d^1 = \xi_d^1(x) = \sqrt{\ln\left(100\left(x - \frac{12}{25}\right)\right)} \\ \xi_d^2 = \xi_d^2(x) = \sqrt{\ln\left(100\left(x - \frac{17}{25}\right)\right)}. \end{cases} \tag{3.89}$$

The exact statistics of the physical cell average $\bar{u}_i$ can be computed exactly for each cell $\mathcal{C}_i =$

$\left[x_i - \frac{|\mathcal{C}_i|}{2}, x_i + \frac{|\mathcal{C}_i|}{2}\right]$ (in the limit of $|\mathcal{C}_i| \to 0$). For the mean, they are defined as

$$\mathcal{E}(\bar{u}_i) = \begin{cases} 0 & \text{if} \quad x_i \leq A_1'^{,x} \text{ or } x_i \geq B_2'^{,x} \\ \frac{5}{3}\left(\xi_d^1(x_i) - \frac{1}{5}\right) & \text{if} \quad x_i \in [A_1'^{,x}, A_2'^{,x}] \\ \frac{5}{3}\left(\xi_d^1(x_i) - \xi_d^2(x_i)\right) & \text{if} \quad x_i \in [A_2'^{,x}, B_1'^{,x}] \\ \frac{5}{3}\left(\frac{4}{5} - \xi_d^2(x_i)\right) & \text{if} \quad x_i \in [B_1'^{,x}, B_2'^{,x}]. \end{cases} \tag{3.90}$$

Concerning the variance, they can be obtained as (and not as $\text{Var} = \mathcal{E}((\bar{u}_i)^2) - (\mathcal{E}(\bar{u}_i))^2$)

$$\text{Var} = \mathcal{E}(\bar{u}_i) - (\mathcal{E}(\bar{u}_i))^2 \quad \forall x_i \in [0,1], \tag{3.91}$$

because in this specific case ($\bar{u}(x,\xi,t) = 1$)

$$\int_\Xi \bar{u}(x_i,\xi,t)^2 p(\xi)\mathrm{d}\xi = \int_\Xi \bar{u}(x_i,\xi,t) p(\xi)\mathrm{d}\xi = \mathcal{E}(\bar{u}_i). \tag{3.92}$$

In Figure 3.16, the spatial convergence for the aSI scheme and for the full scheme, employing only the MHM with the superbee limiter (3.71), are reported for the mean 3.16(a) and the variance 3.16(b) (L_2 norms). Similar curves are obtained for L_1 and L_∞ norms but are not reported here for brevity. The computations are performed over equally spaced meshes in the physical space Ω with 51, 101, 201, 401 and 601 points. The aSI scheme is applied with a coarsest level of 16 cells ($m_0 = 4$), a finest level of 256 stochastic cells ($m = 4$) and a threshold equal to $\varepsilon = 10^{-3}$. The polynomial reconstruction is the quadratic polynomial with and without ENO selection of the stencil. The average number of stochastic cells employed is equal to 39 when the ENO selection is employed and 40 with the centered stencil.

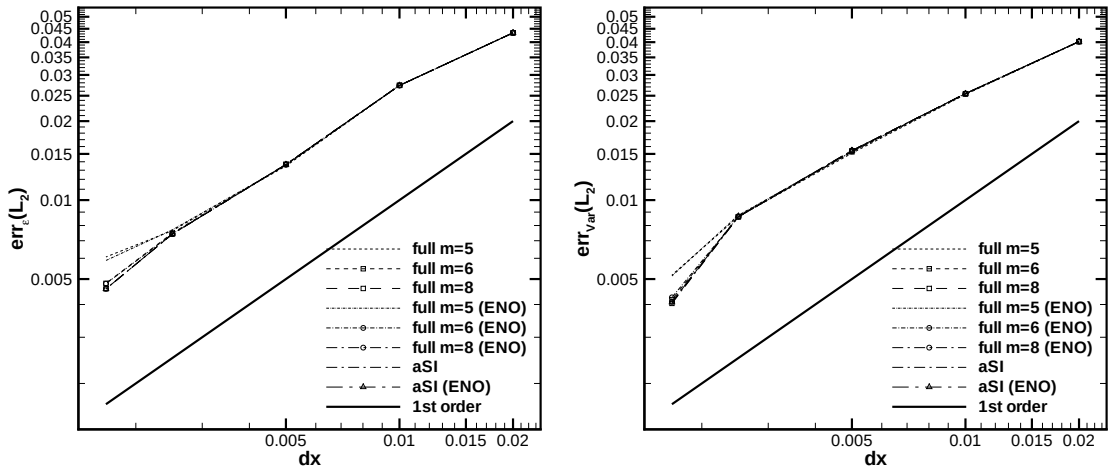

(a) (b)

Figure 3.16: Spatial convergence for the linear advection problem with discontinuous initial condition (3.86). The statistics of the solution (mean (a) and variance (b)) obtained with (aSI) and without (full) compression are reported for the MHM method with the superbee limiter (3.71).

The Figure 3.16 shows that the aSI scheme is able to preserve the accuracy and the order of convergence of the full scheme with a reduction of the computational cost with respect to the full

solution obtained over a grid of 256 cells ($m = 8$). The aSI scheme requires a computational effort equivalent to a computation carried out on about 40 equally spaced stochastic cells. The full solutions on 32 ($m = 5$) and 64 ($m = 6$) cells are then reported in order to compare the efficiency of the scheme with respect to a solution obtained with a similar computational effort. However, the aSI scheme performs better with respect to both the full solution at 32 and 64 cells. Moreover, the quality with respect to the full solution of 256 cells is only slightly degraded. In figures 3.17 and 3.18, the statistics of the solution are reported over the entire physical space (the mesh of 601 points) and compared to the exact solution (see (3.90)) obtained on 2001 equally spaced points in the physical space. The solutions obtained with the full scheme with 32 and 64 stochastic cells exhibit the well-known staircase phenomenon, i.e. in presence of discontinuous solutions the statistics are constituted by a series of *plateau*. The presence of the plateau is due to the lower resolution associated to the discretization of the stochastic space with respect to the resolution of the physical space. The staircase phenomenon is more evident for the coarser case (32 cells), reduces slightly with 64 cells, and disappear with 256 cells. The aSI scheme automatically refines the space where a higher resolution is required. Remark that the staircase problem disappears by using aSI even if the (average) number of cells employed is lower than 64 (see Figure 3.17(b) and 3.18(b)).

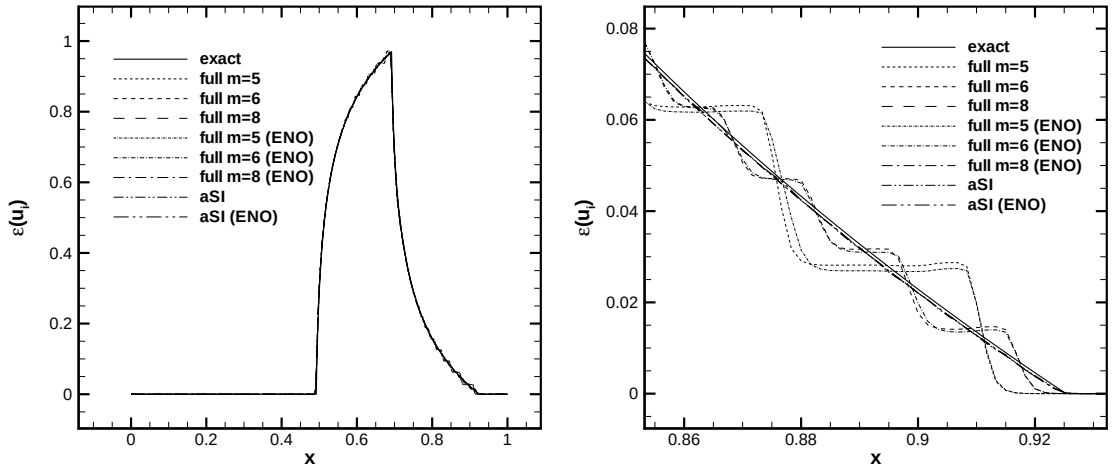

(a) (b)

Figure 3.17: Expectancy for the cell averaged solution of the linear advection equation with discontinuous initial condition (3.86) at the final time $t = 0.4$. The whole physical domain is represented in (a), while in the Figure (b) a zoom in the shock region is reported. The mesh is constituted by 601 equally spaced points.

The ability of aSI scheme to refine only locally the space allows to increase locally the resolution along the stochastic space. In Figure 3.19, the distribution of the stochastic cells over Ω at the final time step $t = 0.4$ is reported. It is evident that the higher computational effort is located in the region of the strong gradients; comparing the Figure 3.18 and 3.19, it is evident that the two peaks associated to the local higher computational effort (in terms of stochastic cells) corresponds to the two peaks in the variance of the solution. In Figure 3.19, the number of points employed by the aSI scheme with and without the ENO selection of the stencil are also reported. The ENO selection of the stencil reduces the number of cells employed. Morevoer, comparing the average number of stochastic cells employed for each computation, it is evident that the efficiency of the ENO selection increases with the spatial resolution. This is due to the global representation of the solution $u(x, \xi, t)$ over cells $\mathcal{C}_i \times \Xi_j$. Higher is the spatial resolution, sharper are the resulting discontinuities, so the

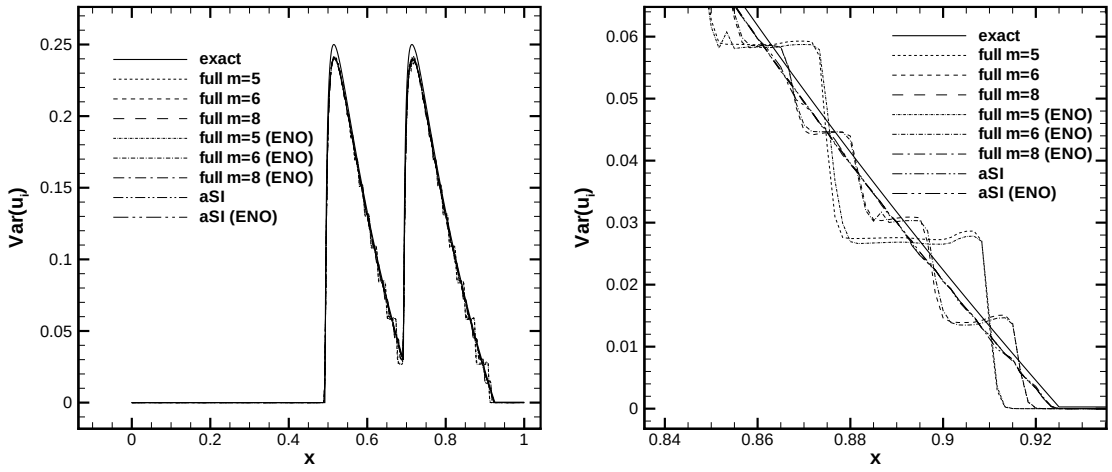

(a) (b)

Figure 3.18: Variance for the cell averaged solution of the linear advection equation with discontinuous initial condition (3.86) at the final time $t = 0.4$. The whole physical domain is represented in (a), while in the Figure (b) a zoom in the shock region is reported. The physical mesh is constituted by 601 equally spaced points.

ENO becomes more useful in order to gain in terms of accuracy (with the SI algorithm) and in terms of compression capabilities (with the TE algorithm). Figure 3.19(b) displays that for too coarse spatial resolution, the ENO selection of the stencil can be negative in terms of both accuracy and compression. The solution becomes smoother and smoother by decreasing the spatial resolution, so a centered stencil becomes the best choice.

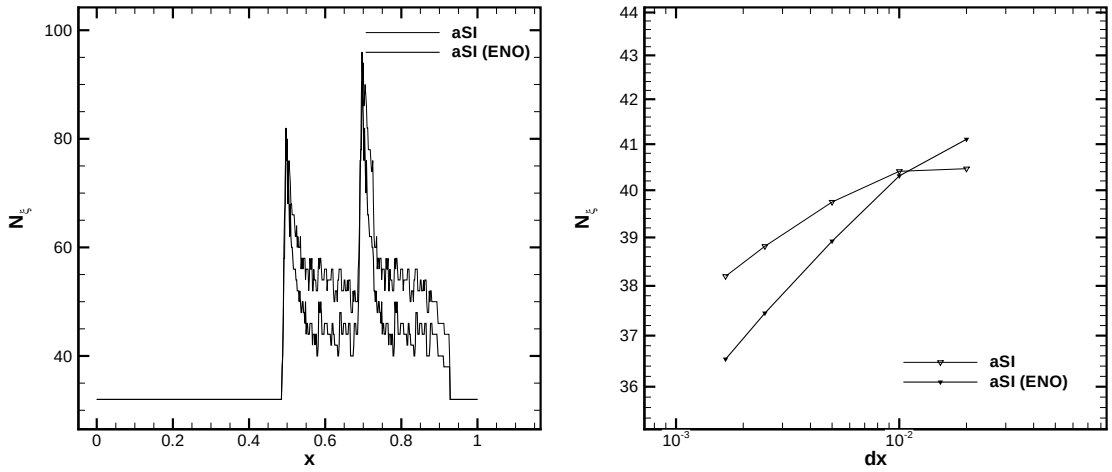

(a) (b)

Figure 3.19: Evolution of the number of stochastic cells employed in each physical location for the aSI scheme with and without the ENO reconstruction (a) for the linear advection equation with discontinuous initial condition. The average number of stochastic cells employed by the aSI scheme as function of the physical space resolution is reported in (b).

3.2.5.2 Inviscid Burgers equation

In this section, the aSI algorithm is applied to the solution of the inviscid Burgers equation

$$\frac{\partial u(x,\xi,t)}{\partial t} + \frac{\partial f(u(x,\xi,t))}{\partial x} = 0 \quad x \in [0,1] \quad \text{and} \quad t \in [0,T], \tag{3.93}$$

where the flux function is defined as $f = f(u(x,\xi,t)) = \frac{1}{2}u^2(x,\xi,t)$.

We assume the following uncertain initial condition, with the random parameter uniformly distributed $\xi \sim \mathcal{U}[0,1]$,

$$u(x,\xi,0) = \begin{cases} H(\xi) & \text{if} \quad x \in [A_1^x, A_2^x] \\ 0 & \text{if} \quad \text{otherwise.} \end{cases} \tag{3.94}$$

The initial condition is represented by a hat function with a different amplitude dependent (non linearly) from the random parameter, $H(\xi) = \frac{1}{3}\xi^2 + \frac{1}{100}\xi + \frac{9}{10}$. To obtain the exact solution it is necessary to consider the two elementary solutions of the Riemann problem of the inviscid Burgers equation (see [LeVeque 2002] for further details). The first case at the left of the hat function ($x = \frac{1}{10}$) is the Riemann problem with $u_l < u_r$ that admits as solution a rarefaction wave (depending on the uncertainty parameter) as follows

$$u(x,\xi,t) = \begin{cases} 0 & \text{if} \quad x \leq A_1^x \\ F(x) & \text{if} \quad x \in [A_1^x, A_1^x + H(\xi)t] \\ H(\xi) & \text{if} \quad x > A_1^x + H(\xi)t, \end{cases} \tag{3.95}$$

where the solution inside the rarefaction wave is $F(x) = (x + A_1^x)/t$.

Knowing the function $H(\xi)$, the exact solution for the uncertain rarefaction wave can be computed. Let us consider now the right of the hat initial function ($x = \frac{1}{2}$), where the solution of the Riemann problem is a shock wave traveling with an uncertain speed $s = H(\xi)/2$. The complete solution of the Riemann problem is then

$$u(x,\xi,t) = \begin{cases} H(\xi) & \text{if} \quad x < A_2^x + st \\ 0 & \text{if} \quad x > A_2^x + st. \end{cases} \tag{3.96}$$

We solve the problem (3.93) until a time equal to $T = 0.6$, with the initial condition (3.94) defined by $A_1^x = B_1^x = \frac{1}{10}$ and $A_2^x = B_2^x = \frac{1}{2}$. The solution appears as sketched in Figure 3.20, where the tail of the fan is at rest ($x = \frac{1}{10}$) while the position of the head is a function of the random parameter and its value is bounded between the slower moving fan ($A_1'^{,x} = \frac{1}{10} + H(0)t$) and the fast moving fan ($B_1'^{,x} = \frac{1}{10} + H(1)t$). The random parameter corresponding to a physical position $x \in [A_1'^{,x}, B_1'^{,x}]$ can be found after some algebraic manipulations analytically, by solving for ξ the equation $x = A_1^x + H(\xi)t$ for $A_1'^{,x} \leq x \leq B_1'^{,x}$, $\xi_F = \xi_F(x)$ (see Figure 3.20 for the locus ξ_F). Following a similar procedure, the value of the random parameter corresponding to the shock position $\xi_{SW} = \xi_{SW}(x)$ can be found analytically, solving for ξ the equation $x = A_2^x + \frac{1}{2}H(\xi)t$ for $A_2'^{,x} \leq x \leq B_2'^{,x}$.

The statistics of the solution can be computed analytically for each cell $\mathcal{C}_i$ as follows. For the expectancy of the physical cell averaged value $\bar{u}_i$, it holds that

$$\mathcal{E}(\bar{u}_i) = \begin{cases} 0 & \text{if} \quad x_i \leq A_1^x \text{ or } x_i \geq B_2'^{,x} \\ F(x_i) & \text{if} \quad x_i \in [A_1, A_1'^{,x}] \\ \displaystyle\int_0^{\xi_F(x_i)} H(\xi)\mathrm{d}\xi + F(x_i)(1-\xi_F(x_i)) & \text{if} \quad x_i \in [A_1'^{,x}, A_2'^{,x}] \\ \displaystyle\int_{\xi_F(x_i)}^{\xi_{SW}(x_i)} H(\xi)\mathrm{d}\xi + F(x_i)(1-\xi_F(x_i)) & \text{if} \quad x_i \in [A_2'^{,x}, B_1'^{,x}] \\ \displaystyle\int_{\xi_{SW}(x_i)}^{1} H(\xi)\mathrm{d}\xi & \text{if} \quad x_i \in [B_1'^{,x}, B_2'^{,x}]. \end{cases} \tag{3.97}$$

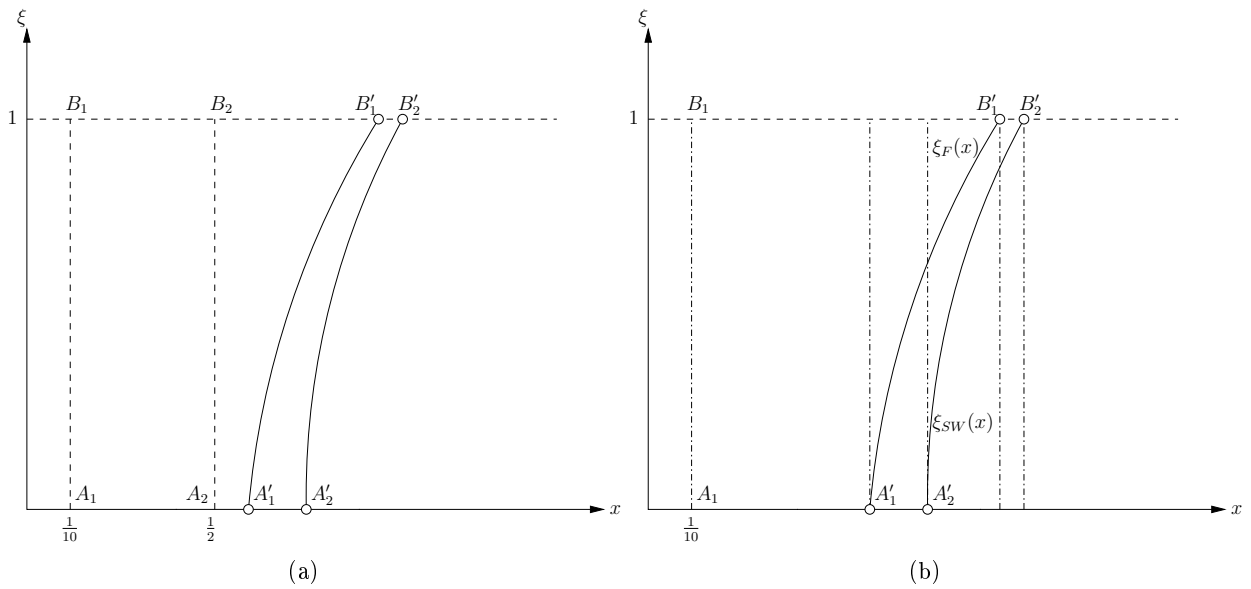

Figure 3.20: Schematic representation of the evolution between the initial condition (points A_1, A_2, B_1, B_2) and the final condition at time $t = 0.6$ (points A'_1, A'_2, B'_1, B'_2) (a). The regions in which the exact solution should be computed, at the final time $t = 0.6$, are reported in (b).

All the integrals in the equation (3.97) can be computed analytically.

Moreover, the variance is easily analytically computed, due to the polynomial behavior of $H(\xi)$, as follows

$$\mathrm{Var}(\bar{u}_i) = \begin{cases} 0 & \text{if} \quad x_i \leq A_1'^{,x} \text{ or } x_i \geq B_2'^{,x} \\ \displaystyle\int_0^{\xi_F(x_i)} H^2(\xi)\mathrm{d}\xi + F^2(x_i)(1-\xi_F(x_i)) - \mathcal{E}^2(\bar{u}_i) & \text{if} \quad x_i \in [A_1'^{,x}, A_2'^{,x}] \\ \displaystyle\int_{\xi_F(x_i)}^{\xi_{SW}(x_i)} H^2(\xi)\mathrm{d}\xi + F^2(x_i)(1-\xi_F(x_i)) - \mathcal{E}^2(\bar{u}_i) & \text{if} \quad x_i \in [A_2'^{,x}, B_1'^{,x}] \\ \displaystyle\int_{\xi_{SW}(x_i)}^{1} H^2(\xi)\mathrm{d}\xi - \mathcal{E}^2(\bar{u}_i) & \text{if} \quad x_i \in [B_1'^{,x}, B_2'^{,x}]. \end{cases} \tag{3.98}$$

The (stochastic) inviscid Burgers problem (3.93) is solved over a set of equally spaced physical meshes with 51, 101, 201, 401 and 601 points. The time space is discretized using 600 time steps of constant length $\Delta t = 1 \times 10^{-3}$. The error norms in L_2, with respect to the exact stochastic solution (see equations (3.97) and (3.98)), are reported in Figure 3.21. Similar results are obtained for L_1 and L_∞ norms, but are not reported here for brevity. The reference solution is the full computation performed with the SI scheme and a 256 ($m = 8$) equally spaced stochastic cells. This solution is compressed by means of the aSI scheme with a coarsest level of $m_0 = 4$ and a finest level of $m = 8$ with a threshold equal to $\varepsilon = 10^{-4}$. For both the full SI and the aSI schemes the computations are performed employing quadratic polynomial reconstruction with and without the ENO selection of the stencil. For each computation, the average number of stochastic cells is evaluated obtaining the equivalent number of equally spaced stochastic cells (with the same computational cost). The evolution of the number of stochastic cells associated to the different (physical) spatial resolutions are reported in Figure 3.24(b) for the aSI scheme with and without the ENO procedure. Moreover, SI scheme is applied over 16 ($m = 4$) and 32 ($m = 5$) equally spaced stochastic cells. These resolutions are chosen because the average number of stochastic cells employed by the aSI scheme varies between these values. The SI scheme fails to converge with the expected first order slope both with and without the ENO, because of the appearance of the staircase phenomenon. The stochastic

resolution is not high enough with respect to the physical resolution, as evident looking at the three last spatial resolutions in Figure 3.21.

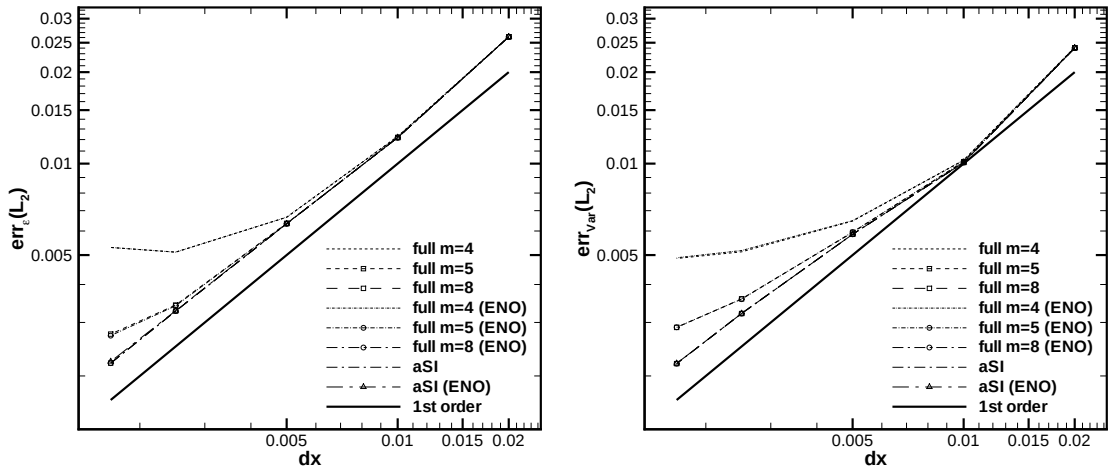

(a) (b)

Figure 3.21: Spatial convergence for the Burgers equation with an uncertain hat initial condition (3.94). The statistics of the solution (mean (a) and variance (b)) obtained with (aSI) and without (full) compression are reported for the MHM method with superbee limiter (3.71).

The staircase phenomenon is evident in Figures 3.22 and 3.23, where the expectancy and the variance of the solution are reported over the 601 points physical mesh (the exact solution is evaluated over a mesh of 2001 equally spaced points). In particular, figures 3.22(b) and 3.23(b) show a zoom of the curves in the region, where the (uncertain) shock wave propagates (see Figure 3.20). As expected, increasing the number of stochastic cells, even equally spaced, reduces the staircase phenomenon (from 16 to 32 cells). It disappears at 256 cells. Note that the aSI scheme, with an overall computational cost similar to the two coarse full simulations, produces better results (without the appearance of the staircase phenomenon) concentrating the computational effort, *i.e.* the number of cells, in the regions where the solution is less regular. The capability to refine and derefine during the simulation following the evolution of the solution in the physical/stochastic space makes the aSI scheme more efficient, yielding results that nearly coincide with the full reference solution.

As already discussed for the solution of the linear advection equation with discontinuous initial condition, the presence of the ENO selection of the stencil makes the computations progressively more efficient increasing the physical resolution. This effect is evident in Figure 3.24(b), where the (average) number of stochastic cells employed is reported as a function of the physical resolution. In Figure 3.24(a), the direct comparison between the aSI scheme with and without the ENO selection of the stencil over the finest 601 points physical mesh is shown. With lower resolution meshes, there is no advantage in using the ENO procedure due to the representation of the solution over cells in the overall physical/stochastic space. However, the slope associated to the average number of stochastic cells shows that the solutions are represented by a narrow discontinuity (due to the increase of the spatial resolution). As a consequence, the non-oscillatory interpolation helps to avoid the so-called *pollution* of the stencil, *i.e.* the propagation of the interpolation error in the neighboring cells of a discontinuity. Again, the combination of the aSI scheme and the use of the ENO procedure for the polynomial interpolation, becomes even more efficient as the spatial resolution is increased. This is a desired property for any intrusive UQ scheme.

In the following section, the aSI scheme is applied to non linear system of stochastic partial

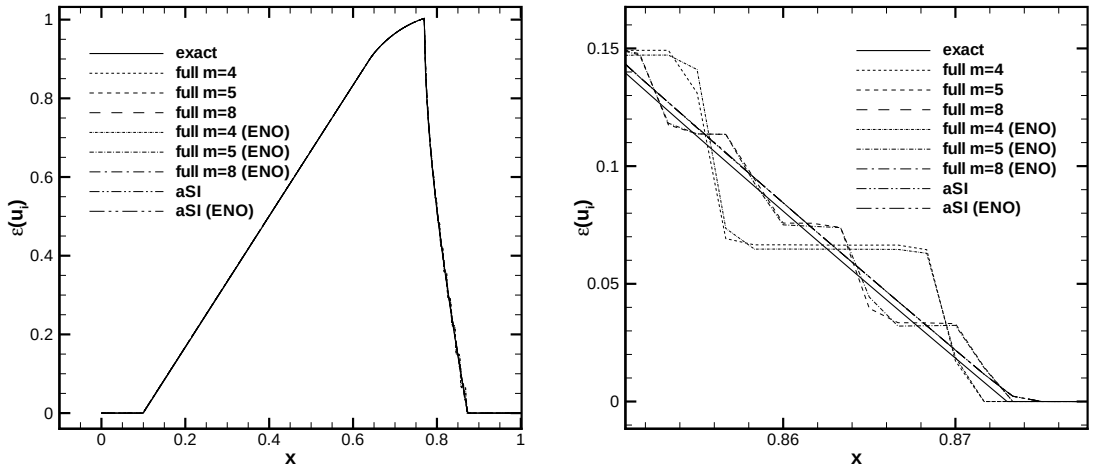

(a) (b)

Figure 3.22: Expectancy for the cell-averaged solution of the inviscid Burgers equation at the final time $t = 0.6$. The whole physical domain is represented in (a), while in Figure (b) a zoom in the shock region is reported. The physical mesh is constituted by 601 equally spaced points.

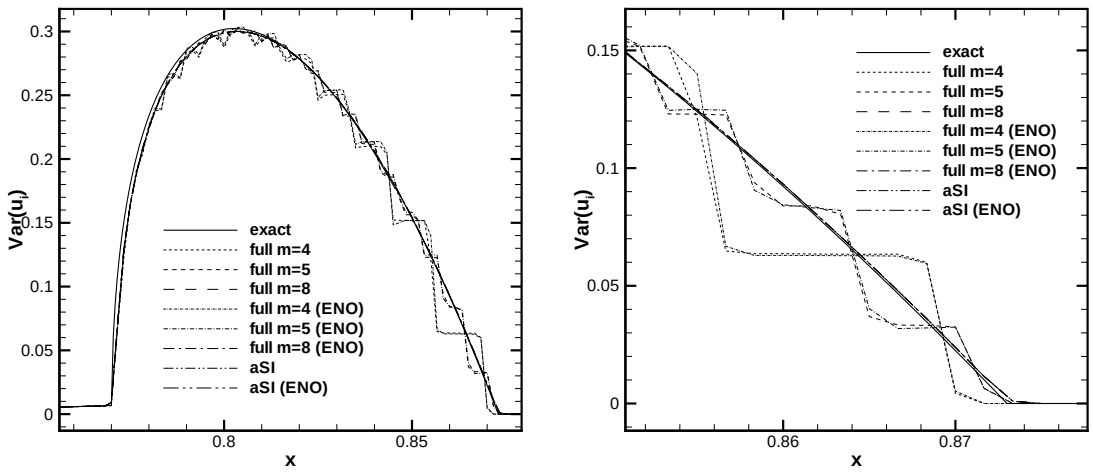

(a) (b)

Figure 3.23: Variance for the cell-averaged solution of the inviscid Burgers equation at the final time $t = 0.6$. Two different zooms in the shock region are reported. The physical mesh is constituted by 601 equally spaced points.

differential equations.

3.2.5.3 Uncertain shock tube

In this section, the solution of the uncertain shock tube problem is reported. The problem can be modeled by the well-known 1D Euler equations

$$\frac{\partial \mathbf{u}}{\partial t} + \nabla \cdot \mathbf{f}(\mathbf{u}) = \mathbf{0} \tag{3.99}$$

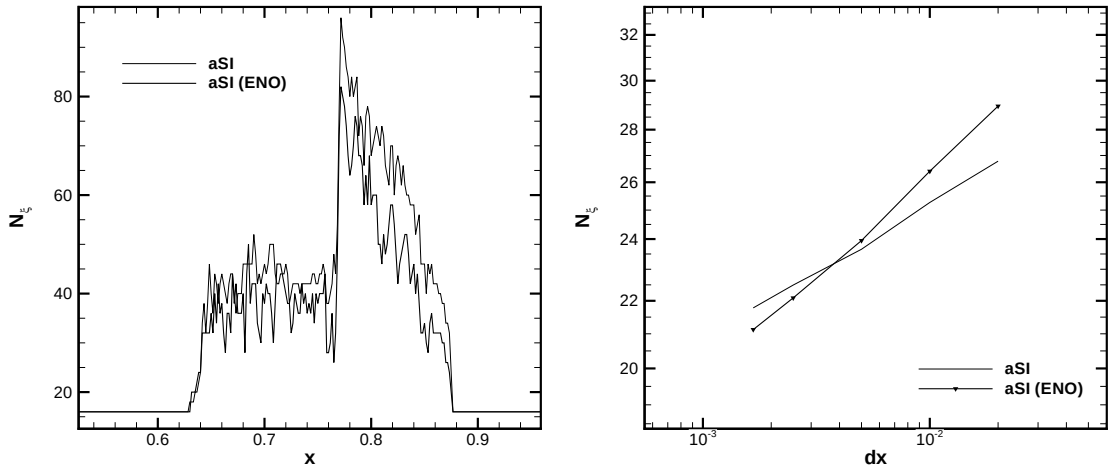

(a) (b)

Figure 3.24: Evolution of the number of stochastic cells employed for each physical location for the aSI scheme with and without the ENO reconstruction (a) for the inviscid Burgers equation. The average number of stochastic cells employed by the aSI scheme as a function of the physical space resolution is reported in (b).

where the vector of conservative variables, the density ρ, the momentum $m = \rho u$ and the total Energy E^t, $\mathbf{u} \in \mathbb{R}^3$ and the flux vector $\mathbf{f}(\mathbf{u}) \in \mathbb{R}^3$ are

$$\mathbf{u} = \begin{pmatrix} \rho \\ m \\ E^t \end{pmatrix} \quad \mathbf{f}(\mathbf{u}) = \begin{pmatrix} m \\ \dfrac{m^2}{\rho} + \Pi(\mathbf{u}) \\ \dfrac{m}{\rho}\left(E^t + \Pi(\mathbf{u})\right). \end{pmatrix} \tag{3.100}$$

The pressure $\Pi(\mathbf{u})$ (as function of the conservative variables) can be derived for a polytropic ideal gas as follows

$$\Pi(\mathbf{u}) = (\gamma - 1)\left(E^t - \frac{1}{2}\frac{|m^2|}{\rho}\right). \tag{3.101}$$

The initial condition for the uncertain shock tube problem is derived from the classical Sod test case [Sod 1978], where an uncertainty of the density at the left state ($x < x_d$ for $t = 0$) is introduced:

$$\mathbf{u}_L(x, \xi, t) = \begin{pmatrix} \rho_L(\xi) \\ 0 \\ \dfrac{p_L}{\gamma - 1} \end{pmatrix} \quad \mathbf{u}_R(x, \xi, t) = \begin{pmatrix} \rho_R \\ 0 \\ \dfrac{p_R}{\gamma - 1}. \end{pmatrix}, \tag{3.102}$$

In particular, the density on the left state is dependent from an uniformly distributed random parameter $\xi \sim \mathcal{U}[0, 1]$: $\rho_L(\xi) = 0.3 + 1.6\xi$. The values of the pressures are $p_L = 1$ and $p_R = 0.1$, while the right value of the density is $\rho_R = 0.125$. The total energy E^t is obtained (considering the gas at the rest in the whole domain) as a function of the local pressure and the ratio between specific heats, that for a diatomic gas can be assumed equal to $\gamma = 1.4$.

As pointed out by Toro [Toro 1997], analyzing the eigenvalue structure of the Euler equations, the Riemann problem for the 1D Euler equations (see figure 3.25) generates (for $t > 0$) four states, where

two are not known (variables are indicated with a star in the following). The Riemann problem for the solution of the 1D Euler equation can be reduced to the solution of a single non-linear algebraic equation for the pressure in the star region $p^\star$ from which the other quantities can be computed. With an uncertain shock tube problem, the dependence of $p^\star$ from the random parameter $p^\star = p^\star(\xi)$ should be considered. Unfortunately, this dependence cannot be computed explicitly. In this paper, only the case involving a left moving rerefaction fan and a right moving shock wave are considered. Moreover, initial conditions (3.102) produce this wave structure for all the random parameter taken into account. The problem is further complicated by the presence of complex functions that should be integrated to compute the exact statistics required. The solution strategy employed is the following. For each physical location, where the exact statistics should be computed, the solution along the stochastic space is divided into smooth regions (where the numerical quadrature with a large number of points produces fair well-converged results even for non-polynomial functions). The main issue is to determine the location of a discontinuity. This task can be accomplished solving an algebraic non-linear equation for the random parameter that can be formulated to involve all (but not only) the derivative available for the solution of the deterministic Riemann problem. After the subdivision of the random space in more regions, where the quadrature can be done numerically without accuracy loss (to the desired global accuracy), the statistics are computed in order to obtain the desired reference solutions.

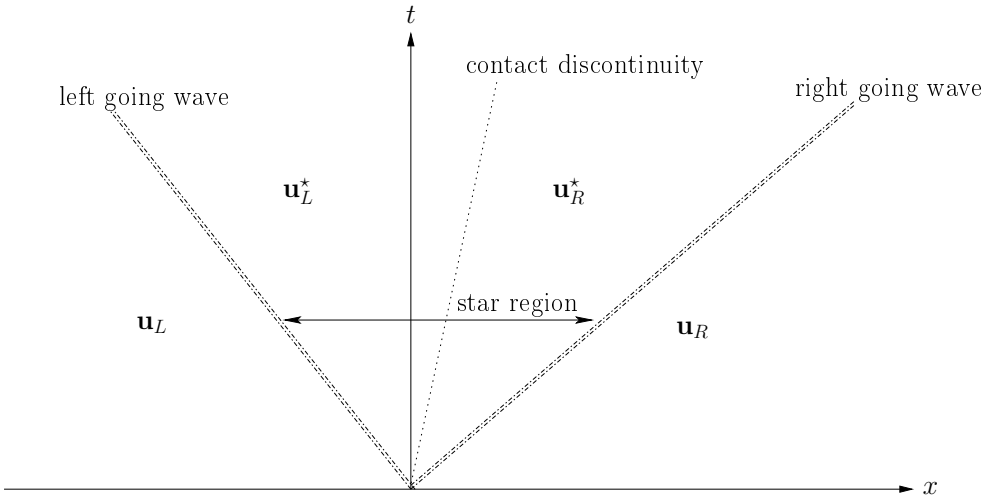

Figure 3.25: Riemann wave structure for the 1D Euler equation.

Details of the numerical procedure to obtain the reference solution of the stochastic Riemann problem are reported in [21].

Simulations are performed over a physical domain $\Omega = [-\frac{1}{5}, \frac{6}{5}]$ until a final time $t = 0.31$ with the position of the diaphragm equal to $x_d = 0.42$. The time space is divided in 6200 equal time steps of length $\Delta t = 5 \times 10^{-5}$. The simulations are carried out over equally spaced meshes of 201, 401, 801 and 1001 points employing the aSI scheme based on the MHM with a van Leer limiter (see equation (3.72)).

In figure 3.26, the spatial convergence is reported for both the mean (3.26(a)) and the variance (3.26(b)) in L_2 for the density ρ. The aSI method is obtained with a coarsest level of 4 ($m_0 = 2$) cells and a finest level of 256 ($m = 8$) stochastic cells with $\varepsilon = 10^{-4}$, while the reference solution is the full SI scheme with 256 cells. The aSI scheme has used an average number of stochastic cells between the two levels $m = 5$ and $m = 6$ (see figure 3.29(b)), so the other solutions are computed by means of the SI scheme for comparison. For all the schemes, both the centered second order polynomial reconstruction and the non-linear ENO one are used. The difference between the two polynomial reconstructions is difficult to appreciate because the spatial resolution is too poor for a

sharp representation of the discontinuities. In this sense, there is no advantage in using the ENO reconstruction (for the aSI scheme and the SI scheme). The first order of convergence is attained for the expectancy of the density ρ, while, even with the SI scheme, the variance exhibits a lower rate of convergence 3.26(b). This behavior clearly indicates that even the solution employing 256 stochastic cells is not fully converged for moments higher than the expectancy.

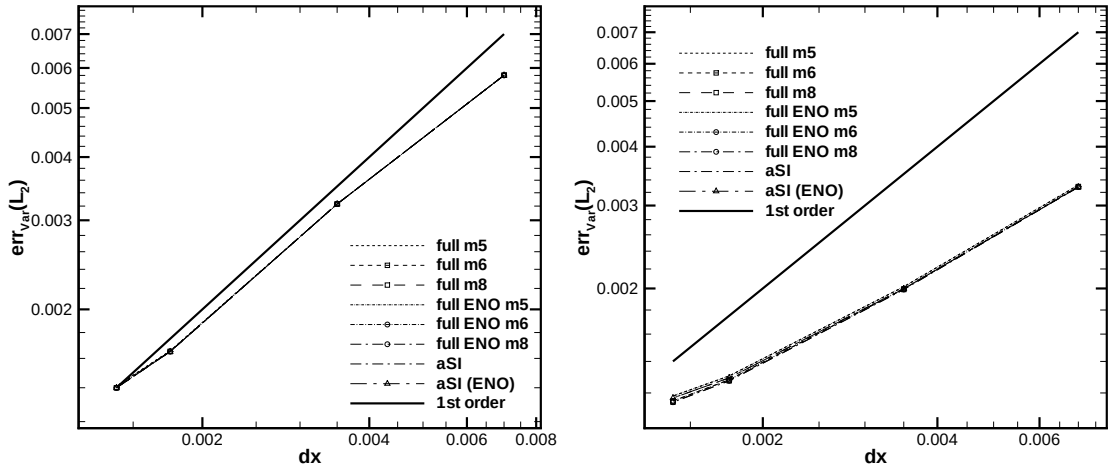

(a) (b)

Figure 3.26: Spatial convergence for the stochastic shock tube problem equation with uncertain initial condition (3.102). The statistics of the solution (mean (a) and variance (b)) obtained with (aSI) and without (full) compression are reported for the MHM method with van Leer limiter (3.72).

However, the aSI scheme displays the required properties: it saves the order of accuracy of the full SI scheme, both for mean and variance (see figure 3.26), and the degradation of the accuracy is strongly limited. Moreover, as already shown in the previous numerical results, the phenomenon of the staircase approximation of the statistics is prevented by the adaptation in the stochastic space. As shown in figure 3.27, note that all the numerical solutions are very similar to the exact solution 3.27(a) obtained over a mesh of 2001 equally spaced points in the physical space. By zooming (3.27(b)), the presence of the typical staircase phenomenon for both the SI scheme with 32 and 64 stochastic cells appears. The solution obtained with the aSI scheme agree very well with its full counterparts.

As already demonstrated for the mean, even for the variance, the presence of the staircase approximation is prevented by the refinement of the stochastic space (see figure 3.28). Even if curves nearly coincide in figure 3.28(a), in the shock region the presence of the typical step pattern is evident for the full SI solution with 32 and 64 equally spaced stochastic cells (see 3.28(b)).

The lower order of convergence attained for the variance, even for the non compressed solution, highlights that the error in the stochastic space dominates the global error. As already demonstrated, the efficiency of the ENO selection of the stencil is related to the sharp representation of the discontinuities. In this case, the results with and without the ENO selection of the stencil are very similar. No advantages, even in term of compression, are observed. This issue is evident in figure 3.29(a), where the number of stochastic cells, along the physical domain, are reported. The region associated to the discontinuity spreads over a larger domain and, globally, the presence of non-centered stencils degradates the quality of prediction. This issue is well known in the ENO literature [Aràndiga 2004]. A possible cure, outside the scope of the present paper, would be the introduction of WENO type of interpolation. Employing a WENO type of interpolation, the correct centered stencil could be

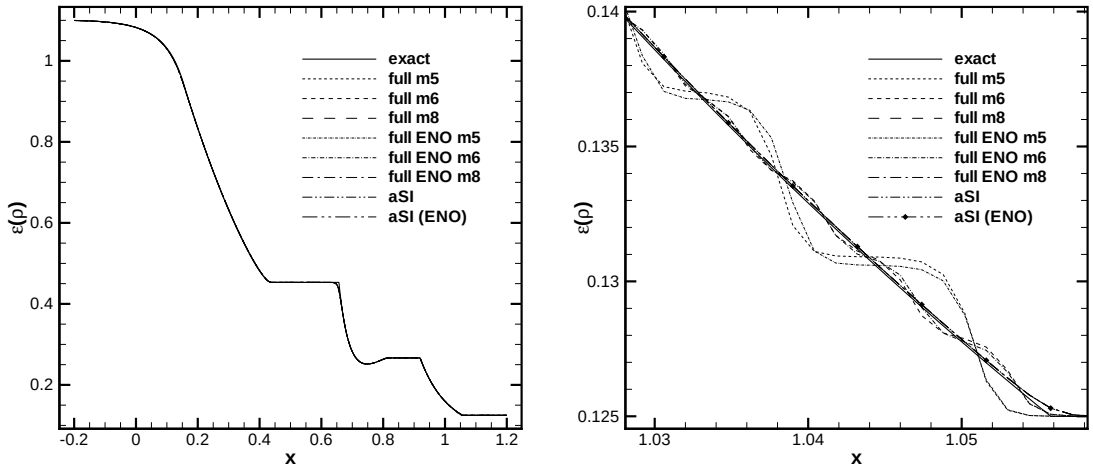

(a) (b)

Figure 3.27: Density Expectancy for the cell averaged solution of the uncertain shock tube problem at the final time $t = 0.31$. The whole physical domain is represented in (a), while in the figure (b) a zoom in the shock region is reported. The physical mesh is constituted by 1001 equally spaced points.

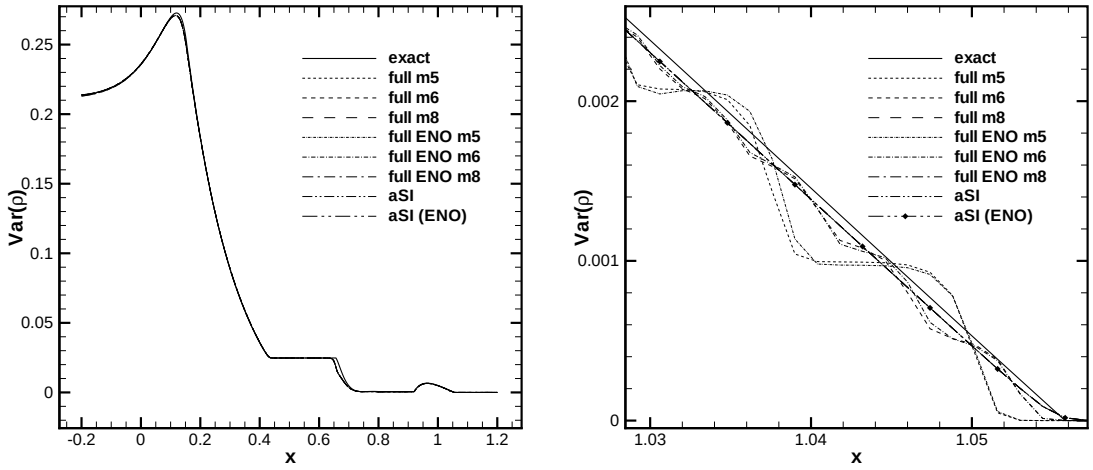

(a) (b)

Figure 3.28: Density Variance for the cell averaged solution of the uncertain shock tube problem at the final time $t = 0.31$. The whole physical domain is represented in (a), while in the figure (b) a zoom in the shock region is reported. The physical mesh is constituted by 1001 equally spaced points.

recovered without strong degradation of the prediction (the author already introduced a WENO interpolation in [Abgrall 2013a] in the context of the MR point-value setting).

The evolution of the average number of stochastic cells employed by the aSI scheme with and without the ENO interpolation is reported in 3.29(b). In this case, there is no intersection between the two curves, revealing that in this case the ENO interpolation gives no advantage, even for high

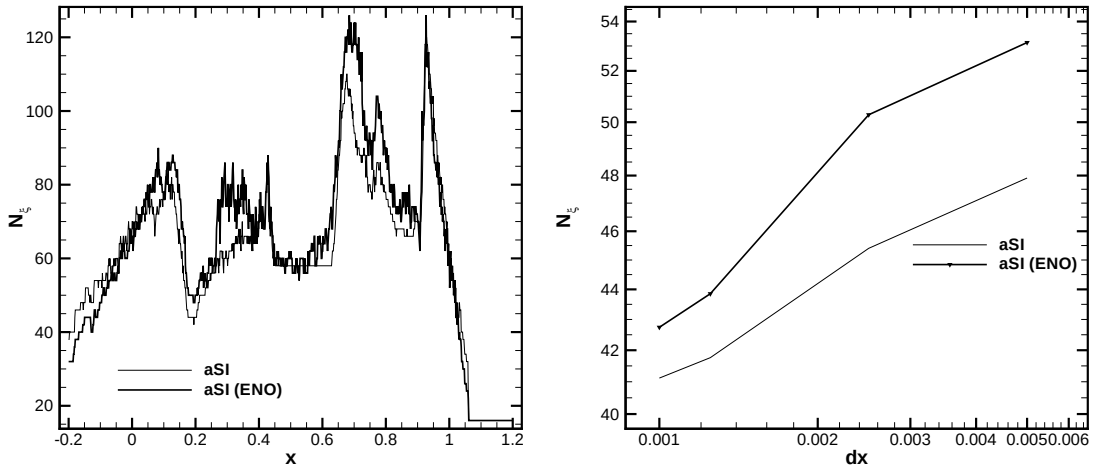

(a) (b)

Figure 3.29: Evolution of the number of stochastic cell employed for each physical location for the aSI scheme with and without the ENO reconstruction for the shock tube problem. The average number of stochastic cells employed by the aSI scheme as function of the physical space resolution has been reported in (b).

physical space resolutions.

3.2.6 Concluding remarks

In this section, a classical MR Harten framework, in its cell average setting, has been coupled to the Semi-Intrusive (SI) scheme. The overall numerical scheme is the so-called adaptive-SI scheme. We demonstrated that it preserves the convergence properties of the original SI scheme with a strong saving in terms of computational cost. Different test-cases have been presented to demonstrate the efficiency and the accuracy properties of the aSI scheme. The linear advection equation has been solved for initial smooth and discontinuous solution to demonstrate the capability of the stochastic scheme to preserve the accuracy related to the deterministic MUSCL-Hancock method (MHM). A second test-case has been focused on the inviscid Burgers equation. We demonstrated the capability of the method to automatically refine/derefine following the changes in the regularity of the solution in the coupled stochastic/physical space. In particular, a smooth solution has been considered, in the stochastic space, as initial condition, where shock waves velocities are directly related to the parameter in the stochastic space. The final test case proposed has been the Euler system of equation to solve an uncertain shock tube problem. The aSI scheme has been demonstrated to be efficient also in the case of vectorial problems. For the computation of the convergence curves, an original strategy for the semi-analytical solution of the stochastic shock tube problem has been also developed following and extending the classical numerical procedure for the solution of the Riemann problem for the Euler equations. The generality of the approach is not limited to second order scheme, but can be easily extended to higher order numerical formulation for the physical space and time discretizations. In the present work, both the linear and non-linear MR framework have been presented in which the selection of the stencil to obtain the reconstruction operators can be obtained by a data-dependent procedure. The ENO selection of the stencil has been also introduced. Considering the numerical results presented, note that the advantages related to the non-linear schemes are very limited. This issue is related not to the non-linear procedure itself but to the peculiarity of the SI scheme that produces representations of the solution in a combined

physical stochastic space. The representation of discontinuous solution along the stochastic space can recover a smoother behavior when the physical spatial resolution is not high enough. This has been demonstrated showing that the importance of the ENO scheme increases with the physical space resolution. To improve the global properties of the scheme, two further steps seem useful. The first is the introduction of the WENO reconstruction instead of the ENO interpolation recovering the correct stencil in all the regions in which the solution is smooth, as it has been already presented for the point-value setting [Abgrall 2013a]. The other step could be to increase the polynomial order for the reconstruction. This should improve both accuracy and compression capabilities. The extension and the analysis of the aSI scheme for a moderate number of dimension is actually underway. Some highlights are given in Section 11.3.

3.3 Other works on intrusive methods

In this manuscript, the SI method is presented in details. Then, the TE algorithm for cell-averaged representation is coupled with the SI, thus yielding a global formulation for the aSI scheme.

Other works on the same research axis are not reported in the manuscript. In particular, the TE algorithm has been formulated first on node representation in [4] (See Section 12.6). Then, it has been applied to the approximation of stochastic ODEs [4] and to stochastic systems of partial differential equations [24]. This framework is efficient and very flexible; it allows to couple together different deterministic solvers(first order/high-order FV solvers, finite elements) and different time discretization. It is also able to treat time varying discontinuous non-classical pdf. Moving from the TE method, recently, an high-order numerical method for solving efficiently sPDE has been proposed [22], based on the reduction of the number of points employed in the physical/stochastic space by means of an adaptive technique. A weak coupling is performed in this case, since the number of points in the stochastic space varies according to the physical space, but the number of points in the physical space remains unchanged. A high-order ENO reconstruction is used for the stochastic space. The focus of this research is on non-linear hyperbolic systems with discontinuous solutions in both physical and stochastic spaces. Two different test cases are considered: the scalar Burgers equation and the Euler system of equations, in particular the simulation of a perfect gas flow in a shock-tube configuration.

Moreover, the aSI method has been recently incorporated into a DEM (Discrete Equation Method) formulation for two-phase flows. The idea is to build a very efficient tool for studying uncertainty propagation in high-fidelity multiphase code. Some highlights of this method are provided in Section 11.3.

Chapter 4

Uncertainty propagation and statistical moment decomposition

Contents

In this chapter, I present some results obtained on ANOVA-based analysis and uncertainty propagation. Some basic definitions for decomposing high-order statistics are provided. I present some results showing the importance of considering kurtosis sensitivity indices when ranking a set of uncertainties. Finally, an ANOVA-based analysis is applied to the simulation of a turbulent flow in a pipe.

4.1 High-order decomposition

4.1.1 HO statistics definitions and functional decomposition

Let us consider a real function $f = f(\boldsymbol{\xi})$ with $\boldsymbol{\xi}$ a vector of random inputs $\boldsymbol{\xi} \in \Xi^d = \Xi_1 \times \cdots \times \Xi_n$ ($\Xi \subset \mathbb{R}^d$) and $\boldsymbol{\xi} \in \Xi^d \longmapsto f(\boldsymbol{\xi}) \in L^2(\Xi^d, p(\boldsymbol{\xi}))$, where $p(\boldsymbol{\xi}) = \prod_{i=1}^{d} p(\xi_i)$ is the probability density function of $\boldsymbol{\xi}$.

We can define the central statistical moment of f of order n as

$$\mu^n(f) = \int_{\Xi^d} (f(\boldsymbol{\xi}) - E(f))^n p(\boldsymbol{\xi}) \mathrm{d}\xi, \tag{4.1}$$

where $E(f)$ indicates the expected value of f

$$E(f) = \int_{\Xi^d} f(\boldsymbol{\xi}) p(\boldsymbol{\xi}) \mathrm{d}\xi. \tag{4.2}$$

In the following, we indicate with σ^2, the variance (second-order moment), with s the skewness (third-order), and with k the kurtosis (fourth-order).

Let us apply the definition of the Sobol functional decomposition [Sobol 2001] to the function f as follows

$$f(\boldsymbol{\xi}) = \sum_{i=0}^{N} f_{\boldsymbol{m_i}}(\boldsymbol{\xi} \cdot \boldsymbol{m_i}), \tag{4.3}$$

where the multi-index $\boldsymbol{m}$, of cardinality $card(\boldsymbol{m}) = d$, can contain only elements equal to 0 or 1. Clearly, the total number of admissible multi-indices $\boldsymbol{m_i}$ is $N+1 = 2^d$; this number represent the total number of contributes up to the dth-order of the stochastic variables $\boldsymbol{\xi}$. The scalar product between the stochastic vector $\boldsymbol{\xi}$ and $\boldsymbol{m_i}$ is employed to identify the functional dependences of $f_{\boldsymbol{m_i}}$. In this framework, the multi-index $\boldsymbol{m}_0 = (0, \dots, 0)$, is associated to the mean term $f_{\boldsymbol{m}_0} = \int_{\Xi^d} f(\boldsymbol{\xi}) p(\boldsymbol{\xi}) \mathrm{d}\xi$. As a consequence, $f_{\boldsymbol{m}_0}$ is equal to the expectancy of f, *i.e.* $E(f)$. Let us assume, in the following, to order the N multi-indices $\boldsymbol{m_i}$ in the following way:

$$\begin{aligned}
\boldsymbol{m}_1 &= (1, 0, \dots, 0) \\
\boldsymbol{m}_2 &= (0, 1, \dots, 0) \\
&\vdots \\
\boldsymbol{m}_d &= (0, \dots, 1) \\
\boldsymbol{m}_{d+1} &= (1, 1, 0, \dots, 0) \\
\boldsymbol{m}_{d+2} &= (1, 0, 1, 0, \dots, 0) \\
&\vdots \\
\boldsymbol{m}_N &= (1, \dots, 1).
\end{aligned} \tag{4.4}$$

Except the term $\boldsymbol{m}_0$, that should be the first in the series, the remaining N multi-indices $\boldsymbol{m_i}$ should be classified with respect to a prescribed criterion. However, this criterion does not affect in any way the successive ANOVA functional decomposition.

The decomposition (4.3) is of ANOVA-type in the sense of Sobol [Sobol 2001] if all the members in Eq. (4.3) are orthogonal, *i.e.* as follows

$$\int_{\Xi^d} f_{\boldsymbol{m_i}}(\boldsymbol{\xi} \cdot \boldsymbol{m_i}) f_{\boldsymbol{m}_j}(\boldsymbol{\xi} \cdot \boldsymbol{m}_j) p(\boldsymbol{\xi}) \mathrm{d}\boldsymbol{\xi} = 0 \quad \text{with} \quad \boldsymbol{m_i} \neq \boldsymbol{m}_j, \tag{4.5}$$

and for all the terms $f_{\boldsymbol{m_i}}$, except f_0, holds

$$\int_{\Xi^d} f_{\boldsymbol{m_i}}(\boldsymbol{\xi} \cdot \boldsymbol{m_i}) p(\xi_j) \mathrm{d}\xi_j = 0 \quad \text{with} \quad \xi_j \in (\boldsymbol{\xi} \cdot \boldsymbol{m_i}) \,. \tag{4.6}$$

Each term $f_{\boldsymbol{m_i}}$ of (4.3) can be expressed as

$$f_{\boldsymbol{m_i}}(\boldsymbol{\xi} \cdot \boldsymbol{m_i}) = \int_{\Xi^{d-\mathrm{card}(\hat{\boldsymbol{m}}_{\boldsymbol{i}})}} f_{\boldsymbol{m_i}}(\boldsymbol{\xi} \cdot \boldsymbol{m_i}) p(\bar{\boldsymbol{\xi}}_i) \bar{\boldsymbol{\xi}}_i \quad - \sum_{\substack{\boldsymbol{m}_j \neq \boldsymbol{m_i} \\ \mathrm{card}(\hat{\boldsymbol{m}}_j) < \mathrm{card}(\boldsymbol{m_i})}} f_{\boldsymbol{m}_j}(\boldsymbol{\xi} \cdot \boldsymbol{m}_j), \tag{4.7}$$

where the multi-indexes, $\hat{\boldsymbol{m}}_{\boldsymbol{i}}$, have cardinality equal to the number of non-null elements in $\boldsymbol{m_i}$ and $\bar{\boldsymbol{\xi}}_i$ contains all the variables not contained in $(\boldsymbol{\xi} \cdot \boldsymbol{m_i})$, *i.e.* $(\boldsymbol{\xi} \cdot \boldsymbol{m_i}) \cup \bar{\boldsymbol{\xi}}_i = \boldsymbol{\xi}$.

The functional decomposition (4.3) is usually employed [Sobol 2001] to compute the contribution of each term to the overall variance, as shown in the next section. In [Abgrall 2012], we present how decomposing and computing HO statistical moments. Here, for the sake of brevity, we illustrate how computing variance in details.

4.1.2 Polynomial Chaos framework

This section and the following are devoted to show how variance can be easily computed in the polynomial chaos framework. If a polynomial chaos formulation is used, an approximation $\tilde{f}$ of the function f is provided

$$f(\boldsymbol{\xi}) \approx \tilde{f}(\boldsymbol{\xi}) = \sum_{k=0}^{P} \beta_k \Psi_k(\boldsymbol{\xi}), \tag{4.8}$$

where P is computed according to the order of the polynomial expansion n_0 and the stochastic dimension of the problem d

$$P + 1 = \frac{(n_0 + d)!}{n_0! d!}. \tag{4.9}$$

Each polynomial $\Psi_k(\boldsymbol{\xi})$ of total degree n_o is a multivariate polynomial form which involve tensorization of 1D polynomial form by using a multi-index $\boldsymbol{\alpha}^k \in \mathbb{R}^d$, with $\sum_{i=1}^{d} \boldsymbol{\alpha}_i^k \leq n_0$:

$$\Psi_k(\boldsymbol{\xi} \cdot \boldsymbol{m}^{\star,k}) = \prod_{\substack{i=1 \\ m_i^{\star,k} \neq 0}}^{d} \psi_{\alpha_i^k}(\xi_i) \tag{4.10}$$

where the multi index $\boldsymbol{m}^{\star,k} = \boldsymbol{m}^{\star,k}(\boldsymbol{\alpha}^k) \in \mathbb{R}^d$ is a function of $\boldsymbol{\alpha}^k$: $\boldsymbol{m}^{\star,k} = (m_1^{\star,k}, \ldots, m_d^{\star,k})$, with $m_i^{\star,k} = \alpha_i^k / \left|\left|\alpha_i^k\right|\right|_{\neq 0}$.

Remark that, for each polynomial basis, $\psi_0(\xi_i) = 1$ and then $\Psi_0(\boldsymbol{\xi}) = 1$. Then, the first coefficient β_0 is equal to the expected value of the function, *i.e.* $E(f)$. The polynomial basis is chosen accordingly to the Wiener-Askey scheme in order to select orthogonal polynomials with respect to the probability density function $p(\boldsymbol{\xi})$ of the input. Thanks to the orthogonality, the following relation holds

$$\int_{\Xi} \Psi_i(\boldsymbol{\xi}) \Psi_k(\boldsymbol{\xi}) p(\boldsymbol{\xi}) \mathrm{d}\xi = \delta_{ij} \langle \Psi_i(\boldsymbol{\xi}), \Psi_i(\boldsymbol{\xi}) \rangle \tag{4.11}$$

where $\langle \cdot, \cdot \rangle$ indicates the inner product and δ_{ij} is the Kronecker delta function.

The orthogonality can be advantageously used to compute the coefficients of the expansion in a non-intrusive PC framework

$$\beta_k = \frac{\langle f(\boldsymbol{\xi}), \Psi_k(\boldsymbol{\xi}) \rangle}{\langle \Psi_k(\boldsymbol{\xi}), \Psi_k(\boldsymbol{\xi}) \rangle}, \quad \forall k. \tag{4.12}$$

Several approaches can be used to estimate PC coefficients. The approach used in this manuscript is generally based on quadrature formulae, namely a non-intrusive formulation (see [Ghanem 2003, Le Maître 2010a] for details). When the number d of variables is large, quadrature formulae based on tensor product of a 1D formula require too many numerical evaluations and Sparse Grid integration based on Smolyak's construction is preferred.

4.1.3 Variance decomposition

Considering that variance can be easily computed as (the interested reader can refer to [Abgrall 2012])

$$\sigma^2 = E(f^2) - E(f)^2 = \sum_{k=1}^{P} \beta_k^2 \langle \Psi_k^2(\boldsymbol{\xi}) \rangle, \tag{4.13}$$

it can be decomposed following

$$\sigma_{\boldsymbol{m_i}}^2 = \sum_{k \in K_{\boldsymbol{m_i}}} \beta_k^2 \langle \Psi_k^2(\boldsymbol{\xi}) \rangle, \tag{4.14}$$

where $K_{\boldsymbol{m_i}}$ represent the set of indexes in associated to the variable contained in the vector $(\boldsymbol{\xi} \cdot \boldsymbol{m_i})$:

$$K_{\boldsymbol{m_i}} = \left\{ k \in \{1, \dots, P\} \,|\, \boldsymbol{m}^{\star,k} = \boldsymbol{m}^{\star,k}(\boldsymbol{\alpha}^k) = \boldsymbol{m_i} \right\} \tag{4.15}$$

If a total sensitivity index is needed, *i.e.* it is necessary to compute the overall influence of a variable, it can be computed summing up all the contributions in which the variable is present

$$\mathrm{TSI}_j = \sum_{\xi_j \in (\boldsymbol{\xi} \cdot \boldsymbol{m_i})} \sigma^{2,\mathrm{SeI}}_{\boldsymbol{m_i}} \tag{4.16}$$

Here, definitions are provided for the variance, but all this can be extended to high-order moments ([Abgrall 2012]), thus defining for example total sensitivity indexes for kurtosis too:

$$\mathrm{TSI}^k_j = \sum_{\xi_j \in (\boldsymbol{\xi} \cdot \boldsymbol{m_i})} k^{\mathrm{SeI}}_{\boldsymbol{m_i}}, \tag{4.17}$$

where $k^{\mathrm{SeI}}_{\boldsymbol{m_i}}$ is the conditional contribution associated to a specific multi-index for the kurtosis (See [Abgrall 2012] for more details).

In the following section, we illustrate a simple test-case for displaying the importance of decomposing HO moments.

4.1.4 On the advantages of high-order indexes for global Sensitivity analysis

The importance of including high-order conditional terms computation in the statistics analysis is demonstrated in this section by means of several model functions. Note that this kind of approach is conceived in order to extend the global sensitivity analysis based on the variance. Anyway, in some situations, criteria based on statistical moments are not adequate and moment independent criteria should be adopted. The interested reader should refer to [Plischke 2013] for a discussion in this sense.

The first model function is the well-known Ishigami function

$$f(\boldsymbol{\xi}) = (1 + 0.1\xi_3^4)\sin(\xi_1) + 7\sin(\xi_2)^2 \quad \text{where} \quad \xi_i \sim \mathcal{U}(-\pi, \pi). \tag{4.18}$$

For this function, the first-order Sensitivity Indexes (SeI) contribution (for variance, skewness and kurtosis) computed for to the third variable ξ_3 are equal to zero. In Figure 4.1, sensitivity indexes are reported for variance, skewness and kurtosis.

Remark that the interaction between the third and the first variable is not negligible, obtaining a $k^{\mathrm{SeI}}_{\boldsymbol{m_i}}$, for $\boldsymbol{m_i} = (1, 0, 1)$, higher than 0.4. Also the interaction between the three variables is almost equal to 0.2 for the kurtosis but it is zero for both variance and skewness. It is also interesting to note that, even if the ranking of the variables it is not directly affected by the choice of the order of Sensitivity Indexes (SeI) (*i.e.* for the variance, skewness or kurtosis), the three indexes provide complementary results. For instance, the relative importance of first-order terms is about 0.75 for the variance, while it is only 0.15 for the kurtosis. The analysis of the table 4.1, where the total sensitivity indexes are reported, confirms that the ranking of the variables is nearly the same for each statistical moment.

Let us consider now, the classical Sobol function (four dimension)

$$f(\boldsymbol{\xi}) = \prod_{i=1}^{4} \frac{|4\xi_i - 2| + a_i}{1 + a_i}, \tag{4.19}$$

where $\xi_i \sim \mathcal{U}(0, 1)$. Two possible choices of the coefficients are considered here

- $a_i = (i - 1)/2$ the so called linear g-function f_{glin}

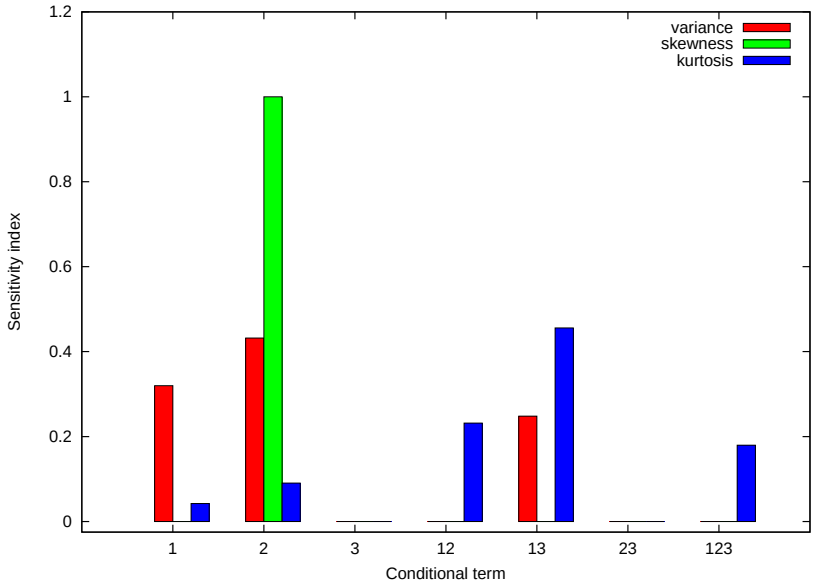

Figure 4.1: Sensitivity indexes for the Ishigami function (4.18) obtained with a PC series with total degree $n_0 = 7$.

Variable	TSI	TSI^s	TSI^k
ξ_1	0.57	0.00	0.91
ξ_2	0.43	1.00	0.50
ξ_3	0.25	0.00	0.64

Table 4.1: Total sensitivity indexes for the Ishigami function (4.18) based on a PC series with total degree $n_0 = 7$.

- $a_i = i^2$ the so called quadratic g-function f_{gquad}.

In figure 4.2, Sensitivity Indexes (SeI) for the linear g-function f_{glin} are reported. Looking at figure 4.2, several differences can be noticed between the sensitivity indexes computed on the variance or on other high-order moments. The variance-based ranking illustrates that the first-order sensitivity indexes are higher than the second order one, while these last ones are higher than the third and fourth order ones. This is not the case for skewness and kurtosis, where the second-order contributions are higher than the first-order and third-order ones. This behavior reveals that the variance is able to catch the absolute ranking of the variables in terms of first-order contributions, but the importance associated to higher-order interactions between the parameters is totally lost. From a practical point of view, underestimating the importance of high-order interactions between variables can lead to wrong decisions in a dimension reduction strategy. The variance based only on first-order contributions exceeds 0.8, while skewness and kurtosis do not attain 0.1. This can be demonstrated to be very influential if the probability distribution for reduced models is considered (see [23]). However, in table 4.2, the total sensitivity indexes for the four variables are reported. It is evident that the ranking of variables is not influenced by the statistical moment, but their relative importance can vary significantly.

The same functional form can lead to slightly different results if the quadratic function coefficients are considered. In Figure 4.3, the sensitivity indexes for the g-function with a quadratic dependence of the coefficients are reported. In this case, the difference between the first order contribution and high-order terms is even more evident. Considering the variance, first-order contributions exceed 0.98, while a value larger than 0.5 is computed for high-order interactions when considering skewness and kurtosis. In this case, the contribution of the first variable exceeds 0.8, but in order to attain

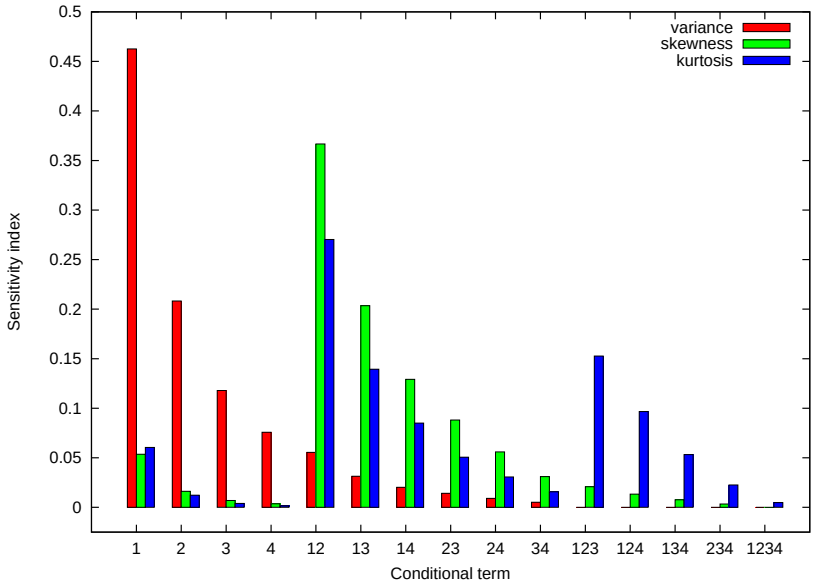

Figure 4.2: Sensitivity indexes for the linear g-function f_{glin} (4.19) obtained with a PC series with total degree $n_0 = 5$.

Variable	TSI	TSI^s	TSI^k
ξ_1	0.57	0.79	0.86
ξ_2	0.29	0.56	0.64
ξ_3	0.17	0.36	0.44
ξ_4	0.11	0.24	0.31

Table 4.2: Total sensitivity indexes for the linear g-function function (4.19) based on a PC series with total degree $n_0 = 5$.

this level, it is necessary to include contributions related to the first variable and the second-order interaction between the first and second variable. In the table 4.3, total sensitivity indexes are reported for the four variables. In this case, variance contributions for both the third and fourth variables are below 0.05, while for both skewness and kurtosis, only the fourth variable contribution takes a TSI value of 0.04. A low level of TSI for the variables ξ_3 and ξ_4 could suggest to truncate the dimensionality of the model to the first two variables or neglect the contributions related to the order higher than one. This case is analyzed in the following section in order to demonstrate the importance of high-order sensitivity indexes analysis.

Variable	TSI	TSI^s	TSI^k
ξ_1	0.82	0.95	0.97
ξ_2	0.14	0.47	0.44
ξ_3	0.04	0.13	0.12
ξ_4	0.01	0.04	0.04

Table 4.3: Total sensitivity indexes for the quadratic g-function f_{gquad} (4.19) based on a PC series with total degree $n_0 = 5$.

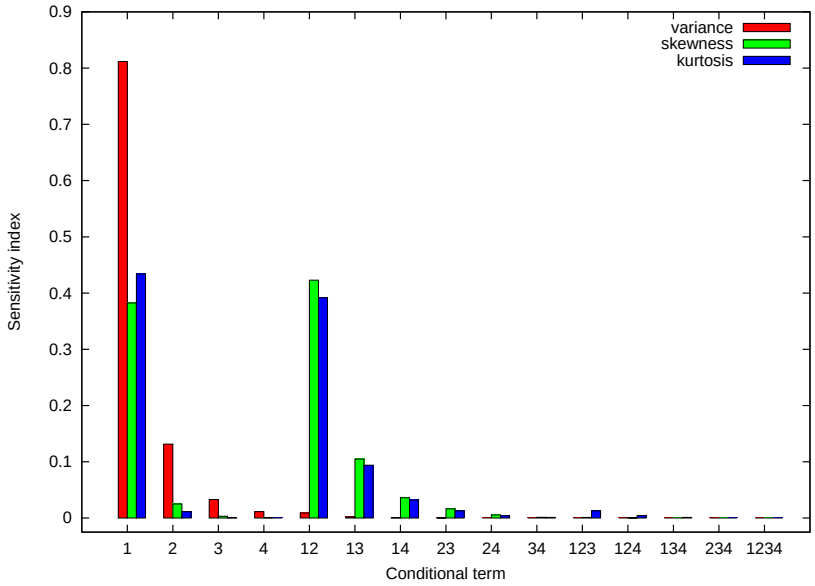

Figure 4.3: Sensitivity indexes for the quadratic g-function f_{gquad} (4.19) obtained with a PC series with total degree $n_0 = 5$.

Let us now consider the following functions:

$$\begin{aligned} f_1 &= \xi_1 e^{\frac{\xi_2}{\xi_3^2+1}} + \xi_1\xi_2 \\ f_2 &= \prod_{i=1}^{3} \frac{2\xi_i + 1}{2}, \end{aligned} \tag{4.20}$$

where the parameters are $\xi_i \sim \mathcal{U}(0,1)$.

Sensitivity indexes associated to the first function f_1 are reported in Figure 4.4. For the function f_1, the most important variable is ξ_1. For the variance, the first-order sensitivity index relative to ξ_1 is also the most important SeI. On the contrary, for both skewness and kurtosis, the highest SeI is associated to the second-order interaction between the first and the second variable. In this case, the inspection of the total sensitivity indexes, reported in the table 4.4, suggests that the third variable ξ_3 is meaningless with respect to the variance. The TSI associated to ξ_3 are lower than the limit proposed in [Gao 2010] to identify a negligible uncertainty that could be frozen. However, if this information is used together with the high-order total sensitivity indexes information, the choice of freezing the third variable should be considered more carefully. This reflects the importance of the third variable in the actual form of the probability density function of f_1 even if its variance is not heavily influenced by it. The results of a model reduction decision, totally based on variance measures, is further discussed in the following section.

Variable	TSI	TSI^s	TSI^k
ξ_1	0.79	0.96	0.97
ξ_2	0.26	0.96	0.67
ξ_3	0.02	0.10	0.10

Table 4.4: Total sensitivity indexes for the first function f_1 (4.20) based on a PC series with total degree $n_0 = 7$.

The last example, *i.e.* the function f_2, is reported here to underline the difference between the measure of sensitivity associated to the variance and to the higher-order moments. In particular, the

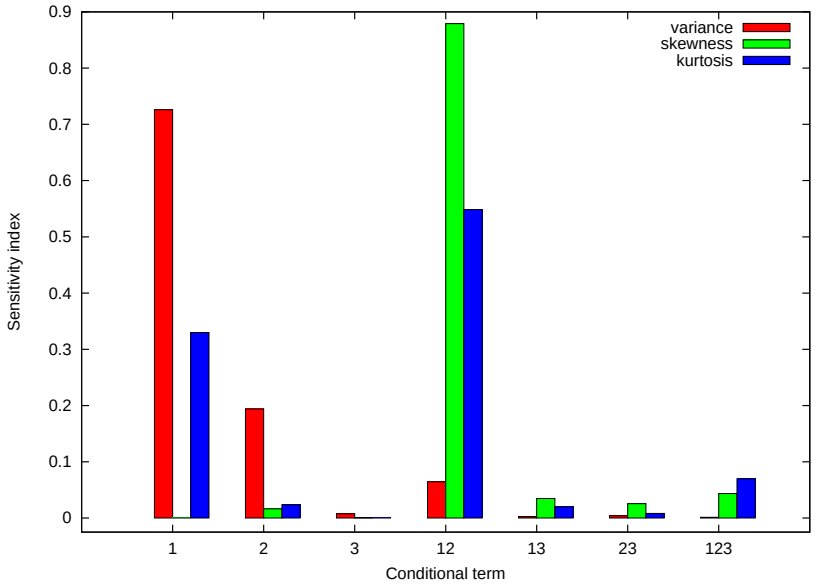

Figure 4.4: Sensitivity indexes for the first function f_1 (4.20) obtained with a PC series with total degree $n_0 = 7$.

functional form of f_2 (4.20) includes an equal contribution of three variables. However, looking at the figure 4.5, it is possible to note that the variance is concentrated only on first-order contributions of the single variables and their sum exceeds 0.9. The skewness and kurtosis contributions, on the contrary, are concentrated on second-order interaction. For kurtosis, the third-order interaction is the highest contribution. The skewness associated to a model including only first-order contribution does not include the skewness information about the probability distribution of the output.

Values for the total sensitivity indexes are reported in table 4.5 for this case. It is interesting to note that the sum of the total sensitivity indexes over the three variables is much more higher for skewness and kurtosis with respect to the variance. Then, they refer, correctly, to an intrinsically high-order (of interaction) function (see equation (4.20) for f_2 definition).

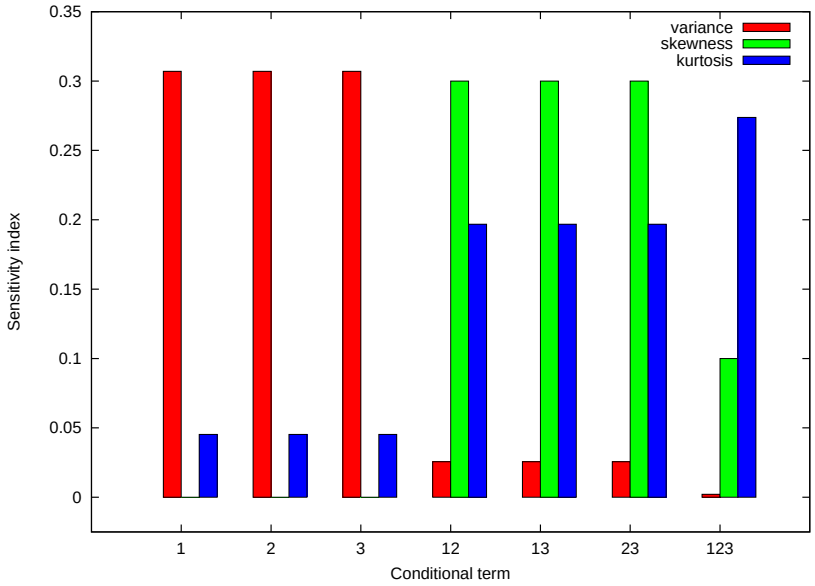

Figure 4.5: SeI for the function f_2.

Variable	TSI	TSI^s	TSI^k
ξ_1	0.36	0.70	0.71
ξ_2	0.36	0.70	0.71
ξ_3	0.36	0.70	0.71

Table 4.5: Total sensitivity indexes for the first function f_2 (4.20) based on a PC series with total degree $n_0 = 7$.

4.1.5 Dimension reduction

In this section, the problem of reducing the number of dimensions is analyzed through some numerical test-cases based on the results obtained in the previous section. The first test-case is represented by the quadratic g-function (4.19). From the analysis conducted in the previous section (see table 4.3), note that the third and fourth variables seem to be meaningless for the variance-based indexes. Their total sensitivity indexes sum up to 0.05 for the variance, while exceed 0.15 for both skewness and kurtosis. Considering only the sensitivity indexes computed on the variance, the decision-maker could be tempted to neglect the variables ξ_3 and ξ_4. In this case, the ANOVA expansion does not include the terms containing ξ_3 and ξ_4, as follows

$$\begin{aligned} f_{G1} &= f_0 + f_1(\xi_1) + f_2(\xi_2) + f_{12}(\xi_1, \xi_2) \\ f_{G2} &= f_0 + f_1(\xi_1) + f_2(\xi_2) + f_{12}(\xi_1, \xi_2) + f_3(\xi_3) + f_{13}(\xi_1, \xi_3) + f_{23}(\xi_2, \xi_3) + f_{123}(\xi_1, \xi_2, \xi_3), \end{aligned} \tag{4.21}$$

where in the first case f_{G1} both are neglected; on the contrary for f_{G2} only ξ_4 is neglected. In this case, the ANOVA terms and the statistics can be computed analytically. In the table 4.6, the percentage errors, for the first four central moments, are reported with respect to the analytical exact solution for both the reduced models f_{G1} and f_{G2}.

Function	Variance	Skewness	Kurtosis
f_{G1}	4.7997	29.236	15.039
f_{G2}	1.2369	7.7705	4.0632

Table 4.6: Percentage $\left(\frac{abs(\mu-\mu_{ex})}{\mu_{ex}} \times 100\right)$ errors related to the reduced g-function f_{G1} and f_{G2}.

In table 4.6, it is evident that an error of only 5% on the variance can correspond to a much greater error on the higher moments. This behavior is justified looking at the Figure 4.6, where the probability density function is computed for both f_{G1} and f_{G2} and compared with the complete function (4.19). In this case, the model with only the first two variables can not reproduce the tails while a good approximation is attained in the middle part. However, this test-case clearly shows that considering only the sensitivity indexes based on the variance could be very risky in a decision-making process. In this case, the pdf results to be analytically bounded between 0.4 and 1.8. If the third variable is included in the reduced model, both variance and skewness are computed with an error lower than 5%, while the error on the kurtosis remains lower than 8%. The total sensitivity indexes associated to the fourth variable is reported in table 4.3 and it is lower than 5% for the three moments. The improvement of the model given by including the third variable is evident in Figure 4.6, where the pdf of the reduced model allows recovering much better the pdf of the complete function.

From a practical point-of-view, the dimension reduction is commonly applied by freezing the neglected parameters. For an analytical function, it is possible to compute the constant values to choose, for both ξ_3 and ξ_4, in order to obtain a reduced model that preserves both the expectancy and the variance of the original complete model. Of course, both requirements cannot be satisfied at

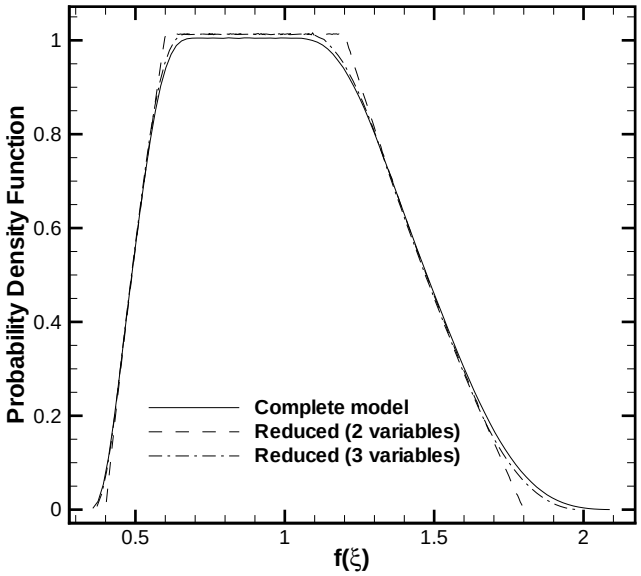

Figure 4.6: PDFs for the complete g-function and the reduced models (see equations 4.21).

the same time, but a set of values satisfying the mean and the variance can be obtained analytically requiring that

$$\begin{aligned} \frac{|4\bar{\xi_j} - 2| + a_j}{1 + a_j} &= 1 \\ \left(\frac{|4\bar{\xi_j} - 2| + a_j}{1 + a_j}\right)^2 &= \int_0^1 \left(\frac{|4\xi_j - 2| + a\text{æ}}{1 + a_j}\right)^2 \mathrm{d}\xi_j. \end{aligned} \tag{4.22}$$

The following values can be analytically computed for the two variables: $\xi_3 = \{1/4, 3/4, 91/120, 29/120\}$ and $\xi_4 = \{1/4, 3/4, 77/102, 25/102\}$.

In Figure 4.7, the pdf associated to the complete quadratic g-function with parameters ξ_3 and ξ_4 frozen, are reported with the complete pdf and the totally reduced one.

From Figure 4.7, it is evident that freezing some parameters in order to assure the correctness of the mean and the variance, yields pdf very close to that one obtained by neglecting entirely the ANOVA terms. From a practical point-of-view, the analysis of the reduced model can be carried out both with the ANOVA reduced model (if it is analytically possible to compute the integrals) and by freezing the parameter to neglect by satisfying the requirement on the expectancy and variance.

The numerical test-cases presented here, can be resumed by stating that the information coming from the sensitivity indexes associated to the variance seem to be incomplete in order to understand the true dependence of a model from its variables. In particular, the variance seems to give a too predominant role to the low-order interactions with respect to the sensitivity indexes associated to skewness and kurtosis. As a consequence, the sensitivity indexes on the skewness and on the kurtosis could contribute to understand much better the interactions between some subsets of variables. Please refer to [23] for a more detailed discussion about the application of high-order sensitivity indices on the truncation strategy in a dimension-reduction framework.

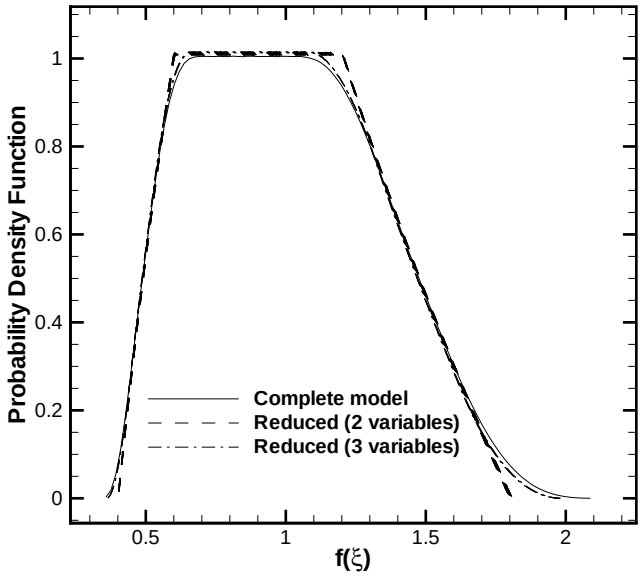

Figure 4.7: PDFs for the complete g-function and the reduced models.

4.2 ANOVA-based analysis in RANS/LES models

In this section, we apply the uncertainty propagation method based on Polynomial Chaos described in Sections 4.1.2 and 4.1.3 to the stochastic simulation of turbulent flows. Other studies have been focused on the effect of different sources of uncertainty in RANS [Simon 2010, Han 2012] and LES [Lucor 2007, Meldi 2011, Meldi 2012] simulations. In this study, the focus is on the comparison between stochastic RANS and LES simulations with respect to the experimental data for a specific configuration.

4.2.1 Flow configuration

The turbulent flow in a pipe with an axisymmetric expansion experimentally studied by Dellenback *et al.* [Dellenback 1987] is considered. This choice relies on two main reasons : i) it covers a variety of flow regimes, displaying recirculating flow regions and high turbulence levels, ii) it is a well documented experiment allowing for a fine comparison between measurements and computations. This experiment has already been used by Schlüter *et al.* [Schlüter 2004] as a reference for (deterministic) numerical simulations in an hybrid RANS/LES context and by Gyllenram and Nilsson [Gyllenram 2008] as a validation test-case for a modified $k-\omega$ turbulence model. A sketch of the experimental configuration is given in Figure 4.8 where the plane generating the full geometry by rotation around the z-axis is displayed : the fluid is flowing from left to right, entering the pipe at $z=-2D$ with or without swirl and leaving the expansion at $z=10D$. Measurements with laser Doppler anemometer are available upstream of the expansion located in $z=0$, allowing for a proper description of the mean inflow quantities such a time-averaged axial and tangential velocity. Available probe locations downstream the expansion are also indicated in Figure 4.8. This incompressible flow configuration is described by two non-dimensional parameters : the Reynolds number Re based on the fluid kinematic viscosity, the inlet diameter D and the bulk velocity U_b and the swirl number S_w describing the level of swirl the inlet flow. The swirl number is defined as the ratio between

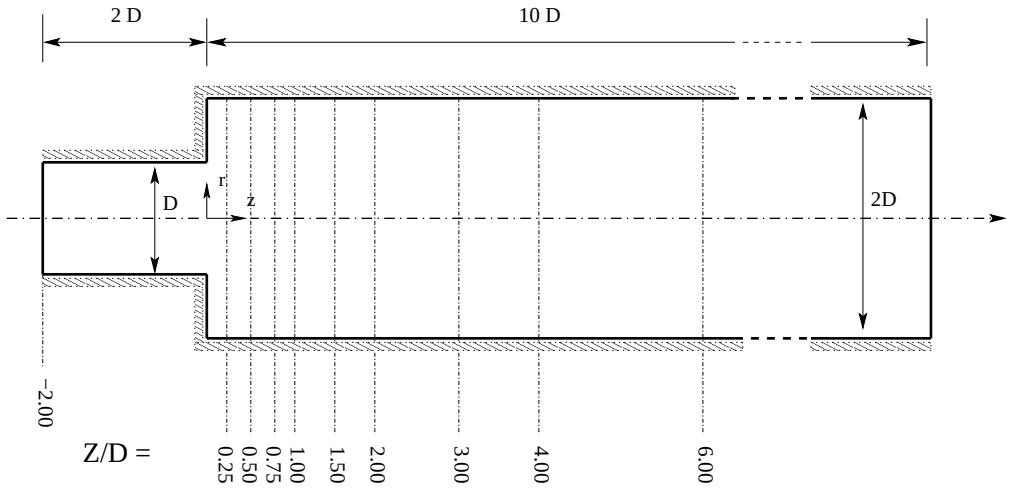

Figure 4.8: Experimental configuration of Dellenback.

angular momentum flux and axial momentum flux :

$$S_w = \frac{1}{R}\frac{\int_0^R r^2 \langle u_z \rangle \langle u_\theta \rangle \, dr}{\int_0^R r \langle u_z \rangle^2 \, dr}, \tag{4.23}$$

where $R = D/2$, r is the radial coordinate (see Fig. 4.8) and $\langle u_z \rangle$, $\langle u_\theta \rangle$ denote respectively the time-averaged streamwise and tangential velocity components. The experiment is reported performed for a Reynolds number $Re = 30000$ and two values of the swirl number : a no-swirl configuration ($S_w = 0$) and a strong swirl configuration ($S_w = 0.6$). The baseline flow (BF) configuration with a bulk velocity yielding $Re = 30000$ and no swirl (NS) will be denoted from now on BFNS test-case; similarly BFHS will denote the baseline flow at $Re = 30000$ with high swirl ($S_w = 0.6$).

4.2.2 Turbulence modeling and numerical tools

The incompressible turbulent flow considered in this study is governed by the instantaneous Navier-Stokes equations expressing mass and momentum conservation :

$$\begin{cases} \dfrac{\partial u_i}{\partial x_i} = 0, \\ \dfrac{\partial u_i}{\partial t} + \dfrac{\partial u_i u_j}{\partial x_j} = -\dfrac{1}{\rho}\dfrac{\partial p}{\partial x_i} + \dfrac{\partial}{\partial x_j}\left(\nu \dfrac{\partial u_i}{\partial x_j}\right), \end{cases} \tag{4.24}$$

where u_i, p, ρ and ν are respectively the velocity components, the pressure, the (constant) density and kinematic viscosity. For high level turbulent flows, it is not possible to perform direct numerical simulation (DNS) *i.e.* to solve directly these equations with the computing resources available because of the too large range of fluid motion scales to account for. Some modeling of a part of the flow dynamics is needed to overcome this limitation. The Reynolds-Averaged Navier-Stokes (RANS) approach solves the mean flow and attempts to model the fluctuating field. The governing equations take the form :

$$\begin{cases} \dfrac{\partial \langle u_i \rangle}{\partial x_i} = 0, \\ \dfrac{\partial \langle u_i \rangle \, \langle u_j \rangle}{\partial x_j} = -\dfrac{1}{\rho}\dfrac{\partial \langle P \rangle}{\partial x_i} + \dfrac{\partial}{\partial x_j}\left((\nu + \nu_T)\dfrac{\partial \langle u_i \rangle}{\partial x_j}\right). \end{cases} \tag{4.25}$$

where $\langle u_i \rangle$ denotes the time-averaged velocity field components and $\langle P \rangle$ is the modified mean pressure. The influence of the fluctuations on the mean flow is described by the turbulent stress tensor $\nu_T \frac{\partial \langle u_i \rangle}{\partial x_j}$ with the turbulent viscosity ν_T to be modeled in order to close the system. Several standard turbulence models can be applied to define ν_T and perform RANS simulations [Platteeuw 2008]. In the present work, the standard $k-\varepsilon$ model has been retained [Jones 1972], where ν_T is expressed as a function of the turbulent kinetic energy k and the dissipation ε of this turbulent energy. These two additional turbulent quantities are themselves determined by solving transport equations which are not detailed here.

Alternatively, the large-eddy simulation (LES) approach proposes to solve only the filtered velocity field $\bar{u}_i$, where the filtering operation allows to separate the scales of the flow motion at the grid level, with the small motion scales taken into account by a subgrid-scale model. The filtered velocity field is computed as the solution of the filtered Navier-Stokes equations :

$$\left\{ \begin{array}{l} \dfrac{\partial \bar{u}_i}{\partial x_i} = 0, \\ \dfrac{\partial \bar{u}_i}{\partial t} + \dfrac{\partial \bar{u}_i\ \bar{u}_j}{\partial x_j} = -\dfrac{1}{\rho}\ \dfrac{\partial \bar{P}}{\partial x_i} + \dfrac{\partial}{\partial x_j}\left((\nu + \nu_{SGS}) \dfrac{\partial \bar{u}_i}{\partial x_j} \right). \end{array} \right. \tag{4.26}$$

where the eddy viscosity ν_{SGS} must be defined to close system (4.26). The standard dynamic Smagorinsky model [Germano 1991] will be used in this study : the eddy viscosity is computed as $\nu_{SGS} = (C\ \Delta)^2\ \left|\bar{S}\,(x,t)\right|$, where $\left|\bar{S}\,(x,t)\right|$ is the norm of the filtered strain rate tensor. This expression defines ν_{SGS} algebraically so that no additional equation needs to be solved; the C coefficient is dynamically computed following Germano's definition [Germano 1991].

The $k-\varepsilon$ model is not necessarily the best choice for an accurate RANS computation of the flow under study and the dynamic Smagorinsky model is not the sole choice of subgrid model. Let us emphasize however our objective is not to investigate the accuracy of RANS modeling with respect to LES but to assess the comparative behavior of both approaches when uncertainties are introduced in the flow description. In this respect, the $k-\varepsilon$ model on one hand and the dynamic Smagorinsky model on the other hand, which are commonly used models, remain valid choices.
Both RANS and LES approaches have been used such as implemented into the open source finite volume code OpenFOAM [1]. In systems (4.25) and (4.26), convective and viscous fluxes are discretized with a second order accurate central differencing scheme. The pressure-velocity coupling is insured by using the PISO algorithm [Issa 1986]. To avoid spatial oscillations of the pressure field over the collocated grid arrangement, Rhie and Chow pressure-weighted interpolation is applied [Rhie 1983]. Moreover, for system (4.26), time advancement is performed by using a Crank-Nicholson scheme.
For RANS steady simulations, the outflow boundary condition is based on extrapolation conditions which require the derivatives of all quantities in the direction normal to the boundary be zero. However, this condition is known to be not satisfactory in unsteady flows [Ferziger 1997]. A convective outflow condition [Orlanski 1976] is thus used for LES unsteady simulations.
For both RANS and LES computations, the profiles of the time-averaged streamwise and orthoradial velocities are imposed at the inlet boundary, from the measured data of Dellenback *et al.* [Dellenback 1987]. These profiles depend on the bulk velocity U_b and the swirl number S_w. Since the first measure point in the inlet section is located outside the boundary layer, the imposed velocity profiles are smoothly connected to the zero value at the wall by a zero-pressure gradient turbulent boundary layer velocity distribution.
When the LES approach is applied, this time-averaged profile must be completed to define the

[1] www.openfoam.com

time-dependent inlet velocity distribution :

$$\bar{u}_{i,\mathrm{LES}}(t) = \langle u_{i,\mathrm{EXPE}} \rangle (U_b, S_w) + \gamma_i \sqrt{\frac{2}{3}\, k_i}, \tag{4.27}$$

where $\langle u_{i,\mathrm{EXPE}} \rangle$ is the experimental time-averaged velocity depending on U_b and S_w, k_i is the inlet turbulent kinetic energy and γ_i is a sequence of random numbers conditioned so that each distribution has zero mean and unit variance. The inlet boundary condition (4.27) is applied for the BFNS configuration only. Indeed, Schlüter *et al.* [Schlüter 2004] have shown that turbulent fluctuations can be neglected when strong swirl is considered so that $\bar{u}_{i,\mathrm{LES}}(t) = \langle u_{i,\mathrm{EXPE}} \rangle$ for BFHS.
When the RANS approach is used, the condition $\bar{u}_{i,\mathrm{RANS}} = \langle u_{i,\mathrm{EXPE}} \rangle$ is systematically used. However, additional inlet conditions have to be defined for the additional transport equations of k and ε. The inlet value of k and ε are computed from the bulk velocity U_b and estimated values of the turbulence intensity T_i and the characteristic turbulence length scale L_t, following the classical relations :

$$k = \frac{3}{2}\,(T_i\, U_b)^2 \qquad \varepsilon = \frac{k^{3/2}}{L_t}, \tag{4.28}$$

In conclusion, the RANS inlet boundary condition depends on a set of 4 physical parameters : U_b, S_w, T_i and L_t. The LES inlet boundary condition solely depends on U_b and S_w for BFHS and also depends on T_i for BFNS. For BFNS and BFHS, $U_b = 0.452\,m/s$ corresponds to $Re = 30000$ and $S_w = 0$ or $S_w = 0.6$. The turbulence intensity T_i is estimated equal to 0.03, leading to velocity fluctuation about 3% of the bulk velocity, and the turbulence characteristic length scale L_t equal to 5% of the inlet radius. Note that these quantities are rarely available from experimental data and there are no well-established rules to determine their values. This is an additional motivation to quantify uncertainties on the results due to uncertainties on such inlet levels.

4.2.3 Setting up the uncertainties

The calculations performed in the previous section assumed exactly known inlet flow conditions when using the RANS or LES numerical modeling; the grid-converged computed results were then compared with measured quantities also assuming exactness of the measurements. In reality, the measured distributions reported in Dellenback *et al.* [Dellenback 1987] must be considered as averaged distributions over a set of experimental realizations. From one realization to another, the inlet bulk velocity U_b and swirl number S_w (for the BFHS configuration) are subject to a level of fluctuation, which lead in turn to some fluctuations in the velocity measurements. We will consider from now on $\overline{U_b} = 0.452\,m/s$ and $\overline{S_w} = 0.6$ (for BFHS) to be mean values around which actual values of U_b and S_w in the series of experiments are uniformly distributed. In other words, U_b and S_w are now stochastic variables described by uniform probability distribution functions (pdf) over the respective intervals $[0.975\,\overline{U_b}, 1.025\,\overline{U_b}]$ and $[0.975\,\overline{S_w}, 1.025\,\overline{S_w}]$. The choice of a 2.5% variance for both U_b and S_w is based on the analysis of the experimental set up description provided by Dellenback *et al.* [Dellenback 1987]. The inlet turbulence characteristics are also subject to uncertainty. However, since no information is available in Dellenback *et al.* [Dellenback 1987] regarding these quantities, the extent of variation for T_i and L_t was estimated from previous calculations on similar configurations [Xia 1997, Yeh 2008, Cole 1998]. The turbulence intensity T_i is assumed to vary between 0.006 and 0.06 following a uniform pdf, *i.e.* the velocity fluctuation is assumed to vary uniformly between 0.6% and 6% of the mean velocity; the characteristic turbulence length-scale is assumed to vary between 0.1% and 10% of the inlet radius R, following a uniform pdf.
The uncertainty on U_b impacts all the simulations through the inlet velocity boundary condition : with or without swirl, using RANS or LES approach. The uncertainty on S_w impacts the simulations with swirl only, since S_w is assumed to remain very close to zero (with a negligible uncertainty) for the configuration without swirl. The uncertainty on T_i impacts all the RANS calculations through

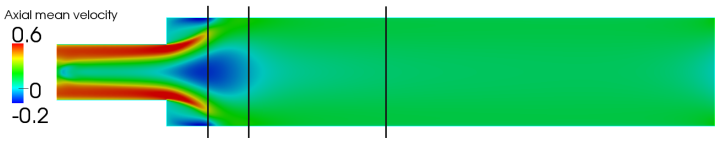

Figure 4.9: High-swirl flow. RANS computations analyzed using PC(3). Mean-value contours ($m\,s^{-1}$) of the time-averaged velocity magnitude. Vertical lines correspond to the sections used for the comparison with experiment (Fig. 4.10 and 4.11).

the inlet boundary condition (4.28) for k and ε and the LES calculation for the configuration without swirl through the inlet boundary condition (4.27). The uncertainty on L_t impacts all the RANS calculations through the inlet boundary condition (4.28) for ε but does not play a role in the LES calculations. The uncertainties taken into account in the study are summarized in Table I. The systematic choice of uniform pdf leads to a maximization of the uncertainty effects, a desirable feature for the present exploratory study. It remains to analyze how these physical (U_b, S_w) and modeling (T_i, L_t) uncertainties impact the numerical solutions provided by the RANS and LES approaches.

Table 4.7: Considered uncertainties for the various computations

Simulations	$U_b\,(m/s)$	S_w	T_i	L_t
RANS with swirl	0.452 ± 0.0113	0.6 ± 0.015	0.006 to 0.06	$0.1\%R$ to $10\%\ R$
RANS without swirl	0.452 ± 0.0113	/	0.006 to 0.06	$0.1\%R$ to $10\%\ R$
LES with swirl	0.452 ± 0.0113	0.6 ± 0.015	/	/
LES without swirl	0.452 ± 0.0113	/	0.006 to 0.06	/

4.2.4 High-swirl configuration

Figure 4.9 displays the central plane of the flow colored by the mean time-averaged axial velocity computed using the RANS computations and PC(3). In particular, a recirculation zone is observed occurring around the flow centerline downstream of the expansion zone.

4.2.4.1 Comparison with experiment

Experimental measurements and simulation results are now compared taking into account the measurement errors and the propagation of uncertainties on the inlet flow conditions in the numerical simulations as detailed in Table I. Figure 4.10 reports the experimental, RANS and LES axial mean velocity distributions along the radial coordinate in several transversal sections, where error bars indicate the computed variance of the numerical solutions (using PC(3) for the RANS results and PC(2) for the LES results) and the experimental error. A tentative estimation of the error levels associated with the measurement instruments used at the time of the experiment (1987) led us to assume the measurement error on the local velocity values to be consistently equal to $\pm 0.04\,m/s$, be it in the inlet section or at any downstream location. Three sections have been considered (see Fig. 4.8), located respectively near the expansion ($L/D = 0.75$), in the center of the computational domain ($L/D = 1.5$) and near the exit ($L/D = 4.0$).
The present analysis provides a more realistic assessment of the predictive properties of the RANS and LES approaches since the stochastic DOE for U_b, S_w, T_i and L_t reproduces the actual variability of the inlet flow conditions encountered in the experiment. Ideally, when the inlet flow conditions

follow the statistical description summarized in Table I, the mean numerical solution should be close to the reported (mean) experimental distribution with a variance associated with the numerical results similar to the estimated experimental error.
When using RANS modeling, the mean axial velocity curves remain systematically far from the experimental distributions (see Fig. 4.10 (a) (b) (c)). This observation is consistent with the well known fact that the turbulent-viscosity assumption leads to inaccurate flow patterns for strong swirling flows. Furthermore, the computed error bars at section $L/D = 0.75$ in the back-flow region close to the centerline $r/R = 0$ (Fig. 4.10 (a)) are much larger than the 2.5% inlet velocity uncertainty, indicating the strong sensitivity of the RANS approach. These computed errors bars tend to reduce rapidly for more downstream sections since they are of the same order than the measurement error bars (assumed consistently equal to the input uncertainty) for $L/D = 1.5$ and smaller for $L/D = 4.0$ but with a computed mean distribution largely overestimated near the flow centerline. When using LES modeling, the picture is quite different since the mean solution is globally in good agreement with the measured distribution *and* the numerical error bars remain similar or even smaller than the experimental error bars in all the sections under study (see Fig. 4.10 (d) (e) (f)).
Another indicator of the statistical flow behavior is the coefficient of variation (standard deviation over mean value) of the axial time-averaged velocity computed at the flow centerline $r/R = 0$ for successive sections. The computed coefficients are reported in Table III along with the assumed experimental coefficient. The RANS coefficient of variation exceeds 100% at sections $L/D = 0.75$ and $L/D = 1.5$ where the swirl effects are significant while it goes down to 6.6% at $L/D = 4.0$ further away from the inlet. Note this drastic reduction does not necessarily imply the RANS prediction is improved at $L/D = 4.0$ (the computed mean distribution remains far from the experimental mean distribution, see Fig. 4.10 (c)); the sensitivity of the computed solution to uncertain inlet conditions is reduced in this flow region far from the inlet while it is particularly high in the first section, closest to the inlet boundary where swirl effects are most significant. The LES coefficient of variation does not depart much from the prescribed value on the inlet conditions and remains in the same range (between 4.75% and 10.2%) along the pipe centerline.

A similar analysis can be performed for the time-averaged tangential velocity distributions

Table 4.8: High-swirl flow. Coefficient of variation (%) for the axial velocity at $r/R = 0$ and successive sections.

L/D	0.75	1.5	4.0
RANS	130.4	106.4	6.6
LES	4.75	10.2	8.0
Experiment	25	40	101

and the computed mean values and variance distributions at the same sections $L/D = 0.75, 1.5$ and 4 are reported in Figure 4.11. As observed in Fig. 4.11 (a,b,c), the error bars for the RANS prediction remain small, inferior to the experimental error. The computed mean distribution remains however systematically far from the measured profile. The RANS approach can be considered as unable to correctly predict the physical flow solution on the basis of a full analysis including the uncertainties on the inlet flow conditions. It must also be noted these physical uncertainties have specifically a great impact on the numerical prediction of the axial velocity in recirculating flow regions.
When using the LES approach, the errors bars on tangential are also small but with a computed mean solution which remains systematically close to the experimental profiles (see Fig. 4.11 (d,e,f)).

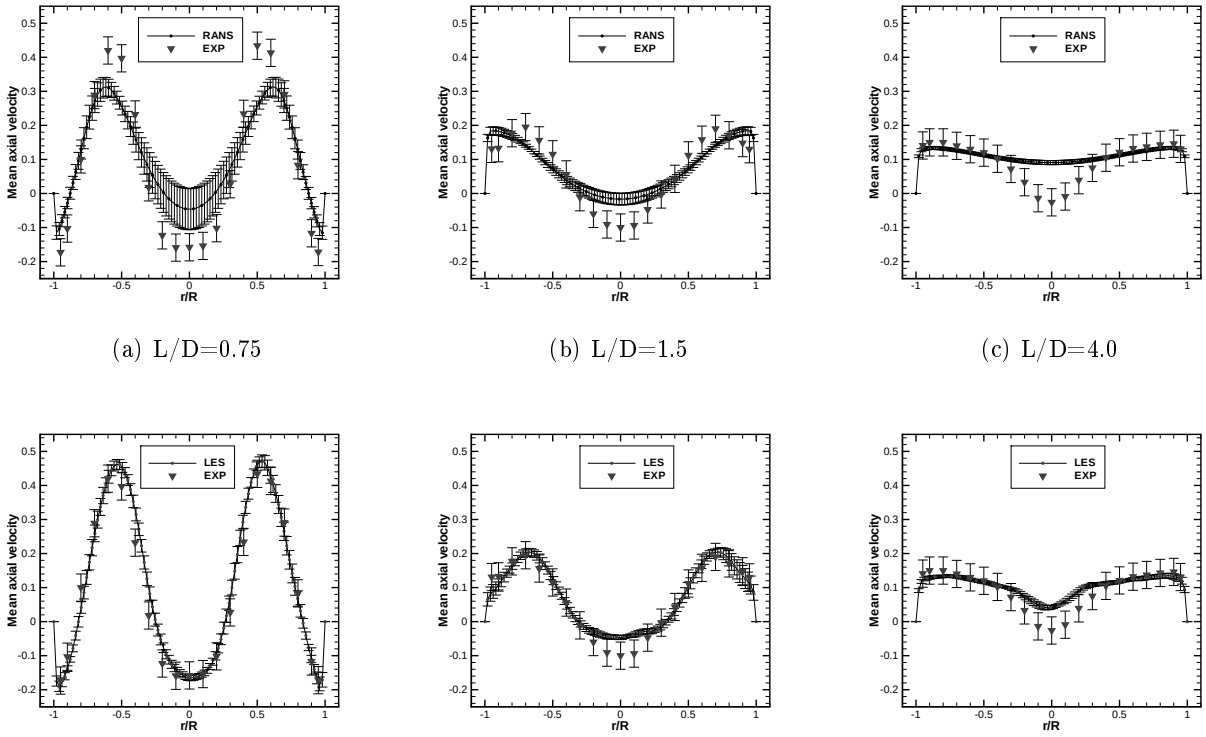

(a) L/D=0.75 (b) L/D=1.5 (c) L/D=4.0

(d) L/D=0.75 (e) L/D=1.5 (f) L/D=4.0

Figure 4.10: High-swirl flow. Statistics of the axial velocity distributions (mean value and standard deviation displayed as error bar) at successive sections (from left to right : upstream to downstream) computed with RANS modeling / PC(3) (top : a,b,c) and LES modeling / PC(2) (bottom : d,e,f). Numerical results are compared with experimental measurements (mean value and assumed experimental error bar).

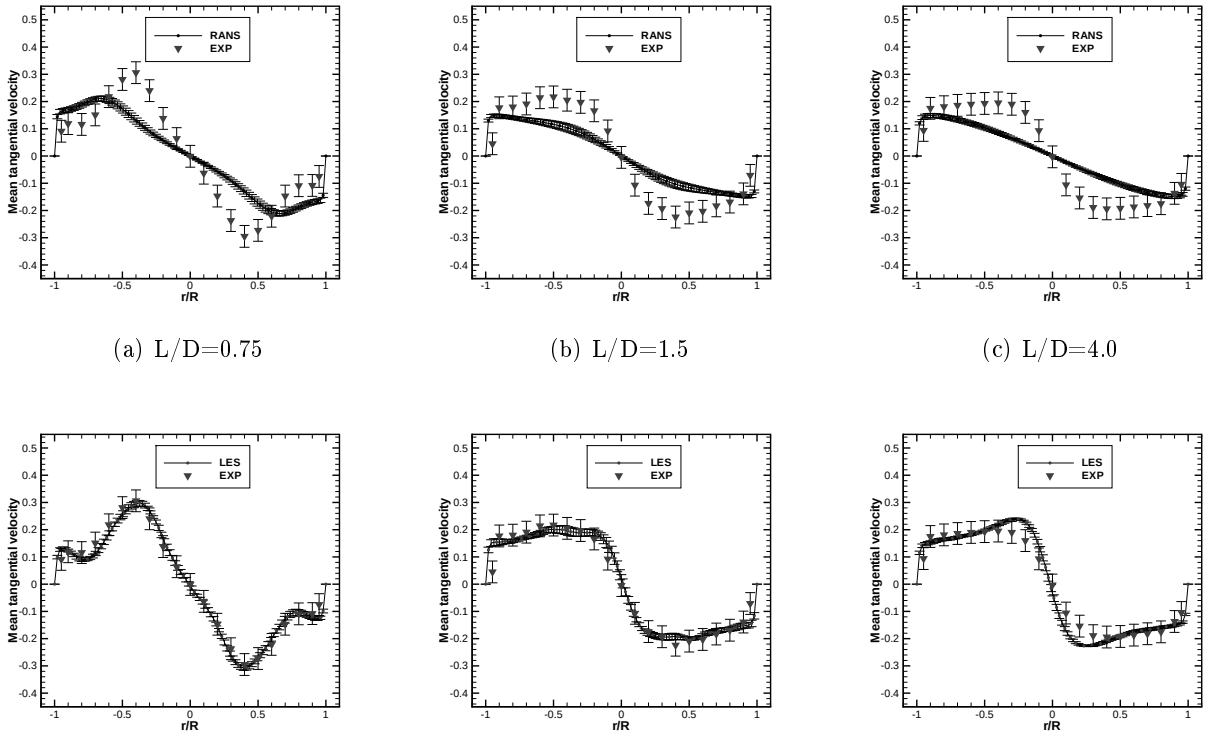

(a) L/D=0.75 (b) L/D=1.5 (c) L/D=4.0

(d) L/D=0.75 (e) L/D=1.5 (f) L/D=4.0

Figure 4.11: High-swirl flow. Statistics of the tangential velocity distributions (mean value and standard deviation displayed as error bar) at successive sections (from left to right : upstream to downstream) computed with RANS modeling / PC(3) (top : a,b,c) and LES modeling / PC(2) (bottom : d,e,f). Numerical results are compared with experimental measurements (mean value and assumed experimental error bar).

Figure 4.12: High-swirl flow. RANS computations analyzed using PC(3). Variance contours ($m^2\,s^{-2}$) of the time-averaged velocity magnitude.

Figure 4.13: High-swirl flow. RANS computations analyzed using PC(3). Contours of T_i uncertainty contribution to the variance of the time-averaged velocity magnitude.

4.2.4.2 Explanation of variance

Since mean flow quantities and their variance are computed at each grid point, it is possible to plot the contours of the variance field for the time-averaged velocity magnitude in order to better understand how the computed uncertainties are spatially distributed in the flow. This analysis will be performed for the RANS approach only since the uncertainties associated with the LES approach were found to remain small. The variance contours plotted in Fig.4.12 indicate the highest values for the variance of the time-averaged velocity magnitude are correlated with the location of the back-flow region well visible in Fig.4.9. Moreover, ANOVA analysis can be applied at each grid point to estimate the contribution of each uncertainty to the global variance and the contours of these uncertainty contributions can be plotted and analyzed. Such a process is successively applied to the four uncertainties taken into account when applying RANS modeling to the high-swirl configuration. The contours of T_i uncertainty contribution to the variance are plotted in Fig.4.13 : they are very similar to the contours of the global variance plotted in Fig.4.13, which indicates the global variance of the RANS computations is essentially produced by the uncertainty on inlet turbulence intensity. The contours of U_b, S_w and L_t uncertainty contributions to the variance of the time-averaged velocity magnitude are respectively plotted in Fig. 4.14, 4.15, 4.16 and illustrate the very weak contribution to the global variance of the uncertainty on bulk velocity, swirl number and turbulence length scale.

Figure 4.14: High-swirl flow. RANS computations analyzed using PC(3). Contours of U_b uncertainty contribution to the variance of the time-averaged velocity magnitude.

Figure 4.15: High-swirl flow. RANS computations analyzed using PC(3). Contours of S_w uncertainty contribution to the variance of the time-averaged velocity magnitude.

Figure 4.16: High-swirl flow. RANS computations analyzed using PC(3). Contours of L_t uncertainty contribution to the variance of the time-averaged velocity magnitude.

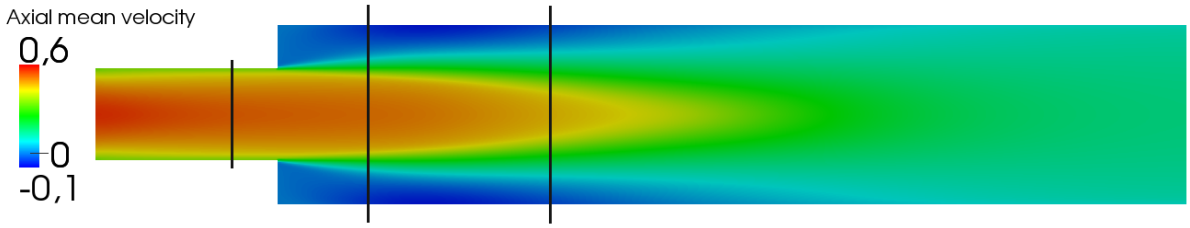

Figure 4.17: No-swirl flow. RANS computations analyzed using PC(3). Mean-value contours ($m\,s^{-1}$) of the time-averaged axial velocity. Vertical lines correspond to the sections used for the comparison with experiment (Fig. 4.18).

4.2.5 No-swirl configuration

Figure 4.17 displays the mean value contours of the time-averaged axial velocity for the no-swirl configuration computed using the RANS approach and PC(3). With respect to the previously studied configuration, the absence of swirl yields a higher velocity in the centerline region of the flow; note also that back-flow regions appear close to the wall immediately downstream of the expansion.

4.2.5.1 Comparison with experiment

As already done for swirling flows, the experimental profiles of the time-averaged axial velocity are plotted in Fig.4.18 along with the mean values of the computed distributions using RANS and LES modeling; the experimental and computed standard deviation are also reported on the same plots. Let us recall the error bar for the local velocity components measurement is systematically assumed equal to $\pm 0.04\,m/s$. Three sections, where experimental data are available, have been considered (see Fig. 4.8), respectively near the inlet ($L/D = -0.50$), in the center of the flow domain ($L/D = 1.0$) and near the exit ($L/D = 3.0$). The measured value at centerline $r/R = 0$ in section $L/D = 1$ is reported but seems spurious when compared to the other nearby measured values in the same section; it will be discarded in the following comments.
When the mean curves computed with RANS modeling are compared with measurements, taking into account their respective error bars, a correct agreement is found between experiment and computation. RANS modeling tends to underpredict, in the mean, the values of axial velocity near the centerline $r/R = 0$ and to slightly overpredict these values near the walls. However, the upper limit of the computed envelope near the centerline is located inside the region bounded by the lower and upper limits of the measured envelope at section $L/D = -0.50$ and $L/D = 1$; this same upper limit of the computed envelope remains slightly below the lower limit of the measured envelope in the downstream section $L/D = 3.0$. In contrast with the previous high-swirl configuration, the variation of the error bars between the far upstream and far downstream sections remains very small. This statistical flow behavior is confirmed by the analysis of the coefficient of variation for the axial velocity along the centerline $r/R = 0$. The values reported in Table IV show this RANS coefficient of variation remains between 4.7 and 5.1. (to be compared with this same coefficient varying from 130.4 to 6.6 when using RANS to compute the high-swirl configuration). The LES prediction is also in very good agreement with the experiments (see Fig. 4.18 (d,e,f)). LES modeling tends to slightly overpredict, in the mean, the axial velocity near the centerline. However the upper limit of the computed envelope in this centerline region tends to coincide with the upper limit of the mea-

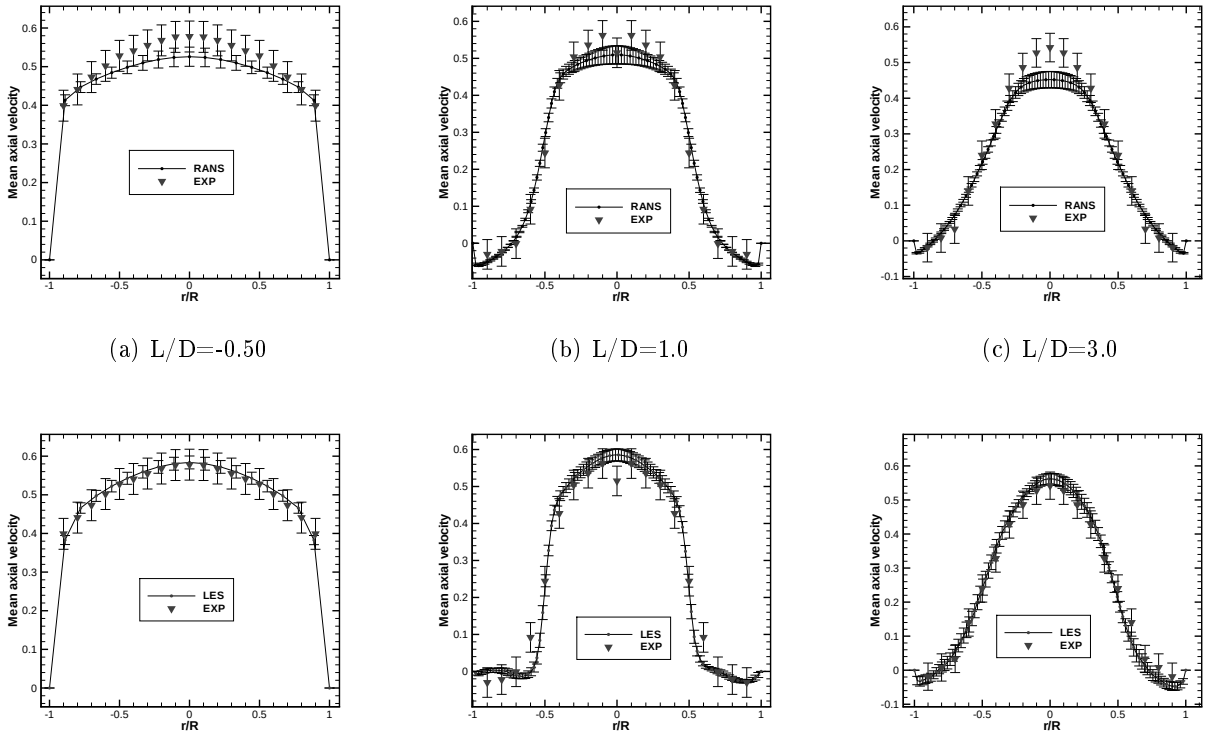

(a) L/D=-0.50 (b) L/D=1.0 (c) L/D=3.0

(d) L/D=-0.50 (e) L/D=1.0 (f) L/D=3.0

Figure 4.18: No-swirl flow. Statistics of the axial velocity distributions (mean value and standard deviation displayed as error bar) at successive sections (from left to right : upstream to downstream) computed with RANS modeling / PC(3) (top : a,b,c) and LES modeling / PC(2) (bottom :d,e,f). Numerical results are compared with experimental measurements (mean value and assumed experimental error bar).

Table 4.9: No-swirl flow. Coefficient of variation (%) for the axial velocity distribution at $r/R = 0$ computed at successive sections.

L/D	−0.5	1.0	3.0
RANS	4.7	4.8	5.1
LES	2.9	2.8	2.9
Experiment	7	7.3	8

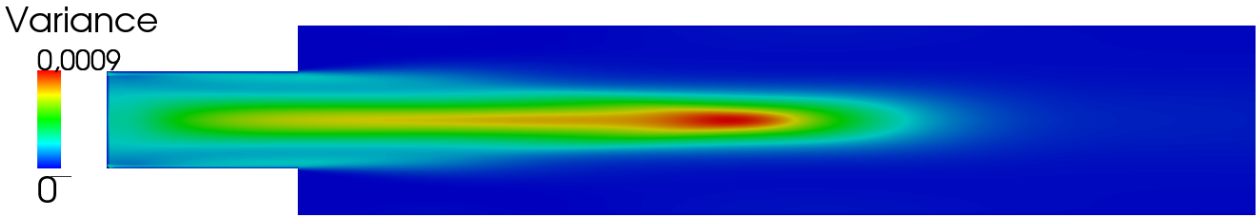

Figure 4.19: No-swirl flow. RANS computations analyzed using PC(3). Variance contours ($m^2\,s^{-2}$) of the time-averaged velocity magnitude.

sured envelope. Moreover the computed error bars for LES are sufficiently small for the numerical envelope to be almost fully included into the measured envelope for the three sections under study. The weak influence of inlet uncertainties on the LES prediction is also apparent in Table 4.9 where the coefficient of variation for the axial velocity at $r/R = 0$ remains below 3%.

4.2.5.2 Explanation of variance

The variance contours of the velocity magnitude in the central plane of the pipe are plotted in figures 4.19 for RANS computations. The maximum value reached by this variance remains well below the previously computed level for the high-swirl configuration (0.0009 against $0.015\,m^2\,s^{-2}$). Moreover this variance reaches its maximum well downstream from the expansion while this maximum was located in the immediate neighborhood of the expansion for the high-swirl case (see Fig.4.12). The contours of the various contributions to this global variance are also reported in Fig.4.20-4.22. In contrast with the high-swirl case where the inlet turbulence intensity T_i was explaining most of the variance, the uncertainties on U_b, L_t et T_i are all significantly contributing to the global variance in this no-swirl case. The uncertainty on bulk velocity explains most of the variance in the inlet region while the downstream peak of the global variance is explained mostly by the uncertainties on the inlet turbulence intensity and turbulence characteristic length scale.

A summary of the ANOVA analysis is proposed in Figure 4.23 where the contributions to the maximum variance of the velocity magnitude are reported for the high-swirl and no-swirl configurations computed using RANS or LES modeling. The contribution of each uncertain inlet parameter to the variance (in %) is plotted for each combination of flow configuration and turbulence modeling, keeping in mind (see Table 3.1.2.1) that S_w is fixed to zero for the no-swirl case and that LES modeling makes use of T_i for the no-swirl case only and does not make use of L_t at all. The overwhelming influence of the T_i uncertainty on the RANS high-swirl computations is clearly illustrated (with a contribution equal to 96% of the variance in that case). For the RANS no-swirl

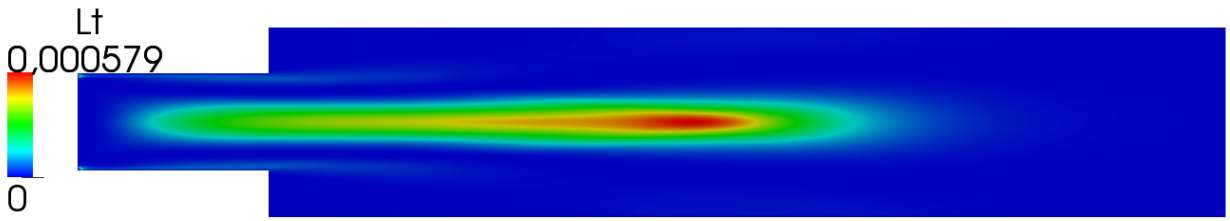

Figure 4.20: No-swirl flow. RANS computations analyzed using PC(3). Contours of L_t uncertainty contribution to the variance of the time-averaged velocity magnitude.

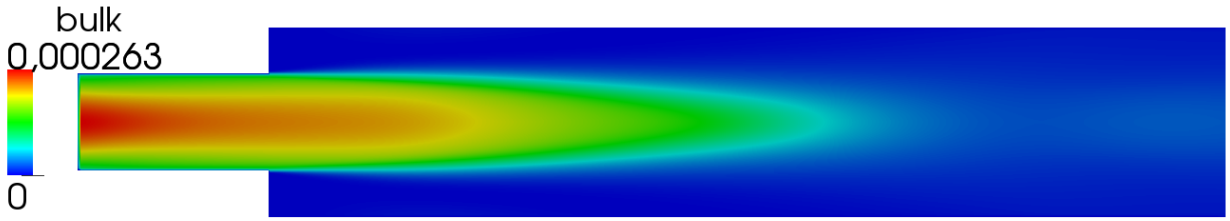

Figure 4.21: No-swirl flow. RANS computations analyzed using PC(3). Contours of U_b uncertainty contribution to the variance of the time-averaged velocity magnitude.

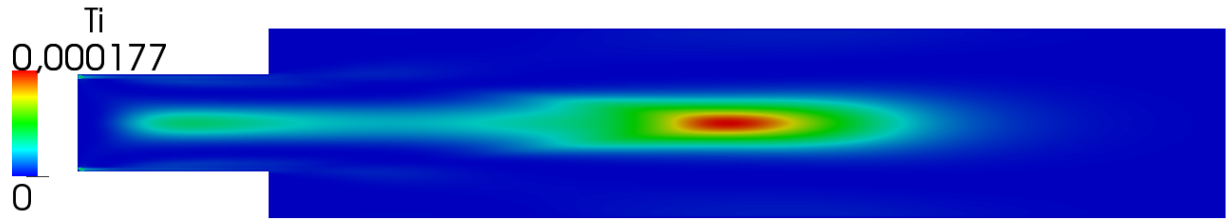

Figure 4.22: No-swirl flow. RANS computations analyzed using PC(3). Contours of T_i uncertainty contribution to the variance of the time-averaged velocity magnitude.

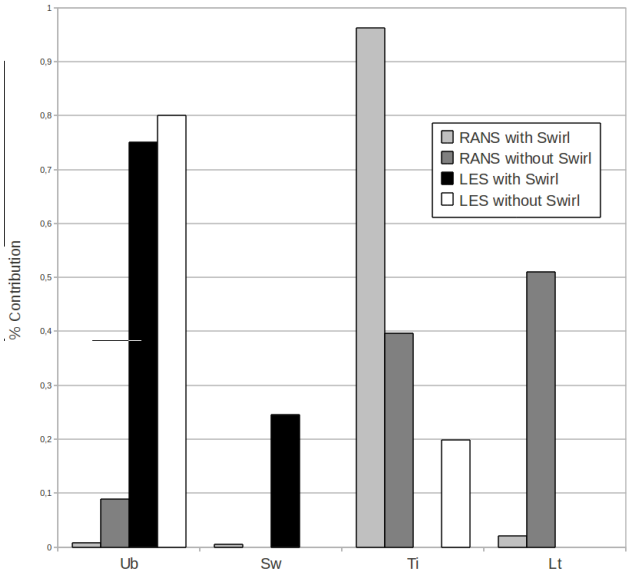

Figure 4.23: High-swirl / no-swirl flows. Analysis of the contributions to the maximal variance of the time-averaged velocity magnitude computed using RANS / PC(3) and LES / PC(2).

case, the uncertainties on both inlet turbulent conditions T_i and L_t contribute to more than 90% of the variance.
The maximum variance associated with the LES computation of the high-swirl flow is explained by both uncertain parameters retained in that case, namely U_b and S_w, with respective contributions of 75% and 24%. Similarly, the maximum variance associated with the LES computation of the no-swirl flow is explained by both uncertain parameters retained in that case, namely U_b and T_i, with respective contributions of 80% and 20%.

4.2.6 Concluding remarks

In this study, a non-intrusive Polynomial Chaos method has been used for taking into account experimental physical uncertainties in numerical simulation of a turbulent flow configuration. Two different ways of treating turbulence has been used, a classical RANS equations system and LES simulations. Statistic computations and analysis of variance allowed evaluating robustness of turbulence models with respect to physical uncertainties and predominant parameters that influence more the global variance. Robustness of different techniques showed to be problem-dependent. In the case of swirling flows, RANS equations are not robust when computing axial velocity in recirculating region, and error bars are much greater than input variations. But, RANS solutions are robust for tangential velocities, that indicate a decoupling between the components of the velocity. When no-swirling flows have been taken into account, RANS solutions show a better agreement with experimental results and a lower sensitivity to inflow uncertainties. This shows the ability to the RANS approach to simulate no-swirling flows in comparison with swirling case. On the contrary, LES solutions show a great agreement with experience and very small error bars in all the cases that we studied. Finally analysis of variance showed that the uncertainty on the turbulence intensity, T_i, needed in the RANS approach is the predominant parameter that contributed more to the variance in the case of swirling flows. When using LES, two uncertainties showed slight differences between them both in swirling and non-swirling flows.

Chapter 5

Inverse problem

Contents

In this chapter, I present the bayesian-based algorithm for treating inverse problem. In particular, it is applied on the rebuilding of free-stream conditions for a reentry vehicle. The other algorithm developed for the inverse problem, *i.e.* the deterministic one, is described in Section 10.1.

5.1 Bayesian-based algorithm: characterization of the uncertain input data for the EXPERT vehicle

Simulation of atmospheric entries of spacecraft is a challenging problem involving many complex physical phenomena, including rarefied gas effects, aerothermochemistry, radiation, and the response of thermal protection materials to extreme conditions. The availability of powerful computational resources and general-purpose numerical algorithms creates increasing opportunities to perform multiphysics simulations of complex systems, in particular in aerospace science. Reliable predictions require sophisticated physico-chemical models as well as a systematic and comprehensive treatment of model calibration and validation, including the quantification of inherent model uncertainties. Conventionally, engineers resort to safety factors to avoid space-mission failure.

The post-flight analysis of a space mission requires accurate determination of the freestream conditions for the trajectory, that is, temperature and pressure conditions and the Mach number in front of the shock. The latters can be rebuilt from the pressure and heat flux measured on the spacecraft by means of a Flush Air Data System (FADS). This instrumentation comprises a set of sensors flush mounted in the thermal protection system to measure the static pressure (pressure taps) and heat flux (calorimeters) (see Figure 5.1). As shown by zur Nieden and Olivier [zur Nieden 2007], state of the art techniques for freestream characterization rely on several approximations, such as the equivalent specific heat ratio approximation, which means that one replaces a complex high temperature effect possibly including thermo-chemical non-equilibrium by an equivalent calorically perfect gas. This approximation is then used, starting from sensors measurements, to reconstruct freestream conditions and prescribe error intervals on these quantities. These techniques do not yet integrate measurement errors nor the heat flux contribution, for which a correct knowledge drives more complex models such as gas surface interaction. In this context, Computational Fluid Dynamics (CFD) supplied with UQ tools permits to take into account chemical effects and to include both measurement errors and epistemic uncertainties on the chemical model parameters in the bulk and at the wall (surface catalysis). Rebuilding the freestream conditions from the FADS data therefore amounts to solving a stochastic inverse problem.

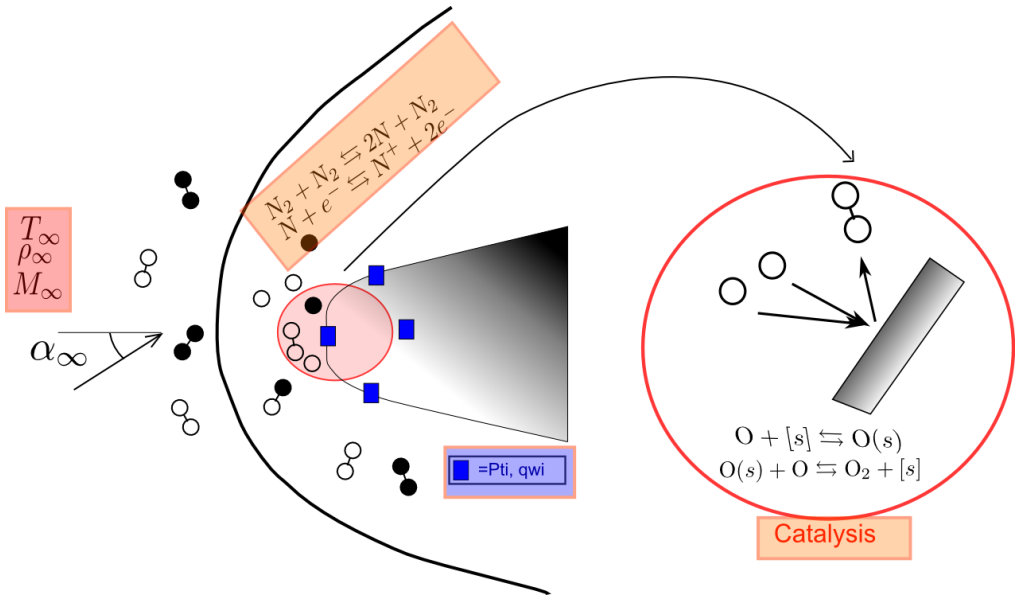

Figure 5.1: RAFLEX Flush Air Data System (FADS), sensors indicated in blue are flush mounted in the thermal protection system to measure the static pressure (pressure taps) and heat flux (calorimeters)

The forward problem, which consists in predicting stagnation-point pressure and heat flux from freestream conditions, is described by a physico-chemical model and solved by suitable numerical methods proposed by Barbante [Barbante 2001]. One point of the trajectory of the European EXPerimental Reentry Test-bed (EXPERT) vehicle is investigated, which has been developed by the European Space Agency as part of its General Technological Research Program. The trajectory point corresponds roughly to the chemical non-equilibrium flow conditions of Table 5.1. The inverse

Flow conditions	Altitude [km]	T_∞ [K]	p_∞ [Pa]	M_∞ [-]
Chemical non-equilibrium	60	245.5	20.3	15.5

Table 5.1: Freestream conditions for one trajectory point of the EXPERT vehicle.

problem is then reduced to determine for instance only freestream pressure and Mach number. The purpose of this study is to propose a new methodology for solving the inverse problem based on a Bayesian setting, that is, probability densities of possible values of freestream conditions are rebuilt from stagnation-point pressure and heat flux measurements. A Bayesian setting offers a rigorous foundation for inferring input parameters from noisy data and uncertain forward models, a natural mechanism for incorporating prior information, and a quantitative assessment of uncertainty on the inferred results [Kaipio 2010].

In Section 5.1.1, the forward model and the associated numerical code are briefly described, as well as the different sources of uncertainty on input data. The latters are parametrized with random variables and propagated into the forward model using the non-intrusive polynomial chaos method described in Sections 4.1.2 and 4.1.3. The impact of the different uncertainties on the stagnation-point measurements is then studied through a sensitivity analysis based on the metamodel obtained with the stochastic spectral method. In Section 5.1.2, the new backward uncertainty propagation method is described, considering measurement errors and the input uncertainties that have the most impact.

5.1.1 Forward problem and sensitivity analysis

5.1.1.1 Physical problem and sources of uncertainty

Here, the quantities of interest are the pressure p_{st} and heat flux q_{st} at the stagnation point. A set of physico-chemical models to simulate high temperature reacting flows is used, including 2D axi-symmetric Navier Stokes equations and gas/surface interaction equations (see Ref. [Barbante 2001]). Indeed, the wall of the spacecraft acts as a catalyzer and promotes combination of atoms. This phenomenon is modeled by a catalytic wall at radiative equilibrium, where the so-called effective catalytic recombination coefficient γ represents the proportion of gas impinging the body that will be recombine. A mixture of 5 species of air is used, namely N, O, N_2, O_2, and NO, with the corresponding Park chemical mechanism [Park 2001]. Input data for the forward model are the freestream pressure p_∞ and Mach number M_∞, the effective catalytic recombination coefficient γ, and the gas reaction rate coefficients of the chemical reactions k_r.

Uncertainties are considered on p_∞, M_∞, and γ, with uniform distributions detailed in Table 5.2. Indeed, only ranges of plausible values are known for these input quantities.

Variable	Distribution	Min	Max
p_∞ [Pa]	Uniform	16.3	24.3
M_∞ [-]	Uniform	13.7	17.3
γ [-]	Uniform	0.001	0.002

Table 5.2: Distributions of M_∞, p_∞, and γ

Uncertainty is also considered on the gas reaction rate coefficients k_r of four chemical reactions of the dissociation reaction. To determine which reactions need to be accounted for, a preliminary triage was done using a 1D code to simulate the stagnation line [Villedieu 2011]. Following the suggestion of Bose *et al.*[Bose 2004], the uncertainty concerns only the pre-exponential factor A_r of the Arrhenius rate equation: $k_r = A_r T^{b_r} \exp(-E_r/RT)$. Since the uncertainties on k_r can be quite large, it is appropriate to consider them on a logarithmic scale ; in particular, $\log_{10}(k_r/k_{r,0})$, with $k_{r,0}$ the recommended rate constant, is commonly assumed to vary following a normal distribution, with probability distribution defined by:

$$P(k_r) \propto \exp\left[-\frac{1}{2}\left(\frac{\log_{10}(k_r/k_{r,0})}{\sigma_r}\right)^2\right] \tag{5.1}$$

where $\pm 2\sigma_r$ (reported in Table 5.3) defines the 95% confidence limits symmetrically bounding $k_{r,0}$.

Gas reaction	Distribution of $\log_{10} k_r$	σ_r
$NO + O \rightarrow N + O + O$	Normal	0.12
$NO + N \rightarrow N + O + N$	Normal	0.12
$O_2 + N_2 \rightarrow 2O + N_2$	Normal	0.10
$O_2 + O \rightarrow 2O + O$	Normal	0.10

Table 5.3: Distributions of $\log_{10} k_r$

5.1.1.2 Numerical tools

To simulate the forward problem the in-house code COSMIC developed by Barbante [Barbante 2001] is used. This solver was designed to approximate hypersonic flow models where chemical non-equilibrium effects need to be accounted for. It relies on a Hybrid Upwind Splitting (HUS) scheme [Coquel 1995], which is an interesting attempt of combining, in a mathematically rigorous

way, Flux Vector Splitting (FVS) and Flux Difference Splitting (FDS) schemes. The design principle combines the robustness of FVS schemes in the capture of nonlinear waves and the accuracy of some FDS schemes in the resolution of linear waves. In particular, COSMIC uses the hybridization of the Van Leer scheme [Leer 1979] and the Osher scheme [Osher 1982] and includes a carbuncle fix.

The boundary conditions are illustrated in the right panel of Figure 5.2 : an axi-symmetric condition is imposed on the y axis, while the wall of the body is modelled by a partially catalytic wall at radiative equilibrium. The mesh used for the computations is given in the right panel of Figure 5.2. Pressure and temperature iso-contours of the flow around EXPERT obtained with COSMIC for input data mean values are shown in Figure 5.3.

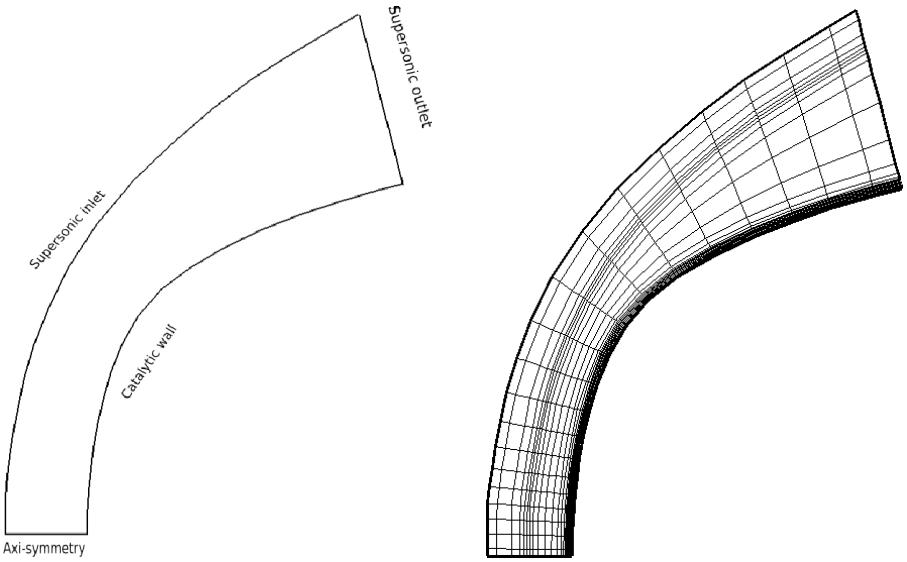

Figure 5.2: Boundary conditions (left) and mesh (right)

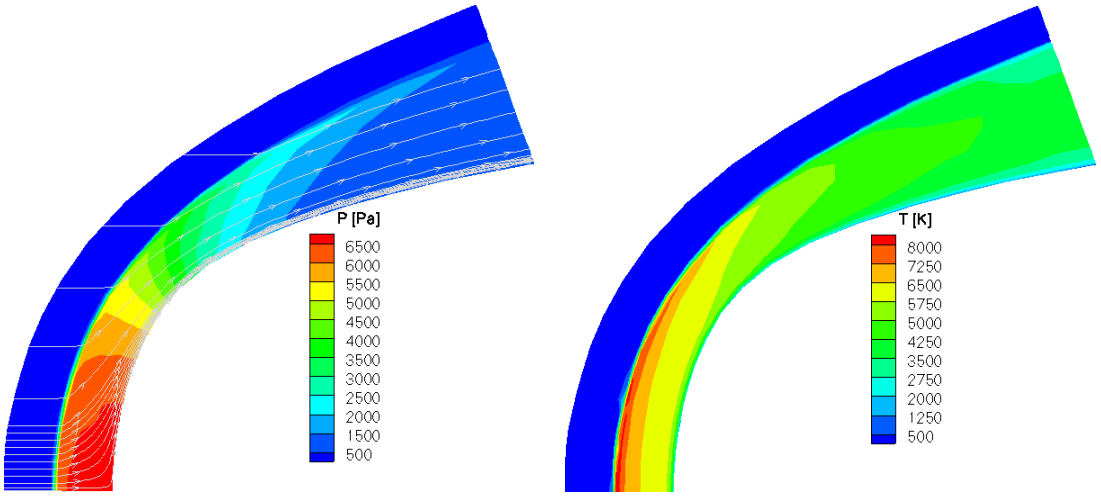

Figure 5.3: Pressure and temperature iso-contours for input data mean values

The stochastic method used in this study to deal with the forward uncertainty quantification is the non-intrusive polynomial chaos described in Sections 4.1.2 and 4.1.3.

5.1.1.3 Numerical results

Propagation of the uncertainties into the forward model has been performed using different polynomial orders No and a Smolyak Fejer quadradure formula of level 6, thus requiring 18947 resolutions of the deterministic code. Means and variances of p_{st} and q_{st} are reported in Table 5.4, while Sobol first order indices S_i and total order indices $S_{T,i}$ are reported in Table 5.5.

	p_{st}			q_{st}		
	No $= 2$	No $= 3$	No $= 4$	No $= 2$	No $= 3$	No $= 4$
μ	$6.49 \cdot 10^3$	$6.49 \cdot 10^3$	$6.49 \cdot 10^3$	$2.75 \cdot 10^5$	$2.75 \cdot 10^5$	$2.75 \cdot 10^5$
σ^2	$1.36 \cdot 10^6$	$1.37 \cdot 10^6$	$1.39 \cdot 10^6$	$9.73 \cdot 10^9$	$2.01 \cdot 10^{10}$	$6.18 \cdot 10^{10}$

Table 5.4: Means (μ) and variances (σ^2) of p_{st} and q_{st} for No $= 2, 3, 4$

		p_{st}			q_{st}		
		No $= 2$	No $= 3$	No $= 4$	No $= 2$	No $= 3$	No $= 4$
p_∞	S_1	$4.00 \cdot 10^{-1}$	$3.99 \cdot 10^{-1}$	$3.93 \cdot 10^{-1}$	$2.06 \cdot 10^{-2}$	$1.07 \cdot 10^{-2}$	$3.49 \cdot 10^{-3}$
	$S_{T,1}$	$4.09 \cdot 10^{-1}$	$4.07 \cdot 10^{-1}$	$4.02 \cdot 10^{-1}$	$3.38 \cdot 10^{-2}$	$6.18 \cdot 10^{-2}$	$4.91 \cdot 10^{-2}$
M_∞	S_2	$5.90 \cdot 10^{-1}$	$5.87 \cdot 10^{-1}$	$5.79 \cdot 10^{-1}$	$5.18 \cdot 10^{-1}$	$2.52 \cdot 10^{-1}$	$8.78 \cdot 10^{-2}$
	$S_{T,2}$	$5.98 \cdot 10^{-1}$	$5.99 \cdot 10^{-1}$	$5.91 \cdot 10^{-1}$	$5.28 \cdot 10^{-1}$	$7.14 \cdot 10^{-1}$	$2.81 \cdot 10^{-1}$
γ	S_3	$6.78 \cdot 10^{-4}$	$6.76 \cdot 10^{-4}$	$2.36 \cdot 10^{-3}$	$1.94 \cdot 10^{-1}$	$9.40 \cdot 10^{-2}$	$1.09 \cdot 10^{-1}$
	$S_{T,3}$	$6.79 \cdot 10^{-4}$	$2.30 \cdot 10^{-3}$	$1.22 \cdot 10^{-2}$	$1.94 \cdot 10^{-1}$	$3.03 \cdot 10^{-1}$	$5.44 \cdot 10^{-1}$
$O_2 + N_2 \rightarrow 2O + N_2$	S_4	$3.72 \cdot 10^{-6}$	$4.54 \cdot 10^{-6}$	$3.07 \cdot 10^{-5}$	$1.86 \cdot 10^{-3}$	$9.31 \cdot 10^{-4}$	$9.64 \cdot 10^{-4}$
	$S_{T,4}$	$2.76 \cdot 10^{-5}$	$1.65 \cdot 10^{-4}$	$8.33 \cdot 10^{-4}$	$7.52 \cdot 10^{-3}$	$2.70 \cdot 10^{-2}$	$3.98 \cdot 10^{-2}$
$O_2 + O \rightarrow 2O + O$	S_5	$2.65 \cdot 10^{-6}$	$3.90 \cdot 10^{-6}$	$1.98 \cdot 10^{-5}$	$1.10 \cdot 10^{-3}$	$6.35 \cdot 10^{-4}$	$5.47 \cdot 10^{-4}$
	$S_{T,5}$	$1.34 \cdot 10^{-5}$	$1.17 \cdot 10^{-4}$	$4.97 \cdot 10^{-4}$	$3.40 \cdot 10^{-3}$	$2.23 \cdot 10^{-2}$	$2.43 \cdot 10^{-2}$
$NO + O \rightarrow N + O + O$	S_6	$2.20 \cdot 10^{-4}$	$2.21 \cdot 10^{-4}$	$3.22 \cdot 10^{-4}$	$6.17 \cdot 10^{-2}$	$3.01 \cdot 10^{-2}$	$1.41 \cdot 10^{-2}$
	$S_{T,6}$	$2.53 \cdot 10^{-4}$	$7.56 \cdot 10^{-4}$	$5.88 \cdot 10^{-3}$	$7.02 \cdot 10^{-2}$	$1.02 \cdot 10^{-1}$	$2.50 \cdot 10^{-1}$
$NO + N \rightarrow N + O + N$	S_7	$6.60 \cdot 10^{-4}$	$6.58 \cdot 10^{-4}$	$2.33 \cdot 10^{-3}$	$1.83 \cdot 10^{-1}$	$8.86 \cdot 10^{-2}$	$1.04 \cdot 10^{-1}$
	$S_{T,7}$	$6.61 \cdot 10^{-4}$	$2.28 \cdot 10^{-3}$	$1.21 \cdot 10^{-2}$	$1.83 \cdot 10^{-1}$	$3.00 \cdot 10^{-1}$	$5.36 \cdot 10^{-1}$

Table 5.5: Sobol first order (S_i) and total order indices ($S_{T,i}$) for No $= 2, 3, 4$

According to Table 5.4, the PC expansions of the stagnation pressure p_{st} and of the stagnation heat flux q_{st} are convergent in the mean-square sense. The interpretation of the indices S_i and $S_{T,i}$ is the following : X_i is an influential input parameter if S_i is important, whereas X_i is not an influential parameter if $S_{T,i}$ is small. Moreover, S_i close to $S_{T,i}$ means that interactions between X_i and the other parameters are negligible. From Table 5.5, p_∞ and M_∞ are observed to have the largest impact on p_{st} with an equivalent magnitude, whereas the effective recombination factor and the reaction rate coefficients have a very small effect on p_{st}. This result was expected since the chemistry usually only influences the heat flux. Moreover, interactions between p_∞ and M_∞ are negligible. The results are rather different when the heat flux is considered: all the inputs are observed to have a non negligible impact on q_{st}, with relatively equivalent orders of magnitude for p_∞, M_∞, γ, k_6, k_7, and smaller orders of magnitude for k_4 and k_5. Moreover, interactions between the different parameters are quite large. Finally, important coefficients of variation (ratio of the standard deviation to the mean) are observed on the stagnation pressure and heat flux: the value on p_{st} is 18%, whereas the value on q_{st} is approximately 52%. A possible way to reduce these uncertainties is to rebuild the probability densities of p_∞ and M_∞, which have an important impact on p_{st} and q_{st}.

5.1.2 Backward uncertainty propagation method

The purpose of this section is to rebuild the probability densities of the freestream conditions p_∞ and M_∞ from noisy observations of stagnation pressure p_{st} and heat flux q_{st}, by taking into account

only the influence of measurement uncertainty concerning p_{st} and the influence of measurement and chemistry uncertainty concerning q_{st}.

5.1.2.1 Bayesian inference for inverse problems

The output of Bayesian inference is not a single value for the model parameters, but a posterior probability distribution that summarizes all available information about parameters. From this distribution, one can calculate means, modes, and high-order moments, compute marginal distributions, or make additional predictions by averaging over the posterior.

Let F denote the forward mathematics model defined as follows : $\mathbf{d} = F(\mathbf{m}, \mathbf{c})$, which yields predictions of the stagnation pressure and heat flux $\mathbf{d} = (p_{\text{st}}, q_{\text{st}})$ as a function of the freestream conditions $\mathbf{m} = (p_\infty, M_\infty)$ and the chemistry coefficients $\mathbf{c} = (\gamma, (k_{\text{r}})_{\text{r}=1,2,3,4})$. The uncertainty on $\mathbf{c}$ is assumed to be known and to follow a distribution $p_{\mathbf{c}}(\mathbf{c}) = p_\gamma(\gamma) \prod_{r=1}^{4} p_{k_{\text{r}}}(k_{\text{r}})$, γ following a uniform distribution detailed in Table 5.2 and k_{r} following lognormal distributions detailed in Table 5.3. In the Bayesian setting, both $\mathbf{m}$ and $\mathbf{d}$ are random variables and Bayes rules are used to define a posterior probability density for the model parameters $\mathbf{m}$, given n observations of the data $\{\mathbf{d}^1, \dots, \mathbf{d}^n\}$:

$$p(\mathbf{m}|\mathbf{d}^1, \dots, \mathbf{d}^n) = \frac{p(\mathbf{d}^1, \dots, \mathbf{d}^n|\mathbf{m}, \mathbf{c}) p_{\mathbf{m}}(\mathbf{m}) p_{\mathbf{c}}(\mathbf{c})}{\int p(\mathbf{d}^1, \dots, \mathbf{d}^n|\mathbf{m}, \mathbf{c}) p_{\mathbf{m}}(\mathbf{m}) p_{\mathbf{c}}(\mathbf{c}) \mathrm{d}\mathbf{m}\mathrm{d}\mathbf{c}}. \tag{5.2}$$

Prior probability $p_{\mathbf{m}}(\mathbf{m})$ represents the degree of belief about possible values of $\mathbf{m} = (p_\infty, M_\infty)$ before observing any data ; p_∞ and M_∞ are a priori assumed to follow uniform distributions, with minima and maxima given in Table 5.2. Data then enters the formulation through the likelihood or joint density of the observations given $\mathbf{m}$ and $\mathbf{c}$, namely $p(\mathbf{d}^1, \dots, \mathbf{d}^m|\mathbf{m}, \mathbf{c})$. A common model assumes independent observations so that independent additive errors account for the deviation between predicted and observed values of $\mathbf{d}$:

$$\mathbf{d}^j = F(\mathbf{m}, \mathbf{c}) + \boldsymbol{\eta}^j, \quad j = 1, \dots, n. \tag{5.3}$$

Because p_{st} and q_{st} can be considered as independent, a typical assumption is $\boldsymbol{\eta}^j \sim \mathcal{N}(\mathbf{0}, \boldsymbol{\Gamma})$, where $\boldsymbol{\Gamma} = \text{diag}(\sigma_{p_{\text{st}}}^2, \sigma_{q_{\text{st}}}^2)$, $\sigma_{p_{\text{st}}}$ and $\sigma_{q_{\text{st}}}$ encompassing measurement errors. In that case, $\mathbf{d}^j|\mathbf{m}, \mathbf{c} \sim \mathcal{N}(F(\mathbf{m}, \mathbf{c}), \boldsymbol{\Gamma})$, and the likelihood is

$$p(\mathbf{d}^1, \dots, \mathbf{d}^m|\mathbf{m}, \mathbf{c}) = \prod_{j=1}^{n} p_{\mathbf{d}^j}(\mathbf{d}^j|\mathbf{m}, \mathbf{c}) = \prod_{j=1}^{n} p_{\boldsymbol{\eta}}(\mathbf{d}^j - F(\mathbf{m}, \mathbf{c}), \boldsymbol{\Gamma}), \tag{5.4}$$

with $p_{\boldsymbol{\eta}}$ the Gaussian density probability of $\mathcal{N}(\mathbf{0}, \boldsymbol{\Gamma})$. Since in general measurement errors are not known with exactness, one can consider $\boldsymbol{\sigma}_{\text{st}} = (\sigma_{p_{\text{st}}}, \sigma_{q_{\text{st}}})$ as hyperparameters of the Bayesian setting that needs to be inferred, with noninformative uniform a priori on $\sigma_{p_{\text{st}}}$ and $\sigma_{q_{\text{st}}}$. For simplicity, measurement errors are here assumed to be known, with $\sigma_{p_{\text{st}}} = 0.1\mu(p_{\text{st}})$ and $\sigma_{q_{\text{st}}} = 0.1\mu(q_{\text{st}})$.

5.1.2.2 Markov Chain Monte Carlo

Markov Chain Monte Carlo (MCMC) encompasses a broad class of methods that simulate drawing samples from the normalized posterior [Gilks 1996]:

$$p(\mathbf{m}|\mathbf{d}^1, \dots, \mathbf{d}^n) \propto p(\mathbf{d}^1, \dots, \mathbf{d}^n|\mathbf{m}, \mathbf{c}) p_{\mathbf{m}}(\mathbf{m}) p_{\mathbf{c}}(\mathbf{c}), \tag{5.5}$$

thus avoiding complex numerical integrations in high dimensions to form the posterior distribution. In this study, the Metropolis-Hastings algorithm is used with single-site updating and Gaussian proposal density to draw samples of $p(\mathbf{m}|\mathbf{d}^1, \dots, \mathbf{d}^n)$ and process as follow :

0. initialize the chain state $\mathbf{m}^{k=0} = (p_\infty^{k=0}, M_\infty^{k=0}) = (\mu(p_\infty), \mu(M_\infty))$

1.a generate $\mathbf{c}^{k,1}$ and a candidate $\widetilde{p}_\infty \sim \mathcal{N}(p_\infty^k, \omega_{p_\infty}^2)$

1.b evaluate the acceptance rate $\alpha(p_\infty^k, \widetilde{p}_\infty) = \min\left\{1, \frac{p(\mathbf{d}^1,\dots,\mathbf{d}^m|\widetilde{p}_\infty, M_\infty^k, \mathbf{c}^{k,1}) p_{p_\infty}(\widetilde{p}_\infty)}{p(\mathbf{d}^1,\dots,\mathbf{d}^m|p_\infty^k, M_\infty^k, \mathbf{c}^{k,1}) p_{p_\infty}(p_\infty^k)}\right\}$

1.c generate $u^{k,1} \sim \mathcal{U}(0,1)$ and update: if $u^{k,1} < \alpha(p_\infty^k, \widetilde{p}_\infty)$, $p_\infty^{k+1} = \widetilde{p}_\infty$, else $p_\infty^{k+1} = p_\infty^k$

2.a generate $\mathbf{c}^{k,2}$ and a candidate $\widetilde{M}_\infty \sim \mathcal{N}(M_\infty^k, \omega_{M_\infty}^2)$

2.b evaluate the acceptance rate $\alpha(M_\infty^k, \widetilde{M}_\infty) = \min\left\{1, \frac{p(\mathbf{d}^1,\dots,\mathbf{d}^m|p_\infty^{k+1}, \widetilde{M}_\infty, \mathbf{c}^{k,2}) p_{M_\infty}(\widetilde{M}_\infty)}{p(\mathbf{d}^1,\dots,\mathbf{d}^m|p_\infty^{k+1}, M_\infty^k, \mathbf{c}^{k,2}) p_{M_\infty}(M_\infty^k)}\right\}$

2.c generate $u^{k,2} \sim \mathcal{U}(0,1)$ and update: if $u^k < \alpha(M_\infty^k, \widetilde{M}_\infty)$, $M_\infty^{k+1} = \widetilde{M}_\infty$, else $M_\infty^{k+1} = M_\infty^k$

3. $k = k+1$, go to 1.a while $k < N_{\text{MCMC}}$, with N_{MCMC} a predefined number of times.

Regardless of the initial chain state, the above algorithm produces a Markov chain that converges to the posterior distribution ; the initial chain state values are here choosen to be the a priori mean values of each component. Nevertheless, the proposal distribution widths vector $\boldsymbol{\omega} = (\omega_{p_\infty}, \omega_{M_\infty})$ have to be chosen carefully in order for the chain to mix well and represent the full posterior distribution in the given number of MCMC steps. If the proposal distribution widths are too large, a great proportion of the proposed moves will be rejected, and the chain will not move very often. On the other hand, if they are too small, most proposed moves will be accepted but the chain will move very slowly through the posterior support. A way to choose $\boldsymbol{\omega}$ efficiently is to plot the empirical autocorrelation at lag s, denoted by $\beta(s)$, for each component of the vector to infer and different proposal distribution widths. Indeed, the autocorrelation quantifies the interdependence of the iterations of a stochastic process, so that an efficient proposal distribution width implies the quickly decay of the autocorrelation with lag along the chain.

In steps 1.b and 2.b, $F(\widetilde{p}_\infty, M_\infty^k, \mathbf{c}^{k,1})$ and $F(p_\infty^{k+1}, \widetilde{M}_\infty, \mathbf{c}^{k,2})$ needs to be computed. The problem is that we can not afford to call COSMIC two times for each iteration of the Markov Chain, since COSMIC is time-consuming (about one hour per simulation) and one needs some thousands of iterations to produce a good sample of the posterior. To tackle this issue, one can rely on a metamodel, which gives an approximation of the outputs of COSMIC as a function of its inputs. Metamodels based on intrusive and non-intrusive stochastic spectral methods have already been proposed in the context of Bayesian inference[Marzouk Y.M. 2007, Y.M. 2009], with PC expansions. PC expansion metamodel functions can be obtained, providing an approximation of the response $(p_{\text{st}}, q_{\text{st}})$ as a function of $(\mathbf{m}, \mathbf{c})$. In Figure 5.4, approximated response surfaces of p_{st} and q_{st} are represented as a function of p_∞ and M_∞ in the top panels, the chemical inputs being fixed to their mean values ; then as a function of $\log_{10}(k_1/k_{1,0})$ and $\log_{10}(k_3/k_{3,0})$ in the bottom panels, the other inputs being fixed to their mean values. These response surfaces are obtained from the metamodels computed with the non-intrusive Polynomial Chaos, with a Sparse Grid integration method and a PC expansion of order $\text{No} = 3$. The response surfaces of p_{st} are well approximated, this assertion was verified by plotting in the same graph the outputs provided by the resolutions of the COSMIC code in Section 5.1.1.3. The PC expansion of p_{st} can therefore be used as a metamodel. Moreover, these surfaces match with the results obtained in Section 5.1.1.3 : p_{st} variates significatively with p_∞ and M_∞, whereas it does not vary a lot with the chemical reaction rates (a similar behavior can be observed when plotting p_{st} as a function of γ, the other parameters fixed to their mean values). However, the response surfaces of q_{st} are not well approximated, because the values are not consistent with the ones obtained with COSMIC (the approximated response surface at the right top panel also reaches negative values, which is obviously unphysical). This behavior is explained by the fact that interactions between the different parameters are quite large (as pointed out in Section 5.1.1.3) and q_{st} strongly depends on all the parameters, so that a global polynomial approximation can not tackle every local variation, which results in an oscillatory behavior. The PC expansion of q_{st} can therefore not be used as a metamodel.

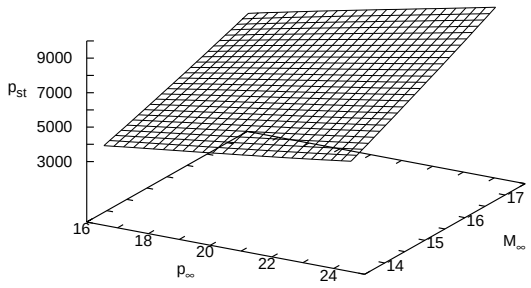

(a) p_{st} as a function of p_∞ and M_∞

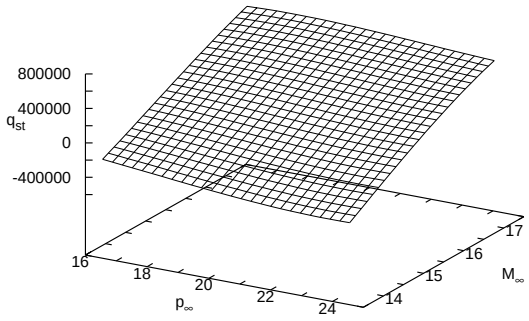

(b) q_{st} as a function of p_∞ and M_∞

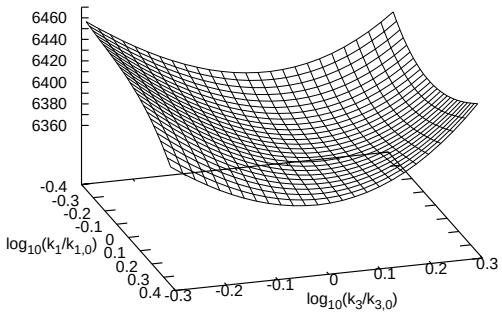

(c) p_{st} as a function of $\log_{10}(k_1/k_{1,0})$ and $\log_{10}(k_3/k_{3,0})$

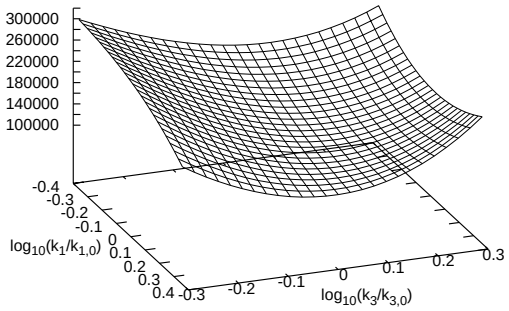

(d) q_{st} as a function of $\log_{10}(k_1/k_{1,0})$ and $\log_{10}(k_3/k_{3,0})$

Figure 5.4: Response surfaces of p_{st} and q_{st} obtained with the non-intrusive Polynomial Chaos, a Sparse Grid integration method, and a PC expansion of order No = 3

To cope with this complication, it was decided to solve first the stochastic inverse problem by considering only the stagnation-point pressure measurements $\{p_{\mathrm{st}}^1, \ldots, p_{\mathrm{st}}^n\}$, for which the PC expansion metamodel can be used, in order to find better a priori distributions for p_∞ and M_∞. Since the chemical inputs have negligible impact on p_{st}, they are fixed to their mean values so that $\mathbf{c}$ does not appear any more in the MCMC algorithm. Moreover, the vector of observations $\{\mathbf{d}^1, \ldots, \mathbf{d}^n\}$ is reduced to $\{p_{\mathrm{st}}^1, \ldots, p_{\mathrm{st}}^n\}$ and we rely on the PC expansion metamodel of p_{st} in steps 1.b and 2.b to compute the likelihood.

5.1.2.3 Numerical results

A noisy data vector $\{p_{\mathrm{st}}^1, \ldots, p_{\mathrm{st}}^{10}\}$ is generated by solving the forward model with COSMIC for a "true" vector of input parameters $(\mathbf{m}, \mathbf{c})$, then perturbing the output value p_{st} $n = 10$ times with independent samples of a Gaussian noise $\eta_i \sim \mathcal{N}(0, \sigma_{p_{\mathrm{st}}}^2)$. For simplicity, $\sigma_{p_{\mathrm{st}}}$ is supposed to be known (see Section 5.1.2.1). The "true" model parameters $\mathbf{m} = (p_\infty, M_\infty)$ is chosen as a sample of p_∞ and M_∞ from their prior (uniform) distributions, while the "true" chemistry coefficients $\mathbf{c} = (\gamma, (k_{\mathrm{r}})_{r=1,2,3,4})$ is chosen as a sample of $p_{\mathbf{c}}$. The generated "true" values considered here are $p_\infty = 19.65, M_\infty = 15, \gamma = 1.86 \cdot 10^{-3}, k_1 = 2.55 \cdot 10^{21}, k_2 = 1.03 \cdot 10^{22}, k_3 = 1.34 \cdot 10^{17}$, and $k_4 = 1 \cdot 10^{17}$. The output obtained for the latter inputs is $p_{\mathrm{st}} = 5.86 \cdot 10^3$ and perturbations of this "true" output, representing 10 independent measurements of p_{st} suffering from errors, can be observed in Figure 5.5.

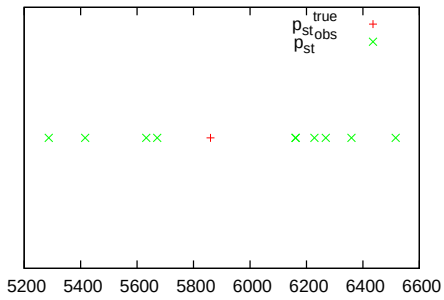

Figure 5.5: "True" p_{st} in red and 10 pseudo-measurements of p_st suffering from error in green

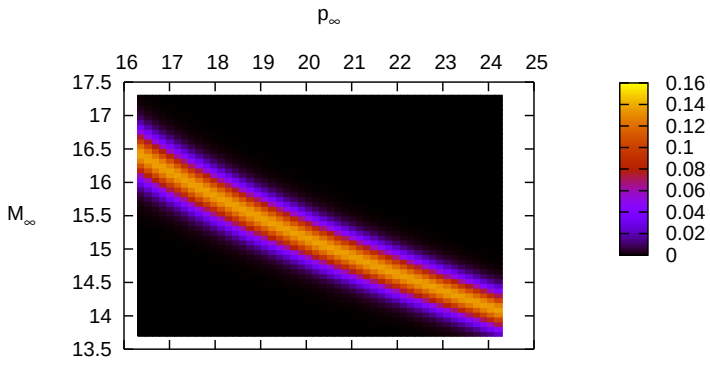

Figure 5.6: Joint posterior density of (p_∞, M_∞)

A first graphical representation of the joint posterior density of (p_∞, M_∞) is obtained in Figure 5.6 by direct evaluations of the normalized posterior (5.5) on the prior intervals of p_∞ and M_∞, relying on the stagnation-point pressure metamodel. The joint density exhibits a ridge spread along a lightly curved line in the (p_∞, M_∞) plane. This density structure suggests a high degree of correlation between the two parameters, which is consistant with the physics of the system. Samples of the posterior $p(\mathbf{m}|p_{\mathrm{st}}^1, \ldots, p_{\mathrm{st}}^{10})$ are then computed through the above MCMC algorithm with a proposal distribution widths vector $\boldsymbol{\omega} = (\omega_{p_\infty}, \omega_{M_\infty}) = (0.9, 0.5)$. Results showing the chain position over 10000 iterations are reported in Figure 5.7, plotted in two dimensions and separately for p_∞ and M_∞. Visual inspection suggests that the chain mixes well and that it moves in the band of Figure 5.6 where the probability is nonzero. In Figure 5.8, the empirical autocorrelation at lag s, namely $\beta(s)$, is plotted for each component of $\mathbf{m}$; $\beta(s)$ decays relatively quickly with lag along the chain, consistent with the good mixing in Figure 5.7. From Figures 5.6 and 5.7, it can be observed that the posterior credible interval of p_∞ remains the same as the prior one, whereas the posterior credible interval of M_∞ is slightly reduced compared to the prior one. Furthermore, the credible couples (p_∞, M_∞) set has been considerably reduced.

From the MCMC sample, the posterior distribution can be summarized in terms of means, standard deviations, and marginal distributions [Gilks 1996]. In order to approximate them, it is important to drop the first $b-1$ iterations of the MCMC sample, where b is commonly called the "burn-in" time, necessary for the chain to reach a good behavior. Let so consider $(p_\infty^k, M_\infty^k)_{k=b,\ldots,K}$; the marginal mean and variance of p_∞ and M_∞ are estimated by

$$\overline{\mu}(p_\infty) = \frac{1}{K-b}\sum_{t=b+1}^{K} p_\infty^k, \quad \overline{\mu}(M_\infty) = \frac{1}{K-b}\sum_{t=b+1}^{K} M_\infty^k, \tag{5.6}$$

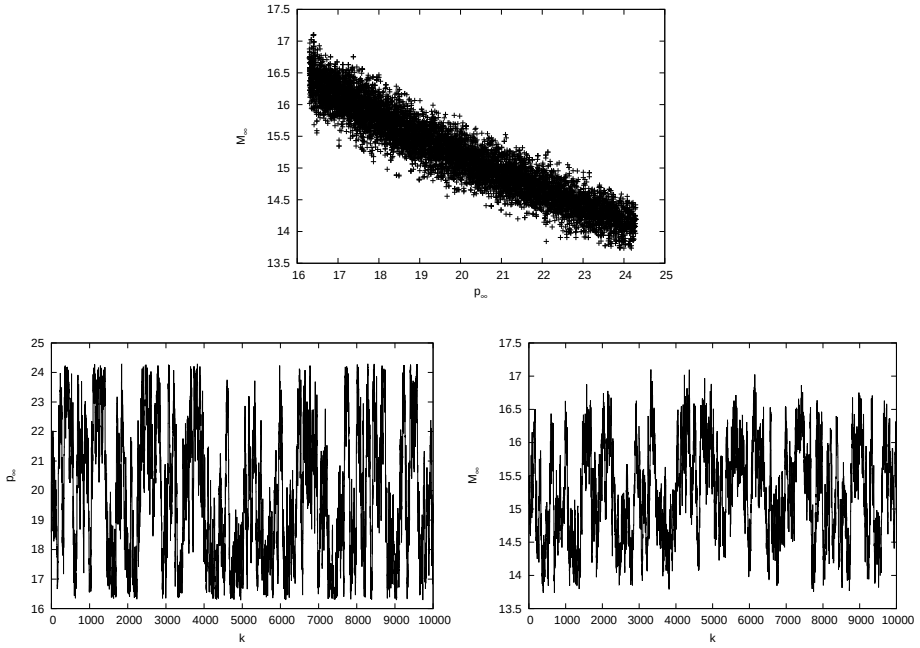

Figure 5.7: MCMC chain over 10000 iterations ; plotted in two dimensions and respectively for p_∞ and M_∞

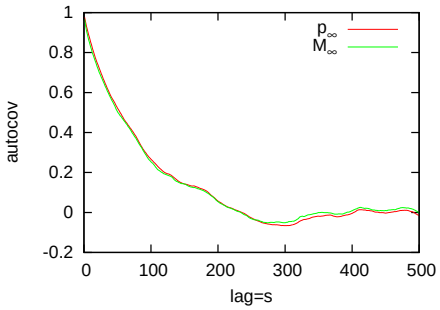

Figure 5.8: Empirical autocorrelation $\beta(s)$ for p_∞ in red and for M_∞ in green

and

$$\overline{\sigma}^2(p_\infty) = \frac{1}{K-b-1}\sum_{t=b+1}^{K}(p_\infty^k - \overline{\mu}(p_\infty))^2, \quad \overline{\sigma}^2(M_\infty) = \frac{1}{K-b-1}\sum_{t=b+1}^{K}(M_\infty^k - \overline{\mu}(M_\infty))^2. \tag{5.7}$$

The values obtained here are $\overline{\mu}(p_\infty) = 20.07$, $\overline{\mu}(M_\infty) = 15.29$, $\sigma(p_\infty) = 2.31$, and $\sigma(M_\infty) = 0.71$. The posterior means are roughly the same as the prior ones, while the posterior standard deviation of p_∞ is the same as the prior one and the posterior standard deviation of M_∞ is slighly smaller as the prior one. Finally, marginal distributions can be estimated by kernel density estimation :

$$p(p_\infty|p_{\text{st}}^1,\ldots,p_{\text{st}}^{10}) \approx \frac{1}{K-b}\sum_{k=b+1}^{K}\mathcal{K}(p_\infty^k|\mathbf{m}^k), \quad p(M_\infty|p_{\text{st}}^1,\ldots,p_{\text{st}}^{10}) \approx \frac{1}{K-b}\sum_{k=b+1}^{K}\mathcal{K}(M_\infty^k|\mathbf{m}^k), \tag{5.8}$$

where $K(p_\infty^k|\mathbf{m}^k)$ (resp. $K(M_\infty^k|\mathbf{m}^k)$) is a density concentrated around p_∞^k (resp. M_∞^k). Here we use a one-dimensional Gaussian kernel, $\mathcal{K} = \mathcal{N}(p_\infty^k, \omega^2)$ (resp. $\mathcal{K} = \mathcal{N}(M_\infty^k, \omega^2)$), with bandwith ω determined by the method of Sheather & Jones [Sheather 1991]. The estimated marginal distributions are plotted in Figure 5.9.

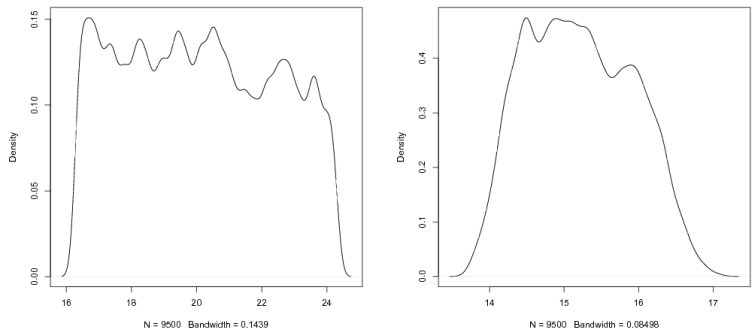

(a) Posterior distribution of p_∞ (b) Posterior distribution of M_∞

Figure 5.9: Marginal distributions of p_∞ and M_∞ obtained with kernel density estimation.

5.1.3 Conclusion

This study deals with the reconstruction of the freestream conditions (p_∞, M_∞) for the trajectory of a re-entry vehicle from measurements of stagnation-point pressure and heat flux $(p_{\text{st}}, q_{\text{st}})$. Prior uniform distributions are first assumed for (p_∞, M_∞) and some chemistry parameters are considered uncertain, with known distribution functions. The impact of the different uncertain inputs on the forward problem simulated by the in-house code COSMIC is studied owing to a non-intrusive stochastic spectral method. Uncertainties on (p_∞, M_∞) are observed to have a large impact on p_{st}, whereas the chemistry uncertainties are observed to have a negligible impact on it. On the contrary, all the input parameters are observed to have a considerable impact on q_{st}. Then, a backward uncertainty propagation method is proposed to solve the inverse problem by taking into account uncertainties due to measurements and model parameters. To this end, a Bayesian framework is used supplied with MCMC algorithms to sample the posterior distribution of (p_∞, M_∞). A major difficulty lies in the fact that one needs to compute the forward problem for each iteration in the Markov chain. A metamodel for p_{st} is computed owing to the non-intrusive spectral method, unfortunately such a metamodel can not be obtained for q_{st} because of the large interactions between the different parameters and the strong dependence of q_{st} on all the parameters. It was therefore decided to solve the stochastic problem only relying on the stagnation pressure measurements and the metamodel for p_{st} in a first step, so as to reduce the a priori on (p_∞, M_∞). On-going efforts consists in considering this new a priori for the resolution of the stochastic inverse problem with measurements of p_{st} and q_{st}, using adaptive algorithm to find the optimal widths vector in the MCMC algorithm and running Markov chains in parallel to accelerate the calculations.

Chapter 6

Robust optimization

Contents

In this Chapter, first I illustrate an ANOVA-based optimization algorithm, relying on the computation of the ranking of most predominant uncertainties (via ANOVA) for some samples in the design space, and on the building of a response surface of the sensitivity indexes (associated to each uncertainty) in the design space. Secondly, another approach for robust design optimization is presented, called Simplex^2 (S2M), based on the merging of the Simplex Stochastic Collocation (SSC) for UQ and the Nelder-Mead (NM) methods for the optimization. This is accomplished by means of a coupled stopping criterion and by the use of an high-degree polynomial interpolation for the space spanned by the design variables. Finally, some efficient techniques are applied to the robust shape optimization of BZT flows.

6.1 Some definitions

Consider the following computational problem for an output of interest $u(\mathbf{x}, t, \mathbf{y}, \boldsymbol{\xi}(\boldsymbol{\omega}))$, that is governed by the numerical discretization of a mathematical model of the engineering system represented by an operator $\mathcal{L}$ (algebraic or differential) and a source term $\mathcal{S}$

$$\mathcal{L}(\mathbf{x}, t, \mathbf{y}, \boldsymbol{\xi}(\boldsymbol{\omega}); u(\mathbf{x}, t, \mathbf{y}, \boldsymbol{\xi}(\boldsymbol{\omega}))) = \mathcal{S}(\mathbf{x}, t, \mathbf{y}, \boldsymbol{\xi}(\boldsymbol{\omega})), \tag{6.1}$$

with appropriate (if needed) initial and boundary conditions.

To make things clearer, let us consider a Computational fluid-dynamics (CFD) example. Then, $\mathcal{L}$ represents the Navier-Stokes equations (system of nonlinear partial differential equations). Initial

and boundary conditions are chosen to simulate the flow around an airfoil in the space coordinate $\mathbf{x}$. The output of interest, u, is the lift of the airfoil (obtained by integration of vertical pressure forces over the surface area of the airfoil). Now, let us imagine to parameterize the shape of the airfoil by means of some design variables collected in the vector $\mathbf{y}$. This means that to a specific realization of $\mathbf{y}$ is associated a particular geometry of the airfoil. Solving the Navier-Stokes equations on a specific airfoil geometry allows to compute a certain value of lift. If some uncertainties are considered, called $\boldsymbol{\xi}$, for example a non-uniform incoming air velocity, then some statistical quantities of the lift can be computed, like the mean and standard deviation, with respect to the uncertainties $\boldsymbol{\xi}$.

Using a more accurate and general mathematical framework, $\mathcal{L}$ and $\mathcal{S}$ are defined on the domain $D \times T \times \Xi^u \times \Xi^d$, where $\mathbf{x} \in D$ and $t \in T$ are the spatial and temporal coordinates with $D \subset \mathbb{R}^{Dim}$, $Dim \in \{1, 2, 3\}$, and $T \subset \mathbb{R}$. The vector $\mathbf{y}$ is defined on the domain $\Xi^d \subset \mathbb{R}^N$ and represents the vector of design variables, where N is the number of design variables. A set of n_ξ second-order random parameters $\boldsymbol{\xi}(\boldsymbol{\omega}) = \{\xi_1(\omega_1), \ldots, \xi_{\mathrm{n}_\xi}(\omega_{\mathrm{n}_\xi})\} \in \Xi^u$ are considered with $\Xi^u \subset \mathbb{R}^{n_\xi}$. The symbol $\boldsymbol{\omega} = \{\omega_1, \ldots, \omega_{\mathrm{n}_\xi}\} \in \Omega \subset \mathbb{R}^{n_\xi}$ denotes events in the complete probability space (Ω, $\mathcal{F}$, P) with $\mathcal{F} \subset 2^\Omega$ the σ–algebra of subsets of Ω and P a probability measure. The random variables $\boldsymbol{\omega}$ are by definition standard uniformly distributed as $\mathcal{U}(0, 1)$. Random parameters $\boldsymbol{\xi}(\boldsymbol{\omega})$ can have any arbitrary probability density $f_\xi(\boldsymbol{\xi}(\boldsymbol{\omega}))$. The argument $\boldsymbol{\omega}$ is dropped from here on to simplify the notation.

Then, the objective of uncertainty propagation is to find the probability distribution of $u(\mathbf{x}, t, \mathbf{y}, \boldsymbol{\xi})$ and its statistical moments $\mu_{\mathrm{u}_i}(\mathbf{x}, t, \mathbf{y})$ given by

$$\mu_{\mathrm{u}_i}(\mathbf{x}, t, \mathbf{y}) = \int_{\Xi^u} u(\mathbf{x}, t, \mathbf{y}, \boldsymbol{\xi})^i f_\xi(\boldsymbol{\xi}) \mathrm{d}\boldsymbol{\xi}, \tag{6.2}$$

where statistical moments remain dependent on the vector of design variables $\mathbf{y}$. A minimization problem can be formulated as follows

$$\min_{\mathbf{y} \subset \Xi^d} \mu_{\mathrm{u}_i}(\mathbf{x}, t, \mathbf{y}), \tag{6.3}$$

where the process of finding solutions of equations (6.1) and (6.3) is referred to as robust design optimization and typically involves only few low-order moments in (6.2).

6.2 ANOVA-based optimization

An efficient strategy based on ANOVA analysis in order to perform robust optimization with multiple sources of uncertainty is proposed and applied to the simulation of turbine cascade in ORCs systems. Standard deviation is chosen as the basic criterion for robust optimization, and then ANOVA is retained as technique of stochastic dimension reduction. Basing on these assumptions, an efficient technique consisting in response surface construction over sensitivity indexes derived from ANOVA analysis in the design variables plan is proposed. The algorithm proposed in this section, that can be divided in two subsequent steps, is presented in details in Section 6.2.1. This algorithm is applied to the optimization of a turbine cascade in a ORCs system (Section 6.2.2). Inlet/outlet conditions and geometrical factors are chosen as design parameters.

6.2.1 Description of the algorithm

In this section, the algorithm for multi-objective robust design optimization is described. The strategy is constituted by two steps, that are schematically represented in figure 6.1.

During the first step (reported in the figure 6.1(a)), the focus is on building a response surface for each TSI_j, *i.e.* $\widetilde{TSI}_j(y)$, in the design space. This step is constituted by the following actions:

- An initial set of N designs (design variables y_l with $l = 1, .., N$) in the design space, i.e. a design of experiment (called hereafter DOE), is generated.
- Eq. 6.2 is solved for each design y_l using the PC expansion or other techniques (quasi-Monte Carlo, collocation, ...).
- TSI_j is computed for each uncertainty j and for each y_l.
- A response surface in the design space for each uncertainty j, $\widetilde{TSI}_j(y)$, is built by using a kriging method based on a DACE approach [Sacks 1989] and the set of $TSI_j(y_l)$, that are computed at the previous step. The advantage of DACE approach is the possibility of implementing an adaptive response surface in order to minimize the statistical error between the real function and the extrapolated one.

During the second step of the algorithm (represented in figure 6.1(b)) the focus is on solving Eq. 6.3. The optimizer is the NSGA algorithm [Deb 2002]. The main tuning parameters of the algorithm are the population size, the number of generations, the crossover and mutation probabilities and the distribution indexes for crossover and mutation operators. Typical values for the last four parameters are, respectively, 0.9, 1, 20 and 20. Remark that the global strategy proposed in this work can be applied for a whatever kind of optimizer.

In order to initialize the Genetic Algorithm, the same initial set of N samples, y_l, considered during the first step, are taken into account. Now, at each iteration of the proposed algorithm, (i.e. for each evaluation of the fitness function), the following operations are performed :

- Supposing a given design y_n, the response surface is used to compute the approximated value of TSI_j, *i.e.* $TSI_j(y_n) \cong \widetilde{TSI}_j(y_n)$, for each uncertainty. Moreover, the 2% criterion on TSI_j [Gao 2010] is applied to build the reduced set of uncertainties to consider. Finally, the stochastic problem, expressed in Eq. 6.2, is solved by means of PC expansion.
- Fitness functions, in terms of mean and variance, are computed and used by the optimizer.

When convergence is reached, the fitness functions of the optimal designs are re-computed by considering the whole set of uncertainties.

6.2.2 Results on complex flows in a turbine cascade

The algorithm described in the previous section is applied to the optimization of a turbine blade, *i.e.* the two dimensional VKI LS-59 cascade [Kiock 1986, Congedo 2011b]. An unstructured CFD dense-gas solver is used to ensure the reliability of the computed results for dense gas flows through a turbine cascade (for more details see [Congedo 2011b]).The two-dimensional flow domain is discretized by a structured C-grid comprised of 192x16 cells. The boundary conditions are imposed as follows: at the inlet and outlet boundaries, non-reflecting boundaries are applied using the method of characteristics; a slip condition is imposed at the wall, which uses multi-dimensional linear extrapolation from interior points to calculate the wall pressure; periodicity conditions are prescribed at the inter-blade passage boundaries. The siloxane dodecamethylcyclohexasiloxane ($C_{12}H_{36}Si6)O_6$), commercially known as D6, is the fluid considered in this study. The physical properties of D6 are reported in Table 6.1. The Peng-Robinson (PRSV) equation is used as thermodynamic model for D6. It depends on the following parameters, the fluid acentric factor ω, the isobaric specific heat in the ideal gas state, i.e. $c_{v\infty}$, and a fluid-dependent parameter n (the mean values of these parameters for D6 are defined in Table 6.2). Performance of the turbine cascade can be evaluated by using several output criteria. Here, the power output per unit depth (PO) expressed as $\delta h \times \dot{m}/w_{mol}$ [W] is taken into account, where δh is the enthalpy variation through turbine stage, $\dot{m}$ is the mass flow rate and w_{mol} is the molecular weight.

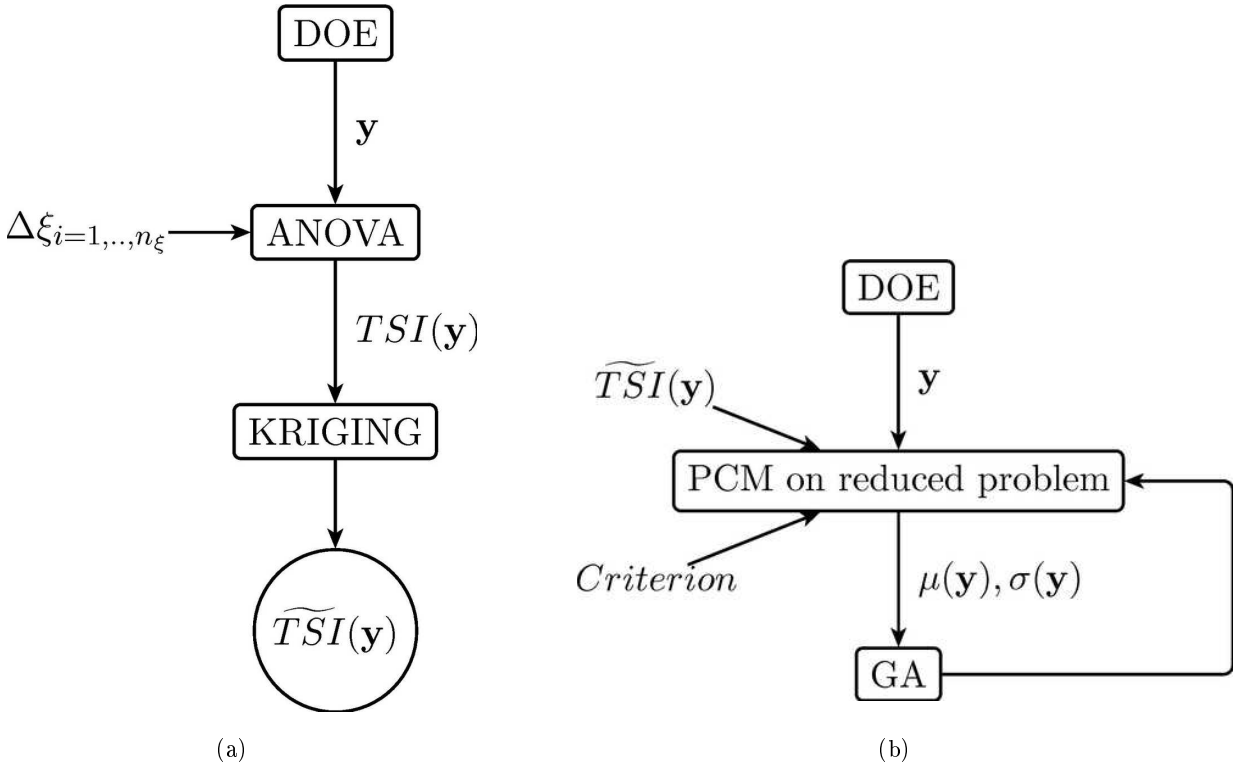

Figure 6.1: Compact scheme for the kriging procedure (a) and the overall optimization strategy (b)

M (g/mole)	$T_c(K)$	$P_c(kPa)$	$T_b(K)$
444.9	645.8	961	518.1

Table 6.1: Thermodynamic data for D6, where M is the percentage molecular weight and T_b is the boiling temperature at 1 atm. Properties are taken from [Colonna 2008b]

Three main sources of uncertainties are considered in this study (globally eight uncertainties): i) the uncertainties on the operating conditions, i.e. inlet total temperature, T_{in}/T_c, inlet total pressure, p_{in}/p_c, angle of incidence β and the stagger angle θ, ii) the uncertainties on the thermodynamic model, i.e. ω, cv_∞ and n, and uncertainties on geometrical parameters, i.e. the blade thickness ϕ. Basing on [Kiock 1986], the 3.0% of uncertainty for the temperature and pressure levels at the inlet conditions has been taken into account. The PRSV thermodynamic model is considered as a good trade-off between the accuracy of thermodynamic properties and the functional complexity since it depends on a limited number of parameters, hence a reduced number of uncertainty sources [Cinnella 2011]. The following uncertainties are retained for this model (see the table 6.2 and Ref. [Cinnella 2011]), listed with their associated error bars: the acentric factor ω (2%), the isobaric specific heat in the ideal gas state and a fluid-dependent parameter n (6%). For the other parameters, it is assumed an uncertainty of 3% for the angle of incidence β and the stagger angle θ, and an uncertainty of 2% for the thickness ϕ.

6.2.2.1 Problem definition

Optimization problem is defined as follows: to find the optimal values for T_{in}/T_c , p_{in}/p_c , β and θ (four design variables) in order to maximize the mean of power output, $\mu(PO)$, and to minimize its standard deviation, $\sigma(PO)$ (two objective-optimization problem). Ranges for each design variable

	n	$c_{v\infty}$	ω
Mean	0.5729	105.86	0.7361
Range	0.5385-0.6073	99.50-112.20	0.7214-0.7508

Table 6.2: Thermodynamic constant for D6, PRSV equation of state, mean and min/max values for the uniform probability density function, data taken from [Colonna 2008c]

p_{in} / p_c	T_{in} / T_c	α	β
0.7-0.98	SCL-1.15	25°-35°	29°-39°

Table 6.3: Ranges of design variables in the optimization plan

are defined in table 6.3. Remark that the lower limit for the temperature is given by the saturation curve limit (SCL). Seeing that CFD code can compute only 1-phase flows, it has to be verified that the uncertainty region does not cross the maximal saturation curve (that can be computed as the upper limit of the 100% confidence intervals when uncertainties on thermodynamic model are taken into account). Finally, the optimization problem consists in finding the optimal values for four design variables where the output to maximize is dependent from eight uncertainties.

6.2.2.2 ANOVA decomposition over the geometric plan and construction of kriging response surface

The algorithm described in figure 6.1(a) is applied on the problem defined in the previous section. A design of experiment (DOE) of 50 elements in the four design variable space is generated. Then, for each design, a quasi-Montecarlo plan (based on Sobol sequences) of two hundred individuals in the stochastic plan is generated and TSI is computed for each uncertainty. The convergence of TSI indexes for each uncertainty and design is verified by increasing the number of individuals until five hundred. Following the approach proposed in this work, the convergence of TSI is much more important than the convergence on the variance since only the correct use of the criterion should be assessed, i.e. it is not important to compute exactly the variance of all the individuals but only of the best individuals. Then, if the stochastic reduction allows obtaining an optimal individual, this one can be analyzed by considering all the uncertainties during the a-posteriori validation. In figures 6.2 and 6.3, TSI contours are reported for each uncertainty in the plan p-T, where the point in the plan p-T is associated to the couple (p_{in} , T_{in}) of inlet thermodynamic conditions. As shown in figure 6.2(a,b), TSI associated to the uncertainty on pin vary from 8% to 44% while vary from 39% to 83% for uncertainty on in T . For the uncertainties on two geometrical parameters, θ and ϕ (see figure 6.2 (c,d)), TSI vary from 7% to 25% and from 0.7% to 2.9%, respectively. TSI associated to the uncertainties on thermodynamic model, i.e. ω , cv_∞ and n (see figure 6.3), and on the geometrical parameter ϕ, are less than 0.29%, then they are negligible with respect to the TSI criterion ([Gao 2010]). Data represented in figures 6.2 and 6.3 are used as the training database for the kriging model, which is then used in order to estimate TSI of each uncertainty for each design generated during the optimization loop.

6.2.2.3 Optimization

As shown in figure 6.1(b), during the optimization loop, for each design y a Polynomial Chaos Method is used on the reduced problem where the reduction is based on the computation of $\widetilde{TSI}_j(y)$ and

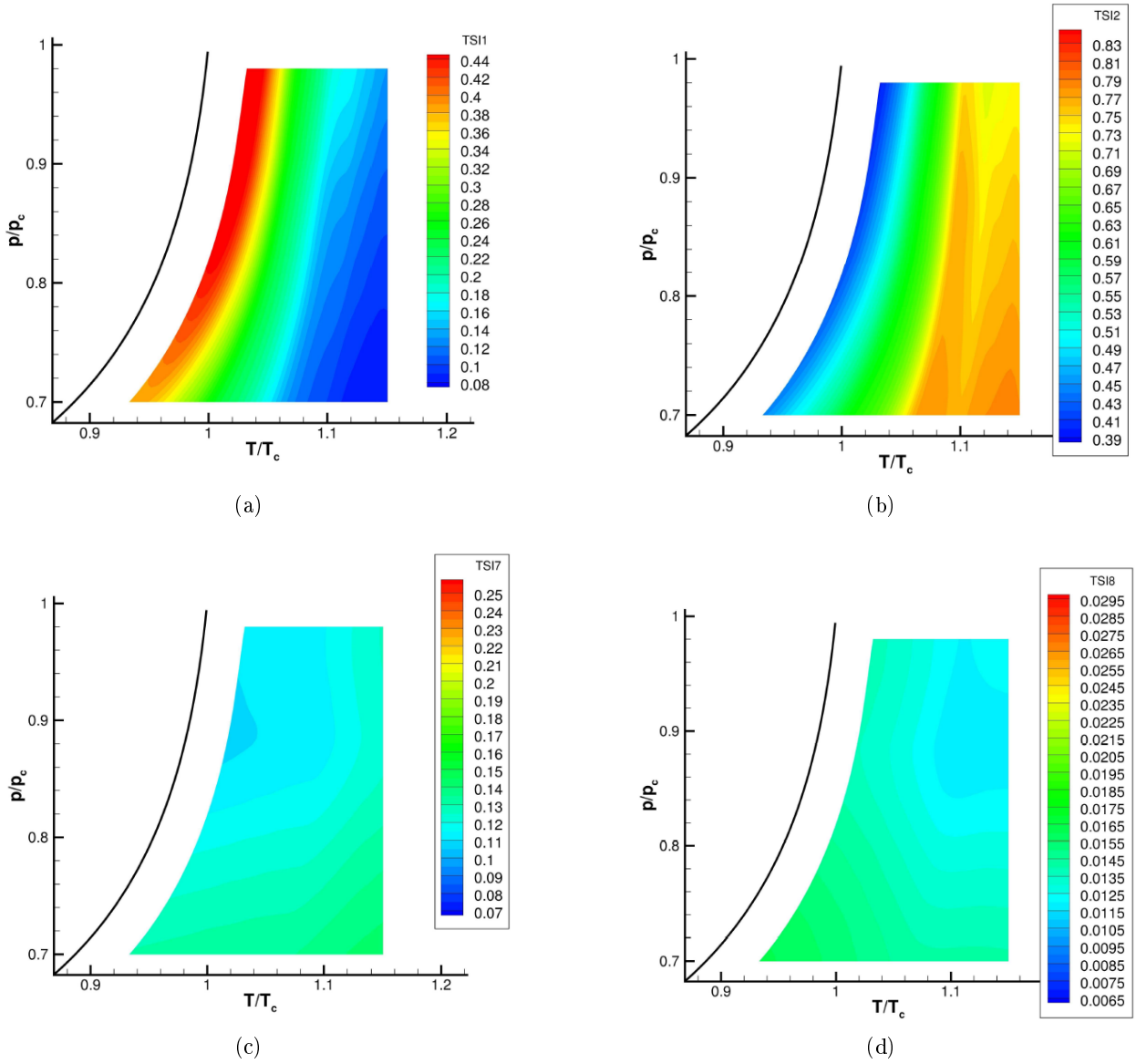

Figure 6.2: TSI contours in the plan p-T for p_in (a), T_in (b), θ (c), φ (d).

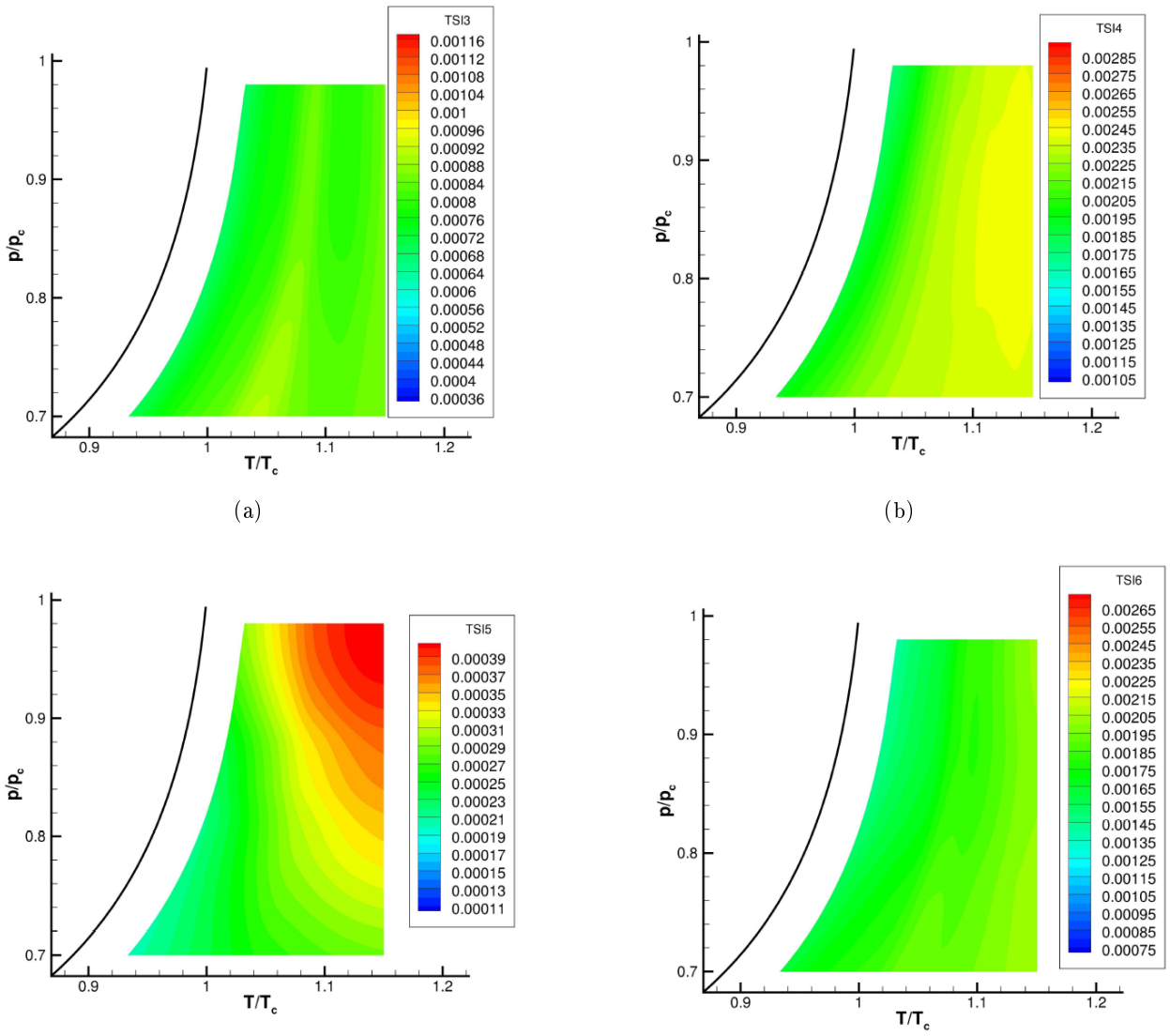

Figure 6.3: TSI contours in the plan p-T for $c_{v,\infty}$ (a), n (b), ω (c), β (6d).

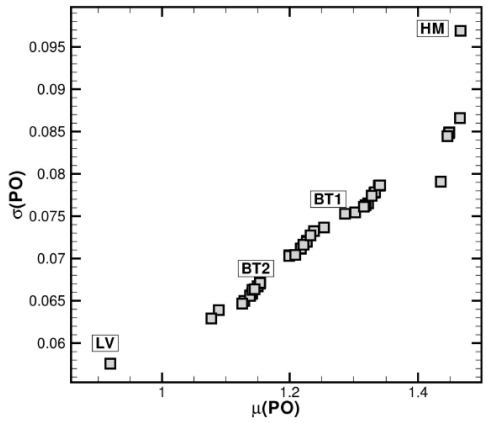

Figure 6.4: Pareto front in the plan μ(PO)âĹŠ σ(PO)

a TSI criterion (2%). For each design of the DOE that has been previously computed for kriging metamodel, the reduced stochastic problem is performed and the statistics are computed in terms of mean and standard deviation for PO. Then, twenty individuals evolved during forty generations. The converged Pareto front is represented in figure 6.4. Various configurations are obtained with a large variation of the PO, going from 0.91 to 1.46. Four individuals are extracted from the Pareto front in order to evaluate differences in the solution: one individual at the lowest variance (denoted hereafter LV), one at the largest mean (denoted HM), and two others, denoted BT1 and BT2, representing potential trade-off between mean and standard deviation. In figure 6.5, the mean pressure is shown in the computational domain for LV, HM, BT1 and BT2. Remark that high inlet turbine pressure are associated to high mean of PO, displaying a strong dependence of turbine performances from thermodynamic inlet conditions. In a similar way, standard deviation of the pressure is reported in figure 6.6. Variance is concentrated around the compression shock location near the trailing edge. Moreover, the variance of PO seems related to the peak of maximal variance of the pressure, i.e. when the maximal variance is lower, variance of PO is lower too.

6.2.2.4 A-posteriori validation and computational cost reduction

Statistics of LV, HM, BT1 and BT2 are validated by performing a complete stochastic computation without uncertainty reduction. The interest is twofold, i.e. to verify that i) the statistic of the optimal individuals can be computed correctly also by performing the reduced stochastic problem, and that ii) LV, HM, BT1 and BT2 belong to the same Pareto front. In figure 6.7, the Pareto front constituted by LV, HM, BT1 and BT2 has been computed by means of the reduced (grey square) and the complete stochastic problem (circle). As shown in the figure, the four designs belong to the same Pareto front also if statistics are evaluated by taking into account all the uncertainties. Moreover, the differences on mean and standard deviation are shorter than 0.5%. In figure 6.8, the coefficient of variation for the pressure has been computed for the LV design by means of the complete and reduced stochastic problem. As it is evident, solutions are very similar. Let us estimate the saving in computational cost realized through the Sobol proposed approach with respect to the complete stochastic problem (using all the uncertainties at the same time). For each individual obtained during optimization, the number of uncertainties varies from 3 to 4 (see figures 6.2 and 6.3 and remember that TSI criterion is of 2%) with respect to 8, that is the global number of uncertainties. This approach displays a strong reduction of stochastic computational cost by preserving the same accuracy.

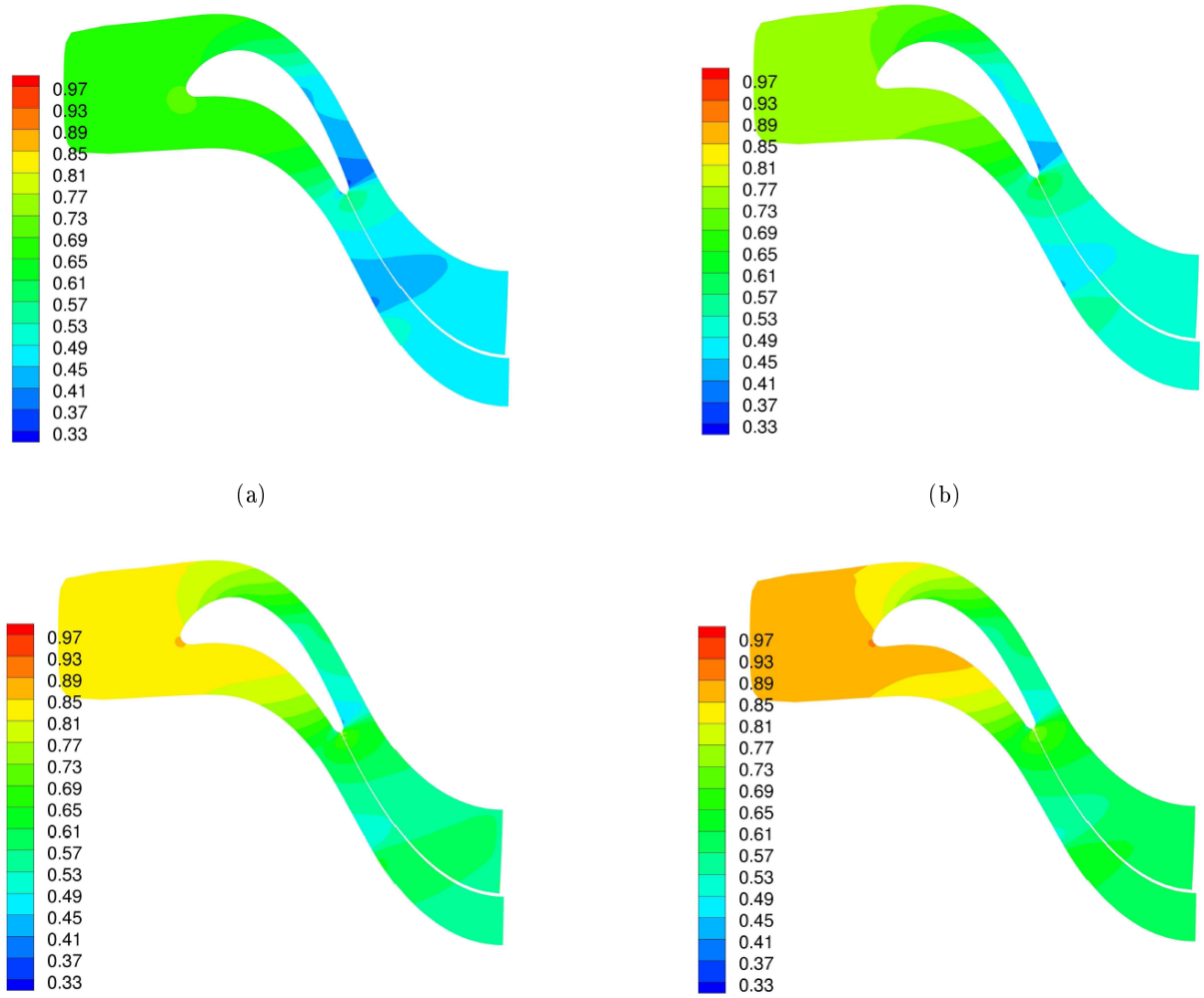

Figure 6.5: Mean of pressure for LV (a), BT2 (b), BT1 (c), HM (d)

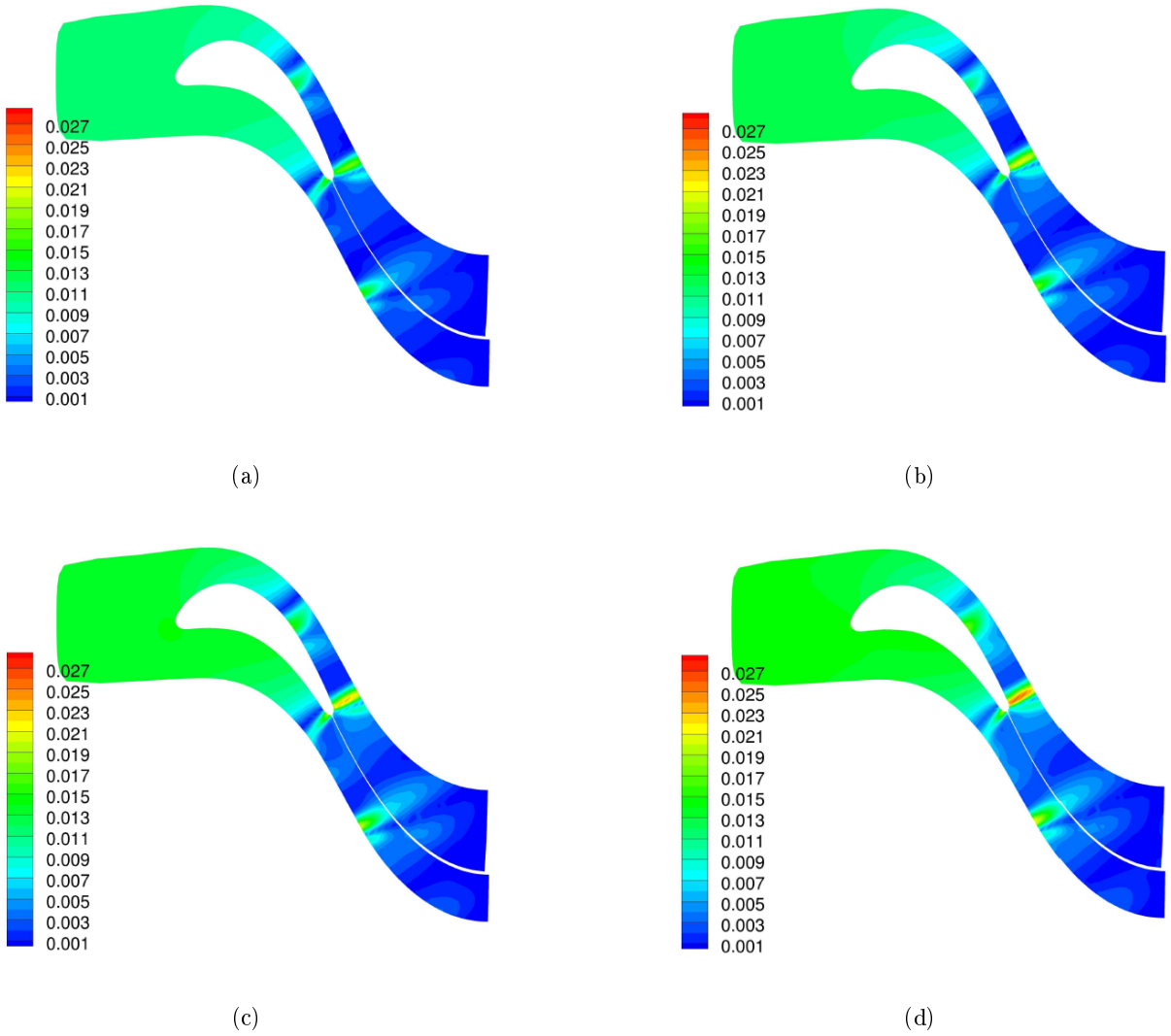

Figure 6.6: Standard deviation of the pressure for LV (a), BT2 (b), BT1 (c), HM (d)

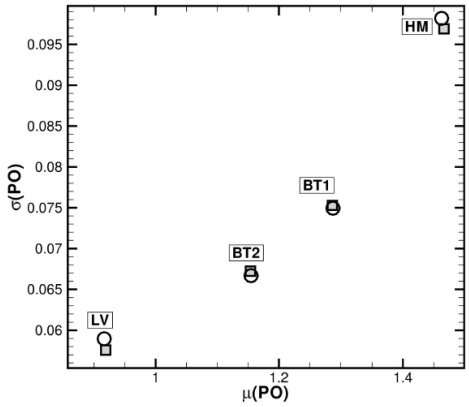

Figure 6.7: Pareto front in the plan $\mu(PO) - \sigma(PO)$. Grey square: reduced, circle: complete

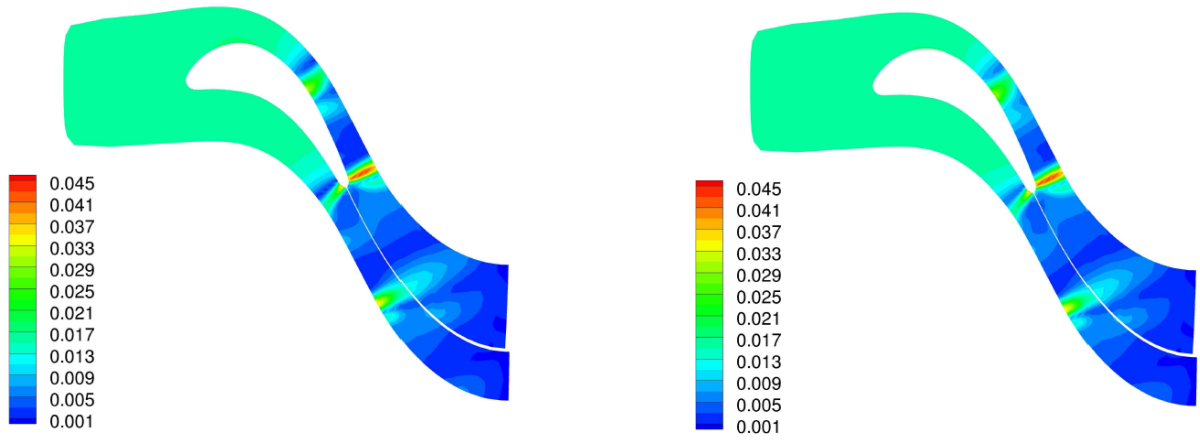

(a) (b)

Figure 6.8: Coefficient of variation of pressure for LV design, reduced (a) and complete (b)

6.3 Simplex^2

In this section, we present the Simplex^2 method, relying on the coupling between two methods based on simplex space representation, the Simplex Stochastic Collocation (SSC) method for UQ and the Nelder-Mead (NM) algorithm for the optimization. The idea is to build a multi-scale strategy based on simplex representation in order to minimize global cost of the robust design.

The SSC method [Witteveen 2012b, Witteveen 2012a] is an efficient algorithm for UQ in computational problems with random inputs and displays super-linear convergence and a linear increase of the initial number of samples with increasing dimensionality. These properties have been demonstrated for uniform and non-uniform distributions, and correlated and uncorrelated parameters.

The NM algorithm is one of the best known algorithms [Nelder 1965] for multi-dimensional unconstrained optimization without derivatives. In many numerical tests, NM method allows obtaining a good reduction in the computational cost by preserving accuracy. Despite its success, very few theoretical results have been demonstrated for this algorithm. More recently, Gao and Han [Gao 2010] proposed a new implementation in which the expansion, contraction and shrink parameters depend on the dimension of the optimization problem that displays good results for high dimensional problems.

6.3.1 Numerical ingredients for robust design optimization

Solving a robust design problem requires an algorithm for solving (6.2) and (6.3). Remark that a non-intrusive formulation for solving (6.2) is considered. This means that the numerical method used to solve (6.1) is not modified for taking into account uncertainties, *i.e.* problem expressed in (6.1) is solved several times for different samples of $\boldsymbol{\xi}(\boldsymbol{\omega})$. Now, let us focus our attention to the resolution of (6.2) and (6.3). Classical approaches for robust design optimization are based on two different and independent methods for solving (6.2) and (6.3), respectively.

In this section, the SSC method (for solving (6.2)) and the NM algorithm (for solving (6.3)) are described.

6.3.1.1 Simplex Stochastic Collocation

In local UQ methods such as the multi-element stochastic collocation approach [Foo 2010, Ma 2010] the weighted integrals in (6.2) defined over the parameter space Ξ^u are computed as a summation of

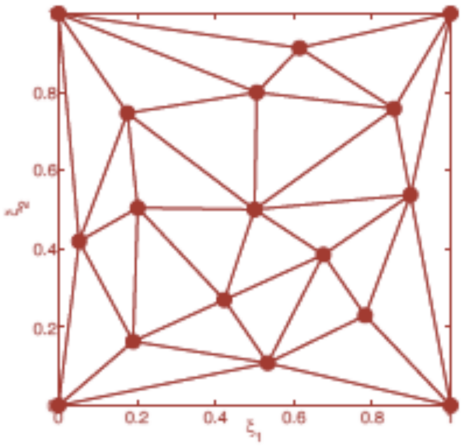

Figure 6.9: Simplex Elements (Triangles in 2D)

integrals over n_e disjoint subdomains $\Xi^u = \bigcup_{j=1}^{n_\mathrm{e}} \Xi_j^u$

$$\mu_{\mathrm{u}_i}(\mathbf{x}, t, \mathbf{y}) \approx \sum_{j=1}^{n_\mathrm{e}} \int_{\Xi_j^u} u(\mathbf{x}, t, \mathbf{y}, \boldsymbol{\xi})^i f_\xi(\boldsymbol{\xi}) \mathrm{d}\boldsymbol{\xi} + \varepsilon, \tag{6.4}$$

where ε is the error involved in the approximation.

Main features of SSC method ([Witteveen 2012b, Witteveen 2012a]) are i) the possibility to compute an error estimate, ii) the adaptive H-refinement and iii) P-refinement capabilities, iv) treating non-ÂŋâĂŘhypercube parameter spaces, v) treating discontinuities in the stochastic space. Properties i,ii,iii) will be presented here since they are the main ingredients for the S2M method, that is proposed in this paper and will be presented in the next section. Other properties of SSC methods, such as iv,v) will be not described here (for more details see [Witteveen 2012b, Witteveen 2012a]).

In the SSC approach [Witteveen 2012b, Witteveen 2012a], the integrals in the simplex elements Ξ_j^u are computed by approximating the response surface $u(\boldsymbol{\xi})$ by an interpolation $w(\boldsymbol{\xi})$ of n_s samples $\mathbf{v} = \{v_1, \ldots, v_{n_\mathrm{s}}\}$. In figure 6.9, an example of simplex elements in 2 dimensions is reported.

Sample v_k is computed by solving (6.1) for realization $\boldsymbol{\xi}_k$ of the random parameter vector $\boldsymbol{\xi}$

$$\mathcal{L}(\mathbf{x}, t, \mathbf{y}, \boldsymbol{\xi}_k; v_k(\mathbf{x}, t, \mathbf{y})) = \mathcal{S}(\mathbf{x}, t, \mathbf{y}, \boldsymbol{\xi}_k), \tag{6.5}$$

for $k = 1, \ldots, n_\mathrm{s}$.

The interpolation of the samples $w(\boldsymbol{\xi})$ consists of a piecewise polynomial function

$$w(\boldsymbol{\xi}) = w_j(\boldsymbol{\xi}), \qquad \text{for } \boldsymbol{\xi} \in \Xi_j^u, \tag{6.6}$$

with $w_j(\boldsymbol{\xi})$ a polynomial interpolation of degree p of the samples $\mathbf{v}_j = \{v_{k_{j,0}}, \ldots, v_{k_{j,N_s}}\}$ at the sampling points $\{\boldsymbol{\xi}_{k_{j,0}}, \ldots, \boldsymbol{\xi}_{k_{j,N_s}}\}$ in element Ξ_j^u, where $k_{j,l} \in \{1, \ldots, n_\mathrm{s}\}$ for $j = 1, \ldots, n_\mathrm{e}$ and $l = 0, \ldots, N_s$, with N_s the number of samples in the simplexes.

The polynomial interpolation $w_j(\boldsymbol{\xi})$ in element Ξ_j^u can then be expressed in terms of a truncated Polynomial Chaos expansion

$$w_j(\boldsymbol{\xi}) = \sum_{m=0}^{P} c_{j,m} \boldsymbol{\Psi}_{j,m}(\boldsymbol{\xi}). \tag{6.7}$$

where the polynomial coefficients $c_{j,m}$ can be determined from the interpolation condition

$$w_j(\boldsymbol{\xi}_{k_{j,l}}) = v_{k_{j,l}}, \tag{6.8}$$

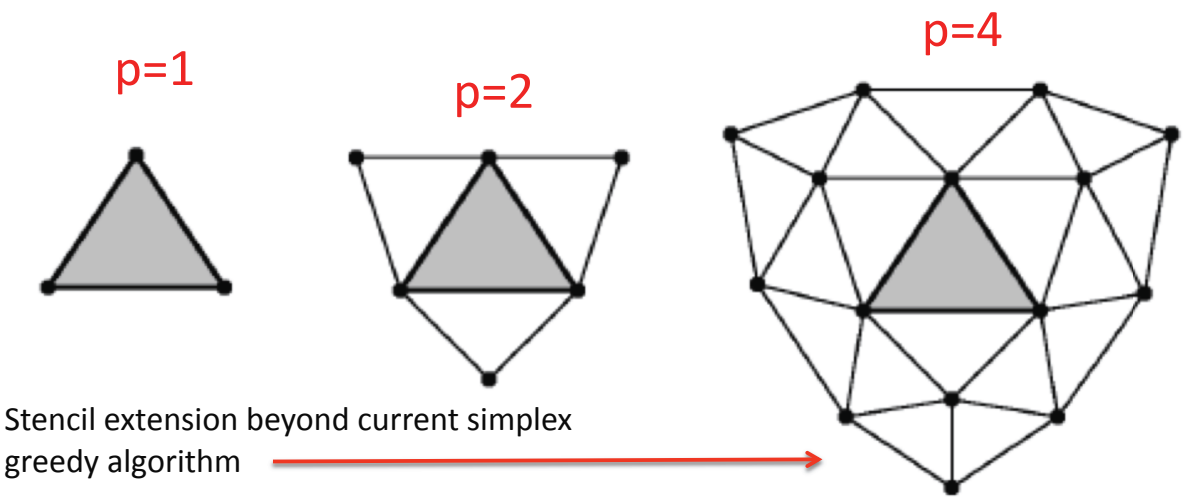

Figure 6.10: P-refinement in 2D stochastic space.

for $l = 0, \ldots, N_s$, which leads to a matrix equation, that can be solved in a least-squares sense for $N_s > P$. Note that a one-to-one correspondence exists between the choice of stochastic variable ξ_i and the polynomials $\Psi_{j,m}$. For instance, if ξ_i is a normal/uniform variable, the corresponding $\Psi_{j,m}$ are Hermite/Legendre polynomials (see [Witteveen 2012b]).

Concerning the i) property, the error ε is estimated using hierarchical surpluses considering in each element Ξ^u_j, the difference between interpolated and exact value. In this way, both local and global error in each simplex can be computed, thus identifying the simplex element, where the error is the largest one.

Concerning H-refinement, SSC has two components: i) simplex selection (based on the previous error estimator), and ii) simplex splitting, designed to avoid clustering. Basic principles are displayed in figure 6.11: a) simplex element where ε is the largest is selected for refinement, b) a region is selected for node insertion, c) random node insertion (guaranteed away from the others). Remark that a threshold, ε_{SSC}, is generally fixed for deciding when stopping the refinement, *i.e.* when $\varepsilon < \varepsilon_{SSC}$, refinement is stopped.

When using SSC, the error convergence of first degree SSC decreases for an increasing n_ξ. To cure this issue, a P-refinement criterion for higher degree SSC has been conceived. In practice, the idea is to use higher degree polynomial interpolation stencil based on Newton-Cotes quadrature. In figure 6.10, it is shown for a 2D stochastic space, how more than 3 samples can be used to construct better approximates by enlarging the stencil. The choice of the optimal polynomial degree p is selected based on the number of uncertainties n_ξ and the required order of convergence. A super-linear convergence can be obtained for smooth responses (see [Witteveen 2012b] for more details).

Then, SSC is constituted by the following operations:

- Initial discretization (2^{n_ξ} vertexes of the hypercube enclosing the probability space Ξ^u and one sampling point in the interior)
- $n_{s_{\text{init}}}$ initial samples v_k computed by solving $n_{s_{\text{init}}}$ deterministic problems (6.1) for the parameter values corresponding to the initial sampling points $\boldsymbol{\xi}_k$ located in Ξ^u only
- Polynomial approximation (Eq. 6.7) and P-refinement
- Error estimate and H-refinement according to the threshold ε_{SSC}

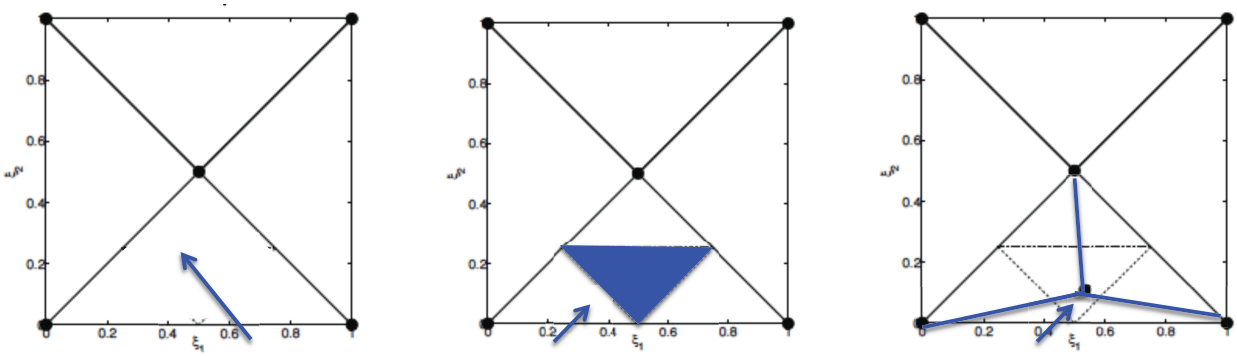

(a) (b) (c)

Figure 6.11: H-refinement

Finally, the probability distribution function and the statistical moments μ_{u_i} of $u(\boldsymbol{\xi})$ given by (6.4) are then approximated by the probability distribution and the moments μ_{w_i} of $w(\boldsymbol{\xi})$

$$\mu_{\mathrm{u}_i}(\mathbf{x}, t, \mathbf{y}) \approx \mu_{\mathrm{w}_i}(\mathbf{x}, t, \mathbf{y}) = \sum_{j=1}^{n_{\mathrm{e}}} \int_{\Xi_j^u} w_j(\mathbf{x}, t, \mathbf{y}, \boldsymbol{\xi})^i f_{\xi}(\boldsymbol{\xi}) \mathrm{d}\boldsymbol{\xi}, \tag{6.9}$$

in which the multi-dimensional integrals are evaluated using a weighted Monte Carlo integration of the response surface approximation $w(\boldsymbol{\xi})$ with $n_{\mathrm{mc}} \gg n_{\mathrm{s}}$ integration points.

6.3.1.2 Nelder-Mead Algorithm

The Nelder-Mead (NM) method is one of the most popular for solving optimization problem, like in (6.3). It uses also a simplex representation in the space spanned by the design variables; this consists of $N+1$ vertices if N is the dimension of vector $\mathbf{y}$. The method generates new designs by extrapolating the behavior of the objective function measured at each one of the basic designs, that constitute the geometric simplex. At each iteration, the vertices of the simplex are ordered according to the objective function values. Then, the algorithm uses four operators, *i.e.* reflection, expansion, contraction and shrink. Simplex structure evolves until the optimal point is found.

For more details concerning NM algorithm, see [Gao 2010].

6.3.2 Optimization Algorithms

In this section, the optimization algorithms are introduced and described. First, the principles of the decoupled approach are drawn. Then, the Simplex^2 method is presented.

6.3.2.1 Decoupled approach

As already explained before, using a decoupled approach for robust design optimization, means that the algorithm used for the evaluation of a given design (solving (6.2) for a design y) is completely decoupled from the algorithm used for the optimization (finding the best y in order to solve (6.3)). Implementation of this approach is very easy, but the most significant challenge consists in solving (6.2) for each design y by finding a good trade-off between accuracy and computational cost.

In this work, a decoupled approach is performed using the NM algorithm as optimizer and the SSC as stochastic method for solving (6.2). This is retained as a reference in order to estimate performances of the proposed approach, the Simplex^2 method introduced in the next section.

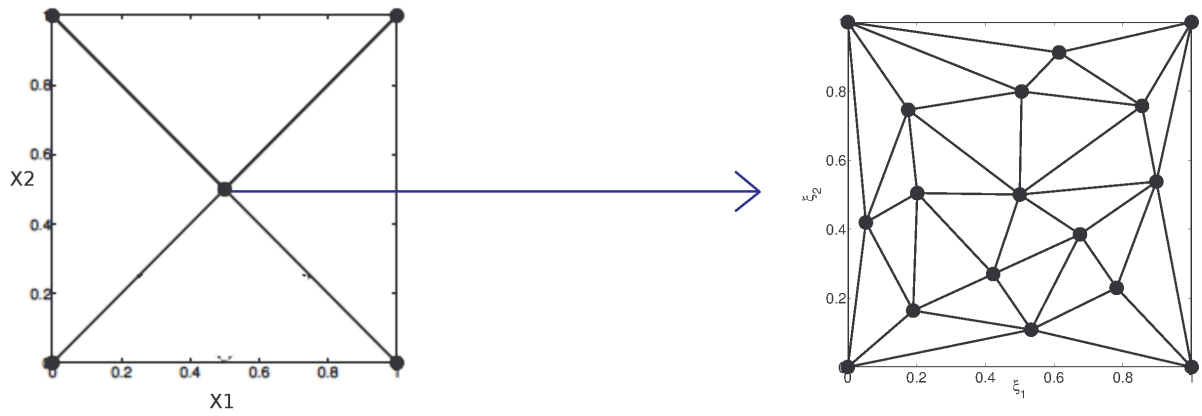

Figure 6.12: Two types of simplexes in Simplex^2 Method.

6.3.2.2 Simplex^2 Method

In this section, the Simplex^2 (S2M) method is presented. It is an efficient multi-scale coupling of SSC and NM methods, based on two different levels of the simplex tessellation. Let us consider the design variable space, and generate an initial Design of Experiment (2^N vertexes of the hypercube enclosing the probability space Ξ^u and one sampling point in the interior). In figure 6.12, a case with two design variables is considered, with designs varying in $[0, 1]$. To each design, that is one of the simplex vertex, a simplex in the stochastic space is associated (micro-scale) (see again figure 6.12). Then, there is one geometric simplex (macro-scale) constituted by the set of designs, and there are a number of stochastic simplex that is equal to the number of designs. Remark that in the formulation of the algorithms and the examples we show below we assume that the uncertain variables and the design parameters are independent for simplicity, then the geometric simplex and each of the stochastic simplex do not share the same space. It is possible to use the same approach for cases in which some of the design variables are uncertain; this will be explored in a future work.

The Simplex^2 Method is based on the following ideas:

1. A stopping criterion for the H-refinement in the stochastic space that is driven from the size of the geometric simplex. The idea is to have some more refined stochastic simplex for only particular designs (close to the optimal solution), and very coarse stochastic simplex for bad designs (thus permitting to save computational cost).

2. An high-degree interpolation (P-refinement) on the geometric simplex

3. The use of the above-mentioned interpolation for having an estimator for the NM operators that can be very expensive. Then, NM Method could be accelerated with respect to the classical version by using this response surface.

4. The error introduced by the interpolating polynomials is estimated in order to decide whether or not using the interpolation during the algorithm steps

Let us focused on the stopping criterion for the H-refinement. Consider the space spanned by the design variables Ξ^d, and an element i of Ξ^d as Ξ^d_i. To each vertex of the element i corresponds a design point y. To each design point y_o, the stochastic simplex tessellation of Ξ^u is associated, thus the problem is to compute $\mu_{\mathrm{u}_i}(\mathbf{x}, t, \mathbf{y_o})$. To solve this problem, the SSC method is applied. For the NM algorithm, it is necessary to focus the attention to the simplex constituted by the best N+1 designs, where N is the number of design variables, considering that $\mu_{\mathrm{u}_i}(y_1) < \mu_{\mathrm{u}_i}(y_2) ... < \mu_{\mathrm{u}_i}(y_{N+1})$ (for a minimization problem). As shown in the previous section, if the error is larger than a prescribed

threshold ε_{SSC}, then a H-refinement on the stochastic simplex is performed. First fundamental feature of S2M is to compute the threshold error for the H-refinement for each stochastic simplex as follows

$$\varepsilon_{SSC} = \mu_{\mathrm{u}_i}(y_{N+1}) - \mu_{\mathrm{u}_i}(y_1), \tag{6.10}$$

where N represents the number of design variables. Note that the same threshold is used for each stochastic simplex. This criterion determines a strong coupling between SSC and NM methods, and it is a fundamental property of S2M method. This permits to obtain very refined stochastic simplex associated to the best design, while coarser stochastic simplex for bad designs. Remark that this criterion can be applied the first time only after the evaluation of μ for each design point in the initial geometric simplex.

Second important feature of S2M method is constituted by the building of the Polynomial approximation (Eq. 6.7) with P-refinement, that has been described in the previous section for SSC, on the geometric simplex by considering the whole set of designs generated during the optimization. The idea is to build a metamodel for accelerating some operators of NM algorithm. Note that a uniform probability density function is retained since the design space is considered (each design is considered to have the same probability). The polynomial interpolation $w_j(\boldsymbol{y})$ (6.7) on Ξ^d is then constructed (denoted P1 in the following), by solving (6.7) on Ξ^d using all the designs generated during the optimization. The P-order is chosen according to the number of design variables, as done in SSC. This allows computing an approximation of μ_{u_i}, *i.e.* $\mu_{\mathrm{u}_i,P1}$, by means of P1. During the optimization, only for the points accepted (see step 8 in the S2M algorithm reported in the following), the error between the response surface P1 and the exact values, *i.e.* ε_{POL}, is computed as follows

$$\varepsilon_{POL} = \left|\mu_{\mathrm{u}_i} - \mu_{\mathrm{u}_i,P1}\right|. \tag{6.11}$$

Then, this error can be computed on one or more points depending on the number of designs generated during one iteration of the NM algorithm (see step 8 in the S2M algorithm reported in the following). If this error is less than $\varepsilon_{SSC}/10$, then the response surface P1 is used as metamodel for some operators in the next iteration of S2M method, thus permitting a strong reduction of the computational cost.

Let us draw the last important remarks. The choice of the initial Design of Experiment in the design space is completely arbitrary. S2M method is general with respect to this choice. What we did generally, is to generate an initial geometric DOE basing on a given number of points (using for example a Latin-Hypercube distribution), since no H-refinement is used for the geometric simplex. For the stochastic simplex, we use systematically the vertexes and the center of the hypercube, where the h-refinement is used for generating new samples. According to the order of the statistical moment, such as for example mean and standard deviation, the refinement of each stochastic simplex associated to a given design, can change. Obviously, computing standard deviation demands generally much more points than for the mean. As a consequence, the refinement of the stochastic simplex for a fixed design can vary according to the statistical moment to optimize.

We now outline the S2M method. Let assume that the objective is to minimize a given function constituted by statistics of a given output, for example to minimize the mean μ.

One iteration of S2M method

1. **Order**. Order μ_{u_i} using the tie-break rules given in [Gao 2010] and the following relation

$$\mu_{\mathrm{u}_i}(y_1) < \mu_{\mathrm{u}_i}(y_2) \ldots < \mu_{\mathrm{u}_i}(y_{N+1}). \tag{6.12}$$

2. **Gravity**. Compute the center of gravity y_0 of all points except y_{N+1}.

3. **Response surface**. If $\varepsilon_{POL} < \varepsilon_{SSC}/10$, use $\mu_{\mathrm{u}_i,P1}$ in order to estimate μ_{u_i} during the iteration steps, otherwise use SSC.

4. **Reflection**. Compute the reflection point, *i.e.* $y_r = y_0 + \alpha(y_0 - y_{N+1})$ with $\alpha = 1$. Evaluate $\mu_{\mathrm{u}_i}(y_r)$. If $\mu_{\mathrm{u}_i}(y_1) < \mu_{\mathrm{u}_i}(y_r) ... < \mu_{\mathrm{u}_i}(y_N)$, then accept y_r. Then go to 8.

5. **Expansion**. If $\mu_{\mathrm{u}_i}(y_r) < \mu_{\mathrm{u}_i}(y_1)$, then compute the expansion point $y_e = y_0 + \Gamma(y_0 - y_{N+1})$ with $\Gamma = 2$. Evaluate $\mu_{\mathrm{u}_i}(y_e)$. If $\mu_{\mathrm{u}_i}(y_e) < \mu_{\mathrm{u}_i}(y_r)$, then replace y_{N+1} with y_e. If $\mu_{\mathrm{u}_i}(y_e) > \mu_{\mathrm{u}_i}(y_r)$, then replace y_{N+1} with y_r. Then go to 8.

6. **Contraction**. If $\mu_{\mathrm{u}_i}(y_r) > \mu_{\mathrm{u}_i}(y_N)$, perform a contraction between y_0 and the better of y_{N+1} and y_r.
   Outside Contraction:
   If $\mu_{\mathrm{u}_i}(y_N) < \mu_{\mathrm{u}_i}(y_r) < \mu_{\mathrm{u}_i}(y_{N+1})$, perform an outside contraction, $y_c = y_0 + \gamma(y_r - y_0)$ with $\gamma = 0.5$. Evaluate $\mu_{\mathrm{u}_i}(y_c)$. If $\mu_{\mathrm{u}_i}(y_c) < \mu_{\mathrm{u}_i}(y_r)$, then replace y_{N+1} with y_c, otherwise go to 7.
   Inside Contraction:
   If $\mu_{\mathrm{u}_i}(y_r) > \mu_{\mathrm{u}_i}(y_{N+1})$, perform an inside contraction, $y_c = y_0 - \gamma(y_0 - y_{N+1})$ with $\gamma = 0.5$. Evaluate $\mu_{\mathrm{u}_i}(y_c)$. If $\mu_{\mathrm{u}_i}(y_c) < \mu_{\mathrm{u}_i}(y_{N+1})$, then replace y_{N+1} with y_c. , otherwise go to 7.

7. **Shrink**. Consider N points $y_i = y_1 + \sigma(y_i - y_1)$ with $\sigma = 0.5$, and evaluate $\mu_{\mathrm{u}_i}(y_i)$ by means of SSC. Then go to 8.

8. **Update**. For the points accepted, if the response surface has been used, compute the exact values by means of SSC and evaluate the error between the response surface P1 and the exact values, *i.e.* ε_{POL}. Update the response surface P1 with the new points.

This algorithm has been implemented in Matlab exploiting some specific functions for Delaunay triangulation (*DELAUNAYN*), for enclosing Delaunay triangle (*TSEARCH*) and for generating Sobol sequences (*SOBOLSET*).

6.3.3 Numerical Results

6.3.3.1 Rosenbrock stochastic problem

Several stochastic formulations of the Rosenbrock optimization problem exist [Yang 2010]. In this work, we propose a version in which a non-linear dependence on a stochastic variable is included. More precisely, we consider the following function

$$f(\mathbf{y}) = \sum_{i=1}^{N-1} \left[(1 - y_i)^2 + 100\sqrt{\xi_i + \alpha}\left(y_{i+1} - y_i^2\right)^2 \right] \tag{6.13}$$

where ξ_i are uniform random variables in $[0, 1]$ and α is taken equal to 1. This stochastic function has the same global optimum of its deterministic counterpart at (1,1,1,...).

We show results obtained by comparing two different formulations. In the first one, SSC and NM methods have been used in a decoupled way, *i.e.* the NM method is used in its traditional version and SSC method is seen as a black-box, as it has been described in section 6.3.2.1. The second formulation is the S2M method described in section 6.3.2. The problem defined by (6.13) is considered with $N = 2$, then with two design variables and one uncertainty. First, we apply S2M method for minimizing $\mu(f)$. In table 6.4, results obtained in terms of deterministic evaluations are reported for each formulation (Decoupled and S2M), where N_{DOE} indicates the number of initial designs in the optimization space used as starting point for identifying N+1 starting points needed for NM (Design Of Experiment, DOE), N_{0-DOE} is the global number of deterministic evaluations employed for the DOE, and N_0 is the number of deterministic evaluations necessary for convergence.

The exact same optimal design is obtained (the optimal fitness function is nearly 10^{-6} where the optimal theoretical fitness is equal to zero) when considering either the standard or the S2M

Table 6.4: Rosenbrock problem with $N = 2$. N_0 number of deterministic evaluations excluding the DOE

N_{DOE}	Formulation	N_0 (N_{0-DOE}) for $\min(\mu)$	N_0 (N_{0-DOE}) for $\min(\mu + \sigma)$
10	Decoupled	707 (102)	753 (109)
10	S2M	352 (102)	374 (109)
20	Decoupled	707 (200)	739 (211)
20	S2M	360 (200)	377 (211)
40	Decoupled	494 (396)	520 (418)
40	S2M	246 (396)	227 (418)

Table 6.5: Rosenbrock problem with $N = 3$. N_0 number of deterministic evaluations excluding the DOE

N_{DOE}	Formulation	N_0 (N_{0-DOE}) for $\min(\mu)$	N_0 (N_{0-DOE}) for $\min(\mu + \sigma)$
40	Decoupled	3674 (1969)	3358 (1989)
40	S2M	888 (1969)	695 (1989)

algorithm. However, the S2M method shows an important advantage in terms of computational cost, *i.e.* allowing a reduction of about 50% for N_0 with respect to the decoupled formulation. Simplex evolution in the design variables space is reported in figure 6.13 (on the left). For the optimal individual, the stochastic response surface with respect to the uncertainty is nearly coincident with the exact solution, as shown in figure 6.13 (on the right).

The same optimization is performed in order to minimize $\mu(f)+\sigma(f)$, and the results are reported in in table 6.4. Results obtained by using S2M confirm the reduction of about 50% for N_0.

Now, let us consider a case with $N = 3$: three design variables and two uncertainties. Two optimization runs are performed for minimizing $\mu(f)$ and $\mu(f) + \sigma(f)$, respectively (N_{DOE} equal to 40 samples in the geometric simplex is used for each formulation). The results in terms of N_0 are reported in table 6.5. Results obtained with S2M are extremely encouraging because we observe a reduction for N_0 of 75.8% and 79.3% by minimizing $\mu(f)$ and $\mu(f) + \sigma(f)$, respectively. These first results show the potentiality of the proposed approach on a classical problem of robust optimization. In the next section, a more complex algebraic functions is taken into account, *i.e.* the function proposed by Yang [Yang 2010].

6.3.3.2 Realistic case

The proposed S2M approach is finally applied to a more realistic case of robust optimization of the aerodynamic performance of a race-car multi-component wing. In this case the analysis is based on a computational fluid dynamic (CFD). The geometry and the associated mesh are illustrated in figure 6.14. The velocity field for the base configuration is illustrated in figure 6.15. We consider the horizontal position of the flap with respect to the main wing as the main design variable, x, while we assume that uncertainty is represented by a non-uniform incoming air velocity, represented in terms of a single uniform random variable. The physical justification for this choice is the fact that race cars operate in close vicinity to each other and the wings typically operate in *dirty* environments.

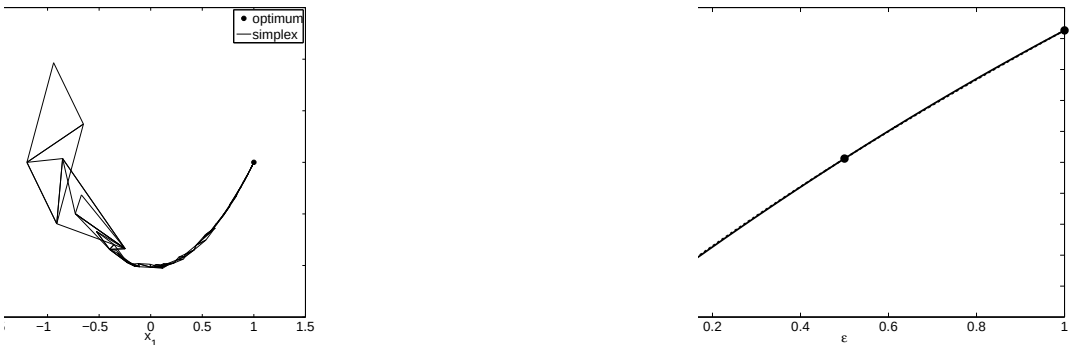

(a) (b)

Figure 6.13: Left: Simplex evolution in the geometric plan. Right: Response surface in the stochastic simplex for the optimal individual

Table 6.6: Realistic problem. N_0 number of deterministic evaluations excluding the DOE

N_{DOE}	Formulation	N_0 (N_{0-DOE}) for $\max(\mu(C_L))$	N_0 (N_{0-DOE}) for $\max(\mu(C_L)-\sigma(C_L))$
10	Decoupled	550 (112)	748 (146)
10	Coupled	201 (112)	262 (146)

It is of paramount importance that the wing aerodynamic performance - specifically the downforce (lift) and drag - are not sensitive to the variability in the incoming airflow.

Decoupled formulation and S2M method are compared in terms of computational cost in order to maximize μ and $\mu-\sigma$ of C_L and C_L/C_D (where C_L and C_D are the lift and drag coefficient respectively). For each case, the same optimum is obtained by using both formulations. For C_L, the maximal value for $\mu(C_L)$ is 0.0041343 obtained at $x = 0.016563$ (the associated optimal design is indicated with G1 hereafter), while the maximal value for $\mu(C_L)-\sigma(C_L)$ is 0.0040705 that is obtained at $x = 0.020391$ (G2). For C_L/C_D, the maximal value for $\mu(C_L/C_D)$ ($\mu(C_L/C_D)-\sigma(C_L/C_D)$) is 28.4129 (25.5571) at $x = 0.041263$ (G3) ($x = 0.041259$ (G4)).

Results in terms of computational cost are summarized in tables 6.6 and 6.7 for C_L and C_L/C_D, respectively. With respect to the decoupled formulation, using S2M permits a reduction of 63.5% for $\mu(C_L)$ and of 65.0% for $\mu(C_L)-\sigma(C_L)$. Concerning C_L/C_D, a reduction of 57.5% for $\mu(C_L/C_D)$ and of 60.9% for $\mu(C_L/C_D)-\sigma(C_L/C_D)$ is obtained using S2M with respect to the decoupled formulation. These trends confirm the good performances of the proposed method observed for simple problems before.

In figure 6.16, the optimal geometries are reported, *i.e.* G1, G2, G3 and G4, showing the effect of the optimization goal on the result. It is worth to remark that the two profiles obtained optimizing the statistical moment for C_L are slightly different while the profiles obtained optimizing C_L/C_D are nearly coincident. The results are also reported in terms of friction coefficient on the airfoil to illustrate the uncertainty present; 99% confidence intervals are drawn in Figure 6.17 and 6.18.

Table 6.7: Realistic problem. N_0 number of deterministic evaluations excluding the DOE

N_{DOE}	Formulation	N_0 (N_{0-DOE}) for $\max(\mu(C_L/C_D))$	N_0 (N_{0-DOE}) for $\max(\mu(C_L/C_D)-\sigma(C_L/C_D))$
10	Decoupled	1002 (170)	1153 (203)
10	S2M	426 (170)	451 (203)

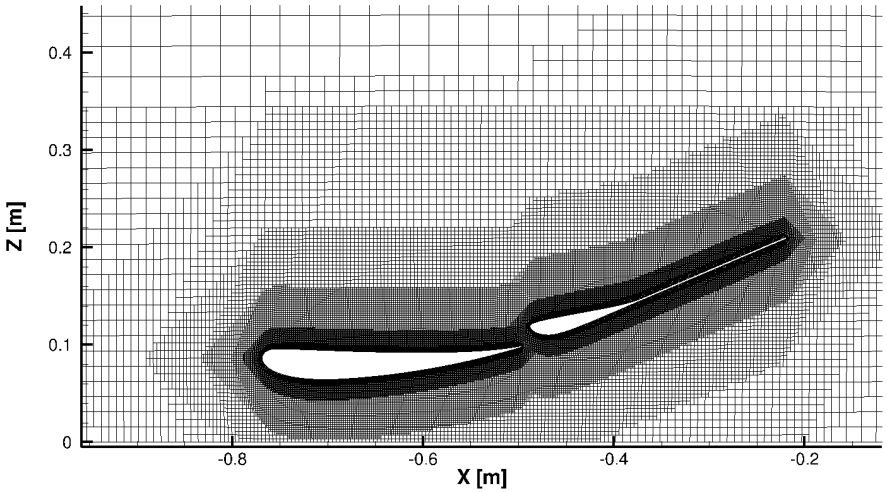

Figure 6.14: Geometry and associated mesh of the multi-component airfoil

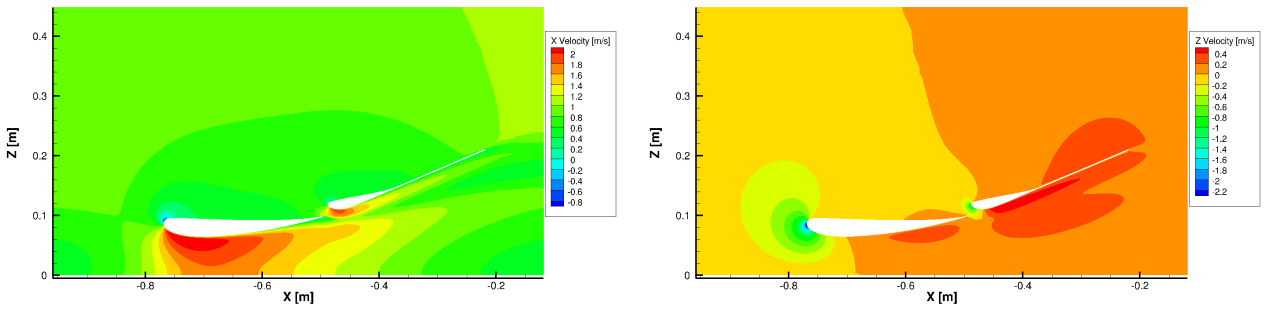

(a) (b)

Figure 6.15: X (a) and Z (b) component velocity field

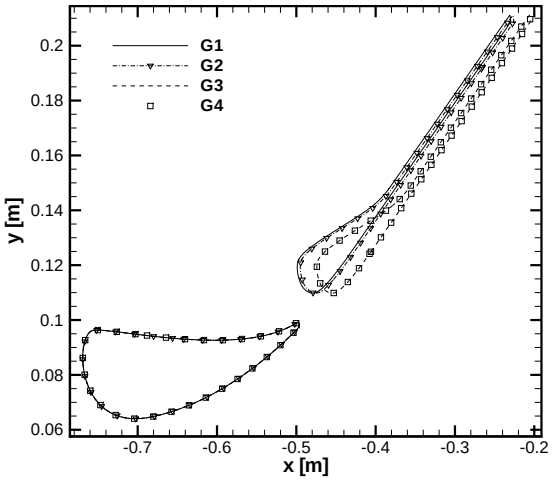

Figure 6.16: Optimal geometries

6.4 Application to the shape optimization of BZT flows

6.4.1 Baseline configuration and sources of uncertainty

Let us consider now some efficient techniques for the shape optimization of BZT flows. The steady transonic inviscid flow of a dense gas over a symmetric profile is considered as baseline configuration for investigating a shape optimization process taking into account uncertainties; this choice, over for instance a turbine cascade geometry, is mainly motivated by the objective of cost reduction when performing this preliminary study. The initial profile is a sonic arc for a perfect gas (with $\gamma = 1.4$) flow, that is the shape around which the flow is nowhere supersonic even when the inflow Mach number is getting close to unity. Note it is possible to theoretically derive the shape of a sonic arc in the case of a perfect gas or a real gas described by the Van der Waals equation of state, as reported in [Z. Rusak 2000]. The fluid considered is the heavy fluorocarbon PP10 (C13F22), with critical properties reported in Table 6.8. The thermodynamic (reduced) conditions of the free-stream are $p_r = 0.985$, $\rho_r = 0.622$ with a freestream Mach number $M_\infty = 0.95$ (there is no incidence, only a half-airfoil being computed). The set of operating conditions is denoted from now on as $input_O = M_\infty, p_r, \rho_r$. The saturation curve for PP10 constructed by means of the PRSV equations is reported with the iso-Γ curves in Fig. 6.19: it can be observed the chosen set for $input_O$ lies near the inversion region ($\Gamma \approx \%$ 0.3) yet not too close to ensure the thermodynamic state remains in the monophasic region even when uncertainties introduce fluctuations in this thermodynamic state. This configuration has also been previously studied by the authors: in [Congedo 2007] for a similar optimization process but without taking into account the uncertainty and in [Cinnella 2011] for analyzing the sole thermodynamic uncertainties independently from any optimization process. In accordance with now well-established conclusions from previous studies [Cramer 1992, Cinnella 2005b, Z. Rusak 2000], the use of a BZT gas allows a significant increase of the critical Mach number as well as the divergence Mach number: for the present sonic arc geometry, the drag divergence occurs for a freestream Mach number of about 0.83 in the case of the perfect gas flow and 0.91 in the case of the dense gas flow (Fig. 6.20). All the flow computations performed in the study use a half C-grid made of $100x32$ cells, with a mean height of the first cell closest to the wall equal to 0.001 chords and an outer boundary located

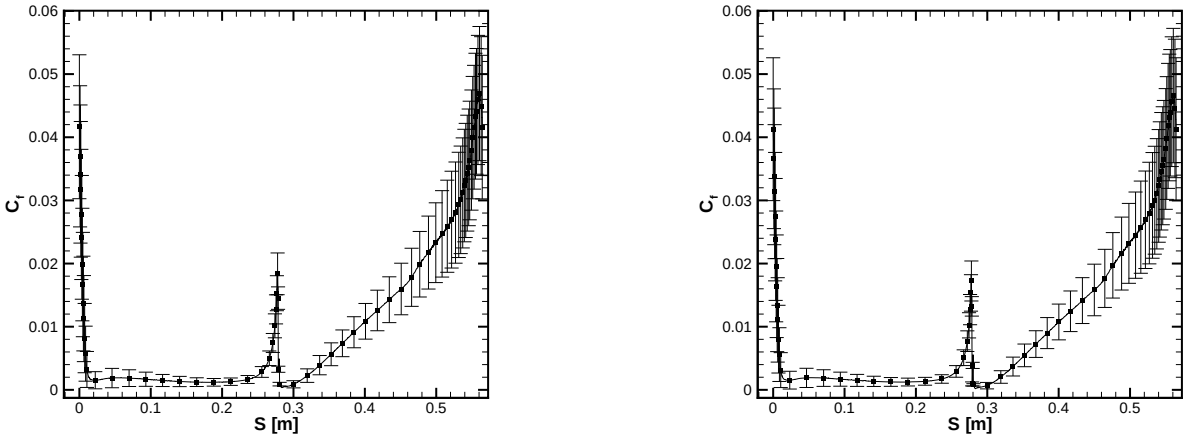

(a)

(b)

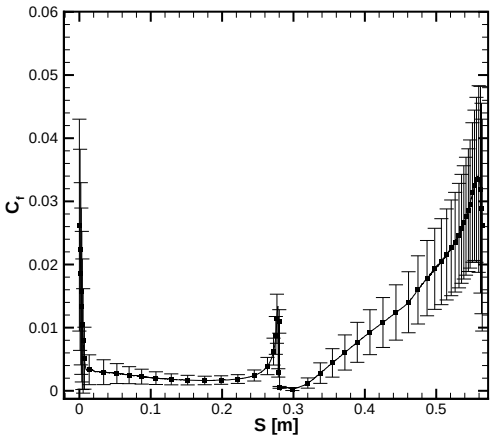

(c)

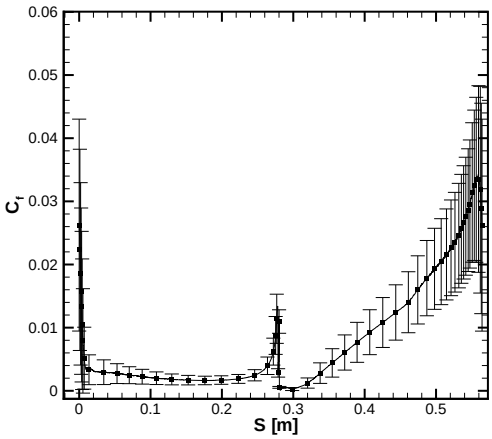

(d)

Figure 6.17: Mean and error bars (standard deviation) of the friction coefficient on the front flap for G1 (a), G2 (b), G3 (c) and G4 (d)

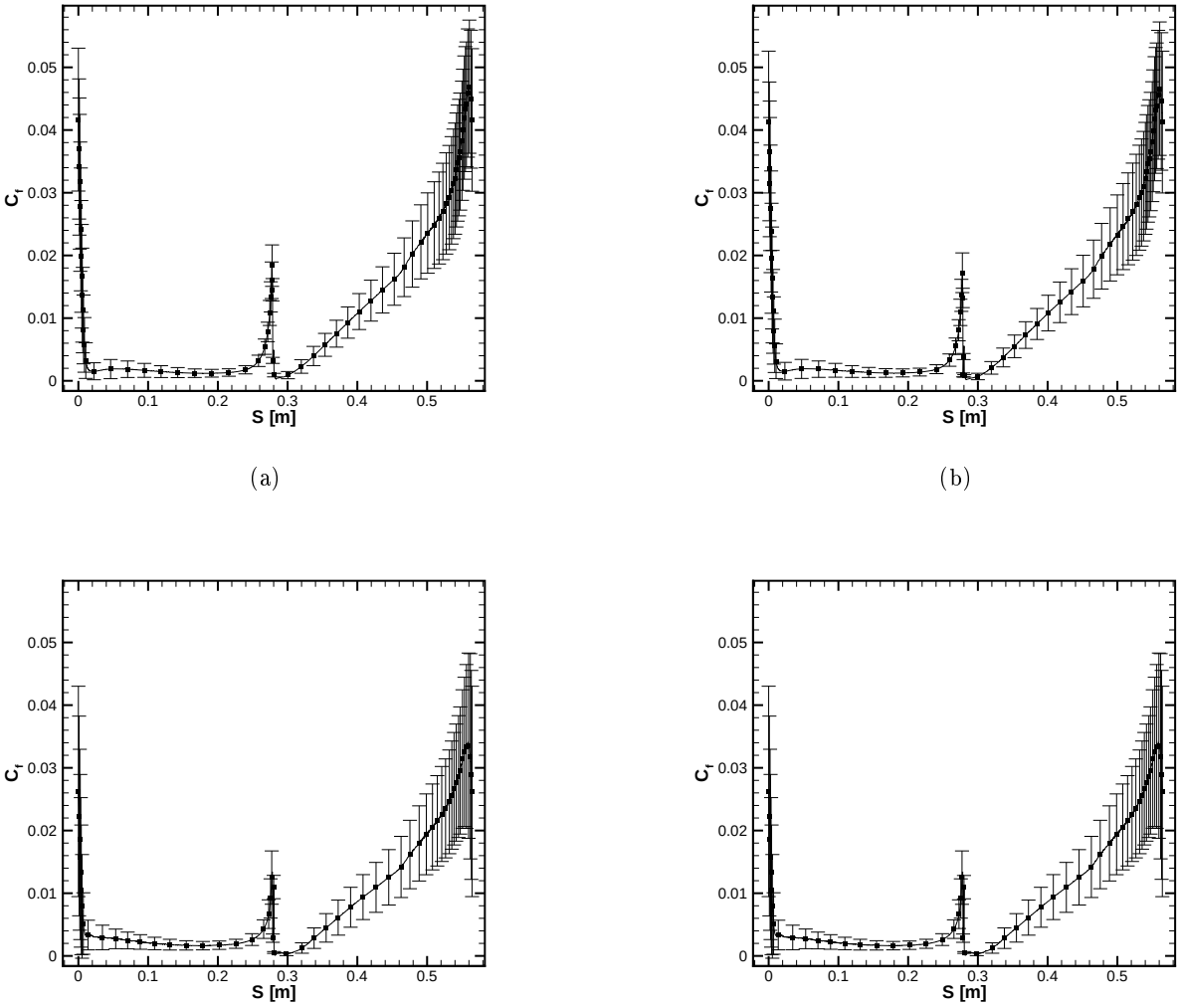

(a) (b)

(c) (d)

Figure 6.18: Mean and error bars (standard deviation) of the friction coefficient on the rear flap for G1 (a), G2 (b), G3 (c) and G4 (d)

Property	P_c (atm)	T_c (K)	Z_c	T_c (K)	n	$C_{v,\infty}(T_c)/R$	ω
	16.2	630.2	0.2859	467	0.5255	78.37	0.4833

Table 6.8: Mean values adopted for the fluid considered, the PP10.

		Mean values	Max variation	PDF
Input_G $\{X_1, X_2, X_3\}$	Decoupled Coupled	{0.044993, 0.040517, 0.060488}	0.7%	Uniform/Gaussian Uniform
Input_O $\{M_\infty, p_n, p_t\}$	Decoupled Coupled	{0.95, 0.985, 0.622}	1%	Uniform/Gaussian Gaussian
Input_T $\{\omega, n, c_{v,\infty}(T_c)/R\}$	Decoupled Coupled	{0.5255, 78.37, 0.4833}	3%	Uniform/Gaussian Gaussian

Table 6.9: Summary of the mean values, maximal variation and probability density function (PDF) for $input_G$, $input_O$ and $input_T$.

at 10 chords from the airfoil surface. This grid represents a reasonable trade-off between accuracy and computational cost, given the number of CFD runs required by the stochastic solver. Some considerations about the effect of the computational grid on the quality of the stochastic simulations are reported in [Cinnella 2011] where stochastic simulations have been performed with uncertainties on the physical properties of the dense gas only: it was demonstrated, for a flow configuration similar to the one studied here, the proposed level of grid refinement is sufficient to provide a reasonable representation of the flow solution expectancy and variance. The sonic arc is defined by a Bézier polynomial [Congedo 2007] using six points of fixed position along the airfoil unit chord as indicated in Fig. 6.21. The arc being symmetric with respect to x/c = 0.5, the geometry is constructed on [0, 0.5] and then reflected on [0.5, 1.0]. The first and last point are, respectively, fixed to (0, 0) and (0.5, 0.06), the airfoil thickness normalized by the chord being chosen equal to 0.12. The position of the fifth control point is fixed to (0.426, 0.06) to ensure the tangent to the profile at mid-airfoil (x/c = 0.5) is horizontal. The y-coordinates of the three internal points are left free and form a set of geometric parameters denoted as $input_G = y_1, y_2, y_3$. The parameters defining the set $input_O$ of operating conditions are supposed to display a 1% variation with respect to their prescribed average values. This choice allows to deal with a significant uncertainty while remaining in a monophasic region; for a stronger variation of $input_O$ parameters, the flow could enter the liquid-vapour mixture region, which must be avoided since the flow solver does not include two-phase flow models. The physical properties of the PRSV model defining the set $input_T$ are affected by a very strong uncertainty (see [Zamfirescu 2008]), reflected in a 3% variation with respect to their mean values, which are reported in Table 6.8 and correspond to the heavy fluorocarbon PP10. Note it has been checked again that all the possible thermodynamic states for the chosen uncertainty ranges always remain in the monophasic region. The geometric tolerances are taken into account by injecting uncertainties on the Bezier parameters of $input_G$: a maximal variation of 0.7% is considered. A summary of the mean values and uncertainty intervals associated with the three sources of uncertainties and the nine uncertain parameters is provided in Table 6.9.

6.4.2 Problem formulation

Our aim is to find an optimal shape for an isolated symmetric airfoil which provides a robust minima for the drag coefficient. Robust means this shape simultaneously minimizes the mean value and the variance of the drag coefficient computed when taking into account the physical uncertainties of the problem gathered in the previously defined sets $input_T$, $input_O$ and $input_G$. Note this bi-objective

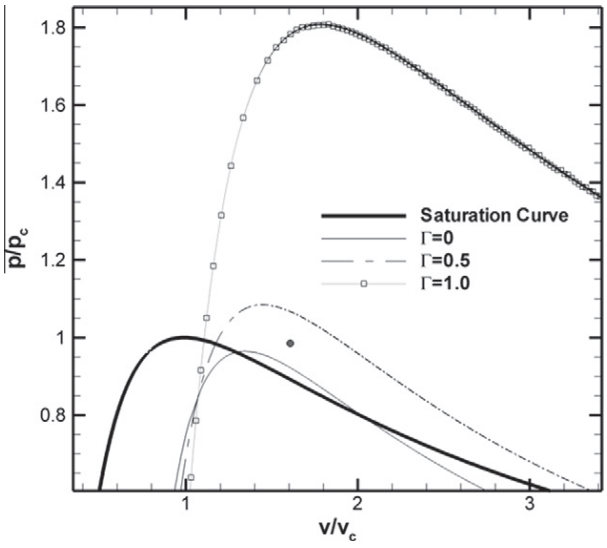

Figure 6.19: Saturation curve and iso-gamma for the PP10, computed by means of PRSV equation, filled point the chosen operating condition.

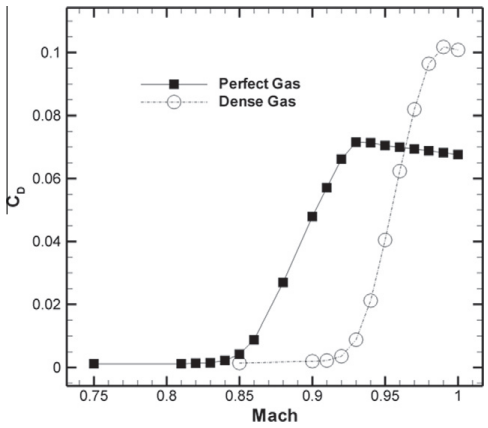

Figure 6.20: Drag coefficient of the sonic arc at zero incidence as a function of Mach number for a perfect and dense-gas flow.

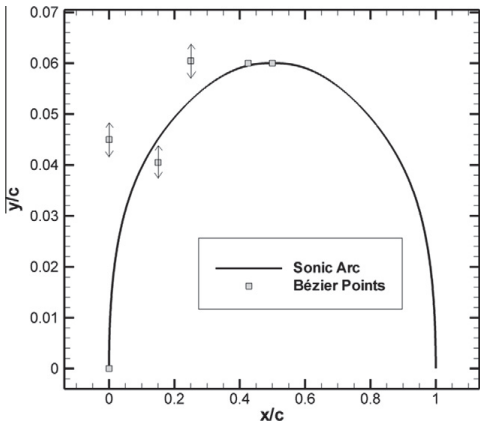

Figure 6.21: Baseline profile with its interpolating Bézier points.

problem possesses a set of solutions, forming the global Pareto front and corresponding to various trade-off between a low mean value and a low variance. In mathematical terms, the problem to solve is expressed as:

$$\min_{y_1,y_2,y_3} (mean(C_D), \sigma(C_D)) \tag{6.14}$$

with y_1, y_2, y_3 varying in the solution space S, made of intervals defined as $[\overline{y}_i - \delta y_i; \overline{y}_i + \delta y_i]$ with y_i the reference mean value for the geometric parameter y_i (these reference mean values are those used to reproduce the baseline sonic arc) and δyi 10% of the corresponding mean value $\overline{y}_i$. The drag coefficient C_D is a function of $input_T = x, nexp, cv_\infty(T_c)/R$, $input_O = M_\infty, p_r, \rho_r$ and $input_G = y_1, y_2, y_3$. With the non-intrusive statistical approach considered in this paper, the stochastic simulation allowing to compute the mean and the variance of C_D reduces to perform series of CFD evaluations using specific sets of values for $input_T$, $input_G$ and $input_O$, which are chosen as reported in the previous section. For a given shape in the previously prescribed domain of geometric definition, a single evaluation corresponds to a particular combination of $input_G$, $input_O$ and $input_T$; the global set containing all the possible variations of the uncertain inputs is called Uncertain Design of Experiment (UDOE). Three input data define the UDOE: (i) the mean values of $input_G$, $input_T$ and $input_O$ parameters (the mean values of $input_T$ and $input_O$ are fixed throughout the optimization problem), (ii) the maximal variations associated with these parameters, (iii) the density probability distribution associated with each of these parameters. The UDOE is a set of combinations for $input_G$, $input_T$ and $input_O$, determined by the quadrature formulae used to compute the PC coefficients. For every combination, a CFD evaluation is performed giving a computed C_D value; when such a value has been obtained for each element of the UDOE, the mean value and variance of the drag coefficient are estimated using the non-intrusive Polynomial Chaos described in Sections 4.1.2 and 4.1.3. A shape optimization procedure including uncertainties is made of two steps schematized in Fig. 6.22. The first step is the generation of a DOE for the variables of the optimization problem; in the present case a set of initial mean values for $input_G$ is generated in the solution space S. Using the non-intrusive Polynomial Chaos, a UDOE is built for each value of $input_G$ in the initial DOE; a grid is then generated for each distinct value of $input_G$ and the flow is computed on each of this grid using the CFD code with the corresponding values of $input_T$ and $input_O$ in the UDOE. The mean value and variance of the drag coefficient are computed from the set of values associated with the UDOE and once this computation has been performed for all the values of $input_G$ in the initial DOE the first generation for solving Eq. 6.14 is available.

The second step corresponds to the optimization process itself. In the present work the NSGA algorithm [59] is applied to obtain the optimal Pareto set associated with Eq. 6.14. The main tuning parameters of the algorithm are the population size, the number of generations, the crossover and mutation probabilities pc, pm and the so-called sharing parameter r used to take into account the relative isolation of an individual along a dominance front. Typical values for pc, pm are, respectively, 0.9 and 0.1; values of r are retained following a formula given in [Deb 2002] that takes into account the population size and the number of objectives. Using the values of the objective functions $mean(C_D)$, $\sigma(C_D)$ and selection, cross-over, mutation genetic operators, a new population of mean values for the $input_G$ parameters is generated in S. For each member of the population (viz. airfoil shape) a UDOE is built, which differs from the ones previously used by the values of $input_G$ only since the mean values of $input_T$ and $input_O$ are fixed once for all in the present problem. A grid is generated for each new shape and a CFD run is performed for the corresponding $input_T$, $input_O$ in the UDOE. The quantities $mean(C_D)$, $\sigma(C_D)$ are then computed using the non-intrusive PC and a new population of potentially improved individuals is obtained which is evolved by applying the genetic operators. This procedure is repeated until a convergence criterion is satisfied (typically the variation of the Pareto set is required to decrease below a prescribed threshold).

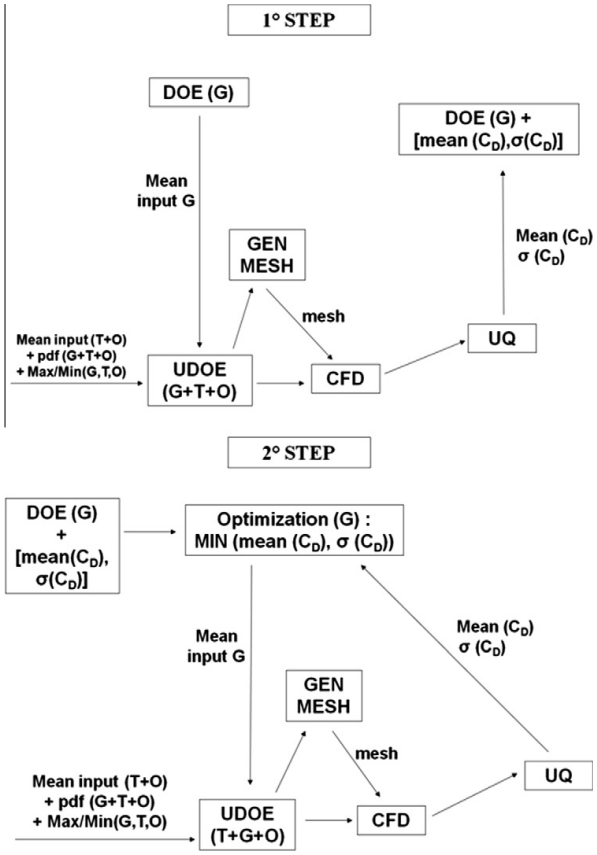

Figure 6.22: Fully coupled approach for optimization problem.

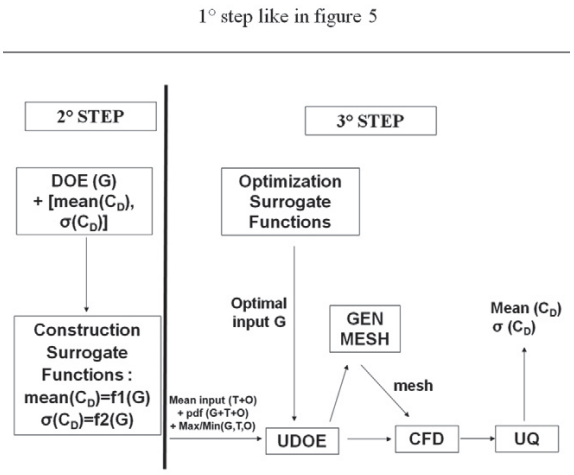

Figure 6.23: Approach using surrogate models for optimization problem.

6.4.3 Approach using surrogate models

As a first way to reduce the computational cost of a fully coupled approach, a preliminary analysis on the baseline sonic arc is performed which allows to assess the contribution of each uncertain parameter to the drag coefficient variance (ANOVA-type sensitivity analysis) so as to retain only the most influential ones in the UDOE used within the optimization process. A second way to achieve this CPU reduction is the massive use of surrogate models. The optimization process relying on surrogate models is also decomposed in two steps (see Fig. 6.23): the first step is identical to the one described for the fully coupled approach but with a size of UDOE which can be reduced thanks to the previous sensitivity analysis and with a size of DOE that can be different (larger in particular) because it will only slightly impact the global cost of the process; in the second step, the DOE of mean values for $input_G$ or DOE (G) with their associated computed values for the mean and variance of C_D is used in order to build a surrogate function for each of these objectives: $mean(C_D) = f1(input_G) = f1(y_1, y_2, y_3)$, $variance(C_D) = f2(input_G) = f2(y_1, y_2, y_3)$ where y_1, y_2, y_3 corresponds to a (mean) value in the S solution space. These simple mathematical functions (approximately) account for the uncertainties effects with a very modest computational cost. A Pareto optimal set for the simultaneous minimization of f1 and f2 is readily obtained. For every member of this optimal set, the non-intrusive PC can then be used to compute a correct final estimate for mean (C_D) and variance (C_D), following the approach previously described and used for every population individual at each generation in the fully coupled approach. Since the final population produced by NSGA is usually entirely distributed along the global Pareto front, the total cost of the approach can be estimated as: total cost = (unit CFD cost) x (size of initial DOE) x 2 x (size of UDOE), where the factor 2 corresponds to the initial computations of Mean (C_D) and Variance (C_D) and to the final a posteriori computations. The cost of optimization for the surrogate functions f1, f2 is negligible with respect to the unit CFD cost. Note however the size of the UDOE must be reduced for the calculation to remain tractable hence the total number of uncertain parameters must be reduced as much as possible and the preliminary ANOVA analysis remains a compulsory step.

6.4.4 Preliminary Anova-based screening

When computing the dense gas flow over the baseline sonic arc, nine parameters are considered uncertain, which are classified into three distinct sources: the three design parameters $input_G$ describing the geometry, the three parameters $input_O$ defining the operating condition for the flow

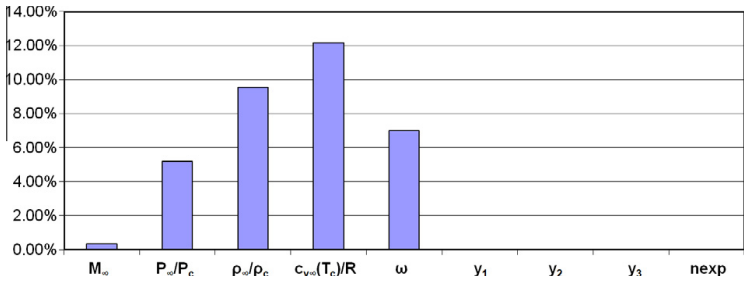

Figure 6.24: Analyse of variance for the stochastic dense gas simulation when uncertainties on geometry ($input_G$), operating conditions ($input_O$), and thermodynamic models ($input_T$) are taken in account (coupled analysis, Sparse Grid Method order 4).

and the three parameters $input_T$ closing the gas thermodynamic model. The mean values, maximal variations and pdf type for each parameter are summarized in Table 6.9.

All the sources of uncertainty ($input_T$ and $input_G$ and $input_O$) are simultaneously taken into account in order to assess possible interactions between the geometry, the operating conditions and the thermophysical parameters that might contribute to the variance of C_D. If the UDOE is generated using again a third-order PC, its size will grow up to $4^9 = 262144$. In view of this extremely high computational cost, it is decided to resort to the Sparse Grid Method (SGM) [Congedo 2011c] to perform this fully coupled analysis. To improve the reliability of this analysis, the SGM is applied not only with a third-order polynomial (yielding a UDOE of size 871) but also with a fourth-order one (yielding a UDOE of size 3463), allowing an assessment of the convergence and accuracy of the statistical analysis. A uniform pdf is assumed for the geometrical parameters of $input_G$, corresponding to a worst case scenario where all the parameters are equally important; a Gaussian distribution is assumed for $input_T$ and $input_O$ since the previous analysis has shown the difference between a Gaussian and Uniform pdf remains slight. The ANOVA analysis is performed for a third-order and fourth-order polynomial; the hierarchy of the most influential parameters and the contribution of each uncertainty to the global variance is analyzed. The results obtained with the two plans are very similar: the hierarchy is identical with minor differences in the decomposition of the variance as reported in Fig. 6.24. The fourth-order analysis is displayed in Fig. 6.25 and yields the following comments: the uncertainty on the operating Mach number is the most influential with a contribution to more than 89% of the variance; the first-order effects on the operating Mach number, pressure and density explain 99.5% of the variance. The drag coefficient stochastic model is of *additive* form with negligible interaction effects. Going back to the third-order/ fourth-order comparison, the difference for the three most dominant parameters ($input_O$) does not exceed 10% so that the results of the ANOVA analysis can be considered as converged. The uncertainties on the geometry ($input_G$) and the thermodynamic model ($input_T$) produce negligible effects with respect to the operating conditions.

6.4.5 Optimization using surrogate functions

The preliminary analysis described in the previous section showed that the number of uncertainties that should be evaluated during the optimization procedure could be reduced to the three uncertainties on the operating conditions ($input_O$). Since $input_T$ is fixed, it no longer appears in the schematic view of the optimization process displayed in Fig. 6.26. Similarly, the set of mean values for $input_G$ given by the initial DOE (G) is directly used to generate a population of airfoil shapes, without impacting the UDOE, the sole input of which is given by the mean values for $input_O$, hence denoted UDOE (O). The remainder of the first step is identical to the one described in Fig. 6.23,

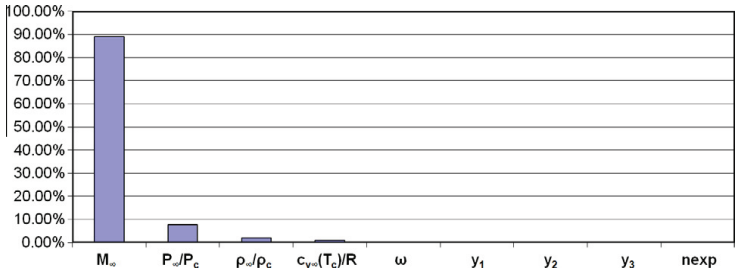

Figure 6.25: Analyse of variance for the stochastic dense gas simulation when uncertainties on geometry ($input_G$), operating conditions ($input_O$), and thermodynamic models ($input_T$) are taken in account (coupled analysis, Sparse Grid Method order 4).

with the generation of (mean value, variance) couples for the drag coefficient associated with each element of DOE (G). The second step is also left unchanged with the design of surrogate functions $f1(input_G)$, $f2(input_G)$ for $mean(C_D)$ and $variance(C_D)$. The third step of a posteriori UQ assessment for optimal shapes undergoes the same simplification as the start of the first step: the mean value and variance of the drag coefficient for an optimal shape are computed using the non-intrusive PC on UDOE (O). The proposed strategy of optimization taking into account uncertainties involves three types of choices: the method for generating DOE (G), the method for deriving the surrogate functions and the UQ method for generating UDOE (O). Three distinct strategies corresponding to three different combinations of methods have been considered in order to assess to what extent the optimal values obtained for $input_G$ are independent from these choices. In strategy 1, a Quasi Monte Carlo (QMC) geometric DOE (G) with 20 individuals is used; the UDOE (O) is built from a third-order Sparse Grid Method. QMC is similar to the usual Monte Carlo simulation but uses quasi-random sequences instead of (pseudo) random numbers; these sequences are deterministic and fill the space more uniformly than random sequences (known as low discrepancy sequences, i.e. the Sobol sequences). The surrogate functions f1, f2 are built from the values (mean (C_D), variance (C_D)) associated with DOE (G) using a multi-layered perceptron (MLP) neural network, with a cross validation method enabling to select 4 hidden units so that each neural network has a 3x4x1 architecture. In strategy 2, a QMC geometric DOE (G) with 40 individuals and a UDOE (O) also based on a QMC distribution are considered. The surrogate functions are derived using the same MLP than for strategy 1. In strategy 3, DOE (G) is generated using a Box Wilson DOE (based on fractional factorial design) of 15 individuals and UDOE (O) is generated using the same Sparse Grid Method as strategy 1. The surrogate functions are derived using the same MLP than for strategy 1. The set of optimal solutions obtained using these three strategies are displayed in Fig. 6.27, both in the objective plane (f1, f2) and in the parameter planes (y_1, y_2) and (y_1, y_3). Let us recall the solution space for y_1, y_2, y_3 is defined as $[0.04049, 0.04949]x[0.03646, 0.04457]x[0.05444, 0.06654]$; the Pareto fronts in the parameter space are very similar: they correspond to the upper limit of variation for y_1 and y_2 with the third parameter y_3 varying on $[0.0544, 0.0599]$ for strategy 3, on $[0.0575, 0.0600]$ for strategy 1 and $[0.0540, 0.0570]$ for strategy 2.

Three individuals are selected on each Pareto front in the objective plane, corresponding respectively to the minimum of f1, the minimum of f2 and a point at mid-distance between the previous ones. In the final step of the optimization, an a posteriori UQ is performed for these individuals, that is (f1, f2) are replaced by (mean (C_D), variance (C_D)) computed using an UDOE (O) based on the Sparse Grid Method with a fourth-order polynomial (83 CFD evaluations are performed for each geometry to quantify the effects of the three uncertainties $input_O$) or on the Quasi Monte Carlo method (with 64 CFD evaluations for each geometry). The use of two distinct strategies for computing the

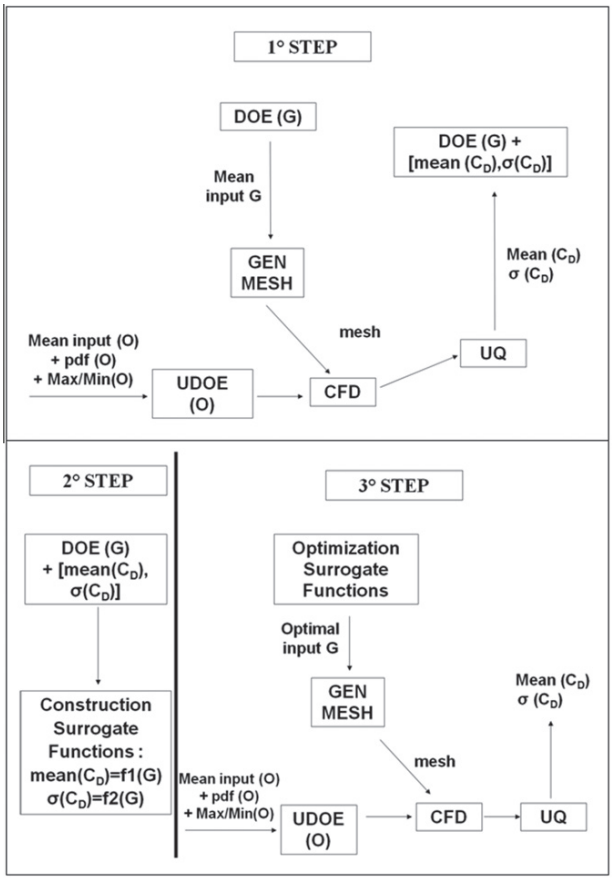

Figure 6.26: Approach using surrogate models for optimization problem after preliminary analysis.

mean and variance of the drag coefficient aims at offering some cross-validation for the conclusions that will be drawn regarding the proposed optimal shapes. These choices of UDOE (O) are also applied to the baseline sonic arc to compute the mean value and variance associated with this initial geometry. Besides, a classical deterministic minimization of the drag coefficient is also performed, where $input_T$ and $input_O$ are equal to their mean values given in Table 6.9 and $input_G$ vary in the parameter space S. This single-objective minimization of the drag coefficient is performed using the same genetic algorithm as the one used for the bi-objective minimization of (mean (C_D),variance (C_D)). The geometric parameters defining this classical optimum are reported in Fig. 6.27 along with the Pareto fronts for strategy 1, 2 and 3 in the parameter space. It is interesting to note this classical optimum seems to belong to these Pareto fronts; however, it is mandatory to carry out the analysis in the plane of the real (and not surrogate) objective functions, which is done in Fig. 6.28, respectively, using SGM and QMC for computing (mean (C_D), variance (C_D)). The nine individuals (three on each Pareto front for strategy 1, 2 and 3) are numbered in Figs. 6.27-6.28, in order to see exactly how the Pareto points move in the objective plane in Fig. 6.28 with respect to the optimization of the surrogate functions in Fig. 6.27. Though all the optimal shapes produced by Strategy 1, 2 and 3 as well as the deterministic optimization dominate or are not dominated by the baseline configuration, it must be noted the surrogate functions (f1, f2) introduce a significant error level with respect to the *exact* objective functions. In particular, the shapes corresponding to a Pareto set in the (f1, f2) plane are no longer forming such a Pareto front in the (mean (C_D), variance (C_D)) plane. A keypoint however is that a global Pareto front can be obtained by gathering shapes produced by the optimization strategies with uncertainties and the deterministic shape. This latter solution correspond to a minimal value for mean (C_D) along the Pareto front but a maximal value

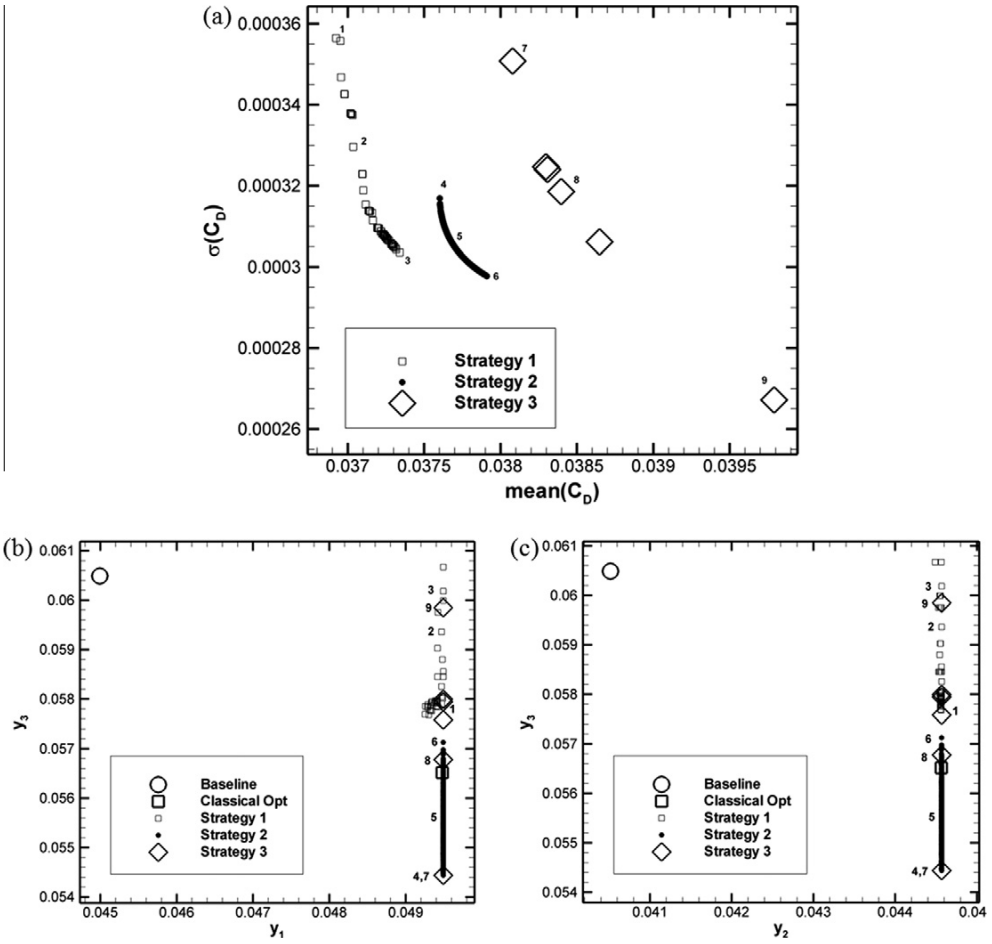

Figure 6.27: Mean and variance of the drag coefficient (a), and position of Pareto front in the parameters plan $y_1 - y_3$ (b) and $y_2 - y_3$ (c), of the optimal individuals issued from the different strategies.

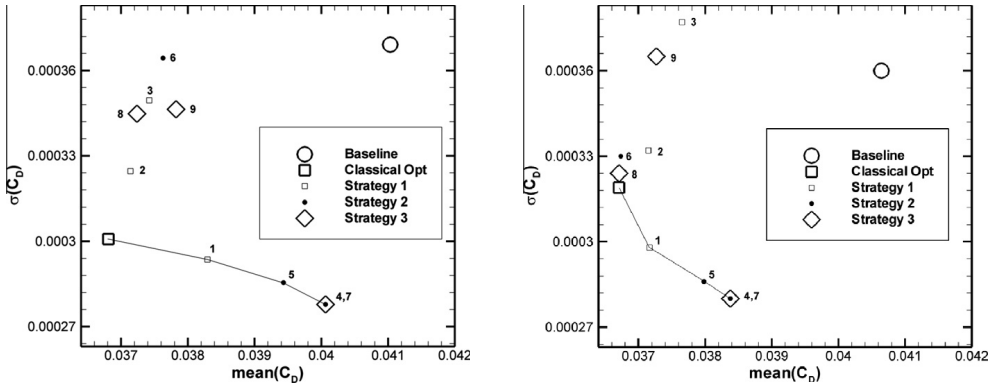

Figure 6.28: Comparison of different optimal individuals by using an UDOE based on the Sparse Grid Method (on the left) and on the Quasi Monte Carlo Method (on the right), connected points represent the global Pareto front.

for variance (C_D), where the deterministic C_D is taken into account in the deterministic optimization process. Strategy 2 and 3 provide in particular the same robust optimum corresponding to a minimal value of variance (C_D) along the Pareto front but to a maximal value for mean (C_D), remaining however below the mean value provided by the baseline configuration. The same conclusions can be drawn from both UDOE (O) (generated either by SGM or by QMC): the maximum difference on the mean drag prediction is 6% and 4.5% on the variance prediction. Moreover, the global Pareto fronts featured in Fig. 6.28 are composed of the same individuals (1, 4, 5, 7 and the classical optimum), though one is concave while the other is convex. This difference in the mean and variance drag prediction can be explained by considering the specific behaviour of dense gas flows. When uncertainties on thermodynamic model and operating conditions are considered at the same time, the freestream Mach number can be close to the critical Mach number for some particular uncertain inputs. In this case, values of CD can be strongly reduced, that makes statistics hard to compute. Then, mean and variance computations depend on the size of UDOE, that is why two strategies can give slightly different results. A Monte Carlo computation would be necessary in order to have a reference results for mean and variance, but it is unfeasible given the computational cost. Several remarks can be made by comparing the different strategies. Concerning strategies 1 and 2, enriching the DOE makes the surrogate functions more predictive, then the approximation of mean and variance (as function of parameters y_1,y_2 and y_3) is improved. In fact, with strategy 2 two individuals belonging to Pareto front are obtained (individuals 4 and 5), as shown in Fig. 6.28. Seeing the complexity in mean and variance computations, two strategies (1 and 3) can give slightly different results if few design points are considered. Geometries of the Pareto front are very similar, with differences on y3 parameter, while y_1 and y_2 are the same. The parameter y_3 is equal to 0.0544 for individuals 4 and 7, to 0.0556 for 5, to 0.0565 for the classical optimum and to 0.0578 for individual 1. Along the Pareto front, lower y_3 is linked with an increase of mean (C_D). Geometry of individual 5 is very similar to geometries 4-7 (difference up to 0.4%, while geometries 1-6-8 are similar to the classical optimum (differences up to 0.3%). Even if y_3 of individual 8 is close to those ones of individual 1 and of the classical optimum, individual 8 does not belong to the Pareto front. This means there is a non-linear behaviour in the proximity of y_3 of the classical optimum. This fact could be confirmed by means of Monte Carlo in order to have a better estimate for statistical quantities.

6.4.6 Concluding remarks

The predictive numerical simulation of a dense gas flow through an ORC turbine must take into account two types or sources of physical uncertainties: the physical properties of the fluid and the operating conditions at the turbine inlet. When designing the geometry of the turbine so as to optimize its efficiency, the geometrical uncertainties on the manufactured shape must also be accounted for. Shape optimization including the quantification of the effect of uncertainties means solving a multi-objective problem where, typically, the mean value and the variance of the initial objective are computed using uncertainty quantification tools. In this section, the feasibility of performing such an optimization for realistic computational costs is assessed on a simplified configuration (drag minimization under uncertainties for the BZT flow over an isolated symmetric airfoil) and a general procedure applicable to more complex problems is proposed.

Part II

Numerical simulation of complex thermodynamically flows and ORC-applications

Chapter 7

Numerical simulation of single-phase non reacting flows

Contents

In this chapter, I describe the basic ingredients to be modified in CFD codes for considering real-gas effects.

7.1 From a usual perfect gas CFD code to a real-gas CFD code

I resume briefly here the work demanded for the modification of an existing CFD code for taking into account complex thermodynamic models. This section describes the main features of the two dense gas flow solvers which are used in the present numerical study. Since these solvers rely on very different ingredients, a high level of confidence in the numerically predicted performance is achieved when these solvers are found to provide close results. Some details about the boundary conditions treatment specific to turbomachinery flows are also provided since this was found to be an important point to ensure accurate computations of global turbine properties such as efficiency.

7.1.1 Basic modifications to perform

Using a perfect gas equation of state is straightforward because of the direct relation between the pressure and the internal energy. The van der Waals equation is more complicated of the PGF equation of state, but it's always possible to write a direct relation between pressure and internal energy. If more accurate models are demanded, such as Martin-Hou, Peng-Robinson, Span-Wagner equations, in these cases it is not possible to derive an explicit relation between pressure and internal energy. Generally, an iterative method is necessary to compute thermodynamic properties (for example to compute the primitive variables by starting from the conservative variables). Newton-Raphson Method is used because of its good accuracy and convergence velocity (For details in the implementation see [Cinnella 2005a]). Generally, if a different equation of state is used, it is necessary to change all the formulations that adopt implicitly a PFG equation of state. Obviously it is taken for granted that the computation of thermodynamic properties changes starting from different thermodynamic relations (typically sound of speed and internal energy). For a very detailed description

of the main thermodynamic properties with the different equation of state see [Cinnella 2011]. For what concerns the solvers described in this manuscript (described in the next section), the numerical schemes formulations are independent from the equation of state. A different formulation for the non-reflecting boundary conditions based on method of characteristic is used (typically the computation of Riemann invariants changes, because it is usually written by considering a PFG equation of state).

7.1.2 Evolution of the CFD code

- Structured Grid Solver:
  The governing equations are discretized using a cell-centered finite volume scheme of third-order accuracy for structured multi-block meshes, which allows computing flows governed by an arbitrary equation of state. The scheme is constructed by correcting the dispersive error term of the second-order-accurate Jameson's et al. scheme [Cinnella 2005b]. The use of a scalar dissipation term simplifies the scheme implementation with highly complex equations of state and greatly reduces computational costs. To preserve the high accuracy of the scheme on non-Cartesian grids, the numerical fluxes are evaluated using weighted discretization formulas, which take into account the stretching and the skewness of the mesh: this ensures truly third-order accuracy on moderately deformed meshes and at least second-order accuracy on highly distorted meshes (see [Cinnella 2005b] for details). The equations are then integrated in time using a four-stage Runge-Kutta scheme. Local time stepping and implicit residual smoothing are used to efficiently drive the solution to the steady state. The good accuracy properties of this numerical solver have been demonstrated in previous works [Cinnella 2005b, Cinnella 2005a], and will not be further discussed here.

- Unstructured Grid Solver:
  The UGS is also based on a cell-centered finite-volume discretization but formulated on a general unstructured grid dividing the spatial domain into a finite number of triangles or quadrangles; the time rate of change of the cell-averaged state vector w is balanced with the area-averaged (inviscid) fluxes across the cell faces. The fluxes are computed across each cell face using the HLL scheme; second-order spatial accuracy is ensured by means of a MUSCL-type reconstruction process on the conserved variables, where the gradient estimates required at each cell center are obtained through a least-square formula. When the solver is applied to the computation of flows containing discontinuities, the reconstruction formula includes a limitation step which ensures oscillation-free shock-capturing. Fast convergence to steady state is provided by making the scheme implicit using a simple first-order Rusanov-type implicit stage allowing the use of large CFL numbers (that is solved by an inexpensive point-relaxation technique). The UGS is validated against the SGS solver for inviscid flows of dense gases past airfoils in [Congedo 2007].

7.1.3 Evolution of the boundary conditions

For a dense-gas turbine blades configuration, suitable boundary conditions should be imposed. For inviscid flows, a no-slip wall boundary condition is applied along the blade. At the inlet and outlet boundary, characteristic conditions based on the conservation of Riemann invariants are applied (Refer to [Colonna 2004] for a detailed description of characteristic boundary conditions for flows governed by a general equation of state). For a subsonic inlet in a two-dimensional flow, three physical quantities have to be prescribed while a fourth quantity is extrapolated from the interior of the computational domain, by imposing the conservation of the appropriate Riemann invariant. For turbomachines, it is common practice to impose stagnation thermodynamic conditions at inlet and

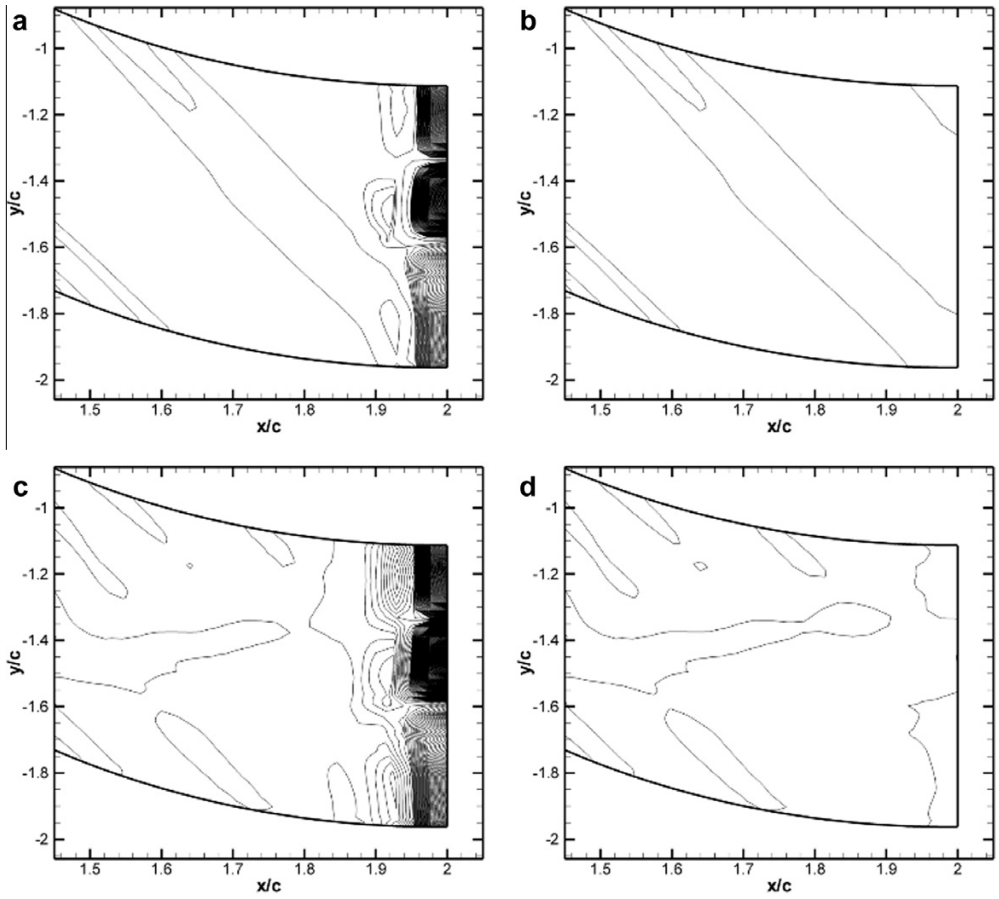

Figure 7.1: Typical computed fields for entropy (top) and enthalpy (bottom) fields, close up of the outlet region for different choices of the extrapolated thermodynamic variable in the subsonic outlet boundary condition. Left: density-based extrapolation; right: entropy-based extrapolation.

the flow direction. Here, the imposed thermodynamic quantities are the inlet entropy s and the inlet stagnation enthalpy H. At the turbine outlet, the boundary condition depends on whether the flow is subsonic or supersonic. In the first case, one single flow property (typically the static pressure) is imposed, while the remaining quantities (velocity components and a thermodynamic state variable) are extrapolated from the interior of the domain. Two different choices of extrapolated state variable have been assessed : the density and the entropy. When the extrapolated thermodynamic quantity is the density, the numerical implementation is straightforward, but spurious oscillations appear on the entropy and static enthalpy fields, close to the outlet. Conversely, when the extrapolated variable is the entropy, the solution of a nonlinear system of equations of the form

$$\begin{cases} s = s\left(\rho, T\right) \\ p = p\left(\rho, T\right) \end{cases} \tag{7.1}$$

is required to compute the conservative variables at boundary points. In turn, the computed solutions are now smooth: Figure 7.1 displays typical entropy and static enthalpy fields for the flow through a turbine cascade computed using the UGS solver and the density or entropy as extrapolated thermodynamic quantity at outlet. Since the smoothness of the entropy and enthalpy fields at turbine outlet is essential for an accurate computation of the turbine stage efficiency and power output, the choice of entropy as extrapolated variable has been systematically retained, both for SGS and UGS. If the flow is supersonic at turbine outlet, the outlet state is simply extrapolated from the adjacent interior cells.

7.2 Hypotheses and models for dense gas RANS Equations

Since the full resolution of the NS equation requires the consideration of a big range of length and time scales, the compressible Reynolds-averaged Navier-Stokes equations RANS equation are used to limit the computer costs. The simulation of turbulent dense gas flows is based on the following working hypotheses: (a) flow conditions are supposed to be sufficiently far from the thermodynamic critical point, so that dense gas effects such as dramatic variations of the fluid specific heat and compressibility can be neglected; in these conditions, density fluctuations will not be as huge as in near-critical conditions and subsequently the turbulence structure will not be affected significantly; (b) at least for equilibrium boundary layers, the mean flow behavior can be predicted adequately using RANS completed by an eddy viscosity turbulence model; similarly, the turbulent heat transfer can be modelled through a *turbulent Fourier law*, as usual for PFG flows, where the turbulent thermal conductivity is computed in a classical way by introducing a turbulent Prandtl number, assumed to be roughly constant and O(1) throughout the flow. Hypothesis (a) is justified by the fact that the flows of interest for this study actually do not evolve in the immediate neighborhood of the critical point; and in fact, if inviscid analyses and computations show an uncommon variation of the fluid speed of sound (and hence compressibility) with pressure perturbations, nevertheless the magnitude of these variations is approximately of the order of those occurring in perfect gases. Moreover, peculiar dense gas phenomena related to flow heating or cooling are excluded from considerations, since the airfoil wall is supposed to be adiabatic. On the contrary, Hypothesis (b) should be considered with some caution. On the one hand, if Hypothesis (a) is verified, it seems quite reasonable to apply to compressible dense gas flows turbulence models initially developed for incompressible flows of perfect gases and currently extended in the common practice to compressible PFG flows; on the other hand, more or less strong pressure gradients and shock waves characterizing the outer inviscid flow are likely to affect the boundary layer, which can no longer be considered an 'equilibrium' one; this is also true for the reference PFG flows considered in the study, characterized by strong shock waves and shock/boundary layer interactions. Thus, aerodynamic performance predictions will necessarily be affected by deficiencies inherent with the chosen turbulence model. Nevertheless, since investigations are intended to provide trends of behavior more than accurate values of the computed aerodynamic coefficients, use of hypothesis (b) represents a means of obtaining preliminary information about realistic dense gas flows with a reasonable computational expense.

7.2.1 Some accurate thermodynamic models

In this section, some thermodynamic models mentioned in this manuscript are introduced. For a more detailed presentation about equations of state, please refer to [Cinnella 2010, Cinnella 2011].

7.2.1.1 Peng-Robinson

Peng and Robinson (1976) proposed a cubic EoS of van der Waals type in the form:

$$p = \frac{RT}{v-b} - \frac{a}{v^2+2bv-b^2}. \tag{7.2}$$

where p and v denote respectively the fluid pressure and its specific volume, a and b are substance-specific parameters related to the fluid critical-point properties p_c and T_c and representative of attractive and repulsive molecular forces. To achieve high accuracy for saturation-pressure estimates of pure fluids, the temperature-dependent parameter a in Eq. (7.2) is expressed as

$$a = \left(0.457235 R^2 T_c^2/p_c^2\right) \cdot \alpha\left(T\right), \tag{7.3}$$

while

$$b = 0.077796 RT_c/p_c. \tag{7.4}$$

These parameters are not completely independent, since isothermal lines in the p-v plane should satisfy the thermodynamic stability conditions of zero curvature and zero slope at the critical point. Such conditions allow computing the critical compressibility factor $Z_c = (p_c v_c)/(RT_c)$ as the solution of a cubic equation. The correction factor α in Eq. (7.3) is given by

$$\alpha\left(T_r\right) = \left[1 + K\left(1 - T_r^{0.5}\right)\right]^2, \tag{7.5}$$

with

$$K = K_0 + K_1\left(1 + T_r^{0.5}\right)\left(0.7 - T_r\right) \text{ for } T_r < 1 \quad \left(K_1 = 0 \,\text{for}\, T_r \geq 1\right), \tag{7.6}$$

and

$$K_0 = 0.378893 + 1.4897153\omega - 0.1713848\omega^2 + 0.0196554\omega^3. \tag{7.7}$$

The parameter ω is the fluid acentric factor and K_1 is obtained by fitting measured saturation pressures at set temperature over a large range from close to the triple point up to the critical pressure. The other needed information to complete the thermodynamic model, namely the ideal-gas isochoric specific heat of the fluid, is approximated through a power law, *i.e.*,

$$c_{v,\infty}\left(T\right) = c_{v,\infty}\left(T_c\right)\left(\frac{T}{T_c}\right)^n \tag{7.8}$$

with n a fluid-dependent parameter. The power law, already used in [Cinnella 2010] and [Congedo 2011a], is preferred to a polynomial form, used for example in [Guardone 2010], because it allows for an explicit dependence on physical parameters affected by uncertainties while introducing negligible differences in the temperature range of interest w.r.t. the polynomial form (lower than 0.001% for the conditions of the experiment).

7.2.1.2 RKS equation

The Redlich-Kwong equation is commonly considered as one of the best available two-parameter equations of state. The modified Redlich-Kwong equation of state (by Soave [Soave 1972]) is given by

$$p = \frac{RT}{v - b} - \frac{a_c \alpha\left(T\right)}{v\left(v + b\right)} \tag{7.9}$$

where p being the fluid pressure, T the absolute temperature, v the specific volume, R the gas constant, $a_c = 0.42747R^2T_c^2/p_c$. The function $\alpha(T)$ is an adimensional relationship depending on the reduced temperature $T_r = T/T_c$ and the substance acentric factor ω,

$$\alpha\left(T\right) = \left[1 + m\left(1 - T_r^{0.5}\right)\right]^2 \tag{7.10}$$

with $m = 0.48 + 1.57\omega - 0.176\omega^2$.

The RKS equation of state is supplemented again by Eq. 7.8 to compute the ideal gas contribution to the specific heat at constant volume. The RKS model in non-dimensional forms depends on three uncertain parameters, namely, the acentric factor ω, the exponent n and the reduced ideal-gas constant-volume specific heat at the critical temperature $c_{v\infty}(T_c)$.

7.2.1.3 Martin-Hou

The comprehensive thermal equation of state of Martin and Hou [Martin 1955] is considered to provide a realistic description of the gas behaviour close to saturation conditions. It reads

$$p = \frac{RT}{v - b} + \sum_{i=2}^{5} \frac{f_i(T)}{\left(v - b\right)^i} \tag{7.11}$$

where $b = RT_c(1-\beta/15)/p_c$ with $b = 20.533 - 31.883Z_c$, and the functions $f_i(T)$ are of the form $f_i(T) = A_i + B_iT + C_iexp(-kT/T_c)$, with T_c the critical temperature and $k = 5.475$. The gas-dependent coefficients A_i, B_i, C_i can be expressed in terms of the critical temperature and pressure, the critical compressibility factor, the Boyle temperature (which may be expressed as a function of the critical temperature), and one point on the vapour pressure curve. The MAH equation of state is supplemented again by Eq. 7.8 to compute the ideal gas contribution to the specific heat at constant volume. Globally, the MAH thermodynamic model requires the knowledge of six material- dependent parameters. Precisely, the uncertain material-dependent parameters considered in this study are the critical pressure p_c , the critical temperature T_c, the critical compressibility factor Z_c , the normal boiling temperature T_b, the exponent n, and the reduced ideal-gas constant-volume specific heat at the critical temperature $c_{v\infty}(T_c)$.

7.2.1.4 Span-Wagner

In [Cinnella 2011, Colonna 2006b], a state-of-the art multiparameter thermodynamic model has been considered, based on 12-term Span-Wagner (SW) equation of state. The SW equation is defined as follows

$$\begin{aligned}\psi(\tau,\delta) =& \psi^0(\tau,\delta) + n_1\delta\tau^{0.25} + n_2\delta\tau^{1.125} + n_3\delta\tau^{1.5} + n_4\delta^2\tau^{1.375} \\ &+ n_5\delta^3\tau^{0.25} + n_6\delta^7\tau^{0.875} + n_7\delta^2\tau^{0.625} + n_8\delta^5\tau^{1.75} + n_9\delta^5\tau^{1.75} \\ &+ n_{10}\delta^4\tau^{3.625}e^{-\delta^2} + n_{11}\delta^3\tau^{14.5}e^{-\delta^3} + n_{12}\delta^4\tau^{12}e^{-\delta^3}\end{aligned} \tag{7.12}$$

where ψ is the reduced Helmoltz energy (i.e., normalized with RT), ψ^0 is the ideal-gas contribution to the Helmoltz free energy, and the remaining terms represent a real-gas correction, which depends on the reduced density $\delta = \rho/\rho_c$ and on the inverse of the reduced temperature $\tau = T_c/T$. In Eq. (7.12), n_1,...,n_{12} are substance-specific coefficients. The relation (7.12) is valid for many classes of non-polar and weakly polar fluids and its parameters have been determined in the literature for different classes of fluids simultaneously.

For the calculation of caloric properties, the SW EOS (Eq. (7.12)) is supplemented by the ideal gas contribution to the specific heat at constant pressure, approximated here with the Aly-Lee equation [Colonna 2008b]:

$$c_{p,\infty} = \alpha + \gamma\left[\frac{\chi/T}{\sinh(\chi/T)}\right]^2 + \delta\left[\frac{\varepsilon/T}{\cosh(\varepsilon/T)}\right]^2 \tag{7.13}$$

where the coefficients depend on the substance under consideration. Pressure and internal energy can be computed as a function of the reduced Helmotz energy (7.12) and the ideal gas (7.13) contribution to the specific heat at constant pressure through the standard thermodynamic relations [Colonna 2006b].

7.2.2 Laws for viscosity and thermal conductivity

Viscous effects in flows of dense gases have remained largely unexplored. One of the most important differences between dense gases and perfect gases is the downward curvature and nearly horizontal character of the isotherms in the neighborhood of the critical point and upper saturation curve in the p-v plane: the region of downward curvature of the isotherms is associated with the aforementioned reversed behavior of the sound speed in isentropic perturbations. In the same region, the specific heat at constant pressure, c_p , can become quite large: this strongly influences the development of the thermal boundary layer and its coupling with the viscous boundary layer in high-speed flows. In the dense gas regime the dynamic viscosity μ and the thermal conductivity k cannot be longer considered independent of the temperature and pressure, even in flows with relatively small temperature

variations. On the other hand, the well-known Sutherland law, commonly used to represent viscosity variation with temperature, becomes invalid, as it is based on the hypothesis that the gas molecules act as non-interacting rigid spheres, and intermolecular forces are neglected. The complexity of the behavior of μ in the dense regime can be anticipated by recalling that the viscosity of liquids tends to decrease with increasing temperature, whereas that of gases tends to increase: the dense gas regime is a transition between these two qualitatively different behaviors. Similarly, the classical approximation of nearly constant Prandtl number ($Pr = \mu c_p/k \approx const$) cannot be used any more. As the thermal conductivity has roughly the same variation as viscosity with temperature and pressure, the behavior of Pr tends to be controlled by variations of c_p. In regions where c_p becomes large, strong variations of Pr can be observed, contrarily to what happens in perfect gases. Nevertheless, if the immediate vicinity of the thermodynamic critical point is excluded from considerations, the Prandtl number remains of order one, similar to perfect gases. In contrast, the Eckert number ($Ec = {U_0}^2/(c_p T_0)$, where U_0 and T_0 refer to a suitable reference state) decreases significantly. Small flow Eckert number implies reduced sensitivity of the boundary layer to friction heating that remains negligible even at moderately large supersonic Mach numbers. Moreover, for flows past adiabatic walls the temperature, and thus also the density, is almost constant across the boundary layer. The fluid viscosity and thermal conductivity are evaluated using the method proposed in [Chung 1984]. The viscosity (measured in μPoise) is related to the absolute temperature through the formula:

$$\mu = 40.785 \frac{F_c M_w^{0.5} T^{0.5}}{V^{2/3} \Omega_v} \tag{7.14}$$

where M_w is the molecular weight in g/mol and V_c is the critical volume in cm^3/mol. The coefficient F_c is given by $F_c = 1 - 0.2756\omega + 0.059035{\delta_r}^4 + \xi$, where ω is the acentric factor, δ_r is a dimensionless dipole moment, and ξ is a special correction for highly polar substances. The viscosity collision integral Ω_v is provided by

$$\Omega_v = A\left(T^*\right)^{-B} + Cexp\left(-DT^*\right) + Eexp\left(-FT^*\right), \tag{7.15}$$

where $T^* = 1.2593(T/T_c)$, $A = 1.16145$, $C = 0.52487$, $D = 0.77320$, $E = 2.16178$ and $F = 2.43787$.

The thermal conductivity k is provided by:

$$\frac{kM_w}{\mu C_v} = \frac{3.75\Psi}{C_v/R}, \tag{7.16}$$

where M_w is the molecular weight in Kg/mol, c_v is the constant volume specific heat in $J/(molK)$, R is the universal gas constant in $J/(molK)$, and the coefficient Ψ is equal to

$$\Psi = 1 + \alpha_1 \frac{0.215 + 0.28288\alpha_1 - 1.061\beta + 0.26665\Xi}{0.6366 + \beta\Xi + 1.061\alpha_1\beta}, \tag{7.17}$$

with $\alpha_1 = (C_v/R)3/2$, $\beta = 0.78620.7109\omega + 1.3168\omega^2$, $\Xi = 2.0 + 10.5(T/T_c)^2$.

7.3 Organization of this part

This part illustrates some results of interest for ORC-systems and dense-gas flows. First, Chapter 8 illustrate some dense-gas results through a turbine cascade. Then, in Chapter 9, reliability of several thermodynamic models is estimated for several fluids of interest in dense-gas framework. Finally, Chapter 10 presents several studies on the appearance and reproducibility of a Rarefaction Shock Wave (RSW).

Chapter 8

Physics of dense-gas flows and their use in ORC-systems

Contents

The previously described flow solvers are now applied to the computation of inviscid transonic dense gas flows through a turbine cascade. In a first step, the reliability of the numerical simulation is established by cross-validation of the results provided by both solvers. Next, a parametric study of the turbine efficiency sensitivity to the thermodynamic conditions is performed for a series of operating points selected in the neighbourhood of the thermodynamic region $\Gamma = 0$. The performance obtained for a molecularly complex fluid (D5) is compared with that provided by a lighter (toluene) and a heavier (dodecamethylcyclohexasiloxane D6) fluid and the role played by dense gas effects is emphasized.

8.1 Turbine configuration

The configuration taken into account in this study is the von-Karman Institute LS-59 plane cascade (VKI LS-59) of rotor blades. The turbine geometry and experimental data (for air flow) are available in [Kiock 1986]. For all of the following computations the flow inlet angle is taken equal to 30^o and the pressure ratio to 1.82, which corresponds to an isentropic exit Mach number equal to 1 in the case of a diatomic perfect gas flow. The computational domain is discretized by a C-shaped grid, selected after a grid refinement study. Initially three grids of increasing refinement (192 x 16, 384 x 32 and 768 x 64 cells) have been considered; the medium grid is shown in Fig. 8.1 and the finer and coarser grids are generated by respectively doubling and halving the number of cells of this medium grid in each direction. The mean height of the first cell closest to the wall is about $2.5x10^{-2}$ chord on the medium grid. Roache's grid convergence index (GCI) represents an estimate of how far the numerical solution is from its asymptotic value. When based on the computed isentropic efficiency and estimated for the finer and medium grid, GCIs of 0.06% and 0.27% (respectively 0.07% and 0.12%) are found for SGS (respectively UGS) assuming an order of convergence equal to 2.2 (respectively 1.8) based on previous experience. In all cases, the solution is well within the asymptotic range so that the medium grid is retained for all subsequent computations. Fig. 8.2 shows the results provided by the SGS and the UGS for the perfect-gas case. The isentropic Mach number distributions along the blade are in reasonable agreement with experimental data available for a flow of air through the cascade

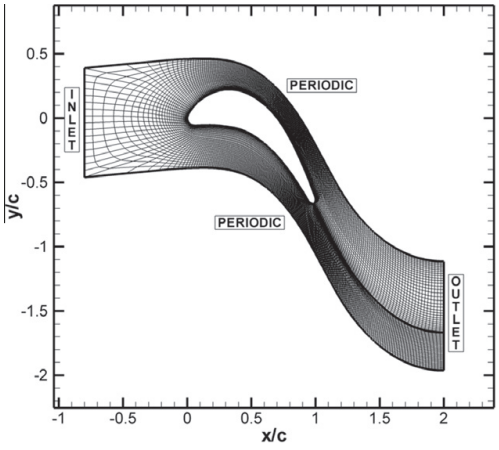

Figure 8.1: View of the computational grid (384 × 32 cells).

[Kiock 1986]. The oscillations close to x/c = 1 (where x is the chordwise coordinate and c the chord) are due to the fact that the inviscid flow model cannot correctly capture the flow physics around the blunt trailing edge of the blade. The performance of the turbine cascade is evaluated by using three criteria, namely:

- the turbine isentropic efficiency, $\eta = \frac{\Delta h}{\Delta h_{ideal}}$, where h is the static enthalpy, δ represents the variation of a flow property between turbine inlet and outlet boundaries. The non-dimensional parameter η quantifies the thermodynamic losses due to entropy generation during turbine expansion or, translated into an energetic viewpoint, states how efficiently the available enthalpy jump is converted by the turbine
- the dimensional enthalpy jump δh, in kJ/mol, is directly related to the amount of work generated by expanding a kmole of fluid and provides information about the turbine dynamics;
- the relative temperature variation, $\frac{\Delta T}{T_{inlet}}$ is equal to the Carnot inlet efficiency of the cycle and provides information about first-principle efficiency.

The outlet flow angle will also be monitored since it is an important parameter for the design of subsequent stages following the cascade under consideration.

8.2 Choice of operating conditions

To investigate the role of dense gas effects in the chosen turbine configuration for a large variety of thermodynamic inlet conditions a parametric study is performed for inlet temperatures ranging approximately between $0.96T_c$ and $1.01T_c$ and pressures between $0.62p_c$ and $1.03p_c$. For D5, this corresponds to dimensional inlet conditions $594K \leq T_{inlet} \leq 625K$ and $6.8atm \leq p_{inlet} \leq 11.3atm$. A grid of operating point is constructed by selecting 5 equally spaced reduced temperatures in the interval [0.96, 1.01]. For each temperature, eight points are considered, ranging from close-to-saturation conditions up to low-density conditions (about 0.25 ρ_c). According to the SW EoS, all the operating points, shown in Fig. 8.3, are located inside the single-phase vapor region. However, due to the sensitivity of the saturation curve to the thermodynamic model, some of these points fall inside a two-phase region for the PRSV and MAH models. Since the numerical codes considered in this study do not handle two-phase flows, some points of the grid (represented by filled symbols in Fig. 8.3) are discarded for analyzes based on the PRSV and MAH models.

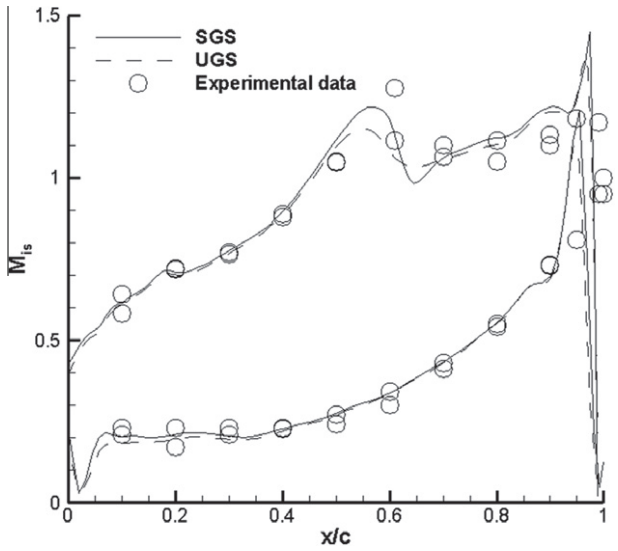

Figure 8.2: Perfect gas flow through the VKI-LS59 cascade, Mach number distribution along the blade wall: comparison of SGS and UGS solvers.

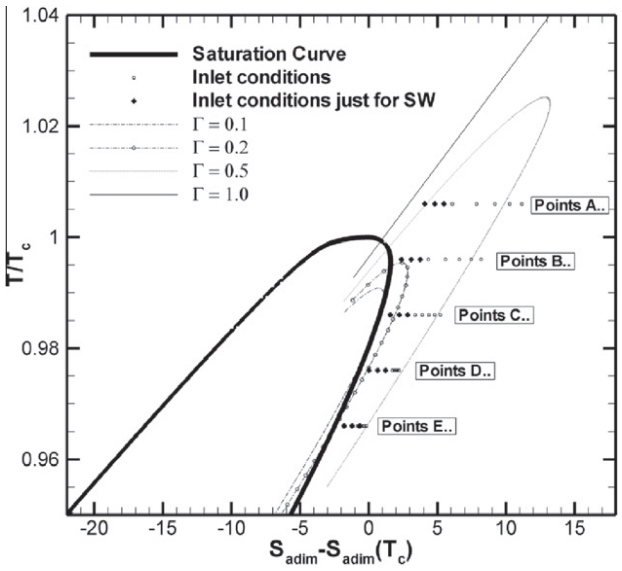

Figure 8.3: Temperature-entropy diagram for D5 (SW EoS) and operating points used in the parametric study.

8.3 Cross validation of dense-gas flow solvers

Since no experimental data are available for dense gas flows through a turbine cascade, both the SGS and UGS solvers are systematically applied for the whole set of operating conditions given in Fig. 8.3 and their computed performance parameters (η, Δh, $\frac{\Delta T}{T_{inlet}}$) compared. The solution residuals are always reduced at least by six orders of magnitude for both solvers. Typical solutions provided by SGS and UGS are displayed in Fig. 8.4 for operating conditions ($p/p_c = 0.622$, $\rho/\rho_c = 0.276$) and the SW EoS. The computed Mach number contours and Mach number distributions along the blade are almost superimposed; a similar result is obtained for different operating conditions and thermodynamic models. More quantitative conclusions can be drawn from the analysis of the differences on global performance parameters computed using SGS and UGS. The relative differences on (η, Δh, $\frac{\Delta T}{T_{inlet}}$) and the outlet flow angle computed by both solvers for the three choices of EoS and their respective selected set of single-phase operating points are displayed in Fig. 8.5 as a function of the inlet compressibility factor. The overall maximal relative difference between the SGS and UGS codes on isentropic efficiency, a quantity known to be sensitive to numerical diffusion, does not exceed 1.7%. This quite small error is not necessarily negligible since the expected efficiency improvements deriving from the use of dense organic working fluids have been estimated around 3% [Brown 2000]. It must be pointed out however that the predicted trends are the same for both solvers, with SGS, based on a centered third-order scheme, systematically predicting a slightly higher efficiency than UGS, based on an up-wind second-order scheme. Errors of the same order (relative difference less than about 1.5%) are observed for the computed enthalpy jump, whereas relative errors drop below 0.6% for the temperature variation and below 0.75% for the outlet flow angle. The relative errors are minimal when the SW model is considered, slightly increase with the PRSV model and are maximal for the MAH model. This trend is correlated with the predicted extent of the inversion zone using the three models: none with the SW model and maximal for the MAH model. Since the MAH model predicts lower values of Γ than the other two models in the considered range of operating conditions, this implies $\left(\frac{\partial a}{\partial \rho}\right)_{s,MAH} < \left(\frac{\partial a}{\partial \rho}\right)_{s,PRSV} < \left(\frac{\partial a}{\partial \rho}\right)_{s,SW}$ according to formula (1). For a given expansion rate, the speed of sound varies more abruptly when the MAH EoS is used, and this affects in turn the numerical dissipation generated by SGS and UGS, leading to greater relative errors. In conclusion, the SGS and UGS considered in this study yield very similar flow fields and turbine performance trends, within a numerical uncertainty of 2% at most. This justifies a physical analysis of the flow field in the turbine cascade and of its energetic performance, purely based on numerical results provided by the SGS solver (retained for its higher space accuracy-order).

8.4 Analysis of turbine performance: Influence of the thermodynamic model

The flow sensitivity to the thermodynamic model is first analyzed, with the SW results taken as reference to compute the relative errors produced by the PRSV and MAH models on the global performance parameters (see Fig. 8.6). The isentropic efficiency predicted by the PRSV and MAH models are in excellent agreement with the reference SW model for the whole range of operating conditions, translated again into an inlet compressibility factor: the computed error is between 0.3% and 0.4% for the PRSV EoS and less than 0.1% for the MAH EoS. The enthalpy jump is more sensitive to the thermodynamic model with error ranging from 3% to 6% for PRSV; the MAH model still provides errors smaller than 1% over most of the considered conditions. The temperature variation is found to be a much more sensitive parameter, with both PRSV and MAH models exhibiting errors of about 10% and the MAH model slightly more accurate than PRSV. This result can be explained when recalling the same inlet pressure and density conditions have been used for the

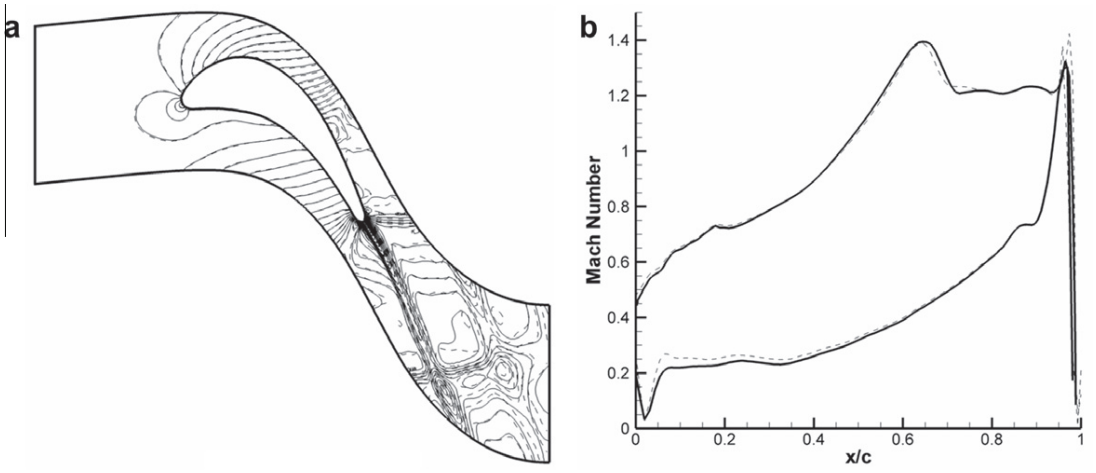

Figure 8.4: Typical numerical results of the SGS and UGS solvers for dense-gas flow through the LS59 cascade. (a) IsoMach lines and (b) mach distribution along the blade. Solid line (SGS), dashed line (UGS).

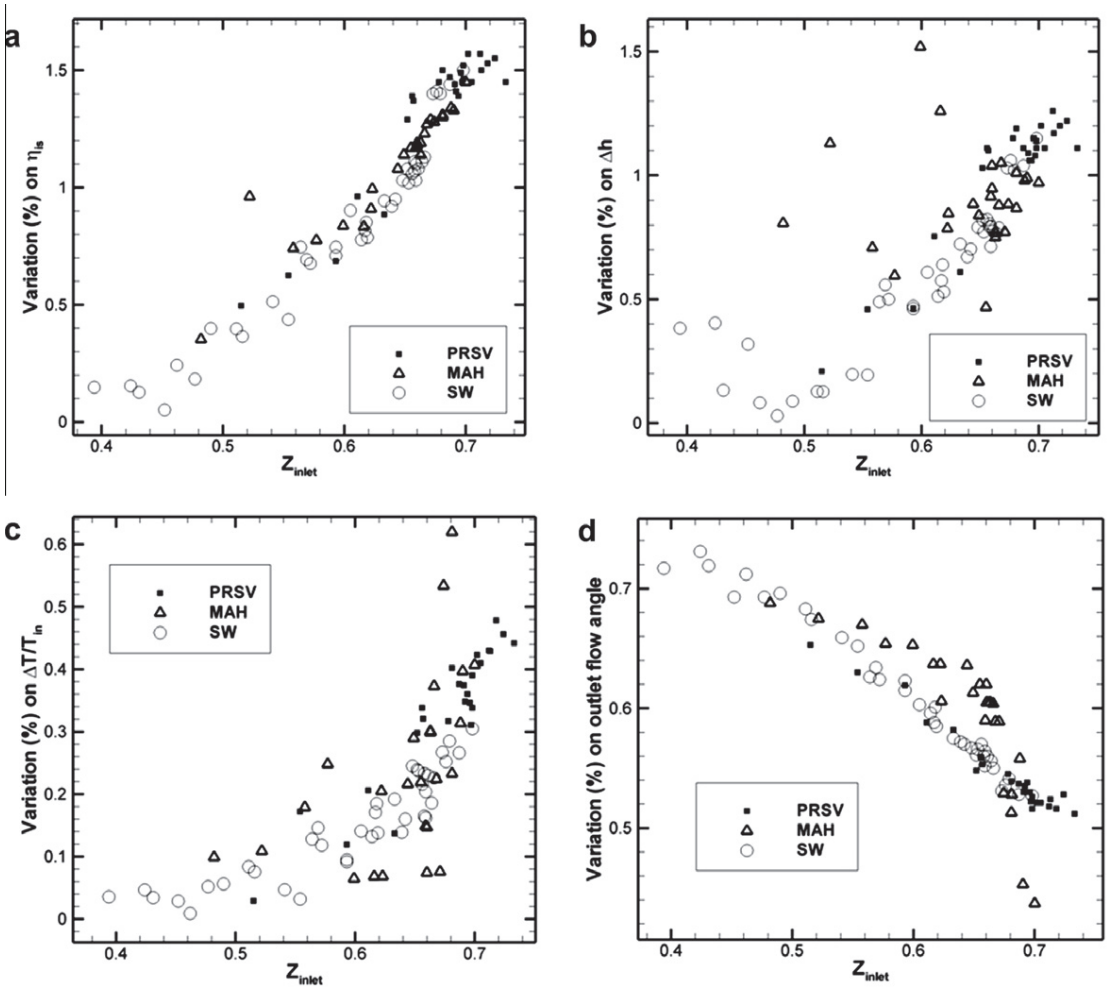

Figure 8.5: Relative differences on turbine performance parameters computed by the SGS and UGS. (a) Isentropic efficiency, (b) enthalpy jump, (c) temperature variation, and (d) outlet flow angle.

three models, which leads to slightly different inlet temperatures (differences up to 4% with respect to the SW model have been observed). The most significant differences on the inlet temperature and consequently on the temperature variation are observed for points lying further away from the saturation curve (but still well within the dense gas region). This means the inlet compressibility factor cannot be retained as the only indicator of non-ideal thermodynamic behavior of the working fluid; the fundamental derivative also plays a key role via the fluid heat capacities, which depend on the sound speed derivatives. Finally, the computed outlet flow angles obtained with the PRSV and MAH models remain in excellent agreement with those associated with SW (see Fig. 8.6d) since the relative error is below 0.2% for the PRSV EoS and below 0.5% for the MAH EoS. In conclusion, the simple PRSV model appears as an interesting alternative to the much more complex SW EoS since it requires only a few thermodynamic inputs to correctly reproduce the qualitative behavior of dense gas flows for a low computational cost. When using SGS, the cost per iteration associated with the SW model is about three times the cost associated with the PRSV model (the MAH model being only 10% more expensive than PRSV). Moreover, it was also observed the convergence of the solver to a steady state was also faster with the PRSV model than with MAH or SW EoS. The average number of iterations needed to decrease the residual by six orders of magnitude with the SW model is about 36% larger than with the PRSV model and 20% larger than the MAH model. The overall computa- tional cost of the PRSV EoS is eventually four times smaller than the cost of the SW model and 20% lower than the cost of the MAH model.

8.5 Influence of the working fluid

To investigate the effect of the working fluid on turbine performance, a parametric study is also performed for toluene (chemical formula C7H8), a lighter fluid of common use in ORCs. The reduced inlet conditions considered for the study are the same as for D5 and the computations are based on the PRSV model. The global performance parameters (η, Δh, $\frac{\Delta T}{T_{inlet}}$) are compared in Fig. 8.7a-c for D5 and toluene. For the studied range of conditions, toluene provides slightly (about 1%) higher efficiencies than D5. Note however that, if the reduced operating conditions are the same for both fluids, the critical pressure is about 40 atm for toluene while it is close to 12 atm for D5. Since the critical temperatures of D5 and toluene are close to each other, both fluids may operate in the same range of temperature but with substantially different operating pressures. In ORCs, high operating pressures increase the technological complexity of the sealings. The enthalpy jump for D5 is about 8% greater than for toluene, which means a higher power output for the given pressure ratio. The relative temperature jump for both fluids display substantially different behaviors. The heat capacity of toluene is much lower than that of D5, so that for a given expansion rate starting from the same inlet conditions, the outlet temperature is much lower in the lighter fluid. When specific heats tend to infinity, isentropic transformations tend toward isothermal ones. The lower temperature variation in D5 makes this high heat capacity fluid more suitable for cogeneration purposes. Similar trends have been observed using the PRSV EoS though the predicted efficiency is a bit lower, ranging from 0.893 to 0.906 (against[0.899, 0.910] with the SW model, as displayed in Fig. 8.7a).

8.6 Role of non-classical gas-dynamics effects

Our last sequence of analysis will be focused on the role of non-classical gas dynamic effects on turbine performance. For a qualitative assessment of this role, the analysis can be restricted to the simple PRSV model, which predicts the existence of an inversion zone for D5. The operating point P_{BZT} = (p/p_c = 1.04, ρ/ρ_c = 0.913) is selected in the close vicinity of the inversion zone (for locating P_{BZT} see the point (2.13, 1.01) in the plan s-T represented in Fig. 8.8a), so that the flow evolves in the neighborhood of the negative nonlinearity region (but not through it) during the

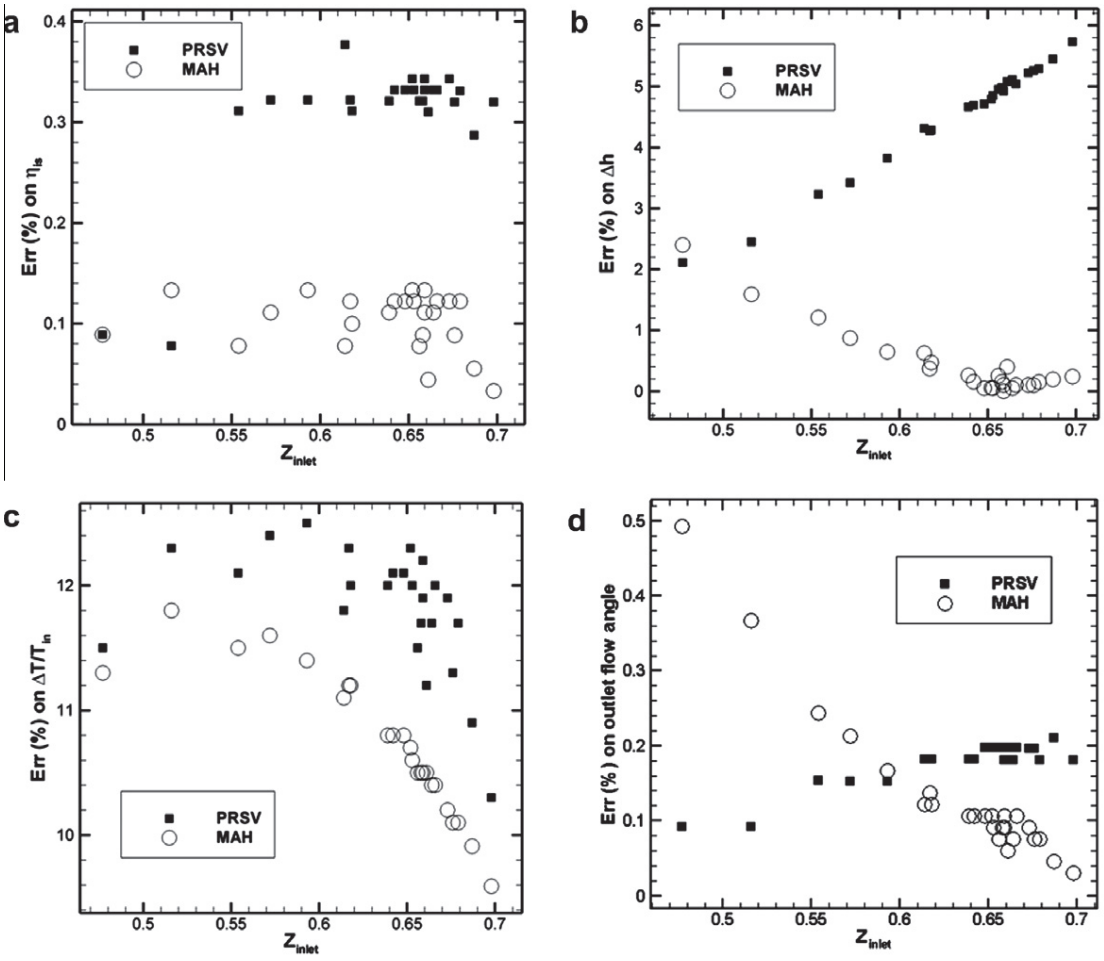

Figure 8.6: Relative errors on turbine performance parameters predicted by different thermodynamic models. (a) Isentropic efficiency, (b) enthalpy jump, (c) temperature variation, and (d) outlet flow angle.

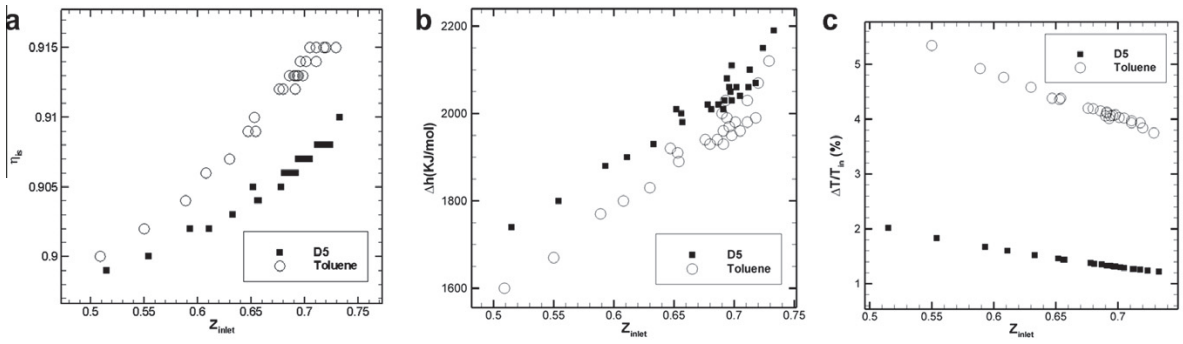

Figure 8.7: Performance parameters for the LS59 cascade. SW model, SGS solver. (a) Isentropic efficiency, (b) enthalpy jump, and (c) temperature variation.

expansion. For these conditions, the fundamental derivative is about 1.1 at turbine inlet but takes values close to zero at the blade wall, due to the dropping pressure. According to formula (1), the sound speed quickly increases, limiting the growth of the Mach number during the expansion and reducing shock strength. Losses associated to shock waves are then reduced and turbine efficiency increases to 91.5%, which is 1-2.5% higher than efficiencies measured with the PRSV EoS in the previous parametric study, where inlet conditions remained far away from the inversion zone and led to flows with a higher Mach number upstream of the shocks. The iso-Mach lines and Mach number distributions along the blade are plotted respectively in Figs. 8.9a and 10c for P_{BZT} and in Figs. 8.9b and 8.9c for the operating point $P_{DG} = (p/p_c = 0.622, \rho/\rho_c = 0.276)$ (see the point (5.86, 0.99) in the plan s-T represented in Fig. 8.8a) yielding higher values of the fundamental derivative during flow expansion (Fig. 8.9d). As expected, for operating conditions closer to the inversion zone, the maximum Mach number in the cascade is decreased, shocks are weaker and the turbine isentropic efficiency increases. Note that the maximum Mach Number is reduced by about 2% at most. This rather limited reduction is due to the pressure ratio imposed on the turbine, that has been chosen sufficiently high to generate a good performance in terms of Δh for the geometry used in this study. For this choice of the operating conditions, the fluid pressure drops quickly, driving the flow below the small BZT region. As a consequence, BZT effects are restricted to a small portion of the flow field, and the Mach number may reach supersonic values. The resulting gain derived from BZT or quasi-BZT effects is slightly less impressive than the one observed for instance in flows over isolated airfoils, as shown in [Congedo 2007], where subsonic Mach number can be achieved. On the other hand the enthalpy jump at P_{BZT} is 1529 kJ/mol, against 2069 kJ/mol for P_{DG}, which means the efficiency improvement is obtained at the expense of a lower work output per mole of operating fluid. In terms of power output, this lower specific work is however counter-balanced by the higher fluid density in the neigh- borhood of the BZT region. The temperature variation DT/Tinlet at $PBZT$ and P_{DG} is respectively equal to 3% and 1.3%. This higher temperature variation and the lower enthalpy drop at P_{BZT} conditions are related to the lower heat capacities in the neighborhood of the saturation curve. Thus working at lower C also improves the Carnot efficiency in this case. Beneficial effects due to negative nonlinearities may be maximized with a working fluid displaying a larger inversion zone, hence with a higher molecular complexity. To validate such a strategy, computations are performed for a heavier cyclic siloxane of the same family as D5, namely dodecamethylcycloexasiloxane also known as D6. The existence of an inversion zone for this fluid is predicted for any choice of the thermodynamic model. The PRSV model is adopted again, for the sake of consistency with previous calculations, and Fig. 8.10 displays the inversion zone and iso-Γ curves in the T-s plane computed for D6 with the PRSV model. Comparing Fig. 8.10 and Fig. 8.8a, it is easy to check the predicted inversion zone is much larger for D6 than for D5 (note the same observation holds when other models are used). For the choice of operating condition $P_{D6} = (p/p_c = 1.05, \rho/\rho_c = 0.99)$ (see the point (2.07, 1.01) in the plan s-T represented in Fig. 8.10), the fundamental derivative is about 1.4 at turbine inlet, but takes negative values at the blade wall, because of the dropping pressure. The associated growth of the Mach number is limited during the expansion and the shock strength reduced (see Figs. 8.11acd). Losses associated to shock waves remain limited and turbine efficiency increases to 92.1%. The enthalpy jump is 1499 kJ/mol while the temperature variation is equal to 2.6%. For the sake of comparison, the behavior of a non-BZT fluid, namely toluene, is also reported in Figs. 8.11bcd with operating conditions $P_{TOL} = (p/p_c = 0.953, \rho/\rho_c = 0.648)$ which are close to the saturation curve so as to avoid entering the biphase region during the expansion. In these conditions, the isentropic efficiency reduces to 88.1% for toluene, due to the appearance of stronger shocks. The enthalpy jump is equal to 1.514 kJ/mol, close to the value obtained for D5 at P_{BZT} conditions. This analysis demonstrates an inlet condition close to the saturation curve is not sufficient in itself to yield an increase in the isentropic efficiency; this feature remains specific to dense gas fluids such as D5 and D6.

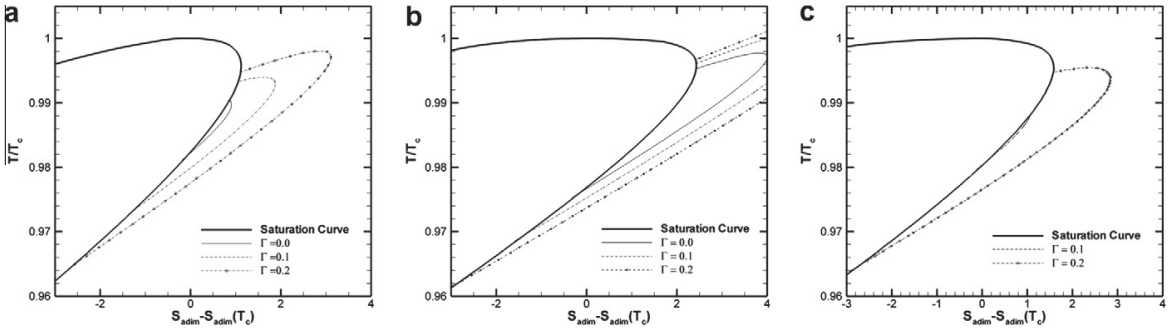

Figure 8.8: Close-up of the dense-gas region for D5. (a) PRSV model, (b) MAH model, and (c) SW model.

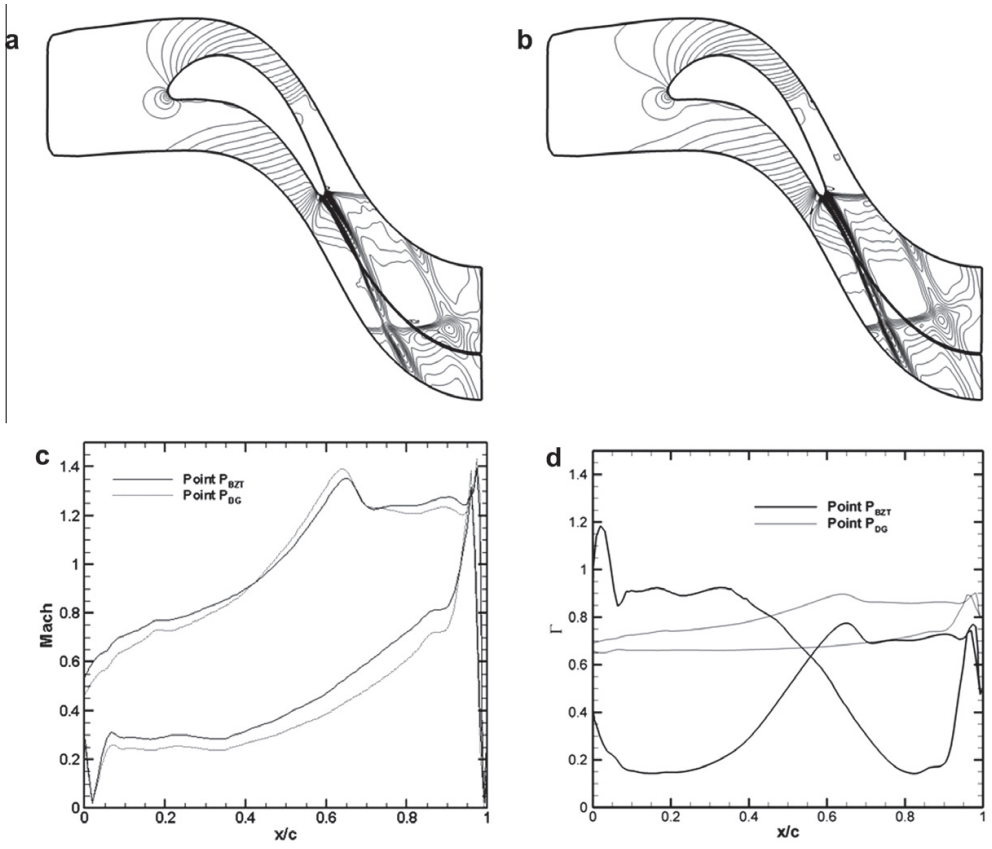

Figure 8.9: iso-Mach lines for P_{BZT} (a) and P_{DG} (b), Mach number (c) and C (d) distributions along the blade wall (working fluid D5, PRSV EoS). Point P_{BZT} is close to the inversion zone of the fluid.

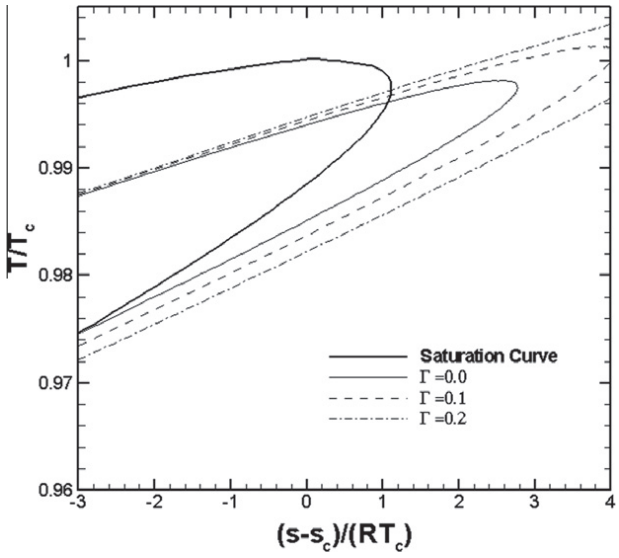

Figure 8.10: Close-up of the dense-gas region for D6 (PRSV model).

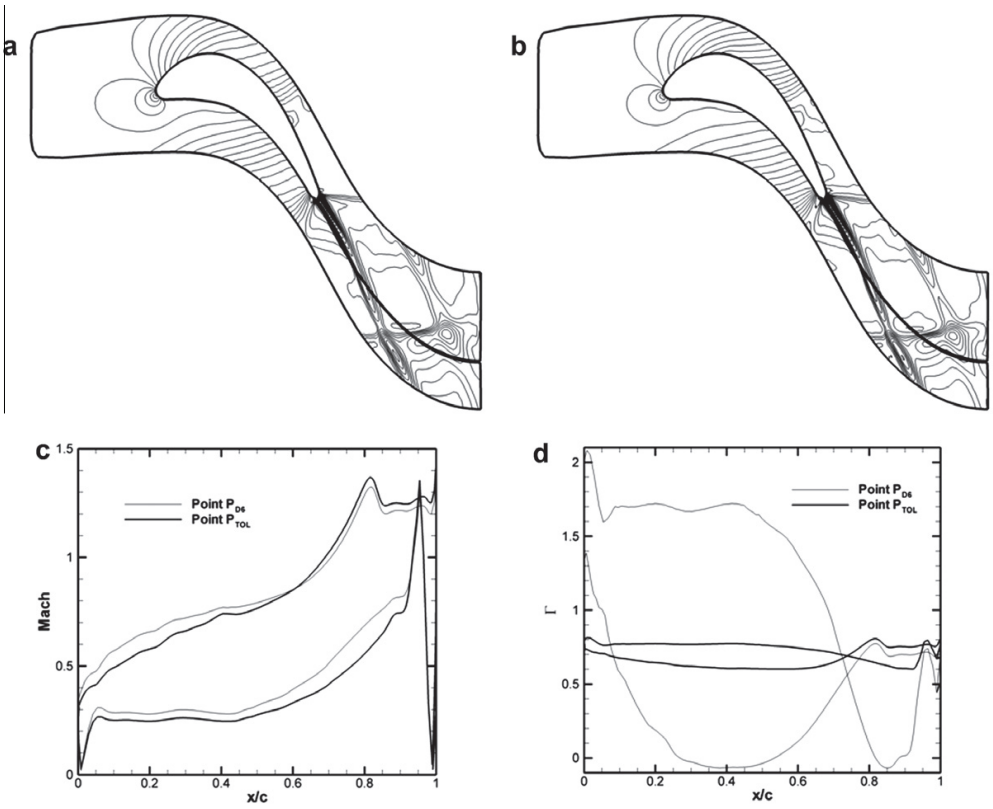

Figure 8.11: iso-Mach lines for PD6 (a) and PTOL (b), Mach number (c) and C (d) distributions along the blade wall (working fluid D6 and toluene, PRSV EoS).

Chapter 9

Reliability of thermodynamic models for dense-gas flows

Contents

This section investigates the sensitivity of numerically computed flow fields to uncertainties in thermodynamic models for complex organic fluids. Precisely, the focus is on the propagation of uncertainties introduced by some popular thermodynamic models to the numerical results of a computational fluid dynamics solver for flows of molecularly complex gases close to saturation conditions (dense gas flows). A chaos collocation method is used to perform both a priori and a posteriori tests on the output data generated by thermodynamic models for dense gases with uncertain input parameters. A priori tests check the sensitivity of each equation of state to uncertain input data via some reference thermodynamic outputs, such as the saturation curve and the critical isotherm. A posteriori tests investigate how the uncertainties propagate to the computed field properties and aerodynamic coefficients for a flow around an airfoil placed into a transonic dense gas stream.

9.1 Introduction

No generally accepted experimental proof of non-classical gasdynamic behavior is available, as several attempts have failed to provide evidence (see Ref. [Colonna 2003] for a review). The detection of BZT behavior is related to a large extent to the possibility of accurately estimating the position and extent of the inversion zone or, in other words, to the accurate evaluation of Γ.

More generally, reliable simulations of compressible flows with complex thermodynamic behavior require the quantification of thermodynamic modelling errors, especially for those applications that look for improvements of the order of a few percents of the system performance. This is actually the case for energy conversion cycles (see, for instance, Ref. [Brown 2000]). The uncertainty associated to the estimation of the thermodynamic behavior of a fluid is due both to the mathematical form of the equation of state chosen to represent it and to the difficulty of providing reliable input thermodynamic properties (like critical properties, acentric factor, etc.) to build the model coefficients. Countless equations of state (EOS) have been proposed in the literature, diversified according to the substance to be modelled. Equations of state based on theoretical and analytical criteria, such as the van der Waals, Redlich-Kwong, Peng-Robinson, Martin-Hou equations, and many other (see, for instance, Ref. [Reid 1987]), allow modelling the thermodynamic behaviour of a fluid for an extended range of operating conditions provided that some thermodynamic inputs (e.g., critical temperature and

pressure, acentric factor and other) are available for the substance of interest. However, such data are typically affected by more or less significant experimental errors. For instance, the determination of critical-point data is a delicate issue, because of the highly sensitive thermodynamic response close to critical conditions and also because complex substances may decompose, totally or partly, at temperatures close to the critical one. In this case, critical point values just rely on estimations.

For simple fluids, large and accurate experimental data sets are available (pressure-density-temperature, or $p\rho T$, data, speed of sound, etc.), which enables the derivation of reference multiparameter equations of state reproducing the fluid thermodynamic properties with the same level of uncertainty affecting the measurements themselves. These can be as low as 0.01% for many substances of common use Ref. [Span 2001, Span 2003]. For more complex fluids, the available data sets are often insufficient to establish reference equations of state. In this case, a way of increasing the accuracy and/or the applicability range of the thermodynamic model is to develop analytical equations of state with a large number of expansion terms (for instance, virial expansion terms), along with suitable thermodynamic constraints, which allow to determine the equation coefficients from a minimal amount of thermodynamic input data. The more complex the equation of state, the larger number of thermodynamic inputs is required to determine the coefficients, compared to simple equations of state. As a consequence, care has to be taken if too scarce or inaccurate data are available, since even if the (deterministic) accuracy is theoretically increased, larger modelling uncertainties appear because of the increased number of uncertain parameters. Clearly, this is a major concern for many molecularly complex industrial fluids; namely, very little data are available for fluids falling into the category of dense gases and, more particularly, for candidate BZT fluids. The scarcity of reliable data is also a major difficulty for the construction of so-called 'technical' equations of state for dense gases. These are semi-empirical equations of state based on a smaller number of parameters than reference EOS and using a fixed mathematical form for a given class of substances (see Ref. [Span 2003]). For instance, Ref. [Colonna 2006b] provides a listing of available data for selected siloxanes. These are essentially restricted to critical properties, normal boiling temperatures, vaporization enthalpies, and acentric factors along with a few saturated liquid and vapor data and p-T data for some of the fluids. The experimental uncertainties for these data are definitely higher than for state-of-the-art data for 'common' fluids (from 3% up to 25% for some data). The present work investigates the sensitivity of some thermodynamic models of common use for the simulation of dense gas flows to uncertain thermodynamic input data. Precisely, we focus on the sensitivity of some important thermodynamic output (such as the saturation pressure at different temperatures and the fundamental derivative of gasdynamics) for two fluids frequently considered in the dense gas literature and for different choices of the thermodynamic model (thermal and caloric equations of state). The chosen fluids are a heavy fluorocarbon (studied, for instance, in Refs. [Brown 2000, Cinnella 2007]) and a siloxane (considered in Refs. [Colonna 2007, Cinnella 2008a]). The thermodynamic models under investigation include two cubic equations of state, namely, the Redlich-Kwong EOS with the modification proposed by Soave [Soave 1972] the Peng-Robinson-Stryjek-Vera (PRSV) equation of state [Stryjek 1986], and the five-term virial equation of state of Martin and Hou [Martin 1955]. These analytical equations of state may be applied to potentially any substance and have been implemented in computational fluid dynamics (CFD) codes for dense gas simulations since they offer a good compromise between accuracy and computational cost. In the past, they have been often applied to the investigation of negative nonlinearity region of organic fluids [Lambrakis 1972, Cramer 1992] and to the analysis of dense gas flows Ref. [Brown 2000, Cinnella 2007, Cinnella 2008a, Cramer 1992]. In addition to the previous ones, we also consider a thermodynamic model based on a multiparameter technical equation of state [Span 2003], whose coefficients have been optimized for siloxanes in Ref. [Colonna 2006b]. After performing a series of a priori tests to check the sensitivity of the equations of state to input thermodynamic data, we quantify the impact of such uncertainties on the flow fields predicted by a dense gas numerical solver, with focus on aerodynamic output data such as pressure and force

coefficients. The application case taken into account for these a posteriori tests is a transonic dense gas flow past an airfoil.

9.2 Sources of uncertainty

The role of a thermodynamic model is to reproduce as accurately as possible the thermodynamic properties of a given substance, especially when measured data are not available or too scarce. The main sources of uncertainty associated to a thermodynamic model are the functional form of the model and the values taken by the substance-specific coefficients. These are related directly or indirectly to some input thermodynamic properties that can be measured or just estimated. For simple fluids, the available data allow to develop very complex multiparameter equations of state whose coefficients may be optimized to a fitting accuracy of the same order of the experimental uncertainty. For the molecularly complex fluids of interest here, the experimental data are much scarcer and difficult to obtain. In these conditions, the use of simpler models may be safer than the use of complex ones, even if complex models are theoretically expected to perform better if they could be properly optimized. The three analytical equations of state described in the previous Section 7.2.1 (RKS, PRSV, MAH) have a mathematical form depending directly on given thermophysical properties; namely, the critical temperature and pressure and the acentric factor (RKS and PRSV models), and additionally the critical compressibility factor and the Boyle temperature (MAH model). For the calculation of caloric properties, the equations of state are supplemented by the ideal gas contribution to the specific heat at constant volume, which depends on $c_{v\infty}(T_c)$ and the power-law exponent n. Table 9.1 lists the values found in the literature for the input thermodynamic parameters needed by the preceding EOS for the two fluids under investigation. For PP10, the data are taken from Refs. [Lambrakis 1972, Cramer 1992] and for D5 from Ref. [Colonna 2006b] and references cited therein. Uncertainty estimation requires taking into account probability distributions for the input thermodynamic properties required by the previous models. Inspection of the available literature allows only a rough estimation of typical ranges of variation of such properties for PP10 and D5. For PP10, no thermodynamic data are available to assess the accuracy of any thermodynamic model, as discussed for instance in Ref. [Guardone 2004]. The critical point data are based on manufacturer data, without any precise uncertainty quantification. The dilute gas specific heat is estimated by power-fitting results from the group contribution procedure of Rihani and Doraiswamy [Rihani 1965], which may lead to errors as high as 25% on the true value. This represents possibly the largest source of uncertainty in the thermodymamic models. Finally, even if only manufacturer data are available for PP10, estimates provided for lighter fluids with similar chemical structures show that the expected errors may be of the order of 3%-4% for vapor pressure data and 15%-20% on the critical specific volume. Concerning D5, a little bit more information is available. For instance, data reviewed in Ref. [Colonna 2006b] show somewhat smaller error intervals both on critical point data (of the order of 1%-2%) and the ideal-gas specific heat (approximately 6%). Because of the lack of information about uncertainties on the fluid properties and the associated probability distributions, and since the aim of the present study is to analyse the sensitivity of the proposed models more than to give accurate quantitative estimates of the confidence intervals on the computed results, we assume in the following that the input properties are described by probability density distributions with means equal to values adopted for most deterministic computations available in the literature (see, e.g., Refs. [Cinnella 2007, Cinnella 2008a]) and variation coefficients (i.e., ratio of the standard variation to the mean) of about 3%, which is maybe optimistic for some of the considered properties, but is expected to lead to a conservative estimate of the variability of the results. Differently from the preceding models, the coefficients of the SW thermal EOS are obtained by taking into account uncertainties on the experimental data used for the calibration procedure. Full information about the weighting strategy is unfortunately not available, so that we are not able to judge about the

Property	p_c (atm)	T_c (K)	Z_c	T_e (K)	n	$c_{v,\infty}(T_c)/R$	ω
PP10	16.0[a] ÷ 16.2[b]	630.2[b] ÷ 632.2[a]	0.2831[a] ÷ 0.2859[b]	463.2[a] ÷ 467[b]	0.5255[a]	78.37[a]	0.4833[b]
D5[c]	10.2 ÷ 11.5	617.4 ÷ 619	0.237 ÷ 0.274	484.1	0.5208[d]	76.0[d]	0.6658

Table 9.1: Ranges for different thermodynamic properties and parameters of PP10 and D5.

A	B	C	D
-4.1975	0.22390	-1.6880×10^{-4}	6.0140×10^{-8}

Table 9.2: Mean values of coefficients the specific heat at constant pressure for D5.

sensitivity of the equation to the weighting criteria. Thus, we choose to adopt the thermal SW EOS with fixed coefficients and carry out a sensitivity analysis on the effect of the chosen caloric model only. Precisely, we perturb the coefficients of Eq. 7.12, whose deterministic values (taken from Ref. [Colonna 2006b]) are provided in Table 9.2. We assume that these coefficients are represented by random variables with means as in Table 9.2 and variation coefficients equal to 3%. In addition to variation intervals, stochastic analyses also require information about the form of the probability density functions (pdfs) for each uncertain parameter. When these informations are not available, a reasonable choice could be to assume a Gaussian distribution. For PP10 and D5, information about possible input pdfs is lacking. Thus, we check the influence of the mathematical form for the input pdf by comparing results obtained for normal and uniform distributions with the same mean. For the last one, the variation interval is equal to $\mu \pm 3\sigma$; μ being the mean and σ the standard deviation of the corresponding normal distribution.

9.3 Results

In this section, we apply a Chaos Collocation Method to the propagation of thermodynamic uncertainties through the selected thermodynamic models (Section 9.3.1) and study how they affect the predicted thermodynamic behavior of the fluids under investigation. Than, we propagate these uncertainties through the dense gas flow solver and quantify their effect on the computed solutions (Section 9.3.2).

9.3.1 Uncertain state diagrams

We first perform a priori tests on the sensitivity of the thermodynamic models under investigation models to uncertain input parameters. To measure such a sensitivity, we consider the uncertain state diagrams in the Amagat (pressure/volume) plane and compute error bars on the liquid/vapour coexistence curve, the critical isotherm and two curves of crucial importance for dense gas flows, namely, two isolines of the fundamental derivative of gas dynamics. Specifically, we investigate the effect of thermodynamic uncertainties on the shape and location of the $\Gamma = 0$ and $\Gamma = 1$ isolines of the p-v plane, on the size (area) of the inversion zone in the non-dimensional p-v plane, denoted as $A(\Gamma < 0)$, and on the minimal value of C on the critical isotherm, i.e., $\Gamma_{min,T_c} = min_v \Gamma(T_c, v)$. The numerical results presented in the following are obtained by using a Chaos Collocation method with an expansion polynomial order equal to 3. Numerical tests show that this is sufficient to ensure converged statistics for the quantities of interest. Two fluids have been selected for this study: PP10 and D5. For PP10, the simpler models RKS and PRSV have been tested against the more complex

MAH model. For this last model, two cases have been considered: in the first one, referred-to as MAH (6), all the six uncertain parameters described in Section 9.2 are perturbed simultaneously and in the second one (MAH (3)), just three model parameters are assumed to vary, namely, the critical pressure and temperature and $c_{v\infty}(T_c)/R$. First of all, we investigate the influence of pdf chosen to model input uncertainties for the most challenging case, i.e., MAH (6). We consider two types of pdf: Gaussian distributions of the form $\mathbb{N}(\mu, 0.03\mu)$, where μ is the mean value of the uncertain parameter of interest, and uniform distributions in the range $\mu \pm \delta$, where δ was chosen equal to 0.09μ. The mean values of the perturbed parameters for PP10 are in Table 9.1. Table 9.3 shows the mean and the standard deviation for the area of the inversion region computed in the two cases. The results obtained with the two pdf are quite similar for all the models. The corresponding uncertain state diagrams, reported in Fig. 9.1, exhibit only slight differences. For this reason, only the normal distribution has been retained for the subsequent computations. Figures 9.2 and 9.3 shows the uncertain state diagrams and a close-up of the inversion zone for PP10, as predicted by the RKS, the PRSV, and the MAH models (with six and three uncertain parameters). For all of the models, the mean stochastic solution is almost superposed to the deterministic solution obtained by taking input parameter equal to the mean values of the distribution. Moreover, the simpler RKS and PRSV models provide similar mean curves and display similar (modest) sensitivity to the input uncertainties. In fact, error bars on the results are of the same order of the supposed uncertainty range for input quantities. The multiparameter MAH model predicts quite different mean curves with respect to the previous cubic models and appears to be much more sensitive to thermodynamic uncertainties then RKS and PRSV; actually, the results are affected by greater error bars, which become particularly large for the Γ isolines. The great sensitivity of the predicted results to the mathematical form of the thermodynamic model and/or to the input thermodynamic data may explain why tentatives of designing experimental setups for dense gas flows (namely, dense gas shock tubes for the study of nonclassical waves) based on preliminary numerical data provided by the MAH model were not successful; very small deviations of the actual flow behavior from the predicted one may result in very different values of the fundamental derivative of gas dynamics, which makes the conditions of the experiments very hard to be controlled. This adds to the difficulty of fine-tuning the experimental conditions due to technological implementation details of the experimental setup and to fluid decomposition problems. For a more quantitative evaluation of the results, Table 9.4 reports the mean values of the computed area of the inversion zone size and of the minimum value of Γ on the critical isotherm for the three models, as well as the corresponding standard deviations. For the simpler models, the mean values are very close to the deterministic ones. However, the associated standard deviations are non negligible (10%-30% of the mean). For the MAH model (three and six uncertain parameters), standard deviation varies from 30% up to 60% of the mean. In terms of amplification factors (defined as the ratios of the output over the input coefficient of variation), for the area of the inversion region, we get 3.3, 10, 10, and 20 for RKS, PRSV, MAH (3) and (6), respectively. The minimal value of the fundamental derivative on the critical isotherm Γ_{min} displays an even higher sensitivity, since it may change its sign according to the fluctuations of the model parameters. Note that the MAH model predicts a much larger inversion zone compared to the RKS and PRSV models. Thus, simpler cubic equations like the RKS and the PRSV may be even more conservative in terms of predictions of BZT effects. A similar analysis has been carried out for D5, a more promising candidate as ORC working fluid. For this fluid, we consider the RKS, PRSV, and MAH models along with the possibly more accurate SW model [Span 2003, Colonna 2006b]. For the last model, only the caloric properties are perturbed, as discussed previously. Inspection of Figures 9.4 and 9.5 shows that the mean stochastic solution is almost superposed to the deterministic solution for all the models. The simpler RKS, PRSV, and more complex SW model provide similar mean curves and display similar (modest) sensitivity to the input uncertainties. Output coefficients of variation for the quantities of interest are of the same order of those used for input quantities.

Model	$\mu(A(\Gamma<0))$	$\sigma(A(\Gamma<0))$	$\mu(\Gamma_{\min,T_c})$	$\sigma(\Gamma_{\min,T_c})$
Gaussian	0.3274×10^{-1}	0.2327×10^{-1}	-0.29655×10^{-1}	0.13656×10^{-0}
Uniform	0.3146×10^{-1}	0.2103×10^{-1}	-0.28809×10^{-1}	0.12953×10^{-1}

Table 9.3: Mean and standard deviations for the area of the inversion zone and the minimum value of the fundamental derivative Γ along the critical isotherm, PP10 fluid, and MAH model. Effect of the mathematical form of the pdf for input quantities.

Model	$\mu(A(\Gamma<0))$	$\sigma(A(\Gamma<0))$	$A(\Gamma<0)\vert_{\text{det}}$	$\mu(\Gamma_{\min,T_c})$	$\sigma(\Gamma_{\min,T_c})$	$\Gamma_{\min,T_c}\vert_{\text{det}}$
RSK	0.8705×10^{-2}	0.2678×10^{-2}	0.8664×10^{-2}	0.1418×10^{-0}	0.1522×10^{-1}	0.1420×10^{-0}
PRSV	0.6409×10^{-2}	0.1345×10^{-2}	0.6388×10^{-2}	0.1702×10^{-0}	0.1454×10^{-1}	0.1703×10^{-0}
MAH (3)	0.3237×10^{-1}	0.1427×10^{-1}	0.2842×10^{-1}	-0.2924×10^{-1}	0.1062×10^{-0}	-0.3009×10^{-1}
MAH (6)	0.3274×10^{-1}	0.2327×10^{-1}	—	-0.2966×10^{-1}	0.1366×10^{-0}	—

Table 9.4: Means and standard deviations for the area of the inversion zone and the minimum value of the fundamental derivative Γ along the critical isotherm. Fluid: PP10.

On the contrary, MAH exhibits significant error bars for the $\Gamma = 1$ contour, as already observed for PP10. Moreover, the $\Gamma = 1$ contour has a monotonic behavior, i.e., pressure increases when specific volume tends toward unity; this is in contrast with predictions of other models. All the models, except SW, predict an inversion zone. Table 9.5 provides quantitative results for the area of the inversion region and Γ_{min}. For D5, the area of the inversion zone is zero or close to zero according to all the models. As a consequence, the standard deviation is as high as 90% of the mean. Remark that the SW always predicts positive values of Γ, at least in the range of perturbed coefficients considered here, so that the standard deviation of the inversion zone is equal to zero. For Γ_{min}, the coefficients of variation range from 15% to 25%, according to the chosen model.

In summary, the main results of the present a priori analysis are (1) the MAH model is much more sensitive to uncertain input parameters than simpler cubic equations and produces unreliable results when applied to substances lacking of high-quality experimental information; specifically, its use is not recommended for substances like PP10 or D5 and (2) the PRSV model shows good stability in the presence of uncertain inputs and provides results close to the reference SW model in terms of size the inversion region (close to zero) and Γ_{min}.

Model	$\mu(A(\Gamma<0))$	$\sigma(A(\Gamma<0))$	$A(\Gamma<0)\vert_{\text{det}}$	$\mu(\Gamma_{\min,T_c})$	$\sigma(\Gamma_{\min,T_c})$	$\Gamma_{\min,T_c}\vert_{\text{det}}$
RSK	0.2527×10^{-2}	0.1822×10^{-2}	0.2287×10^{-2}	0.2205×10^{-0}	0.2826×10^{-1}	0.2206×10^{-0}
PRSV	0.1097×10^{-2}	0.1073×10^{-2}	0.6430×10^{-3}	0.2448×10^{-0}	0.2655×10^{-1}	0.2449×10^{-0}
MAH (3)	0.2091×10^{-1}	0.1378×10^{-1}	0.1922×10^{-1}	0.1594×10^{-0}	0.3837×10^{-1}	0.1589×10^{-0}
MAH (6)	0.2269×10^{-1}	0.2015×10^{-1}	—	0.2006×10^{-0}	0.4929×10^{-1}	—
SW	0.0	0.0	0.0	0.2755×10^{-0}	0.3164×10^{-1}	0.2748×10^{-0}

Table 9.5: Means and standard deviations for the area of the inversion zone and the minimum value of the fundamental derivative Γ along the critical isotherm. Fluid: D5.

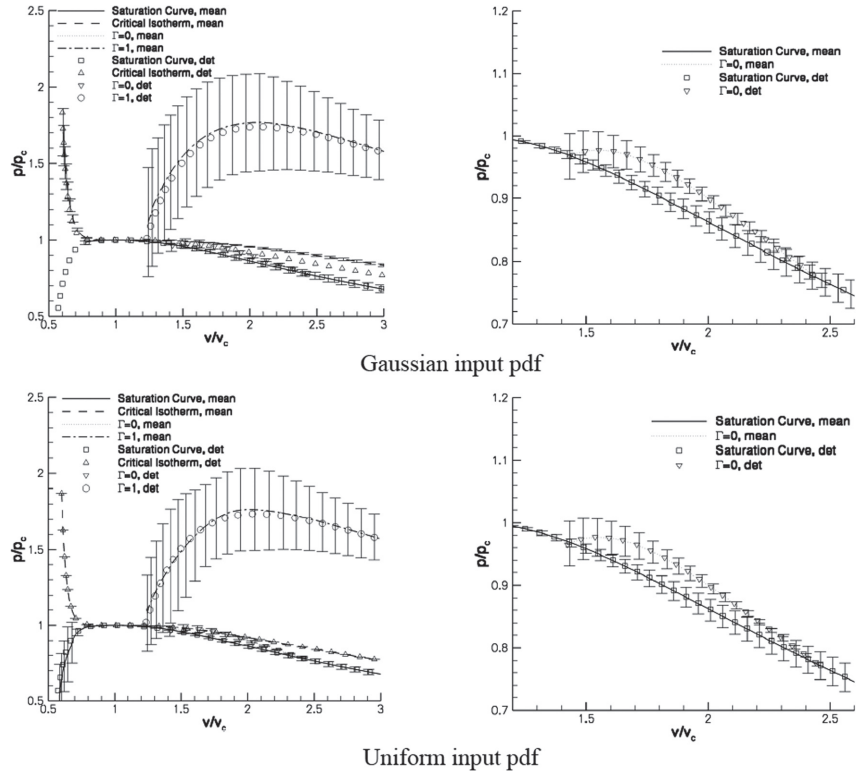

Figure 9.1: Uncertain state diagrams (left) and close-up of the inversion zone (right). MAH model, fluid PP10. Effect of the mathematical form of the pdf for the input quantities.

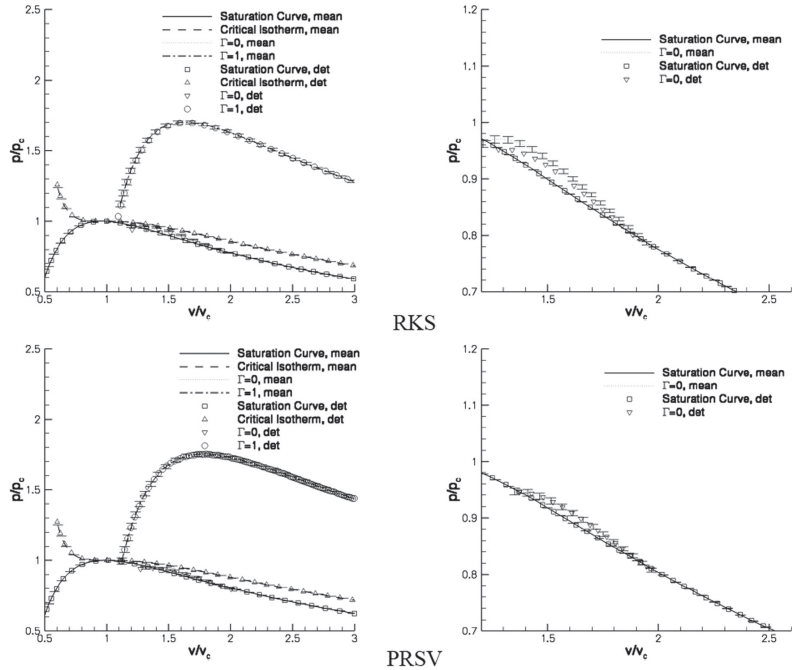

Figure 9.2: Uncertain state diagrams (left) and close-up of the inversion zone (right). Fluid PP10. Top to bottom: RKS and PRSV models.

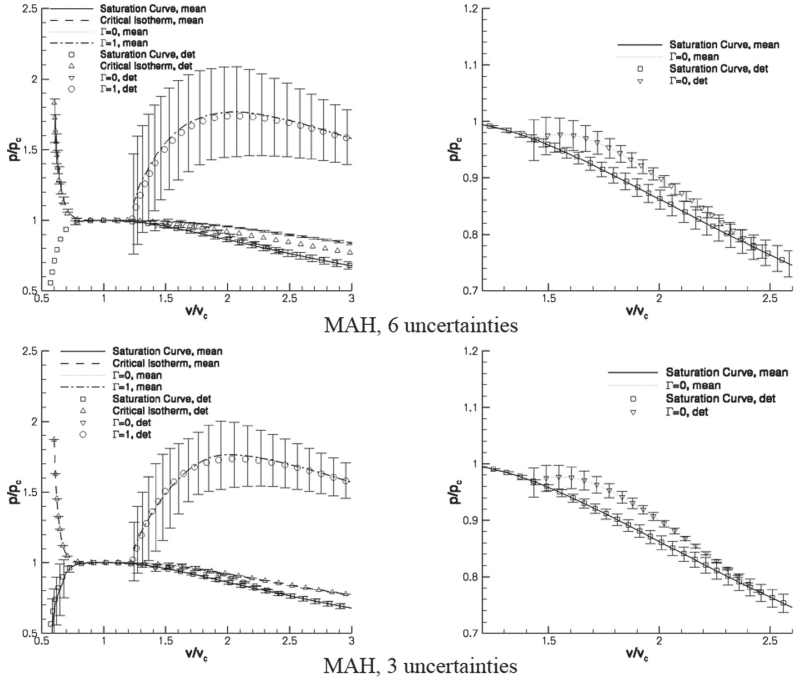

Figure 9.3: Uncertain state diagrams (left) and close-up of the inversion zone (right). Fluid PP10. Top to bottom: MAH model with 6 and 3 uncertain parameters.

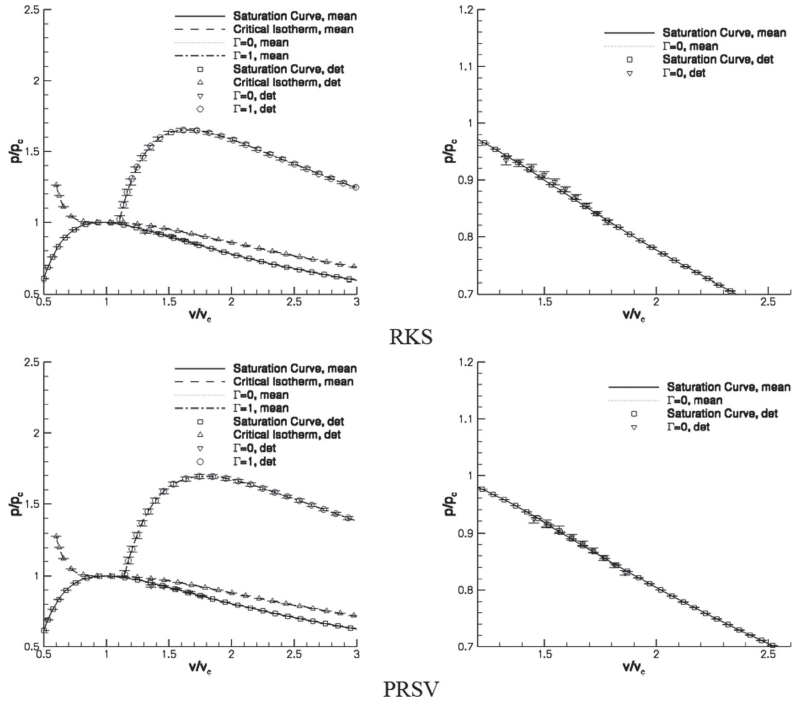

Figure 9.4: Uncertain state diagrams (left) and close-up of the inversion zone (right). Fluid D5. Top to bottom: RKS and PRSV models.

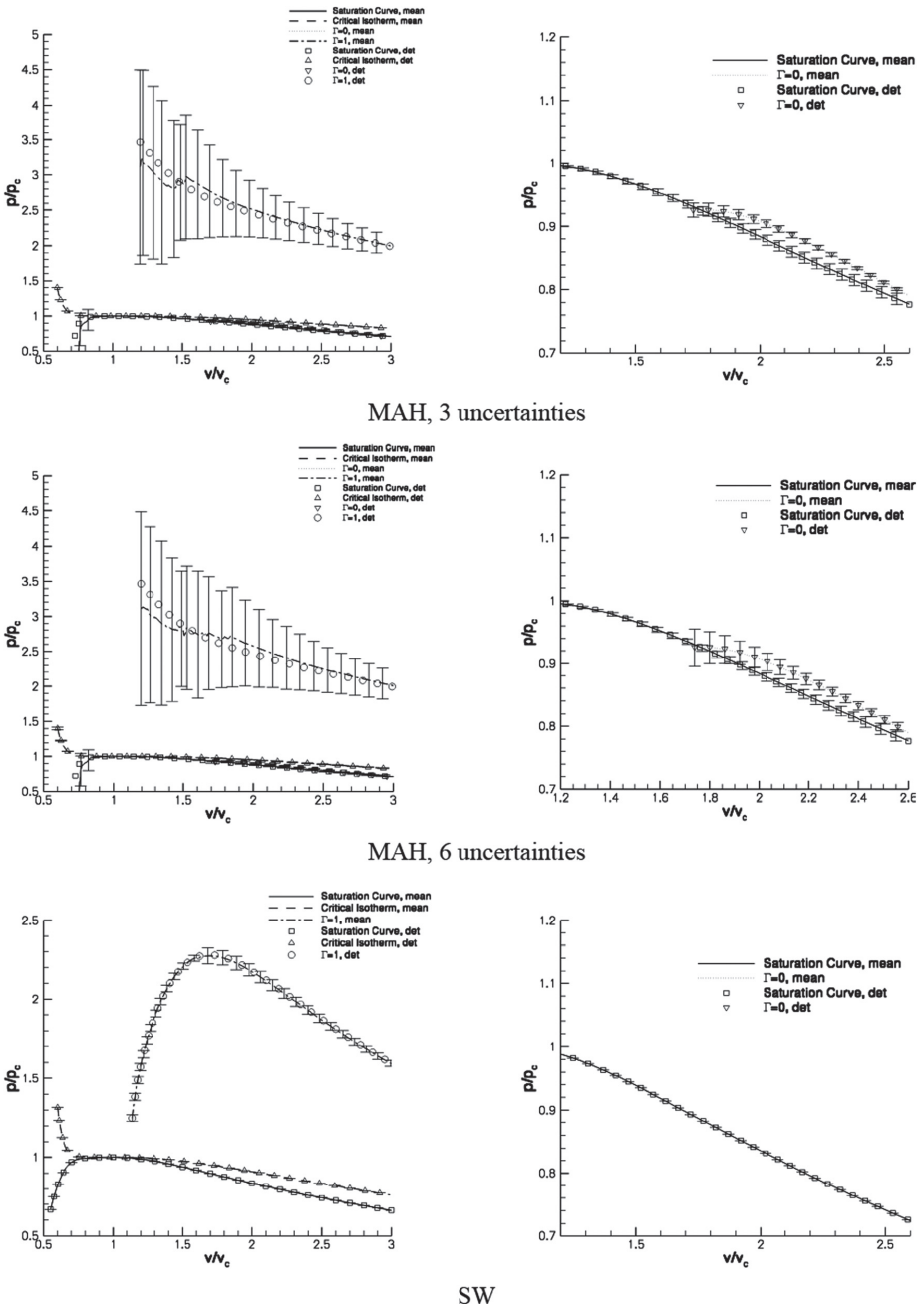

Figure 9.5: Uncertain state diagrams (left) and close-up of the inversion zone (right). Fluid D5. Top to bottom: MAH model, with 6 and 3 uncertain parameters, and SW model.

9.3.2 Uncertainty propagation through the dense gas solver

As a second step, a posteriori tests are performed to study the propagation of thermodynamic uncertainties to the numerical results for a steady transonic inviscid flow of a dense gas over a NACA0012 airfoil at $M_\infty = 0.95$ and 0° angle of attack. The thermodynamic conditions of the free-stream are fixed (no uncertainty) and correspond to $p_r = 0.985$ and $\rho_r = 0.622$. In these conditions, the lift and moment coefficients are equal to zero, but wave drag exists. Thereby, we focus our analyses on the drag coefficient. Since this quantity is very sensitive to mesh resolution, we perform a preparatory mesh study to check the independency of the computed stochastic results on the computational grids. Because of the flow symmetry, only one half of the computational domain is simulated, with symmetry conditions enforced on the axis. Figure 9.6 shows the effect of grid density on the stochastic and deterministic results computed by using the MAH model with normal distributions for the input thermodynamic data. The distribution parameters are reported in Table 9.6. The mean values correspond to the thermodynamic properties of PP10. The coefficients of variation σ/μ of the input distributions are limited to about 1.5%. This choice avoids that large variations of the input parameters may drive the flow into the humid vapour region, for the chosen thermodynamic free-stream conditions, since the flow solver is not equipped with two-phase models. This is a limitation of the proposed method, which will be investigated in future research. The results are computed using increasingly fine half C-shaped grids composed by $50x16$, $100x32$, and $200x64$ cells, respectively. The mean height of the first cell closest to the wall is equal to 0.001 chords for the medium grid. The outer boundary is located 10 chords away from the airfoil. The stochastic results take into account only three uncertain input parameters, namely, the critical temperature and pressure and the ideal critical heat capacity. Computations are carried out using second-order chaos polynomials. Grid convergence of the mean stochastic solution (Fig. 9.6(a)) is slightly slower than that of the deterministic one for this very sensitive case characterized by significant dense gas effects. Nevertheless, convergence of the solution standard deviation (Fig. 9.6(b)) is quite satisfactory, and the medium grid solution provides already a reasonable representation of the solution expectancy and variance. In the following, we compute solutions using the mean grid, but apply Richardson extrapolation (REX) [Cinnella 2013] to the drag coefficients obtained on two coarse grids of increasing density. Fig. 9.6(c) displays the reconstructed probability density function of the drag coefficient for the different computational grids and the REX method. The corresponding means and standard deviations are also provided in the legend. The REX technique provides a distribution in fair agreement with the fine grid one, for computational cost that is only slightly higher with respect to medium grid computations and is, therefore, retained for the subsequent drag computations.

Second, we check the effect of the chaos polynomial order used to reconstruct the stochastic solutions. Computations with chaos polynomials ranging form 1st to 5th order have been performed for case MAH (3) with input distributions chosen as in the preceding series of computations. Fig. 9.7 displays the mean and the standard deviation of the drag coefficient as functions of the chaos polynomial order. A satisfactory convergence is achieved by using second-order chaos polynomials, which are thereby retained for the rest of the study. As stressed before, accurate information about probability function distributions of the input stochastic parameters is not available. A priori tests carried out using normal distributions and uniform distributions characterized by the same mean and range $\pm 3\sigma$, indicated that the distribution shape affects only marginally the thermodynamic output (see Section 9.3.1). Here, we check how these small differences propagate through the dense gas solver. We choose case MAH (3) and compare the results obtained with the normal input distributions of Table 9.6 (PP10) for uniform distributions characterized by the same mean values and a variation interval equal to $\pm 3\sigma$. Fig. 9.8 shows the distributions of the mean pressure coefficient and of its standard deviation around the airfoil. The mean fields are only slightly affected by the choice of the input distribution, whereas the standard deviation field changes significantly. The affected zone is wider when considering normal distributions, and the peak value, located close to

the airfoil wall in a region characterized by a weak shock wave, is higher. The reason is that when the normal distribution is considered, a greater number of quadrature points produce an extended inversion zone. As a consequence, the probability of capturing nonclassical phenomena is higher when using a normal distribution. This is confirmed by inspection of the computed mean and standard deviations for the drag coefficient; if the mean is only slightly sensitive to the input distribution ($\mu = 0.3161 \cdot 10^{-2}$ for the normally distributed case and $\mu = 0.3031 \cdot 10^{-2}$ for the uniform one), the standard deviation is more than double when normally distributed variables are considered ($0.3692 \cdot 10^{-2}$ vs $0.1560 \cdot 10^{-2}$). Moreover, the output distribution associated to normally distributed input parameters is highly non normal and characterized by lower values of the mean and higher values of the standard deviation. The lower mean drag is due to the fact that nonclassical effects are encountered for a greater number of quadrature points. Since the output solution exhibits a higher sensitivity when using a normal distribution, we consider this choice as the more conservative (worst case possible), and thus, we consider normally distributed input parameters in all subsequent computations. We now consider the propagation of thermodynamic uncertainties for different choices of the working fluid and of the thermodynamic model. The first series of results concerns flows of PP10. The thermodynamic models taken into account are the RKS, PRSV, and MAH (with 3 and 6 uncertain parameters). The uncertain input parameters in the thermodynamic models are assumed to be normally distributed, with means and standard deviations listed in Table 9.5. The reference quantities used to investigate the sensitivity of the computed flow-field to the uncertain thermodynamic model are the drag coefficient and the pressure coefficient. Four series of results are considered in the following: the first and the second one have been obtained by means of the RKS and PRSV models with three uncertain parameters (namely, ω, $c_{v\infty}(T_c)/R$, and n). The third and fourth series have been obtained via the multiparameter MAH model and differ between them for the number of uncertain parameters included in the simulations. In one case, just three model parameters are assumed to vary, namely, the critical pressure and temperature and $c_{v\infty}(T_c)/R$. In the second one, all of the free parameters in the MAH model are assumed as random variables. Figure 9.9 shows the iso-contours of the mean pressure coefficient and its standard deviation for the four cases under study. The deterministic distributions obtained by setting the model parameters to the mean values of the chosen distributions are also reported for reference. For the RKS and PRSV models, the mean solution provided by the chaos collocation method is very similar to the deterministic one. As it could be expected, the region of strongest sensitivity is located around the shock wave. The output distribution is almost symmetric, and the mean location of the shock wave almost coincides with the deterministic one. This is better shown by inspection of Figure 9.10 that displays the wall distributions of the pressure coefficient, with error bars corresponding to $\mu \pm \sigma$. For simpler models, the standard deviation of the pressure coefficient is negligible almost everywhere, except in the shock region, where it takes values up to 40% of the mean. For the MAH model, the appearance of nonclassical nonlinearities amplifies the uncertainties on the input parameters significantly. This result in a considerable dispersion of the computed drag coefficient. Figure 9.11 shows the computed probability density function for the drag coefficient, c_d. This has been obtained via Monte-Carlo sampling over 500 points of the output distribution reconstructed via Eq. (12). For the RKS and the PRSV models, the drag coefficient is characterized by almost normal pdfs. The C_D distribution for RKS exhibits a higher mean than the PRSV one, which is consistent with the fact that the first model predicts a smaller inversion zone and, consequently, more reduced dense gas effects. On the other hand, the RKS model is also slightly less sensitive than PRSV to input uncertainties, and the associated standard deviation is lower. Numerical values for the mean and standard deviation of the drag coefficient, along with the corresponding deterministic values, is provided in Table 9.7. Figures 9.9 and 9.10 also provide results for the comprehensive MAH model. Several remarks are in order. First of all, both the deterministic and the mean stochastic solutions provided by this model strongly differ from those given by the simpler ones. This is due to the fact that, for the chosen

p_c	T_c	Z_c	T_e	n	$c_{v,\infty}(T_c)/R$
$\aleph(16.2, 0.27)$	$\aleph(630.2, 10.5)$	$\aleph(0.286, 0.005)$	$\aleph(467, 7.7)$	$\aleph(0.526, 0.009)$	$\aleph(78.3, 1.31)$

Table 9.6: Distributions of the uncertain parameters used for a posteriori tests. PP10.

Model	$\mu(c_d)$	$\sigma(c_d)$	$(c_d)_{\text{det}}$
RKS	0.6253×10^{-1}	0.7724×10^{-3}	0.6214×10^{-1}
PRSV	0.5175×10^{-1}	0.1177×10^{-2}	0.5150×10^{-1}
MAH, 3 unc.	0.3161×10^{-2}	0.3692×10^{-2}	0.2587×10^{-2}
MAH, 6 unc.	0.4344×10^{-2}	0.6169×10^{-2}	—

Table 9.7: Mean and standard deviations of the computed drag coefficient for different models. Working fluid PP10.

fluid properties and far-field thermodynamic conditions, the MAH model predicts the flow to evolve essentially within or in the immediate neighbouring of the inversion zone. In such conditions, the flow physics is dramatically affected by dense gas effects. Namely, compression shock waves tend to disintegrate and the flow field is almost smooth. Unfortunately, no experimental data are available for this problem, so that there is no mean of determining which models gives the more realistic results. It is quite universally accepted that the MAH model is one of the more accurate models for the computation of thermodynamic properties of fluorinated substances, whenever high-quality data for validation are available. Nevertheless, when applied to substances for which scarce and/or uncertain data are available, the MAH model provides results for the location and extent of the inversion zone that are extremely sensitive to the model parameters, as demonstrated by the preceding a priori tests. As a consequence, the aerodynamic field displays a much greater sensitivity to the input parameter than in the previous computations with the simpler models. Note that the solution computed by considering only three well-chosen uncertain parameters is quite close to that computed by allowing all the model parameters to vary. This demonstrates that the dispersion of the computed results may be quantified with reasonable accuracy using a reduced number of uncertain parameters, that is, with a substantial reduction in the global computational cost. The computed probability density functions for the drag coefficient obtained in the two cases are also shown in Figure 9.11. In this case, the results display significant non-Gaussian interactions, with more dispersion of the data on the high-C_D side of the curve. High-drag values are associated to the presence of a stronger shock wave in the solution, i.e., gas behaviour is closer to the ideal-gas one. The drag coefficient is affected by a very large uncertainty, with standard deviation which is larger than the mean value for both the case with 3 and the case with 6 uncertain model parameters. In the first case, however, the mean drag coefficient is about 20% lower than in the second one (see Table 9.7), in spite of the relatively similar mean pressure coefficient distribution at the wall. This indicates that integrated values are more sensitive than local ones, essentially because of large uncertainties on the shock location. Finally, we remark that the computed means are higher than the deterministic drag coefficient, since small changes in the model parameter produce large variations in the size of the inversion zone, which increases the probability for the flow to evolve outside it.

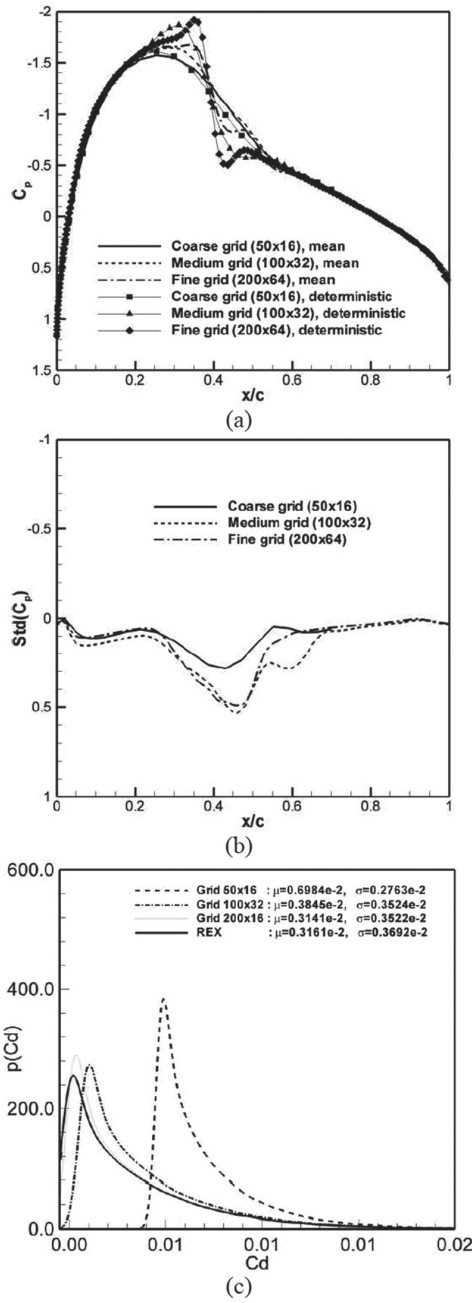

Figure 9.6: Effect of mesh density on the computed results. (a) Mean pressure coefficient at the wall, (b) standard deviation, and (c) probability density distribution of the drag coefficient. The results have been obtained by using the MAH equation with 3 uncertain parameters.

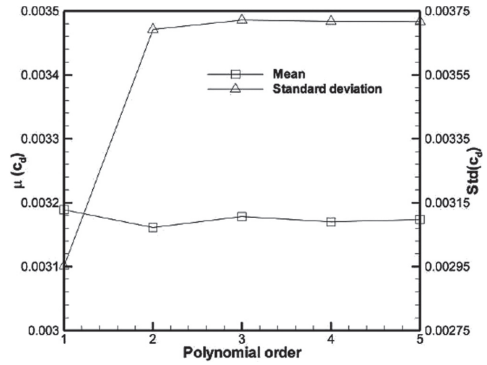

Figure 9.7: Effect of the chaos polynomial order on the mean and standard deviation of the stochastic drag coefficient. The results have been obtained by using the MAH equation with 3 uncertain parameters.

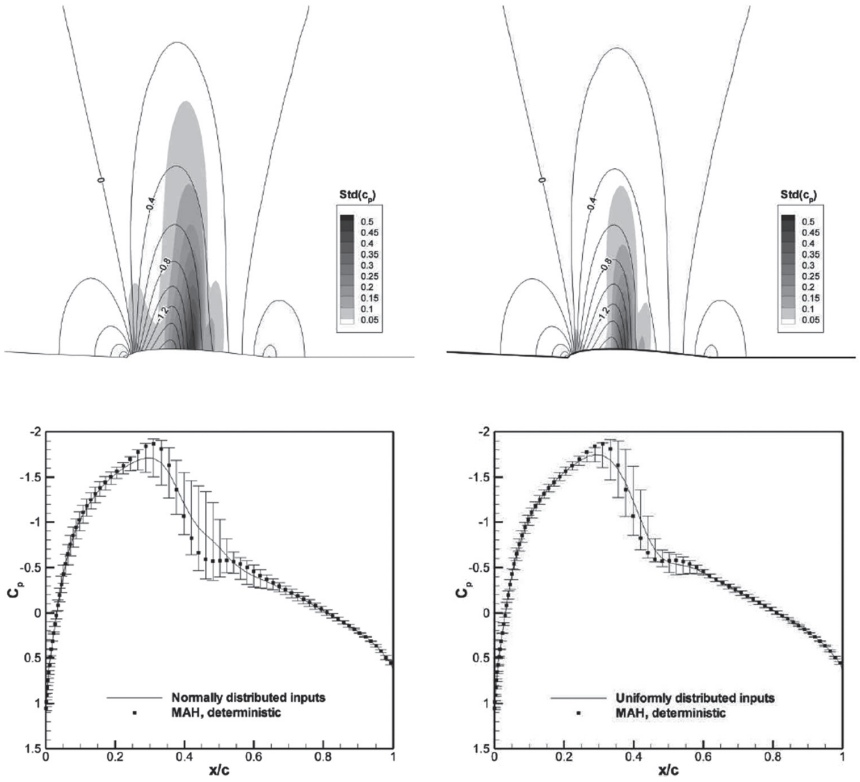

Figure 9.8: Results of stochastic computations for case MAH (3) using normally (left column) and uniformly (right column) distributed input parameters. Top: stochastic pressure coefficient fields (line: mean field; flood: standard deviation). Bottom: pressure coefficient distributions at the wall.

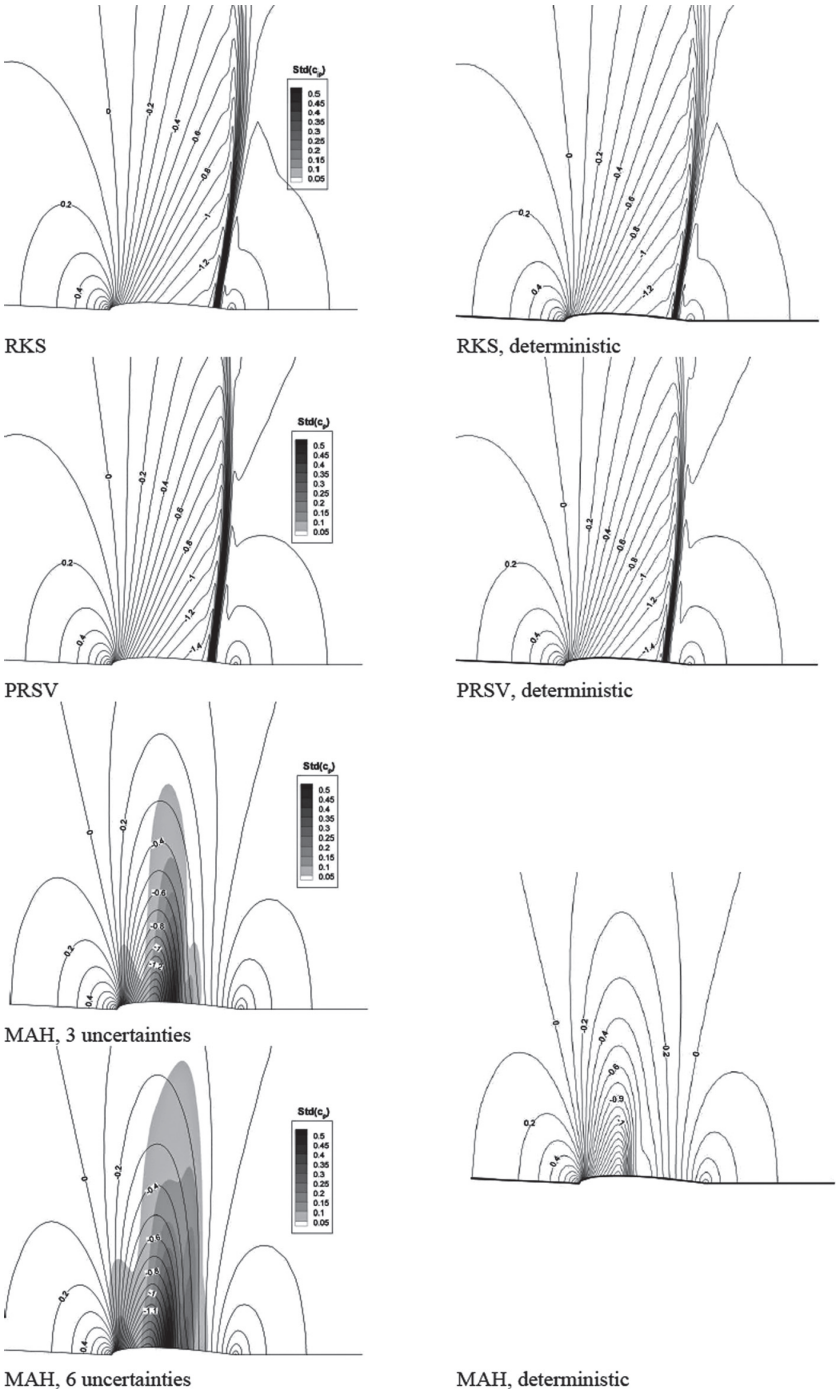

Figure 9.9: Results of stochastic computations for normally distributed input parameters. Working fluid is PP10. Left: stochastic pressure coefficient field, mean value; middle: standard deviation; right: deterministic pressure coefficient field associated to the most probable (mean) values of the input parameters.

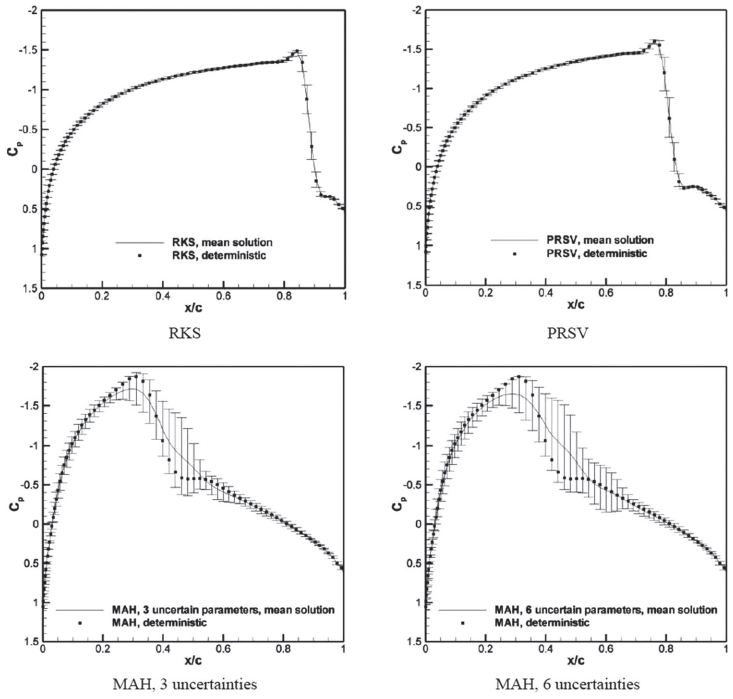

Figure 9.10: Results of stochastic computations for normally distributed input parameters. Working fluid is PP10. Pressure coefficient along the airfoil surface: mean value μ and uncertainty bars $\mu \pm \sigma$.

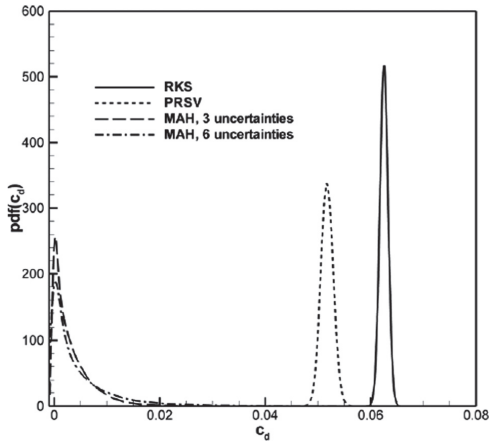

Figure 9.11: Probability density functions for the drag coefficient C_D (working fluid PP10).

Chapter 10

Rarefaction Shock Wave

Contents

A computational method for taking into account backward uncertainty propagation in flow problems is presented and applied to the study of rarefaction shock waves (RSW) in a dense-gas shock tube. Previous theoretical and numerical studies have shown that a RSW is relatively weak and that the prediction of its occurrence and intensity are highly sensitive to uncertainties on the initial flow conditions and on the fluid thermodynamic model. The objective of this study is to introduce an innovative, flexible and efficient algorithm combining computational fluid dynamics (CFD), uncertainty quantification (UQ) tools and metamodel-based optimization in order to obtain a reliable estimate for the RSW probability of occurrence and to prescribe the experimental accuracy requirements ensuring the reproducibility of the measurements with sufficient confidence. Moreover, a second study is presented which is focused on exploring the possibility of using a two-phase shock tube for the reproduction of a RSW.

10.1 Feasibility study on RSW appearance considering UQ and experimental set-up

The purpose of the present study is twofold. First, an efficient and flexible algorithm is described for computing the uncertainty levels to be achieved on input parameters of a flow problem (such as measured initial flow conditions) so as to ensure a prescribed level of uncertainty on the experiment output. Secondly, the proposed algorithm is applied to the prediction of occurrence for a rarefaction shock wave in the FAST experiment (see Figure 10.1). Note the methodology proposed and followed

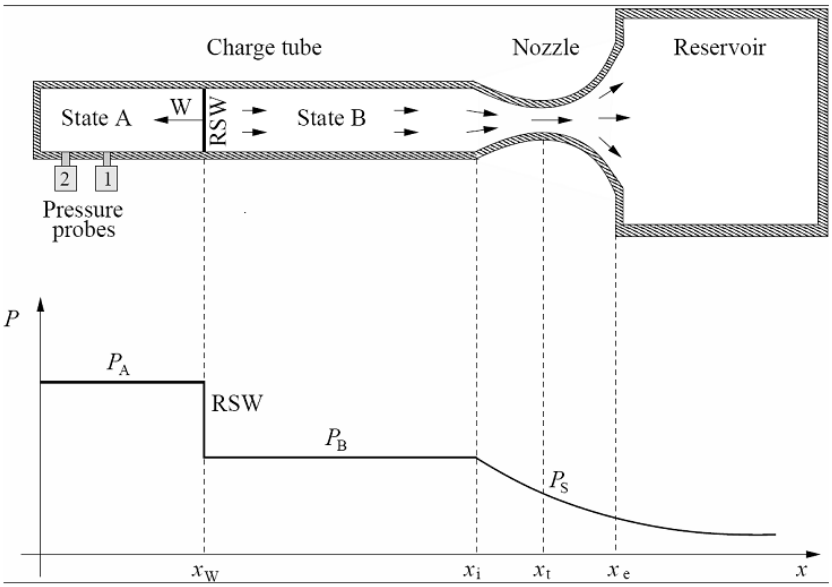

Figure 10.1: Schematic view (top) of the FAST setup and of a rarefaction shock wave experiment. Qualitative pressure profile (below) along the shock tube some time after the opening of the valve located at $x = x_i$.

in this study can also be easily extended to tackle the complex problem of turbomachinery design in the particular case of ORC turbines exploiting nonclassical gas dynamics effects.

10.1.1 CFD solvers for dense gas flows

zFlow is a CFD code capable of treating dense-gas flows [Colonna 2004, Colonna 2003, Colonna 2008c, Harinck 2009, Harinck 2010, Rebay 2009, Turunen-Saaresti 2010a]. It is linked to the FluidProp library [Colonna 2005], which implements a wide variety of thermodynamic models. zFlow can solve the Euler and the RANS equations coupled with the high- or low-Reynolds number k-ω turbulence models in 1D, 2D and 3D. Other distinguishing features are a high resolution upwind space discretization method for the advective parts of the equations suited to general unstructured and hybrid grids and the use of an implicit time-integration scheme which proved to be crucial for the effective computations of fluids modeled with complex and therefore very computationally demanding equations of state.

The NZDG code has been developed at LEGI in Grenoble [Congedo 2007, Congedo 2011a]. It solves the quasi-1D Euler equations with second-order accuracy in time and space. The convective fluxes are discretized using the Roe numerical flux and a second-order limited MUSCL variable reconstruction. The Roe average for dense gas flows is computed with the simplified approach proposed in [Cinnella 2006] and the slope limiter introduced in the linear reconstruction is of the Van Albada type. Second-order accuracy in time and robust time-integration are achieved using a three-level implicit formula to approximate the physical time-derivative, within a dual-time sub-iterative approach to solve the resulting non-linear system.

10.1.2 Sources of Uncertainty

Two main sources of uncertainties are considered in this study: i) the uncertainties on the fluid initial state (p, T) in the charge tube of the FAST, denoted as IC uncertainties from now on and ii) the uncertainties on the thermodynamic model denoted as TD uncertainties hereafter. These

uncertainties affecting the flow simulation can be propagated either in the sole PRSV EoS (Eq. (7.2)) or in the EoS coupled with the unsteady Euler equations describing the flow evolution in the shock-tube. The first approach is referred to as an *a priori* strategy for analyzing uncertainty and is used in Section 10.1.4 to determine the best initial condition for the shock tube experiment. The second approach is called *a posteriori* and is applied in Section 10.1.5 and 10.1.6, respectively in a forward and backward-propagation mode. The goal of solving the forward uncertainty propagation problem is to quantify the impact of prescribed IC and TD uncertainty levels on the RSW probability of occurrence. The study of the backward uncertainty problem yields the estimation of the IC and TD uncertainty levels allowing to ensure a prescribed probability of occurrence for the RSW in the shock tube. In the present work, the uncertain parameters will be systematically assumed to follow a uniform probability density function; consequently, these parameters will be described by their intervals of variation denoted $\%IC, \%TD$.

10.1.2.1 Uncertainties in the initial conditions of the experiment

The initial conditions (IC) for the experiment (and for the simulation) are prescribed so as to maximize the Mach number of the rarefaction shock wave and thus makes its detection easier, according to the method briefly described in [Colonna 2008a]. The maximum achievable accuracy on the temperature and pressure levels in the charge tube has been deduced from the measurement instruments and hardware specifications to be 0.4% for the pressure and 0.1% for the temperature [Colonna 2008a]. Both the specification of the IC conditions and the accuracy achievable with the FAST instrumentation and control are still subject of investigation and the results of this work will help directing the efforts. In this study, initial left state (pressure p_L and temperature T_L) and right state (p_R and T_R) are assumed uncertain.

10.1.2.2 Uncertainties on the thermodynamic model

See Section 9.2 for the model-uncertainties of PRSV model.

10.1.3 Backward uncertainty propagation algorithm

10.1.3.1 Definition of the inverse problem

The objective of the study is to find optimal uncertainty bars on input data ensuring target statistic properties for the output of interest. Obviously, if uncertainty bars are reduced on the input data, the variability of the output in terms of statistical moments will be also reduced. However, reducing the uncertainty bars on input data can be costly or simply unfeasible because, for instance, of measurement tools tolerance that limit the practically achievable accuracy. Using the notations introduced in the previous section, the *inverse problem* to solve can be mathematically expressed as:

$$\underset{\boldsymbol{\xi}}{min}(|\mu_{\mathrm{u}_i} - Q|) \quad \text{and} \quad \underset{\boldsymbol{\xi}}{max}\,(\|\Delta\boldsymbol{\xi}\|) \tag{10.1}$$

where the uncertain parameters $\{\xi_1, \ldots, \xi_{\mathrm{n}_\xi}\}$ vary in a solution space made of intervals defined as $\left[\overline{\xi_i} - \Delta\xi_i \,;\, \overline{\xi_i} + \Delta\xi_i\right]$ with $\overline{\xi_i}$ the reference mean value for ξ_i and with $\Delta\boldsymbol{\xi} = \{\Delta\xi_1, \ldots, \Delta\xi_{\mathrm{n}_\xi}\}$. The quantity Q denotes the target value for the moment of interest μ_{u_i}, and $\|\boldsymbol{\xi}\|$ is a L2-norm.

The problem defined by Eq. (10.1) is a particular optimization problem, where the vector $\Delta\boldsymbol{\xi}$ defining the extent of the solution space is used at the same time to build a fitness function to minimize. The problem defined by Eq. (10.1) can be typically formulated by an experimentalist when setting up an experiment: it aims at finding which uncertainty bars should be ensured for the input parameters in order to ensure a given statistic property for the output of interest. Remark that uncertainty bars in that case would be usually fixed according to the tolerance of the measurement

tools. Looking for the maximum values of uncertainty bars on the input parameters that allow to preserve the reproducibility of the experiment (by satisfying a prescribed statistical property Q on the output moment μ_{u_i}) can be interpreted as a way to relax as much as possible the constraints on the measurement tools to be used in the experiment without compromising the quality of the measurement.

10.1.3.2 Definition of efficient strategies to solve the stochastic inverse problem

The present study is focused on a flexible algorithm, independent of the way to compute μ_{u_i} in Eq. (10.1). The basic structure of this algorithm is presented in Fig. 10.2. For each design vector defined by a set of values for the error bars $\Delta\xi_{i=1,..,n_\xi}$, a stochastic simulation is performed by coupling a non-intrusive stochastic method with the CFD code used as a black box to yield an estimate for μ_{u_i}. This process is applied to an initial population of design vectors which is evolved using a genetic algorithm (GA); after a few generations, an Artificial Neural Network (ANN) is coupled with the GA in order to reduce the optimization cost (for more details concerning the ANN, see [Congedo 2007, Cinnella 2008b]), *i.e.* the CFD and UQ calculation are replaced with an inexpensive ANN response. The algorithm is processed until a convergence criterion is met. Since Eq. (10.1) defines a bi-objective optimization problem, its solution is not necessarily unique; when applied to the study of RSW in the fast shock tube (see Section 10.1.6) the outcome of the method will be however a single set of optimal error bars, $\Delta\xi_{OPT-i=1,..,n_\xi}$, improving the reproducibility of the experiment. This so-called full approach algorithm displays several advantages. The use of GA decouples the optimization operators from the stochastic ones. The same algorithm can be used regardless of the cost function definition, order of the statistical moment of interest, thus offering a great flexibility. The computational cost of the method can be measured by counting the numbers of CFD simulations required in order to achieve convergence. The overall cost is the product of the number of stochastic evaluations (computation of μ_{u_i} for a given design vector) needed by the optimization algorithm (directly related to the population size, number of generations, use of ANN) multiplied by the number of CFD evaluations needed by the UQ method to compute each value of μ_{u_i}. Using the PC approach described in Section 4.1.2 with the 8 uncertainties reported in Section 10.1.2, at least dozens of CFD runs will be needed for the stochastic evaluation of a given design; for an 8-parameter problem the GA will need at least a few hundreds design computations to yield a nearly converged solution or set of solutions. Consequently, thousands of CFD runs are likely to be needed in order to solve the problem defined by Eq. (10.1), which can represent an excessive computational cost. A reduced-cost approach is consequently proposed hereafter, as an alternative to the previous brute-force approach. The proposed reduced-cost algorithm is schematized in Fig. 10.3 and is based on the following steps:

1. Assuming the moments of interest μ_{u_i} used in the formulation of Eq. (10.1) include the variance σ of a physical quantity, perform a preliminary ANOVA analysis with a set of initial values for $\Delta\xi_{i=1,..,n_\xi}$.

2. Find the $n_{\xi'}$ most influential parameters $\xi_{i=1,..,n_{\xi'}}$ and discard the $(n_\xi - n_{\xi'})$ negligible ones to build a new vector, $\Delta\boldsymbol{\xi}' = \Delta\xi'_{i=1,..,n_{\xi'}}$ where $\Delta\xi'_1$, ..., $\Delta\xi'_{n_{\xi'}}$ are ordered by decreasing rank of influence.

3. Apply GA and ANN to solve Eq. (10.1) with the subset of error bars $\Delta\xi'_{i=1,..,n_R}$ starting with $n_R = 1$.

4. When the optimization algorithm reaches convergence, an optimal set $\Delta\xi'_{OPT-i=1,..,n_R}$ is generated. Since the GA is coupled with the meta-model derived from the ANN, an a-posteriori stochastic analysis should be performed by considering $n_{\xi'}$ with the theoretically optimal

$\Delta\xi'_{OPT-i=1,..,n_R}$ and the initial $\Delta\xi'_{i=n_R,..,n_{\xi'}}$) in order to check the solution provided by the optimizer remains optimal or at least improves the objective $|\mu_{u_i} - Q|$ with respect to the initial vector $\Delta\xi_{i=1,..,n_\xi}$.

5. If the error bars ($\Delta\xi'_{OPT-i=1,..,n_R}$) are not physically acceptable (typically because they are well below the physically achievable measurement accuracy), then increase n_R by one (thus increasing the number of degrees of freedom for finding a solution of Eq. (10.1)) and restart from Step 3.

The computational cost of the above algorithm is strongly reduced with respect to the full approach, first of all because of the reduction of the number of uncertain parameters, based on the preliminary ANOVA analysis. The progressive increase of the number of variable error bars $\Delta\xi'_i$ may also significantly contribute to the speed-up of the algorithm if using $n_R < n_{\xi'}$ is sufficient to yield physically acceptable error bars $\Delta\xi'_{OPT-i=1,..,n_R}$.

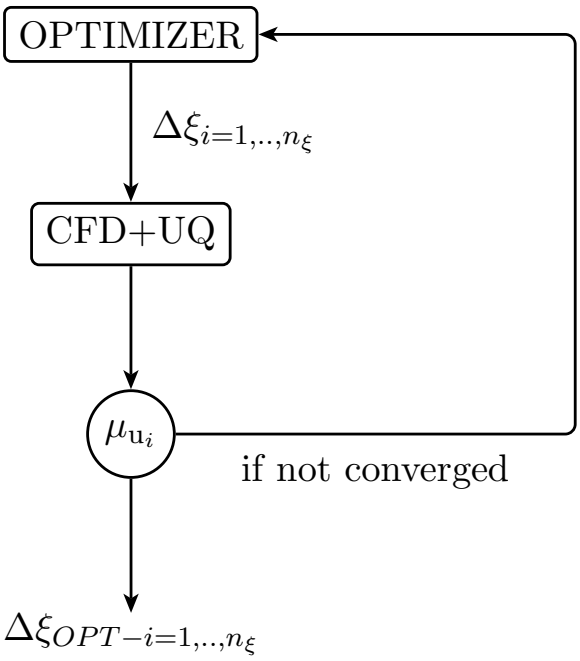

Figure 10.2: Brute-force or full approach algorithm for stochastic inverse design.

10.1.4 Preliminary analysis on dense gas shock-tube

The FAST setup is the outcome of several studies aimed at determining the best option in order to generate and measure a rarefaction shock wave, the most dramatic of the predicted nonclassical gas dynamics effects. The principles of operation and the design of the FAST are reported in [Colonna 2008a], where the results of a preliminary computation for the initial fluid thermodynamic states in the charge tube and in the reservoir (Fig. 10.1) are reported. The PRSV EoS was then adopted and the recommended fluid thermodynamic state in the charge tube corresponds to the PA point ($p = 9.12$ bar, $v = 4.92 \cdot 10^{-3}$ m^3/kg, $T = 368.97$°C) of Fig. 10.4 located on the D_6 saturation curve. The thermal control system of the setup is designed to achieve a small degree of superheating, in order to avoid condensation, which could hamper the interpretation of the results.

Recently, a rigorous theory has been developed, see [Guardone 2010], which allows for the computation of the operating conditions leading to the RSW with maximum intensity or wave Mach

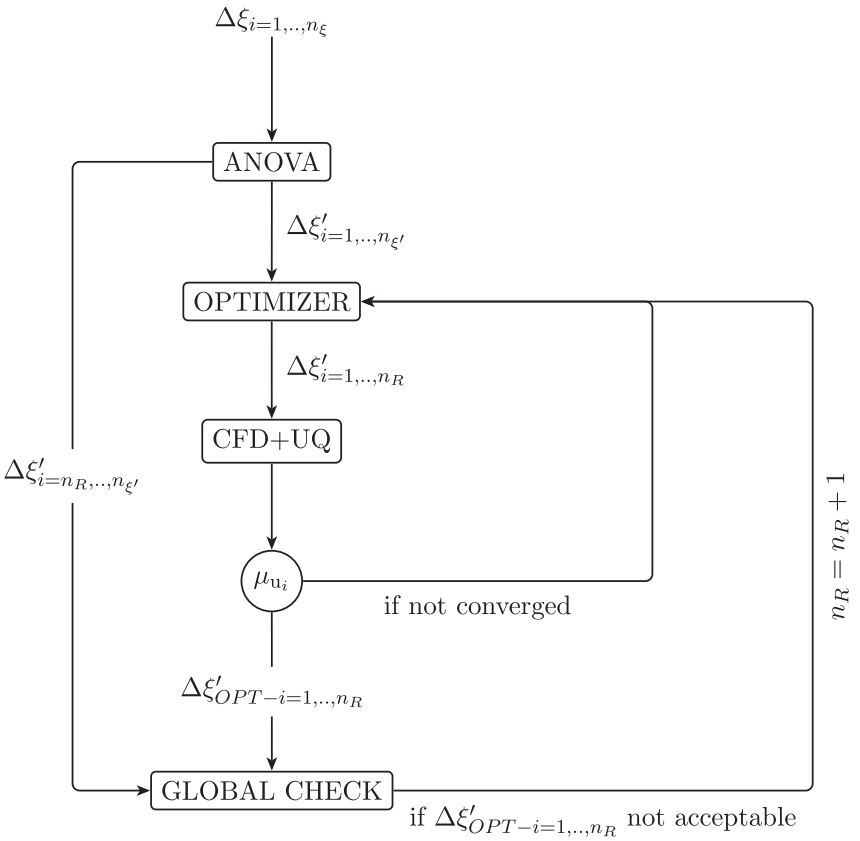

Figure 10.3: Reduced-cost algorithm for stochastic inverse design.

number, thus maximizing the effect and easing its measurement. Using this theory and a multi-parameter equation of Span-Wagner (SW) type, the conditions in the charge tube that maximize the wave Mach number have been computed as $T \approx 371°\text{C}$, $v \approx 4.0 \cdot 10^{-3}\ m^3/\text{kg}$). These values correspond to a higher pressure and temperature when compared to the preliminary estimation reported in [Colonna 2008a]. This theory has not been employed yet in our investigation, as it would demand for additional work in order to obtain the initial conditions for the FAST experiment with the PRSV thermodynamic model in place of SW. The validity of the methodology herein described remains unaffected and the results we obtain here are therefore possibly sub-optimal. The continuation of this work will be aimed at selecting more favorable initial conditions and better characterizing the source of uncertainty related to measurement and control system, thanks to operational experience. With reference to Fig. 10.1, state A must therefore be in the superheated vapor region if both IC and TD uncertainties are taken into account. According to preliminary method described in [Colonna 2008a] state A must also be located within the inversion region ($\Gamma(p,T) < 0$) and should maximize the strength of the RSW.

In order to better understand the left state effect on the RSW characteristics, a parametric study is first performed by varying the IC: while the left state (pressure p_L and temperature T_L) varies in a region between the saturation curve and the $\Gamma = 0$ curve, the right state is obtained by fixing a pressure ratio p_R/p_L consistent with the value used in [Colonna 2008a] and a right temperature $T_R = T_L$. A CFD computation using NZDG for each combination of $(p_L, T_L), (p_R, T_R)$ is performed and the Mach associated to the RSW is stored. The resulting Mach contours are plotted in the p-v plane in Fig. 10.4 and illustrate a left state close to the saturation curve is required in order to obtain the wave Mach number greater than unity, which is a mandatory feature of the RSW. Consequently, an optimal choice of initial left state should meet the following requirements when

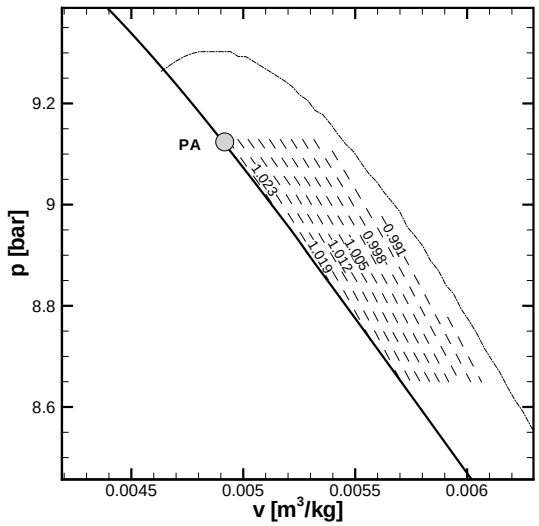

Figure 10.4: Dashed lines: iso-Mach contours of RSW, where each point of the contour represents the shock tube left state in the Amagat diagram; solid line: saturation curve; dashdotted line: $\Gamma = 0$ line.

IC and TD uncertainties are included in its *a priori* stochastic analysis: (R_1) is in the single-phase vapor region, (R_2) is close to the saturation curve.
An automatic procedure has been set up to compute such a state, which relies on an *a priori* analysis based on thermodynamic considerations only; the *a posteriori* analysis based on CFD computations including the PRSV EoS is discussed in the next Section. The algorithm used to automatically detect an initial left state satisfying the aforementioned requirements is based on three steps: in the first step, a discretization of the p-v plane has been generated by moving along isobaric and isentropic curves; in the second step, the uncertainty region is computed using the given IC uncertainty levels on initial pressure and temperature and a Monte Carlo approach; in the third step, it is verified that the uncertainty region does not cross the maximal saturation curve (computed with the TD uncertainties taken into account) and that the chosen point is located as close as possible to the saturation curve. This analysis yields a new initial left state, denoted P1 ($p = 9.09$ bar, $v = 5.25 \cdot 10^{-3}$ m^3/kg, $T = 369.63$°C) from now on, plotted in Fig.10.5 with its associated uncertainty region. It can be checked that this uncertainty region satisfies the requirements (R_1) and (R_2); more precisely the P1 uncertainty region has a single point in common with the maximal saturation curve computed with the TD uncertainties taken into account. The RSW Mach number associated with P1 is equal to 1.010, with $M_{RSW} = \frac{W}{a_A}$ (see Fig. 10.1); for point PA, $M_{RSW} = 1.023$. The robustness of point P1 for successfully performing the FAST experiment, that is ensuring with maximum likelihood the occurrence of a RSW in the shock tube, is assessed in the following *a posteriori* analysis.

10.1.5 Forward uncertainty propagation problem

The stochastic properties of the RSW generated in the shock tube with uncertain IC and TD are computed in order to assess the probability of occurrence for the RSW. A detailed cross-validation of the two numerical codes used to compute the dense gas flows is first described and the convergence of the stochastic method is analyzed; the occurrence of RSW for P1 initial conditions is discussed next.

The deterministic solution has been verified by means of comparisons between the zFlow and NZDG numerical codes. In this first numerical study, the initial conditions are taken from

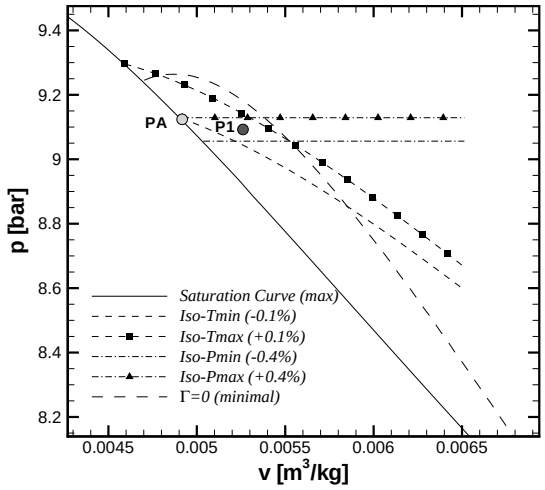

Figure 10.5: Robust point (P1) obtained by means of an automatic *a priori* procedure along with its associated uncertainty region.

[Colonna 2008a] and the Riemann problem solutions provided by both codes are compared at a non-dimensional time $t/t_c = 2.5$ (where $t_c = L/\sqrt{p_c v_c}$ with $L = 1\,m$). The verification drawn for this time instant remains valid for subsequent time steps. As shown in Fig. 10.6, solutions obtained on the same grid are very similar with only a slight difference near the expansion shock. In this region, the NZDG solution appears a bit less dissipative than the zFlow solution. Both numerical solutions are superimposed in the nozzle region. The same trends are observed for the density and Mach number distributions. Seeing that the results are very similar, only the NZDG code has been used in the following computations. A mesh of 2000 cells has been retained, after a convergence study not reported here for the sake of brevity. Each deterministic computation takes about 5 minutes on a Intel Westmere-EP processor.

Statistic computations have been performed for various sources of uncertainty (on initial conditions IC and/or thermodynamic model TD) and with various stochastic methods for a comprehensive validation of the results. The stochastic solutions provided by the PC method have been compared with Monte Carlo computations taken as reference. Comparisons have been made at different time steps with uncertainty sources taken into account separately (IC or TD) and together (IC+TD). In this work, when coupled uncertainties are considered (IC+TD), PC is systematically applied with Sparse Grid integration in order to reduce computational cost. Remark also that every stochastic result presented in the following, has been obtained after a convergence study (on the number of realizations for Monte Carlo method, and on the polynomial order for PC), not reported here for brevity.

The P1 conditions produced by the a priori analysis have been retained for the left initial state. The reference solution obtained for the pressure distribution using a Monte Carlo technique for uncertain IC and TD is reported in Fig. 10.7. The mean stochastic solution and the deterministic solution differ near the RSW, the latter being sharper as expected. In Fig. 10.7, the region between the maximal and minimal pressure distributions along the tube represents the variability region for the stochastic solution when all the uncertainty sources are taken into account. In Fig. 10.8, the pressure standard deviation along the tube is compared for PC, SSC and Monte Carlo at a non-dimensional time of 2.5, when only IC uncertainties are taken into account. Monte Carlo and PC solutions show a great similarity with a difference of only 1% on the computed standard deviation

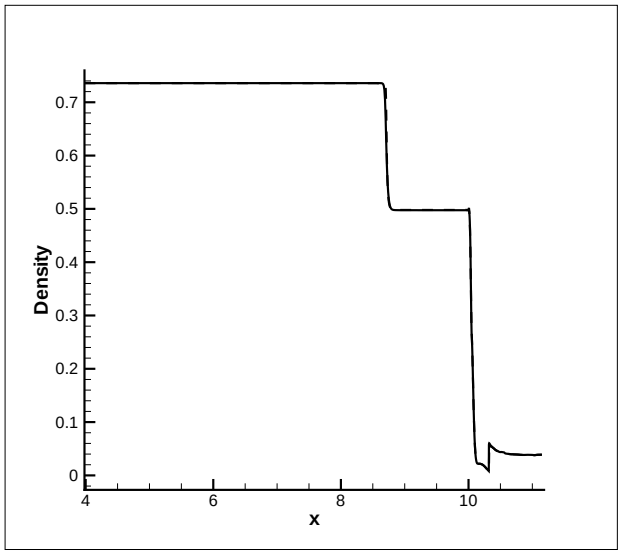

(a)

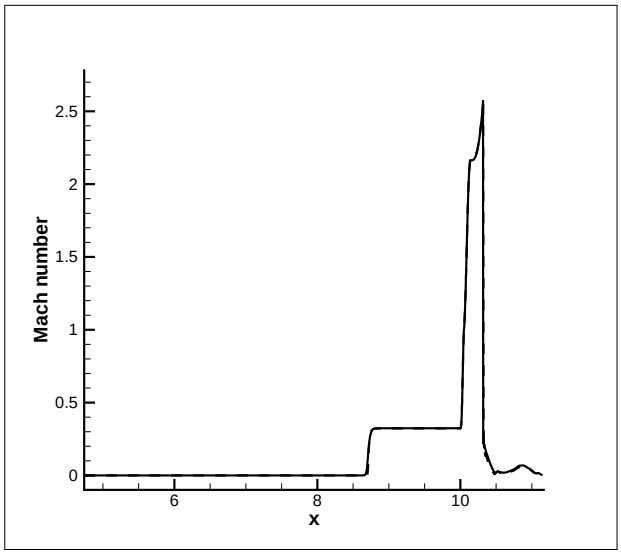

(b)

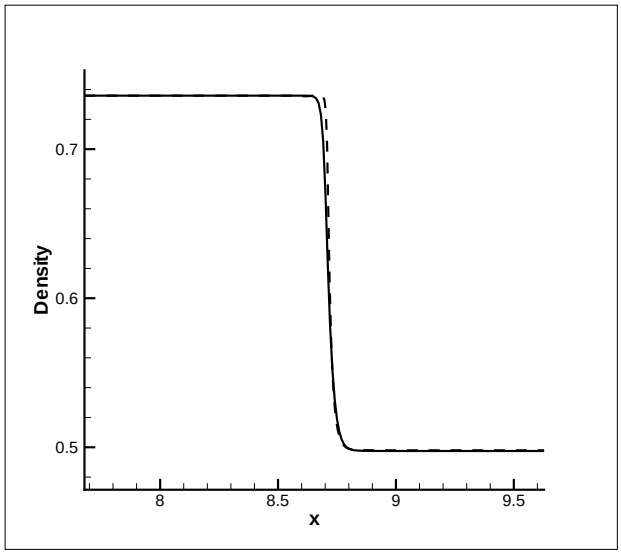

(c)

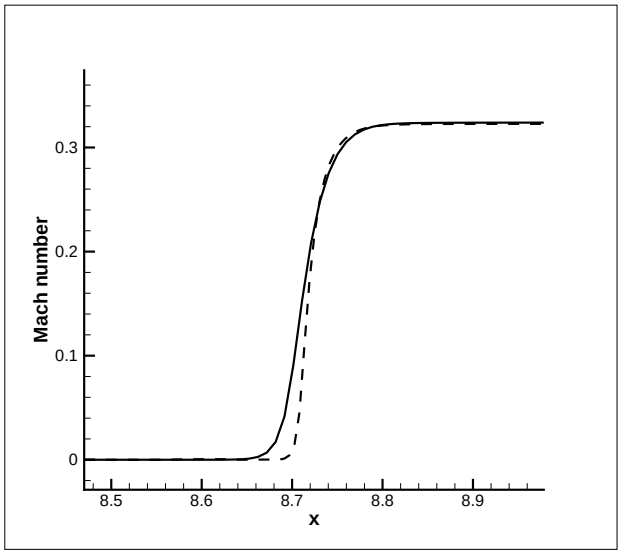

(d)

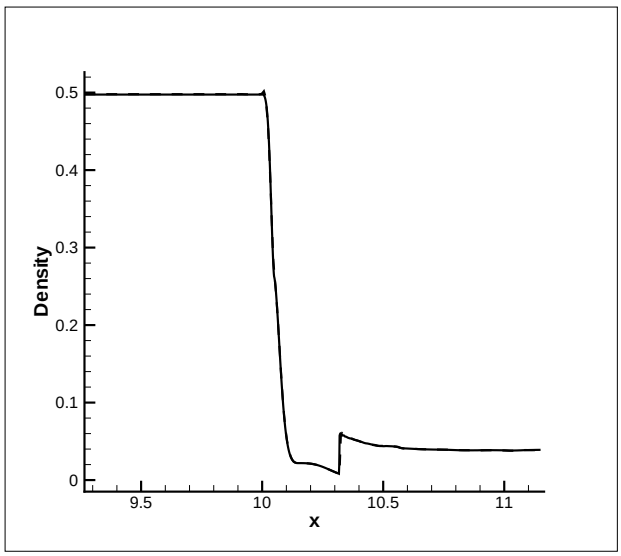

(e)

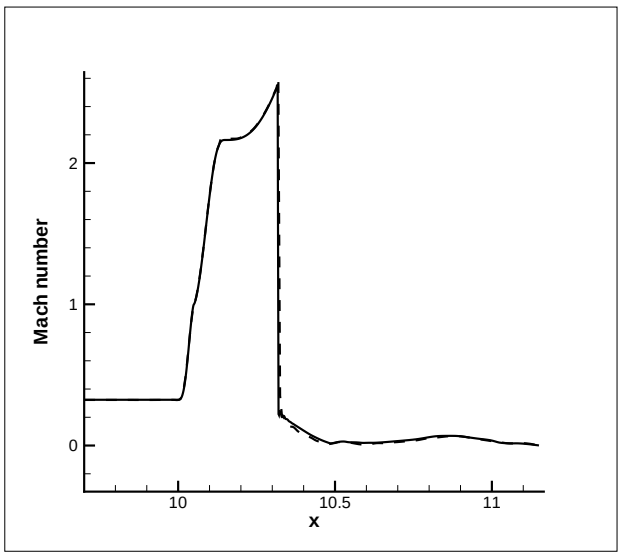

(f)

Figure 10.6: Solid line: zFlow; dashed line: NZDG. (a,c,e) Density (v_c/v); (b,d,f) Mach number. Solution along the tube (a,b), close-up on the expansion shock region (c,d), close-up on the nozzle region (e,f). Non-dimensional time $t/t_c = 2.5$, x expressed in [m].

	IC	TD	$IC + TD$
X_s	0.12	0.09	0.14
U_s	0.45	0.31	0.49
M_s	0.38	0.50	0.46

Table 10.1: % variation between Monte Carlo and PC on position X_s, velocity U_s and Mach number M_s of the shock, when uncertainties on initial conditions and thermodynamic models are considered separately (IC and TD), and together (IC+TD).

peak, as shown in Fig. 10.8. For PC method only 81 computations are necessary (only four uncertain parameters are considered and a second order PC) with respect to 5000 Monte Carlo evaluations. The SSC method is found to be less accurate in the peak region with a difference of 7.5% with respect to Monte Carlo ; note however that the SSC results have been obtained with fewer (only 35) computations.

In Table 10.1, comparisons of Monte Carlo and PC results are reported in terms of the RSW position, velocity and Mach number at a non-dimensional time of 2.5. The values provided in Table 10.1 express the difference on the computed coefficient of variation (standard deviation divided by the mean value). These variations have been computed when each source of uncertainty (IC or TD) is considered separately and when they are simultaneously taken into account. The difference between Monte Carlo and PC remain below 0.5% in all the cases, which confirms again that accurate statistics can be computed with very few solution evaluations using PC. Note the differences in statistic computations have been compared at several non-dimensional time steps, 1.5, 2.0, 2.5, and the same trends have been systematically observed.

The influence of each source of uncertainty on RSW properties is now analyzed using PC stochastic results. The coefficients of variation for the RSW features are reported in Table 10.3. The uncertainties on initial conditions are clearly dominant for the shock position and velocity; when analyzing the shock Mach number, uncertainties on IC and TD are of comparable level. In Fig. 10.9, the distribution of the non-dimensional pressure standard deviation is reported along the tube, where uncertainties on IC and TD are considered separately or simultaneously. The solutions for IC and IC+TD are almost coincident (see in particular the close-up on the shock region displayed in Fig. 10.9). The same analysis has been performed at different times (1.5, 2.0, 2.5) and similar conclusions can be drawn.

Since Monte Carlo computations have been performed in this study, owing to the reduced computational cost of the quasi-1D flow, it is possible to compute the probability distribution for the Mach number of the left-running wave. Specifically we are interested in computing the probability for the RSW Mach number to be less than unity since $M_{RSW} > 1$ is a necessary condition to observe a RSW. As shown in Fig. 10.10, this probability is equal to 27.8%, a clearly unsatisfactory prospect for the reproducibility of the experiments since the RSW will likely be observed roughly three times in four shock tube shots. In order to increase the probability for the RSW Mach number to be greater than unity, it is necessary to reduce the level of variability on the IC and TD uncertainty sources while remaining within realistic bounds as far as physical accuracy is concerned. This means solving an inverse stochastic design problem of the form given by Eq. (10.1) thanks to the computational strategies described in Section 10.1.3.2. The next Section will be devoted to the application of the reduced-cost algorithm to determine the maximum uncertainty levels compatible with a prescribed probability for the left-running wave Mach number to be greater than unity.

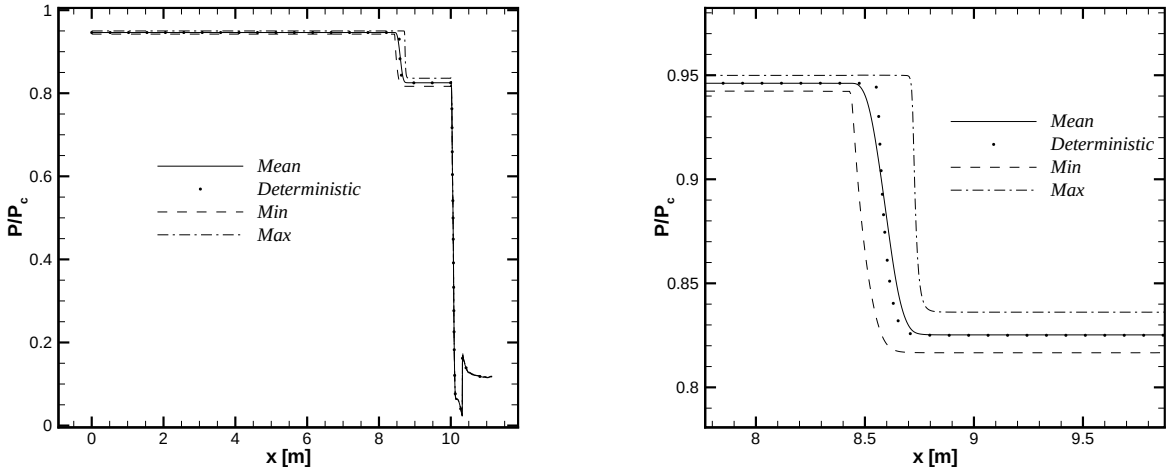

(a) (b)

Figure 10.7: (a) Mean, maximal and minimal pressure along the tube computed by means of Monte Carlo computation (uncertainties on initial conditions and thermodynamic model); (b) close-up on the expansion shock region. Non-dimensional time $t/t_c = 2.5$.

ω	K_1	n	$c_{v,\infty}(T_c)/R$
0.740	-0.02798	0.5095	105.88

Table 10.2: Mean values of parameters of the adopted fluid thermodynamic model (PRSV + power law for $c_{v,\infty}$) for the D_6. Values are taken from [Colonna 2008b].

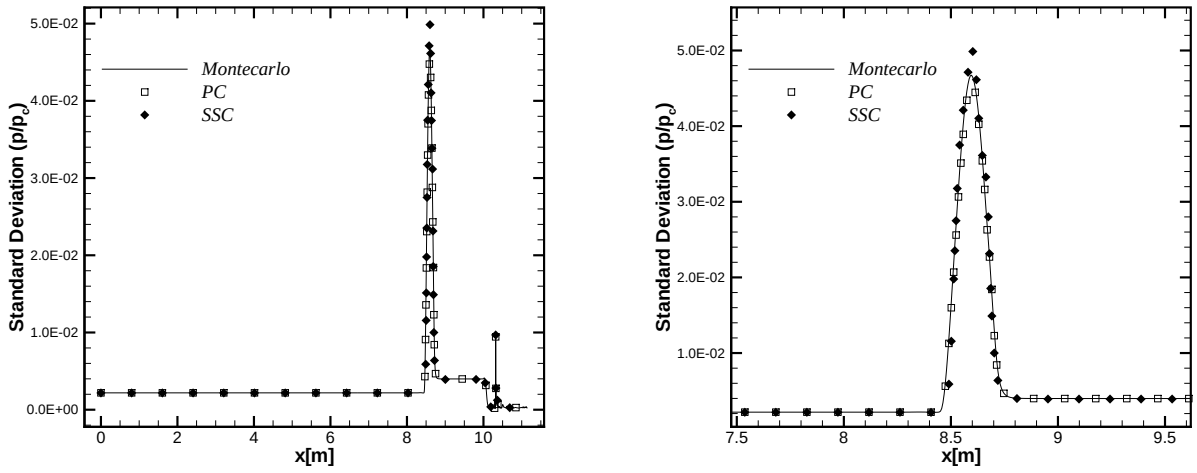

(a) (b)

Figure 10.8: (a) Comparison of pressure standard deviation between Monte Carlo, PC and SSC (uncertainties on initial conditions); (b) close-up on the expansion shock region. Non-dimensional time $t/t_c = 2.5$.

	IC	TD	$IC+TD$
X_s	0.58	0.06	0.59
U_s	3.21	0.31	3.24
M_s	0.80	0.39	0.90

Table 10.3: Computed coefficient of variation (in %) using PC for the position X_s of the RSW, the velocity U_s and the Mach number M_s of the RSW, when sources of uncertainties are considered separately (IC and TD) or together (IC+TD). Non-dimensional time $t/t_c = 2.5$.

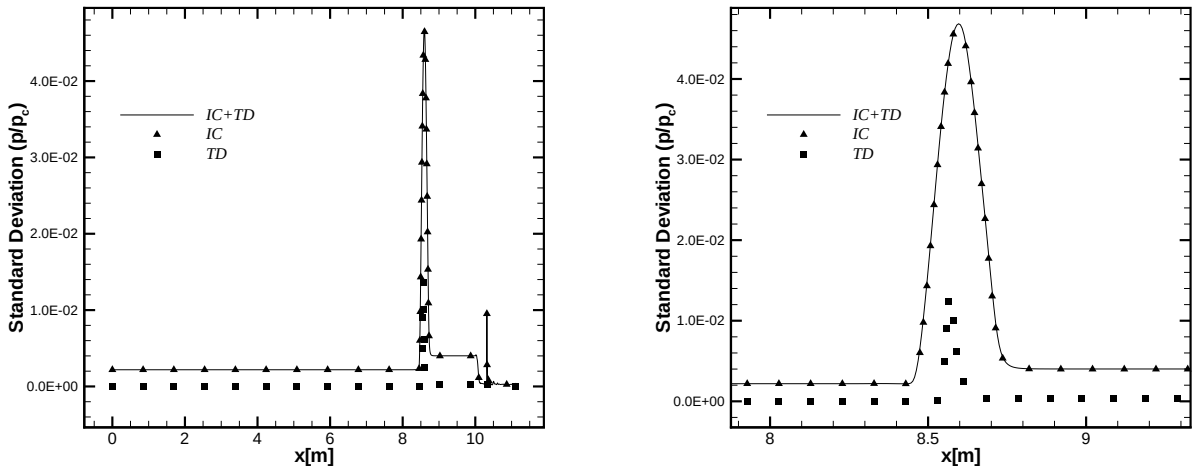

(a) (b)

Figure 10.9: (a) Standard deviation of pressure along the shock tube using PC, when uncertainties on initial conditions (IC) and thermodynamic model (TD) are considered separately and together (IC+TD); (b) close-up on the expansion shock region. Non-dimensional time $t/t_c = 2.5$.

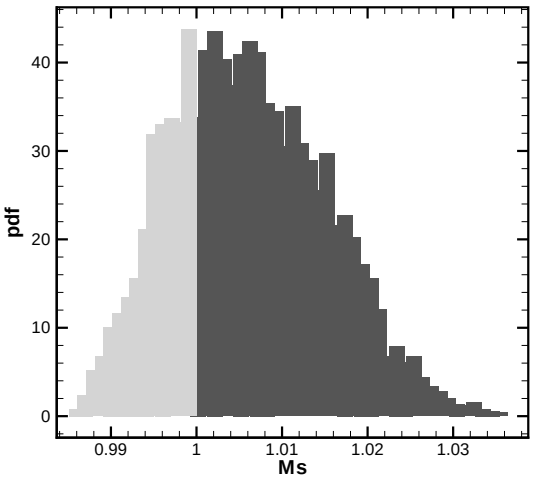

Figure 10.10: Probability density function for the left-running wave Mach number, computed from Monte Carlo results. Probability for the Mach to be inferior to unity equal to 27.8%.

10.1.6 Backward uncertainty propagation problem

Assessing the reduction of the IC and TD uncertainty required to increase the probability for M_{RSW} to be greater than unity can be cast as an inverse analysis problem solved by coupling statistical tools and optimization algorithms. The problem can also be defined as finding the maximum uncertainty bars for the uncertain parameters which allow minimizing the probability for the RSW Mach number to be less than unity, that is

$$\min_{\%IC,\%TD} \left(Prob\left(M<1\right)\right) \quad \text{and} \quad max\left(\%IC,\%TD\right), \tag{10.2}$$

where it is recalled that $\%IC$ denotes the extent of variation for the initial conditions around point P1 while $\%TD$ denote the extent of variation of the thermodynamic properties around the mean values summarized in Table 10.2.
The full optimization problem Eq. (10.2) is hard to solve directly because of its computational cost. Indeed, computing the probability with a good degree of accuracy requires large Monte Carlo ensembles of computations. Since the uncertainty bars must be optimized, ensemble runs have to be performed for every set of parameters considered during the optimization, which is obviously unfeasible. On the other hand, PC could be considered since, as previously demonstrated, it offers good accuracy with a limited computational cost. However, if PC provides accurate evaluations of the solution statistics, such as the mean value and the standard deviation, it is typically not appropriate to evaluate the probability for the Mach number to be less than unity (it is in fact a biased estimator and tail probabilities are affected by the truncation in the expansion). The optimization problem described in Eq. (10.2) is instead converted into the following equivalent reliability problem, where the maximum uncertainty bars allowing to minimize the quantity $|\mu-\sigma-1|$ are looked for:

$$\min_{\%IC,\%TD}\left(|\mu-\sigma-1|\right) \quad \text{and} \quad max\left(\%IC,\%TD\right), \tag{10.3}$$

where μ is the mean of the RSW Mach number and σ its standard deviation. Both quantities can be accurately computed using PC.

The problem (10.3), where PC is used for statistics, remains hard to solve because of the large number of uncertain parameters (eight). Cost reduction is achieved using the algorithm (see Fig. 10.3) previously introduced in section 10.1.3.2, which relies on an ANOVA analysis, stochastic dimension reduction and a metamodel-based optimization. The ANOVA analysis, or analysis of the contributions to the variance, is useful to find the input parameters that contribute the most to the output uncertainty. Once the uncertain inputs are ranked, only a subset of those most significant is considered, so that the cost of the stochastic optimization is reduced. In addition, metamodels can be constructed for the output $|\mu-\sigma-1|$ using sampling computations (a few generations of the genetic algorithm) and neural networks [Congedo 2011a], thus allowing a further reduction of the number of objective function evaluations requiring a full CFD simulation. Finally, a Monte Carlo computation is performed with the optimized parameters obtained from the previous step and $Prob(M<1)$ is assessed. An ANOVA analysis based on a Polynomial Chaos expansion (starting from a Sobol plan of 5000 realizations) and 8 uncertainties is first performed. The contribution of each parameter to the global variance is then computed. As indicated in Fig. 10.11, T_L, $c_{v,\infty}\left(T_c\right)$ and P_L contribute 92% of the variance, and uncertainty on T_L alone contributes 60%. Some uncertain parameters, such as p_R, T_R and K_1, have not been reported in Fig. 10.11 because of their negligible contribution. These results hold also when different times are considered (1.5, 2.0) and therefore a representative stochastic computation inside the optimization loop can be carried out by considering only the uncertainty on T_L; if a better estimate is necessary, $c_{v,\infty}\left(T_c\right)$ and P_L should also be included in the stochastic analysis inside the optimization loop. In any case, the other uncertainties can be neglected since their respective contribution to the variance is inferior to the maximal contribution by more than

one order of magnitude. This results in a substantially smaller computational cost (for a discussion about more systematic reduction criteria by using ANOVA, see [Gao 2011]). Problem (10.3) is first solved with only T_L uncertain. The optimal solution of problem (10.3) is then completed by a Monte Carlo computation, where the other uncertainties retained after ANOVA analysis, i.e. $c_{v,\infty}(T_c)$ and P_L, are used for the stochastic analysis. Monte Carlo simulation allows for the computation of the probability for the RSW Mach number to be less than unity. It is found that the probability for the left-running wave Mach number to be inferior to 1 decreases to 19.1% when the error bars on T_L are equal to 0.04% (0.26°C). The recommended uncertainty bars obtained from the inverse analysis must be analyzed with respect to the accuracy levels that can be experimentally achieved. Since such a level of accuracy on the temperature might be unfeasible, the possibility to increase the uncertainty bars on T_L if uncertainty on $c_{v,\infty}(T_c)$ were reduced was also investigated. The uncertainty on $c_{v,\infty}(T_c)$, *i.e.* 6%, is linked to the lack of available experimental data and it is deemed prudential [Nannan 2007]. The second optimization run performed with uncertain T_L and $c_{v,\infty}(T_c)$ shows that if the uncertainty on $c_{v,\infty}(T_c)$ is reduced to 1%, it is then possible to achieve a maximal uncertainty of 0.06% (0.39°C) on T_L which yields a reduced probability of 18.9% for the RSW Mach number to be less than unity (see Fig. 10.12). This means that if a large effort to improve the thermodynamic characterization is carried out (hence reducing uncertainty on the thermodynamic model), more realistic error bars on T_L can be tolerated. However, since this probability is not yet negligible, a more challenging optimization problem has been considered. The idea is to find the maximal uncertainty bars allowing to minimize $|\mu - 2\sigma - 1|$, that is to solve the following optimization problem:

$$\min_{\%IC,\%TD}(|\mu - 2\sigma - 1|) \quad \text{and} \quad max\,(\%IC, \%TD) \tag{10.4}$$

In this case, uncertainty on T_L, $c_{v,\infty}(T_c)$ and P_L have been simultaneously taken into account. After optimization, it is found that error bars for T_L, P_L and $c_{v,\infty}(T_c)$ should be respectively reduced to 0.035% (0.23°C), 0.1% (0.009 bar), and 0.5%. A Monte Carlo computation eventually leads to a 0.8% probability (see Fig. 10.12 on the right) for the left-running wave Mach number to be less than 1 (to be compared with the initially obtained 27.8% probability). According to these results, the experiment can be performed with a high degree of confidence in that case; however, achieving in practice the required precision on the initial conditions and the thermodynamic model might be extremely challenging. Since different initial conditions have been proposed in [Guardone 2010] along with a Span-Wagner type equation for the thermodynamical description of the fluid, the proposed methodology should be applied to this alternative problem set-up in order to check whether less stringent accuracy requirements can be obtained in that case.

10.2 Preliminary study on an improved system

Following the previous study, I focused my attention to a possible improvement of the FAST setup by investigating the feasibility of a RSW in a two-phase shock-tube configuration. For this reason, a DEM-based code for multiphase flow is modified for taking into account complex TD models. Moreover, a detailed study on RSW is performed considering the influence of vapor fraction in mixtures.

10.2.1 Discrete Equation Method (DEM)

The present study is based on a five-equation model with a single pressure and a single velocity. It is obtained imposing the asymptotic reduction of a seven equation model following the lines of Abgrall [Abgrall 2006]. So, a DEM [Abgrall 2003] scheme is used, applying the asymptotic reduction to a discrete level.
Actually, the DEM method has already been extensively explained in [Abgrall 2006, Abgrall 2003],

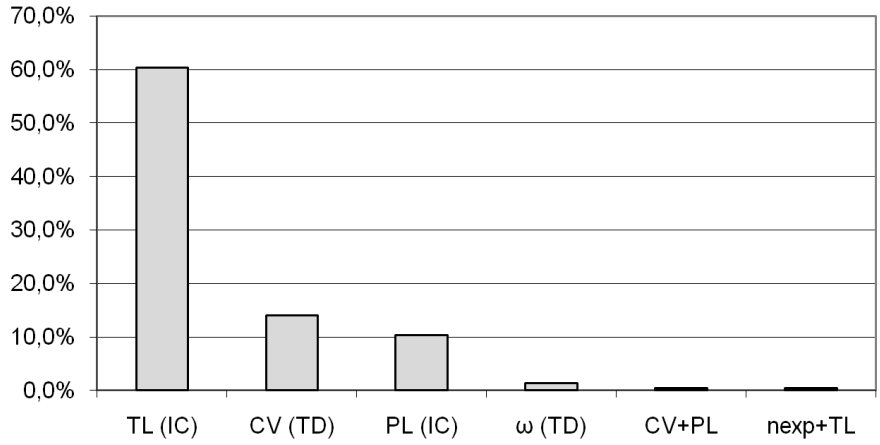

Figure 10.11: % contribution to the variance of the Mach number for each uncertainty, results obtained from ANOVA analysis.

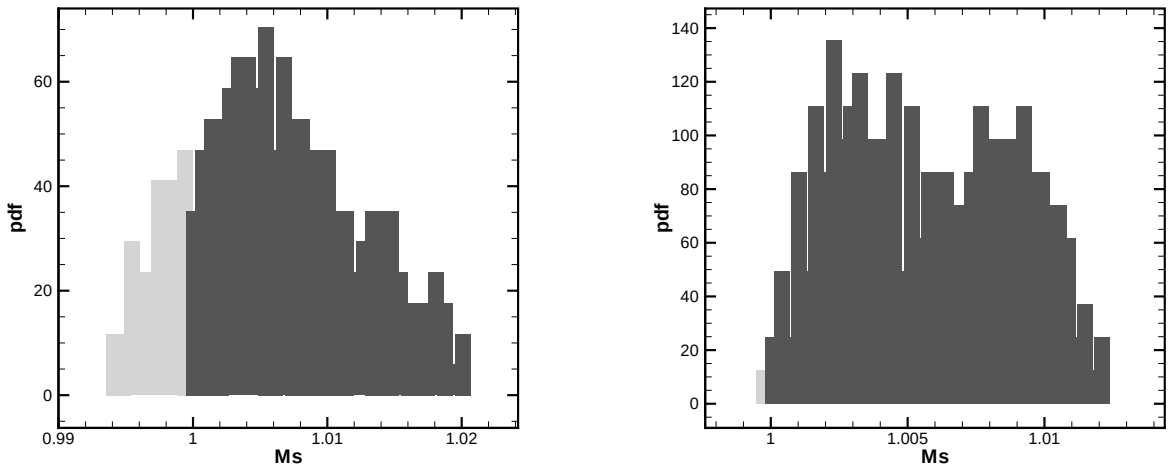

(a) (b)

Figure 10.12: Probability density function for the left-running wave Mach number, computed from Monte Carlo results for the problem described by equation (10.3) (a) and by equation (10.4) (b).

thus I recall the main idea and the final formulation.

10.2.1.1 The five equations model

The well known Baer & Nunziato [Baer 1986] model is composed by the conservative equations of each phase and one transport equation for each volume fraction of phases (in this case no heat and mass transfer is considered):

$$\begin{cases} \dfrac{\partial \alpha_1}{\partial t} & = -\mathbf{u}_I \cdot \nabla \alpha_1 & +\mu(p_1 - p_2) \\ \dfrac{\partial \alpha_1 \rho_1}{\partial t} + div(\alpha_1 \rho_1 \mathbf{u}_1) & = 0 & \\ \dfrac{\partial \alpha_1 \rho_1 \mathbf{u}_1}{\partial t} + div(\alpha_1 \rho_1 \mathbf{u}_1 \otimes \mathbf{u}_1) + \nabla(\alpha_1 p_1) & = p_I \nabla(\alpha_1) & +\lambda(\mathbf{u}_2 - \mathbf{u}_1) \\ \dfrac{\partial \alpha_1 \rho_1 E_1}{\partial t} + div(\alpha_1(\rho_1 E_1 + p_1)\mathbf{u}_1) & = p_I \mathbf{u}_I \cdot \nabla(\alpha_1) & +\lambda \mathbf{u}_I \cdot (\mathbf{u}_2 - \mathbf{u}_1) + \\ & & -\mu p_I (p_1 - p_2) \\ \dfrac{\partial \alpha_2}{\partial t} + \mathbf{u}_I \cdot \nabla \alpha_2 & = & -\mu(p_1 - p_2) \\ \dfrac{\partial \alpha_2 \rho_2}{\partial t} + div(\alpha_2 \rho_2 \mathbf{u}_2) & = 0 & \\ \dfrac{\partial \alpha_2 \rho_2 \mathbf{u}_2}{\partial t} + div(\alpha_2 \rho_2 \mathbf{u}_2 \otimes \mathbf{u}_2) + \nabla(\alpha_2 p_2) & = p_I \nabla(\alpha_2) & -\lambda(\mathbf{u}_2 - \mathbf{u}_1) \\ \dfrac{\partial \alpha_2 \rho_2 E_2}{\partial t} + div(\alpha_2(\rho_2 E_2 + p_2)\mathbf{u}_2) & = p_I \mathbf{u}_I \cdot \nabla(\alpha_2) & -\lambda \mathbf{u}_I \cdot (\mathbf{u}_2 - \mathbf{u}_1) + \\ & \underbrace{\qquad\qquad}_{Non\ conservative\ terms} & \underbrace{+\mu p_I (p_1 - p_2)}_{Relaxation\ terms} \end{cases} \tag{10.5}$$

where the subscripts 1 and 2 refer to the two phases k. α_k, ρ_k, $\mathbf{u}_k$, p_k, E_k are the volume fraction, the density, the velocity vector, the pressure and the total energy, respectively for each phase k. The last one is defined as $E_k = e_k + 0.5u_k^2$. The interface velocity and the pressure are indicated with u_I and p_I, respectively. These last one are defined in [Baer 1986] as $u_I = u_2$ and $p_I = p_1$, with 1 and 2 that correspond to the gas and the liquid phases, respectively. More complex definitions of interface variables are given in [Abgrall 2003, Ambroso 2012].
λ and μ represent the dynamic compaction viscosity and the relaxation velocity parameter, respectively.
The system (10.5) can be expressed in vectorial form:

$$\frac{\partial U}{\partial t} + \frac{\partial}{\partial x} F(U) + B(U) \frac{\partial \alpha_1}{\partial x} = S(U) \tag{10.6}$$

or, after some manipulation:

$$\frac{\partial U}{\partial t} + FT(U) = S(U) \tag{10.7}$$

where

$$U = \begin{pmatrix} \alpha_1 \\ \alpha_1 \rho_1 \\ \alpha_1 \rho_1 \mathbf{u}_1 \\ \alpha_1 \rho_1 E_1 \\ \alpha_2 \\ \alpha_2 \rho_2 \\ \alpha_2 \rho_2 \mathbf{u}_2 \\ \alpha_2 \rho_2 E_2 \end{pmatrix}, \qquad FT(U) = \frac{\partial}{\partial x} F(U) + B(U) \frac{\partial \alpha_1}{\partial x},$$

$$F(U) = \begin{pmatrix} 0 \\ \alpha_1\rho_1\mathbf{u}_1 \\ \alpha_1(\rho_1\mathbf{u}_1 \otimes \mathbf{u}_1) + p_1 \\ \alpha_1(\rho_1 E_1 + p_1)\mathbf{u}_1 \\ 0 \\ \alpha_2\rho_2\mathbf{u}_2 \\ \alpha_2(\rho_2\mathbf{u}_2 \otimes \mathbf{u}_2) + p_2 \\ \alpha_2(\rho_2 E_2 + p_2)\mathbf{u}_2) \end{pmatrix}$$

$$B(U) = \begin{pmatrix} \mathbf{u}_I \\ 0 \\ -p_I \\ -p_I\mathbf{u}_I \\ \mathbf{u}_I \\ 0 \\ -p_I \\ -p_I\mathbf{u}_I \end{pmatrix}, \quad S(U) = \begin{pmatrix} \mu(p_1 - p_2) \\ 0 \\ \lambda(\mathbf{u}_2 - \mathbf{u}_1) \\ \lambda\mathbf{u}_I \cdot (\mathbf{u}_2 - \mathbf{u}_1) - \mu p_I(p_1 - p_2) \\ -\mu(p_1 - p_2) \\ 0 \\ -\lambda(\mathbf{u}_2 - \mathbf{u}_1) \\ -\lambda\mathbf{u}_I \cdot (\mathbf{u}_2 - \mathbf{u}_1) + \mu p_I(p_1 - p_2) \end{pmatrix}.$$

Supposing the mechanical equilibrium, the equality of pressure and velocity can be obtained in the limit of a stiff mechanical relaxation as in [Kapila 2001, Murrone 2005], *i.e.* the relaxation parameters, λ and μ are taken as infinite:

$$\mu = \frac{1}{\varepsilon}, \qquad \lambda = \frac{1}{\varepsilon}, \quad where \quad \varepsilon \to 0^+. \tag{10.8}$$

Thus, the asymptotic development allows to find the solution such that the relaxation terms go to zero (for more details concerning asymptotic development, Refs. [Murrone 2005, Abgrall 2006, Abgrall 2013c] are strongly recommended). Then, after some algebraic manipulations of system (10.5), the reduced model is so obtained:

$$\begin{cases} \dfrac{\partial\alpha_1}{\partial t} + \mathbf{u} \cdot \nabla\alpha_1 = \dfrac{\rho_2 c_2^2 - \rho_1 c_1^2}{\frac{\rho_1 c_1^2}{\alpha - 1} + \frac{\rho_2 c_2^2}{\alpha_2}} \text{ div } \mathbf{u} \\ \dfrac{\partial\alpha_1\rho_1}{\partial t} + \nabla(\alpha_1\rho_1\mathbf{u}) = 0 \\ \dfrac{\partial\alpha_2\rho_2}{\partial t} + \nabla(\alpha_2\rho_2\mathbf{u}) = 0 \\ \dfrac{\partial\rho\mathbf{u}}{\partial t} + \nabla(\rho_k\mathbf{u} \otimes \mathbf{u} + p) = 0 \\ \dfrac{\partial E}{\partial t} + \nabla((E + p)\mathbf{u}) = 0 \end{cases} \tag{10.9}$$

where $\rho = \alpha_1\rho_1 + \alpha_2\rho_2$, $E = \alpha_1\rho_1 e_1 + \alpha_2\rho_2 e_2$, p and $\mathbf{u}$ are the mixture density, mixture total energy, the mixture pressure and the mixture velocity, respectively. Finally, c_k is the sound of speed of each phase.

We remember that $\alpha_1 + \alpha_2 = 1$, so only a single phase is considered in the unknowns of the system that, for the system 10.9 are: α_1, ρ_1, ρ_2, e_1, e_2, p and u. In order to close the system (10.9), an equation of state (EOS) for each pure phase is needed for defining all the needed thermodynamic properties. This model involves mechanical equilibrium between the phases at any time, as it is evident for the presence of only one pressure p and only one velocity vector, $\mathbf{u}$, in the system (10.9). The computations presented in this work rely on the five-equation model.

10.2.1.2 The numerical scheme

The DEM approach has been derived in [Abgrall 2003] and in [Abgrall 2006] for the five-equations model, so only the main lines of the scheme are recalled.
First, remember that the DEM consists into applying at a discrete level the same procedure used to obtain a compressible multiphase model, *i.e.*:

1. let us suppose that each pure fluid is governed by the Euler equations,
2. let us introduce, for each phase, the characteristic function X_k that satisfies the topological equation:
$$\frac{\partial X_k}{\partial t} + \sigma \cdot \nabla X_k = 0, \;\; with \;\; X_k = \begin{cases} 1 & \text{if } (\vec{x},\text{t}) \text{ belongs to phase k} \\ 0 & \text{otherwise} \end{cases} \tag{10.10}$$
where σ is the interface velocity between the two phases.
3. An averaging procedure, $\mathcal{E}(\cdot)$, as in Drew and Passmann [Drew 1998], is applied to Euler equations (see [Abgrall 2003]).
4. A statistical average is performed in order to obtain an approximation of the mean quantities.

In particular, to obtain the semi-discrete numerical approximation of the two-phase system 10.9, two steps are needed. In the first step, the DEM method, before described, is applied to a seven equations model, *i.e.* to the system 10.5. After obtaining its semi-discrete numerical approximation, a relaxation procedure is applied, always at a discrete level, in order to reach a mechanical equilibrium.

Now, let us suppose that at time t, the computational domain Ω is divided into the cells $\mathcal{C}_i =]x_{i-1/2}, x_{i+1/2}[$, but at time $t = t + s$ (with s small), the interface in $x_{i+1/2}$ is assumed to move at a velocity $\sigma_{i+1/2}$ and the interface in $x_{i-1/2}$ moves at a velocity $\sigma_{i-1/2}$. So, the cell $\mathcal{C}_i$ evolves in $\bar{\mathcal{C}}_i =]x_{i-1/2}+s\sigma_{i-1/2}, x_{i+1/2}+s\sigma_{i+1/2}[$ (see figure 10.13). The cell may be either smaller or larger than the original ones $\mathcal{C}_i$, depending on the signs of the velocities. Then, let us denote with $F(U_L, U_R)$

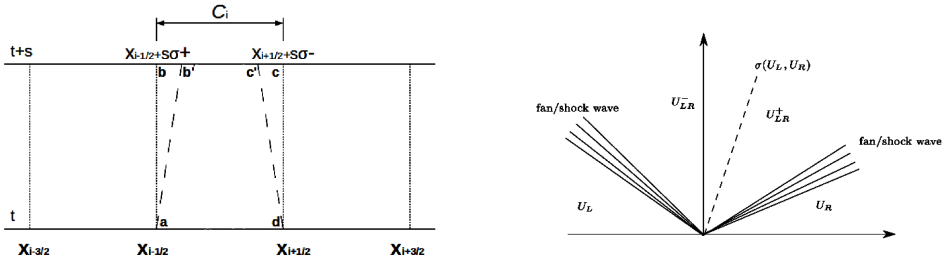

Figure 10.13: a) Subdivision of computational domain. b) The various states in the Riemann problem between states U_L and U_R.

the Godunov numerical flux between the states U_L and U_R, and with $F^{lag}(U_L, U_R)$ the flux across the contact discontinuity between the states U_L and U_R (see figure 10.13). The relation between the two fluxes is:

$$F^{lag}(U_L, U_R) = F(U^+_{LR}) - \sigma(U_L, U_R)U^+_{LR} = F(U^-_{LR}) - \sigma(U_L, U_R)U^-_{LR},$$

where the superscripts $\pm$ denote the state on the right and on the left of the contact discontinuity as in figure 10.13.

The semi-discrete scheme for the reduced five equations model in 1D is:

$$\begin{cases} \dfrac{\partial \alpha_1}{\partial t} = FT(U_1) + \dfrac{\alpha_1\alpha_2}{\alpha_2\rho_1a_1^2 + \alpha_1\rho_2a_2^2}\left\{ \dfrac{FT(U_8)}{\alpha_2\rho_2\chi_2} - \dfrac{u_2FT(U_7)}{\alpha_2\rho_2\chi_2} + \dfrac{\frac{{u_2}^2}{2} - \varepsilon_2 - \rho_2\kappa_2}{\alpha_2\rho_2\chi_2}FT(U_6) + \right. \\ \qquad \left. + \dfrac{\rho_2^2\kappa_2FT(U_1)}{\alpha_2\rho_2\chi_2} - \dfrac{FT(U_4)}{\alpha_1\rho_1\chi_1} + \dfrac{u_1FT(U_3)}{\alpha_1\rho_1\chi_1} - \dfrac{\frac{{u_1}^2}{2} - \varepsilon_1 - \rho_1\kappa_1}{\alpha_1\rho_1\chi_1}FT(U_2) - \dfrac{\rho_1^2\kappa_1FT(U_5)}{\alpha_1\rho_1\chi_1} \right\} \\ \dfrac{\partial \alpha_1\rho_1}{\partial t} = FT(U_2) \\ \dfrac{\partial \alpha_2\rho_2}{\partial t} = FT(U_6) \\ \dfrac{\partial \rho u}{\partial t} = FT(U_3) + FT(U_7) \\ \dfrac{\partial \rho E}{\partial t} = FT(U_4) + FT(U_8) \end{cases} \tag{10.11}$$

where χ_k and κ_k, are defined as following:

$$\chi_k = \left(\frac{\partial e_k}{\partial P_k}\right)_{\rho_k} \quad ; \quad \kappa_k = \left(\frac{\partial e_k}{\partial \rho_k}\right)_{P_k} \tag{10.12}$$

where e_k is the phase internal energy.
As explained before, the vector $FT(U_j)$, with $j = 1, ..., 8$, is the sum of two contributions, *i.e.* of the flux of hyperbolic system (conservative term) and of the non-conservative term, obtained for each equation of the system (10.5). The correspondence of the semi-discrete system (10.11) with the model (10.9) has been demonstrated in [Abgrall 2006]. Note that this method allows to begin with two different thermodynamic states of phases, arriving, finally, to a mechanical equilibrium. On the contrary, a direct discretization of the system (10.9) imposes immediately the equality of initial pressure and velocity of the phases. The next step is, now, to define the vector $FT(U_j)$ that for each component will be composed by a conservative and a non-conservative terms:

$$\begin{aligned} FT(U_j) = \frac{1}{\triangle x}\,\mathcal{E}\left(X(x_{i+1/2},t)F(U^*_{i+1/2}) - X(x_{i-1/2},t)F(U^*_{i-1/2})\right) + \\ + \frac{1}{\triangle x}\left(\mathcal{E}([X]_{j=0})F^{lag}(U_i^-, U_{i-1}^+) - \mathcal{E}([X]_{j=N})F^{lag}(U_i^+, U_{i+1}^-)\right), \end{aligned} \tag{10.13}$$

where $U^*_{i+1/2}$ (or $U^*_{i+1/2}$) denotes the solution of Riemann problem between U_i^+ and U_{i+1}^- (respectively,U_{i-1}^+ and U_i^-). $[X]_{j=0}$ and $[X]_{j=N}$ are the jump of X at the beginning and at the end of computational cell, respectively.

Following the procedure demonstrated in [Abgrall 2003, Abgrall 2006], the idea of DEM method is to avoid the introduction of approximated estimation of fluxes expectancy that, on the contrary, is estimated basing on the probability to find in two neighbor cells the same phase or two different phases (see the "flow patterns" in the table 10.4). As a consequence, the flux indicator can be indicated as in the following:

$$\beta^{(l,r)}_{i+1/2} = sign(\sigma(U_i^l, U_{i+1}^r)) = \begin{cases} 1 & if\ \ \sigma(U_i^l, U_{i+1}^r) \geq 0, \\ -1 & if\ \ \sigma(U_i^l, U_{i+1}^r) < 0, \end{cases}$$

where l and r indicate the phase at the left and the right of interface, respectively.
Thus, the conservative and non-conservative terms of (10.13) can be developed supposing the four instances. Again, for sake of clarity, let us briefly recall the main ideas of this strategy [Abgrall 2003, Abgrall 2006].

Flow Patterns	Jump indicator	Flux Indicator
$\Sigma_1 - \Sigma_2$	$[X]_{1,1} = 0$	$\left(\beta^{(1,2)}_{i+1/2}\right)$
$\Sigma_1 - \Sigma_1$	$[X]_{1,2} = \begin{cases} -1 \ if \ \sigma(1,2) > 0 \\ 0 \quad otherwise \end{cases}$	1
$\Sigma_2 - \Sigma_1$	$[X]_{2,1} = \begin{cases} 1 \ if \ \sigma(2,1) > 0 \\ 0 \quad otherwise \end{cases}$	$\left(\beta^{(2,1)}_{i+1/2}\right)$
$\Sigma_2 - \Sigma_2$	$[X]_{2,2} = 0$	0

Table 10.4: The various flow configurations at cell boundary $i + 1/2$.

The terms of equation (10.13) can be defined as:

$$\mathcal{E}\left(X(x_{i+\frac{1}{2}},t)F(U^*_{i+\frac{1}{2}})\right) = P_{i+\frac{1}{2}}(\Sigma_1 - \Sigma_1)F(U^{(1)}_i, U^{(1)}_{i+1}) + \\ + P_{i+\frac{1}{2}}(\Sigma_1 - \Sigma_2)\left(\beta^{(1,2)}_{i+\frac{1}{2}}\right)F(U^{(1)}_i, U^{(2)}_{i+1}) + P_{i+\frac{1}{2}}(\Sigma_2 - \Sigma_1)\left(\beta^{(2,1)}_{i+\frac{1}{2}}\right)F(U^{(2)}_i, U^{(1)}_{i+1})$$

$$\mathcal{E}\left(X(x_{i-\frac{1}{2}},t)F(U^*_{i-\frac{1}{2}})\right) = P_{i-\frac{1}{2}}(\Sigma_1 - \Sigma_1)F(U^{(1)}_{i-1}, U^{(1)}_i) + \\ + P_{i-\frac{1}{2}}(\Sigma_1 - \Sigma_2)\left(\beta^{(1,2)}_{i-\frac{1}{2}}\right)F(U^{(1)}_{i-1}, U^{(2)}_i) + P_{i-\frac{1}{2}}(\Sigma_2 - \Sigma_1)\left(\beta^{(2,1)}_{i-\frac{1}{2}}\right)F(U^{(2)}_{i-1}, U^{(1)}_i)$$

$$\mathcal{E}\left([X]_N F^{lag}(U^{N(w)}_i, U^-_{i+1})\right) = P_{1+1/2}(\Sigma_1, \Sigma_2)\left(\beta^{(1,2)}_{i+1/2}\right)F^{lag}(U^{(1)}_i, U^{(2)}_{i+1}) + \\ - P_{1+1/2}(\Sigma_2, \Sigma_1)\left(\beta^{(2,1)}_{i+1/2}\right)F^{lag}(U^{(2)}_i, U^{(1)}_{i+1})$$

$$\mathcal{E}\left([X]_0 F^{lag}(U^+_{i-1}, U^0_i)\right) = -P_{1-1/2}(\Sigma_1, \Sigma_2)\left(\beta^{(1,2)}_{i-1/2}\right)F^{lag}(U^{(1)}_{i-1}, U^{(2)}_i) + \\ + P_{1-1/2}(\Sigma_2, \Sigma_1)\left(\beta^{(2,1)}_{i+1/2}\right)F^{lag}(U^{(2)}_{i-1}, U^{(1)}_i)$$

It remains to evaluate the term of probability, $P_{i\pm1/2}(\Sigma_p, \Sigma_q)$ (see [Abgrall 2003]). For simplicity the final formulation for $i + 1/2$ is as follows:

$$\begin{cases} \mathcal{P}_{i+1/2}(\Sigma_1, \Sigma_1) & := \mathcal{P}\left(X(x^-_{i+1/2}) = 1 \ and \ X(x^+_{i+1/2}) = 1\right) & = \min\left(\alpha^{(1)}_i, \alpha^{(1)}_{i+1}\right) \\ \mathcal{P}_{i+1/2}(\Sigma_1, \Sigma_2) & := \mathcal{P}\left(X(x^-_{i+1/2}) = 1 \ and \ X(x^+_{i+1/2}) = 0\right) & = \max\left(\alpha^{(1)}_i - \alpha^{(1)}_{i+1}, 0\right) \\ \mathcal{P}_{i+1/2}(\Sigma_2, \Sigma_1) & := \mathcal{P}\left(X(x^-_{i+1/2}) = 0 \ and \ X(x^+_{i+1/2}) = 1\right) & = \max\left(\alpha^{(2)}_i - \alpha^{(2)}_{i+1}, 0\right) \\ \mathcal{P}_{i+1/2}(\Sigma_1, \Sigma_2) & := \mathcal{P}\left(X(x^-_{i+1/2}) = 0 \ and \ X(x^+_{i+1/2}) = 0\right) & = \min\left(\alpha^{(2)}_i, \alpha^{(2)}_{i+1}\right). \end{cases}$$

where Σ_k indicates the phase, with $k = 1, 2$.

10.2.2 Thermodynamic closure

As previously mentioned, we deal with pure fluid and artificial mixture zone, thus the EOS must be able to describe flows both in pure fluids and mixture zones. In this section, first we describe three EOSs, *i.e.* the Stiffened Gas (SG) EOS, the Peng-Robinson (PRSV) EOS and the Span-Wagner (SW) EOS. Secondly, we build the mixture EOS using the SG EOS for each phase. Then, the mixture EOS using PRSV (or SW) and the SG for the gas and the liquid phase, respectively, is described.

10.2.2.1 Stiffened Gas EOS for pure fluid

The Stiffened Gas EOS is usually used for shock dynamics and its robustness for simulating two-phase flow with or without mass transfer has been amply demonstrated, see for example [Abgrall 2003, Murrone 2005, Goncalves 2009, Abgrall 2006, Saurel 2007]. It can be written as follows:

$$P(\rho, e) = (\gamma - 1)(e - q)\rho - \gamma P_\infty, \tag{10.15a}$$

$$e(\rho, T) = Tc_v + \frac{P_\infty}{\rho c_v} + q \tag{10.15b}$$

$$h(T) = \gamma c_v T, \tag{10.15c}$$

where p, ρ and e are the pressure, the density and the energy, respectively. The polytropic coefficient γ is the constant ratio of specific heat capacities $\gamma = c_p/c_v$, P_∞ is a constant reference pressure and q is the energy of the fluid at a given reference state. Moreover, T, c_v and h are the temperature, the specific heat at constant volume and the enthalpy, respectively. The speed of sound, defined as $c^2 = (\frac{\partial P}{\partial \rho})_s$ can be computed as follows:

$$c^2 = \gamma \frac{P + P_\infty}{\rho} = (\gamma - 1)c_p T \tag{10.16}$$

where c^2 remains strictly positive (for $\gamma > 1$). It ensures the hyperbolicity of the system and the existence of a convex mathematical entropy [Harten 1998].

10.2.2.2 *SG EOS based mixture*

The EOS for the mixture can be easily obtained using the EOS of the single phases. In this section, we consider the mixture obtained supposing a SG EOS for each phase. The aim is now to obtain the mixture pressure, the starting point is the mixture energy equation:

$$\rho E = \alpha_1 \rho_1 e_1 + \alpha_2 \rho_2 e_2. \tag{10.17}$$

The energy of each phase, e_k, can be replaced by (10.15a), obtaining the mixture total energy as a function of the phase pressure. Under pressure equilibrium, we obtain the following expression for the pressure mixture:

$$P(\rho, e, \alpha_k) = \frac{\rho(E - \frac{\alpha_1 \rho_1 q_1}{\rho} - \frac{\alpha_2 \rho_2 q_2}{\rho}) - \left(\frac{\alpha_1 \gamma_1 P_{\infty,1}}{\gamma_1 - 1} + \frac{\alpha_2 \gamma_2 P_{\infty,2}}{\gamma_2 - 1}\right)}{\frac{\alpha_1}{\gamma_1 - 1} + \frac{\alpha_2}{\gamma_2 - 1}} \tag{10.18}$$

In this study, the term q is assumed to be equal to zero for each phase.

10.2.2.3 *Real EOS-SG based mixture*

We consider a mixture, obtained using the SG EOS for the liquid and a complex EOS for the gas (PRSV or SW). In the case of SG EOS (see section 10.2.2.1), we have shown how the pressure mixture can be easily obtained from the energy and the density of each phase. If a PRSV or a SW EOS is considered, it is not possible togive a closed form of the pressure as a function of the energy and the density. The procedure shown in section 10.2.2.2 for the SG EOS can not be used in this case. Under pressure equilibrium, the following system of two equations is obtained:

$$\begin{aligned} P_1(T_1, \rho_1) &= P_2(T_2, \rho_2) \\ \rho E &= \alpha_1 \rho_1 e_1 + \alpha_2 \rho_2 e_2. \end{aligned} \tag{10.19}$$

where P_1 represents the pressure state computed for the phase 1 described by the PRSV (or SW) EOS, and P_2 the pressure of the phase 2 described by SG EOS. Note that the unknowns are T_1 and T_2.

Replacing P_2 using Eq. (10.15a) in the first equation of the system (10.19), the liquid temperature T_2 can be expressed as a function of the gas temperature T_1 (where P_1 is a function of T_1 and ρ_1 using Eq. (7.12)):

$$T_2 = \frac{P_1(T_1, \rho_1) + P_{\infty,2}}{(\gamma_2 - 1)\rho_2 c_{v,\infty_2}} \tag{10.20}$$

Using Eq. (10.15b) for e_2 in the mixture energy equation (second equation of the system (10.19)), we obtain:

$$\rho E = \alpha_1 \rho_1 e(T_1, \rho_1) + \alpha_2 \rho_2 \left[T_2 c_{v,\infty_2} + \frac{P_{\infty,2}}{\rho_2} + q \right]. \tag{10.21}$$

Replacing T_2 in the Eq. (10.21) using (10.20), it is possible to derive a relation between the gas temperature, T_1, and the mixture energy. This is a function $E = E(T_1)$ that depends only on T_1. Solving iteratively Eq. (10.23) by using a Newton-Raphson method, the value of the gas temperature T_1 can be computed. Once T_1 is obtained, the mixture pressure can be easily computed using Eq. (7.12).

Let us detail the previous equation in detail for PRSV EOS. Replacing P_1 as a function of T_1 and ρ_1 using Eq. (7.2) and P_2 using Eq. (10.15a) in the first equation of the system (10.19), the liquid temperature T_2 can be expressed as a function of the gas temperature T_1:

$$T_2 = \left[\frac{T_1 R_1}{\dfrac{1}{\rho_1} - b_1} - \frac{\alpha(T_1) a_1}{\dfrac{1}{\rho_1^2} + \dfrac{2b_1}{\rho_1} - b_1^2} + P_{\infty,2} \right] \frac{1}{(\gamma_2 - 1)\rho_2 c_{v,\infty_2}} \tag{10.22}$$

Replacing the energy e_k of each phase for e_1 and using Eq. (10.15b) for e_2 in the mixture energy equation (second equation of the system (10.19)), we obtain:

$$\begin{aligned} \rho E = \alpha_1 \rho_1 \Bigg[& e_c + \frac{c_{v,\infty}(T_c)}{(n+1)T_c^n}(T_1^{n+1} - T_c^{n+1}) \\ & - \frac{a}{2\sqrt{2}b} \left(\alpha(T_1) - T_1 \frac{d\alpha(T)}{dT} \right) \log \left| \frac{V + b(1+\sqrt{2})}{V + b(1-\sqrt{2})} \right| \Bigg] \\ & + \alpha_2 \rho_2 \left(T_2 c_{v,\infty_2} + \frac{P_{\infty,2}}{\rho_2} + q \right). \end{aligned} \tag{10.23}$$

As described before, by replacing T_2 in the Eq. (10.23) using the Eq. (10.22), it is possible to derive a relation between the gas temperature, T_1, and the mixture energy. Since the function $E = E(T_1)$ depends exclusively on T_1, Eq. (10.23) can be solved by using a Newton-Raphson method.

10.2.2.4 *Definition of χ_k and κ_k*

Two thermodynamics-dependent properties are χ_k and κ_k (see Eq. (10.12)). If a more complex equation of state is used, it is not possible to explicitly compute these coefficients. Using standard thermodynamics, we have

$$\chi_k = \left(\frac{\partial e_k}{\partial P_k} \right)_{\rho_k} = \frac{\left(\frac{\partial e_k}{\partial T_k} \right)_{\rho_k}}{\left(\frac{\partial P_k}{\partial T_k} \right)_{\rho_k}}, \tag{10.24a}$$

$$\kappa_k = \left(\frac{\partial e_k}{\partial \rho_k} \right)_{P_k} = \left(\frac{\partial e_k}{\partial \rho_k} \right)_{T_k} - \frac{\left(\frac{\partial p_k}{\partial \rho_k} \right)_{T_k} \left(\frac{\partial e_k}{\partial T_k} \right)_{\rho_k}}{\left(\frac{\partial P_k}{\partial T_k} \right)_{\rho_k}}. \tag{10.24b}$$

For SG EOS, it is trivial to compute these coefficients as follows:

$$\chi_k = \left(\frac{\partial e_k}{\partial P_k}\right)_{\rho_k} = \frac{1}{(\gamma-1)\rho}, \tag{10.24c}$$

$$\kappa_k = \left(\frac{\partial e_k}{\partial \rho_k}\right)_{P_k} = -\frac{P+\gamma P_\infty}{(\gamma-1)\rho^2}. \tag{10.24d}$$

For a more complex EOS, derivatives in Eqs. (10.24) can be easily computed, once thermal and caloric EOS are known (for example using Eqs. (7.2) in the case of a PRSV model).

10.2.3 Results

10.2.4 TC1: validation of PRSV equation of state in quasi-single phase fluid

We consider the test case presented by Fergason et al. [Fergason 2001], where a rarefaction shock is observed in a single-phase shock tube configuration. This non-classical phenomenon has been observed numerically in the literature [Thompson 1973, Congedo 2012, Colonna 2006a], even if an experimental confirmation of the rarefaction shock wave still does not exist. Only an accurate EOS, such as the PRSV EOS, can describe a so particular gas thermodynamic behavior. For this reason, this test-case represents a good validation for checking the EOS implementation.

The shock tube is filled out with only one fluid, the FC70, but for numerical reasons, each chamber contains a very weak volume of fraction of water ($\alpha_l = 10^{-8}$). Initial conditions for the left and right states are specified in table 10.6. The diaphragm is located at $x = 2.5$ m (the tube is 5 m long). Results obtained with DEM are validated with the numerical results obtained by means of the *NZDG* code (see [Congedo 2012] and Section 10.1.1 for more details), comparing the profiles at a time of $t = 0.3$ s.

Table 10.5 provides the fluid properties of FC70 and the corresponding PRSV EOS parameters, *i.e.* the fluid acentric factor ω and the n coefficient (see Eq. 7.8), taken from [Guardone 2005].

FLUID	SG EOS					
	γ	P_∞ $[Pa]$	C_p $[\frac{J}{KgK}]$	C_v $[\frac{J}{KgK}]$	q	q'
Liq. Dodecane	2.35	4×10^8	2534	1077	0	0
Vap. Dodecane	1.025	0	2005	1956	0	0
Water	4.4	6×10^8	18392	4180	0	0
	PRSV EOS					
	$\frac{C_{v,\infty}}{R}$		n		ω	
FC70	118.7		0.493		0.7584	
Dodecane	60.4		0.69277		0.575	
D6	105.88		0.5095		0.74	
	SW EOS					
D6	n_1	n_2	n_3	n_4	n_5	n_6
	1.691561	-3.379625	0.386090	0.0645989	0.105890	$0.454568x10^{-4}$
	n_7	n_8	n_9	n_{10}	n_{11}	n_{12}
	0.741692	-0.0881026	-0.173733	-0.109513	-0.0626956	0.0374599
	α		γ	χ	δ	ε
	468.7		981.2	1792.1	686.7	786.8

Table 10.5: EOS coefficients for liquid and gas phases.

In Figure 10.14, the evolution of dimensionless[1] pressure, density, Mach and the fundamental derivative of gas dynamics Γ along the tube axis are shown. The negative value of Γ allows us

[1] computed with respect to the critical point

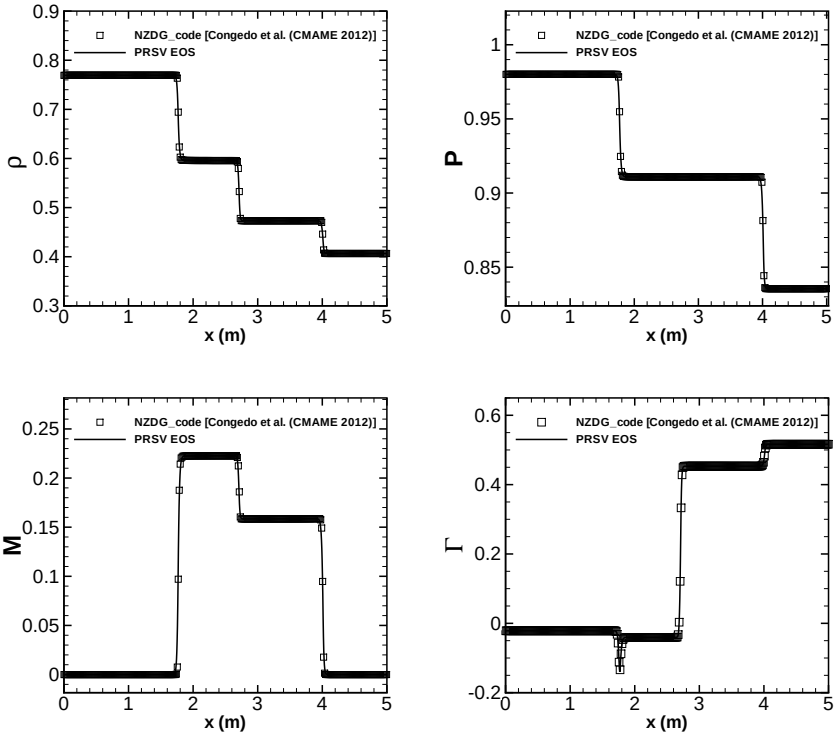

Figure 10.14: Comparison of the DEM results with the ones obtained with the *NZDG* code for a quasi-single phase shock-tube flow in terms of density, pressure, Mach and the fundamental derivative of gas dynamics Γ.

to identify the zone where a rarefaction shock wave can appear [Thompson 1973, Congedo 2012, Colonna 2006a]. Consequently, a non-classical discontinuity wave field displaying a rarefaction shock wave can be observed on $x = 1.8$ m (see Figure 10.14), whereas we observe a compression shock wave on $x = 4.0$ m. The results obtained with the DEM code and the *NZDG* code [Congedo 2012] show a perfect agreement.

10.2.5 TC2: Rarefaction shock waves (RSW) in a two-phase flow, influence of gas volume fraction

A contribution of this study is to demonstrate the numerical evidence of a RSW in a two-phase flow. So, let us suppose we have the same fluid initial conditions of the TC1 test case, except for the initial gas volume fraction. We assume a mixture of FC70 and water at different volume percentages. In particular, two initial conditions are imposed for both sides of the tube, *i.e.* $\alpha_g = 0.5$ and $\alpha_g = 0.1$, corresponding to the case TC2(a) and TC2(b), respectively. A PRSV EOS is used for modelling the gas phase, since SG is too simplified in order to observe complex effects, such as BZT effects.

Plots of fundamental derivative of gas dynamics Γ, vapor density, mixture density, velocity, pressure and gas temperature profiles are reported in Figure 10.15. Let us focus on the solution with $\alpha_g = 0.5$. As it can be observed, a RSW appears. In fact, a rarefaction happens at $x = 1.7$. Note that the corresponding Γ is negative. This means that only rarefaction shocks are admissible (while the compression shocks are forbidden) due to the second principle of thermodynamics. The other structures that can be observed are a contact discontinuity at $x = 2.6$, and a compression at $x = 3.75$. Note that this is a compression shock since the corresponding Γ is positive.

Let us now focus on the influence of the gas volume fraction. In particular, comparison between the computations at $\alpha = 1$ (*i.e.* the TC(1) presented in the previous section), $\alpha_g = 0.5$(TC2(a)) and

$\alpha_g = 0.1$ (TC2(b)) are shown at $t = 0.03$s and are reported in Figure 10.15.

The main differences are related to the velocity of each structure, *i.e.* rarefaction shock, contact discontinuity and compression shock, and to the values of the intermediate states (region between the compression and the contact or between the rarefaction and the contact). Note that velocities of the rarefaction shock (contact discontinuity) increases when the gas volume fraction decreases (increases). Consequently, as it can be observed looking at Γ, that the RSW is located at $x = 1.8m$, $x = 1.7m$ and $x = 0.9m$ for $\alpha_g = 1$, $\alpha_g = 0.5$ and $\alpha_g = 0.1$, respectively (see figure 10.15). A non-linear behavior of the compression shock velocity is observed with respect to α_g. In particular, the velocity is the slowest at $\alpha_g = 0.5$, while at $\alpha_g = 0.1$, it is faster with respect to $\alpha_g = 1.0$. Remark that the mixture velocity and the Mach is radically reduced when the gas volume fraction decreases (see figure 10.15). Concerning the intermediate states, vapor density and pressure are higher when α_g is lower.

Finally, results display a strong influence of the gas volume fraction on some specific properties of the RSW. This is a precious indication for the set-up of an experience in order to maximize the probability of occurrence of the RSW with respect to modeling and experimental uncertainties.

10.2.6 TC3: Influence of thermodynamic model

Beneficial effects of negative nonlinearities may be maximized with a working fluid displaying a larger inversion zone, hence with a higher molecular complexity. To validate such a strategy, computations are performed for a heavier cyclic siloxane, namely dodecamethylcycloexasiloxane also known as D6. The existence of an inversion zone for this fluid is predicted for any choice of the thermodynamic model. Properties are taken from [Guardone 2010]. The main properties for D6 are given in the table 10.5.

In this section, we focus on the influence of the thermodynamic model. In figure 10.16a, a close-up of the saturation and iso-Γ curves obtained by means of PRSV and SW are reported. A discrepancy exists between these two equations for predicting the saturation curve and the inversion region (where Γ is negative), thus predicting different values for Γ. Concerning D6, a question exists concerning which thermodynamic model is the most accurate. In particular, the higher robustness of the PRSV equation when coupled with CFD solvers with respect to more complex and potentially more accurate multi-parameter equations of state has been discussed in [Cinnella 2010, Congedo 2011c].

The choice of initial conditions, *i.e.* left and right states (in terms of specific volume and pressure) is performed in order to highlight BZT effects and to display the importance of an accurate thermodynamic model. For these reasons, two initial conditions are considered. They are reported in Figure 10.16b. In particular, red (black) points represent the left/right conditions (obviously left states are the points at higher pressure). The left condition corresponding to the first choice, is near the saturation curve, and, as it can be seen in Figure 10.16b (red points), Γ is predicted as negative using both EOS. Note that the left condition is chosen for being inside the vapor region when using also PRSV. The left condition corresponding to the second choice, is inside the inversion region for SW, but not for PRSV. Dimensional values for pressure and density of both conditions are reported in table 10.6.

We now focus on the effect of these initial conditions on the RSW appearance in two-phase flow simulations. A mixture of D6 and water at the same volume fraction ($\alpha_G = 0.5$) is considered. In figure 10.17, plots of several variables are reported when using the first initial condition for both PRSV and SW. Similar structures are observed, *i.e.* a RSW (note that Γ is negative for both EOS during the rarefaction at $x = 2.1$), a contact discontinuity and a compression shock. Pressure evolution is very similar for both EOS, while larger differences are observed for density, velocity and Mach number. Temperature prediction is different when using PRSV with respect to SW, in particular a maximal difference of 0.6% is computed.

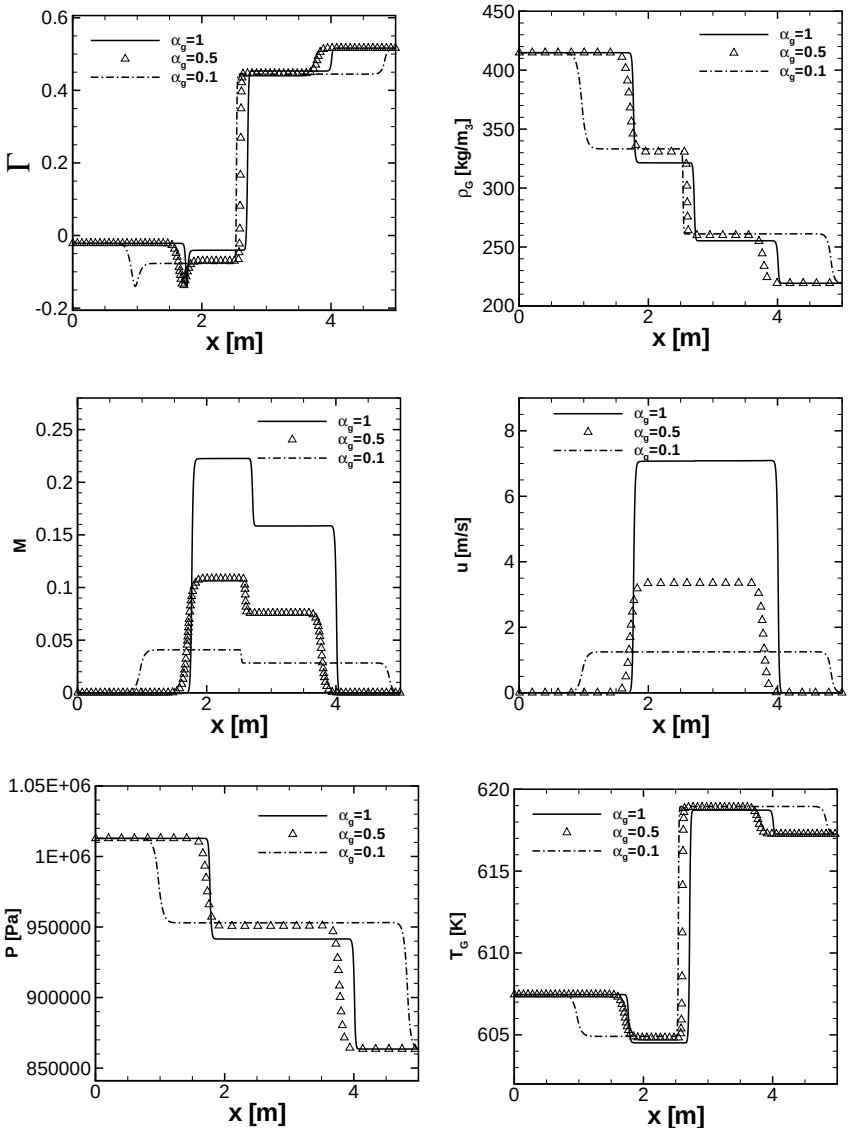

Figure 10.15: Comparison between fundamental derivative of gas dynamics Γ, vapor density, mixture density, velocity, pressure and gas temperature profiles obtained for TC1($\alpha_g = 1$), TC2(a)($\alpha_g = 0.5$) and TC2(b)($\alpha_g = 0.1$) test cases.

The figure 10.18 illustrates results obtained by using a second couple of points for the left/right conditions (black points in Figure 10.16b). Note that the pressure profiles are nearly coincident and that the observed differences for the other variables are concentrated on the values of the intermediate states, except for the temperature. This last one has the same behavior than the previous point in terms of differences between PRSV and SW. Anyway, a strong difference exists between PRSV and SW: the appearance of a RSW is no more observed for PRSV. In particular, compression shocks and contact discontinuity are observed for both EOS, while the rarefaction is a shock when using SW and a wave when using PRSV. This confirms the important sensitivity of this phenomenon to the initial conditions and to the influence of the thermodynamic model. At the same time, this introduces the possibility of using a two-phase flow for setting-up a better experience, that could maximize the occurrence of the RSW.

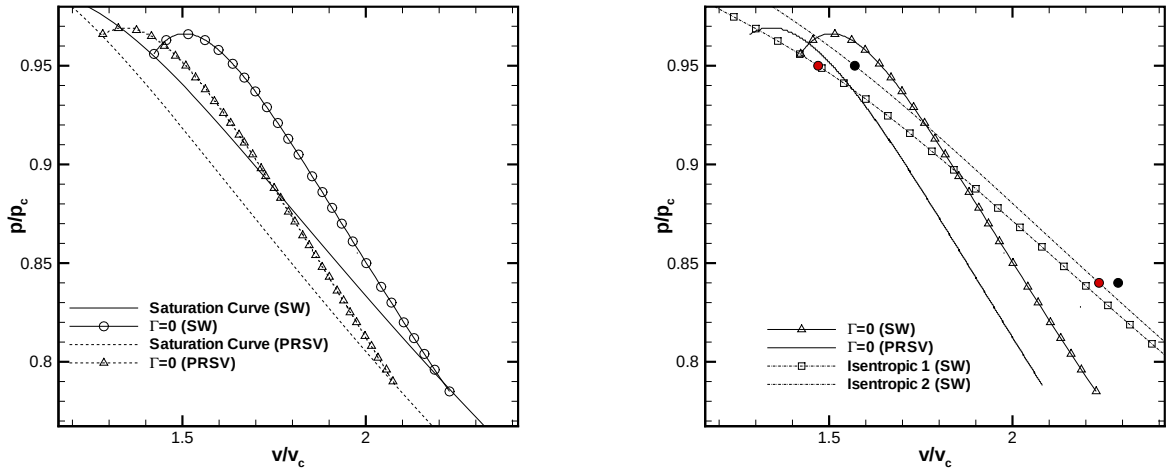

(a) (b)

Figure 10.16: Close-up of saturation curve and the inversion region for the D6 fluid by using PRSV and SW equations (a). Location of left and right states along the isentropes (b).

n^o	Fluid	Test Case (TC) conditions						Aim
		Left			Right			
		α	$\rho\ [\frac{kg}{m^3}]$	P [MPa]	α	$\rho\ [\frac{kg}{m^3}]$	P [MPa]	
TC1	FC70	1-ε	414.819	1.0128	1-ε	219.2398	0.8635	(i) Validation PRSV EOS. (ii) RSW for a quasi-single phase fluid
	Water	ε	1000		ε	1000		
TC2(a)	FC70	0.5	470.398	7.0766	0.5	248.991	0.8635	(i) RSW observation in a BIPHASE flow. (ii) Influence of initial gas volume fraction on RSW.
	Water	0.5	1000		0.5	1000		
TC2(b)	FC70	0.1	470.398	7.0766	0.1	248.991	0.8635	
	Water	0.9	1000		0.9	1000		
TC3(a)	D6	1-ε	187.992	0.91295	1-ε	123.596	0.80724	(i) Influence of thermodynamic model on RSW observation. (ii) Comparison of PRSV-SW EOS in multiphase flows.
	Water	ε	1000		ε	1000		
TC3(b)	D6	1-ε	176.0179	0.91295	1-ε	120.782	0.80724	
	Water	ε	1000		ε	1000		

Table 10.6: Initial conditions for all test cases. $\varepsilon = 10^{-8}$. For all test cases, in the right and left part, u_k=0.

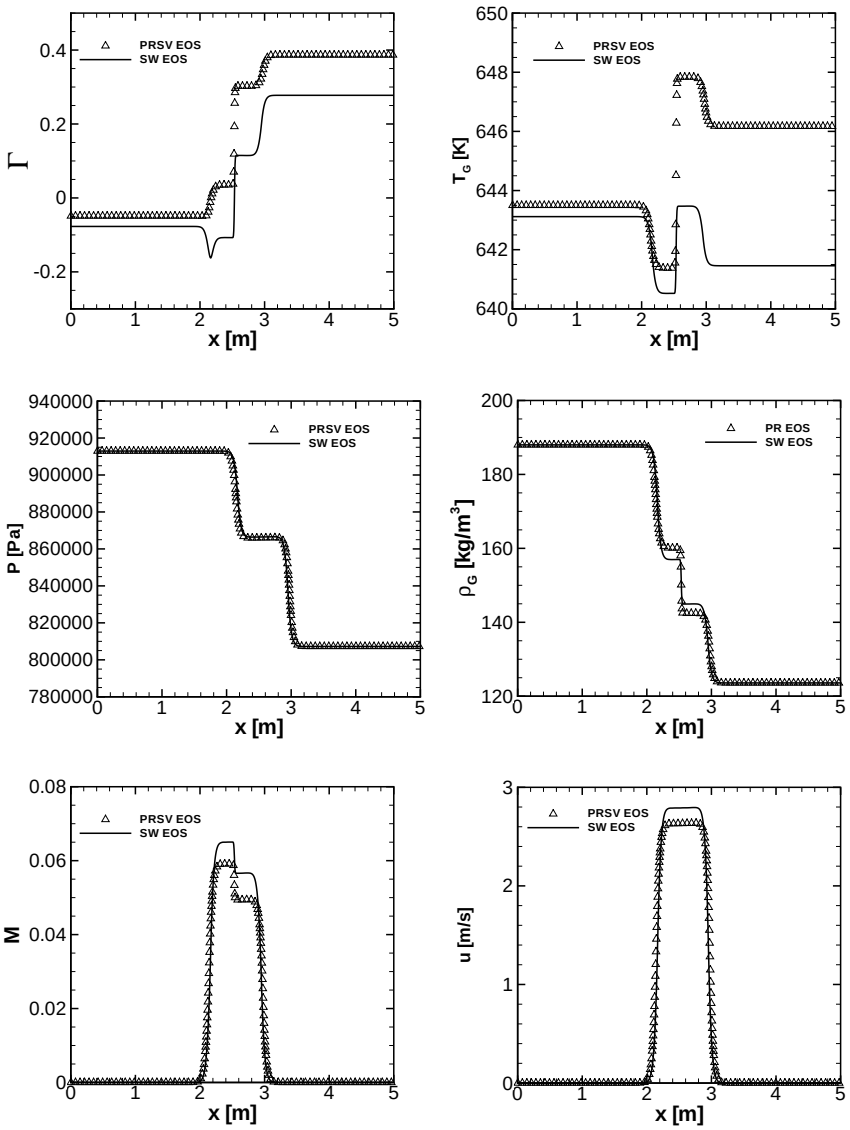

Figure 10.17: Vapor volume fraction, vapor density, mixture density, velocity, pressure and gas temperature profiles for TC3(a) test case.

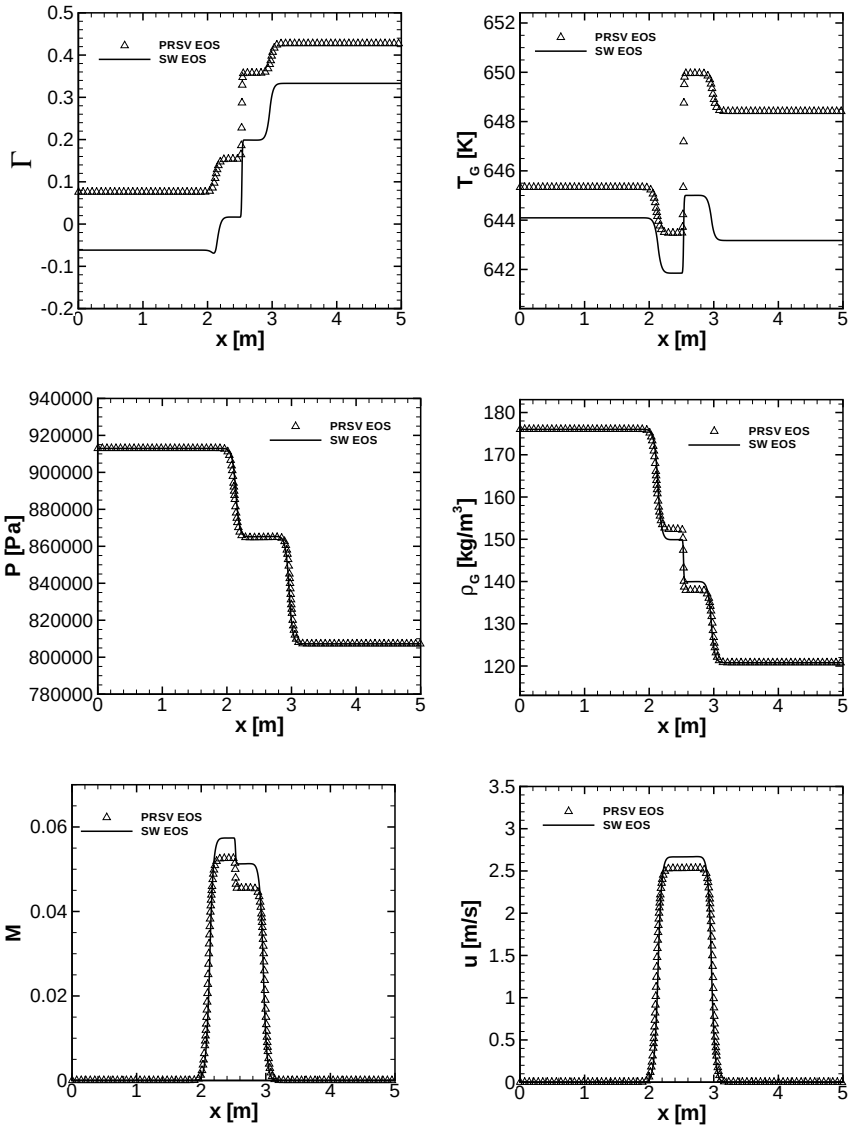

Figure 10.18: Vapor volume fraction, vapor density, mixture density, velocity, pressure and gas temperature profiles for TC3(b) test case.

Chapter 11

Some conclusions and perspectives

Contents

In this section, I have summarized the main results that I have obtained along the various axes of my research activity. In particular, what has been done and what should be done are described for each specific topic. Finally, highlights on some works currently in progress are provided.

11.1 Methods and Algorithms

Intrusive schemes

The effort towards the development of intrusive schemes for computational fluid-dynamics can be fully justified if a very high accuracy in describing shock-dominated flow is required. In my opinion, research should be directed in three main directions. The first issue to handle is related to the degree of intrusiveness of the approach (in terms of flexibility and work needed to perform modifications in a given deterministic code). The second point is related to the number of dimensions that can be handled intrusively without using some reduction strategy based on non-intrusive approach. The third point is the possibility to automatically refine/coarsen the mesh in the coupled physical/stochastic space, by ideally capturing and following for example the structure of a shock propagating in both spaces.

The formulation of the **Semi-Intrusive (SI)** method could be an option for increasing the accuracy of the stochastic solution by retaining in some way a lower degree of intrusiveness. For this very reason, this method is said semi-intrusive because it requires only a limited amount of modifications in a deterministic flow solver to quantify uncertainty on the flow state when the flow solver includes uncertain variables. It can be considered as very easy to implement in comparison with other intrusive methods, such as Polynomial Chaos. This method proves to be very efficient to deal with probability density function of any form, long-term integration and discontinuities in the stochastic space. Let us emphasize that up to now results have been obtained with SI systematically using an uniform grid in the stochastic space, without any kind of adaptivity according to the probability density function; there is clearly an interesting potential for further improvements along this line of adaptivity in the stochastic space for the SI method.

Though SI represents a very good option for UQ, its use for real problem with a high number of uncertainties remains very expensive. For this reason, the Harten multi-resolution technique has been considered, modified for the UQ framework (formulation of TE method) and then coupled with the SI method, yielding the aSI method.

The TE method, inspired from the classical Harten's framework, allows building, in a very general manner, stochastic numerical schemes starting from any type of deterministic schemes and handling a large class of problems, from unsteady to discontinuous solutions. Its formulations allows to recover the results of the classical multiresolution approach concerning the interpolation theory, but with an extension to uncertainty quantification problems. The TE method is extended to the spatial-TE (sTE), for partial differential equations and applied to the heat equation. Moreover, the flexibility of the proposed method is demonstrated by proposing a simple algorithm coupling together high-resolution schemes in the physical and in the stochastic spaces at the same time, and by applying it to the Burgers equation. These methods are not reported in this manuscript. Any interested reader might refer to [22,24].

The TE method, in its cell average setting, has been coupled with the Semi-Intrusive (SI) scheme. The overall numerical scheme is the so-called **adaptive-SI scheme**. We demonstrated that it preserves the convergence properties of the original SI scheme with a large saving in terms of computational cost. Different test-cases have been presented to demonstrate the efficiency and the accuracy properties of the aSI scheme. The linear advection equation has been solved for initial smooth and discontinuous solution to demonstrate the capability of the stochastic scheme to preserve the accuracy derived from the deterministic MUSCL-Hancock method (MHM). A second test-case has been focused on the inviscid Burgers equation. We demonstrated the capability of the method to automatically refine/coarsen following the changes in the regularity of the solution in the coupled stochastic/physical space. In particular, a smooth solution has been considered, in the stochastic space, as initial condition, where shock waves velocities are directly related to the parameter in the stochastic space. The final test case proposed has been the Euler system of equation to solve an uncertain shock tube problem. The aSI scheme has been demonstrated to be efficient also in the case of vectorial problems. For the computation of the convergence curves, an original strategy for the semi-analytical solution of the stochastic shock tube problem has been also developed following and extending the classical numerical procedure for the solution of the Riemann problem for the Euler equations. This paper represented the first effort to introduce a MR framework into the SI method. The generality of the approach is not limited to second order scheme, but can be easily extended to higher order numerical formulation for the physical space and time discretization. In this work, both the linear and non-linear MR framework have been presented in which the selection of the stencil to obtain the reconstruction operators can be obtained by a data-dependent procedure. The ENO selection of the stencil has been also introduced. Considering the numerical results presented, note that the advantages related to the non-linear schemes are very limited. This issue is not related to the non-linear procedure itself but to the peculiarity of the SI scheme that produces representations of the solution in a combined physical/stochastic space. The representation of a discontinuous solution in the stochastic space can recover a smoother behavior when the physical spatial resolution is not high enough. This has been demonstrated showing that the importance of the ENO scheme increases with the physical space resolution. To improve the global properties of the scheme, two further steps seem useful. The first is the introduction of the WENO reconstruction instead of the ENO interpolation in order to recover the correct stencil in all the regions where the solution is smooth. The other step could be to increase the polynomial order for the reconstruction. This should improve both accuracy and compression capabilities. The extension and the analysis of the aSI scheme for a moderate number of dimension is ongoing. In particular, aSI method has been extended for taking into account up to three dimensions in the stochastic space. Some highlights of this work have been presented in Section 11.3.

In order both to illustrate the flexibility of the aSI method and to yield an accurate stochastic numerical code for multiphase flow, the aSI method has been very recently incorporated into a DEM (Discrete Equation Method) formulation. Some highlights of this work have been presented in Section 11.3.

High-order decomposition

Global sensitivity analysis aims at determining contributions of each uncertainty to the variability of the studied output. This is a very active research field, since the most part of engineering applications are someway dependent on a huge number of physical and modeling uncertainties. Though several studies focused on ANOVA decomposition, low-cost computation by means of Polynomial-Chaos method or global criterion including several orders of statistical moments, very few studies exist on the extension of the ANOVA analysis to high-order statistical moments. In this field, my contribution can be summarized in the following points :

- A correlation was found between the functional decomposition, as depicted by Sobol, and the polynomial chaos development. This permitted to clearly identify each term of the decomposition, drawing also a practical way to compute all these terms.
- Computing skewness was shown to be of great importance for an exhaustive and complete stochastic analysis.
- Sensitivity indices based on kurtosis decomposition have been introduced. The importance of ranking the predominant uncertainties in terms not only of the variance but also of higher order moments (then extending the ANOVA analysis also to higher order statistic moments), was demonstrated with an algebraic function, where all the decomposition terms can be calculated analytically.
- How to compute high-order decomposition based on the Polynomial Chaos development is presented by estimating also the required computational cost.

Future works will be oriented towards adaptive strategies for the reduction of the global computational cost in the computation of the proposed indices.

Inverse problem

Concerning inverse problem, a very rich literature exist on the topic. Actually, some specific issues for CFD applications exist, since a massive use of CFD computations is not feasible in practice due to the high computational cost of each computation. One of the most interesting option is to build efficient metamodels in order to obtain a response surface to use instead of the very-expensive CFD simulation. These metamodels should be sufficiently robust for yielding a low approximation error also in spaces with a very large number of dimensions. In this manuscript, I have presented two methods, one deterministic and a Bayesian-one for handling inverse problem. In both cases, the overall algorithms have included a Polynomial Chaos framework for computing statistics or generating an accurate response surface.

In particular, the reconstruction of the free-stream conditions (p_∞, M_∞) for the trajectory of a re-entry vehicle from measurements of stagnation-point pressure and heat flux $(p_{\rm st}, q_{\rm st})$ has been performed. Prior uniform distributions are first assumed for (p_∞, M_∞) and some chemistry parameters are considered uncertain, with known distribution functions. The impact of the different uncertain inputs on the forward problem simulated by the in-house code COSMIC is studied using a non-intrusive stochastic spectral method. Uncertainties on (p_∞, M_∞) are observed to have a

large impact on p_{st}, whereas the chemistry uncertainties are observed to have a negligible impact on it. On the contrary, all the input parameters are observed to have a considerable impact on q_{st}. Then, a backward uncertainty propagation method is proposed to solve the inverse problem by taking into account uncertainties due to measurements and model parameters. To this end, we rely on a **Bayesian framework** supplied with MCMC algorithms to sample the posterior distribution of (p_∞, M_∞). A major difficulty lies in the fact that one needs to compute the forward problem for each iteration in the Markov chain. A metamodel for p_{st} is computed taking advantage from the non-intrusive spectral method; unfortunately such a metamodel can not be obtained for q_{st} because of the large interactions between the different parameters and the strong dependence of q_{st} on all the parameters. It was therefore decided to solve the stochastic problem only relying on the stagnation pressure measurements and the metamodel for p_{st} in a first step, so as to reduce the a priori on (p_∞, M_∞). On-going efforts consist in considering this new a priori for the resolution of the stochastic inverse problem with measurements of p_{st} and q_{st}, using adaptive algorithm to find the optimal widths vector in the MCMC algorithm and running Markov chains in parallel to accelerate the calculations.

Robust Optimization: Simplex2

Concerning robust design optimization, a large set of methods exist, but very few are focused on an efficient coupling between the information coming from the stochastic and the optimization spaces. In this perspective, the Simplex^2 method has been conceived. In particular, it is based on a multi-scale strategy, based on simplex tessellation on both uncertainty and design space in order to minimize the cost of robust optimization procedures. In particular, we coupled the SSC method employed for uncertainty quantification with the well-known Nelder-Mead optimization algorithm. The efficiency of the former is based on high degree polynomial interpolation and randomized refinement sampling, while the basic properties of the Nelder-Mead algorithm are improved by accelerating some evaluations by means of response surface built by performing a high-degree polynomial interpolation with P-refinement on the geometric simplex. The robustness and the excellent performances of the S2M method are obtained (i) by using a coupled stopping criterion, (ii) by a high-degree polynomial interpolation with P-refinement on the design space. Moreover, the error introduced by the interpolating polynomials is estimated in order to decide whether to use the interpolation in the design domain during the algorithm steps.

Robust Optimization: ANOVA-based analysis

Another possibility for reducing the global cost of the robust design relies on a dimension reduction strategy that is adapted to the design. The idea is to reduce the number of dimensions in the stochastic problem associated to a given design based on an ANOVA analysis. ANOVA analysis is used to perform a variance-based decomposition and to compute the Total Sensitivity Indices (TSI) for each uncertainty and an initial set of designs. Then, a response surface is generated for each TSI in the design space, that is used during the optimization loop. In this way, the uncertainties with a TSI lower than 2% (TSI criterion) can be discarded in the reduced stochastic problem associated to any design. During the optimization, the stochastic problem associated to a given design is reduced, thus decreasing the cost of the statistics estimation. This method is general and can be used with a deterministic black box solver.

The proposed robust-optimization algorithms are very efficient for treating high-dimensional problem. Further efforts are necessary for including high-order statistics by reducing the global computational cost.

11.2 Dense-gas physics

High-fidelity turbine computations

The design of ORC turbines using dense gases to achieve improved performances relies in a crucial way on the availability of accurate and efficient CFD tools because of the scarcity or even lack of available experimental set-up. The reliability of the CFD tools depends on the solution methods used to solve the conservation laws governing the dense gas flows and the choice of models retained to describe the thermodynamic behavior of these fluids. The results presented in this manuscript have demonstrated reliable numerical results could be obtained for turbine cascades using a BZT gas as working fluid since highly similar performances were computed by two distinct solvers. It was also pointed out a proper treatment of the outlet boundary condition was required to ensure a correct calculation of performance indices such as turbine isentropic efficiency, enthalpy jump and normalized temperature variation. The influence of the thermodynamic model on the performance prediction was investigated as well and it was found the simple Peng-Robinson-Stryjeck-Vera equation of state offers an interesting compromise between the accuracy level of the thermodynamic description and the computational cost of the CFD tool when used for turbine design. It must be emphasized the reliability study of the numerical tool (cross-validation of the solvers and investigation of the EoS influence) was performed on a large range of upstream thermodynamic conditions in order to account for the variability of the flow behavior encountered in practical applications. With the high level of confidence achieved regarding the output of dense gas flow simulations in turbine cascade, it was then possible to numerically investigate the influence of the choice of working fluid on turbine performance and the exact role of non-classical dense gas effects. The global performance parameters $(\eta, \delta h, \delta T/T_{inlet})$ provided by toluene, a fluid of common use in ORCs, were compared with those obtained using the BZT fluid D5; the analysis was performed using both the SW and PRSV EoS for a large range of operating conditions in order to check the comparison was only weakly dependent on the thermodynamic model. The BZT fluid consistently displayed attractive characteristics with respect to the conventional fluid: a higher power output for a given pressure ratio and a lower temperature variation well suited for cogeneration purposes. The beneficial effects of working in the inversion zone associated with a BZT fluid such as D5 or D6 were also demonstrated and quantified. While the present analysis has been restricted to the well-known LS-59 plane cascade geometry, the design of optimized ORC turbine working with BZT fluids remains however the final objective of our work. The next step towards this goal is the coupling of the present reliable BZT flow solvers with a shape optimization loop that takes into account the existing uncertainties on the thermodynamic model for such BZT fluids and the fluctuating inlet conditions typical of ORC sources.

Concerning dense-gas flows, currently developed numerical codes require the use of adapted turbulence models. These ones should be calibrated with respect to high-fidelity (DNS) turbulent flow simulations, since experimental data are not available.

Robustness of thermodynamic models

Another important aspect for improving the reliability of dense gas numerical simulation is related to the robustness of thermodynamic models. In this manuscript, for the first time in the literature, thermodynamic uncertainties in real gas flows past airfoils have been quantified. Propagation uncertainty performed for thermodynamic models of common use for dense gases shows that more complex models, used to achieve a more accurate description of the fluid thermodynamic response, may be more sensitive to uncertainties on the fluid thermo-physical properties because of the larger number of input parameters they require. Uncertainties are particularly critical when dense gas or non-classical gas dynamic effects are to be quantified. Two working fluids considered in the literature as possible candidates for dense gas experiments, namely, PP10 (a fluorocarbon) and D5 (a siloxane)

were analyzed with thermodynamic uncertainties propagated through a dense gas flow solver. The flow case selected for the computation is a transonic inviscid dense gas flow over a symmetric airfoil. For both fluids, the largest error bars on the solution are achieved in the region close to the shock, because of the highly nonlinear behavior of the flow-field. For simple thermodynamic models like RKS or PRSV, the mean stochastic solution is almost superimposed with the deterministic one, and the output distribution is almost Gaussian with standard deviation being within roughly 10% of the mean, at worst, i.e., approximately the order of magnitude of the input dispersion. For the MAH model, on the other hand, the computed results are much more sensitive to model parameter uncertainties, and the output distribution for the drag coefficient exhibits significant non-Gaussian interactions. For all the models, the sensitivity is higher for PP10 than for D5; this is related to the more extended region of nonclassical nonlinearity predicted for PP10, which deeply alters its gas dynamic behavior. For D5, a state-of-the art multiparameter thermodynamic model has also been considered, based on a 12-term SW equation of state. For this model, we restricted our investigation to uncertainties introduced by the caloric model, since uncertainties on the fluid thermal properties like p-v-T and saturation data are already taken into account in the regression procedure used to calibrate the model's coefficients by applying some weighting criteria to the calibration data. These are known in detail for the substance of interest, and their investigation, which requires going through the model optimization procedure, is not relevant for our purpose. For thermodynamic operating conditions well inside the dense gas region, the selected caloric uncertainties are amplified even if the SW model does not predict any inversion region for D5; specifically, a 3% variation of the caloric properties may produce variations of the drag coefficient of about 6%. If anyway, the flow thermodynamic conditions are moved to lower pressures and density, the thermodynamic behavior of the fluid becomes closer to that of a perfect gas, and the effects of thermodynamic uncertainties on the computed solutions become almost negligible.

Rarefaction shock wave

Since no experimental evidence of a RSW exist, the use of more accurate numerical simulation by means of uncertainty quantification tools is of great interest for estimating the probability of occurrence of this phenomenon, at least from a numerical point of view. Works presented in this manuscript investigate the efficiency of an existing experimental configuration for reproducing the RSW. Secondly, the possibility of using a new setting considering two-phase flows is explored, though further studies are still necessary. For estimating the reliability of the experiment in the FAST shock tube facility at TU Delft, an algorithm has been introduced to handle stochastic inverse problem with high efficiency and a reduced computational cost. The expected output of the flow problem (the unconventional Rarefaction Shock Wave) is very sensitive to uncertainties in the initial experimental conditions and in the parameters of the thermodynamic models adopted to describe the fluid.

The numerical deterministic simulation of the FAST experiment has been assessed by comparing two available CFD codes capable of treating dense-gas flows. Regarding the stochastic computations, the good accuracy provided by the PC approach for a reduced computational cost has been demonstrated by comparison with a Monte Carlo strategy. By considering only the thermodynamic model and its uncertainties, we first defined in a simplified way a robust initial condition P_1 for the shock tube experiment, that is an initial condition which maximizes the strength of the RSW while arguably preventing condensation in the charge tube. This initial condition may not be the best that could be actually obtained using the FAST setup to generate and measure a RSW. However using alternative conditions associated with a more complex equation of state would demand further work on the formulation of the equation of state, a task which is not relevant for our purpose.

Using this initial condition P_1, a forward uncertainty propagation problem based on full CFD simulations was considered, with the variability in both the initial conditions and the thermodynamic

model accounted for. The probability for the RSW Mach number to be less than unity was found to be equal to 27.8%, a value considered too high for ensuring a satisfactory reproducibility of the phenomenon. An inverse analysis has then been performed in order to determine how much the input uncertainties had to be reduced to decrease this probability. A preliminary ANOVA analysis was applied to obtain the most influential input parameters thus reducing the overall complexity of the stochastic problem. The left state temperature and pressure as well as the ideal-gas specific heat at constant volume were found to be the most influential parameters, contributing to 92% of the variance. Only these parameters were therefore considered for the inverse analysis, allowing the preservation of a high accuracy while benefiting from a strong reduction of the computational cost. The inverse analysis provided maximum admissible error levels on the initial conditions of the experiment to ensure the probability to obtain a RSW Mach number less than unity remains below 1% so that the experiment can be performed with a high degree of confidence. Unfortunately, such requirements on the experimental uncertainties seem hardly achievable and a trade-off between the needed accuracy and the number of experiments must be investigated. The method described in this paper remains a relevant tool to numerically investigate the sources of uncertainties in a delicate flow experiment and help directing the efforts towards the reduction of the experimental uncertainties. For the FAST experiment, different initial conditions - with a more complex equation of state - will be considered in order to further increase the estimated RSW Mach number.

A second work is focused on exploring the possibility of using a two-phase shock tube for the reproduction of a RSW. A semi-discrete scheme for the resolution of interface problems has been modified for taking into account complex equations of state. A reduced five equation model, under the hypothesis of pressure and velocity equilibrium, is used and discretized through the Discrete Equations Method (DEM), assuming no mass and heat transfer.

Then, the system is coupled with a mixture equation of state, that has been formulated for a general EOS, thus permitting real EOS-SG based mixture. In this case, SG has been systematically used for the liquid phase, while three EOS have been considered for the gas phase, *i.e.* SG, PRSV and SW. The PRSV EOS implementation has been validated by comparing the results obtained with the DEM code with the ones of a single-phase (vapor) code [Congedo 2012]. In particular, the operating conditions and the working fluid have been chosen in order to reproduce a rarefaction shock wave. A perfect agreement has been obtained between the DEM and the NZDG code. Then, a two-phase shock tube (liquid and vapor Dodecane) has been considered, where the influence of using a different equation of state has been evaluated. It has been observed that, for conditions closer to the saturation curve, considering a more complex equation of state, *i.e.* the PRSV EOS, is of prominent importance for achieving good predictions. Finally, the proposed method has been applied to the simulation of a rarefaction shock wave, displaying BZT effects in a two-phase flow for the first time in the literature. In particular, the influence of the initial conditions and of the thermodynamic model (by comparing PRSV with a very accurate technical EOS, *i.e.* SW EOS) has been analyzed for assessing which conditions could maximize the intensity of the rarefaction shock. It has been observed that the velocity of each structure in the flow, *i.e.* rarefaction shock, contact discontinuity and compression shock, is strongly influenced by the gas volume fraction. In particular, the velocity of RSW increases when the gas volume fraction decreases. Concerning the influence of the thermodynamic model, it has been noted that the accuracy in capturing thermodynamic behavior near the saturation curve and the inversion region, has a strong impact on the reproducibility of the RSW. This is a confirmation of the sensitivity of RSW to the initial conditions and to the thermodynamic model. Nevertheless, using a two-phase flow for illustrating a RSW could be very useful for a better control of the experiment in order to maximize the probability of occurrence, since no constraint for having strictly a vapor flow needs be imposed.

Future work will be focused on the implementation of the mass transfer terms. Moreover, a feasibility study on the new two-phase experimental setting for reproducing a RSW will be performed,

taking into account physical and modeling uncertainties.

11.3 Some works in progress

In this section, I mention some of my current research works.

11.3.1 SI-DEM numerical scheme for stochastic multiphase flow

A new scheme for the numerical approximation of a five-equations model taking into account uncertainty quantification (UQ) has been formulated. In particular, the Discrete Equation Method (DEM) for the discretization of the five-equations model is modified for including a formulation based on the adaptive Semi-intrusive (aSI) scheme, thus yielding a new intrusive scheme (sDEM) for simulating stochastic two-phase flows. Some preliminary results are shown here.

The numerical simulation of a shock tube filled out with water and air at the same volume fraction ($\alpha_k = 0.5$) on the right and on the left of a diaphragm (located at x=0.5m), is performed. The gas volume fraction on the left state is dependent on an uniformly distributed random parameter $\xi \sim \mathcal{U}[0,1]$: $\alpha_G(\xi) = \alpha_G \pm 0.1\xi$ and its propagation in the shock tube is observed. Simulations are performed over a physical domain $\Omega = [0,1]$ until a final time $t = 193.744\ \mu s$. The time space is divided in 1900 equal time steps of length $\Delta t = 1 \times 10^{-7}$. The simulations are carried out over equally spaced meshes of 101, 201, 401 and 801 points employing the aSI scheme based on the MUSCL method with a Superbee limiter.

In figure 11.1(a), the spatial convergence is reported for both the mean and the variance in L_1 norm for the density ρ. It has been obtained with the aSI method with a level of 128 ($m = 7$) stochastic cells. Results obtained by the aSI method have been compared with the ones obtained by a full SI scheme, in terms of L1 norm (figure 11.1(b)), showing a perfect overlapping of the curves.

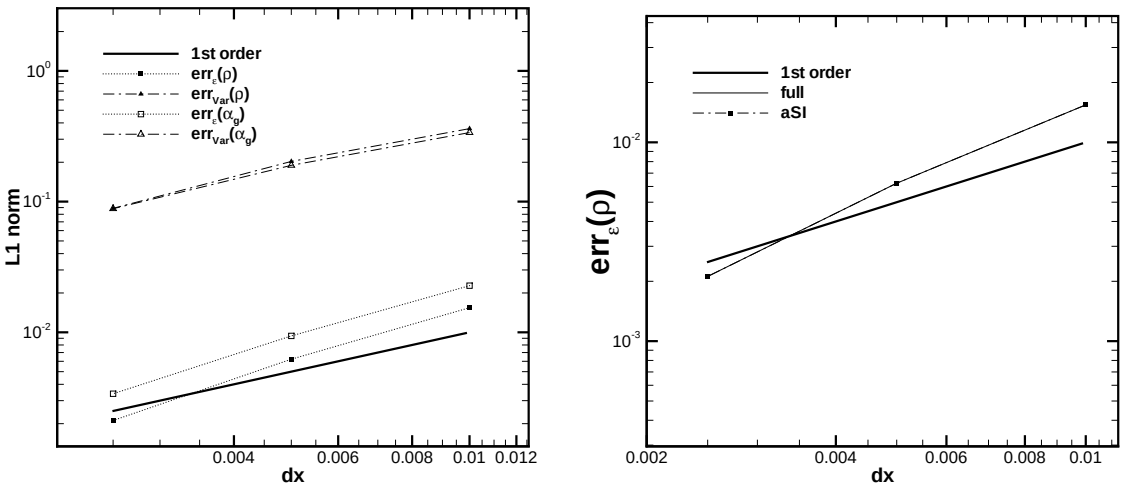

(a) (b)

Figure 11.1: (a) Spatial convergence for the stochastic shock tube problem with an uncertain volume fraction as initial condition. L1 norms are shown for the density expectancy and variance of the solution. (b) Comparison between aSI and full SI scheme obtained with a level of 128 (m=7) is shown on the stochastic spatial convergence of the density expectancy.

11.3.2 Extension of aSI scheme to 2D/3D

The adaptive-SI scheme has been already successfully extended to problems with 2D and 3D stochastic space. Some preliminary results have already been obtained for different test cases employing a linear reconstruction operator. For instance, the classical Sod test case is solved considering an initial condition depending on two random parameters. In particular, both density and pressure of the left state are assumed to be uniformly distributed. In figure 11.2, the results for both the expectancy and the variance, over the whole physical space, are reported as a function of the spatial resolution. Despite the strong reduction achieved by the adaptive procedure in terms of computational cost, the expected first order convergence, for the statistics of each conservative variable, is achieved. The extension of the approach to a high-order non-linear multiresolution reconstruction operator is underway.

11.3.3 High-order residual distribution schemes for dense-gases

Second and third order simulations with the non-linear residual-distribution (RD) scheme are performed, for two and three dimensional problems, with complex thermodynamic laws. The ability of the numerical solver to preserve the monotonicity of the solutions near strong shocks and the good convergence properties of the scheme for fluids which require more complex model that the ideal gas are verified. The flow over a two-dimensional turbine cascade with real gas effects is now considered. The configuration studied is the VKI LS-59 plane cascade of rotor blades, with the PRSV and the SW equations of state. Simulations have been performed on a sequence of three uniformly refined grids. The coarsest grid, made of 2 241 triangles, is shown in Fig. 11.3, finer grids are obtained by splitting each triangle into four sub-elements.

Simulations are performed with the PRSV and the SW equations of state, for the D5 working fluid. In all the cases, the operating condition is chosen such that at the inlet boundary $P/P_c = 0.6217864$ and $\rho/\rho_c = 0.2759043$ and the flow angle is 30°, at the outflow boundary the pressure ratio $P^t_{\text{in}}/P_{\text{out}} = 1.82$ is imposed, where P^t_{in} is the total pressure at the inflow and P_{out} is the static pressure at the outflow.

The Jacobian-free method with the LU-SGS preconditioner is used to make the scheme converge to the steady state, which is considered to be reached when the L^2 norm of the density residual has dropped at least by ten orders of magnitude. In Fig. 11.4 the convergence histories on the three levels of grids for the PRSV model are reported; a similar behavior is obtained with the SW equation of state. Note that the residual of the second order simulation on the coarsest grid could not be reduced by more than four orders of magnitude.

In Fig. 11.5, the Mach number contours of the third order simulations on the finest grid are displayed for the PRSV equation of state. From the inflow boundary on the left hand side of the domain, the fluid accelerates to supersonic velocities through the passage formed by the blade cascade. At the blade trailing edge, an over-expansion region can be observed and a weak shock appears downstream.

In Fig. 11.6, the distributions of the Mach number on different grids and with different accuracy orders are reported for the PRSV and SW models. The oscillations of the Mach number observed at the trailing edge are due to the fact that the inviscid flow model cannot correctly capture the separation around the blunt trailing edge of the blade, as also observed in Section 8. Increasing the order of approximation allows to reach a grid independent solution more efficiently than refining the mesh. Furthermore, the discontinuities are better resolved with the high-order approximation than the second order one, for the same number of degrees of freedom.

Finally, in Fig. 11.7 , the distributions of Mach number and pressure over the blade are reported for the third order RD solutions on the different grids; the solutions obtained with the cell-centered FV solver of Section 8 are also reported for the sake of comparison. Taking the third order simulation

on the finest grid as a reference, it can be observed that, for approximately the same number of degrees of freedom along the blade, the third order RD simulation is closer to the reference value with respect to the FV solution. Note also that the shock is always much better resolved with the third order RD scheme.

11.4 Short-term and long-term overall perspectives

I intend to preserve the current balance I have established between the development of methods and algorithms for reliable numerical simulations and their application in the aerospace and energy fields. As demonstrated (hopefully) in this memoir, I am indeed convinced that the analysis and design of real-life systems which are bound to introduce a large number of uncertainties not necessarily described by conventional pdfs is the best fuel for the continuous development of UQ methods and robust optimization techniques.

Some short-term objectives have been already mentioned in the previous paragraph for some specific methods or applications. Main actions in the long-term are resumed here :

- Concerning intrusive methods, the aim is to extend the aSI scheme for handling a large number of uncertainties by using high-order non-linear multiresolution reconstruction operator. A massive parallelization of the stochastic space is demanded. This algorithm will be applied to the stochastic simulation of shock-dominated compressible flows in dense-gas flows and hypersonic flows.

- Adaptive dimension-reduction strategy for problems featuring a very large number of uncertainties will be investigated. Particular attention will be devoted to the coupling of high-order decomposition with some recent approaches proposed in literature (for example [Doostan 2011, Yang 2012]). Further studies concerning very efficient and flexible optimization strategies are under way, with a focus on high-order statistical moments. This numerical framework will be used for the robust design of ORC cycles. It is planned to insert the local approach devoted to the numerical simulation of the sole turbine stage into a more global analysis of the whole cycle. The flexibility of the analysis and its potential to contribute to innovative designs will lead us to derive performance indices such as efficiencies based on the first and second laws as well as the net specific work of the cycle.

- Efficient Bayesian approaches will be used for including directly experimental data in the numerical framework. In this case, a massive use of metamodels is demanded, since the CFD is too expensive if complex effects are taken into account. This algorithm will be then used for improving the numerical prediction for aerospace application.

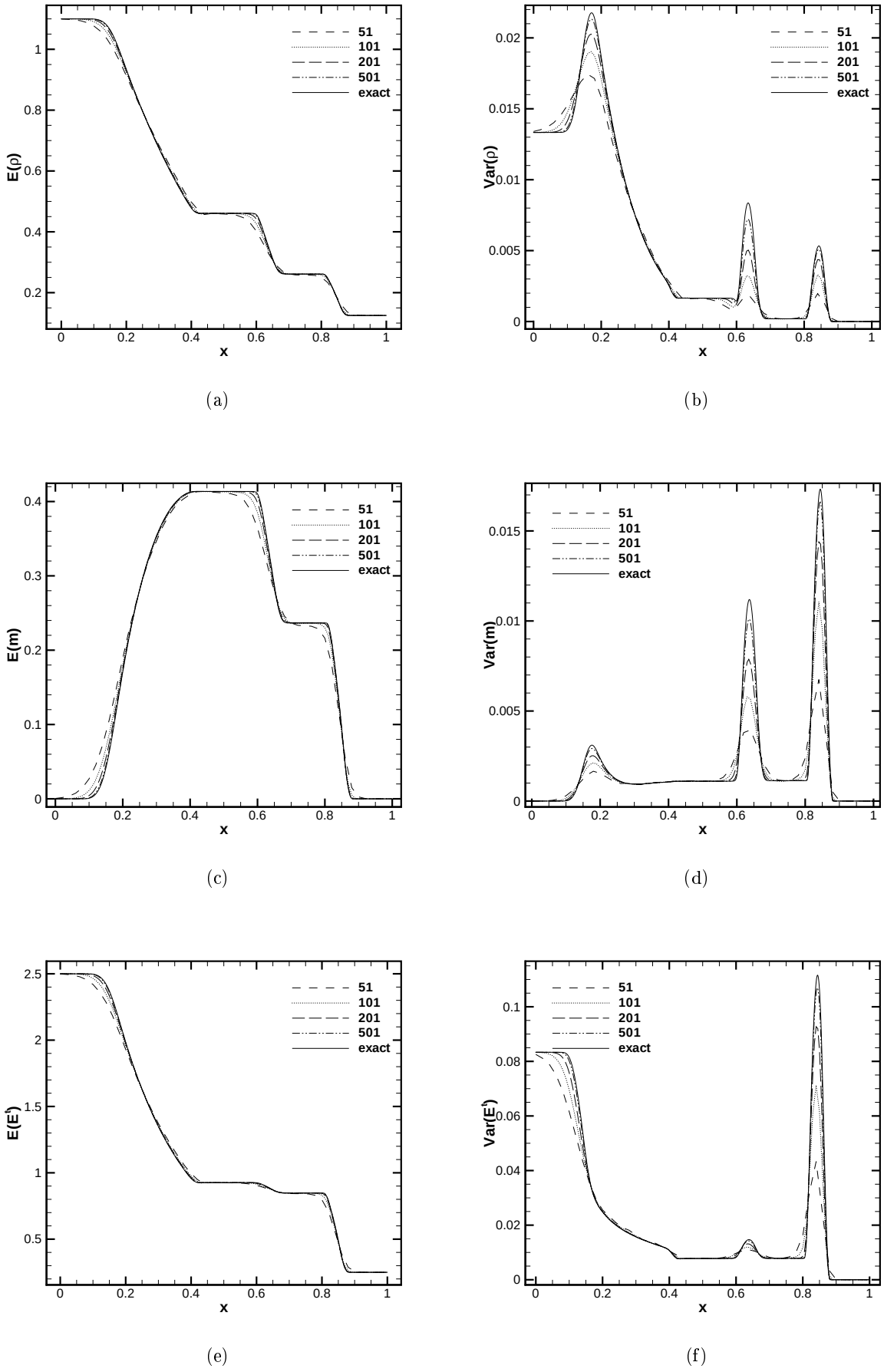

Figure 11.2: Expectancies for the uncertain shock tube for the density (a), momentum (c) and total energy (e). The variance of these quantities is reported respectively in (b), (d) and (f).

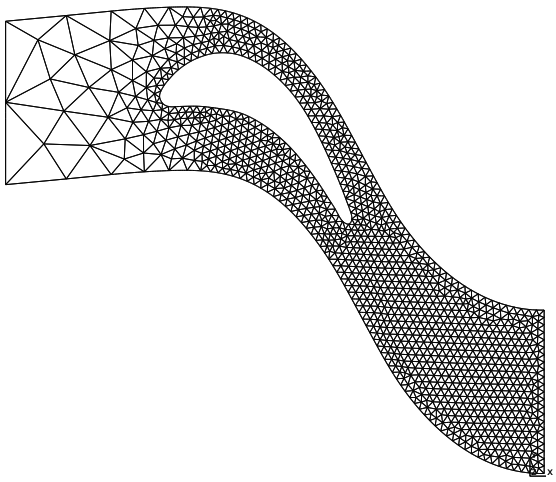

Figure 11.3: Coarsest grid used for the simulations of the turbine cascade.

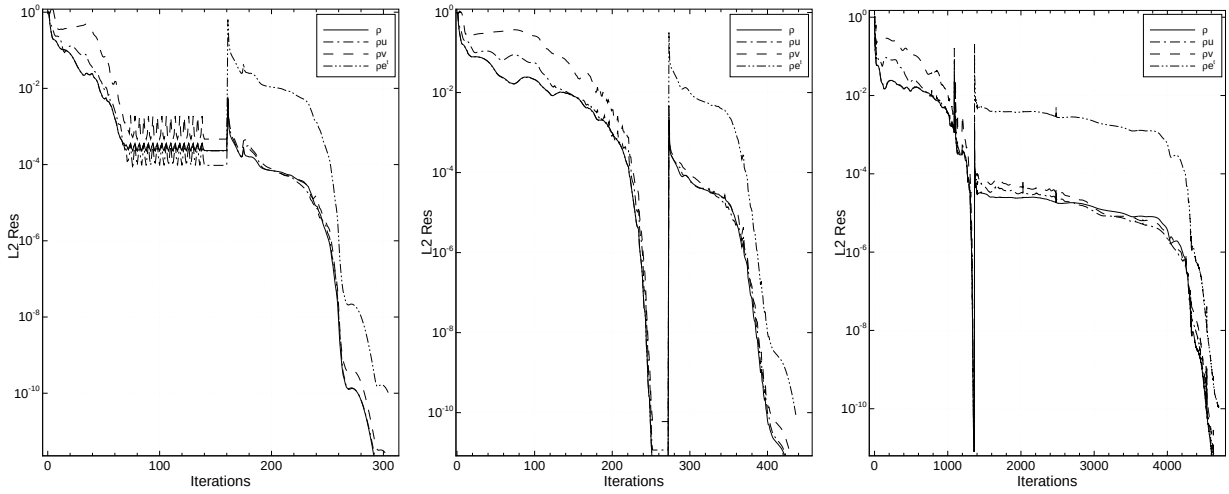

(a) Coarse (b) Medium (c) Fine

Figure 11.4: Convergence histories of the second and third order simulations (order sequencing used) with the PRSV models for three uniformly refined girds.

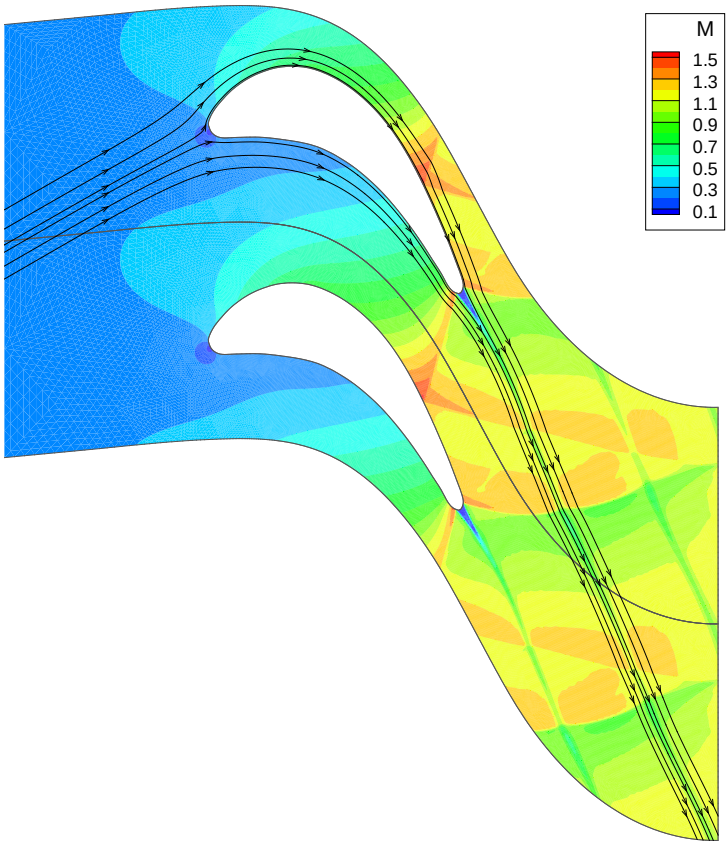

Figure 11.5: Mach number contours over the turbine cascade for the third order simulation on the finest grid. Streamlines are also reported.

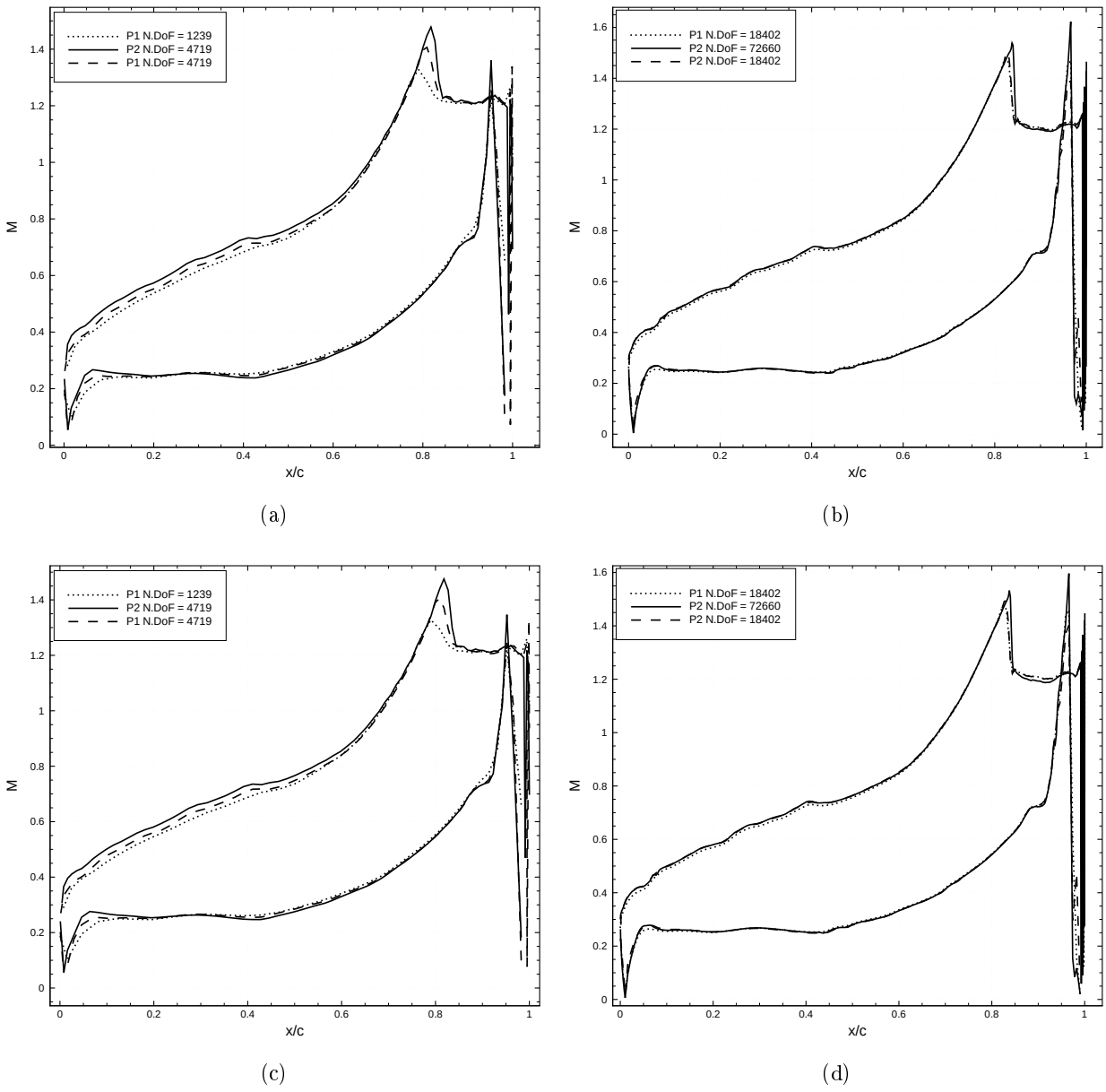

Figure 11.6: Mach number profiles over the blade on different grids with linear and quadratic approximation of the solution. Top row: PRSV, bottom row: SW models.

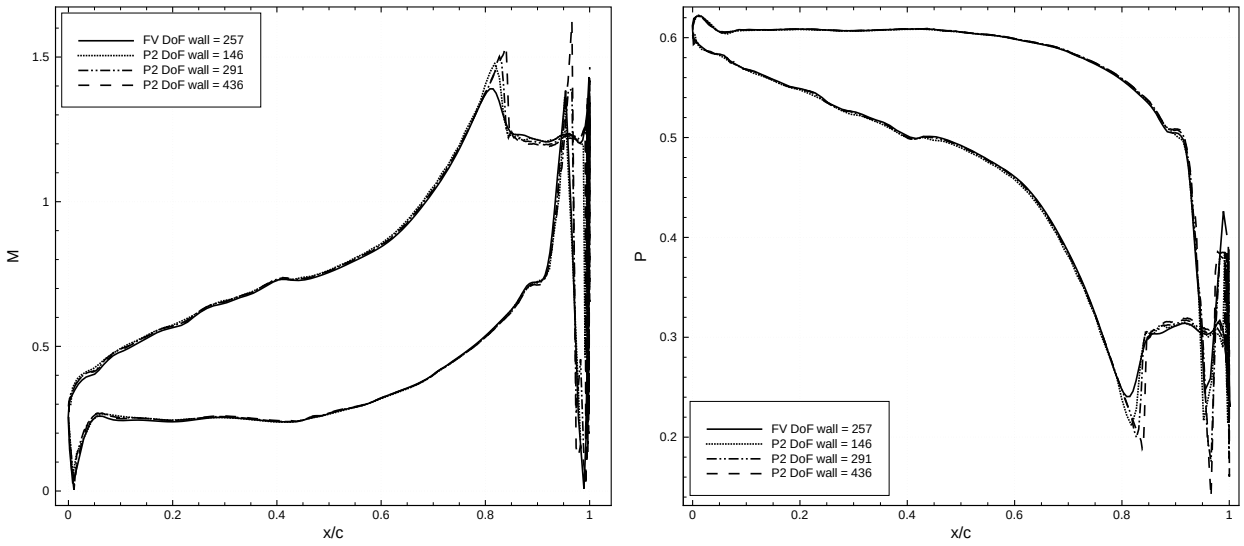

(a) (b)

Figure 11.7: Mach number (a) and pressure (b) distributions along the blade for the third order RD solution and the cell-centered FV solver. In the legend is reported the number of degrees of freedom along the blade of the different simulations.

Chapter 12

Academic Achievements

Contents

12.1 Curriculum

Doctorat(s) :

- Doctorat en Systèmes Énergétiques, Mention: Excellent, 18 juillet 2007, Università del Salento, Lecce (Italie)

Autres diplômes (à partir du niveau Master) :

- Mastère de Recherche EFA (Énergie, Fluides, Aérodynamique), Mention: Très Bien, Date : 30 Juin 2005, Établissement ayant délivré le diplôme : École Nationale Supérieure d'Arts et Métiers, Paris.
- *Laurea*[1] en Ingénierie des Matériaux, Note: 110/110 cum laude, Date : 10/12/2003, Università di Lecce, Italie.

12.2 Awards

1. **Prix de la Meilleure communication** au 44ème Colloque d'Aérodynamique Appliquée, qui s'est tenu à Nantes en Mars 2009 à la présentation intitulée : Quantification of thermodynamic uncertainties in real gas flows ayant pour auteurs : P. Cinnella, P.M. Congedo, L. Parussini, V. Pediroda. Organisme d'attribution : Commission Aérodynamique de la 3AF (Association Aéronautique Astronautique de France).

2. **Fellowship** de l'Université de Stanford pour la participation au Center for Turbulence Research (CTR) Summer Program 2010.

3. **Prime d'excellence scientifique**, INRIA 2012.

4. **Fellowship** de l'Université de Stanford pour la participation au Center for Turbulence Research (CTR) Summer Program 2012.

[1] Titre italien, délivré après cinq années d'études après le baccalauréat, équivalent à un Diplôme d'Ingénieur

12.3 Research supervision

Thèse

1. Gianluca Geraci, Année 2010-2013, Co-direction d'une thèse, Méthodes innovantes pour la prise en compte des incertitudes dans la simulation numérique en mécanique des fluides, INRIA Bordeaux Sud-Ouest. Part prise dans l'encadrement : 80%. Ce travail consiste dans l'extension de la méthode semi-intrusive à des approches de type multi-resolution à la Harten. La méthode a été déjà validée sur des cas connus dans la littérature et elle est très compétitive. Plusieurs papiers sont déjà publiés et soumis. Un autre axe de travail consiste dans la conception d'une stratégie qui permet de décomposer un problème stochastique selon les moments d'ordre plus élevé.

2. Francesca Fusi, Année 2013-2016, Co-direction d'une thèse, Méthodes innovantes pour l'optimisation robuste d'aubes d'hélicoptère, Politecnico di Milano et INRIA Bordeaux Sud-Ouest. Part prise dans l'encadrement : 50%. Les méthodes qu'on est en train de développer, se basent sur des approches type "multi-fidelity" et sur des méthodes de quantification d'incertitudes à moindre coût, conçues pour des problèmes non-stationnaires. Un papier vient d'être soumis à une conférence.

Post-Doc

1. Julie Tryoen, Année 2011-2013 : Co-direction d'un post-doc, INRIA Bordeaux Sud-Ouest. Part prise dans l'encadrement : 50%. Ce travail porte sur deux axes principaux: i) l'utilisation d'une méthode de type bayésien pour prendre en compte les données expérimentales dans la calibration de modèles et la résolution d'un problème inverse ; ii) l'extension de la méthode semi-intrusive pour prendre en compte des approches de type bayésien permettant de considérer les incertitudes expérimentales dans la simulation numérique.

2. Maria Giovanna Rodio, Année 2011-2013 : Co-direction d'un post-doc, INRIA Bordeaux Sud-Ouest. Part prise dans l'encadrement : 50%. Ce travail porte sur la simulation numérique des écoulements diphasiques avec des méthodes de type Discrete Equation method (DEM). La difficulté consiste dans la modélisation thermodynamique d'un gaz qui présente un comportement complexe dans la région monophasique et qui peut présenter un comportement non-convexe dans la région diphasique. Dans la littérature, on résout généralement ce problème en utilisant une équation plus simple, qui par contre ne peut pas prédire des effets de gaz réel. Pour cette raison, on a mis en place une méthode qui pourrait permettre de résoudre ce problème. Cette activité se développe dans le cadre de la plateforme, ORComp. Une deuxième activité repose sur l'application d'approche de type bayésien aux modèles thermodynamiques utilisés proche de la courbe de saturation.

3. Kunkun Tang, Année 2013-2014 : Co-direction d'un post-doc, INRIA Bordeaux Sud-Ouest/ANDRA. Part prise dans l'encadrement : 80%. Ce travail porte sur le développement de méthodes efficaces à moindre coût pour faire une décomposition de moments statistiques d'ordre plus élevé. Le but est ensuite d'appliquer ces méthodes à des problèmes multi-physiques caractérisés par un grand nombre d'incertitudes.

Master 2 et PFE

1. Romain Barelli and Ly-Vy Luong, Università di Lecce et ENSAM (Paris), Juin 2006, Projet PFE. Part prise dans l'encadrement : 50%. Ce travail a porté sur la mise en place dans le code NS3 d'un calcul d'écoulement de gaz dense dans des aubes de turbine. En plus, un couplage

avec un algorithme génétique a été réalisé, ceci a permis des calculs d'optimisation de forme de turbine. L'intérêt de ces travaux consiste dans la conception d'une géométrie de turbine adaptée pour l'exploitation des effets de gaz dense, objectif atteint pour la première fois.

2. Florian Rolé, Année 2008-2009: ENSE3, Grenoble INP, Co-direction d'un stage de 2ème année, Simulation numérique d'écoulements de gaz denses autour d'aubes de turbines . Part prise dans l'encadrement : 50%. Ce travail a porté sur l'implémentation de la loi d'état de Peng-Robinson dans le code NS3 pour la simulation d'écoulement dans des aubes de turbine. De plus il y a eu un couplage du code avec les librairies FluidPROP, qui contient les données thermodynamiques de plusieurs catégories de fluides. La version du code couplée avec la librairie a été comparé avec la version où on avait codé en dur l'équation d'état, ceci a permis de comparer les performances et la précision obtenues.

3. Birte Schmidmann (Université de Kaiserslautern), Année 2011 : Co-direction d'un stage, INRIA Bordeaux Sud-Ouest. Part prise dans l'encadrement : 30%. Ce travail a porté sur l'implémentation de méthodes numériques d'ordre élevé pour la simulation des écoulements hypersoniques. Je me suis occupé d'aider l'étudiant dans la résolution des problèmes numériques.

4. Razaaly Jamal Nassim, Année 2012 : Direction d'un stage, INRIA Bordeaux Sud-Ouest. Part prise dans l'encadrement : 100%. Ce travail consiste dans le développement d'une plateforme numérique à utiliser pour la simulation des cycles ORC. Cette interface permet de lier ensemble un code de quantification d'incertitude, un code d'optimisation et un code permettant de décrire un cycle ORC du point de vue thermodynamique à l'aide de Fluidprop (conçu à l'Université de Delft pour calculer les propriétés thermodynamiques des fluides).

5. Razaaly Jamal Nassim, Année 2013, Direction d'un projet PFE, INRIA Bordeaux Sud-Ouest. Part prise dans l'encadrement : 100%. Le travail porte sur l'extension de la méthode à résidus distribués aux écoulements régis par des lois d'état complexes. La méthode numérique a été modifiée et plusieurs lois ont été implémentées. Le code ainsi modifié a été appliqué à la simulation des plusieurs configurations 2D et 3D.

6. Abdallah Mansouri, Année 2013 : Direction d'un stage, INRIA Bordeaux Sud-Ouest. Part prise dans l'encadrement : 100%. Le travail porte sur l'application des méthodes de type bayésien à l'optimisation robuste et à la calibration de modèles thermodynamiques complexes.

7. Marc Duvernet, Année 2013 : Direction d'un stage, INRIA Bordeaux Sud-Ouest. Part prise dans l'encadrement : 100%. Le travail consiste dans la construction de métamodèles dans des espaces à grande dimension. L'idée est de pouvoir utiliser une surface de réponse à moindre coût au lieu de plusieurs calculs de fluides, qui peuvent s'averer très chers.

TER

1. Marie-Laetitia KHOURY-HELOU , Zaki ABIZA, Année 2010-2011: ENSEIRB-MATMECA, Bordeaux, TER de deuxième année.
   Part prise dans l'encadrement : 100%. Ce travail a porté sur l'implémentation d'une équation de Peng-Robinson dans un code de simulation pour reproduire un choc de détente dans un tube à choc.

2. Mohamad Samer , Razaaly Jamal Nassim, Année 2011-2012, ENSEIRB-MATMECA, Bordeaux, TER de deuxième année. Part prise dans l'encadrement : 100%. Il s'agit d'une étude de l'influence des incertitudes physiques sur la conception des modèles thermodynamiques complexes. En particulier, on travaille actuellement sur des méthodes efficaces pour améliorer la

stabilité des équations d'état, pour pouvoir les utiliser dans des codes de simulation numérique pour les gaz réels.

3. Fatmi Amine, Bordet Aurélien, Année 2011-2012, ENSEIRB-MATMECA, Bordeaux, TER de deuxième année. Part prise dans l'encadrement : 100%. Le travail porte sur la modélisation et la simulation des cycles ORC (Organic Rankine Cycles). L'idée consiste à mettre en place une approche couplée en faisant en même temps la simulation numérique de la turbine ORC et l'analyse globale du cycle. Ensuite la boucle a été liée à une méthode d'optimisation pour pouvoir calculer les conditions idéales de fonctionnement du système.

4. Marc Duvernet, Mickael Capelli, Année 2012-2013, ENSEIRB-MATMECA, Bordeaux, TER de deuxième année. Part prise dans l'encadrement : 100%. Le travail consiste dans l'implémentation d'une méthode de type bayésien pour la reconstruction des conditions amont à partir des conditions à la paroi.

5. Claire Morel, Fabien Gadichau, Année 2012-2013, ENSEIRB-MATMECA, Bordeaux, TER de deuxième année. Part prise dans l'encadrement : 100%. Le travail consiste dans l'étude de l'effet thermique dans des écoulements cavitants. En particulier, la contribution des termes conducitfs et convéctifs dans l'équation de Rayleigh-Plesset est prise en compte.

12.4 Collective tasks

1. **Responsable de l'équipe associée AQUARIUS (INRIA-Bordeaux and Stanford University).** Cette équipe rassemble trois groupes de recherches (Bacchus à INRIA Bordeaux Sud-Ouest, le Département de Mécanique et le Département Aéronautique et Aérospatial à l'Université de Stanford). Sa mission est l'excellence scientifique sur deux thématiques à très fort potentiel, c'est-à-dire la quantification des incertitudes et la simulation des écoulements à grand nombre de Reynolds (basée sur des méthodes d'enrichissement de la couche limite).

2. **Activité de Révision** pour Physics of Fluids, Journal of Computational Physics, Computers and Fluids, International Journal for Numerical Methods in Fluids, International Journal of Environmental Engineering, Engineering Computations, Journal of Marine Science and Technology, Biomedical Signal Processing and Control.

3. **Participation au comité de lecture et de révision** des *Technical Publications* pour la conférence *ASME 2010 10th Biennial Conference on Engineering Systems Design and Analysis (ESDA 2010)*, Istanbul, Turkey from 12 to 14 July 2010.

4. **Participation au comité de lecture et de révision** des *Technical Publications* pour la conférence AIAA 2012 12th Non-deterministic conference, Hawai, USA, avril 2012.

5. **Participation au comité de lecture et de révision** des *Technical Publications* pour la conférence AIAA 2013 13th Non-deterministic conference, Hawai, USA, avril 2013.

6. **Membre des Commissions d'examens** des cours suivants :

   - Fluidodinamica II (Dynamique des Fluides II), cours de 2ème cycle, Università del Salento, 2007/2008.
   - Fluidodinamica (Dynamique des Fluides), cours de 1er cycle, Università del Salento, 2007/2008.
   - Fluidodinamica numerica (Dynamique des Fluides Numérique), cours de 2ème cycle, Facoltà di Brindisi, Università del Salento, 2007/2008.

7. **Co-Organisation** de la conférence HONOM2013, tenue à INRIA-Bordeaux en mars 2013.

8. ***Chairman* à la session Eurogen 2011.**
J'ai été le *Chairman* dans la session de *Optimization and Uncertainty* dans le cadre de EUROGEN 2011, International Conference on Evolutionary and Deterministic Methods for Design, Optimization and Control with Applications to Industrial and Societal Problems, qui s'est tenu à Capoue, Italie. Cette conférence, qui se tient tous les deux ans, réunit les meilleurs experts d'optimisation au monde, et est une des conférences plus connues dans le domaine de l'optimisation.

9. **Chairman** à une session de la conférence Honom 2013, tenue à Bordeaux en mars 2013.

10. *Participation* au **comité de sélection** concernant le poste de MC/UPMC 0876 "Propagation des incertitudes, optimisation, contrôle robuste en CFD", Université Pierre et Marie Curie.

11. Expertise pour l'évaluation des projets de l'Idex de Sorbonne Paris Cité, Février 2013.

12. **Gestion du site web** de l'équipe BACCHUS, de l'équipe associée AQUARIUS, et de la conférence HONOM2013.

13. **Référent de l'équipe** pour l'organisation interne du nouveau bâtiment INRIA.

14. **Organisation de rencontres** appelés *Brainstorming*, avec les thésards de l'équipe Bacchus pour les habituer à présenter leur travaux et éventuellement les aider dans leurs travaux.

15. Presentation de l'outil Mendeley aux chercheurs de INRIA Bordeaux Sud-Ouest, Avril 2013.

12.5 Teaching

CM+TD

1. Année 2013-2014 : ENSEIRB-MATMECA, Bordeaux, TD (20h) de Mécanique des Fluides II, 2ème année.

2. Année 2013-2014 : ENSEIRB-MATMECA, Bordeaux, CM (30h) de Simulation numérique des écoulements fluides, 3ème année.

3. Année 2013-2014 : ENSEIRB-MATMECA, Bordeaux, TD (24h) de Analyse Numérique II, 1ère année.

4. Année 2012-2013 : ENSEIRB-MATMECA, Bordeaux, TD (20h) de Mécanique des Fluides II, 2ème année.

5. Année 2012-2013 : ENSEIRB-MATMECA, Bordeaux, CM (30h) de Simulation numérique des écoulements fluides, 3ème année.

6. Année 2012-2013 : ENSEIRB-MATMECA, Bordeaux, TD (24h) de Analyse Numérique II, 1ère année.

7. Année 2011-2012 : ENSEIRB-MATMECA, Bordeaux, TD (24h) de Analyse Numérique II, 1ère année.

8. Année 2009-2010: Ense3, Grenoble INP, Cours de troisième année d'école d'ingénieurs, niveau M2, Optimisation pour l'ingénieur, 8h de bureau d'études (BE).

9. Année 2008-2009: Ense3, Grenoble INP, Cours de première année *énergie et enjeux*, 4 de travaux dirigés (TD).

10. Année 2007-2008: Responsable du cours de 2ème cycle *Fluidodinamica II* (Dynamique des Fluides II), à l'Università del Salento (Italie), 24 heures de cours magistraux (CM) + 12 heures de travaux dirigés (TD).

11. Année 2007-2008: Università del Salento (Italie), Cours *Fluidodinamica Numerica* (Mécanique des Fluides Numérique), Master *Prototypage Numérique*, 8 h.

TER

1. Année 2012-2013: ENSEIRB-MATMECA, Bordeaux, TER de deuxième année sur le problème inverse dans les capsules aérospatiales, 6h.

2. Année 2012-2013: ENSEIRB-MATMECA, Bordeaux, TER de deuxième année sur l'effet thermique dans des écoulements cavitants, 6h.

3. Année 2011-2012: ENSEIRB-MATMECA, Bordeaux, TER de deuxième année sur la prise en compte des incertitudes dans les équations d'état complexes, 8h.

4. Année 2011-2012: ENSEIRB-MATMECA, Bordeaux, TER de deuxième année sur la modélisation et la simulation numérique des cycles ORC, 8h.

5. Année 2010-2011: ENSEIRB-MATMECA, Bordeaux, TER de deuxième année sur la simulation numérique en gaz dense, 8h.

Encadrement

- 2 thèse de doctorat
- 3 post-doc
- 2 PFE
- 5 stage de Master II
- 5 stage de type TER

12.6 Publications

Nombre de Publications	Depuis 2010	Globale
Articles dans des revues internationales avec comité de lecture	14	20
Chapitre de Livres	4	8
Articles soumis	4	4
Conférences internationales avec comité de lecture	25	41
Communication sans actes	1	9
Rapport de Recherche	13	13
Séminaires invités	14	21
Autres	0	3
GLOBALE	75	119

Articles dans des revues internationales avec comité de lecture

1. J. Tryoen, P.M. Congedo, R. Abgrall, N. Villedieu, T. Magin, Bayesian-based Method with metamodels for rebuilding free-stream conditions in atmospheric entry flows. Accepted with revisions in AIAA Journal.

2. R. Abgrall, M.G. Rodio, P.M. Congedo, Two-phase flow numerical simulation with real-gas effects: application to rarefaction shock waves. Accepted with revisions in European Journal of Mechanics/B Fluids.

3. M.G. Rodio, P.M. Congedo, Robust Analysis of cavitating flows in Venturi tube. Accepted with revisions in European Journal of Mechanics/B Fluids.

4. R. Abgrall, P.M. Congedo, G. Geraci, A One-Time Truncate and Encode Multiresolution Stochastic Framework. In press on Journal of Computational Physics.

5. P.M. Congedo, J. Witteveen, G. Iaccarino, 2013, A simplex-based numerical framework for simple and efficient robust design optimization. Computational Optimization and Application 56, 1, pp. 231-251.

6. P.M. Congedo, G. Geraci, R. Abgrall, V. Pediroda, L. Parussini, 2013, TSI metamodels-based multi-objective robust optimization. Engineering Computations 30, 8.

7. R. Abgrall, P.M. Congedo, A semi-intrusive deterministic approach to uncertainty quantifications in non-linear fluid flow problems. Journal of Computational Physics 2013, 235, pp. 828-845.

8. P.M. Congedo, G. Balarac, C. Duprat, C. Corre, Numerical prediction of turbulent flow using RANS and LES with uncertain inflow conditions. International Journal for Numerical Methods in Fluids 2013, Volume: 72, Issue: 3, pp. 341-358.

9. P. Cinnella, P.M. Congedo, 2013, Convergence behaviours of Genetic Algorithms for Aerodynamic Optimisation Problems. International Journal of Engineering Systems Modelling and Simulation, Vol. 5, No. 4, 2013, pp. 197-216.

10. P.M. Congedo, C. Corre, P. Colonna, J. Witteveen, G. Iaccarino, Backward uncertainty propagation method in flow problems: application to the prediction of rarefaction shock waves, Comput. Methods Appl. Mech. Engrg. 2012, Volume: 213-216, Issue: 1, pp. 314-326.

11. P. Cinnella, P.M. Congedo, V. Pediroda, L. Parussini, Quantification of uncertainties in compressible flows with complex thermodynamic behavior, Physics of Fluids 2011, 23, pp. 116101.

12. C. Duprat, G. Balarac, O. Metais, P.M. Congedo, O. Brugière, A wall-layer model for large-eddy simulations of turbulent flows with/out pressure gradient, Physics of Fluids 2011, 23, pp. 015101.

13. P.M. Congedo, C. Corre, P. Cinnella, Numerical Investigation of dense-gas effects in turbomachinery, Computers and Fluids 2011,Volume: 49, Issue: 1, pp. 290-301

14. P.M. Congedo, C. Corre, J.M. Martinez, Shape Optimization of an Airfoil in a BZT Flow with Multiple-source Uncertainties, Comput. Methods Appl. Mech. Engrg. 2011, Volume: 200, Issue: 1-4, pp. 216-232.

15. P. Cinnella, P.M. Congedo, V. Pediroda, L. Parussini, Quantification of Thermodynamic Uncertainties in Real Gas Flows, International Journal of Engineering Systems Modelling and Simulation, Vol. 2, Nos. 1/2, 2010, pp. 12-24 .

16. P. Cinnella, P.M. Congedo, Optimal airfoil shapes for viscous transonic flows of Bethe-Zel'dovich-Thompson fluids, Computer and Fluids, Volume: 37, Issue: 3, March, 2008, pp. 250-264 .

17. P. Cinnella, P.M. Congedo, Inviscid and viscous behavior of dense gas flows past an airfoil, J. Fluid Mech. 580(2007), 179-217.

18. P.M. Congedo, C. Corre, P. Cinnella, 2007,Airfoil shape optimization for transonic flows of Bethe-Zel'dovich-Thompson fluids. AIAA Journal, Vol. 45, No.6, pp.1303-1316.

19. P. Cinnella, P.M. Congedo, 2005, Aerodynamic performance of transonic BZT flows past an airfoil, AIAA Journal, Vol. 43, No.2, pp.370-378.

20. P. Cinnella, P.M. Congedo, 2005, Numerical solver for dense gas flows. AIAA Journal, Vol.43, No.11, pp. 2457-2461.

Articles soumis

21. R. Abgrall, P.M. Congedo, G. Geraci, G. Iaccarino, An adaptive multiresolution semi-intrusive scheme for UQ in compressible fluid problems

22. R. Abgrall, P.M. Congedo, G. Geraci, G. Iaccarino, Non-linear Multiresolution framework for Uncertainty Quantification in Computational Fluid Dynamics.

23. R. Abgrall, P.M. Congedo, G. Geraci, G. Iaccarino, Decomposition and Computation of high-order statistics.

24. R. Abgrall, P.M. Congedo, G. Geraci, Toward a Unified Multiresolution Scheme in the Combined Physical/Stochastic Space for Stochastic Differential Equations.

Chapitre de Livres

25. R. Abgrall, P.M. Congedo, G. Geraci, G. Iaccarino, Adaptive strategy in multiresolution framework for uncertainty quantification. Proceedings of the 2012 Summer Program, Center for Turbulence Research, Stanford University, pp. 209-218.

26. R. Abgrall, P.M. Congedo, G. Geraci, An Adaptive Multiresolution Inspired Scheme for Solving the Stochastic Differential Equations. Proceedings of MASCOT11, pp. 1-10.

27. P.M. Congedo, J. Witteveen, G. Iaccarino, Simplex-simplex approach for robust design optimization, EUROGEN 2011 Proceedings, ECCOMAS Thematic Conference, pp. 554-569.

28. P.M. Congedo, G. Geraci, R. Abgrall, V. Pediroda, L. Parussini, Efficient ANOVA decomposition and metamodel-based multi-objective robust optimization, EUROGEN 2011 Proceedings, ECCOMAS Thematic Conference, pp. 493-504.

29. P.M. Congedo, C. Corre, P. Colonna, J. Witteveen, G. Iaccarino, Robust simulation of non-classical gas-dynamics phenomena. Proceedings of the 2010 Summer Program, Center for Turbulence Research, Stanford University, pp. 27-40.

30. P.M. Congedo, P. Cinnella, C. Corre, Efficient Numerical Simulation of Dense Gas Flows Past Airfoils and Wings. Computational Fluid Dynamics 2008, Part 16, pp. 295-300, Springer-Verlag.

31. P.M. Congedo, P. Cinnella, C. Corre, Shape Optimization for Dense Gas Flows in Turbine Cascades. Computational Fluid Dynamics 2006, Part 6, pp. 555-560, Springer-Verlag.

32. P. Cinnella, P.M. Congedo, D. Laforgia, Transonic Flows of BZT Fluids Through Turbine Cascades. Computational Fluid Dynamics 2004, Part VI, pp. 227-232, Springer-Verlag.

Conférences internationales avec comité de lecture

33. R. Abgrall, P.M. Congedo, D. De Santis, G. Geraci, Stochastic analysis and robust optimization of an experimental setting for converging shock waves studies, MASCOT 2013, San Lorenzo de El Escorial, Spain.

34. R. Abgrall, P.M. Congedo, G. Geraci, A high-order adaptive semi-intrusive finite volume scheme for stochastic partial differential equations, MASCOT 2013, San Lorenzo de El Escorial, Spain.

35. F. Fusi, P.M. Congedo, G. Quaranta, A. Guardone, Multi-fidelity approach for aerospace applications, EUROGEN 2013, Las Palmas de Gran Canaria. Spain.

36. R. Abgrall, P.M. Congedo, G. Geraci, G. Iaccarino, Multi-objective design optimization using high-order statistics for CFD applications, EUROGEN 2013, Las Palmas de Gran Canaria. Spain.

37. P. M. Congedo, P.M. Congedo, L. Parussini, V. Pediroda, Optimization under uncertainty of horizontal ground heat exchangers, EUROGEN 2013, Las Palmas de Gran Canaria. Spain.

38. P.M. Congedo, G. Geraci, D. De Santis, On the predictive estimation of converging shock waves, Congrés Français de Mécanique, Bordeaux, 2013.

39. M.G. Rodio, J. Tryoen, P.M. Congedo, Construction d'un modèle thermodynamique fiable et robuste pour les mélanges liquide-vapeur, Congrés Français de Mécanique, Bordeaux, 2013.

40. P.M. Congedo, M. Ricchiuto, Robust simulation of shallow water long wave run-up, Congrés Français de Mécanique, Bordeaux, 2013.

41. M.G. Rodio, P.M. Congedo, Robust estimation of the thermal effect considering convective and conductive heat transfer in hydrogen cavitating flow, EUROTHERM SEMINAR 96, September 2013, Bruxelles, Belgium.

42. J. Tryoen, P.M. Congedo, T. Magin, Characterization of the freestream conditions in the VKI Longshot facility, EUROTHERM SEMINAR 96, September 2013, Bruxelles, Belgium.

43. R. Abgrall, P.M. Congedo, G. Geraci, A high-order non-linear multiresolution scheme for stochastic-PDE, Honom 2013, March 2013, Bordeaux, France.

44. R. Abgrall, P.M. Congedo, G. Geraci, G. Iaccarino, High-order statistics-based robust design optimization, 11th International Conference on Structural Safety & Reliability, June 2013, New York, USA.

45. J. Tryoen, P.M. Congedo, R. Abgrall, N. Villedieu, T. Magin, Sensitivity analysis and characterization of the uncertain input data for the EXPERT vehicule, 51st AIAA Aerospace Sciences Meeting, January 2013, Grapevine, USA.

46. M. Ricchiuto, P.M. Congedo, G. Geraci, R. Abgrall, Uncertainty propagation in shallow water long wave runup simulations, 1st International Conference on Frontiers in Computational Physics: Modeling the Earth System, December 2012, Boulder, USA.

47. P.M. Congedo, C. Corre, R. Abgrall, Robust performance assessment for an oscillating airfoil using a Time-Spectral Method and a non-intrusive uncertainty propagation method, ICCFD7 - International Conference on Computational Fluid Dynamics, July 2012, Island of Hawaii, United States.

48. R. Abgrall, M.G. Rodio, P.M. Congedo, Efficient algorithm for viscous two-phase flows with real gas effects, ICCFD7 - International Conference on Computational Fluid Dynamics, July 2012, Island of Hawaii, United States.

49. R. Abgrall, M.G. Rodio, P.M. Congedo, Innovative formulation for the numerical simulation of uncertain shock waves in dispersed two-phase flows, ECCOMAS 2012, September 2012, Vienna, Austria.

50. P.M. Congedo, J. Witteveen, G. Iaccarino, A simplex-simplex approach for mixed aleatory-epistemic uncertainty quantification, 14th Non-deterministic Approaches Conference, April 2012, Honolulu, Hawai, USA.

51. R. Abgrall, P.M. Congedo, G. Geraci, An adaptive semi-intrusive finite-volume scheme for the solution of stochastic partial differential equations, MASCOT 2011 - 11TH MEETINGS ON APPLIED SCIENTIFIC COMPUTING AND TOOLS, Oct 2011, Rome, Italy.

52. P.M. Congedo, C. Duprat, G. Balarac, C. Corre, Effects of inlet uncertainties on prediction of turbulent flows using RANS and LES simulations, AIAA Paper 2011-3869, 20th AIAA Computational Fluid Dynamics Conference, Jun 2011, Honolulu, Hawaii, USA

53. P.M. Congedo, P. Cinnella, S. Hercus, C. Corre, Efficient robust optimization techniques for uncertain dense gas flows, CFD & Optimization - ECCOMAS Thematic Conference, May 2011, Antalya, Turkey.

54. P.M. Congedo, C. Corre, J.P. Thibault, G. Iaccarino, Global analysis of Organic Rankine cycles integrating local CFD simulations and uncertainty, First International Seminar on ORC Power Systems, September 2011, Delft, Netherlands.

55. P.M. Congedo, J. Witteveen, G. Iaccarino, Simplex-simplex approach for robust design optimization, EUROGEN 2011, International Conferences on Evolutionary Computing for Industrial Applications. - ECCOMAS Thematic Conference, Sep 2011, Capua, Italy

56. R. Abgrall, P.M. Congedo, S. Galera, , G. Geraci, Semi-intrusive and non-intrusive stochastic methods for aerospace applications, 4th European Conference for Aerospace Sciences, Saint Petersburg, Russia (2011)

57. P.M. Congedo, G. Geraci, R. Abgrall, V. Pediroda, L. Parussini, Efficient ANOVA decomposition and metamodel-based multi-objective robust optimization, EUROGEN 2011, International Conferences on Evolutionary Computing for Industrial Applications. - ECCOMAS Thematic Conference, Sep 2011, Capua, Italy

58. R. Abgrall, P.M. Congedo, C. Corre, S. Galera, A simple semi-intrusive method for uncertainty quantification of shocked flows, comparison with a non-intrusive polynomial choas method, ECCOMAS CFD 2010, 14-17 June 2010, Lisbon, Portugal.

59. C. Duprat, O. Brugière, P.M. Congedo, G. Balarac, O. Metais, A wall model for LES of turbulent flows with/out pressure gradient, ERCOFTAC Workshop Direct and Large Eddy Simulation 8, July 2010, Eindhoven, The Netherland.

60. P. Cinnella, P.M. Congedo, V. Pediroda, L. Parussini, Quantification of thermodynamic uncertainties in real flows, 44eme Colloque d'Aérodynamique Appliquée, Nantes, avril 2009.

61. M. Giordano, P.M. Congedo, P. Cinnella, Nozzle Shape Optimization for Wet-Steam Flows, 19th AIAA Computational Fluid Dynamic Conference, San Antonio, June 2009.

62. P. Cinnella, P.M. Congedo, V. Pediroda, L. Parussini, Quantification of uncertainties in compressible flows with complex thermodynamic behavior, 39th AIAA Fluid Dynamic Conference, San Antonio, June 2009.

63. P.M. Congedo, P. Cinnella, C. Corre, 2008, Aerodynamic performance of turbulent dense gas flows past airfoils and wings, 5th ICCFD, Seoul, July 2008.

64. M.G. De Giorgi, P.M. Congedo, M.G. Rodio, A. Ficarella, 2008, Shape optimization for cryogenic cavitating flows past an isolated hydrofoil, 2008 ASME Heat Transfer /Fluids /Solar /Nano Conferences, Jacksonville, August 2008.

65. Pietro M. Congedo, S. Collura, Paolo M. Congedo, 2008, Modeling And Analysis of Natural Convection Heat Transfer In Nanofluids, presented to the 2008 ASME Heat Transfer /Fluids /Solar /Nano Conferences, Jacksonville, August 2008.

66. P. Cinnella, P.M. Congedo, 2008, Accurate and Computationally Efficient Equations of State for the Numerical Simulation of Dense Gas Flows, 38th AIAA Fluid Dynamic Conference, Seattle, June 2008.

67. P. Cinnella, P.M. Congedo, 2007, GA-Hardness of Aerodynamic Optimization Problems: Analysis and Proposed Cures, 37th AIAA Fluid Dynamic Conference, Miami, June 2007.

68. P.M. Congedo, P.Cinnella, , C. Corre, 2006, Shape optimization for dense gas flows through turbine cascades, 4th International Conference on Computational Fluid Dynamics (ICCFD 4), Ghant, Belgium, July 2006.

69. P.Cinnella, P.M. Congedo, 2006, GA-Hardness of dense-gas flow optimization problems, Paper 522-151. Proceedings of 15th IASTED International Conference on Applied Simulation and Modelling, Rhodes, Greece, June 2006. ISBN: 0-88986-561-2, pp. 489-494.

70. P.Cinnella, P.M. Congedo, 2005, Optimal airfoil shapes for viscous dense gas flows, Paper 2006-3881, 36th AIAA Fluid Dynamic Conference, San Francisco, june 2006.

71. P.Cinnella, P.M. Congedo, D. Laforgia, 2004, Investigation of BZT transonic flows past an airfoil using a 5th power virial equation of state. Proceedings ECCOMAS 2004 (on CD-ROM), European Conference on Computational Mechanics and Applied Sciences, Jyv$^{\prime}$askyl$^{\prime}$a,Finland, 24-28 july 2004. ISBN: 951-39-1868-8.

72. P. Cinnella, P.M. Congedo, D. Laforgia, 2004, Transonic BZT flows through turbine cascades, Proceedings ICCFD3, 3rd International Conference on Computational Fluid Dynamics,- Toronto, Canada, 12-16 july 2004.

73. P. Cinnella, P.M. Congedo, 2004, A numerical solver for dense gas flows, AIAA Paper 2004-2137. 34h AIAA Fluid Dynamics Conference and Exhibit, Portland, Oregon, 28 june-1er july 2004.

Communication sans actes

74. M. Ricchiuto, P.M. Congedo, Robust Code-to-Code Validation by Means of Parameter Uncertainty Propagation and Anova, 2013 SIAM Conference on Mathematical & Computational Issues in the Geosciences, June 2013, Padova, Italy.

75. P.M. Congedo, C. Corre, Optimization under uncertainty of tear substitute rheological properties, International modeFRONTIER Users' Meeting 2010, May 2010, Trieste, Italy.

76. V. Pediroda, L. Parussini, P. Cinnella, P.M. Congedo, Simulation of real-gas flow with uncertainty analysis, 2nd International Workshops on Advances in Computational Mechanics, March 29-31, 2010, Yokohama, Japan.

77. P.M. Congedo, C. Corre, J.M. Martinez, Uncertain shape optimization for dense gas flows, 62nd Annual Meeting of the American Physical Society's Division of Fluid Dynamics (DFD), Minneapolis, November 2009

78. P.M. Congedo, C. Corre, Simulation d'écoulements de gaz denses en turbines, Congrés FranÃğais de Mécanique 2009, Marseille.

79. P. Cinnella, P.M. Congedo, 2004, Analysis and Optimization of Viscous Dense Gas Flow, 18h AIMETA Congress of Theoretical And Applied Mechanics, September 2007.

80. P.M. Congedo, P. Cinnella, C. Corre, 2008, Efficient numerical simulation of three-dimensional Bethe-Zel'dovich-Thompson Fluid Flows, 5th ECCOMAS, Venice, July 2008.

81. P. Cinnella, P.M. Congedo, 2008, Optimal Blade Shapes For Viscous Dense Gas Flows Through Turbine Cascades, 5th ECCOMAS, Venice, July 2008.

82. P. Cinnella, P.M. Congedo, 2008, Computationally Efficient Models For The Numerical Simulation Of Thermodynamically Complex Flows, 5th ECCOMAS, Venice, July 2008.

Rapport de Recherche

83. G. Bellas-Chatzigeorgis, N. Villedieu, M. Panesi, P.M. Congedo, T.E. Magin, Propagation of uncertainties related to a complex detailed chemical mechanism, VKI Research Report.

84. P.M. Congedo, T.E. Magin, M. Duvernet, J. Tryoen, B. Van Hove, Development of a post-flight methodology for the analysis of flight data, VKI Research Report.

85. J. Tryoen, P.M. Congedo, R. Abgrall, T. Magin, N. Villedieu, Sensitivity analysis and characterization of the uncertain input data for the EXPERT vehicle, INRIA Research Report RR-8360.

86. R. Abgrall, M.G. Rodio, P.M. Congedo, 2012, Towards an efficient algorithm for the simulation of viscous two-phase flows with real gas effects, INRIA Research Report RR-8173.

87. M.G. Rodio, P.M. Congedo, 2012, Quantifying uncertainties in a Venturi multiphase configuration, INRIA Research Report RR-8180.

88. R. Abgrall, P.M. Congedo, G. Geraci, G. Iaccarino, 2012, Decomposition of high-order statistics, INRIA Research Report RR-8193.

89. R. Abgrall, P.M. Congedo, G. Geraci, G. Iaccarino, 2012, Non-polynomial expansion for stochastic problems with non-classical pdfs, INRIA Research Report RR-8191.

90. R. Abgrall, P.M. Congedo, G. Geraci, 2012, Numerical investigation on the Total Sensitivity Index influence in the solution of stochastic partial differential equations, INRIA Research Report RR-7911.

91. R. Abgrall, P.M. Congedo, G. Geraci, 2012, Toward a Unified Multiresolution Scheme in the Combined Physical/Stochastic Space for Stochastic Differential equations, INRIA Research Report RR-7996.

92. R. Abgrall, P.M. Congedo, G. Geraci, 2012, A One-time Truncate and Encode Multiresolution Stochastic Framework, INRIA Research Report RR-7967.

93. M. Ricchiuto, P.M. Congedo, G. Geraci, R. Abgrall, 2011, Numerical methods for a reliable prediction of long water-wave phenomena: uncertainty quantification for tsunami rump, INRIA Research Report RR-7809.

94. R. Abgrall, P.M. Congedo, S. Galera, 2011, A semi-intrusive deterministic approach to uncertainty quantification in non-linear fluid flow problems, INRIA Research Report RR-7820.

95. P.M. Congedo, G. Geraci, R. Abgrall, 2011, On the use of the Sparse Grid technique coupled with Polynomial Chaos, INRIA Research Report RR-7579.

Mémoire de Master Recherche

96. Optimisation de forme pour des écoulements de gaz denses, Thèse de Mastère, Ecole Nationale Supérieure d'Arts et Métiers, 30 juin 2005.

97. Simulazione Numerica di Flussi di Gas Denso. Tesi di Laurea in Ingegneria dei Materiali. Università degli Studi di Lecce. 10 dicembre 2003.

Thèse

98. Analysis and Optimization of Dense Gas Flows : Application to Organic Rankine Cycles, Thèse de Doctorat, Università del Salento, Lecce, 18 juillet 2007.

Séminaires invités

99. Stochastic methods for shocked flows and robust optimization, Short course on UQ controls at CERFACS, Toulouse, June 2013.

100. Uncertainty analysis and numerical flow simulation, invited, Workshop BIS2013 (Berkeley, INRIA, Stanford), Stanford, May 2013.

101. Quantification of uncertainties in numerical simulation, Quantification d'incertitude et calcul intensif Workshop (Journée thématique du GDR MASCOT NUM), Mar 2013, Grenoble, France.

102. Uncertainty Quantification and Robust Design in Complex Flow Simulations, International Workshop on Uncertainty Quantification and Design Optimization, February 2013, Trieste, Italy.

103. Introduction to Uncertainty Quantification, invited, Uncertainty Quantification for Aerospace Applications, von Karman Institute, October 2012

104. New perspectives for robust design optimization, invited, Complex modeling, Convergence, and Uncertainty Quantification, Uppsala, Sweden, June 2012

105. Innovative Contributions and work in progress for quantifying uncertainties in fluid flow problems, invited, Workshop BIS2012 (Berkeley, INRIA, Stanford), Paris, France, May 2012

106. Semi-intrusive multiresolution schemes for UQ : Application to unsteady discontinuous flows, invited, SIAM Conference on Uncertainty Quantification, Raleigh, USA, April 2012

107. Quantification des incertitudes en Mécanique des fluides, invited, Première rencontre GAMNI-MAIRCI : Précision et Incertitudes, Paris, France, February 2012

108. Chercher aujourd'hui pour l'énergie de demain, invited, Unithé ou Café, une rencontre ouverte à tous, INRIA Bordeaux Sud-Ouest, décembre 2011

109. Simulation robuste de phénomènes non-classiques en dynamique des gaz, invited, Séminaires modélisation et calculs, IMB-Bordeaux, janvier 2011

110. Robust optimization for uncertain dense gas flows, invited, UQ seminars, Stanford University, mai 2011

111. A simple, flexible, generic deterministic approach to UQ in non linear problems: description of the method, invited, RTO-AVT-VKI Short course on uncertainty quantification, Bruges, mai 2011

112. Numerical method for uncertainty quantification and prediction of high reynolds number flows, invited, CITRIS/INRIA Workshop, Berkeley, mai 2011

113. Contribution à la modélisation, la simulation et l'optimisation robuste des écoulements complexes : Applications aux cycles de Rankine à fluide organique, invited, Seminaire Arts et Métiers, ParisTech, Paris, mars 2010

114. Les incertitudes en thermo-hydraulique, invited, Atelier thermo-hydraulique du PCR-ANSF, Grenoble, juin 2010

115. Uncertain shape optimization for dense gas flows, invited, Université de Trieste (Italie), Trieste, mai 2010

116. Modélisation thermodynamique, optimisation et prise en compte des incertitudes dans la simulation d'écoulements de gaz réel, invited, CEA, Saclay, 11 mars 2009

117. Simulation et Optimisation d'écoulements de gaz dense, invited, LEGI, Grenoble, Août 2008.

118. Dense gas flows: exploitation of non-classical properties, invited, Cha-Cha Days, College of Charleston, South Carolina, Octobre 2006.

119. Introduction to dense gas flows: exploitation of non-classical properties for energy applications, invited seminar, National Institute of Aerospace (NIA), Hampton, Virginia, Août 2006.

Bibliography

[Abgrall 1994a] R. Abgrall. *On essentially non-oscillatory schemes on unstructured meshes: Analysis and implementation.* J. Comput. Phys., vol. 114, no. 1, pages 45–58, 1994. (Cited on page 25.)

[Abgrall 1994b] Remi Abgrall. *On Essentially Non-oscillatory Schemes on Unstructured Meshes: Analysis and Implementation*, September 1994. (Cited on page 48.)

[Abgrall 1997a] R Abgrall and T Sonar. *On the use of Mühlbach expansions in the recovery step of ENO methods.* Numerische Mathematik, no. 1997, pages 1–25, 1997. (Cited on page 41.)

[Abgrall 1997b] R. Abgrall and Th. Sonar. *On the use of Mahlbach expansions in the recovery step of ENO methods.* Numer. Math., vol. 76, no. 1, pages 1–25, 1997. (Cited on page 25.)

[Abgrall 1998] Remi Abgrall and Ami Harten. *Multiresolution Representation in Unstructured Meshes.* SIAM Journal on Numerical Analysis, vol. 35, no. 6, pages 2128–2146, 1998. (Cited on pages 40 and 41.)

[Abgrall 2003] R. Abgrall and R. Saurel. *Discrete Equations for Physical and Numerical Compressible Multiphase Mixtures.* Journal of Computational Physics, vol. 186, pages 361–396, 2003. (Cited on pages 192, 194, 196, 197, 198 and 199.)

[Abgrall 2006] R. Abgrall and V. Perrier. *Asymptotic Expansion of Multiscale Numerical Scheme For Compressible Multiscale Flow.* Society for Industrial and Applied Mathematics, vol. 5, pages 84–115, 2006. (Cited on pages 192, 195, 196, 197 and 199.)

[Abgrall 2011] Remi Abgrall, Pietro Marco Congedo and Stephane Galéra. *A semi-intrusive deterministic approach to uncertainty quantifications in non-linear fluid flow problems.* Rapport technique, INRIA, 2011. (Cited on page 40.)

[Abgrall 2012] R Abgrall, PM Congedo, G Geraci and Iaccarino G. *Decomposition of high-order statistics.* Rapport technique, INRIA, 2012. (Cited on pages 72, 73 and 74.)

[Abgrall 2013a] R Abgrall, P M Congedo and G Geraci. *A high-order non-linear multiresolution scheme for stochastic PDEs.* In European Workshop on High Order Nonlinear Numerical Methods for Evolutionary PDEs: Theory and Applications (HONOM 2013), 2013. (Cited on pages 68 and 70.)

[Abgrall 2013b] R. Abgrall and P.M. Congedo. *A semi-intrusive deterministic approach to uncertainty quantification in non-linear fluid flow problems.* Journal of Computational Physics, vol. 235, pages 828–845, 2013. (Cited on page 25.)

[Abgrall 2013c] R. Abgrall and M.G. Rodio. *Discrete Equation Method (DEM) for the Simulation of Viscous, Compressible, Two-phase Flows.* Computers and Fluids, 2013. Submitted. (Cited on page 195.)

[Abusam 2003] A. Abusam, K.J. Keesman and G. van Straten. *Forward and backward uncertainty propagation: an oxidation ditch modelling example.* Water Research, vol. 37, pages 429–435, 2003. (Cited on page 7.)

[Abusam 2009] A. Abusam, K.J. Keesman and G. van Straten. *Forward and backward probabilistic simulations in Geotechnical engineering.* Contemporary Topics in In Situ Testing, Analysis, and Reliability of Foundations (GSP 186), vol. 186, pages 332–339, 2009. (Cited on page 7.)

[Agarwal 2009] Nitin Agarwal and N.R. Aluru. *A domain adaptive stochastic collocation approach for analysis of MEMS under uncertainties.* Journal of Computational Physics, vol. 228, no. 20, pages 7662–7688, November 2009. (Cited on pages 8 and 30.)

[AIAA 1998] AIAA. Guide for the verification and validation of computational fluid dynamics simulations. AIAA-G-077-1998, 1998. (Cited on page 3.)

[Ait-Sahalia 2007] Y. Ait-Sahalia and R. Kimmel. *Maximum likelihood estimation of stochastic volatility models.* Journal of Financial Economics, vol. 83, pages 413–452, 2007. (Cited on page 7.)

[Ambroso 2012] A. Ambroso, C. Chalons and P.-A. Raviart. *A Godunov-type method for the seven-equation model of compressible two-phase flow.* Computers and Fluids, vol. 54, pages 67–91, 2012. (Cited on page 194.)

[Arandiga 2000] F Arandiga and Rosa Donat. *Nonlinear multiscale decompositions: The approach of A. Harten.* Numerical Algorithms, vol. 23, pages 175–216, 2000. (Cited on page 40.)

[Aràndiga 2004] Francesc Aràndiga and Ana MarÄśÌĄa Belda. *Weighted ENO interpolation and applications.* Communications in Nonlinear Science and Numerical Simulation, vol. 9, no. 2, pages 187–195, April 2004. (Cited on page 67.)

[Arandiga 2009] F. Arandiga, G. Chiavassa and Rosa Donat. *Harten framework for multiresolution with applications: From conservation laws to image compression.* Boletín SEMA, vol. 31, no. 31, pages 73–108, 2009. (Cited on pages 40 and 43.)

[Asokan 2004] V. Asokan and N. Zabaras. *Stochastic inverse heat conduction using a spectral approach.* International Journal for Numerical Methods in Engineering, vol. 60, pages 1569–1593, 2004. (Cited on page 7.)

[Babuška 2010] Ivo Babuška, Fabio Nobile and RauÌĄl Tempone. *A Stochastic Collocation Method for Elliptic Partial Differential Equations with Random Input Data.* SIAM Review, vol. 52, no. 2, page 317, 2010. (Cited on page 8.)

[Baer 1986] M.R. Baer and J.W. Nunziato. *A Two-phase mixture theory for deflagration to detonation transition (ddt) in reactive granular materials.* International Journal of Multiphase Flow, vol. 12, pages 861–889, 1986. (Cited on page 194.)

[Barbante 2001] P.F. Barbante. *Accurate and efficient modelling of high temperature non-equilibrium air flows.* PhD thesis, von Karman Institute, Rhode-Saint-Genèse, Belgium, 2001. (Cited on pages 98 and 99.)

[Barth 1990] T. J. Barth and P. O. Frederickson. *Higher order solution of the euler equations on unstructured grids using quadratic reconstruction.* In AIAA paper 90-0013, pages 1–12. AIAA, 1990. (Cited on page 25.)

[Bellman 1961] Richard Ernest Bellman and Bellmann Richard. Adaptive Control Processes: A Guided Tour. Princeton University Press, 1961. (Cited on pages 8 and 12.)

[Beyer 2007] H.-G. Beyer and B. Sendhoff. *Robust optimization âĂŞ a comprehensive survey.* Comput. Methods Appl. Mech. Engrg., vol. 196, pages 3190–3218, 2007. (Cited on page 11.)

[Blatman 2010a] G Blatman and B. Sudret. *A comparison of three metamodel-based methods for global sensitivity analysis: GP modelling, HDMR and LAR-gPC.* Procedia - Social and Behavioral Sciences, vol. 2, no. 6, pages 7613–7614, 2010. (Cited on page 10.)

[Blatman 2010b] G Blatman and B. Sudret. *Efficient computation of global sensitivity indices using sparse polynomial chaos expansions.* Reliability Engineering and System Safety, vol. 95, pages 1216–1229, 2010. (Cited on page 10.)

[Borgonovo 2003] E Borgonovo, G E Apostolakis, S Tarantola and A Saltelli. *Comparison of global sensitivity analysis techniques and importance measures in PSA.* Reliability Engineering & System Safety, vol. 79, no. 2, pages 175–185, 2003. (Cited on page 10.)

[Borgonovo 2007] E Borgonovo. *A new uncertainty importance measure.* Reliability Engineering & System Safety, vol. 92, no. 6, pages 771–784, 2007. (Cited on page 10.)

[Borgonovo 2012] E Borgonovo, W Castaings and S Tarantola. *Model emulation and moment-independent sensitivity analysis: An application to environmental modelling.* Environmental Modelling & Software, vol. 34, pages 105–115, 2012. (Cited on page 10.)

[Bose 2004] D. Bose, M. Wright and T. Gokçen. *Uncertainty and Sensitivity Analysis of Thermochemical Modeling for Titan Atmospheric Entry.* 37th AIAA Thermophysics Conference, Portland, Oregon, 2004. (Cited on page 99.)

[Brown 2000] B. P. Brown and B. M. Argrow. *Application of Bethe-Zel'dovic-Thompson fluids in organic Rankine cycle engines.* J. Power Sources, vol. 16, page 1118, 2000. (Cited on pages 6, 12, 156, 163 and 164.)

[Caniou 2011] J Y Caniou and B Sudret. *Distribution-based global sensitivity analysis in case of correlated input parameters using polynomial chaos expansions.* In ICASP2011, 2011. (Cited on page 10.)

[Carlberg 2008] K. Carlberg and C. Farhat. *A compact proper orthogonal decomposition basis for optimization-oriented reduced-order models.* 2008. (Cited on page 11.)

[Carlberg 2011] K. Carlberg, C. Bou-Mosleh and C. Farhat. *Efficient non-linear model reduction via a least-squares Petrov-Galerkin projection and compressive tensor approximations.* International Journal for Numerical Methods in Engineering, vol. 86, no. 2, pages 155–181, 2011. (Cited on page 11.)

[Chantrasmi 2009] Tonkid Chantrasmi and Gianluca Iaccarino. *Computing Shock Interactions under Uncertainty.* AIAA Paper 2009-2284, no. May, pages 1–14, 2009. (Cited on page 8.)

[Chung 1984] T.H. Chung, L.L. Lee and K.E. Starling. *Applications of Kinetic Gas theories and Multiparameter Correlation for Prediction of Dilute Gas Viscosity and Thermal Conductivity.* Industrial Engineering Chemistry Fundamentals, vol. 23, pages 8–23, 1984. (Cited on page 151.)

[Cinnella 2005a] P Cinnella and PM Congedo. *Aerodynamic Performance of Transonic Bethe-Zel'dovich-Thompson Flows past an Airfoil.* AIAA Journal, vol. 43, pages 370–378, 2005. (Cited on pages 12, 145 and 146.)

[Cinnella 2005b] P Cinnella and PM Congedo. *Numerical Solver for Dense Gas flows.* AIAA Journal, vol. 43, pages 2458–2461, 2005. (Cited on pages 129 and 146.)

[Cinnella 2006] P. Cinnella. *Roe-type schemes for dense gas flow computations.* Computers & Fluids, vol. 35, no. 10, pages 1264–1281, 2006. (Cited on page 180.)

[Cinnella 2007] P Cinnella and PM Congedo. *Inviscid and viscous aerodynamics of dense gases.* J. Fluid Mech., vol. 580, pages 179–217, 2007. (Cited on pages 164 and 165.)

[Cinnella 2008a] P Cinnella. *Transonic flows of dense gases over finite wings.* Physics of Fluids, vol. 20, pages 046103:1–17, 2008. (Cited on pages 164 and 165.)

[Cinnella 2008b] P. Cinnella and P. M. Congedo. *Optimal airfoil shapes for viscous transonic flows of Bethe-Zel'dovich-Thompson fluids.* Computers & Fluids, vol. 37, pages 250–264, 2008. (Cited on pages 6 and 182.)

[Cinnella 2010] P. Cinnella, P. M. Congedo, V. Pediroda and L. Parussini. *Quantification of thermodynamic uncertainties in real gas flows.* International Journal of Engineering Systems Modelling and Simulation, vol. 2, no. 1, pages 12–24, 2010. (Cited on pages 7, 148, 149 and 203.)

[Cinnella 2011] P. Cinnella, P.M. Congedo, V. Pediroda and L. Parussini. *Sensitivity analysis of dense gas flow simulations to thermodynamic uncertainties.* Physics of Fluids, vol. 23, page 116101, 2011. (Cited on pages 7, 12, 112, 129, 132, 146, 148 and 150.)

[Cinnella 2013] P. Cinnella and P.M. Congedo. *Convergence behaviours of Genetic Algorithms for Aerodynamic Optimisation Problems.* International Journal of Engineering Systems Modelling and Simulation, vol. 5, pages 197–216, 2013. (Cited on page 172.)

[Cole 1998] D.R. Cole and M.N. Glauser. *Flying hot-wire measurements in an axisymmetric sudden expansion.* Experimental Thermal and Fluid Science, vol. 18, pages 150–167, 1998. (Cited on page 84.)

[Colonna 2003] P. Colonna and P. Silva. *Dense gas thermodynamic properties of single and multicomponent fluids for fluid dynamics simulations.* J. Fluid Eng.-T. ASME, vol. 125, no. 3, pages 414–427, 2003. (Cited on pages 6, 163 and 180.)

[Colonna 2004] P. Colonna and S. Rebay. *Numerical simulation of dense gas flows on unstructured grids with an implicit high resolution upwind Euler solver.* Int. J. Numer. Meth. Fl., vol. 46, no. 7, pages 735–765, 2004. (Cited on pages 6, 12, 146 and 180.)

[Colonna 2005] P. Colonna and T.P. van der Stelt. Fluidprop: A program for the estimation of thermophysical properties of fluids. Energy Technology Section, Delft University of Technology, The Netherlands, 2005. (Cited on page 180.)

[Colonna 2006a] P. Colonna, A. Guardone and N. R. Nannan. *Siloxanes: a new class of candidate Bethe-Zel'dovich-Thompson fluids.* Phys. Fluids, vol. 19, no. 8, pages 1–12, 2006. (Cited on pages 201 and 202.)

[Colonna 2006b] P. Colonna, N. R. Nannan, A. Guardone and E. W. Lemmon. *Multiparameter equations of state for selected siloxanes.* Fluid Phase Equilib., vol. 244, pages 193–211, 2006. (Cited on pages 150, 164, 165, 166 and 167.)

[Colonna 2007] P Colonna, A Guardone and NR Nannan. *Siloxanes: A new class of candidate Bethe-Zel'dovich-Thompson fluids.* Physics of Fluids, vol. 19, no. 086102, 2007. (Cited on page 164.)

[Colonna 2008a] P. Colonna, A. Guardone, N. R. Nannan and C. Zamfirescu. *Design of the dense gas flexible asymmetric shock tube.* J. Fluid Eng.-T. ASME, vol. 130, no. 034501, pages 1–6, 2008. (Cited on pages 5, 7, 12, 181, 183, 184 and 186.)

[Colonna 2008b] P. Colonna, N. R. Nannan and A. Guardone. *Multiparameter equations of state for siloxanes: [(CH3)3-Si-O1/2]2-[O-Si-(CH3)2]i = 1...3, and [O-Si-(CH3)2]6.* Fluid Phase Equilib., vol. 263, no. 2, pages 115–130, 2008. (Cited on pages 112, 150 and 189.)

[Colonna 2008c] P. Colonna, S. Rebay, J. Harinck and A. Guardone. *Real-gas effects in organic Rankine cycle turbine nozzles.* J. Propul. Power, vol. 24, pages 282–294, 2008. (Cited on pages 113 and 180.)

[Congedo 2007] P. M. Congedo, C. Corre and P. Cinnella. *Airfoil Shape Optimization for Transonic Flows of Bethe-Zel'dovich-Thompson Fluids.* AIAA J., vol. 45, no. 6, pages 1303–1316, 2007. (Cited on pages 12, 129, 132, 146, 160, 180 and 182.)

[Congedo 2011a] P. M. Congedo, C. Corre and J.-M. Martinez. *Shape optimization of an airfoil in a BZT flow with multiple-source uncertainties.* Computer Methods in Applied Mechanics and Engineering, vol. 200, no. 1, pages 216–232, 2011. (Cited on pages 149, 180 and 191.)

[Congedo 2011b] Pietro Marco Congedo, C. Corre and P. Cinnella. *Numerical investigation of dense-gas effects in turbomachinery.* Computers & Fluids, no. June, June 2011. (Cited on pages 12 and 111.)

[Congedo 2011c] Pietro Marco Congedo, C. Corre and Jean-Marc Martinez. *Shape optimization of an airfoil in a BZT flow with multiple-source uncertainties.* Computer Methods in Applied Mechanics and Engineering, vol. 200, no. 1-4, pages 216–232, 2011. (Cited on pages 12, 137 and 203.)

[Congedo 2012] P.M. Congedo, P. Colonna, C. Corre, J.A.S. Witteveen and G. Iaccarino. *Backward uncertainty propagation method in flow problems: Application to the prediction of rarefaction shock waves.* Computer Methods in Applied Mechanics and Engineering, vol. 213, pages 314–326, 2012. (Cited on pages 12, 201, 202 and 215.)

[Coquel 1995] F. Coquel and M.S. Liou. *Hybrid Upwind Splitting Scheme by a Field-by-Field Decomposition.* NASA Tech. Memorandum 106823, 1995. (Cited on page 99.)

[Cramer 1992] MS Cramer and GM Tarkenton. *Transonic Flows of Bethe-Zel'dovich-Thompson Fluids.* J. Fluid Mech., vol. 240, pages 197–228, 1992. (Cited on pages 6, 129, 164 and 165.)

[Crestaux 2009] Thierry Crestaux, Olivier Le Maître and Jean-Marc Martinez. *Polynomial chaos expansion for sensitivity analysis.* Reliability Engineering & System Safety, vol. 94, no. 7, pages 1161–1172, July 2009. (Cited on page 10.)

[Deb 2002] K. Deb, A. Pratap, S. Agarwal and T. Meyarivan. *A Fast and Elitist Multiobjective Genetic Algorithm: NSGA-II.* IEEE TRANSACTIONS ON EVOLUTIONARY COMPUTATION, vol. 6, 2002. (Cited on pages 111 and 134.)

[Dellenback 1987] P. A. Dellenback, D. E. Metzger and G. P. Neitzel. *Measurements in Turbulent Swirling Flow Through an Abrupt Expansion.* AIAA Journal, vol. 26, no. 6, pages 669–681, 1987. (Cited on pages 81, 83 and 84.)

[Desceliers 2006] C. Desceliers, R. Ghanem and C. Soize. *Maximum likelihood estimation of stochastic chaos representations from experimental data.* International Journal for Numerical Methods in Engineering, vol. 66, pages 978–1001, 2006. (Cited on page 7.)

[Diwekar 2003] U. Diwekar. *A Novel Sampling Approach to Combinatorial Optimization Under Uncertainty.* Computational Optimization and Applications, vol. 24, pages 335–371, 2003. (Cited on page 11.)

[Doltsinis 2004] I. Doltsinis and Z. Kang. *Robust design of structures using optimization methods.* Comput. Methods Appl. Mech. Engrg., vol. 193, pages 2221–2237, 2004. (Cited on page 11.)

[Doostan 2011] Alireza Doostan and Houman Owhadi. *A non-adapted sparse approximation of PDEs with stochastic inputs.* Journal of Computational Physics, vol. 230, no. 8, pages 3015–3034, April 2011. (Cited on pages 9 and 218.)

[Drew 1998] D.A. Drew and S.L. Passman. Theory of multicomponent fluids, volume 135. Applied Mathematical Sciences, Springer, New York, 1998. (Cited on page 196.)

[Ebert 2013] E. Ebert, L. Wilson, A. Weigel, M. Mittermaier, P. Nurmi, P. Gill, M. Gober, S. Joslyn, B.G. Brown, T.L. Fowler and A. Watkins. *Progress and challenges in forecast verification.* Meteorological Applications, vol. 20, pages 130–139, 2013. (Cited on page 2.)

[Fergason 2001] S. H. Fergason, T. L. Ho, B. M. Argrow and G. Emanuel. *Theory for producing a single-phase rarefaction shock wave in a shock tube.* Journal of Fluid Mechanics, vol. 445, pages 37–54, 2001. (Cited on pages 12 and 201.)

[Ferziger 1997] J. H. Ferziger and M. Perić. Computational methods for fluid dynamics. Berlin ; New York : Springer, 1997. (Cited on page 83.)

[Foo 2008] Jasmine Foo, Xiaoliang Wan and George Em Karniadakis. *The multi-element probabilistic collocation method (ME-PCM): Error analysis and applications.* Journal of Computational Physics, vol. 227, no. 22, pages 9572–9595, November 2008. (Cited on page 30.)

[Foo 2010] Jasmine Foo and George Em Karniadakis. *Multi-element probabilistic collocation method in high dimensions.* Journal of Computational Physics, vol. 229, pages 1536–1557, March 2010. (Cited on pages 8, 10 and 119.)

[G. 1989] Taguchi G. Introduction to quality engineering. American Supplier Institute, 1989. (Cited on page 11.)

[Ganapathysubramanian 2007] B Ganapathysubramanian and Nicholas Zabaras. *Sparse grid collocation schemes for stochastic natural convection problems.* Journal of Computational Physics, vol. 225, no. 1, pages 652–685, July 2007. (Cited on page 8.)

[Gao 2010] Zhen Gao and Jan S. Hesthaven. *Efficient solution of ordinary differential equations with high-dimensional parametrized uncertainty.* Communications in computational physics, pages 1–33, 2010. (Cited on pages 77, 111, 113, 119, 122 and 124.)

[Gao 2011] Z. Gao and J. Hesthaven. *Efficient solution of ordinary differential equations with high-dimensional parametrized uncertainty.* Comm. Comput. Phys., vol. 10, pages 253–278, 2011. (Cited on pages 12 and 192.)

[Germano 1991] M. Germano, U. Piomelli, P. Moin and W. H. Cabot. *A dynamic subgrid-scale eddy viscosity model.* Phys. Fluids A, vol. 3, pages 1760–1765, 1991. (Cited on page 83.)

[Gerritsma 2010] Marc Gerritsma, Jan-Bart van der Steen, Peter Vos and George Em Karniadakis. *Time-dependent generalized polynomial chaos.* Journal of Computational Physics, vol. 229, no. 22, pages 8333–8363, November 2010. (Cited on pages 8, 30 and 32.)

[Gerstner 1998] T. Gerstner and M. Griebel. *Numerical Integration using sparse grids.* Numer. Algorithms, vol. 18, pages 209–223, 1998. (Cited on page 26.)

[Getreuer 2008] Pascal Getreuer and Francois G. Meyer. *ENO multiresolutions Schemes with General Discretizations.* SIAM Journal on Numerical Analysis, vol. 46, no. 6, pages 2953–2977, 2008. (Cited on page 41.)

[Ghanem 2003] R. Ghanem and P. Spanos. Stochastic finite elements: a spectral approach. Dover, 2003. (Cited on page 73.)

[Gilks 1996] W.R. Gilks, Sylvia Richardson and D.J. Spiegelhalter. Markov chain monte carlo in practice. Chapman & Hall, 1996. (Cited on pages 102 and 105.)

[Goncalves 2009] E. Goncalves and R.F. Patella. *Numerical simulation of cavitating flows with homogeneous models.* Computers and Fluids, vol. 38, pages 1682–1696, 2009. (Cited on page 199.)

[Graham 2011] I.G. Graham, F.Y. Kuo, D. Nuyens, R. Scheichl and I.H. Sloan. *Quasi-Monte Carlo methods for elliptic PDEs with random coefficients and applications.* Journal of Computational Physics, vol. 230, no. 10, pages 3668–3694, February 2011. (Cited on page 8.)

[Griebel 2006] Michael Griebel. *Sparse grids and related approximation schemes for higher dimensional problems.* In L. Pardo Todd, A. Pinkus, E. Suli and M.J., editeurs, Foundations of Computational Mathematics (FoCM05), Santander, pages 106–161. Cambridge University Press, 2006. (Cited on page 8.)

[Guardone 2004] A Guardone, L Vigevano and BA Argrow. *Assessment of thermodynamic models for dense gas dynamics.* Physics of Fluids, vol. 16, pages 3878–87, 2004. (Cited on page 165.)

[Guardone 2005] A. Guardone and B. Argrow. *Nonclassical gasdynamic region of selected fluorocarbons.* Physics of Fluids, vol. 17, page 116102(17), 2005. (Cited on page 201.)

[Guardone 2010] A. Guardone, C. Zamfirescu and P. Colonna. *Maximum intensity of rarefaction shock waves for dense gases.* J. Fluid Mech., vol. 642, pages 127–146, 2010. (Cited on pages 149, 183, 192 and 203.)

[Gyllenram 2008] W. Gyllenram and H. Nilsson. *Design and Validation of a Scale-Adaptive Filtering Technique for LRN Turbulence Modeling of Unsteady Flow.* Journal of Fluids Engineering, vol. 130, no. 2, pages 194–204, 2008. (Cited on page 81.)

[Han 2012] Xingsi Han, Pierre Sagaut and Didier Lucor. *On sensitivity of RANS simulations to uncertain turbulent inflow conditions.* Computers & Fluids, vol. 61, no. 0, pages 2 – 5, 2012. (Cited on page 81.)

[Harinck 2009] J. Harinck, P. Colonna and A. Guardone. *The influence of molecular complexity on expanding flows of ideal and dense gases.* J. Fluid Mech., vol. 21, no. 8, pages 086101–1–14, 2009. (Cited on page 180.)

[Harinck 2010] J. Harinck, P. Colonna, A. Guardone and S. Rebay. *Influence of thermodynamic models in 2D flow simulations of turboexpanders.* J. Turbomach., vol. 132, pages 011001–17, 2010. (Cited on page 180.)

[Harten 1987] A. Harten, B. Engquist, S. Osher and S. Chakravarthy. *Uniformly high order accurate essentially non-oscillatory schemes. III.* J. Comput. Phys., vol. 71, page 231âĂŞ303, 1987. (Cited on page 25.)

[Harten 1993] Ami Harten. *Discrete multi-resolution analysis and generalized wavelets.* Applied Numerical Mathematics, vol. 12, no. 1âĂŞ3, pages 153 – 192, 1993. (Cited on pages 40 and 43.)

[Harten 1994] Ami Harten. *Adaptive multiresolution schemes for shock computations.* Journal of Computational Physics, vol. 135, no. 2, pages 260–278, August 1994. (Cited on pages 40 and 43.)

[Harten 1995] Ami Harten. *Multiresolution algorithms for the numerical solution of hyperbolic conservation laws.* Communications on Pure and Applied Mathematics, vol. 48, no. 12, pages 1305–1342, 1995. (Cited on pages 40 and 43.)

[Harten 1998] A. Harten, P.D. Lax, C.D. Levermore and W. Morokoff. *Convex entropies and hyperbolicity for general euler equations.* SIAM Journal of Numerical Analysis, vol. 35, no. 6, pages 2117–2127, 1998. (Cited on page 199.)

[Iaccarino 2008] Gianluca Iaccarino. *Quantification of Uncertainty in Flow Simulations Using Probabilistic Methods.* In VKI Lecture Series - Sept. 8-12, chapitre Non equili. VKI, 2008. (Cited on page 3.)

[Issa 1986] R. I. Issa. *Solution of implicitly discretized fluid flow equations by operator-splitting.* J. Comput. Phys., vol. 62, pages 40–65, 1986. (Cited on page 83.)

[Jensen 2007] H.A. Jensen and M.A. Catalan. *On the effects of non-linear elements in the reliability-based optimal design of stochastic dynamical systems.* Int. J. Non-Linear Mech., vol. 42, pages 802–816, 2007. (Cited on page 11.)

[Jones 1972] W. P. Jones and B. E. Launder. *The prediction of laminarization with a two-equation model of turbulence.* International Journal of Heat and Mass Transfer, vol. 15, pages 301–314, 1972. (Cited on page 83.)

[Kaipio 2010] J. Kaipio and E. Somersalo. Statistical and Computational Inverse Problems. Applied Mathematical Sciences, Vol. 160. Springer, 2010. (Cited on page 98.)

[Kapila 2001] A. K. Kapila, R. Menikoff, J. B. Bdzil, S. F. Son and D. S. Stewart. *Two-phase modeling of deflagration-to-detonation transition in granular materials: Reduced equations.* Physics of Fluids, vol. 13, pages 3002–3024, 2001. (Cited on page 195.)

[Kiock 1986] R. Kiock, F. Lehthaus, N. C. Baines and C. H. Sieverding. *The Transonic Flow Through a Plane Turbine Cascade as Measured in Four European Wind Tunnels.* ASME J Eng Gas Turb Power, vol. 108, no. 2, pages 277–284, 1986. (Cited on pages 111, 112, 153 and 154.)

[Kraichnan 1963] R. H. Kraichnan. *Direct-interaction approximation for a system of several interacting simple shear waves.* Physics of Fluids, vol. 6, no. 11, pages 1603–1609, 1963. (Cited on page 30.)

[Lambrakis 1972] KC Lambrakis and PA Thompson. *Existence of real fluids with a negative Fundamental Derivative* Γ. Physics of Fluids, vol. 15, no. 5, pages 933–935, 1972. (Cited on pages 164 and 165.)

[Le Maître 2004a] Olivier Le Maître. *Multi-resolution analysis of Wiener-type uncertainty propagation schemes.* Journal of Computational Physics, vol. 197, no. 2, pages 502–531, July 2004. (Cited on page 9.)

[Le Maître 2004b] Olivier Le Maître. *Uncertainty propagation using WienerâĂŞHaar expansions.* Journal of Computational Physics, vol. 197, no. 1, pages 28–57, June 2004. (Cited on page 9.)

[Le Maître 2010a] O. Le Maître and O. Knio. Spectral methods for uncertainty quantification. Springer, 2010. (Cited on page 73.)

[Le Maître 2010b] Olivier Le Maître and O.M. Knio. Spectral Methods for Uncertainty Quantification: With Applications to Computational Fluid Dynamics. Springer Verlag, 2010. (Cited on pages 8 and 39.)

[Leer 1979] B. Van Leer. *Towards the ultimate conservative difference scheme. V. A second-order sequel to Godunov's method.* Journal of Computational Physics, vol. 32, no. 1, pages 101–136, 1979. (Cited on page 100.)

[LeVeque 2002] R. J. LeVeque. Finite volume methods for conservation laws and hyperbolic systems. Cambridge University Press, 2002. (Cited on pages 49 and 61.)

[Lucor 2007] Didier Lucor, Johan Meyers and Pierre Sagaut. *Sensitivity analysis of large-eddy simulations to subgrid-scale-model parametric uncertainty using polynomial chaos.* Journal of Fluid Mechanics, vol. 585, page 255, August 2007. (Cited on page 81.)

[Lucor 2012] By D Lucor, J Witteveen, P Constantine, D Schiavazzi and G Iaccarino. *Comparison of adaptive uncertainty quantification approaches for shock wave-dominated flows.* In Center For Turbulence Research, Prooceedings of the Summer Program 2012, pages 219–228, 2012. (Cited on page 9.)

[M. S. Eldred 2008] P. G. Constantine M. S. Eldred C. G. Webster. *Design Under Uncertainty Employing Stochastic Expansion Methods.* In AIAA 2008-6001, pages 1–15. AIAA, 2008. (Cited on page 12.)

[Ma 2009a] X. Ma and N. Zabaras. *An adaptative hierarchical sparse grid collocation algorithm for the solution of stochastic differential equations.* J. Comput. Phys., vol. 228, pages 3084–3113, 2009. (Cited on pages 12, 26 and 30.)

[Ma 2009b] X. Ma and N. Zabaras. *An efficient bayesian inference approach to inverse problems based on an adaptive sparse grid collocation method.* Inverse Problems, vol. 25, page 035013, 2009. (Cited on page 7.)

[Ma 2009c] Xiang Ma and Nicholas Zabaras. *An adaptive hierarchical sparse grid collocation algorithm for the solution of stochastic differential equations.* Journal of Computational Physics, vol. 228, no. 8, pages 3084–3113, May 2009. (Cited on page 8.)

[Ma 2010] Xiang Ma and Nicholas Zabaras. *An adaptive high-dimensional stochastic model representation technique for the solution of stochastic partial differential equations.* Journal of Computational Physics, vol. 229, no. 10, pages 3884–3915, May 2010. (Cited on page 119.)

[Martin 1955] JJ Martin and YC Hou. *Development of an equation of state for gases.* AIChE Journal, vol. 1, pages 142–151, 1955. (Cited on pages 149 and 164.)

[Marzouk Y.M. 2007] Najm H.N. Marzouk Y.M. and L.A. Rahn. *Stochastic spectral methods for efficient Bayesian solution of inverse problems.* Journal of Computational Physics, vol. 224, pages 560–586, 2007. (Cited on page 103.)

[Meldi 2011] M. Meldi, D. Lucor and P. Sagaut. *Is the Smagorinsky coefficient sensitive to uncertainty in the form of the energy spectrum?* Physics of Fluids, vol. 23, no. 12, 2011. (Cited on page 81.)

[Meldi 2012] M. Meldi, M.V. Salvetti and P. Sagaut. *Quantification of errors in large-eddy simulations of a spatially evolving mixing layer using polynomial chaos.* Physics of Fluids, vol. 24, no. 3, 2012. (Cited on page 81.)

[Mitra 2005] G. Mitra. *Introduction: Optimization and Risk Modelling.* Computational Optimization and Applications, vol. 32, pages 5–8, 2005. (Cited on page 11.)

[Monaco 1997] J. F. Monaco, M. S. Cramer and L. T. Watson. *Supersonic flows of dense gases in cascade configurations.* J. Fluid Mech., vol. 330, pages 375–409, 1997. (Cited on pages 6 and 12.)

[Murrone 2005] A. Murrone and H. Guillard. *A five equation reduced model for compressible two-phase flow problems.* Journal of Computational Physics, vol. 202, pages 664–698, 2005. (Cited on pages 195 and 199.)

[Namura 2011] N. Namura, K. Shimoyama, S. Jeong and S. Obayashi. *Kriging/RBF-hybrid response surface method for highly nonlinear functions.* IEEE Congress on Evolutionary Computation, vol. 1, pages 2534–2541, 2011. (Cited on page 11.)

[Nannan 2007] N. R. Nannan, P. Colonna, C. M. Tracy, R. L. Rowley and J. J. Hurky. *Ideal-gas heat capacities of dimethylsiloxanes from speed-of-sound measurements and ab initio calculations.* Fluid Phase Equilib., vol. 257, pages 102–113, 2007. (Cited on page 192.)

[Nelder 1965] J.A. Nelder and R. Mead. *A simplex method for function minimization.* Computer Journal, vol. 7, pages 308–313, 1965. (Cited on page 119.)

[Ngnepieba 2007] P. Ngnepieba and M.Y. Hussaini. *An efficient sampling method for stochastic inverse problems.* Comput. Optim. Appl., vol. 37, pages 121–138, 2007. (Cited on page 7.)

[Oberkampf 2010] W Oberkampf and CJ Roy. Verification and validation in scientific computing. Cambridge University Press, 2010. (Cited on page 4.)

[Orlanski 1976] I. Orlanski. *A simple boundary condition for unbounded hyperbolic flows.* J. Comput. Phys., vol. 21, pages 251–269, 1976. (Cited on page 83.)

[Orszag 1967] S. A. Orszag and L. R. Bissonnette. *Dynamical properties of truncated Wiener-Hermite expansions.* Physics of Fluids, vol. 10, no. 12, pages 2603–2613, 1967. (Cited on page 30.)

[Osher 1982] S. Osher and F. Solomon. *Upwind Difference Schemes for Hyperbolic Systems of Conservation Laws.* Mathematics of Computation, vol. 38, no. 158, pages 339–374, 1982. (Cited on page 100.)

[Park 2001] C. Park, R.L. Jaffe and H. Partridge. *Chemical-Kinetic Parameters of Hyperbolic Earth Entry.* Journal of Thermophysics and Heat Transfer, vol. 15, no. 1, pages 76–90, 2001. (Cited on page 99.)

[Park 2006] G.J. Park, T.H. Lee, K. Lee and K.H. Hwang. *Robust design: an overview.* AIAA J., vol. 44, pages 181–191, 2006. (Cited on page 11.)

[Parussini 2010] L. Parussini, V. Pediroda and C. Poloni. *Prediction of geometric uncertainty effects on Fluid Dynamics by Polynomial Chaos and Fictitious Domain method.* Computers and Fluids, vol. 39, no. 1, pages 137–151, 2010. (Cited on page 11.)

[Pettersson 2013] Per Pettersson. *Uncertainty Quantification and Numerical Methods for Conservation Laws.* PhD thesis, 2013. (Cited on page 9.)

[Platteeuw 2008] P. D. A. Platteeuw, G. J. A. Loeven and H. Bijl. *Uncertainty Quantification Applied to the k-epsilon Model of Turbulence Using the Probabilistic Collocation Method.* In AIAA 2008-2150, pages 1–17. AIAA, 2008. (Cited on page 83.)

[Plischke 2013] Elmar Plischke, Emanuele Borgonovo and Curtis L. Smith. *Global sensitivity measures from given data.* European Journal of Operational Research, vol. 226, no. 3, pages 536–550, May 2013. (Cited on page 74.)

[Poëtte 2012] Gaël Poëtte and Didier Lucor. *Non intrusive iterative stochastic spectral representation with application to compressible gas dynamics.* Journal of Computational Physics, vol. 231, no. 9, pages 3587–3609, May 2012. (Cited on page 9.)

[Quarteroni 2008] Alfio Quarteroni, Riccardo Sacco and Fausto Saleri. Matematica Numerica. Springer, 2008. (Cited on pages 44 and 54.)

[Rabitz 1999] H Rabitz, O Alis, J Shorter and K Shim. *Efficient input-output model representations.* Comput. Phys. Commun., vol. 117, pages 11–20, 1999. (Cited on page 10.)

[Rebay 2009] S. Rebay, P. Colonna, D. Pasquale and A. Ghidoni. *Simulation of the turbulent dense gas flow through the nozzle of an organic Rankine cycle turbine.* Proceedings of the 8th European Turbomachinery Conference, pages 1137–1148, 2009. (Cited on page 180.)

[Reid 1987] R. C. Reid, J. M. Prausnitz and B. E. Poling. The properties of gases and liquids. McGraw-Hill, 1987. (Cited on page 163.)

[Rhie 1983] C.M. Rhie and W. L. Chow. *Numerical study of the turbulent flow past an airfoil with trailing edge separation.* AIAA Journal, vol. 21, pages 1525–1532, 1983. (Cited on page 83.)

[Rihani 1965] D. N. Rihani and L. K. Doraiswamy. *Estimation of heat capacity of organic compounds from group contributions.* Ind. Eng. Chem. Fundam., vol. 4, 1965. (Cited on page 165.)

[Roe 1981] P. L. Roe. *Approximate Riemann solvers, parameter vectors, and difference schemes.* J. Comput. Phys., vol. 43, pages 357–372, 1981. (Cited on page 28.)

[Sacks 1989] Jerome Sacks, William J. Welch, Toby J. Mitchell and Henry P. Wynn. *Design and Analysis of Computer Experiments.* Statistical Science, vol. 4, no. 4, pages 409–423, November 1989. (Cited on page 111.)

[Saltelli 2010] A Saltelli. *Variance based sensitivity analysis of model output. design and estimator for the total sensitivity index.* Comput. Phys. Commun., vol. 181, pages 259–270, 2010. (Cited on page 10.)

[Sankaran 2010] S. Sankaran, C. Audet and A.L. Marsden. *A method for stochastic constrained optimization using derivative-free surrogate pattern search and collocation.* Journal of Computational Physics, vol. 229, pages 4664–4682, 2010. (Cited on page 12.)

[Saurel 2007] R. Saurel, O. Le Metayer, J.Massoni and S. Gavrilyuk. *Shock jump relations for multiphase mixtures with stiff mechanical relaxation . Shock Waves.* Shock Waves, vol. 16, no. 3, pages 209–232, 2007. (Cited on page 199.)

[Schlüter 2004] J. U. Schlüter, H. Pitsch and P. Moin. *Large Eddy Simulation Inflow Conditions for Coupling With Reynolds-Averaged Flow Solvers.* AIAA Journal, vol. 42, no. 3, pages 478–484, 2004. (Cited on pages 81 and 84.)

[Schueller 2008] G.I. Schueller and H.A. Jensen. *Computational methods in optimization considering uncertainties–An overview.* Comput. Methods Appl. Mech. Engrg., vol. 198, pages 242–272, 2008. (Cited on page 11.)

[Sheather 1991] S. J. Sheather and M. C. Jones. *A reliable data-based bandwidth selection method for kernel density estimation.* Journal of the Royal Statistical Society series B, vol. 53, pages 683–690, 1991. (Cited on page 106.)

[Simon 2010] F. Simon, P. Guillen, Pierre Sagaut and Didier Lucor. *A gPC-based approach to uncertain transonic aerodynamics.* Computer Methods in Applied Mechanics and Engineering, vol. 199, pages 1091–1099, March 2010. (Cited on page 81.)

[Smolyak 1963a] S. Smolyak. *Quadrature and interpolation formulas for tensor product of certain classes of functions.* Soviet Math. Dokl., vol. 4, pages 240–243, 1963. (Cited on page 26.)

[Smolyak 1963b] S. A. Smolyak. *Quadrature and interpolation formulas for tensor products of certain classes of functions.* Soviet Math. Dokl., no. 4, pages 240–243, 1963. (Cited on page 8.)

[Soave 1972] G. Soave. *Equilibrium constants from a modified Redlich-Kwong equation of state.* Chem. Eng. Sci., vol. 27, page 1197, 1972. (Cited on pages 149 and 164.)

[Sobol 2001] I Sobol. *Global sensitivity indices for nonlinear mathematical models and their Monte Carlo estimates.* Mathematics and Computers in Simulation, vol. 55, no. 1-3, pages 271–280, February 2001. (Cited on pages 10 and 72.)

[Sod 1978] G.A. Sod. *Finite Difference Methods for Systems of Nonlinear Hyperbolic Conservation Laws.* Journal of Computational Physics, no. 27, pages 1–31, 1978. (Cited on page 65.)

[Span 2001] R. Span, W. Wagner, E. W. Lemmon and R. T. Jacobsen. *Multiparameter equations of state – recent trends and future challenges.* Fluid Phase Equilibria, vol. 183-184, pages 1 – 20, 2001. (Cited on page 164.)

[Span 2003] R Span and W Wagner. *Equations of State for Technical Applications. I. Simultaneously Optimized Functional Forms for Nonpolar and Polar Fluids.* Int J Thermophys, vol. 24, pages 1–39, 2003. (Cited on pages 164 and 167.)

[Stryjek 1986] R. Stryjek and J. H. Vera. *PRSV: an improved Peng-Robinson equation of state for pure compounds and mixtures.* Can. J. Chem. Eng., vol. 64, pages 323–333, 1986. (Cited on page 164.)

[Sudret 2008] B. Sudret. *Global sensitivity analysis using polynomial chaos expansions.* Reliability Engineering and System Safety, vol. 93, pages 964–979, 2008. (Cited on page 10.)

[Thompson 1971] P. A. Thompson. *A fundamental derivative in gas dynamics.* Phys. Fluids, vol. 14, no. 2, pages 1843–1853, 1971. (Cited on pages 5 and 6.)

[Thompson 1973] P. A. Thompson and K. C. Lambrakis. *Negative shock waves.* Journal of Fluid Mechanics, vol. 60, page 187, 1973. (Cited on pages 201 and 202.)

[Toro 1997] E. F. Toro. Riemann solvers and numerical methods for fluid mechanics. Springer, Berlin, 1997. (Cited on pages 49, 50 and 65.)

[Trucano 2006] Timothy G Trucano, L Swiler, T Igusa, William L Oberkampf and M Pilch. *Calibration, Validation, and Sensitivity Analysis: What's What.* Reliability Engineering and System Safety, vol. 91, pages 1331–1357, 2006. (Cited on page 3.)

[Tryoen 2010] J Tryoen, Olivier Le Maître, M Ndjinga and A Ern. *Intrusive Galerkin methods with upwinding for uncertain nonlinear hyperbolic systems q.* Journal of Computational Physics, vol. 229, pages 6485–6511, 2010. (Cited on pages 9 and 39.)

[Tryoen 2011] Julie Tryoen. *Methodes de Galerkin stochastiques adaptatives pour la propagation d'incertitudes parametriques dans les systemes hyperboliques.* PhD thesis, Université Paris-Est, 2011. (Cited on pages 9 and 49.)

[Tryoen 2012] J Tryoen, Olivier Le Maître and A Ern. *Adaptive Anisotropic Spectral Stochastic Methods for Uncertain Scalar Conservation Laws.* SIAM Journal Scientific Computing, vol. 34, pages A2459–A2481, 2012. (Cited on page 9.)

[Turunen-Saaresti 2010a] T. Turunen-Saaresti, J. Harinck, P. Colonna and J. van Buijtenen. *Computational study of a high-expansion ratio radial ORC turbine stator.* J. Eng. Gas Turb. Power., vol. 132, no. 5, pages 011001–17, 2010. (Cited on pages 12 and 180.)

[Turunen-Saaresti 2010b] T. Turunen-Saaresti, J. Harinck, P. Colonna and J. van Buijtenen. *Influence of thermodynamic models in two-dimensional flow simulations of turboexpanders.* J Turbomach - Trans ASME, vol. 132, no. 2, 2010. (Cited on page 12.)

[Villedieu 2011] N. Villedieu, J. Cappaert, J.P. Garcia Galache and T.E. Magin. *Uncertainty Quantification for characterization of high enthalpy facilities.* 4th European Conference for Aerospace Sciences, St Petersburg, Russia, 2011. (Cited on page 99.)

[Wan 2005] X. Wan and G. E. Karniadakis. *An adaptative multi-element generalized polynomial chaos method for stochastic differential equations.* J. Comput. Phys., vol. 209, no. 2, pages 617–642, 2005. (Cited on page 30.)

[Wan 2006a] X. Wan and G. E. Karniadakis. *Multi-element generalized polynomial chaos for arbitrary probability measure.* SIAM J. Sci. Comput., vol. 28, no. 3, pages 901–928, 2006. (Cited on page 30.)

[Wan 2006b] X. Wan and George Em Karniadakis. *Long-term behavior of polynomial chaos in stochastic flow simulations.* Computer Methods in Applied Mechanics and Engineering, vol. 195, no. 41-43, pages 5582–5596, August 2006. (Cited on page 8.)

[Witteveen 2010] Jeroen a. S. Witteveen and Gianluca Iaccarino. *Simplex Elements Stochastic Collocation in Higher-Dimensional Probability Spaces.* In 51st AIAA/ASME/ASCE/AHS/ASC Structures, Structural Dynamics, and Materials Conference 12 - 15 April 2010, Orlando, Florida, numéro April, 2010. (Cited on page 9.)

[Witteveen 2012a] JAS Witteveen and G. Iaccarino. *Refinement criteria for simplex stochastic collocation with local extremum diminishing robustness.* SIAM Journal on Scientific Computing, vol. 34, pages A1522–A1543, 2012. (Cited on pages 119 and 120.)

[Witteveen 2012b] JAS Witteveen and G. Iaccarino. *Simplex stochastic collocation with random sampling and extrapolation for nonhypercube probability spaces.* SIAM Journal on Scientific Computing, vol. 34, pages A814–A838, 2012. (Cited on pages 119, 120 and 121.)

[Witteveen 2013] J.A.S. Witteveen and Gianluca Iaccarino. *Subcell resolution in simplex stochastic collocation for spatial discontinuities.* Journal of Computational Physics, vol. 251, pages 17–52, October 2013. (Cited on page 9.)

[Xia 1997] J.L. Xia, B.L. Smith, A.C. Benim, J. Schmidli and G. Yadigaroglu. *Effect of inlet and oultet boundary conditions on swirling flows.* Computers & Fluids, vol. 26, pages 811–823, 1997. (Cited on page 84.)

[Xu 2003] D. Xu and S. Albin. *Robust optimization of experimentally derived objective functions.* IIE Trans., vol. 35, pages 793–802, 2003. (Cited on page 11.)

[Xu 2007] C Xu and G Gertner. *Extending a global sensitivity analysis technique to models with correlated parameters.* Computational Statistics & Data Analysis, vol. 51, pages 5579–5590, 2007. (Cited on page 10.)

[Xu 2008] C Xu and G Gertner. *Uncertainty and sensitivity analysis for models with correlated parameters.* Reliability Engineering & System Safety, vol. 93, pages 1563–1573, 2008. (Cited on page 10.)

[Yang 2010] X.S. Yang and S. Deb. *Engineering optimization by cuckoo search.* Int. J. Math. Modelling Num. Optimisation, vol. 1, pages 330–343, 2010. (Cited on pages 125 and 126.)

[Yang 2012] Xiu Yang, Minseok Choi, Guang Lin and George Em Karniadakis. *Adaptive ANOVA Decomposition of Stochastic Incompressible and Compressible Flows.* Journal of Computational Physics, vol. 231, no. 4, pages 1587–1614, 2012. (Cited on pages 10 and 218.)

[Yeh 2008] C.-L. Yeh. *Turbulent flow simulation of liquid jet emanating from pressure-swirl atomizer.* Heat Mass Transfer, vol. 44, pages 275–280, 2008. (Cited on page 84.)

[Y.M. 2009] Marzouk Y.M. and X. Dongbin. *A Stochastic Collocation Approach to Bayesian Inference of Inverse Problems.* Communications in Computational Physics, vol. 6, no. 4, pages 826–847, 2009. (Cited on page 103.)

[Z. Rusak 2000] C.W. Wang Z. Rusak. *Low-drag airfoils for transonic flow of dense gases.* Angew. Math. Phys. (ZAMP), vol. 51, pages 467–480, 2000. (Cited on page 129.)

[Zabaras 2008] N. Zabaras and B. Ganapathysubramanian. *A scalable framework for the solution of stochastic inverse problem using a sparse grid collocation approach.* Journal of Computational Physics, vol. 227, pages 4697–4735, 2008. (Cited on page 7.)

[Zamfirescu 2008] C. Zamfirescu, A. Guardone and P. Colonna. *Admissibility region for rarefaction shock waves in dense gases.* J. Fluid Mech., vol. 599, pages 363–381, 2008. (Cited on page 132.)

[zur Nieden 2007] P. zur Nieden and H. Olivier. *Determination of Atmospheric Densities from Reentry Data Flight Data.* Journal of Spacecraft and Rockets, vol. 44, no. 2, 2007. (Cited on page 97.)